Centre Val de Loire UNIVERSITÉ

UNIVERSITÉ D'ORLÉANS

UNIVERSITE D'ORLEANS

ÉCOLE DOCTORALE
ENERGIE, MATERIAUX, SCIENCES DE LA TERRE ET DE L'UNIVERS

Institut des Sciences de la Terre d'Orléans (ISTO)
Bureau de Recherches Géologiques et Minières (BRGM)

THÈSE présentée par :

Armel MENANT

soutenue le : **08 juin 2015**

pour obtenir le grade de : **Docteur de l'université d'Orléans**
Discipline / Spécialité : Sciences de la Terre

Du manteau à la croûte, dynamique de subduction et systèmes minéralisés en Méditerranée orientale

THÈSE dirigée par :

Laurent JOLIVET	Professeur, Université d'Orléans
Laurent GUILLOU-FROTTIER	Ingénieur-Chercheur, BRGM

RAPPORTEURS :

Olivier VANDERHAEGHE	Professeur, Université de Toulouse 3
Philippe YAMATO	Maitre de conférences, Université de Rennes 1

JURY :

Bruno SCAILLET	Directeur de Recherche CNRS, Université d'Orléans (Président)
Claudio FACCENNA	Professeur, Università Degli Studi Roma Tre
Laurent GUILLOU-FROTTIER	Ingénieur-Chercheur, BRGM
Laurent JOLIVET	Professeur, Université d'Orléans
Jeremy P. RICHARDS	Professeur, University of Alberta
Olivier VANDERHAEGHE	Professeur, Université de Toulouse 3
Philippe YAMATO	Maitre de conférences, Université de Rennes 1

Du manteau à la croûte, dynamique de subduction et systèmes minéralisés en Méditerranée orientale

Anciens travaux miniers, Serifos, Grèce

Manuscrit de thèse

Armel Menant

08 juin 2015

Directeur de thèse : Laurent Jolivet
Co-directeur de thèse : Laurent Guillou-Frottier

Institut des Sciences de la Terre d'Orléans (ISTO)
Bureau de Recherches Géologiques et Minières (BRGM)

Ecole doctorale Energie – Matériaux – Sciences de la Terre et de l'Univers
Université d'Orléans

... l'excitation des plongeons du haut des falaises dans les criques pleines d'écume de Mykonos valait toute la cocaïne du monde.

Dan Brown, Le Symbole Perdu

Remerciements

Je m'excuse par avance de la répétition de certains mots dans les quelques lignes qui suivent…

Waouh… Une sacrée expérience que ces 4 ans de thèse. Pour tout ce que ça m'a apporté autant sur le plan scientifique qu'humain, merci à vous Laurent et Laurent ! Laurent, je me souviendrai de toutes les missions de terrain (en Grèce et ailleurs) et conférences. Tout ça a été sacrément enrichissant pour moi, à commencer par le premier jour de terrain sur Syros où il a fallu s'y reprendre à plusieurs fois pour reconnaître rutile, chlorite et autres minéraux rouges, verts, … A quand la prochaine *Conveners party* ? Et Laurent, je vais me rappeler longtemps de notre longue errance dans les rues de Grenoble ! Et un grand merci aussi de m'avoir guidé dans la jungle (administrative) du BRGM.

Je remercie également tous les membres du jury (Olivier Vanderhaeghe, Philippe Yamato, Bruno Scaillet, Claudio Faccenna et Jeremy P. Richards) de bien avoir voulu s'*attaquer* à ce manuscrit de thèse.

Je souhaite aussi citer Daniel Cassard et Cristelle Loiselet pour avoir initié ce projet de recherche grâce à leurs premières observations. Merci aussi à Johann Tuduri, Romain Augier, Guillaume Bertrand, Laurent Bailly, ainsi que les autres chercheurs de l'unité DGR-MIN et de l'ISTO, pour leurs contributions scientifiques, et extrascientifiques pour certains.

Un merci particulier à Lucile, Virginie et Marie-Noëlle pour m'avoir simplifié un grand nombre de démarches administratives.

Je remercie également Bruno Vrielynck pour sa contribution à la réalisation du modèle de reconstructions cinématiques.

Thank you to Taras Gerya for allowing me to use his 3D numerical code and for his invaluable help.

Bien entendu, je remercie Pietro pour toutes nos discussions scientifiques et aussi (et surtout) pour son côté italien et Rabi pour les bonnes rigolades et les bonnes avancées scientifiques sur le terrain (c'est sûr ce sont bien les sédiments de Naxos…).

Je souhaite également citer le BRGM, la région Centre, l'ERC RHEOLITH et le Labex VOLTAIRE pour leur soutien financier au cours de ces 3 (4) années de thèse.

De manière plus impersonnelle, je vais citer mon PC qui a tenu le coup jusqu'au bout malgré mes coups de sang.

Et pour terminer, je remercie mes collègues de bureau qui ont su me supporter : Sarah (et une verveine…), Maxou (vive la ZIM…), sans oublier Fred !

Je n'oublie pas non plus la colloc' de la Villa : Leïla (honneur à la *dame*), David (le frisé), Colin (le bizarre), Malcolm (la pile) et Billa (bien qu'elle sache ce que je pense d'elle) avec qui j'ai passé deux années de *folies* (« j'étais bien plus sage avant »…). Merci à la colloc' des Dyonisiens de m'avoir accueilli pour cette période de fin de thèse au cours de laquelle je n'étais pas des plus drôles : Manon, Ben, Tony, Matthieu, Ségo, Kévin, Jameson, la rousse, la noire et tous les autres reptiles avec ou sans pattes (qui ne sont pas, soit dit en passant, des Mustélidés…) ! Tant qu'on y est, un coup de chapeau à la colloc' du Manoir (Yann, Rabi, Thomas, Léo) et à Hobbitebourg (P'tit Gui et Ananas, vive les mariés !).

Plus en vrac je vais citer, par ordre de grande g***** : Valentin, Kévin, Hugues, Joanna, Matthieu, Seb, Vincent, Hugo, Alex, Nolwenn, Charlène, Momo, Bashar, Doumdoum, et tous ceux que j'aurais pu oublier (désolé d'avance).

Un grand merci à ma famille qui m'a soutenu.

Et enfin et surtout (je ne t'ai pas oubliée) merci pour tout Eloïse…

Table des matières

1. Introduction 21

1.1. Minéralisations, magmatisme, subduction, les premières observations 23

1.2. Attrait économique des zones de subduction 25

1.3. Métallogénie et magmatisme en contexte de subduction 29

1.3.1. Magmatisme et transfert de métaux dans le coin mantellique 30

1.3.2. Zone MASH *: maturation des magmas et partitionnement des métaux 32*

1.3.3. Transition magmatisme-hydrothermalisme et exsolution des métaux 33

1.3.4. Hydrothermalisme et précipitation des métaux 35

1.3.5. Minéralisation et contexte tectonique en domaine de subduction 38

1.4. Evolution de la zone subduction, réponse mantellique et crustale 40

1.4.1. Cinématique de la subduction 41

1.4.2. Subduction et déformation crustale 43

1.4.3. Contraintes sur la dynamique profonde de la subduction 49

1.4.4. Dynamique de subduction : l'apport de la modélisation 54

1.5. Pourquoi s'intéresser à la région Méditerranéenne ? 58

1.6. Objectifs et démarche de cette étude 63

2. Reconstructions cinématiques et évolution du magmatisme en Méditerranée orientale 67

2.1. Abstract 74

2.2. Introduction 75

2.3. Methodology 77

2.4. Geodynamic overview of the eastern Mediterranean region 80

2.4.1. Sedimentary and tectono-metamorphic constraints 82

2.4.2. Magmatic features 95

2.5. Kinematic reconstructions of the eastern Mediterranean region 99

2.5.1. Late Cretaceous (100-65 Ma) 113

2.5.2. Paleocene-Eocene (65-35 Ma) 116

2.5.3. Oligocene-early Miocene (35-15 Ma) 118

2.5.4. Middle-late Miocene (15-5 Ma) 121

2.5.5. Pliocene-Quaternary (5-0 Ma) 124

2.6. Discussion 125

2.6.1. Late Cretaceous and Oligocene to Present slab retreat and back-arc opening 125

2.6.2. Strain partitioning in the Aegean region 129

2.6.3. Successive metamorphic events in the Menderes massif 132

2.6.4. Driving forces acting on the westward extrusion of Anatolia 133

2.6.5. Southward retreat of the subduction zone and magma genesis 135

2.6.6. Modulation of magmatic evolution by slab tearing and mantle plumes 137

2.7. Conclusion 138

3. Distribution des minéralisations et reconstructions de la dynamique de subduction 141

3.1. Extended abstract 160
3.2. Introduction 161
3.3. Ore distribution in eastern Mediterranean since the late Cretaceous 161
3.4. Subduction-related deep processes and ore genesis 163
3.5. Crustal evolution of hydrothermal systems 166
3.6. Conclusion 167

4. Dôme extensifs et contrôle structural des systèmes minéralisés : le cas de l'île de Mykonos 169

4.1. Introduction 175
4.2. Geological and Geodynamic Setting 176
4.3. Detailed Mapping at the Vicinity of the NCDS on Mykonos 178
4.4. Characterization of the Mineralization 179
4.5. Evidence of Successive Tectonic Regimes 183
4.6. Interpretations and Discussion 186
4.7. Conclusion 192

5. Contrôle mantellique et crustal sur la genèse du magmatisme : approche numérique 195

5.1. Abstract 204
5.2. Introduction 205
5.3. Late Cenozoic evolution of the eastern Mediterranean subduction zone 206
5.4. Numerical modeling 209
5.4.1. Modeling approach and setup 209
5.4.2. Parametric study on rheological implications in natural subduction context 213
5.5. Results 214
5.5.1. Asthenospheric vs. lithospheric flow pattern 215
5.5.2. Genesis and transport of partially molten material 220
5.6. Discussion 225
5.6.1. Magmatism and mantle flow 225
5.6.2. Magmatism and lithospheric deformation 228
5.6.3. Implications for the eastern Mediterranean region 229
5.7. Conclusion 232

6. Synthèse générale : dynamique de subduction et minéralisations en Méditerranée orientale ...235

6.1. Crétacé supérieur : une chaîne de type Andine, riche en minéralisations cuprifères 238
6.1.1. Dynamique de subduction et processus mantelliques 238
6.1.2. Dynamique de subduction et processus crustaux 241
6.2. Paléocène-Eocène : accrétion continentale et quiescence de l'activité magmatique et hydrothermale 242
6.2.1. Dynamique de subduction et processus mantelliques 243
6.2.2. Dynamique de subduction et processus crustaux 244
6.3. Oligocène : extension d'arrière-arc et minéralisations à plomb-zinc 245
6.3.1. Dynamique de subduction et processus mantelliques 245

6.3.2. Dynamique de subduction et processus crustaux 246
6.4. Miocène : étirement lithosphérique intense et minéralisations aurifères 247
6.4.1. Dynamique de subduction et processus mantelliques 248
6.4.2. Dynamique de subduction et processus crustaux 250
6.5. Conclusion : processus géodynamiques et métallogénie 253
6.6. Perspectives 255
6.6.1. Quid de l'exploration minérale ? 255
6.6.2. Pistes de recherche 257

7. Références bibliographiques 259
8. *Annexe A.* Lexique 287
9. *Annexe B.* Driving the upper plate deformation by slab rollback and mantle flow 293
10. *Annexe C.* Reconstructions cinématiques : table des rotations et fichier multimédia 305
11. *Annexe D.* Reconstructions cinématiques et distribution des minéralisations : fichier multimédia 319
12. *Annexe E.* Modélisation numérique : méthode et fichiers multimédias 323

Liste des figures

Chapitre 1. Introduction

1.1. carte mondiale de répartition des gisements de type porphyre cuprifère et à molybdène (zones hachurées) 25

1.2. graphique montrant l'évolution du prix du cuivre et de l'or depuis 2002 26

1.3. graphique montrant l'évolution de la production mondiale de cuivre en fonction du type de gisement 27

1.4. diagramme tonnage *versus* teneur en cuivre ou en or des principaux gisements de type porphyre, skarn et épithermal 28

1.5. schéma conceptuel d'une zone de subduction montrant les principaux processus et systèmes magmatiques et hydrothermaux qui peuvent s'y développer 29

1.6. schéma conceptuel de la partie inférieure de l'arc magmatique montrant la genèse et l'évolution des magmas d'arc ainsi que les flux de métaux associés depuis le coin mantellique, jusqu'à la base de la croûte continentale 31

1.7. schéma conceptuel du système magmatique-hydrothermal mis en place dans la croûte supérieure en domaine d'arc 34

1.8. illustrations de la morphologie des différents corps minéralisés qui peuvent se déposer dans un environnement de subduction 36

1.9. schémas conceptuels montrant l'évolution possible d'une zone de subduction et des systèmes magmatiques-hydrothermaux qui y sont associés 40

1.10. carte recensant les principales zones de subduction dans le monde 41

1.11. schémas d'une zone de subduction caractérisée par une marge compressive ou extensive, où figurent les différents vecteurs cinématiques la caractérisant 42

1.12. schéma représentant les principales forces responsables de la dynamique d'une zone de subduction 43

1.13. carte des principales zones de subduction à travers le monde sur laquelle sont représentés tous les séismes connus de magnitude supérieure à 7,5 de 1700 à 1900 et après 1900 44

1.14. graphique montrant la distribution temporelle du volcanisme entre 19 et 22° de latitude sud ainsi que le taux de raccourcissement moyen estimé pour cette région 45

1.15. carte tectonique de la région Méditerranéenne 46

1.16. bloc 3D d'une croute continentale étirée en domaine d'arrière-arc où l'extension est accommodée par plusieurs détachements permettant l'exhumation de la croûte moyenne-inférieure sous la forme de dômes métamorphiques 47

1.17. schéma conceptuel d'une zone de subduction se retirant sous une marge continentale extensive où s'exprime un magmatisme à la fois de type *arc* et *arrière-arc* 49

1.18. cartes de l'activité sismique et profils verticaux de la répartition de ces séismes le long de la zone de subduction du Japon et de la Cordillère des Andes 50
1.19. la tomographie sismique dans le manteau terrestre 51
1.20. la convection mantellique à différentes échelles 53
1.21. l'anisotropie sismique dans le manteau 54
1.22. les modèles géodynamiques globaux 56
1.23. modèles de subduction à l'échelle lithosphérique 57
1.24. reconstructions paléotectoniques de la chaîne Téthysienne au Callovien, Campanien, Lutétien et Tortonien 59
1.25. carte tectonique de la Méditerranée orientale montrant les principales structures actives, les principales zones de suture océanique, les principaux chevauchements constituant la chaîne des Hellénides et des Taurides, les principales structures extensives à faible pendage 60
1.26. modèle tomographique d'anomalies de vitesse des ondes sismiques *P* dans la région Méditerranéenne 61
1.27. modèle numérique 3D montrant l'évolution d'une zone de transition entre subduction océanique et subduction/collision continentale 62

Chapitre 2. Reconstructions cinématiques et évolution du magmatisme en Méditerranée orientale

2.1. succession de cartes de la chaîne ouest-Téthysienne montrant la distribution des minéralisations à or, argent, cuivre et molybdène au Crétacé supérieur, Paléogène et Néogène 69
2.2. tectonic map of the eastern Mediterranean region highlighting the main tectono-metamorphic domains 77
2.3. map of the eastern Mediterranean region showing the main domains used in the kinematic reconstructions 79
2.4. tectonic map showing the main data used to constrain the kinematic evolution of the eastern Mediterranean region, including the stretching lineations in the MCCs, the offset of main structures and the vertical-axis rotations deduced from paleomagnetic studies 80
2.5. present-day cross-sections in the eastern Mediterranean region 81
2.6. diagram showing the main tectonic, metamorphic and magmatic events since the late Cretaceous used to constrain the kinematic reconstructions of the eastern Mediterranean region 83
2.7. detailed tectonic map of the Aegean region 85
2.8. detailed tectonic map of the western and central Anatolian region 91
2.9. paleotectonic maps extracted from the kinematic reconstruction model 100
2.10. reconstructed cross-sections of the Aegean region highlighting the different magma genesis processes 113
2.11. reconstructed cross-sections of the western Anatolian region highlighting the different magma genesis processes 114
2.12. detailed paleotectonic maps of the Rhodope-Aegean-west Anatolian region during the Oligocene-Miocene extension 120

2.13. different motion paths deduced from the kinematic reconstructions of the eastern Mediterranean region 126
2.14. **t**ectonic map showing the correlation between deformation and kinematics of exhumation of the MCCs in the Aegean domain since the Eocene 130

Chapitre 3. Distribution des minéralisations et reconstructions de la dynamique de subduction

3.1. cartes paléotectoniques extraites du modèle de reconstruction cinématique, mettant en évidence la distribution spatiale et temporelle des occurrences minéralisées en Méditerranée orientale depuis le Crétacé supérieur 146
3.2. kinematic evolution of the eastern Mediterranean subduction zone, showing the spatial distribution of compiled mineral occurrences 162
3.3. **s**patial and temporal distribution of magmatism and compiled mineral occurrences in the Balkan-Rhodope-Aegean-west Anatolian region since the late Cretaceous 163
3.4. reconstructed cross-sections of the subduction zone in the Balkan-Rhodope-Aegean region, showing dominant magmatic and ore-forming processes 164
3.5. 3D lateral view from below of the Eastern Mediterranean subduction zone geometry in the middle-late Miocene 166

Chapitre 4. Dômes extensifs et contrôle structural des systèmes minéralisés : le cas de l'île de Mykonos

4.1. carte tectonique de l'archipel des Cyclades où sont identifiés les principaux gîtes et indices minéralisés 174

Chapitre 5. Contrôle mantellique et crustal sur la genèse du magmatisme : approche numérique

5.1. principe de la technique de *marker-in-cell* 199
5.2. schéma synthétisant les principales étapes implémentées dans le code *I3ELVIS* et qui permettent de modéliser les phénomènes de déshydratation, hydratation, fusion partielle et transport de fluides au niveau du coin mantellique 200
5.3. schéma synthétisant l'ensemble les liens (i.e. contrôles et interactions) qui sont mis en évidence à partir de l'observation des modèles numériques 3D entre la dynamique mantellique et crustale d'une zone de subduction et les processus de genèse et transport de roches partiellement fondues 202
5.4. late Cenozoic geodynamic evolution of the eastern Mediterranean region 207
5.5. geophysical maps of the eastern Mediterranean region 208
5.6. initial model setup 212
5.7. evolution of the reference model *2c93-60* 216
5.8. evolution of magmatism in reference model *2c93-60* 217
5.9. asthenospheric and crustal flow evolution and crustal strain rate in performed numerical experiments 218

5.10. time-trench velocity diagram showing the trench migration of both oceanic and oceanic-continental subduction zones obtained from models *2c89-60*, *2c98-100*, *2c84-100* and *1c113-70* and from kinematic reconstructions of the eastern Mediterranean region 219
5.11. subduction geometry of the model *2c98-100*, displaying a relatively strong coupling between both interacting lithospheres 220
5.12. evolution of the model *2c84-100* 221
5.13. evolution of magmatism in model *2c84-100* 222
5.14. evolution of the model 1*c113-70* 223
5.15. evolution of magmatism in model *1c113-70* 224
5.16. view from below of the mantle wedge of selected models, showing the relation between magmatic evolution at the base of the overriding crust and subduction-related asthenospheric flow for two selected time steps 226

Chapitre 6. Synthèse générale : dynamique de subduction et minéralisations en Méditerranée orientale

6.1. cartes tectoniques comparatives de la répartition des gisements métallifères dans le long de la chaine des Balkans en Méditerranée orientale au Crétacé supérieur et le long de la cordillère des Andes à l'actuel 239
6.2. 3D interprétatif de la géométrie de la zone de subduction est-Méditerranéenne au Crétacé supérieur vue de dessous, mettant en évidence une cinématique de cinématique de subduction stable, associée à un faible retrait du panneau plongeant 240
6.3. bloc 3D interprétatif de la géométrie de la zone de subduction est-Méditerranéenne au Paléocène vue de dessous, mettant en évidence une cinématique lente de la subduction associée à un épisode d'accrétion continentale 243
6.4. bloc 3D interprétatif de la géométrie de la zone de subduction est-Méditerranéenne à l'Oligocène vue de dessous, mettant en évidence une accélération du retrait du panneau plongeant associée à l'exhumation du dôme métamorphique du Rhodope en contexte d'arrière-arc 246
6.5. bloc 3D interprétatif de la géométrie de la zone de subduction est-Méditerranéenne au Miocène moyen-supérieur vue de dessous, mettant en évidence une déchirure du panneau plongeant sous le massif du Menderes associée à des flux asthénosphériques toroidaux jusque sous le dôme métamorphique extensif des Cyclades 249
6.6. coupe schématique montrant l'exhumation du dôme métamorphique des Cyclades, accommodée par de grands systèmes de détachements 252
6.7. schémas de synthèse, mettant en évidence les principaux liens, mis en évidence dans ce manuscrit de thèse, qui unissent géodynamique et métallogénie en contexte de subduction et qui permettent d'expliquer la genèse de provinces minéralisées riches en cuivre ou en plomb-zinc et or 253
6.8. carte tectonique de la Méditerranée orientale montrant les principales provinces métallogéniques reconnues ainsi que celles suspectées, au vue du contexte géodynamique similaire 256

Liste des tableaux

Chapitre 5. Contrôle mantellique et crustal sur la genèse du magmatisme : approche numérique

5.1. material properties used in the numerical experiments 211

5.2. range of performed models with variations in the continental crust structure and geothermal gradient in the continental and oceanic lithospheres 214

Annexe C. **Reconstructions cinématiques : table des rotations et fichier multimédia**

C.1. table resuming the succession of total reconstruction poles calculated for each domain 307

Chapitre 1

Introduction

1.1. Minéralisations, magmatisme, subduction, les premières observations 23

1.2. Attrait économique des zones de subduction 25

1.3. Métallogénie et magmatisme en contexte de subduction 29

1.3.1. Magmatisme et transfert de métaux dans le coin mantellique 30

1.3.2. Zone MASH *: maturation des magmas et partitionnement des métaux* 32

1.3.3. Transition magmatisme-hydrothermalisme et exsolution des métaux 33

1.3.4. Hydrothermalisme et précipitation des métaux 35

1.3.5. Minéralisation et contexte tectonique en domaine de subduction 38

1.4. Evolution de la zone subduction, réponse mantellique et crustale 40

1.4.1. Cinématique de la subduction 41

1.4.2. Subduction et déformation crustale 43

1.4.3. Contraintes sur la dynamique profonde de la subduction 49

1.4.4. Dynamique de subduction : l'apport de la modélisation 54

1.5. Pourquoi s'intéresser à la région Méditerranéenne ? 58

1.6. Objectifs et démarche de cette étude 63

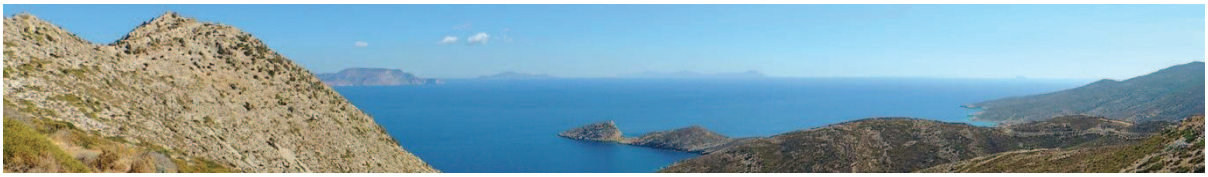

Ce chapitre introductif a pour but d'exposer les motivations à l'origine de ce travail de thèse dont l'objectif est de **mettre en évidence les liens qui existent entre la dynamique de subduction et la genèse de minéralisations**. Plus précisément, il sera question d'identifier **les processus mantelliques et crustaux qui contrôlent à différentes échelles la distribution spatiale et temporelle de ces minéralisations et favorisent la concentration de certains métaux plutôt que d'autres** (notamment le cuivre et l'or).

Cette étude a été réalisée dans la partie orientale de la région Méditerranéenne, dont l'histoire tectonique est dominée depuis le Mésozoïque par une zone de subduction, encore active aujourd'hui. Cette subduction, très largement étudiée depuis une vingtaine d'années, a connu une évolution complexe avec une grande variété de processus tectoniques, métamorphiques, magmatiques et hydrothermaux, ce qui en fait une zone d'étude privilégiée afin d'étudier les interactions entre subduction, magmas et minéralisations.

Dans ce chapitre introductif, après un bref historique sur la mise en évidence des premiers liens entre subduction et systèmes minéralisés, je présente quelques éléments d'économie minérale montrant l'intérêt de ces zones de convergence du point de vue de leur potentiel minier. Je fais ensuite une synthèse des connaissances actuelles vis-à-vis des processus magmatiques et hydrothermaux à l'origine de ces minéralisations, puis de la dynamique crustale et mantellique qui caractérise les environnements de subduction. Dans un troisième temps, je justifie le choix de la Méditerranée orientale comme zone d'étude et finalement, je pose les problèmes que soulève l'intégration des modèles de genèse des minéralisations dans un contexte *dynamique* de subduction et auxquels j'essayerai de répondre tout au long de ce manuscrit.

1.1. Minéralisations, magmatisme, subduction, les premières observations

Depuis des siècles, de grandes civilisations ont connu un important essor économique à travers le monde grâce à l'exploitation de ressources minérales, telles que le cuivre et l'or. Parmi les plus

connues, on retrouve l'empire inca en Amérique du Sud, l'empire grec ou romain en Europe, ou encore la civilisation japonaise en Asie. L'attirance des Hommes pour ces métaux a même donné lieu à de grandes conquêtes comme la colonisation espagnole des Amériques (XV^{e} – XVIII^{e} siècles) ou la ruée vers l'or vers l'Etat de Californie aux Etats-Unis (XIX^{e} siècle).

Ce n'est qu'au XX^{e} siècle, suite aux premières observations relatives à la dérive des continents [*Wegener*, 1920], puis à la découverte de la formation et du recyclage de la lithosphère au niveau des dorsales médio-océaniques et des marges actives [*Dietz*, 1961; *Hess*, 1962] et des premiers modèles cinématiques globaux [*McKenzie & Parker*, 1967; *Le Pichon*, 1968; *Morgan*, 1968], que des liens commencent à être établis entre processus tectoniques et distribution de ces ressources minérales tant convoitées. *Sillitoe* [1972] a ainsi observé que les gisements(*) de type porphyres(*) à cuivre et molybdène se localisent à la frontière des plaques tectoniques, au niveau de chaînes orogéniques(*) que sont la chaîne ouest-Américaine, sud-ouest-Pacifique et Alpine (figure 1.1). De plus, il remarque que ces minéralisations de type hydrothermal(*) sont très souvent associées spatialement à du magmatisme de la série calco-alcaline(*) avec lequel elles possèdent des similitudes du point de vue géochimique et isotopique. Ce magmatisme de type *arc* se développe typiquement à l'aplomb d'une marge active où une lithosphère océanique dense plonge sous une autre lithosphère (océanique ou continentale) moins dense, au cours d'un processus appelé *subduction* [*Coats*, 1962; *Gill*, 1981; *Arculus*, 1994].

Suite à ces premières observations, d'autres types de gisements hydrothermaux, déjà décrits, ont été reconnus comme étant également associés à ces environnements de subduction. Parmi eux, on retrouve les épithermaux(*) à métaux précieux (ex. or, argent) ou métaux de base (ex. cuivre, plomb, zinc) [*Sillitoe*, 1977; *White & Hedenquist*, 1990], les skarns(*) proximaux et distaux riches en cuivre, or, plomb, zinc et/ou fer [*Einaudi & Burt*, 1982; *Meinert*, 1997] et les minéralisations filoniennes ou de remplacement, notamment de type manto(*), riches en métaux de base ou précieux [*Sillitoe*, 1977; *Beaty et al.*, 1990].

(*) Définition du terme en *Annexe A. Lexique*

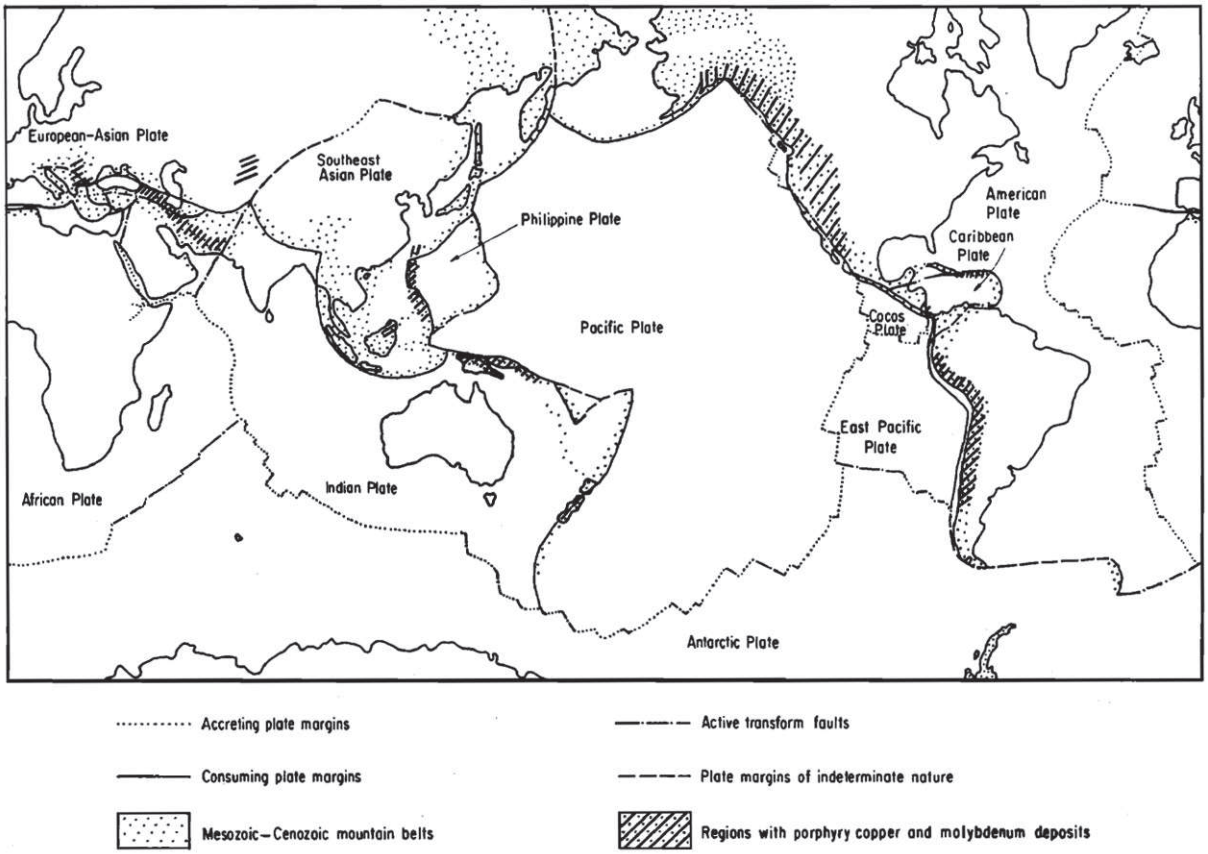

Figure 1.1 : carte mondiale de répartition des gisements de type porphyre cuprifère et à molybdène (zones hachurées). La majorité de ces gisements se répartissent le long de trois grandes chaînes orogéniques (ouest-américaine, sud-ouest-Pacifique et alpine) [*Sillitoe*, 1972].

1.2. Attrait économique des zones de subduction

Depuis ~3300 ans av. J.-C. (i.e. début de l'âge du cuivre), les Hommes ont extrait les métaux du sol pour façonner outils, armes, bijoux, infrastructures, etc. Aujourd'hui encore, et plus que jamais avec le développement de nouvelles technologies, l'exploitation de ces métaux est nécessaire. En raison notamment de ses propriétés électriques et thermiques et de sa résistance à la corrosion, le cuivre est actuellement un métal industriel majeur, au troisième rang en termes de consommation mondiale, après le fer et l'aluminium. C'est également une substance dite critique, caractérisée par un prix qui a fortement augmenté depuis le début du XXI^{e} siècle (figure 1.2a) et une forte demande mondiale qui risque de perdurer en raison de la demande croissante des pays émergents (ex. Inde, Chine) et

l'expansion des technologies de pointe et des technologies dites *vertes* (ex. éoliennes, voitures électriques).

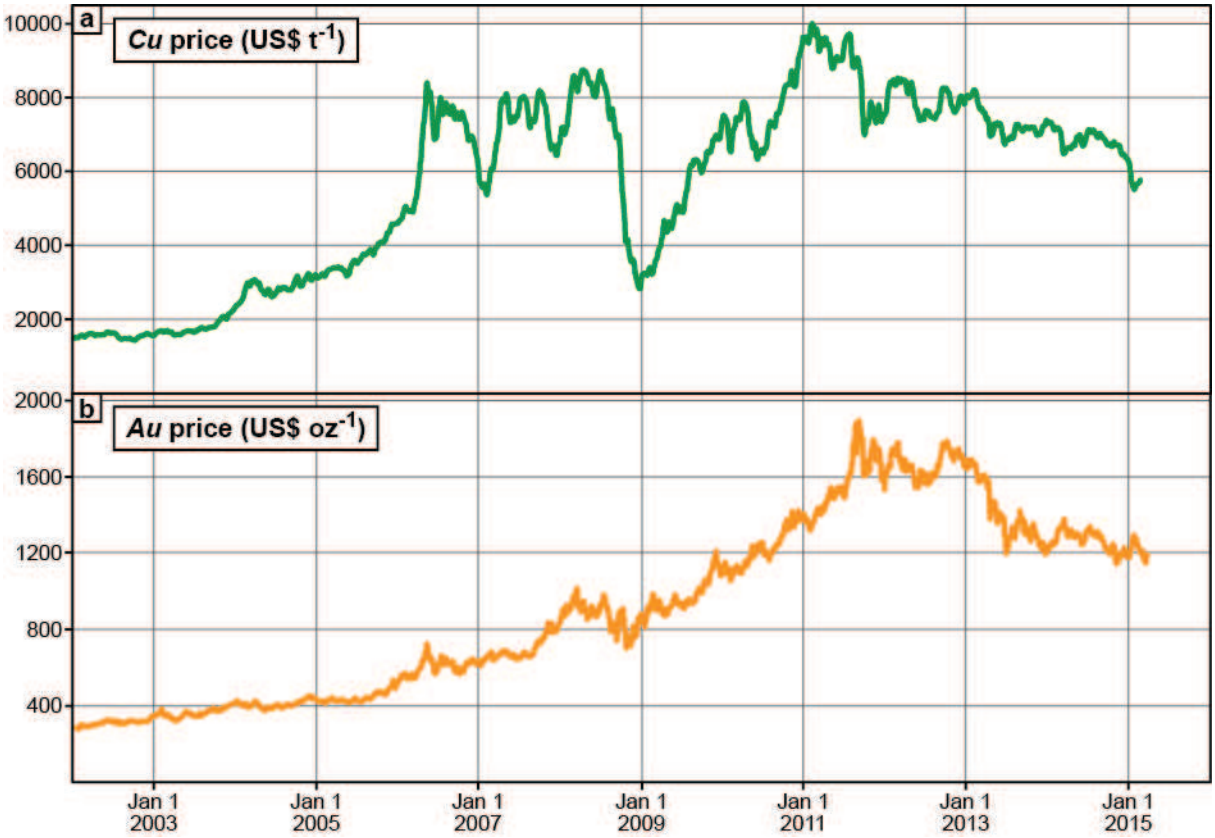

Figure 1.2 : graphique montrant l'évolution du prix du cuivre (a) et de l'or (b) depuis 2002. Source : *www.kitco.com*, *www.lbma.org.uk*, *www.lme.com*, *www.ela.gov*.

Entre 1995 et 2008, la production mondiale de cuivre a ainsi augmentée de près de 50 %, passant de 9,8 à 15,5 Mt (*Critical raw materials for the EU*, rapport pour la Commission Européenne, 2010), avec une majorité de cette production provenant de gisements de type porphyre (i.e. jusqu'à 75-80 % au début du XXI^{e} siècle, en considérant à la fois les porphyres minéralisés et leurs équivalents oxydés par l'altération superficielle, figure 1.3). Une telle tendance montre donc l'intérêt que peut susciter ce type de gisement et donc les environnements de subduction dans lesquels ils se concentrent.

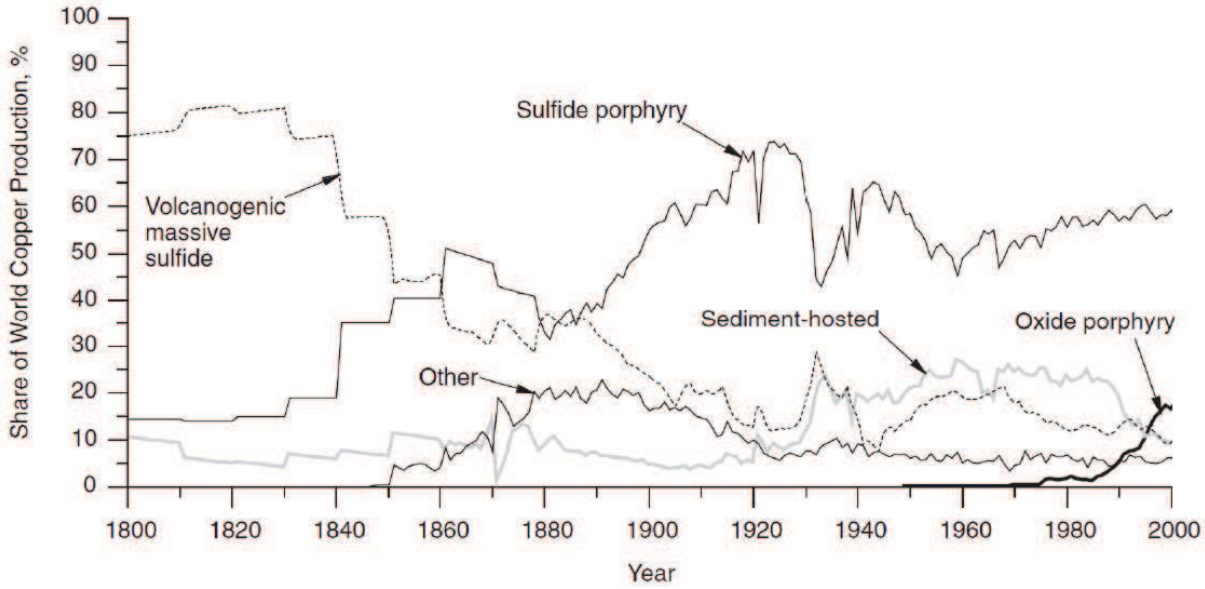

Figure 1.3 : graphique montrant l'évolution de la production mondiale de cuivre en fonction du type de gisement [*Gerst*, 2008].

Ces porphyres sont caractérisés par des teneurs en cuivre, et autres métaux, qui sont généralement faibles mais avec des tonnages très importants (figure 1.4a), ce qui les rend rentables du point de vue économique et justifie leur exploitation. Parmi ces gisements de classe mondiale, se retrouvent les porphyres cuprifères de Chuquicamata et d'El Teniente au Chili, premier pays producteur mondial de cuivre [*Cooke et al.*, 2005; *Richards*, 2005]. D'autres types de gisements comme les skarns peuvent également être associés à ces porphyres et contenir de grandes quantités de cuivre, tout comme le skarn cuprifère d'Antamina au Pérou (figure 1.4a) [*Love et al.*, 2004].

Egalement présent dans les gisements associés aux zones de subduction, l'or est un métal qui, bien que n'étant pas considéré comme critique, est recherché en raison de sa qualité de valeur refuge. Ceci se traduit par une grande stabilité de son prix sur les marchés financiers, notamment lors des crises économiques (ex. la crise économique de la fin des années 2000), à la différence des autres métaux (figure 1.2b). Dans les gisements de type porphyre, l'or se retrouve communément en produit secondaire, donnant une plus-value à l'exploitation principale du cuivre. Il peut même dans certains cas devenir le produit principal de la mine, comme pour les porphyres aurifères de Grasberg en Indonésie et de Bingham aux Etats-Unis [*Sillitoe*, 1997]. L'or peut également se concentrer dans les épithermaux et skarns associés aux porphyres minéralisés, qui sont alors généralement caractérisés par

des tonnages relativement faibles mais des teneurs très importantes, pouvant atteindre les 100 g t^{-1} (figure 1.4b). Parmi les principaux gisements de ce type, on retrouve l'épithermal aurifère de Yanacocha au Pérou et le skarn aurifère de Kucing Lias en Indonésie [*Sillitoe*, 1997; *New*, 2006].

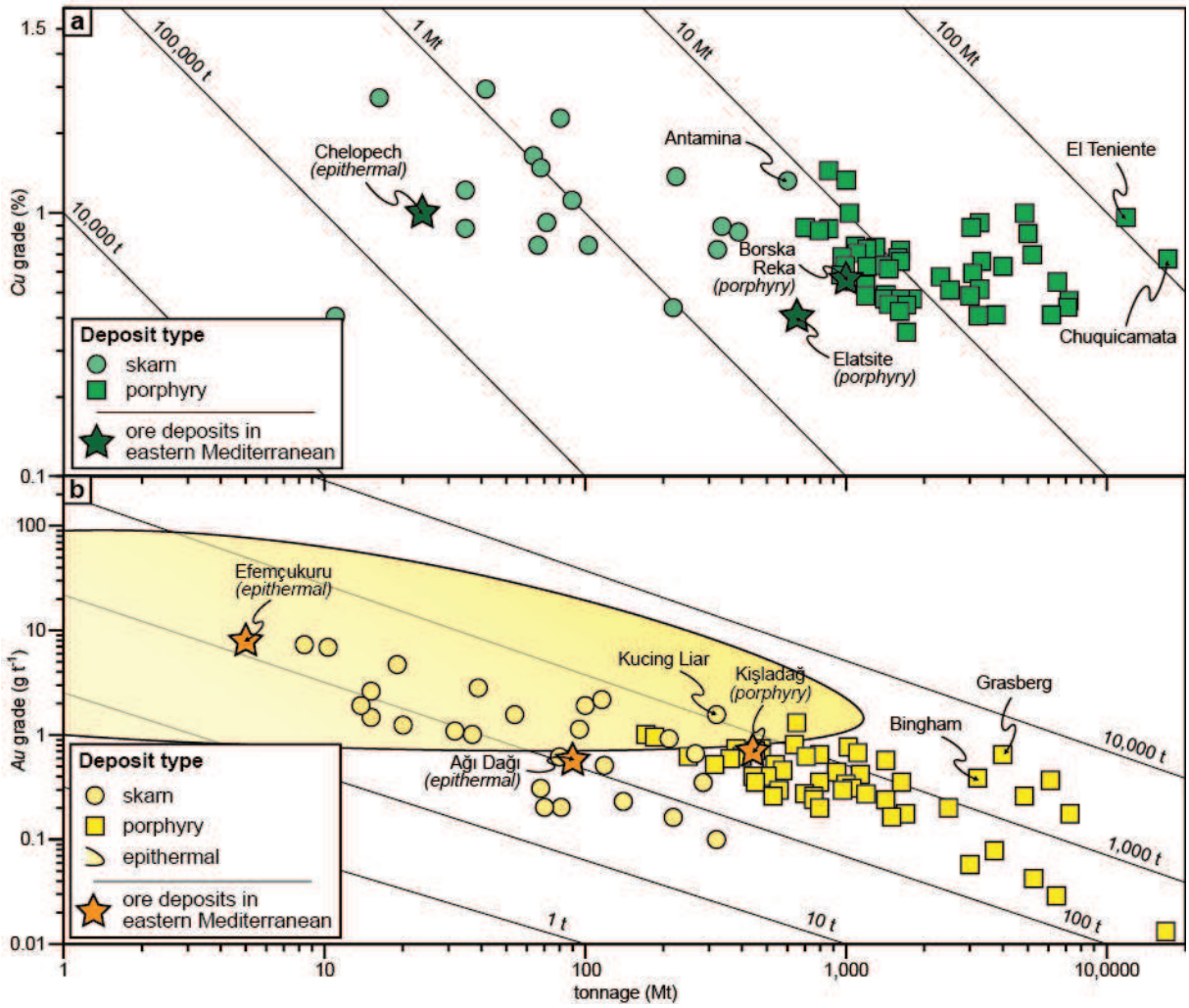

Figure 1.4 : diagramme tonnage *versus* teneur en cuivre (a) ou en or (b) des principaux gisements de type porphyre, skarn et épithermal. Les gisements majeurs en Méditerranée orientale ont également été ajoutés. Données extraites d'après *Jébrak & Marcoux* [2008] et *Singer et al.* [2008], excepté pour les données sur la Méditerranée orientale qui ont été récupérées sur les sites internet des compagnies minières.

Tous ces éléments montrent l'intérêt économique que peuvent représenter ces zones de subduction où se concentrent l'essentiel de la production mondiale de cuivre (figure 1.3), ainsi qu'une part non négligeable de la production mondiale d'or. Il est donc nécessaire de chercher de nouveaux gisements et par conséquent de mieux comprendre les processus qui en sont à l'origine, afin de guider l'exploration minière.

1.3. Métallogénie et magmatisme en contexte de subduction

L'engouement scientifique et économique suscité par ces minéralisations en contexte de subduction a donné lieu à de très nombreuses études afin de comprendre les processus métallogéniques(*) (i.e. de genèse) à l'origine de ces gisements hydrothermaux [ex. *Solomon*, 1990; *Hedenquist & Lowenstern*, 1994; *Sillitoe*, 1997, 2010; *Tosdal & Richards*, 2001; *Richards*, 2003, 2005, 2009; *Sillitoe & Hedenquist*, 2003; *Cooke et al.*, 2005; *Williams-Jones & Heinrich*, 2005; *Seedorff et al.*, 2005; *Groves & Bierlein*, 2007; *Wilkinson*, 2013]. En parallèle, l'amélioration de la compréhension des processus magmatiques dans ces environnements d'arc et du fractionnement des métaux en faveur des phases fluides (i.e. magmas et fluides hydrothermaux) ou solides [ex. *Gill*, 1981; *Tatsumi et al.*, 1983, 1986; *Hildreth & Moorbath*, 1988; *Peach et al.*, 1990; *Schmidt & Poli*, 1998; *Grove et al.*, 2006; *Scaillet*, 2010; *Richards*, 2011] ont permis de développer des modèles conceptuels complets de ces systèmes magmatiques et hydrothermaux, depuis le coin mantellique sus-jacent à la lithosphère en subduction, jusqu'en surface au niveau de la lithosphère constituant la marge active (figure 1.5). Je me focalise ici sur l'évolution d'un arc magmatique en domaine continental mais les processus sont relativement similaires en domaine océanique [ex. *Hedenquist et al.*, 1998].

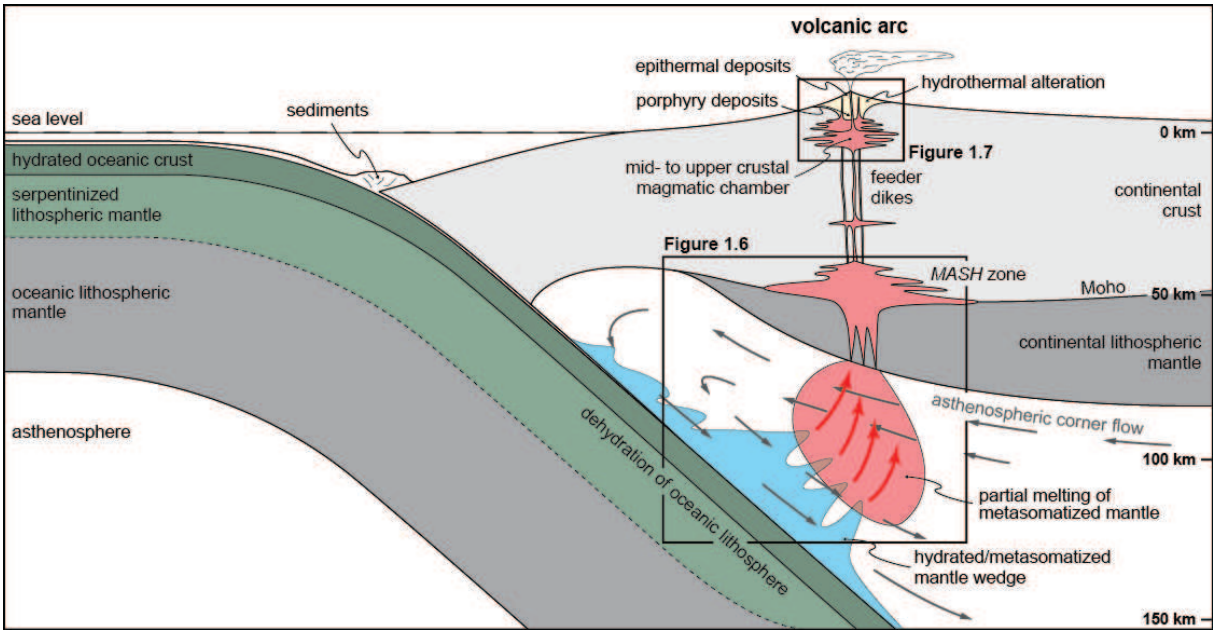

Figure 1.5 : schéma conceptuel d'une zone de subduction montrant les principaux processus et systèmes magmatiques et hydrothermaux qui peuvent s'y développer. *MASH* zone : *melting-assimilation-storage-homogenization* zone. Modifiée d'après *Richards* [2011].

1.3.1. Magmatisme et transfert de métaux dans le coin mantellique

Les magmas silicatés formés dans le domaine d'arc d'une zone de subduction sont issus de la fusion partielle du manteau, dans le coin mantellique sous-jacent (figure 1.5) [*Coats*, 1962; *Gill*, 1981]. Celle-ci ne peut être déclenchée dans les conditions de pression et de température (*P*-*T*) admises pour cette région du manteau, uniquement si ce manteau est hydraté [*Tatsumi et al.*, 1983; *Arculus*, 1994; *Schmidt & Poli*, 1998; *Grove et al.*, 2006]. En effet, la présence d'eau dans le manteau permet d'abaisser le solidus(*) de la péridotite qui le constitue, entrainant ainsi une fusion partielle de cette roche à plus faible température. L'eau nécessaire à ce processus est apportée par la lithosphère océanique subduite (i.e. croûte océanique et manteau lithosphérique) qui a été préalablement hydratée et serpentinisée alors qu'elle constituait encore le plancher océanique. En effet, l'augmentation de la température et surtout de la pression lors de l'enfouissement de ces roches, induit des réactions métamorphiques (i.e. passage progressif de la roche au faciès métamorphique des schistes bleus, puis des éclogites) qui permettent de relâcher l'eau contenue dans les minéraux (figure 1.6) [*Schmidt & Poli*, 1998]. Cette eau ainsi libérée peut ensuite percoler jusque dans les péridotites constituant le coin mantellique qui peuvent alors l'intégrer, notamment sous la forme de minéraux hydratés tels que l'amphibole, la chlorite ou la serpentine [*Schmidt & Poli*, 1998; *Grove et al.*, 2006]. En plus de l'eau, d'autres éléments peuvent être libérés lors de cette déshydratation, tels que le chlore, le soufre ainsi qu'un grand nombre d'éléments incompatibles(*), comme les éléments lithophiles à large rayon ionique (i.e. *LILE*(*)) ou encore la plupart des éléments lithophiles à fort potentiel ionique (i.e. *HFSE*(*)) [*Tatsumi et al.*, 1986; *Arculus*, 1994]. Un tel apport chimique dans le manteau induit indubitablement des modifications chimiques majeures, avec notamment une augmentation du degré d'oxydation (i.e. de la fugacité(*) d'oxygène : fO_2) et de la fugacité du soufre (i.e. fS_2) dans le coin mantellique (figure 1.6) [*Parkinson & Arculus*, 1999; *Jégo & Dasgupta*, 2013].

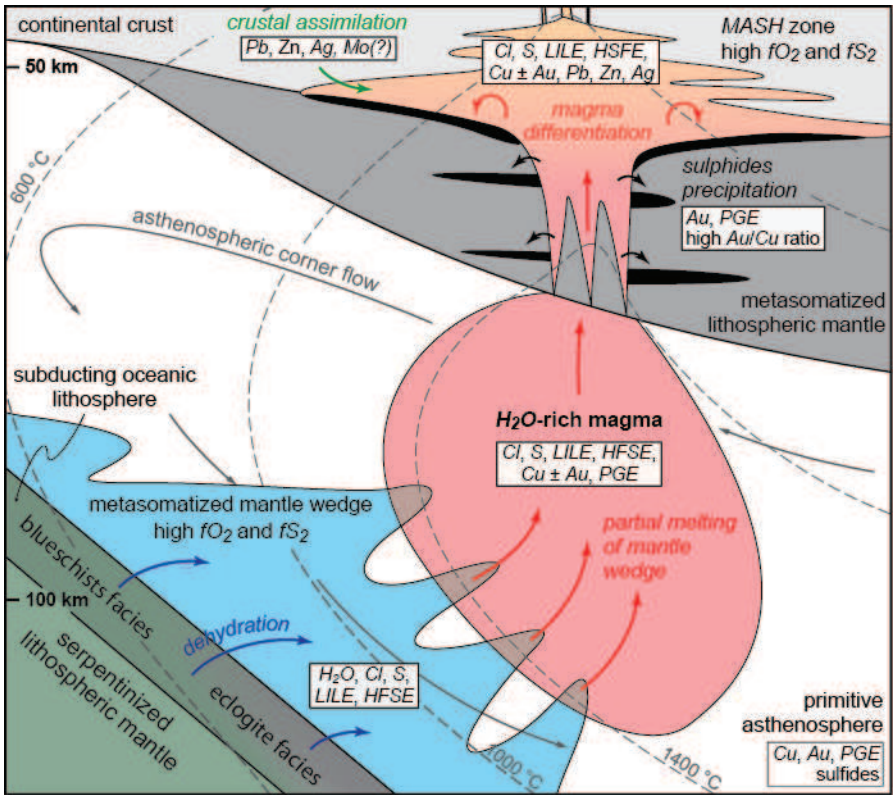

Figure 1.6 : schéma conceptuel de la partie inférieure de l'arc magmatique montrant la genèse et l'évolution des magmas d'arc ainsi que les flux de métaux associés depuis le coin mantellique, jusqu'à la base de la croûte continentale. *MASH* zone : *melting-assimilation-storage-homogenization* zone.

Ce manteau métasomatisé peut ensuite fondre de manière partielle lorsqu'il atteint les régions chaudes du coin mantellique, que ce soit par entrainement par le flux mantellique ou par infiltration directe de la phase fluide aqueuse (figures 1.5 et 1.6) [*Schmidt & Poli*, 1998; *Grove et al.*, 2006]. Le magma silicaté de composition basaltique alors produit peut piéger l'eau présente dans le manteau (jusqu'à 5-6 wt.% H_2O) [*Schmidt & Poli*, 1998; *Pichavant et al.*, 2002], ainsi qu'un grand nombre d'éléments volatils et incompatibles, influençant la composition du produit final, à savoir les magmas d'arc [*Gill*, 1981; *Tatsumi et al.*, 1986]. Présent initialement en faible quantité dans le manteau primitif, les métaux tels que le cuivre, l'or ou les éléments du groupe du platine (i.e. *PGE*(*)) peuvent se concentrer de deux à 800 fois dans ce magma primaire, en fonction notamment de paramètres critiques comme la fO_2 et la fS_2 [*Peach et al.*, 1990; *McInnes et al.*, 1999; *Richards*, 2009, 2011]. En effet, en comparaison des éléments chalcophiles(*) (ex. cuivre), les éléments sidérophiles(*) (ex. or, PGE) sont préférentiellement retenus dans les phases sulfurées plutôt que dans les liquides silicatés

[*Peach et al.*, 1990]. A fS_2 élevée, ces sulfures peuvent coexister avec une phase dominante sulfatée dissoute, bien que le coin mantellique soit fortement oxydé [*McInnes et al.*, 2001], permettant ainsi un fort fractionnement entre éléments chalcophiles et sidérophiles. Il en résulte un magma primaire relativement enrichi en cuivre (sous la forme de complexes sulfatés ou chlorurés) par rapport aux métaux précieux tels que l'or ou les *PGE*, qui sont à l'inverse concentrés dans les phases sulfurées résiduelles (figure 1.7) [*Peach et al.*, 1990; *Richards*, 2009]. Bien que mal contrainte du point de vue mécanique, la remontée de ce magma silicaté entraine des modifications chimiques similaires dans le manteau environnant, maintenant actif ce processus de fractionnement des métaux jusqu'à son arrivée au niveau du Moho, à la base de la croûte.

Sur la base d'études isotopiques, le manteau présent sous le domaine d'arc serait la source principale de ces métaux [*McInnes et al.*, 1999; *Halter et al.*, 2005; *Richards*, 2011], le rôle de la déshydratation et de la fusion partielle des sédiments et de la croûte océanique subduits dans l'apport des métaux étant considéré comme mineur [*Hedenquist & Lowenstern*, 1994; *Richards*, 2011]. Il est également intéressant de noter que *Lee et al.* [2012] ont récemment suggéré que le manteau sous l'arc magmatique n'étant pas enrichi en cuivre, ce qui implique des mécanismes différents, plus superficiels, afin de concentrer ces métaux dans les magmas silicatés [*Wilkinson*, 2013].

1.3.2. Zone MASH *: maturation des magmas et fractionnement des métaux*

En raison d'une densité plus élevée que celle de la croûte [*Herzberg et al.*, 1983], le magma primaire peut être stocké en base de croûte, sous la forme d'un complexe de sills, dans une zone communément appelée la *melting-assimilation-storage-homogenization* (*MASH*) zone ou *zone chaude* (figure 1.5) [*Hildreth & Moorbath*, 1988; *Annen*, 2006]. Ces magmas peuvent alors progressivement se différencier(*) grâce à des processus de cristallisation fractionnée et d'assimilation de la croûte inférieure encaissante (figure 1.6). Le magma résultant, plus riche en silice, montre alors une composition andésitique à dacitique, typique du magmatisme d'arc [*Gill*, 1981; *Annen*, 2006].

Ce fractionnement, et la diminution de température qui y est associée, tend à diminuer la concentration en métaux du magma, qui se retrouvent alors retenus dans des minéraux sulfurés néoformés [*Hedenquist & Lowenstern*, 1994; *Zajacz et al.*, 2012]. Cependant, toujours en raison de

leur plus grande affinité pour ces phases sulfurées [*Peach et al.*, 1990], l'or et les autres éléments sidérophiles s'y retrouvent préférentiellement piégés, se déposant alors sous la forme de cumulats denses (figure 1.6) [*Richards*, 2009; *Wilkinson*, 2013]. A l'inverse, le cuivre présent en grande quantité dans le magma silicaté est moins affecté par ce mécanisme, ce qui entraine une diminution du rapport or/cuivre (i.e. *Au*/*Cu*) du magma différencié [*Richards*, 2009]. La réinjection d'un magma primaire chaud peut néanmoins moduler cette tendance en réapprovisionnant en métaux cette zone *MASH* ainsi qu'en induisant la fusion des cumulats, remobilisant ainsi l'or et les autres métaux piégés [*Richards*, 2009; *Wilkinson*, 2013]. D'autres métaux d'affinité crustale comme le plomb, le zinc, l'argent et possiblement le molybdène peuvent également se concentrer dans le magma à ce moment-là (mais également tout au long de la remontée du magma dans la croûte), par l'intermédiaire des processus d'assimilation crustale (figure 1.6) [*Richards*, 2011].

1.3.3. Transition magmatisme-hydrothermalisme et exsolution des métaux

Une fois différencié, ce magma andésitique à dacitique, moins dense, remonte au travers des roches crustales le long de complexes de dykes, jusqu'à atteindre la croûte supérieure où il s'accumule dans une chambre magmatique (figure 1.5) [*Annen*, 2006]. Au cours de la remontée puis du stockage de ce magma hydraté différencié, la diminution de la pression ainsi que la cristallisation progressive du magma sous la forme d'une intrusion plutonique permettent de diminuer la solubilité de l'eau et de saturer progressivement le magma en éléments volatils. Ces phénomènes induisent alors un mécanisme crucial pour le fractionnement et la concentration des métaux : l'exsolution, entre 600 et 500 °C, d'un fluide aqueux concentrant éléments volatils et métaux (figure 1.7) [*Hedenquist & Lowenstern*, 1994; *Candela & Piccoli*, 2005; *Scaillet*, 2010; *Wilkinson*, 2013]. En effet, la concentration du soufre notamment dans cette phase fluide, vient concurrencer la formation de complexes sulfurés au sein de la chambre magmatique, entrainant leur résorption et la mobilité des métaux [*Scaillet*, 2010; *Richards*, 2011; *Zajacz et al.*, 2012; *Wilkinson*, 2013]. Dans les conditions oxydantes, typiques des domaines d'arc, les métaux tels que le cuivre et l'or sont exsolvés sans fractionnement significatif dans cette phase fluide qui conserve ainsi le même rapport *Au*/*Cu* acquis

précédemment [*Halter et al.*, 2005; *Sillitoe*, 2010; *Richards*, 2011; *Zajacz et al.*, 2012; *Wilkinson*, 2013].

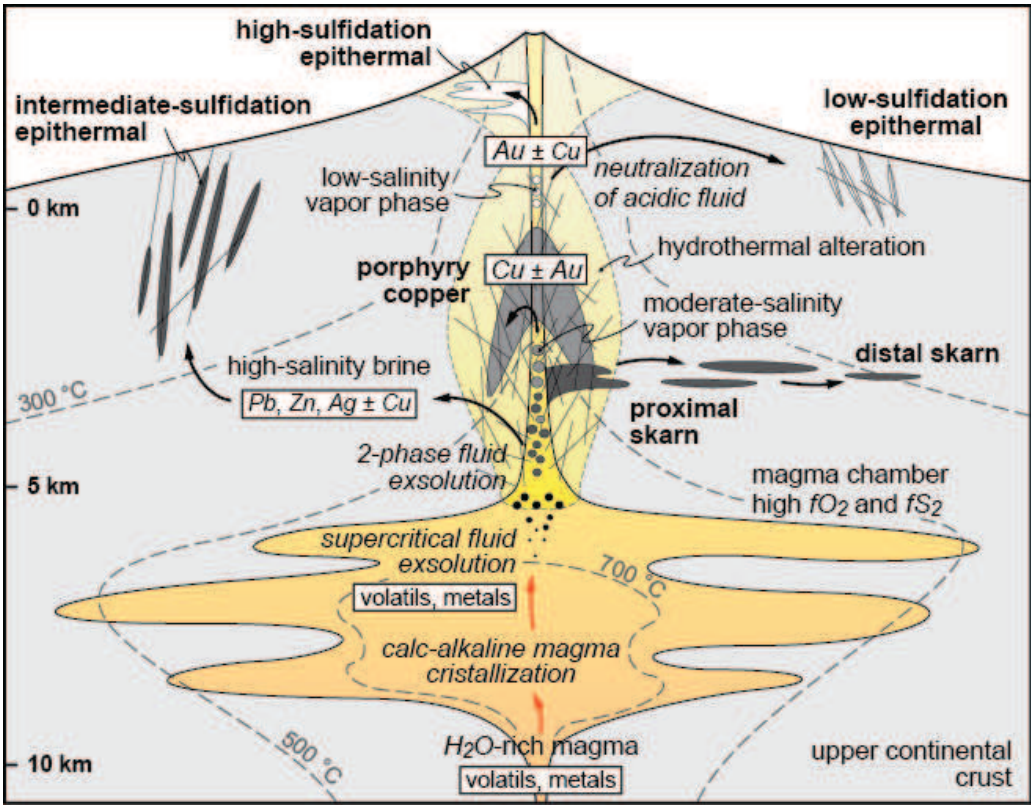

Figure 1.7 : schéma conceptuel du système magmatique-hydrothermal mis en place dans la croûte supérieure en domaine d'arc. Les principaux processus chimiques à l'origine des gisements typiques de ces environnements y figurent. Modifiée d'après *Sillitoe* [2010] et *Richards* [2011].

La composition globale du fluide est dépendante de nombreux paramètres comme la composition et l'état d'oxydation du magma ou encore sa teneur en eau, de même que sa nature est contrôlée par la profondeur à laquelle cette exsolution s'opère. Ainsi, pour des profondeurs supérieures à ~5-6 km, ce fluide sera de nature supercritique(*), alors qu'à plus faible profondeur, deux phases fluides immiscibles coexistent : une saumure fortement saline et une phase vapeur moyennement saline (figure 1.7) [*Hedenquist & Lowenstern*, 1994; *Heinrich et al.*, 1999, 2004; *Candela & Piccoli*, 2005; *Williams-Jones & Heinrich*, 2005; *Sillitoe*, 2010; *Richards*, 2011]. La formation de ces deux fluides induit un fractionnement majeur des métaux et éléments volatils alors présents en solution, avec le soufre, le cuivre et l'or qui se concentrent principalement dans la phase vapeur tandis que le chlore, le plomb, le zinc ou l'argent s'accumulent dans la saumure [*Heinrich et al.*, 1999; *Williams-Jones &*

Heinrich, 2005; *Sillitoe*, 2010; *Richards*, 2011; *Kouzmanov & Pokrovski*, 2012; *Zajacz et al.*, 2012]. Ce fractionnement, et notamment celui du cuivre, reste cependant encore débattu (cf. discussion de *Sillitoe* [2010]), avec un rôle probable de la fS_2 [*Heinrich et al.*, 2004; *Williams-Jones & Heinrich*, 2005].

1.3.4. Hydrothermalisme et précipitation des métaux

Ces deux phases fluides (i.e. saumure et vapeur) peuvent ensuite transporter les métaux jusqu'à ce que leur solubilité dans ces fluides chute et qu'ils précipitent, principalement sous la forme de sulfures [*Sillitoe*, 2010; *Richards*, 2011; *Kouzmanov & Pokrovski*, 2012; *Wilkinson*, 2013]. Différents facteurs tels que la baisse de la pression, de la température ou encore l'interaction avec la roche encaissante ou avec d'autres fluides (ex. météoriques) peuvent conduire à cette précipitation dans des environnements variés, résultant donc en une large gamme de minéralisations avec une morphologie et des altérations associées spécifiques (figure 1.7).

Les porphyres minéralisés sont exclusivement associés aux intrusions plutoniques. La minéralisation peut notamment se présenter sous la forme d'un stockwerk(*) (figure 1.8a), de disséminations, ou de *pipes* bréchiques(*). Outre la gangue(*) de quartz, la paragenèse(*) minérale est principalement composée de minéraux porteurs du cuivre comme la chalcopyrite et la bornite, ainsi que d'autres sulfures comme la pyrite et éventuellement la molybdénite, ainsi que de la magnétite [ex. *Sillitoe*, 2010]. Ces gisements se mettent typiquement en place entre 4 et 8 km de profondeur et à des températures estimées à 425-320 °C [*Sillitoe*, 2010; *Richards*, 2011], à la suite d'une fracturation hydraulique(*) au niveau d'apophyses plutoniques à l'apex de la chambre magmatique (figure 1.7) [*Guillou-Frottier & Burov*, 2003]. Dans de telles conditions, à la fois la saumure et la phase vapeur peuvent contribuer à la précipitation du cuivre alors que l'or reste préférentiellement en solution, notamment si la fS_2 reste élevée [*Hedenquist & Lowenstern*, 1994; *Richards*, 2011; *Kouzmanov & Pokrovski*, 2012]. Ces porphyres cuprifères peuvent néanmoins être enrichis en or si la (ou les) phase(s) fluide(s) minéralisatrice(s), et donc le magma source, possède(nt) un rapport *Au*/*Cu* élevé [*Halter et al.*, 2005].

Figure 1.8 : illustrations de la morphologie des différents corps minéralisés qui peuvent se déposer dans un environnement de subduction. (a) Stockwerk à cuivre et molybdène caractérisant un gisement porphyrique, *Los Tamales project*, Mexique (source : *www.sundanceminerals.com*). (b) *Vuggy silica* à or, caractérisant un gisement de type épithermal acide, *Colquijirca District*, Pérou (source : *J. Tuduri*). (c) Veines rubanées à or et argent caractérisant un gisement de type épithermal neutre, *Golden Cross Mine*, Nouvelle-Zélande (source : *www.sjsresource.com.au*). (d) Minéralisation de remplacement de type manto dans un banc carbonaté, *Morrococha District*, Pérou (source : *J. Tuduri*).

Les épithermaux acides (i.e. *high-sulfidation epithermal deposits*), riches en or, se mettent en place dans un environnement superficiel acide, à l'aplomb du système porphyrique et à des températures inférieures à 300 °C. La formation de ce type de gisement résulte de la condensation, au contact

d'eaux météoriques, d'une phase vapeur d'origine magmatique riche en *HCl* et SO_2 et pauvre en métaux, résultant en un lessivage intense de la partie superficielle de l'édifice volcanique où seul subsiste un résidu siliceux vacuolaire appelé vuggy silica (figure 1.8b) [*White & Hedenquist*, 1990; *Heinrich et al.*, 2004]. Cette roche piège ensuite l'essentiel de la minéralisation aurifère apportée par un fluide modérément à faiblement salin, issu du système porphyrique sous-jacent (figure 1.7). Dans ces systèmes, l'or est généralement associé à l'énargite et la pyrite. Les teneurs en or chutent rapidement latéralement en raison du mélange des fluides minéralisateurs avec les eaux météoriques [*White & Hedenquist*, 1990; *Hedenquist & Lowenstern*, 1994].

Les épithermaux neutres (i.e. *low-sulfidation epithermal deposits*) se mettent en place, tout comme leurs équivalents acides, dans des environnements superficiels de faibles températures mais où le lien avec une source magmatique est moins évident. Ce sont classiquement des veines rubanées (figure 1.8c) à gangue de quartz, adulaire, calcite, minéraux de manganèse (i.e. rhodochrosite et rhodonite), où peuvent se concentrer des métaux précieux comme l'or ou l'argent (notamment sous la forme de tellures), mais également des métaux de base tels que le plomb (i.e. galène), le zinc (i.e. sphalérite) et le cuivre (i.e. chalcopyrite). Contrairement aux épithermaux acides, ces gisements se caractérisent par un fluide minéralisateur qui s'est neutralisé au cours de son transport en réagissant de manière significative avec la roche encaissante et/ou les eaux météoriques (figure 1.7) [*White & Hedenquist*, 1990; *Hedenquist & Lowenstern*, 1994].

Les épithermaux intermédiaires, skarns et autres gisements de remplacement tirent leur origine de la saumure dense qui se sépare de la phase vapeur au sommet de la chambre magmatique. Celle-ci peut transporter des métaux comme le plomb, le zinc, l'argent et dans une moindre mesure le cuivre et l'or à de plus ou moins grandes distances du système magmatique (figures 1.7 et 1.8d) [*Sillitoe & Hedenquist*, 2003; *Sillitoe*, 2010; *Kouzmanov & Pokrovski*, 2012]. Leur morphologie et leur minéralogie peuvent être extrêmement variables, notamment dans le cas des skarns où la roche carbonatée encaissante joue un rôle crucial [*Meinert*, 1997].

Bien que pouvant expliquer la formation de systèmes minéralisés complets dans les domaines d'arc (i.e. porphyres minéralisés, skarns, gîtes de remplacement et épithermaux associés), la succession des processus magmatiques et hydrothermaux décrite ci-dessus n'est qu'une alternative possible à l'évolution de ces systèmes. De nombreux paramètres incluant la composition du coin mantellique et du magma, la variation de fO_2 et de fS_2, ou encore la profondeur d'exsolution des fluides hydrothermaux et ses modalités de transport peuvent modifier cette évolution (cf. discussion de *Sillitoe* [2010] et *Richards* [2011]). Afin de guider l'exploration minière, cette complexité doit être appréhendée car elle influence l'expression de la minéralisation ainsi que les altérations qui y sont associées (figure 1.8), modifiant les métallotectes(*) utiles à cette prospection à une échelle locale à régionale.

1.3.5. Minéralisation et contexte tectonique en domaine de subduction

Bien que les études citées précédemment contraignent bien les mécanismes physico-chimiques à l'origine de ces gisements, elles n'abordent généralement que de manière parcellaire le rôle de la dynamique de la subduction et de l'évolution tectonique qui en résulte. Cet aspect est pourtant crucial car il peut influencer l'évolution du système magmatique-hydrothermal depuis le manteau, jusque qu'en surface. Ainsi, la précipitation des minéralisations dans la croûte supérieure est très souvent contrôlé par des failles résultant de l'état de contrainte dans la croûte [*Sillitoe*, 1997; *Tosdal & Richards*, 2001]. En effet, les fluides minéralisateurs peuvent facilement circuler au travers de ces structures perméables, entrainant une chute de la pression ou encore un mélange avec d'autres fluides (ex. météoriques) qui favorise la baisse de la solubilité des métaux en solution et donc leur précipitation.

A plus grande échelle, les gisements peuvent être regroupés en clusters ou bien s'aligner de manière parallèle ou transverse à l'arc magmatique [*Billa et al.*, 2004; *Sillitoe*, 2010; *Bertrand et al.*, 2014]. Une telle répartition implique des structures d'échelle crustale mais également des processus à l'échelle de la zone de subduction qui peuvent être difficiles à contraindre en raison du manque d'observations directes (ex. géométrie de la lithosphère subduite, processus mantelliques).

Certaines corrélations ont cependant déjà été mises en évidence entre la genèse de gisements porphyriques et épithermaux de grande taille et un régime compressif favorisant le développement de larges chambres magmatiques [ex. *Sillitoe & Hedenquist*, 2003; *Cooke et al.*, 2005]. Cependant, la relaxation des contraintes faciliterait l'exsolution des fluides magmatiques-hydrothermaux enrichis en métaux, suggérant un rôle majeur des changements de régime tectonique sur la précipitation de ces concentrations métalliques [*Tosdal & Richards*, 2001; *Richards*, 2005]. En combinant un modèle de reconstructions paléotectoniques et une base de données recensant les porphyres cuprifères le long de des chaînes Téthysienne et Andine, *Bertrand et al.* [2014] ont récemment confirmé l'importance de ce régime extensif (ou du moins de la relaxation des contraintes compressives) et de la dynamique profonde de la lithosphère plongeante sur la distribution de ces gisements.

D'autres changements majeurs dans ces processus métallogéniques peuvent intervenir lorsqu'une zone de subduction sous une marge continentale évolue vers une zone de collision (figures 1.9a et b) [*Kerrich et al.*, 2000; *Groves & Bierlein*, 2007; *Richards*, 2009]. En effet, la délamination du manteau lithosphérique et l'extension qui peut s'en suivre permettraient la fusion de la base de la croûte (figures 1.9c et d) précédemment enrichie en or et autres métaux sidérophiles alors qu'elle se trouvait en domaine d'arc (figure 1.6). Il en résulte des minéralisations principalement de type épithermal, ainsi que des porphyres minéralisés enrichis en or par rapport à leurs équivalents mis en place à l'aplomb de la zone de subduction [*Richards*, 2009, 2011]. De même, d'autres processus géodynamiques spécifiques comme une inversion de la polarité de la zone de subduction, pourraient avoir favorisé la mise en place de ces systèmes minéralisés riches en or [*Solomon*, 1990].

Ces études montrent l'importance de ces processus tectoniques sur la mise en place de gisements potentiellement exploitables dans les environnements de subduction. Cependant, l'évolution géodynamique de ces zones de convergence peut être très différente de celles proposées par *Grove et al.* [2006] ou encore *Richards* [2009] et mérite d'être considérée aux vues des changements majeurs qu'elle peut induire sur la dynamique crustale mais aussi mantellique et donc sur les mécanismes de genèse de ces minéralisations. De plus, on connait aujourd'hui la complexité tridimensionnelle (3D) des zones de subduction, dès lors que les panneaux plongeants peuvent se déchirer ou se détacher, il convient donc également de considérer cet aspect 3D.

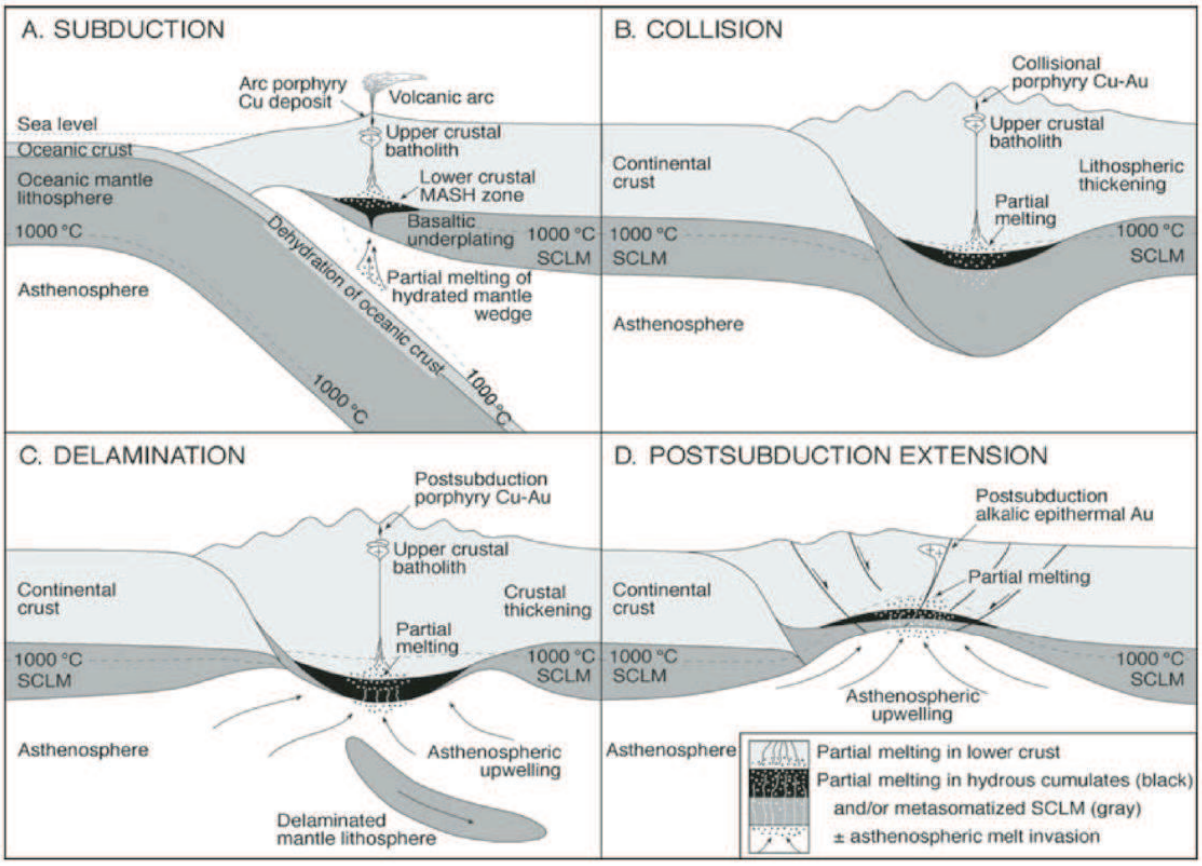

Figure 1.9 : (a, b, c, d) schémas conceptuels montrant l'évolution possible d'une zone de subduction et des systèmes magmatiques-hydrothermaux qui y sont associés [*Richards*, 2009].

1.4. Evolution de la zone subduction, réponse mantellique et crustale

Il existe actuellement un grand nombre de zones de subduction actives à travers le monde avec des géométries diverses, comme l'indique en surface l'allure de leur fosse océanique (traduisant l'interface entre les deux lithosphères) (figure 1.10) [*Jarrard*, 1986; *Heuret & Lallemand*, 2005; *Lallemand et al.*, 2005; *Schellart et al.*, 2007]. Celle-ci varie en longueur (entre 250 et 2 700 km) et peut être plus ou moins courbée avec une nette tendance à être rectiligne pour les longues fosses (et donc les larges lithosphères plongeantes, ex. subduction andine) et très courbée pour les fosses relativement courtes (ex. subductions méditerranéennes). Cette observation traduit une diversité et une complexité de la géométrie 3D des zones de subduction qui induisent nécessairement des évolutions géodynamiques différentes se répercutant à la fois sur la dynamique crustale et mantellique.

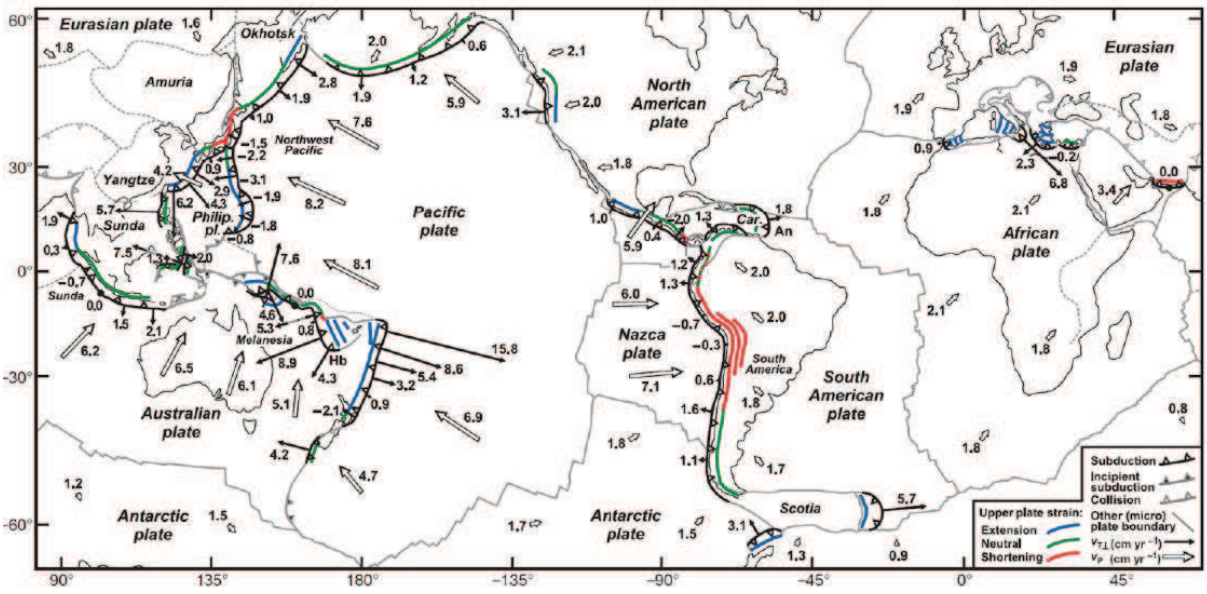

Figure 1.10 : carte recensant les principales zones de subduction dans le monde. Les vitesses des plaques tectoniques sont marquées par les flèches blanches alors que les flèches noires indiquent les vitesses de migration des fosses océaniques [*Schellart et al.*, 2007].

1.4.1. Cinématique de la subduction

Le processus de subduction se traduit par une cinématique en surface mesurable à l'aide de méthodes basées sur l'évolution cinématique long terme (ex. anomalies magnétiques, géométrie des failles transformantes) [ex. *Le Pichon*, 1968] ou encore sur l'évolution actuelle grâce à la géodésie spatiale et en particulier les mesures GPS. Cette cinématique peut alors être caractérisée par plusieurs vecteurs vitesse (figure 1.11) [*Chase*, 1978; *Lallemand et al.*, 2005; *Husson*, 2012] : (1) les vitesses absolues des lithosphères plongeante (V_{sub}) et chevauchante (V_{up}), (2) la vitesse de convergence ($V_c = V_{sub} - V_{up}$), (3) la vitesse de migration de la fosse (V_t) et (4) la vitesse de déformation dans la lithosphère supérieure ($V_d = V_t - V_{up}$). Il est généralement admis que le régime tectonique dans la lithosphère supérieure est indépendant de la vitesse de convergence. En revanche, la vitesse de déformation V_d nous renseigne sur l'état des contraintes et donc sur le régime tectonique qui la caractérise. Ainsi, en considérant des vitesses négatives vers la marge active et des vitesses positives vers l'océan, cette déformation sera compressive si cette différence de vitesses est positive (figure 1.11a, ex. subduction andine) et extensive dans le cas contraire (figure 1.11b, ex. subductions méditerranéennes). Ces simples relations, applicables dans le cas de systèmes 2D, ne sont cependant

pas totalement représentatives des systèmes naturels en 3D (figure 1.10) où une forte composante oblique à la fosse de ces vecteurs vitesse peut résulter en une déformation transpressive(*) ou transtensive(*).

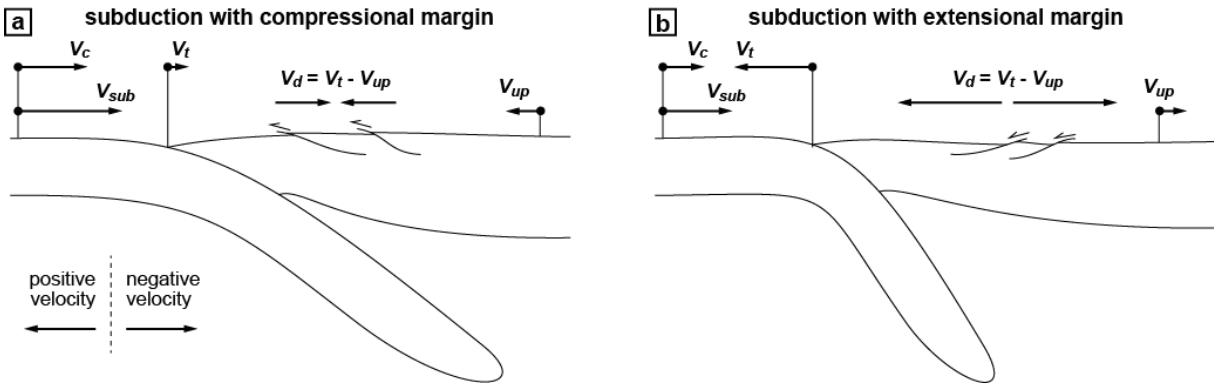

Figure 1.11 : schémas d'une zone de subduction caractérisée par une marge compressive (a) ou extensive (b), où figurent les différents vecteurs cinématiques la caractérisant. V_{sub} : vitesse absolue de la lithosphère plongeante. V_{up} : vitesse absolue de la lithosphère supérieure. V_c : vitesse de convergence. V_t : vitesse de la fosse. V_d : vitesse de déformation dans la lithosphère supérieure. Modifiée d'après *Lallemand et al.* [2005].

Il n'en reste pas moins que l'étude statistique des paramètres cinématiques et de la géométrie des zones de subductions actuelles montre que non seulement la vitesse de la plaque supérieure joue un rôle sur ce régime tectonique dans la plaque supérieure [*Chase*, 1978; *Dewey*, 1980; *Heuret & Lallemand*, 2005], mais également l'angle du panneau plongeant dans le manteau [*Lallemand et al.*, 2005], sa largeur [*Schellart et al.*, 2007; *Loiselet et al.*, 2009], son comportement à l'approche de la limite manteau supérieur-inférieur [*Guillou-Frottier et al.*, 1995; *Faccenna et al.*, 2007a, 2013], son interaction avec les plaques tectoniques avoisinantes [*Yamato et al.*, 2009] ou encore les flux mantelliques [*Heuret & Lallemand*, 2005; *Faccenna & Becker*, 2010; *Husson*, 2012; *Faccenna et al.*, 2013a]. Ces derniers peuvent en effet entrainer un phénomène de succion le long de cette lithosphère en subduction qui est particulièrement efficace en considérant une convection mantellique globale, avec la remontée de panaches mantelliques chaud qui contrebalance la subduction de lithosphères froides [*Conrad & Lithgow-Bertelloni*, 2002; *Yamato et al.*, 2008; *Becker & Faccenna*, 2011; *Faccenna et al.*, 2013a]. Ces observations tendent à rejoindre les conclusions de *Jarrard* [1986] qui

propose que de nombreux paramètres contrôlent la cinématique et donc la dynamique de la subduction en agissant sur les forces motrices et résistives qui la régissent (figure 1.12).

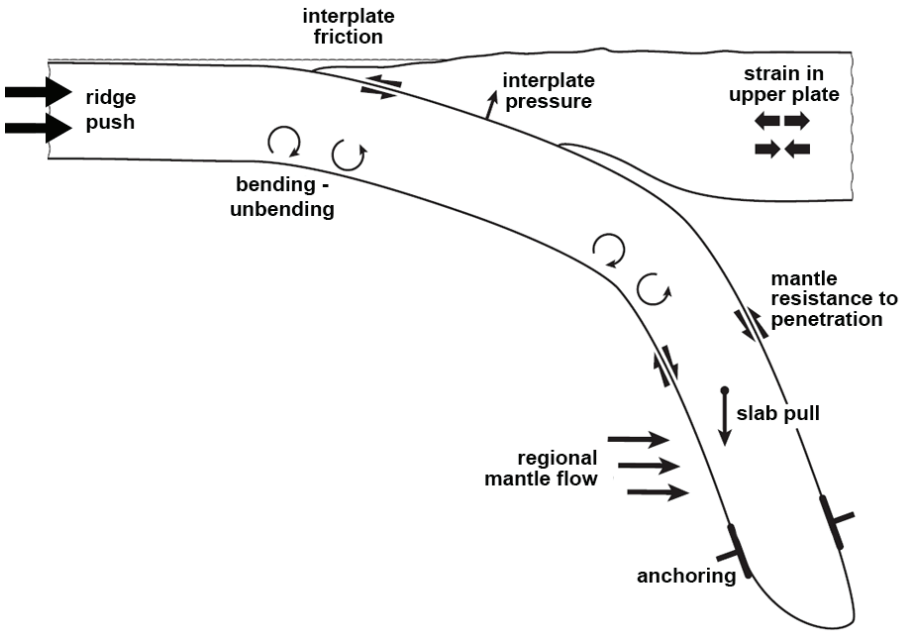

Figure 1.12 : schéma représentant les principales forces responsables de la dynamique d'une zone de subduction. Modifiée d'après *Lallemand et al.* [2005].

1.4.2. Subduction et déformation crustale

Le régime tectonique dans la plaque supérieure (qu'il soit compressif, transpressif, transtensif, extensif, voire neutre, figure 1.10) et donc la balance des forces contrôlant la dynamique de subduction se répercute par l'expression d'une déformation et donc d'une structuration spécifique dans cette croûte.

Les marges continentales compressives : le cas de la Cordillère des Andes. Une déformation compressive intense le long d'une marge continentale comme les Andes peut être caractérisée par le soulèvement d'un plateau qui peut atteindre plus de 4 000 mètres d'altitude (ex. l'Altiplano-Puna), associé à une croûte pouvant atteindre 70-80 km d'épaisseur [*James*, 1971; *McGlashan et al.*, 2008; *Vanderhaeghe*, 2012]. La compression qui opère depuis le Cénozoïque, notamment dans la partie centrale de cette chaîne, se traduit par des taux de raccourcissement pouvant atteindre ~12 mm a^{-1} qui sont majoritairement accommodés par des plissements et des chevauchements dans la croûte

supérieure [*Oncken et al.*, 2006 et références associées]. Une phase extensive à transtensive est également décrite au cours du Paléogène-Néogène inférieur mais reste relativement marginale par rapport à la compression [*Elger et al.*, 2005].

Une des expressions les plus spectaculaires de ces contraintes exercées dans la lithosphère supérieure sont les séismes qui peuvent atteindre, le long de ces zones de subduction, des magnitudes supérieures à neuf sur l'échelle de Richter. Les observations sur ces phénomènes, limitées dans le temps (i.e. quelques siècles tout au plus), laissent à penser que ces séismes de forte magnitude se déclenchent préférentiellement le long des marges présentant un régime tectonique compressif associé à une lithosphère océanique plongeante plutôt jeune (figure 1.13) [*Uyeda & Kanamori*, 1979; *McCaffrey*, 2008].

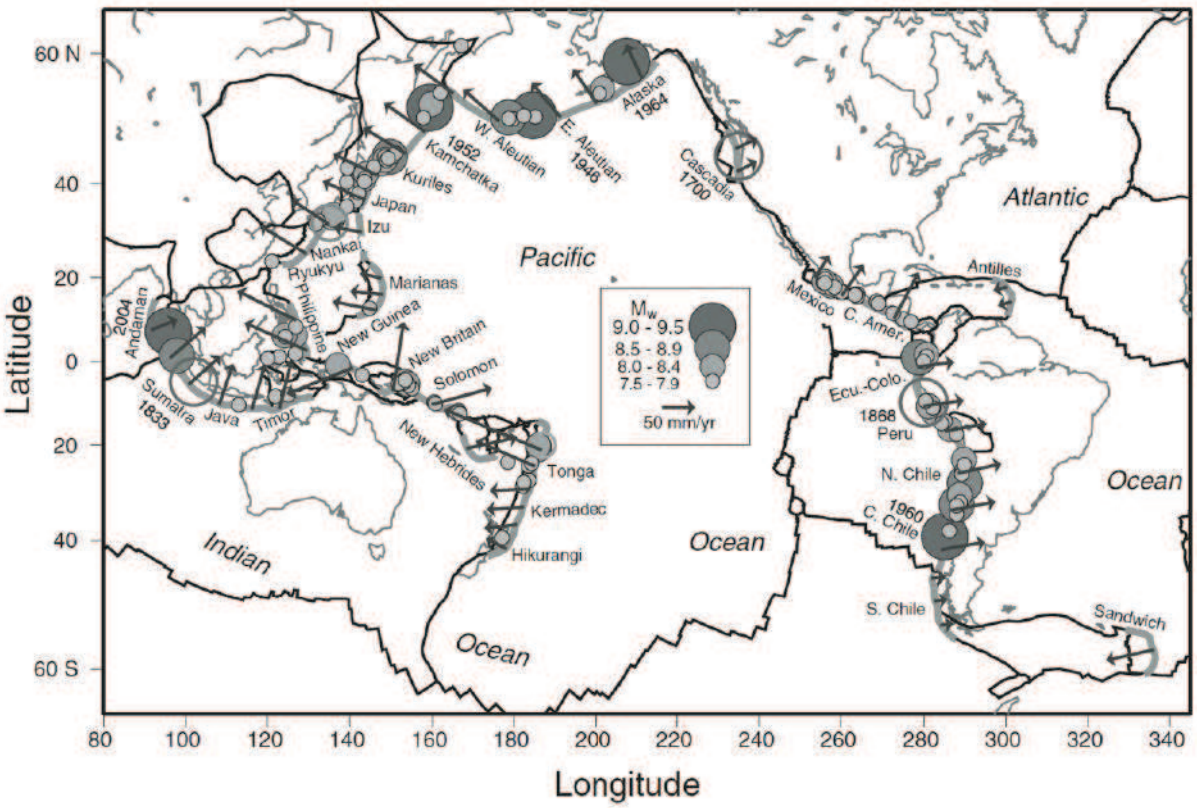

Figure 1.13 : carte des principales zones de subduction (lignes grisées épaisses) à travers le monde sur laquelle sont représentés tous les séismes connus de magnitude supérieure à 7,5 de 1700 à 1900 (cercles vides) et après 1900 (cercles pleins) [*McCaffrey*, 2008].

Une autre caractéristique de ces marges actives compressives est le volcanisme en surface qui représente l'expression ultime des systèmes magmatiques se développant dans ces domaines dits d'*arc*

(cf. *Section 1.3*). Ces magmas appartiennent majoritairement à la série calco-alcaline et présentent un enrichissement en silice qui leur donne une composition intermédiaire andésitique à dacitique [*Gill*, 1981; *Tatsumi et al.*, 1983]. Ces arcs magmatiques peuvent avoir une durée de vie relativement longue et intermittente en contexte compressif, tout comme dans la partie centrale des Andes où l'activité volcanique semble anti-corrélée au développement de la compression à l'Oligocène, exprimé dans la figure 1.14 par le taux de raccourcissement [*Oncken et al.*, 2006 et références associées]. En revanche, l'intense activité volcanique au Miocène pourrait s'expliquer par une possible délamination lithosphérique qui aurait suivi l'épaississement crustal [*Sobolev et al.*, 2006]. Il est également intéressant de noter que cet arc volcanique a migré vers l'est, perpendiculairement à la fosse, sur une distance inférieure à 100 km depuis l'Eocène, en accord avec la migration de la fosse [*Trumbull et al.*, 2006].

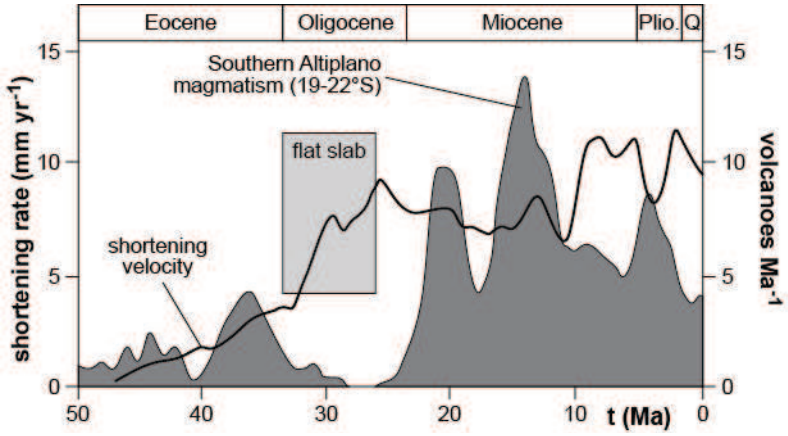

Figure 1.14 : graphique montrant la distribution temporelle du volcanisme entre 19 et 22° de latitude sud ainsi que le taux de raccourcissement moyen estimé pour cette région. Modifiée d'après *Oncken et al.* [2006].

Les marges continentales extensives : le cas de la région Méditerranéenne. Le développement d'une marge continentale extensive est très souvent lié à la vitesse de retrait de la fosse qui surpasse celle de la plaque chevauchante (figure 1.11b) [*Chase*, 1978; *Dewey*, 1980; *Heuret & Lallemand*, 2005]. D'autres facteurs, tels que l'effondrement gravitaire, peuvent également induire de l'extension au niveau de ces marges actives, qu'elles soient associées à un processus de subduction ou de collision [ex. *Burchfiel & Royden*, 1985; *Dewey*, 1988; *Vanderhaeghe*, 2012]. Celui-ci affecte la croûte précédemment épaissie et se développe lorsque les forces propres à cet orogène, telles que l'énergie

potentielle gravitaire, surpassent les forces tectoniques qui maintiennent cette croûte épaisse en équilibre isostatique(*) [*Dewey*, 1988]. Il en résulte un effondrement gravitaire de la chaîne qui peut conduire à l'ouverture de bassins intra-montagneux voir océaniques si le manteau lithosphérique sous-jacent est également affecté [*Vanderhaeghe*, 2012]. L'état thermique de la croûte épaissie, et notamment la présence de roches partiellement fondues dans la croûte inférieure qui peut alors fluer, ainsi que la compétition entre la surrection de la chaîne et son érosion, peuvent également influer sur cet effondrement [*Vanderhaeghe & Teyssier*, 2001; *Vanderhaeghe*, 2012].

Dans la région Méditerranéenne, le moteur principal de la déformation extensive qui affecte la marge Eurasienne est l'accélération du retrait de plusieurs segments de lithosphères plongeantes appartenant à l'océan Néo-Téthys qui migrent rapidement vers le sud à partir de 35-30 Ma [*Jolivet & Faccenna*, 2000] (cf. *Section 1.5*). Cette extension s'est traduite par l'ouverture de plusieurs bassins d'arrière-arc continentaux où l'épaisseur crustale est comprise entre 20 et 30 km (ex. Mer d'Alboran, Mer Egée, figure 1.15) [*Le Pichon & Angelier*, 1979; *Lonergan & White*, 1997; *Faccenna et al.*, 2004; *Tirel et al.*, 2004; *Jolivet & Brun*, 2010]. Cet étirement intense de la croûte a également pu provoquer sa rupture et la formation de plusieurs bassins océaniques, tels que le Bassin Liguro-Provençal ou la Mer Tyrrhénienne [*Malinverno & Ryan*, 1986; *Faccenna et al.*, 1997; *Chamot-Rooke et al.*, 1999].

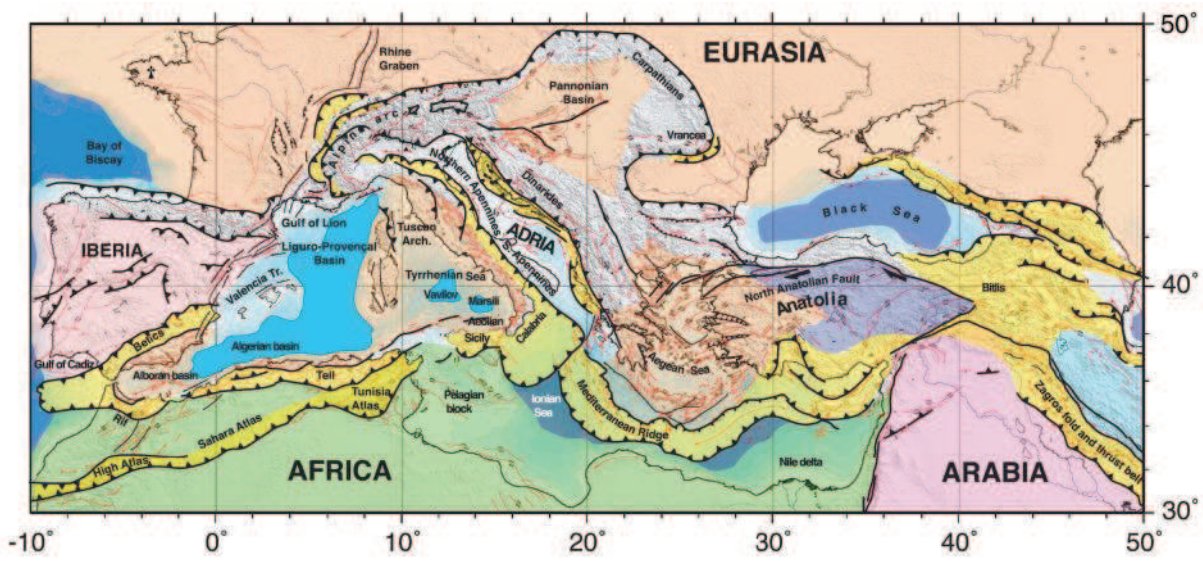

Figure 1.15 : carte tectonique de la région Méditerranéenne. Modifiée d'après *Faccenna et al.* [2014].

Dans ces domaines d'arrière-arc, l'extension est principalement accommodée par de grandes zones de cisaillements ductiles-cassantes à faible pendage : les détachements. Ces structures d'échelle crustale permettent l'exhumation de roches de la croûte moyenne-inférieure, sous la forme de dômes métamorphiques appelés *metamorphic core complexes* (*MCCs*) (figure 1.16). Découvertes dans la province du *Basin & Range* aux Etats-Unis [*Wernicke*, 1981; *Allmendinger et al.*, 1983], ces structures ont ensuite été décrites pour la première fois en mer Egée par *Lister et al.* [1984]. Par la suite, de nombreuses études ont rapporté des structures similaires dans les différents bassins extensifs méditerranéens, permettant ainsi de préciser la cinématique et le timing de l'épisode extensif dans cette région [ex. *Jolivet et al.*, 2008 et références associées].

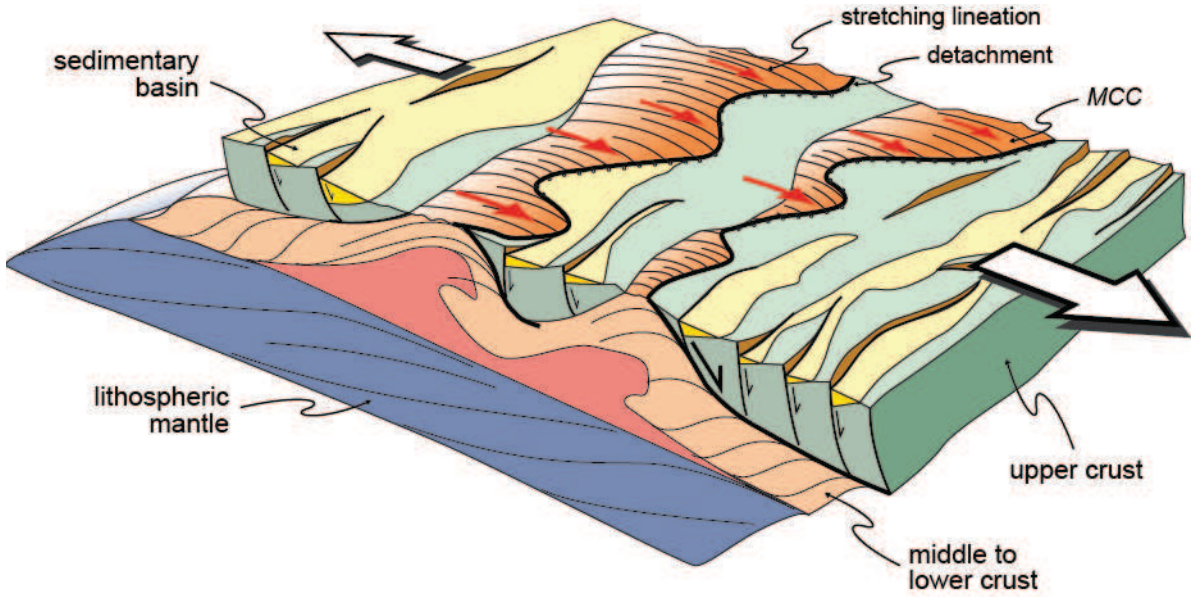

Figure 1.16 : bloc 3D d'une croute continentale étirée en domaine d'arrière-arc où l'extension est accommodée par plusieurs détachements permettant l'exhumation de la croûte moyenne-inférieure sous la forme de dômes métamorphiques. Modifiée d'après *Jolivet et al.* [2009].

La sismicité au niveau de ces marges extensives est globalement caractérisée par des mécanismes au foyer extensifs au niveau des bassins d'arrière-arc et compressifs à proximité de l'interface de subduction [ex. *Faccenna et al.*, 2014 et références associées]. Ces séismes compressifs montrent par ailleurs des magnitudes plus faibles que ceux qui se produisent le long des marges compressives (figure 1.13) [*Uyeda & Kanamori*, 1979]. Cependant, en 2004, un séisme de magnitude 9,2 s'est déclenché dans la région de Sumatra, en Indonésie [ex. *Lay et al.*, 2005], pourtant caractérisée par la

subduction d'une lithosphère océanique ancienne sous une marge active en extension (figure 1.10). Cet évènement laisse à penser que la relation entre sismicité, régime tectonique et dynamique de subduction implique d'autres paramètres, comme la thermicité au niveau de ces marges, qui peuvent également être des facteurs déterminants dans la génération de ces séismes de forte magnitude [*McCaffrey*, 2008].

Le magmatisme qui s'exprime le long des marges actives extensives peut être réparti en deux groupes : (1) un magmatisme calco-alcalin de type *arc*, similaire à celui qui se développe le long de marges compressives comme les Andes et qui trouve son origine dans la fusion partielle du coin mantellique hydraté et (2) un magmatisme calco-alcalin riche en potassium à moyennement alcalin riche en potassium (i.e. shoshonitique), lié au réchauffement de la lithosphère qui caractérise les domaines d'arrière-arc [*Johnson et al.*, 1978; *Hawkesworth et al.*, 1995]. Ce dernier peut résulter de l'étirement et de la délamination de cette lithosphère ainsi que de la remontée asthénosphérique associée, qui peuvent induire la fusion partielle de la croûte inférieure et du manteau lithosphérique sous-jacent (figure 1.17) [*Tatsumi et al.*, 1989; *Hawkesworth et al.*, 1995; *Pe-Piper & Piper*, 2006]. Ces sources magmatiques peuvent avoir été précédemment métasomatisées alors qu'elles se trouvaient au niveau de l'arc magmatique (qui a migré par la suite), ce qui explique la similitude des signatures géochimique et isotopique du magmatisme d'arc et d'arrière-arc [*Johnson et al.*, 1978]. Un étirement intense de la lithosphère peut finalement conduire à l'ouverture d'un bassin océanique où le magma arrivant à la surface montre une composition asthénosphérique appauvrie (i.e. de type *MORB*$^{(*)}$), similaire aux dorsales médio-océaniques [*Tatsumi et al.*, 1989]. Dans la région Méditerranéenne, le retrait des zones de subduction depuis l'Oligocène s'accompagne d'une migration vers le sud sur plus de 600 km de ce magmatisme de type *arc* et *arrière-arc* qui peut même s'initier dès le Crétacé supérieur en Méditerranée orientale, avec l'arc magmatique de cet âge le long de la chaîne des Balkans (cf. C*hapitre 2*) [*Wilson & Bianchini*, 1999; *Harangi et al.*, 2006; *Pe-Piper & Piper*, 2006].

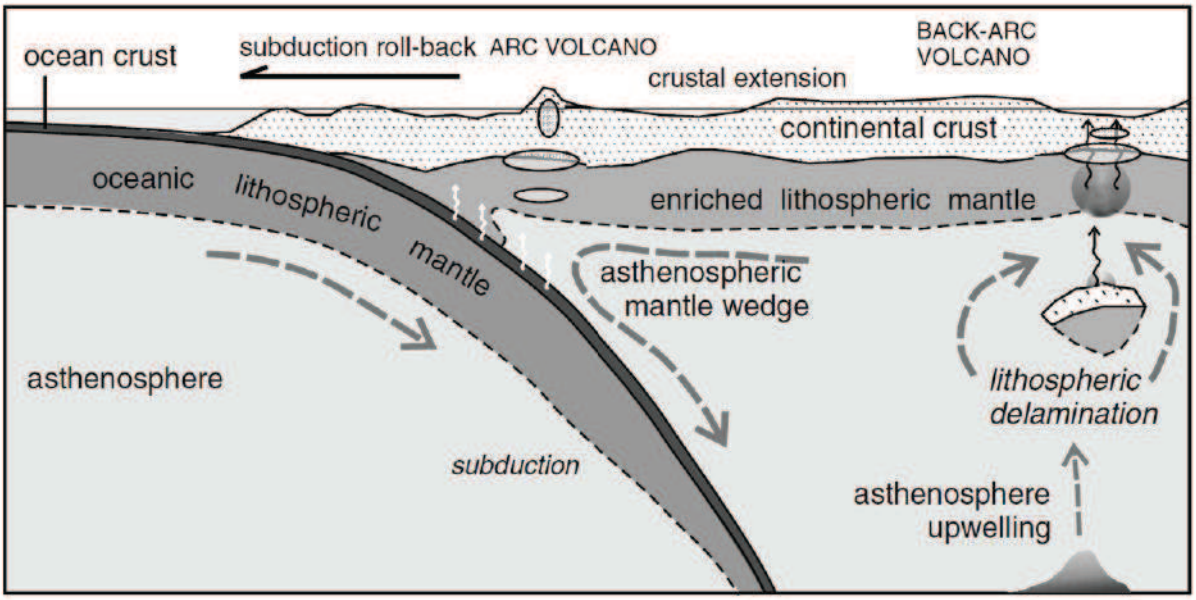

Figure 1.17 : schéma conceptuel d'une zone de subduction se retirant sous une marge continentale extensive où s'exprime un magmatisme à la fois de type *arc* et *arrière-arc* [*Pe-Piper & Piper*, 2006].

La cinématique caractérisant ces zones de subduction ainsi que les processus tectoniques et magmatiques exprimés dans la croûte s'opposent, de par leur observation directe, à des processus plus *inaccessibles*, comme le comportement en profondeur de la lithosphère plongeante et du manteau environnant qui nécessitent, eux, des moyens d'observation indirects. La compréhension de ces mécanismes profonds est pourtant un point crucial du fait du contrôle majeur qu'ils exercent sur la déformation crustale et l'activité magmatique dans ces régions (figures 1.12 et 1.17).

1.4.3. Contraintes sur la dynamique profonde de la subduction

Sismicité et géométrie de la lithosphère en subduction. Le premier paramètre à contraindre concernant la dynamique profonde de la subduction est la géométrie de la plaque plongeante. Celle-ci a été initialement décrite grâce à la sismicité profonde dans ces zones de convergence. En effet, les séismes étant générés uniquement dans la lithosphère cassante, ceux qui se déclenchent à de grandes profondeurs (i.e. supérieures à 100 km) traduisent un mécanisme de rupture dans la lithosphère plongeante froide. Leur alignement forme alors la zone de Wadati-Benioff qui nous renseigne sur l'allure de cette lithosphère en subduction (figure 1.18) [*Wadati*, 1935; *Benioff*, 1955].

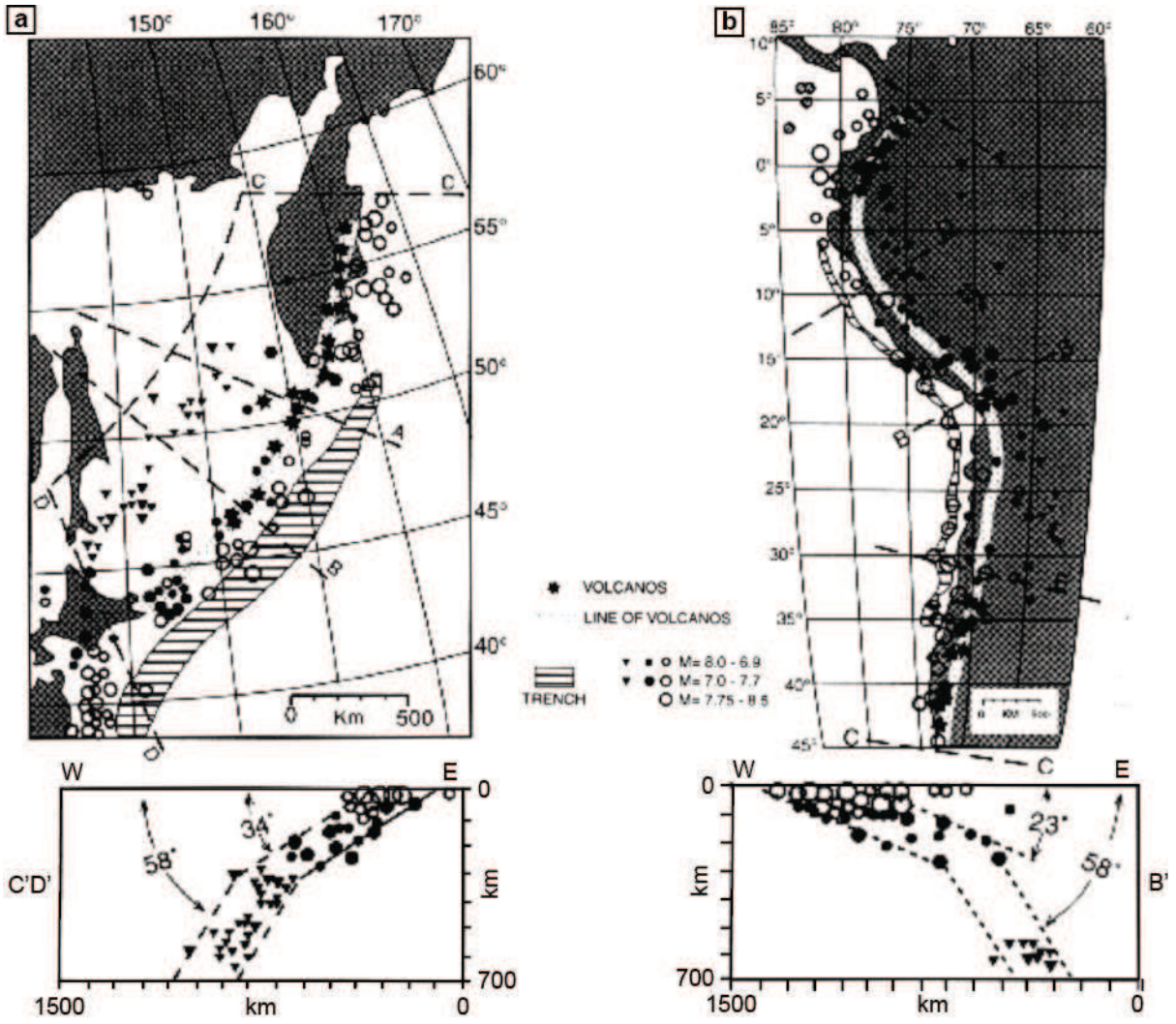

Figure 1.18 : cartes de l'activité sismique et profils verticaux de la répartition de ces séismes le long de la zone de subduction du Japon (a) et de la Cordillère des Andes (b). L'alignement des séismes délimite la zone de Wadati-Benioff qui image la géométrie de la lithosphère en subduction [*Benioff*, 1955].

Tomographie sismique. La vitesse de propagation des ondes sismiques générées par ces séismes a également été utilisée afin de visualiser la structuration profonde des zones de subduction. Celle-ci est en effet dépendante de la densité, et par conséquent, de la nature (i.e. composition chimique) ou encore de la température des roches qu'elles traversent. En partant de cette constatation, des modèles de tomographie sismique ont été développés afin d'imager en 3D les hétérogénéités de densité dans le manteau terrestre [ex. *Sengupta & Toksöz*, 1976; *Fukao et al.*, 1992; *Bijwaard et al.*, 1998; *Kárason & van der Hilst*, 2000; *Li et al.*, 2008]. Extraites de ces modèles, des cartes à des profondeurs données et des coupes verticales permettent de mieux contraindre la géométrie des différentes lithosphères subduites, plus denses que l'asthénosphère environnante (figure 1.19) [ex. *Bijwaard et al.*, 1998;

Kárason & van der Hilst, 2000; *Wortel & Spakman*, 2000; *Piromallo & Morelli*, 2003]. Celles-ci montrent ainsi des variations de pendage dans le manteau supérieur mais également des comportements différents lorsqu'elles atteignent la limite manteau supérieur-inférieur à 660 km de profondeur (figure 1.19b). Enfin, des modèles 3D des anomalies de vitesses sismiques dans le manteau peuvent être réalisés à partir de ces modèles tomographiques, permettant une meilleure visualisation de la géométrie profonde de ces zones de subduction (figure 1.19c) [ex. *Miller et al.*, 2005; *Loiselet*, 2009].

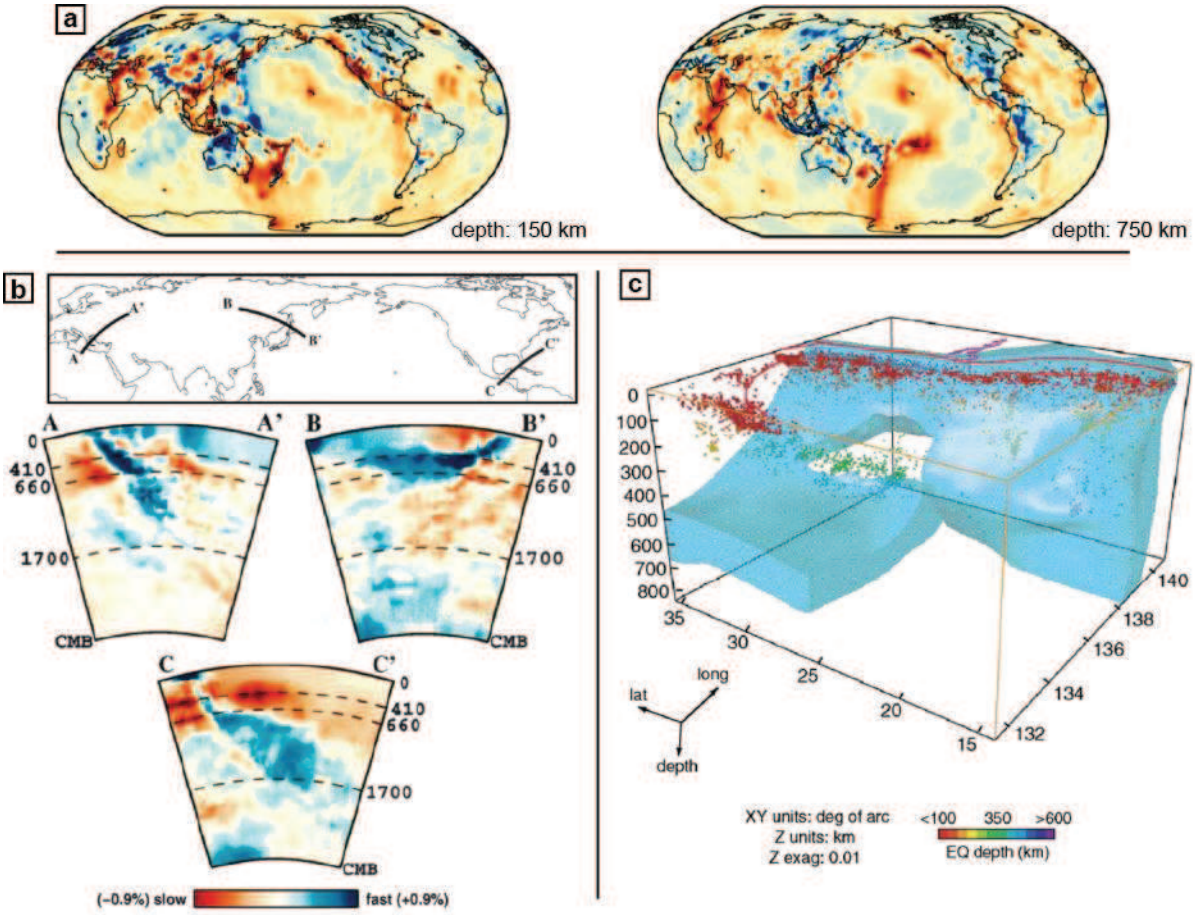

Figure 1.19 : la tomographie sismique dans le manteau terrestre. (a) Cartes mondiales de variations de vitesse des ondes sismiques *P* à 150 et 750 km de profondeur [*Li et al.*, 2008]. (b) Coupes verticales montrant la géométrie de différentes lithosphères en subduction à partir d'un modèle tomographique des ondes *P* [*Kárason & Van der Hilst*, 2000]. *CMB* (*core-mantle boundary*) : limite noyau-manteau. (c) Modèle 3D interprétatif de la géométrie de la lithosphère plongeante sous l'arc Izu-Bonin-Mariannes obtenu à partir d'images tomographiques des ondes *P* [*Miller et al.*, 2005]. Les séismes entre 1967 et 1995 figurent dans ce modèle avec des couleurs indiquant la profondeur de leur épicentre.

Flux asthénosphérique et anisotropie sismique. Un autre processus profond important à contraindre est le flux asthénosphérique qui peut interagir avec la lithosphère plongeante (figure 1.12), modifiant ainsi la dynamique de la zone de subduction et la réponse tectonique en surface [*Heuret & Lallemand*, 2005; *Faccenna & Becker*, 2010; *Husson*, 2012]. Des études récentes ont également montré que ces flux peuvent en partie contrôler directement la déformation de la lithosphère non engagée dans un processus de subduction, en accord avec les premières hypothèses de *Holmes* [1931] sur le couplage entre convection mantellique et dérive des continents [*Jolivet et al.*, 2009; *Becker & Faccenna*, 2011; *Schellart & Moresi*, 2013; *Sternai et al.*, 2014]. *Jolivet et al.* [2009] ont ainsi montré des similitudes entre l'orientation des flux mantelliques (estimée à partir de mesures de l'anisotropie sismique dans le manteau, cf. ci-dessous) et de la déformation finie dans les domaines extensifs d'arrière-arc dans la région Méditerranéenne, qui suggèrent à un couplage asthénosphère-lithosphère dans ces domaines de croûte amincie et chaude. En plus de ce contrôle direct ou indirect (via la déformation du panneau plongeant) sur le régime tectonique des marges actives, ces flux asthénosphériques peuvent entrainer une remontée du manteau profond jusqu'à la base de la lithosphère, notamment s'ils sont caractérisés par une forte composante poloidale (i.e. dans le plan vertical). Cet apport de matériel chaud peut générer de la fusion partielle à la fois de la croûte mais également du manteau, entraînant la mise en place de systèmes magmatiques, potentiellement associés à des systèmes minéralisés (figures 1.9 et 1.17).

A l'échelle du manteau terrestre, le flux asthénosphérique s'organise en grandes cellules convectives, caractérisées par du matériel froid et dense qui s'enfonce au niveau des zones de subduction et du matériel chaud, moins dense, remontant sous la forme de panaches mantelliques (figure 1.20a) [ex. *Parsons & McKenzie*, 1978; *Gurnis*, 1988; *Tackley*, 2000; *Courtillot et al.*, 2003]. Aux abords des zones de subduction, ce flux peut être largement perturbé en raison des géométries complexes des panneaux plongeants, formant ainsi des cellules de convection *locales* (ex. région Méditerranéenne, figure 1.20b) [*Faccenna & Becker*, 2010; *Becker & Faccenna*, 2011].

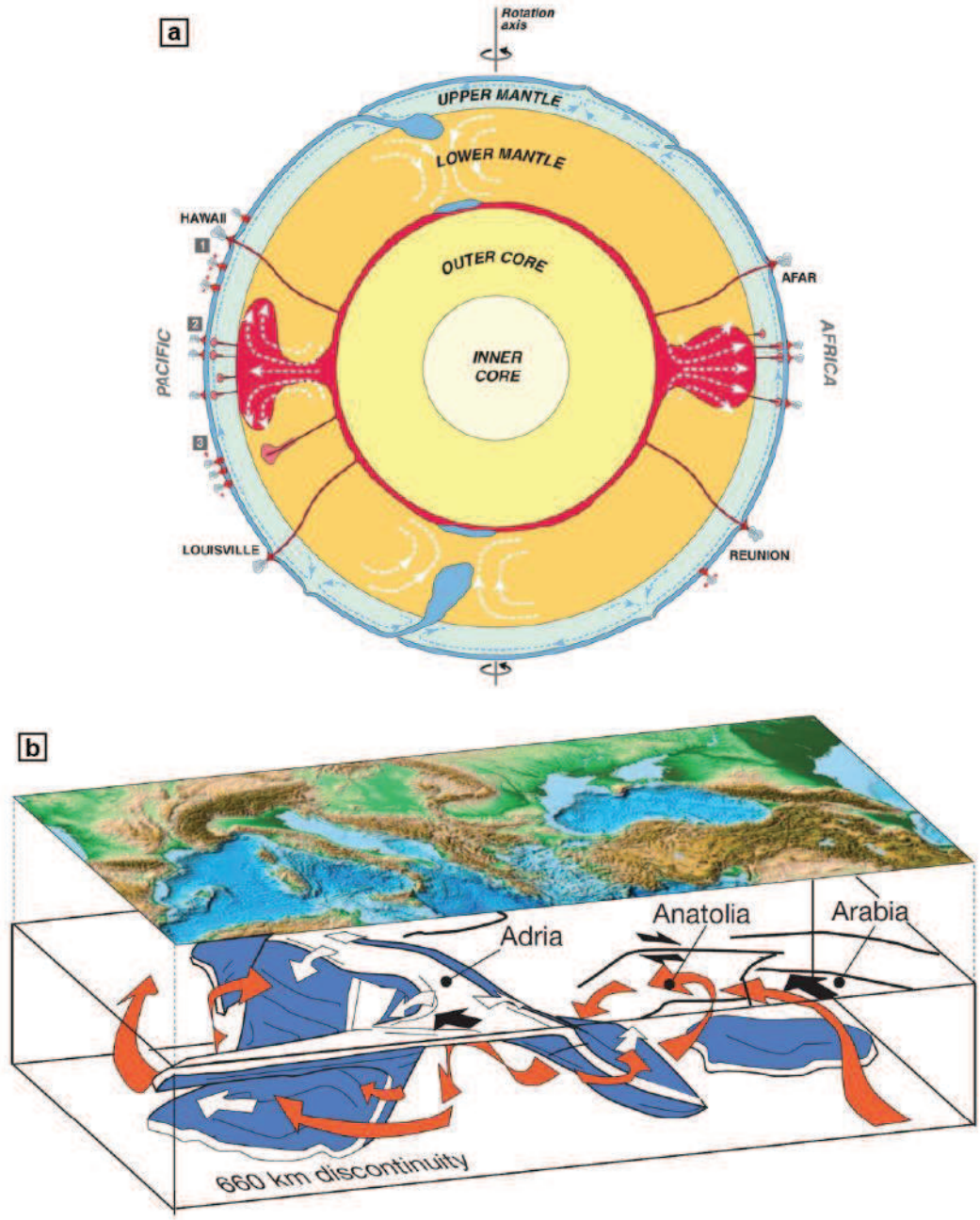

Figure 1.20 : la convection mantellique à différentes échelles. (a) Coupe schématique de la Terre montrant la dynamique mantellique caractérisée par de grandes cellules de convection dans le manteau supérieur et inférieur. [*Courtillot et al.*, 2003]. (b) Bloc schématique de la géométrie des zones de subduction en profondeur et des flux asthénosphériques associés dans la région Méditerranéenne [*Faccenna & Becker*, 2010].

Cette convection à différentes échelles entraine une déformation de la fabrique cristalline de l'olivine qui tend à s'aligner dans le sens de ce fluage, créant ainsi une anisotropie cristalline (ou structurale) dans le manteau [*Zhang & Karato*, 1995; *Karato et al.*, 2008]. Les ondes sismiques qui se déplacent dans le manteau présentent deux composantes orthogonales qui, en traversant un milieu

anisotrope, s'orientent en fonction de cette anisotropie et se propagent à des vitesses différentes (i.e. mécanisme de *shear wave splitting*, figure 1.21a) [*Silver*, 1996; *Savage*, 1999]. En surface, la mesure de ce phénomène permet d'identifier la direction de polarisation de la composante de l'onde la plus rapide ainsi que le temps de retard entre ces deux composantes. Ces paramètres fournissent ainsi des contraintes sur l'orientation ainsi que l'intensité de cette anisotropie cristalline qui peut être interprétée comme un marqueur du flux asthénosphérique, notamment dans les zones de subduction (figure 1.21b) [ex. *Russo & Silver*, 1994; *Long & Silver*, 2008; *Jolivet et al.*, 2009; *Long & Becker*, 2010]. Ces informations restent néanmoins à considérer avec précaution car de nombreux facteurs peuvent modifier le signal sismique (ex. hydratation du manteau, structure de la lithosphère plongeante) [*Faccenda et al.*, 2008; *Karato et al.*, 2008; *Long & Becker*, 2010].

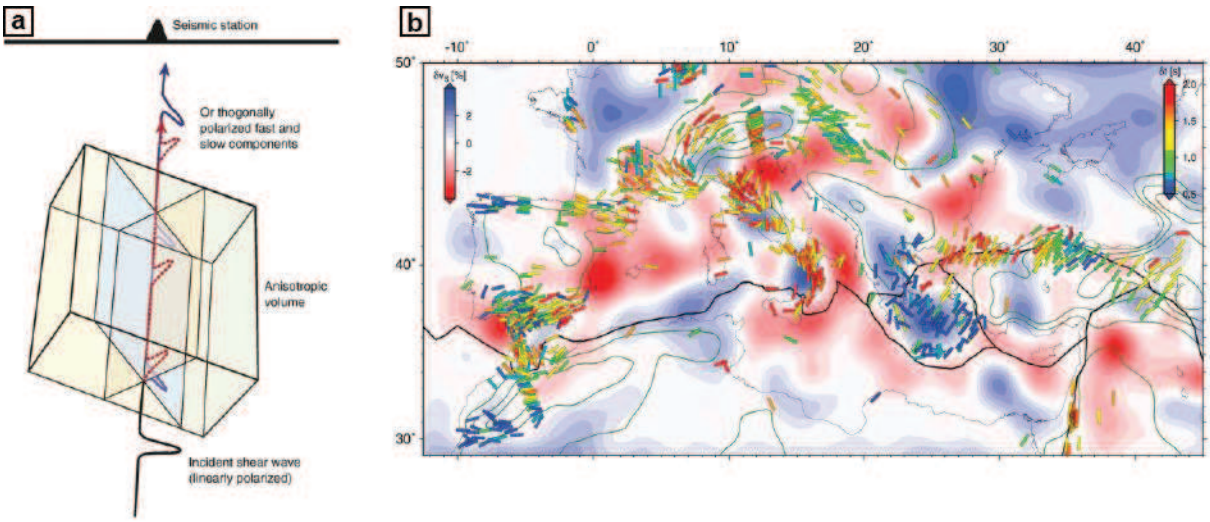

Figure 1.21 : l'anisotropie sismique dans le manteau. (a) Schéma conceptuel de la propagation des ondes sismiques dans un milieu anisotrope [*Long & Becker*, 2010]. (b) carte tomographique des ondes *S* pour la région Méditerranéenne où les anomalies de vitesses (δv_s) entre 100 et 400 km de profondeur sont moyennées. Les mesures d'anisotropie sismique disponibles sont également représentées, leur couleur indiquant le décalage temporel (δt) entre les deux composantes des ondes sismiques [*Faccenna et al.*, 2014 et références associées].

1.4.4. Dynamique de subduction : l'apport de la modélisation

L'ensemble des contraintes géologiques et géophysiques relatives à la dynamique de la subduction a permis d'établir des modèles conceptuels de l'évolution crustale et mantellique de ces zones de convergence (figures 1.5, 1.9, 1.17 et 1.20b). Ces modèles ne considèrent cependant aucune contrainte physique, ce qui amène à de nombreuses discussions quant à leur validité. Le développement de

méthodes de modélisation analogiques ou numériques depuis plusieurs décennies a permis d'y remédier en partie car elles intègrent un certain nombre de lois physiques qui agissent sur les processus géologiques que l'on cherche à contraindre. En contrepartie, ces modèles sont limités par les contraintes matérielles (ex. puissance de calcul), nécessitant une simplification des processus modélisés qui peut également être discutable aux vues de la complexité des systèmes naturels. Il existe plusieurs catégories de modèles, analogiques et numériques, permettant de discuter des processus mantelliques et/ou crustaux qui peuvent régir l'évolution des zones de subduction. Néanmoins, l'ensemble des modèles décris ci-dessous font l'hypothèse que les roches, à l'échelle des temps géologiques, se comportent comme des fluides très visqueux, ce qui permet de décrire leur mouvement (et donc leur déformation) en utilisant une simple loi d'écoulement laminaire (i.e. équations de *Navier-Stokes* ou de *Stokes* dans le cas d'un écoulement lent) couplée à l'équation de transport de la chaleur (par conduction et convection).

Les modèles géodynamiques globaux. Ces modèles sont réalisés à l'échelle du manteau terrestre, ce qui permet de visualiser le flux mantellique global décrit comme la convection d'un fluide visqueux (i.e. l'asthénosphère) [ex. *Hager & O'Connell*, 1981; *Gurnis*, 1988; *Davaille & Jaupart*, 1993; *Tackley et al.*, 1993; *Guillou-Frottier & Jaupart*, 1995; *van Keken et al.*, 1997]. Dans ces modèles, la limite supérieure froide possède un comportement plus rigide (i.e. viscosité plus élevée) que le manteau convectif sous-jacent qui entraine alors le déplacement de blocs rigides le long de zones où la déformation se concentre [*Tackley*, 2000; *Bercovici*, 2003; *Coltice et al.*, 2007, 2013; *Rolf et al.*, 2012]. Un tel système permet d'approximer le mouvement de plaques tectoniques accommodé au niveau de zones de divergence (i.e. rifting continental, dorsales médio-océaniques) et de convergence (i.e. subduction, collision). Ces modèles, initialement définis en 2D (figure 1.22a) [ex. *Gurnis*, 1988], ont ensuite évolué grâce aux nouvelles techniques de modélisation qui ont permis de développer des modèles 3D sphériques, plus complexes et plus proches de la structuration interne réelle de la Terre (figure 1.22b) [ex. *Rolf & Tackley*, 2011]. Bien qu'intégrant une convection mantellique globale qui contrôle le déplacement de lithosphères rigides, ces modèles globaux ne possèdent pas une résolution suffisante pour reproduire certains processus de plus petite échelle (notamment crustaux) actifs dans les environnements de subduction.

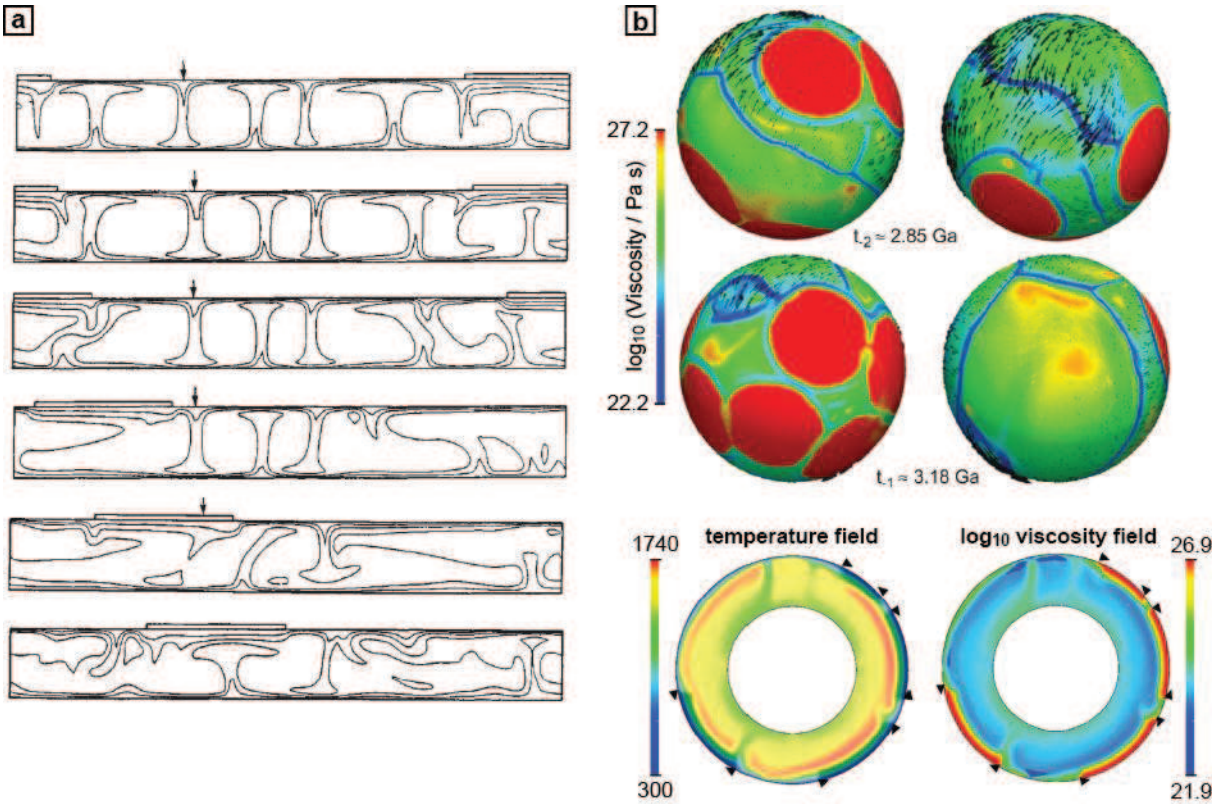

Figure 1.22 : les modèles géodynamiques globaux. (a) Simulation numérique en 2D d'un champ convectif mantellique entrainant des blocs continentaux en surface. Ce champ est visualisé par ses isothermes. La flèche noire indique le plongement de matériel froid [*Gurnis*, 1988]. (b) Modèle 3D sphérique de convection mantellique contrôlant le mouvement de blocs rigides (en rouge) en surface [*Rolf & Tackley*, 2011]. Les deux panels en haut montrent l'évolution de ce modèle pour des pas de temps à 2,85 et 3,18 Ga. En plus des lithosphères continentales en rouge (i.e. forte viscosité), les lithosphères océaniques apparaissent en vert et les zones de divergences (i.e. dorsales médio-océaniques) et de convergence (i.e. subduction) en bleu (i.e. faible viscosité). Le panel du bas montre une section radiale de ce modèle où figure le champ de température (à gauche) et de viscosité (à droite). Les triangles noirs représentent les limites des continents.

Les modèles de subduction à l'échelle lithosphérique. Ces modèles sont réalisés à l'échelle de la zone de subduction afin d'illustrer les mécanismes propres à l'évolution de celle-ci. Ils peuvent être analogiques ou numériques et réalisés en 2D ou en 3D (figure 1.23). Grâce à ces modèles, il a ainsi été possible d'apporter des contraintes physiques sur la nature des flux mantelliques notamment aux limites de ce panneau plongeant [ex. *Guillou-Frottier et al.*, 1995; *Funiciello et al.*, 2003; *Kincaid & Griffiths*, 2003; *Jadamec & Billen*, 2010; *Li et al.*, 2013], les processus d'exhumation des roches dans la croûte [ex. *Burov et al.*, 2001, 2014; *Gerya et al.*, 2002; *Yamato et al.*, 2008], les processus de déformation crustale [*Govers & Wortel*, 2005; *Schellart & Moresi*, 2013; *Capitanio*, 2014; *Sternai et*

al., 2014], la genèse des magmas [ex. *Zhu et al.*, 2009, 2013; *Gerya & Meilick*, 2011; *Bouilhol et al.*, 2015], etc.

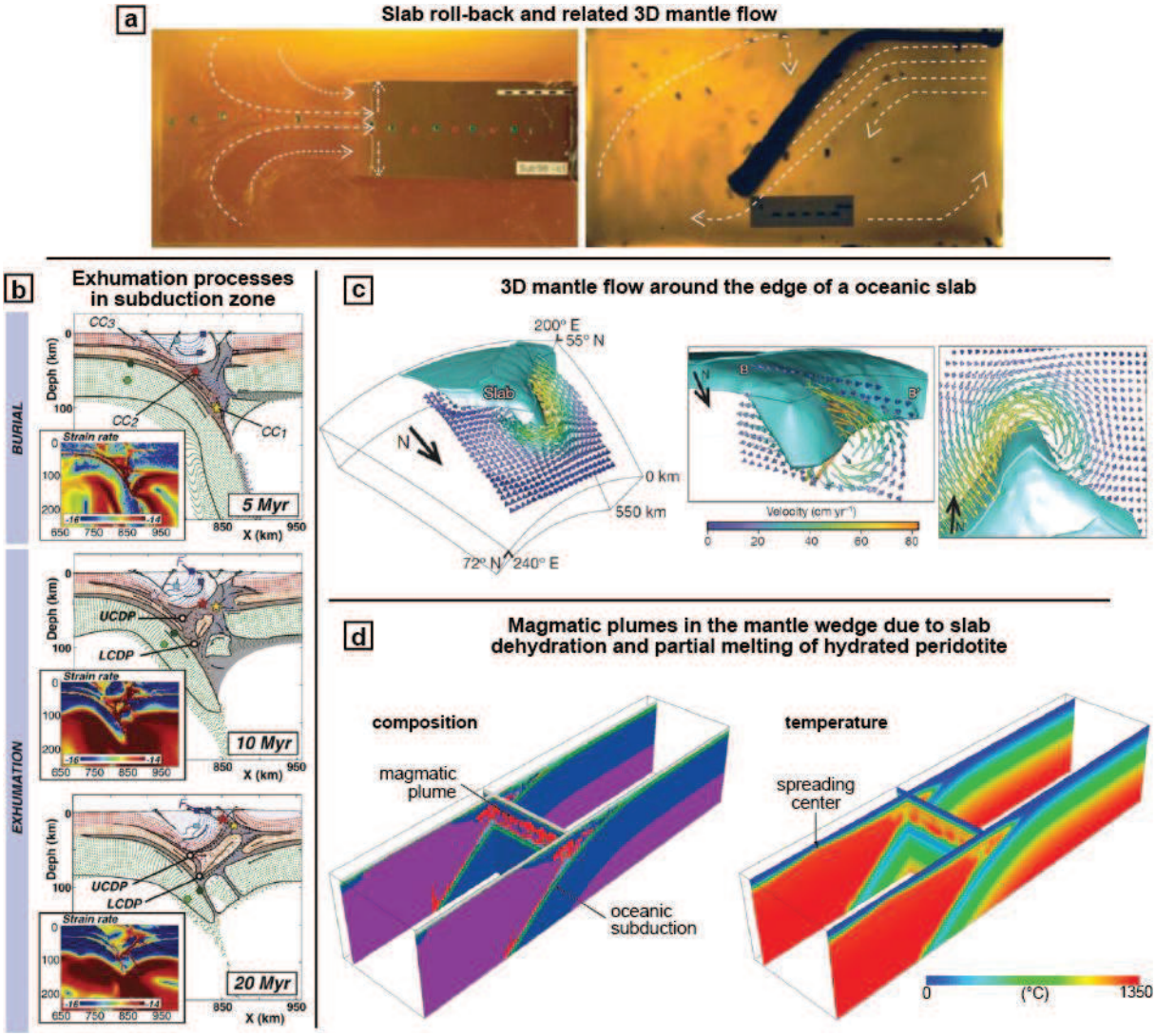

Figure 1.23 : modèles de subduction à l'échelle lithosphérique. (a) Vue du dessus et latérale d'un modèle analogique d'une lithosphère en subduction se retirant spontanément où sont mis en évidence des flux mantelliques toroïdaux (i.e. dans un plan horizontal) et poloïdaux (i.e. dans un plan vertical) [*Funiciello et al.*, 2003]. (b) Modèle numérique 2D d'une subduction continentale mettant en évidence l'exhumation de blocs rigides au sein d'une zone ductile (en gris) [*Yamato et al.*, 2008]. Les taux de déformation pour chacun des pas de temps sont représentés en encart. (c) Modèle numérique 3D montrant la distribution du flux mantellique en bordures d'une lithosphère en subduction [*Jadamec & Billen*, 2010]. (d) Modèle numérique 3D d'une zone de subduction océanique montrant la genèse et la remontée de roches partiellement fondues au niveau du coin mantellique [*Zhu et al.*, 2009].

Ces modèles globaux et lithosphériques sont donc de bons outils afin d'appréhender les liens qui peuvent exister entre dynamique mantellique et crustale, notamment au niveau des zones de subduction. De plus, ils permettent une meilleure visualisation tridimensionnelle de ces processus. Cependant, bien que fournissant des contraintes physiques, ces modèles nécessitent eux-mêmes des contraintes géologiques qui ne peuvent être apportées qu'après un travail poussé d'acquisition de données de terrain et de mesures géophysiques.

1.5. Pourquoi s'intéresser à la région Méditerranéenne ?

La région Méditerranéenne (figure 1.15) constitue l'extrémité ouest de la marge active Téthysienne qui s'étend, à l'est, à travers les chaînes du Zagros et de l'Himalaya, jusqu'à la zone de subduction indonésienne. Dans sa partie occidentale (figure 1.24), la chaîne Téthysienne (parfois appelée chaîne Alpine s.l.) résulte de la convergence depuis le Mésozoïque entre les plaques Afrique et Eurasie qui a induit la fermeture progressive de l'océan Téthys [ex. *Dercourt et al.*, 1986; *Stampfli & Borel*, 2002; *Barrier & Vrielynck*, 2008; *Stampfli & Hochard*, 2009].

L'évolution précoce de ce système est caractérisée par une zone de subduction océanique à vergence nord sous la marge Eurasienne (figure 1.24a). Au cours du temps, plusieurs blocs continentaux (ex. l'Apulie, l'Inde, l'Arabie) se sont successivement séparés de l'Afrique et ont migré vers le nord, jusqu'à interagir avec cette marge active, induisant des épisodes de subduction et/ou de collision continentale qui ont permis la construction de grandes chaînes orogéniques (ex. les Alpes, le Zagros, l'Himalaya, figures 1.24b et c).

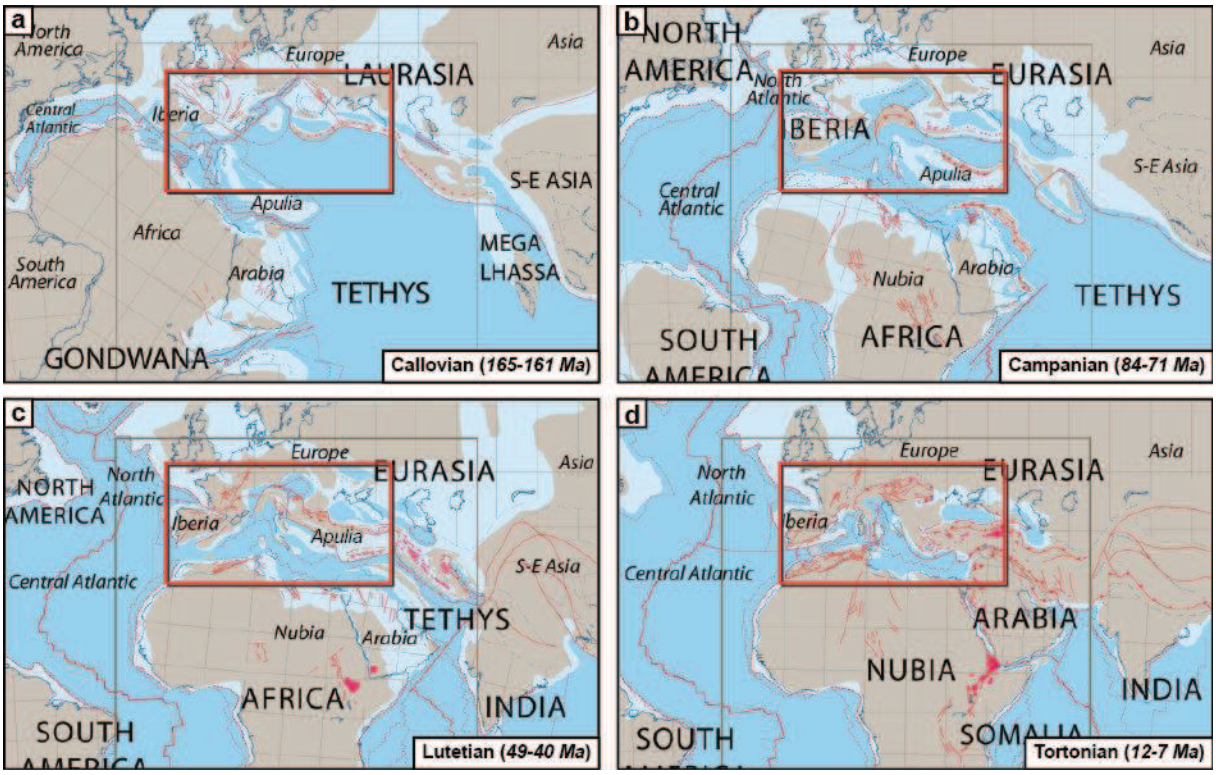

Figure 1.24 : reconstructions paléotectoniques de la chaîne Téthysienne au Callovien (a), Campanien (b), Lutétien (c) et Tortonien (d). Le rectangle rouge localise la région Méditerranéenne (figure 1.15) [*Barrier & Vrielynck*, 2008].

Dans la région Méditerranéenne, et notamment dans sa partie orientale (figure 1.25), cette évolution géodynamique complexe a résulté en une migration progressive vers le sud de la marge active Téthysienne où se sont accrétés plusieurs écailles crustales formant un prisme orogénique (i.e. la chaîne des Hellénides-Taurides, cf. *Chapitre 2*) [ex. *Le Pichon & Angelier*, 1979; *Bonneau & Kienast*, 1982; *Jolivet et al.*, 2003; *van Hinsbergen et al.*, 2005a; *Brun & Sokoutis*, 2010; *Jolivet & Brun*, 2010].

En réponse à l'accélération du retrait de la zone de subduction Hellénique à l'Oligocène, cette chaîne s'est partiellement effondrée sous l'effet de contraintes extensives, permettant l'ouverture d'un vaste domaine d'arrière-arc (i.e. le domaine Egéen) où des roches de la croûte moyenne à inférieure ont été exhumées sous la forme de dômes métamorphiques (i.e. le massif du Rhodope, du Menderes ou encore les Cyclades, figures 1.16 et 1.25) [*Lister et al.*, 1984; *Urai et al.*, 1990; *Gautier et al.*, 1993; *Sokoutis et al.*, 1993; *Bozkurt & Oberhänsli*, 2001; *Vanderhaeghe*, 2004; *Bonev et al.*, 2006; *Brun & Sokoutis*, 2007; *Brun & Faccenna*, 2008; *Gessner et al.*, 2013; *Jolivet et al.*, 2013].

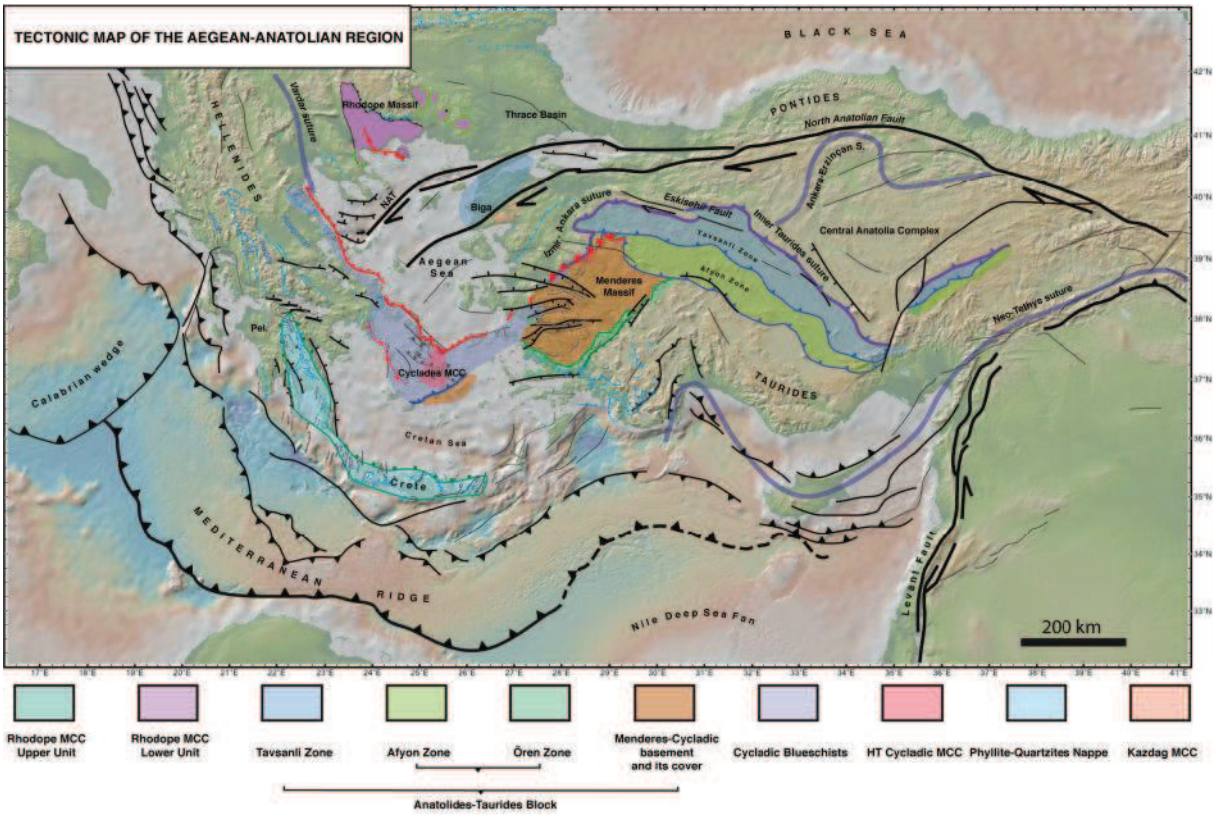

Figure 1.25 : carte tectonique de la Méditerranée orientale montrant les principales structures actives (lignes noires), les principales zones de suture océanique (lignes épaisses violettes ou bleues), les principaux chevauchements constituant la chaîne des Hellénides et des Taurides (lignes fines bleues), les principales structures extensives à faible pendage (i.e. détachements, lignes rouges). Modifiée d'après *Jolivet et al.* [2013].

Dans cette région, mais également dans l'ensemble du domaine Méditerranéen, les données géophysiques disponibles (ex. tomographie sismique, anisotropie sismique, figures 1.21b et 1.26a) suggèrent un ensemble de segments de panneaux plongeants (i.e. anomalies de vitesse des ondes sismiques négatives) qui évoluent de manière indépendante les uns des autres [*De Boorder et al.*, 1998; *Wortel & Spakman*, 2000; *Piromallo & Morelli*, 2003; *Berk Biryol et al.*, 2011; *Salaün et al.*, 2012; *Paul et al.*, 2014]. Cette géométrie contraste avec l'aspect continu du panneau plongeant à plus grande profondeur (i.e. plus ancien) (figure 1.26b), ce qui laisse à penser que des épisodes relativement récents de déchirure et/ou détachement ont affecté cette lithosphère plongeante, complexifiant sa géométrie et par conséquent les flux mantelliques et la déformation crustale associés (figure 1.20b) [ex. *Faccenna et al.*, 2003; *Govers & Wortel*, 2005; *Brun & Sokoutis*, 2010; *Faccenna & Becker*, 2010; *Becker & Faccenna*, 2011; *Özbakır et al.*, 2013; *Jolivet et al.*, 2013].

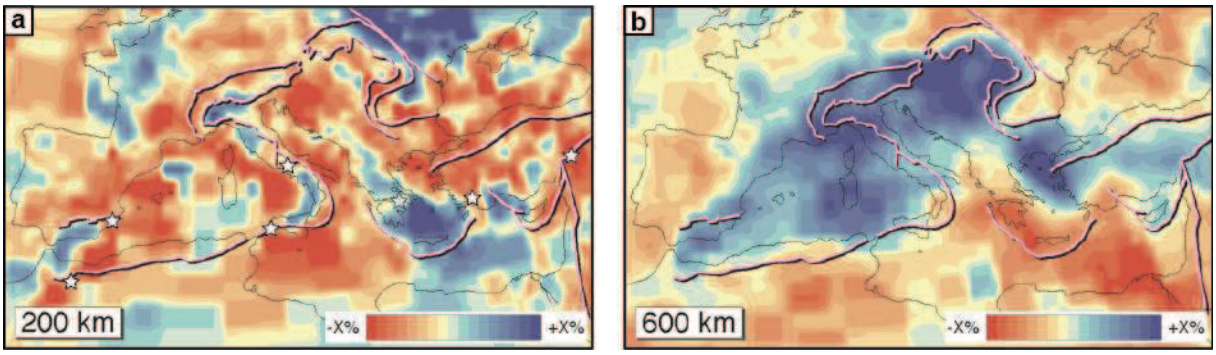

Figure 1.26 : modèle tomographique d'anomalies de vitesse des ondes sismiques *P* dans la région Méditerranéenne [*Wortel & Spakman*, 2000]. (a) Coupe horizontale à 200 km de profondeur. Les étoiles blanches représentent les anomalies de vitesse négative (rouge) pouvant être interprétées comme des déchirures ou détachement des lithosphères subduites. L'étoile apparait en transparence si cette déchirure est hypothétique. (b) Coupe horizontale à 600 km de profondeur montrant une anomalie de vitesse sismique positive continue pouvant être interprétée comme un unique panneau plongeant au niveau de la limite manteau supérieur-inférieur.

Dans une étude récente (i.e. *Sternai et al.* [2014], cf. *Annexe B. Driving the upper plate deformation by slab rollback and mantle flow*), nous avons ainsi montré, grâce à des modèles numériques 3D, que l'interaction entre des processus de retrait de la subduction, collision continentale et déchirure du panneau plongeant contrôle l'ouverture d'un domaine d'arrière-arc conjointement avec l'extrusion latérale d'un bloc continental le long d'une zone localisée de déformation décrochante (figures 1.23c et 1.27a). Cette étude montre également que le flux asthénosphérique sous-jacent toroïdal peut entrainer un cisaillement à la base de la lithosphère, en particulier lorsque celle-ci est chaude et étirée, contrôlant ainsi en partie cette déformation crustale dans le domaine arrière-arc (figure 1.27b). Ces résultats sont en accord avec d'autres modélisations numériques similaires [*Li et al.*, 2013; *Capitanio*, 2014; *Duretz et al.*, 2014; *Magni et al.*, 2014] et montrent également de fortes similitudes en termes de géométrie de la zone de subduction et de déformation crustale avec l'évolution tectonique de la Méditerranée orientale depuis l'Oligocène. En effet, l'interaction entre le retrait de la zone de subduction des Hellénides vers le sud et la collision Arabie-Eurasie plus à l'est a conduit à l'extrusion progressive du bloc Anatolie, notamment accommodé par la faille décrochante nord-Anatolienne qui vient se propage vers l'ouest, jusqu'au domaine extensif d'arrière-arc Egéen (figure 1.25) [*Armijo et al.*, 1999; *Şengör et al.*, 2005; *Faccenna et al.*, 2006; *Reilinger et al.*, 2006; *Le Pichon & Kreemer*, 2010].

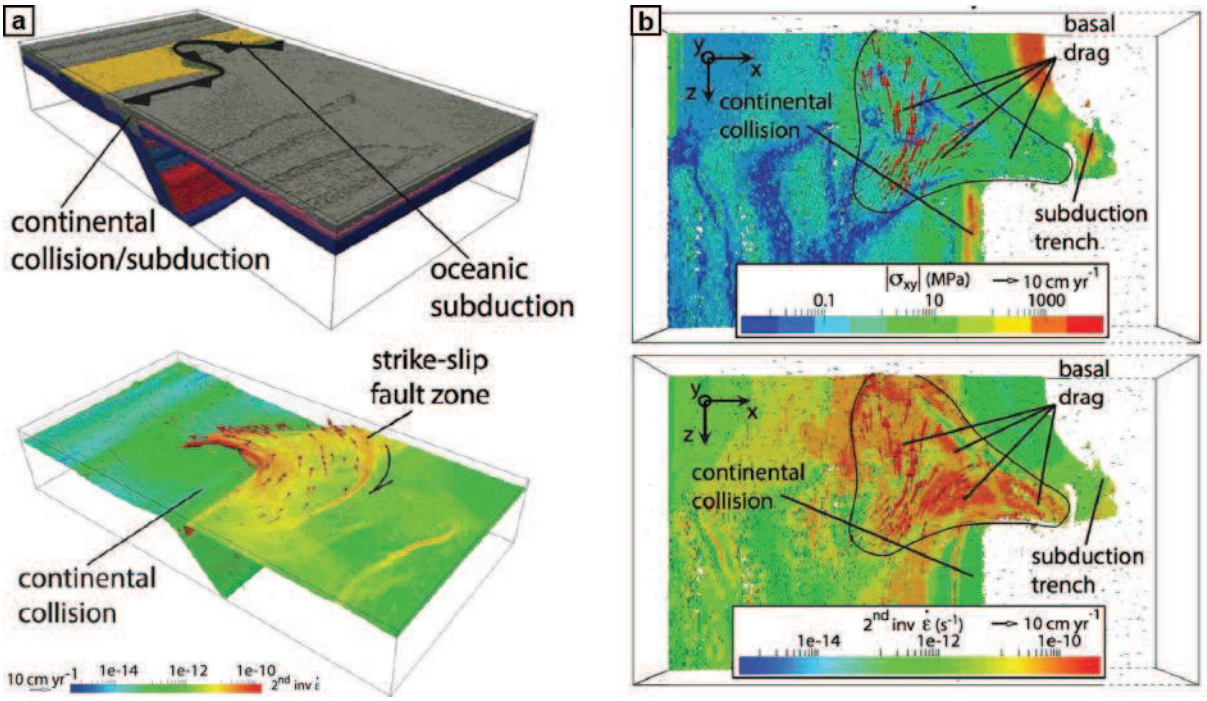

Figure 1.27 : modèle numérique 3D montrant l'évolution d'une zone de transition entre subduction océanique et subduction/collision continentale [*Sternai et al.*, 2014]. (a) Vue 3D du modèle mis en évidence par sa composition (panel du haut). Taux de déformation dans la croûte de la lithosphère supérieure au moment de l'extrusion latérale d'un bloc continental vers le domaine extensif d'arrière-arc (panel du bas). (b) Contrainte cisaillante (panel du haut) et taux de déformation à la base de la croûte de la plaque supérieure (panel du bas). La zone délimitée par la ligne noire est directement en contact avec l'asthénosphère. Pour plus de détails, cf. *Annexe B*.

La région Méditerranéenne, et notamment sa partie orientale, a donc connu une histoire géodynamique longue et complexe où une grande variété de processus crustaux et mantelliques ont été identifiés. Cette évolution depuis le Crétacé supérieur s'est traduite par une succession d'environnements d'arc et d'arrière-arc associés à différentes provinces magmatiques dont l'origine a été largement discutée dans la littérature (cf. C*hapitre 2*) [ex. *Pe-Piper & Piper*, 1989, 2006; *Altherr & Siebel*, 2002; *Keskin*, 2003; *Marchev et al.*, 2004a; *Harangi et al.*, 2006; *Agostini et al.*, 2007; *Dilek & Altunkaynak*, 2009; *Stouraiti et al.*, 2010; *Bolhar et al.*, 2010; *Seghedi et al.*, 2013; *Ersoy & Palmer*, 2013]. Souvent associées à ces systèmes magmatiques, plusieurs provinces métallogéniques ont également été mises en évidence dans cette région [ex. *Janković*, 1997; *Berza et al.*, 1998; *Heinrich & Neubauer*, 2002; *Skarpelis*, 2002; *Marchev et al.*, 2005; *von Quadt et al.*, 2005; *Yigit*, 2009, 2012] avec pour certaines d'entre elles des gisements majeurs en exploitation (figure 1.4). Cependant, de

rares études se sont focalisées sur le lien entre ces minéralisations et la dynamique de la subduction est-Méditerranéenne [*De Boorder et al.*, 1998; *Lips*, 2002; *Neubauer*, 2002; *Loiselet et al.*, 2010; *Bertrand et al.*, 2014; *Richards*, 2014] et aucune n'intègre la complexité 3D de son évolution mantellique et crustale mise en évidence ci-dessus (figures 1.15, 1.20b, 1.25 et 1.26).

1.6. Objectifs et démarche de cette étude

Comme brièvement introduit au début de ce chapitre, l'objectif de ce travail de thèse est d'identifier les processus mantelliques et crustaux se rapportant à l'évolution d'une zone de subduction qui contrôlent la genèse de systèmes minéralisés. L'absence de telles contraintes en Méditerranée orientale justifie le choix de cette zone d'étude, d'autant plus qu'il existe un grand nombre de données géologiques et géophysiques sur cette région, permettant d'établir une évolution tectonique et magmatique robuste.

La finalité d'une telle étude est double et pourrait s'appliquer à d'autres zones de subduction dans le monde, que l'évolution géodynamique soit similaire ou non.

(1) Fournir, dans les régions du globe où l'évolution tectonique et magmatique d'une zone de subduction (passée ou encore active) est bien contrainte, des métallotectes d'ordre régional pour l'exploration minière.

(2) A l'inverse, utiliser les données métallogéniques disponibles sur une région donnée afin de mieux contraindre l'évolution géodynamique d'une zone de subduction donnée.

Afin d'atteindre ces objectifs, l'étude à mener doit être réalisée depuis l'échelle lithosphérique (i.e. de la zone de subduction) jusqu'à l'échelle de l'affleurement afin d'avoir un panel complet des processus et facteurs (notamment structuraux) qui peuvent contrôler la concentration de métaux dans la croûte. Pour ce faire, ce travail de thèse s'est articulé en quatre axes majeurs qui constituent les quatre chapitres suivants de ce manuscrit.

Chapitre 2. Reconstructions cinématiques et évolution du magmatisme en Méditerranée orientale. Ce chapitre compile un grand nombre de données stratigraphiques, pétrologiques, métamorphiques, structurales, paléomagnétiques et magmatiques qui m'ont permis de réaliser de nouvelles reconstructions cinématiques de la région est-Méditerranéenne. Celles-ci décrivent, avec une précision encore jamais atteinte jusqu'à présent, l'évolution géodynamique de cette région depuis le Crétacé supérieur et permettent de discuter des processus mantelliques et crustaux qui ont pu contrôler la déformation crustale et la distribution spatiale et temporelle du magmatisme. Ce chapitre pose ainsi une base géodynamique solide sur laquelle je m'appuierai pour la suite de cette étude.

Chapitre 3. Distribution des minéralisations et reconstructions de la dynamique de subduction. Ce chapitre présente les liens que j'ai mis en évidence entre l'évolution de la zone de subduction est-Méditerranéenne et la distribution spatiale et temporelle des minéralisations et ce, depuis le Crétacé supérieur. Ce travail d'échelle lithosphérique se base sur les reconstructions cinématiques de la région décrites dans le chapitre précédent, auxquelles j'ai intégré un grand nombre d'occurrences minéralisées extraites de différentes bases de données métallogéniques.

Chapitre 4. Dômes extensifs et contrôle structural des systèmes minéralisés : le cas de l'île de Mykonos. Ce chapitre s'intéresse, à travers une étude de terrain, aux minéralisations qui affleurent sur l'île de Mykonos dans l'archipel des Cyclades. Dans cette région, plusieurs dômes métamorphiques ont été exhumés au cours de l'Oligocène-Miocène, le long de systèmes de détachements, associés à une intense activité magmatique. Ce travail d'échelle locale permet ainsi de mettre en évidence les liens génétiques qui existent sur le terrain entre ces grandes structures extensives à faible pendage, les systèmes intrusifs plutoniques et les systèmes minéralisés.

Chapitre 5. Contrôle mantellique et crustal sur la genèse du magmatisme : approche numérique. Ce chapitre présente les facteurs contrôlant la genèse et le transport des magmas dans un environnement de subduction de faible extension latérale que j'ai mis en évidence à partir de modèles numériques 3D. J'ai réalisé ces derniers en utilisant le code *I3ELVIS* développé par Taras Gerya (et

collaborateurs) [ex. *Gerya*, 2010] à l'*ETH Zurich*. Ces résultats permettent d'apporter des contraintes physiques sur les processus mantelliques mais également crustaux qui interagissent avec l'évolution des systèmes magmatiques, pouvant être potentiellement associés à des systèmes minéralisés.

Dans un chapitre final (i.e. *chapitre 6. Synthèse Générale : dynamique de subduction et minéralisations en Méditerranée orientale et ailleurs*), je discute de l'influence de la dynamique mantellique et crustale sur l'activité hydrothermale le long de la zone de subduction est-Méditerranéenne, afin d'identifier les processus cruciaux à la mise en place de grandes provinces métallogéniques. Enfin, je propose de nouvelles pistes de recherche qui pourraient s'inscrire dans la continuité de ce travail de thèse.

Chapitre 2

Reconstructions cinématiques et évolution du magmatisme en Méditerranée orientale

Kinematic reconstructions and magmatic evolution illuminating crustal and mantle dynamics of the eastern Mediterranean region since the late Cretaceous

(article en révision au journal *Tectonophysics*)

2.1. Abstract 74
2.2. Introduction 75
2.3. Methodology 77
2.4. Geodynamic overview of the eastern Mediterranean region 80
2.4.1. Sedimentary and tectono-metamorphic constraints 82
2.4.2. Magmatic features 95
2.5. Kinematic reconstructions of the eastern Mediterranean region 99
2.5.1. Late Cretaceous (100-65 Ma) 113
2.5.2. Paleocene-Eocene (65-35 Ma) 116
2.5.3. Oligocene-early Miocene (35-15 Ma) 118
2.5.4. Middle-late Miocene (15-5 Ma) 121
2.5.5. Pliocene-Quaternary (5-0 Ma) 124
2.6. Discussion 125
2.6.1. Late Cretaceous and Oligocene to Present slab retreat and back-arc opening 125
2.6.2. Strain partitioning in the Aegean region 129
2.6.3. Successive metamorphic events in the Menderes massif 132
2.6.4. Driving forces acting on the westward extrusion of Anatolia 133
2.6.5. Southward retreat of the subduction zone and magma genesis 135
2.6.6. Modulation of magmatic evolution by slab tearing and mantle plume 137
2.7. Conclusion 138

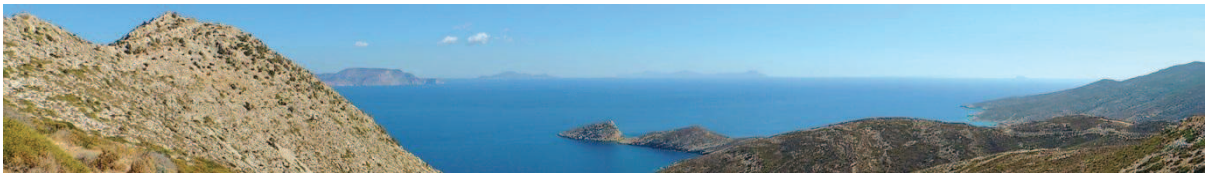

Afin de mettre en évidence le contrôle à l'échelle lithosphérique de la subduction sur la genèse des systèmes minéralisés, il convient dans un premier temps d'étudier leur distribution spatiale et temporelle. Celle-ci peut être discutée dans un premier temps à partir de données métallogéniques géoréférencées sur des cartes géologiques, tectoniques, ou autres (figure 2.1) [ex. *Loiselet et al.*, 2010]. La limite de cette méthode est qu'elle ne prend pas en compte le fait que le contexte géodynamique de la région étudiée a évolué au cours du temps. Afin de visualiser la configuration de la zone de subduction au moment de la mise en place de ces minéralisations, il est donc nécessaire d'intégrer ces données à un modèle de reconstructions cinématiques.

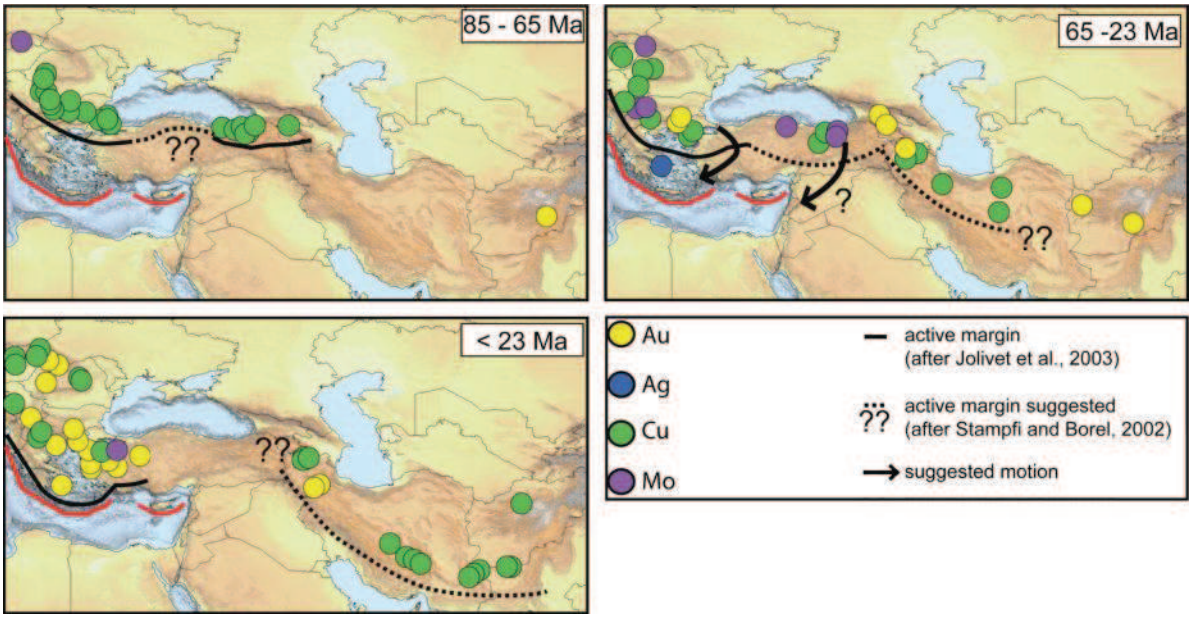

Figure 2.1 : succession de cartes de la chaîne ouest-Téthysienne montrant la distribution des minéralisations à or, argent, cuivre et molybdène au Crétacé supérieur, Paléogène et Néogène [*Loiselet et al.*, 2010]. La marge active est représentée d'après les modèles de reconstructions cinématiques ou paléogéographiques à grande échelle [*Jolivet et al.*, 2003; *Stampfli & Hochard*, 2009].

En Méditerranée orientale, la majorité des reconstructions cinématiques existantes dans la littérature considère l'ensemble de marge active ouest-Téthysienne (figure 1.24) [*Dercourt et al.*, 1986, 1993; *Ricou*, 1994; *Stampfli & Borel*, 2002; *Jolivet et al.*, 2003; *Barrier & Vrielynck*, 2008; *Stampfli & Hochard*, 2009], n'apportant pas assez de détails sur l'évolution tectonique de notre zone

d'étude. Il a donc été nécessaire de réaliser de nouvelles reconstructions cinématiques précises à l'échelle de la Méditerranée orientale, présentées dans ce chapitre.

Ce travail a fait l'objet d'un article scientifique en révision au journal *Tectonophysics* et qui s'intitule *Kinematic reconstructions and magmatic evolution illuminating crustal and mantle dynamics of the eastern Mediterranean region since the late Cretaceous*. Le format de cet article (ex. appel des figures dans le texte, références bibliographiques déplacée dans la section adéquate) a été légèrement modifié par rapport à la version en révision afin de s'adapter à celui de ce manuscrit de thèse.

Dans cet article présenté ci-dessous, après avoir justifié cette démarche, je présente dans un premier temps la méthode que j'ai employée pour réaliser ce modèle de reconstructions cinématiques à l'aide du logiciel de reconstruction tectonique et de visualisation *GPlates* (*www.gplates.org*) [*Boyden et al.*, 2011]. Je compile dans un troisième temps l'ensemble des données stratigraphiques, pétrologiques, métamorphiques, structurales, paléomagnétiques et magmatiques qui ont été utiles à ce travail. Je décris ensuite l'ensemble des cartes et coupes paléotectoniques extraites de ce modèle de reconstructions cinématiques qui s'étendent du Crétacé supérieur à l'actuel (i.e. 25 cartes également disponibles sous la forme d'un film, et 12 coupes reconstruites). Enfin, je discute des implications de ce nouveau modèle de reconstructions cinématiques sur l'évolution de la cinématique crustale et du magmatisme en Méditerranée orientale et de leurs liens avec la dynamique mantellique sous-jacente.

Principe de reconstruction

La cinématique des plaques tectoniques peut être décrite par la rotation de blocs rigides, ce qui se traduit par une déformation entièrement localisée aux limites de ces blocs. Cependant, à l'échelle de la Méditerranée orientale, la déformation peut être beaucoup plus distribuée. Afin de renforcer la précision de mes reconstructions cinématiques, j'ai donc considéré 56 domaines indépendants, définis par des lignes rigides et des zones entièrement déformables, qui ont été intégrés à un modèle global de reconstructions cinématiques, constitué de 30 blocs rigides [*Barrier & Vrielynck*, 2008]. A partir d'une compilation de données géologiques, j'ai ensuite calculé, à l'aide du logiciel *GPlates*, l'ensemble des

rotations finies de chaque bloc afin de définir leur cinématique depuis le Crétacé supérieur, jusqu'à aujourd'hui (cf. *Annexe C*, *table C.1*).

Enfin, pour étudier la distribution spatiale et temporelle du magmatisme dans cette région, j'ai compilé une base de données recensant 512 occurrences magmatiques, caractérisées par leur composition géochimique et leur âge. Chacune de ces occurrences est finalement rattaché cinématiquement au domaine sur lequel elle se met en place, se déplaçant de manière similaire dans le processus de reconstruction.

Principaux résultats

Depuis le Crétacé supérieur, cette région est caractérisée par le retrait vers le sud d'une zone de subduction où interagissent plusieurs lithosphères océaniques et continentales. Au cours de cette évolution, deux épisodes extensifs permettant la formation de bassins d'arrière-arc ont été mis en évidence : (1) au Crétacé supérieur, une extension de relativement faible amplitude a affecté la chaîne des Balkans et des Pontides qui formaient alors une longue marge active linéaire orientée ouest-est et (2) à partir de l'Eocène-Oligocène, un régime extensif plus important a affecté une région comprenant le massif du Rhodope, le domaine Egéen et la partie ouest de l'Anatolie (figure 1.25), en réponse à l'accélération du retrait du panneau plongeant des Hellénides vers le sud. Cette extension devient même particulièrement intense à partir du Miocène moyen alors que la zone de subduction se courbe, en réponse d'une possible déchirure du panneau plongeant sous l'ouest de l'Anatolie.

Dans ce vaste domaine d'arrière-arc, l'exhumation sous la forme de dômes des principales unités métamorphiques identifiées sur le terrain est accommodée par de grands systèmes de détachements d'échelle crustale (ex. *north Cycladic detachment system*, *west Cycladic detachment system*, détachement de Kerdylion) [*Faure et al.*, 1991; *Lee & Lister*, 1992; *Sokoutis et al.*, 1993; *Brun & Sokoutis*, 2007; *Jolivet et al.*, 2010a; *Grasemann et al.*, 2012] alors que la déformation décrochante d'importance moindre, liée à la courbure de la fosse semble être plus distribuée.

La distribution spatiale et temporelle de l'activité magmatique, ainsi que l'évolution de sa composition est en accord avec cette évolution tectonique avec : (1) une migration de premier ordre vers le sud des occurrences magmatiques en accord avec le retrait de la zone de subduction Hellénique

depuis le Crétacé supérieur et (2) une migration de second ordre au cours du Miocène depuis le massif du Menderes à l'est (région ouest-Anatolienne) jusque dans l'archipel des Cyclades à l'ouest, contrôlée par la courbure puis la déchirure du panneau plongeant Hellénique et le flux asthénosphérique chaud associé.

Kinematic reconstructions and magmatic evolution illuminating crustal and mantle dynamics of the eastern Mediterranean region since the late Cretaceous

Armel Menant [(1,2,3)*], Laurent Jolivet [(1,2,3)]

(1) Univ d'Orléans, ISTO, UMR 7327, 45071 Orléans, France

(2) BRGM, ISTO, UMR 7327, BP 36009, 45060 Orléans, France

(3) CNRS/INSU, ISTO, UMR 7327, 45071 Orléans, France

* *Corresponding author: Armel Menant – ISTO*
1A, rue de la Férollerie, 45071 Orléans cedex 2
+33(0)2 38 49 46 60
(armel.menant@cnrs-orleans.fr)

Bruno Vrielynck [(4)]

(4) ISTEP, UPMC-CNRS, UMR 7193, 4 Place Jussieu, 75252 Paris cedex 05, France

2.1. Abstract

The 3D coupling between subduction dynamics and crustal deformation in Mediterranean subduction zones is subject to active discussions and numerous models, notably 3D numerical models, have been recently developed in order to explore this question. Such models require a precise description of the past geological evolution. Based on a compilation of stratigraphic, petrologic, metamorphic, structural, paleomagnetic and magmatic data, we report new kinematic reconstructions of the eastern Mediterranean region since the late Cretaceous, using the principle of non-rigid domains. The motion of the 56 defined deforming domains is calculated, based on published paleomagnetic rotations, direction of motion along the main shear zones such as large-scale detachments in the back-arc regions and amount of displacement of metamorphic units during their exhumation. Extracted from these reconstructions, paleotectonic maps and lithospheric-scale cross-sections illustrate a continuous southward retreating subduction zone since the late Cretaceous with the subduction and accretion of several small continental domains. Separated by a compressional period in the Paleocene-Eocene, two back-arc extensional events are thus highlighted: (1) a slow extension along the Balkans and the Pontides in the late Cretaceous while the trench was long and linear and (2) a sensibly faster extension since the Oligocene in the Aegean-west Anatolian region. Fast rotation of the Hellenides between 15 and 8 Ma that could be associated with slab tearing event below western Anatolia further accelerating this extensional kinematics. Spatial distribution and geochemical signature of magmatic centers produced during this evolution allow us to trace mantle-related processes, such as asthenospheric flow, revealing the deep dynamics that partially control both the emplacement of this magmatism and the crustal kinematics.

2.2. Introduction

Recent studies of Mediterranean subduction zones and back-arc basins have triggered the development of new models of interactions between slab dynamics, related asthenospheric flow and overriding plate deformation [*Faccenna et al.*, 2003; *Kreemer et al.*, 2004; *Jolivet et al.*, 2009, 2013; *Brun and Sokoutis*, 2010; *Faccenna and Becker*, 2010; *Sternai et al.*, 2014]. These models are of different types: (1) conceptual models based on the tectonic history recorded in subduction zones or mountain belts and their back-arc regions, integrating also various geophysical data such as seismic anisotropy or seismic tomography, (2) instantaneous 3D velocity fields in the mantle calculated from the distribution of density anomalies taken from seismic tomography and fitting various proxies such as dynamic topography or seismic anisotropy, (3) long-term 3D models of mantle flow using fully-coupled thermo-mechanical codes or analogue experiments, testing various setups and boundary conditions to explore the space of physical parameters governing the tectonic evolution of the lithosphere. The two latter types of model cannot usually fit sequences of geological events on long geological durations, while conceptual models, familiar to geologists, do not contain any physical constraints other than what is *a priori* reasonable, but usually not tested. The 3D complexity and evolution of the Mediterranean subduction zones however require that the geological evolution is constrained as precisely as possible to serve as tests for these models.

In the eastern Mediterranean region (figure 2.2), several sets of kinematic and paleogeographic reconstructions have already been proposed to constrain its geological evolution [*Dercourt et al.*, 1986, 1993; *Ricou*, 1994; *Jolivet et al.*, 2003; *Barrier and Vrielynck*, 2008; *Stampfli and Hochard*, 2009; *van Hinsbergen and Schmid*, 2012]. All these reconstructions show that the geodynamic evolution of this region is governed by the Africa-Eurasia convergence and involves interactions between several oceanic domains belonging to the Neo-Tethys Ocean and continental blocks previously rifted from the African margin and belonging to the Apulian (or Adria) plate. However, apart from *van Hinsbergen and Schmid*, [2012], these reconstructions often consider the entire western Tethyan active margin, not providing enough details for the smaller-scale eastern Mediterranean

region where a succession of subduction, collision, obduction, slab retreat and tearing events has occurred since the Mesozoic [*Le Pichon and Angelier*, 1979; *Şengör and Yilmaz*, 1981; *Jolivet and Faccenna*, 2000; *Jolivet et al.*, 2003; *Faccenna et al.*, 2006, 2013; *Brun and Faccenna*, 2008; *Dilek and Sandvol*, 2009; *Ring et al.*, 2010; *Brun and Sokoutis*, 2010; *Jolivet and Brun*, 2010]. Detailed kinematic reconstructions are therefore necessary to describe this apparently complex tectonic evolution, especially as there is no consensus about the lithospheric behavior and the crustal-scale structures accommodating this deformation notably during the Oligocene-Miocene back-arc extension [*Walcott and White*, 1998; *Jolivet and Brun*, 2010; *Jolivet et al.*, 2010a; *Philippon et al.*, 2012; *van Hinsbergen and Schmid*, 2012]. In addition, integrating magmatism and its sources is also particularly useful to discuss the interaction between crustal and mantle processes. *Pe-Piper and Piper*, [2006] have thus added to their simplified kinematic reconstructions information about the distribution and geochemical characteristics of magmatic centers through time and then discussed the respective roles of slab retreat and break-off, asthenospheric upwelling, as well as major crustal-scale structures such as strike-slip faults and detachments.

In this paper, we reconstruct the tectonic and magmatic evolution of the eastern Mediterranean region with unprecedented details. First, we review and discuss stratigraphic, petrologic, metamorphic, structural, paleomagnetic and magmatic data, providing information about the tectono-metamorphic history of the different crustal units and their paleogeographic environment. Then, we propose new paleotectonic maps and lithospheric-scale cross-sections of the region for each important time step, illustrating the 3D evolution of the subduction zone geometry. The full set of tectonic reconstructions is also available as a video (cf. *Annexe C, video C.1*). We thus show that the Tethyan subduction zone has worked continuously since the late Cretaceous, with the successive subduction and accretion of several small continents. Its rate of southward retreat and the development of a wide extensional back-arc region are then mainly driven by the width of the slab, suggesting a major role of slab tearing on the increasing rate of this crustal kinematics, notably after 15 Ma in the Aegean-western Anatolian region. Integrated in these reconstructions, the magmatic evolution is used to discuss this dynamics and highlights the importance of the asthenospheric flow on controlling magmatic centers migration as well as crustal kinematics.

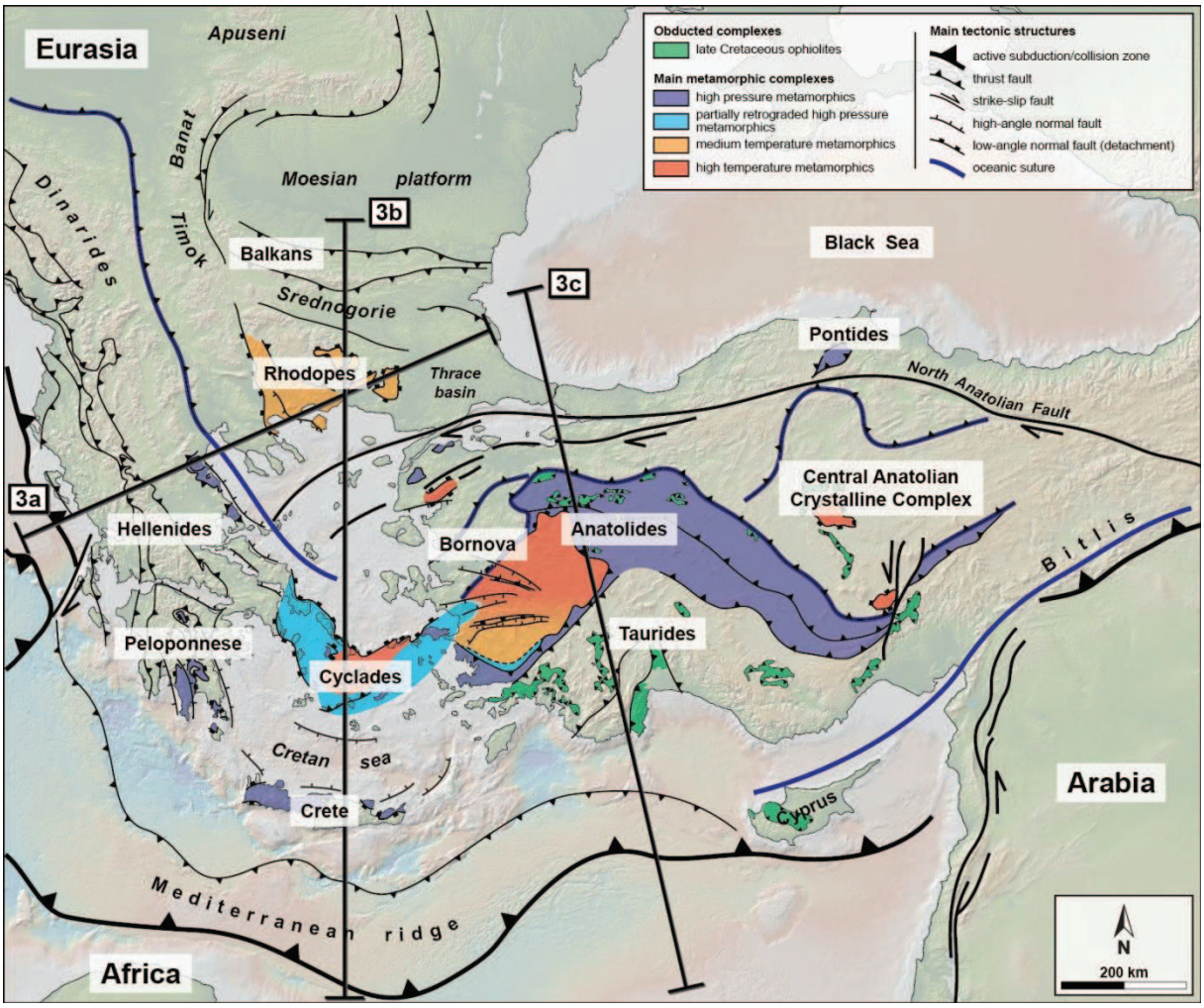

Figure 2.2: tectonic map of the eastern Mediterranean region highlighting the main tectono-metamorphic domains. Modified from *Jolivet et al.* [2013]. Base maps made with *GeoMapApp* (*https://www.geomapapp.org*).

2.3. Methodology

Based on the principle of tectonic plate motions, most kinematic reconstructions consider the relative displacement of rigid polygons (representing different continental or oceanic crustal blocks) relative to one of the polygons considered stable or within an absolute framework. In this case, strain is considered entirely localized at the edges of these polygons. However, at the scale of the eastern Mediterranean region, deformation is widely distributed and defining only rigid polygons is therefore partly misleading. One possible way to approximate this non-rigid behavior at the scale of the studied region is to consider (1) many small rigid polygons or (2) only the rigid boundaries of deforming

polygons. The space between these different polygons is then considered as a fully deforming zone (i.e. principle of "continuously closed plate" [*Gurnis et al.*, 2012] or "deformable topologies" [*van Hinsbergen and Schmid*, 2012]). We decided to use both strategies by defining 56 independently moving domains comprising both rigid lines and intervening deforming areas (figure 2.3). Due to their non-rigid behavior, the domains boundaries are not necessarily defined by rigid lines and can be implicitly defined between two deforming areas. These domains are integrated in a global plate kinematic model constituted by 30 rigid polygons [*Barrier and Vrielynck*, 2008], notably comprising Africa, Arabia, Eurasia and the Moesian platform (figure 2.3). Kinematics of the domains is then defined using a large number of geological data (figure 2.4) including notably (1) paleomagnetism to constrain the amount of vertical axis rotations, (2) direction and amount of displacement on large-scale structures such as strike-slip faults and detachments and (3) the tectonic and metamorphic history (i.e. pressure-temperature-time path) of main tectonic units. The latter also provides information on the burial and exhumation processes affecting these tectonic units, constraining their vertical tectonic evolution. Most of vertical axis rotations considered in this paper result from consistent paleomagnetic measurements over a wide area which is thus considered as a rigid block, moving in response to large-scale crustal (and mantle) processes.

Using the interactive plate-tectonic reconstructions and visualizations software GPlates (www.gplates.org) [*Boyden et al.*, 2011], we reconstruct backward the kinematics of the eastern Mediterranean region from the present-day plate configuration to the late Cretaceous. Relative motions of deforming domains are described by finite rotations given by the geographical coordinates of the rotation pole and the rotation angle. We then obtain for each defined domain a succession of total reconstruction poles, corresponding to the finite rotation from the present-day position to the position at a given time in the past (positive and negative angles of rotation depicting respectively clockwise and counterclockwise rotations) (*Annexe C, table C.1*). All these rotations are defined with respect to the Moesian platform that is considered as belonging to stable Eurasia since the late Cretaceous (figure 2.4) [v*an Hinsbergen et al.*, 2008].

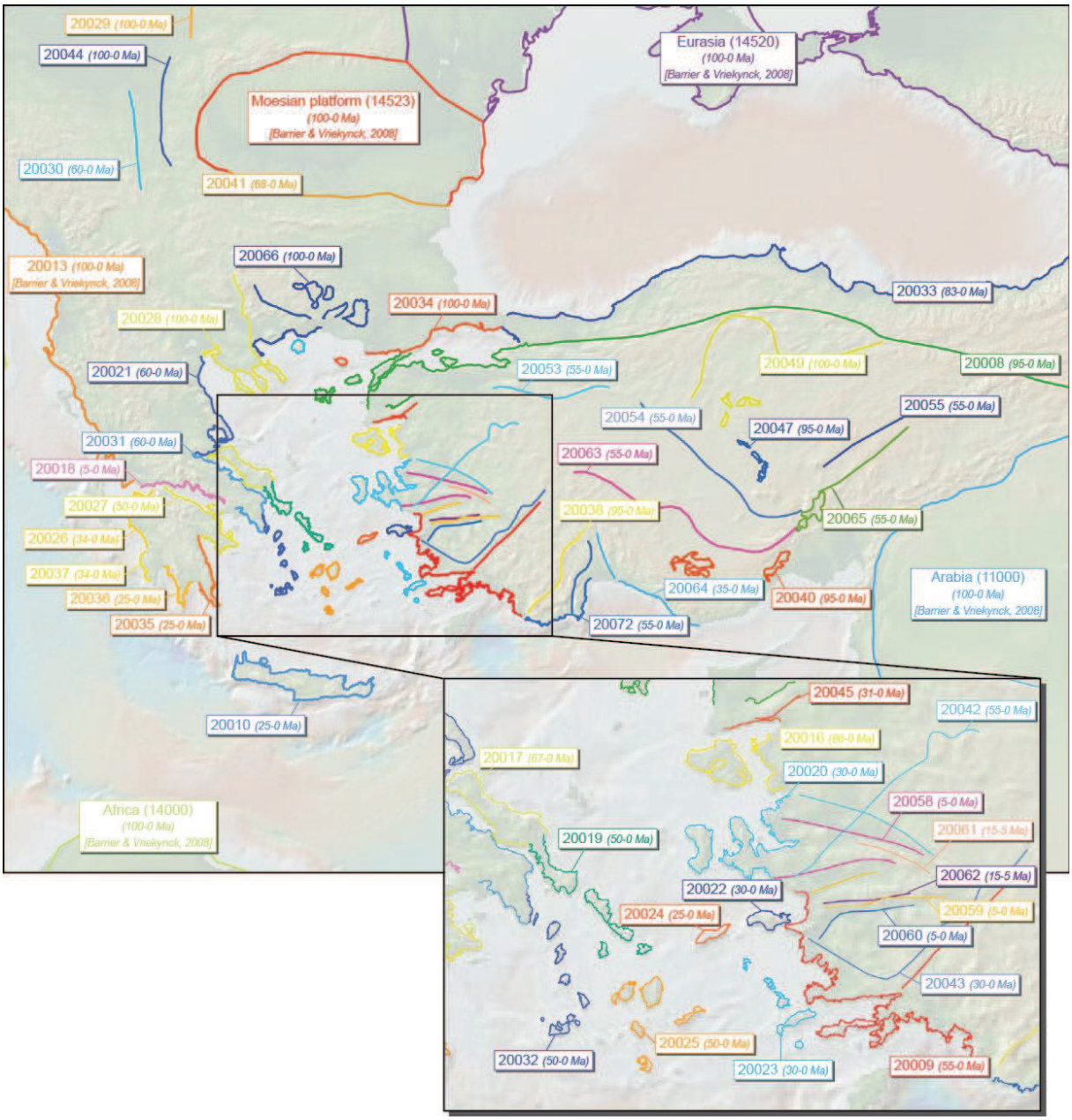

Figure 2.3: map of the eastern Mediterranean region showing the main domains used in the kinematic reconstructions. Each domain has a specific ID (cf. *Annexe C, Table C.1*) as well as an age of appearance and disappearance (in italic). Base maps made with *GeoMapApp* (*https://www.geomapapp.org*).

Finally, in order to discuss the spatial and temporal distribution of the magmatism across the studied area, we have constructed a GIS database of the magmatic products emplaced in this region since the late Cretaceous. We thus consider 512 magmatic centers that are all characterized by their geochemical composition and their period of activity. Each magmatic center is then kinematically attached to the domain it belongs and moves with it in the process of reconstruction.

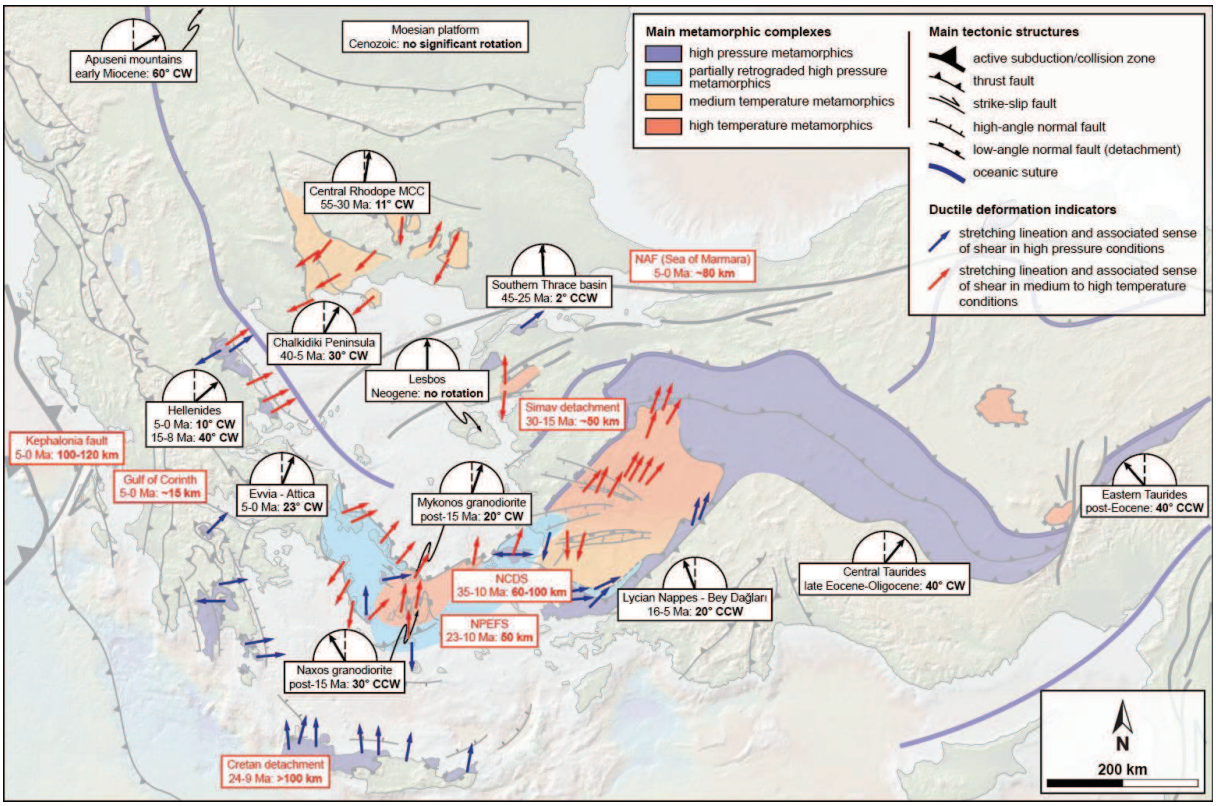

Figure 2.4: tectonic map showing the main data used to constrain the kinematic evolution of the eastern Mediterranean region, including the stretching lineations in the MCCs [*Rimmelé et al., 2006; Bonev & Beccaletto, 2007; Jolivet et al., 2013*], the offset of main structures [*Armijo et al., 1999; Jolivet et al., 2004, 2010b; Brichau et al., 2006, 2008*] and the vertical-axis rotations deduced from paleomagnetic studies [*Kissel & Laj, 1988; Kissel et al., 1993, 2003; Pătraşcu et al., 1994; Morris & Anderson, 1996; van Hinsbergen et al., 2005b, 2008, 2010a; Brun & Sokoutis, 2007; Bradley et al., 2013*]. CW: clockwise rotation. CCW: counterclockwise rotation. NAF: North Anatolian Fault. NCDS: North Cycladic Detachment System. NPEFS: Naxos/Paros Extensional Fault System. Base maps made with *GeoMapApp* (*https://www.geomapapp.org*).

2.4. Geodynamic overview of the eastern Mediterranean region

The geodynamic history of the eastern Mediterranean region has been dominated by the convergence of Africa and Eurasia since the Mesozoic, inducing subduction, collision and obduction processes [*Şengör and Yilmaz*, 1981; *Dercourt et al.*, 1986; *Ricou et al.*, 1986; *Ricou*, 1994]. Accretionary wedges and associated orogenic belts, such as the Hellenides and the Anatolides-Taurides (figures 2.2 and 2.5), were thus formed along this active margin by decoupling of crustal nappes from the subducted lithosphere and their accretion to the overriding plate [*Le Pichon and*

Angelier, 1979; *Jolivet et al.*, 2003; *van Hinsbergen et al.*, 2005a]. These nappes were partially buried within the subduction zone where they underwent a high pressure-low temperature (H*P*-L*T*) metamorphism [*Bonneau and Kienast*, 1982; *Okay*, 1986; *Wijbrans and McDougall*, 1988]. These metamorphic rocks were then partly exhumed in a syn-orogenic context, within the subduction channel or the accretionary wedge, preserving H*P*-L*T* parageneses [*Jolivet et al.*, 2003; *Ring et al.*, 2007, 2010; *Huet et al.*, 2009].

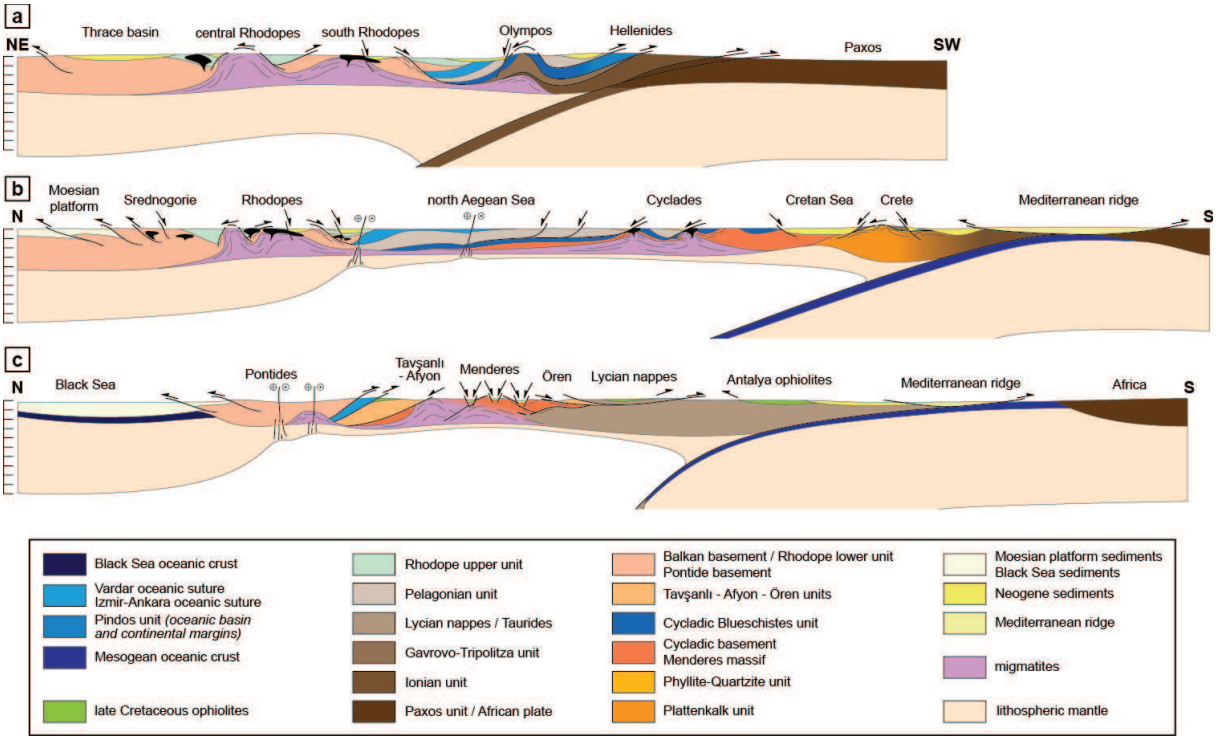

Figure 2.5: present-day cross-sections in the eastern Mediterranean region. See figure 1 for location. Modified from *Jolivet & Brun* [2010]. Crustal thickness in the Aegean and western Anatolian region has been extracted from *Tirel et al.* [2004] and *Karabulut et al.* [2013].

Coevally with the migration of the subduction trench, these accretionary wedges were progressively transferred in the back-arc domain where buried rocks underwent a medium to high temperature-medium pressure (M*T*- to H*T*-M*P*) metamorphism, overprinting the former H*P*-L*T* parageneses [*Altherr et al.*, 1982; *Gautier and Brun*, 1994; *Jolivet and Brun*, 2010]. As a result of different processes such as gravitational collapse or slab retreat, the subsequent collapse of the accretionary wedges and the opening of back-arc basins allowed the exhumation in a post-orogenic context of the lower parts of the stretched crust as Metamorphic Core Complexes (MCCs), such as in

the Rhodope massif, the Cyclades and the Menderes massif (figures 2.2 and 2.5) [*Lister et al.*, 1984; *Sokoutis et al.*, 1993; *Jolivet et al.*, 1994, 2004a; *Lips et al.*, 2001; *Ring et al.*, 2003; *Brun and Sokoutis*, 2007].

2.4.1. Sedimentary and tectono-metamorphic constraints

In the following section, we review the main stratigraphic, petrologic, metamorphic, structural and paleomagnetic data that characterize the different tectonic domains (i.e. the Balkans, the Rhodope massif, the Hellenides, the Cyclades, Crete and the Peloponnese, the Black Sea basin, the Pontides, the Bornova flysch zone, the Central Anatolian Crystalline Complex and the Anatolide-Tauride block) (figure 2.2) in order to constrain our kinematic reconstructions of the eastern Mediterranean region.

The Balkans. Displaying a present-day "L"-shape surrounding the Moesian platform, the Balkans have been part of the Eurasian margin since the Triassic Tethyan rifting [*Georgiev et al.*, 2001; *Okay et al.*, 2001a]. They consist in an orogenic belt where four different areas can be distinguished: the Apuseni, Banat, Timok and Srednogorie regions (figure 2.2). After a compressional period in early Cretaceous times, a late Cretaceous phase of extension developed across the Balkan belt (figure 2.6) with notably the opening of Gosau-type basins in the Banat and Apuseni regions [*Berza et al.*, 1998; *Willingshofer et al.*, 1999]. In the Srednogorie region, transtensional basins formed at the end of the early Cretaceous and evolved in rifting zones until the beginning of the Cenozoic [*Bergerat et al.*, 2010].

An inversion of the Cretaceous extensional structures then occurred and a N-vergent foreland fold and thrust belt has developed throughout the Balkans since the Paleocene and culminated in the middle-late Eocene (figure 2.6) [*Doglioni et al.*, 1996; *Bergerat et al.*, 2010].

Finally, paleomagnetic data acquired in the Apuseni mountains show a ~60° early Miocene clockwise rotation in this part of the belt (figure 2.4) [*Pătraşcu et al.*, 1994].

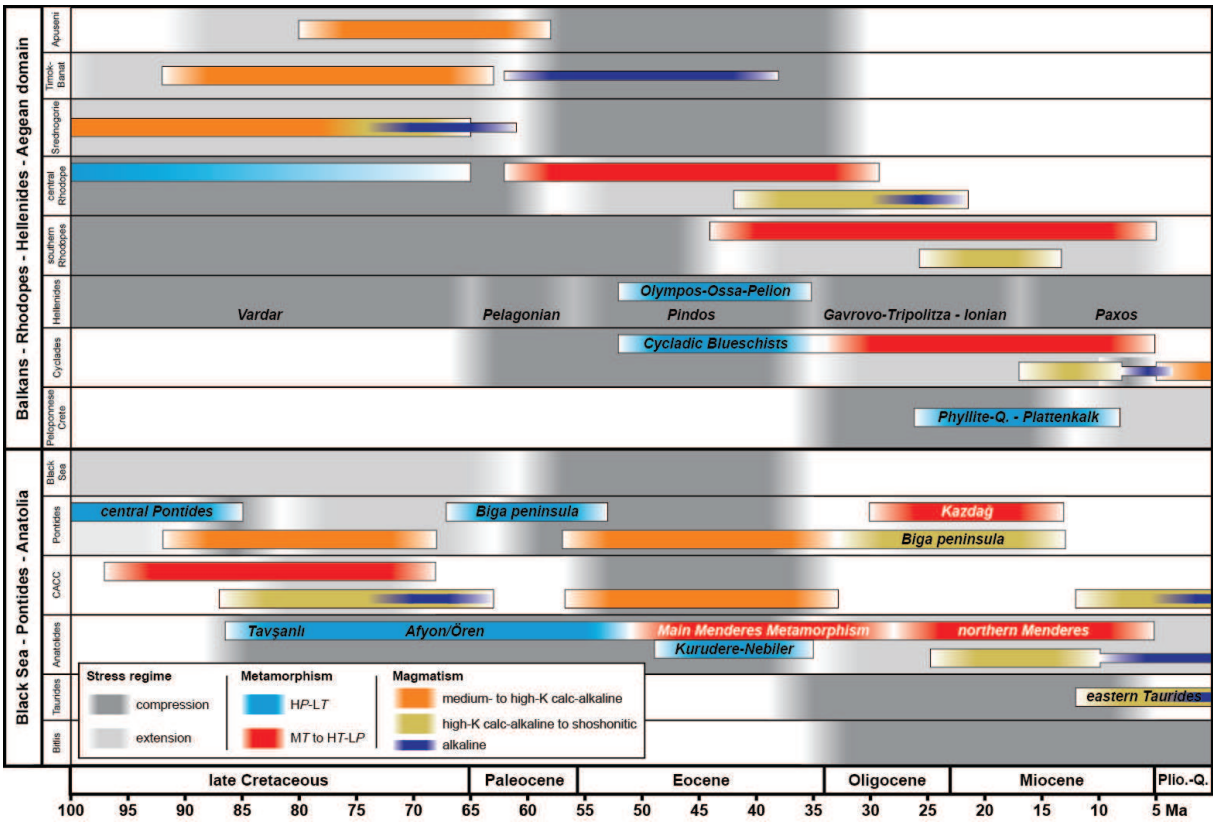

Figure 2.6: diagram showing the main tectonic, metamorphic and magmatic events since the late Cretaceous used to constrain the kinematic reconstructions of the eastern Mediterranean region (see text for references).

The Rhodope massif. Located south of the Balkans, the Rhodope massif is chiefly a stack of nappes partly crosscut by several MCCs (i.e. the central and south Rhodope core complexes) (figure 2.7) [*Burg et al.*, 1990, 1996; *Bonev et al.*, 2006; *Brun and Sokoutis*, 2007]. Stacked units emplaced southward [*Burg et al.*, 1996; *Dinter*, 1998] underwent a H*P* metamorphism (i.e. 12-17 kbar, 750-811 °C) with locally ultra-H*P* conditions, no later than the late Cretaceous (U-Pb crystallization ages on zircon) [*Liati et al.*, 2002; *Bonev et al.*, 2006; *Bauer et al.*, 2007].

Afterwards, a M*T*-M*P* metamorphism (i.e. 8-10 kbar, 560-650 °C) was recorded in the Rhodope massif in the Paleocene and subsequent exhumation of these rocks as a MCC initiated first in the central Rhodope massif ~55 Ma ago below top-to-the NE ductile-brittle detachments (figures 2.4 and 2.6) [*Burg et al.*, 1996; *Bonev et al.*, 2006]. This exhumation is associated with a ~11° clockwise rotation (figure 2.4) [*Brun and Sokoutis*, 2007]. Contemporaneous sedimentation on the hanging wall of these detachments, notably including olistholiths of the underlying metamorphic rocks, indicates the partial exposure at the surface of the central Rhodope core complex in the late Eocene [*Burchfiel et al.*,

2003; *Bonev et al.*, 2006]. Exhumation below these detachments then ceased in the early Oligocene and high-angle normal faulting finally developed [*Marchev et al.*, 2004a; *Wüthrich*, 2009]. Coevally, the Thrace basin progressively opened further east (figure 2.2) in the middle Eocene-late Oligocene, resulting in the deposition of sediments that were then intensively deformed as a result of a tectonic inversion in the lower-middle Miocene [*Turgut and Eseller*, 2000; *Okay et al.*, 2010a]. The amount of extension in the Thrace basin remains however poorly constrained and v*an Hinsbergen and Schmid* [2012] suggested a ~2° counterclockwise rotation of the southern part of this basin to describe its opening (figure 2.4).

Further south, exhumation of the southern Rhodope core complex started ~40 Ma ago, accommodated by the top-to-the SW Kerdylion detachment whose hanging wall (i.e. the Vertiskos unit) has stayed in near-surface conditions since the early-middle Eocene (figures 2.4 and 2.7) [*Sokoutis et al.*, 1993; *Brun and Sokoutis*, 2007; *Wüthrich*, 2009; *Kydonakis et al.*, 2014]. Based on paleomagnetism [*Kondopoulou and Westphal*, 1986] and on the curvature of the stretching lineations in the MCC, *Brun and Sokoutis* [2007] consider a ~30° clockwise rotation of the hanging wall of the Kerdylion detachment (including the Chalkidiki Peninsula) with the major part of the rotation occurring in the final stage of exhumation of the south Rhodope core complex after 15 Ma [*van Hinsbergen et al.*, 2008]. Since the middle Miocene, sedimentary basins have also developed over the whole MCC, controlled by normal faults [*Brun and Sokoutis*, 2007].

The Hellenides. Located southwest of the Rhodope massif, the Hellenides is a W- to SW-vergent nappe stack constituted by several continental and oceanic units of low-metamorphic grade (figures 2.2, 2.5 and 2.7) [*Aubouin*, 1959; *van Hinsbergen et al.*, 2005a].

The Vardar suture zone is the most internal part of the Hellenides and represents the remnant of a wide oceanic basin that was partially obducted southward, over the Pelagonian carbonate platform in latest Jurassic times [*Ricou et al.*, 1986; *Schmid et al.*, 2008]. This oceanic basin closed in the latest Cretaceous to Paleocene during the accretion of the ~200 km wide Pelagonian carbonate platform (figure 2.6) [*Ricou et al.*, 1998; *van Hinsbergen et al.*, 2005a].

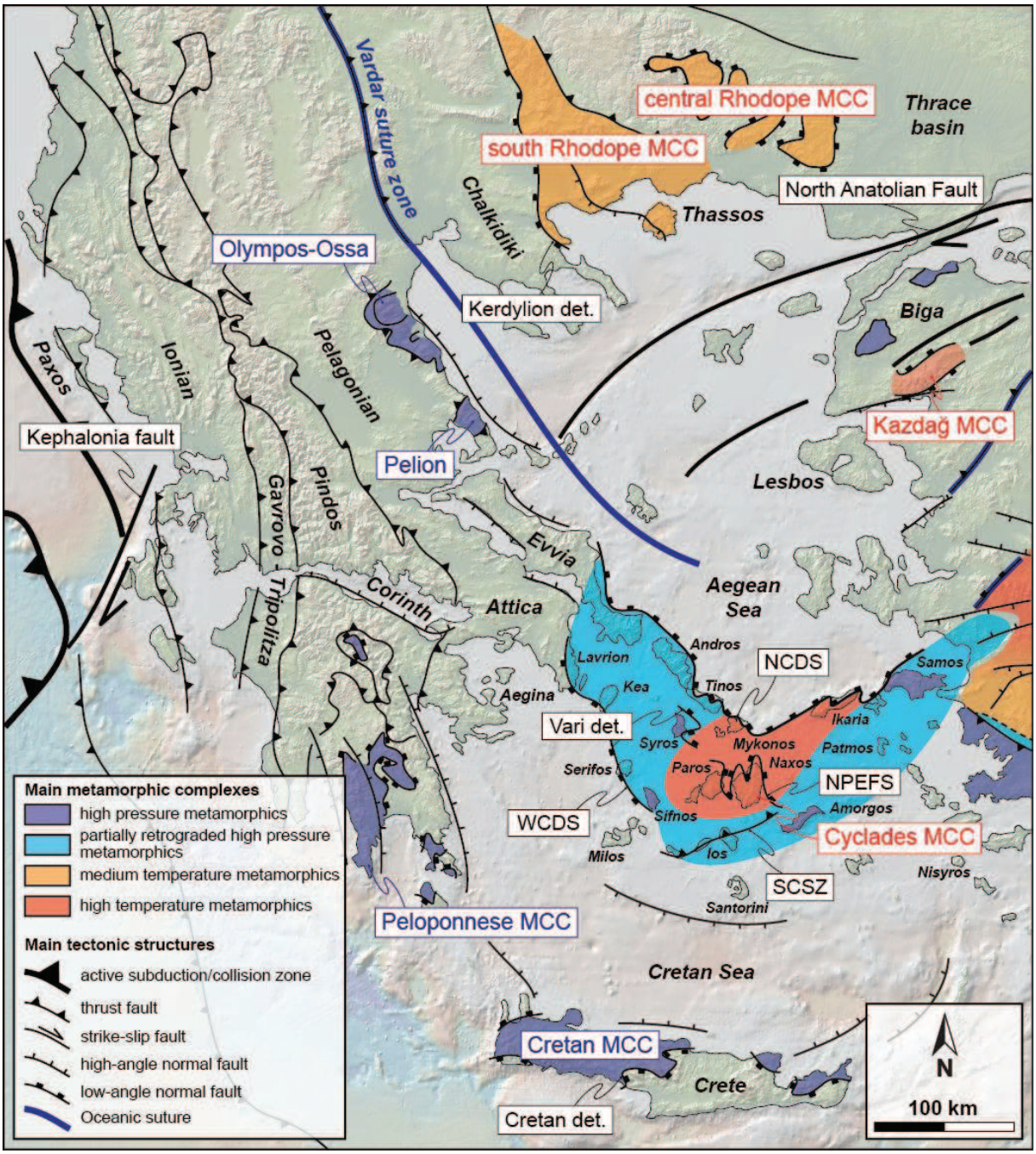

Figure 2.7: detailed tectonic map of the Aegean region. NAF: North Anatolian Fault. NCDS: North Cycladic Detachment System. NPEFS: Naxos/Paros Extensional Fault System. SCSZ: South Cycladic Shear Zone. WCDS: West Cycladic Detachment System. Base maps made with *GeoMapApp* (*https://www.geomapapp.org*).

Underthrusted below the Pelagonian nappe in the late Paleocene-Eocene, the Pindos nappe was originally an oceanic basin with its continental margins [*Aubouin*, 1959], extending from the northwest in the Dinarides with the Budva-Cukali zone [*Robertson and Karamata*, 1994] to the

southeast in the Aegean domain and possibly as far as the Lycian basin in the Taurides [*Bonneau*, 1984]. This basin had an original width of at least 300 km [*van Hinsbergen et al.*, 2005a].

In the Oligocene, the Pindos nappe overthrusted the Gavrovo-Tripolitza nappe, consisting in a ~150 km wide carbonate platform (figure 2.4) [*Aubouin*, 1959; *Sotiropoulos et al.*, 2003; *van Hinsbergen et al.*, 2005a]. Coevally, the Gavrovo-Tripolitza nappe overthrusted the Ionian platform whose original width is also estimated at around 150 km (figure 2.6) [*van Hinsbergen et al.*, 2005a].

Finally, forming the most external part of the Hellenides, the Paxos nappe (or Pre-Apulian nappe) consists in a carbonate platform that was underthrusted below the Ionian nappe in the Miocene (figure 2.6). This platform has no lateral continuation in eastern Greece where the Mesogean oceanic lithosphere has been subducting since the early-middle Miocene [*Underhill*, 1989; *Le Pichon et al.*, 2002]. Along this oceanic subduction zone, a sedimentary wedge, called the Mediterranean ridge, has finally developed since ~15 Ma against the Hellenic thrust belt (figures 2.2 and 2.5) [*Le Pichon et al.*, 1982, 2002; *Chaumillon et al.*, 1996; *Kopf et al.*, 2003; *Yem et al.*, 2011]. At the junction between the Paxos platform and the Mesogean oceanic basin, a strike-slip fault, the Kephalonia fault has been active since ~5 Ma, accommodating 100-120 km of dextral offset (figure 2.4) [*Finetti*, 1982; *Kreemer and Chamot-Rooke*, 2004; *Royden and Papanikolaou*, 2011].

As shown by paleomagnetism, the Hellenides underwent a significant rigid rotation during its accretion, with ~40° clockwise rotation between 15 and 8 Ma and an additional 10° clockwise rotation since the Pliocene (figure 2.4) [*Kissel and Laj*, 1988; *van Hinsbergen et al.*, 2005b]. A recent study shows however a larger Pliocene-Quaternary clockwise rotation of ~23° in the southeastern Hellenides (figure 2.4), suggesting a recent tectonic decoupling between these two parts of the orogenic belt [*Bradley et al.*, 2013].

The Cyclades. Located in the center of the extensional Aegean region, the Cyclades partly expose the buried parts of the Hellenides, exhumed since the Eocene as MCCs in low, medium and/or high temperature environments (figures 2.5 and 2.7) [*Bonneau*, 1984; *Lister et al.*, 1984; *Faure and Bonneau*, 1988; *Gautier and Brun*, 1994; *Jolivet et al.*, 1994, 2003, 2004a; *van Hinsbergen et al.*, 2005c; *Ring et al.*, 2010; *Grasemann et al.*, 2012].

The buried Pindos oceanic basin and its continental margins underwent a H*P*-L*T* metamorphism (i.e. ~15-20 kbar, ~500 °C) whose metamorphic peak is dated at around 50 Ma, forming the Cycladic Blueschists unit and the Cycladic basement [*Bonneau and Kienast*, 1982; *Bonneau*, 1984; *Wijbrans and McDougall*, 1988; *Tomaschek et al.*, 2003; *Lagos et al.*, 2007]. Exhumation of these metamorphic units first occurred between 45 and 35-30 Ma in a syn-orogenic context, following a cold retrograde path (figure 2.6) [*Altherr et al.*, 1979; *Bonneau and Kienast*, 1982; *Trotet et al.*, 2001]. These Eocene H*P*-L*T* parageneses are particularly well preserved in Syros and Sifnos islands (Cyclades) where syn-orogenic extensional shear zones, such as the Vari detachment in Syros (figure 2.7), show respectively top-to-the ENE and top-to-the N senses of shear (figure 2.4) [*Trotet et al.*, 2001; *Keiter et al.*, 2004; *Ring et al.*, 2011; *Roche et al.*, submitted]. In Ios island, a coeval top-to-the S structure, called the South Cycladic Shear Zone (SCSZ), is observed at the base of the Cycladic Blueschists unit (figure 2.7). This structure has been interpreted first as an extensional shear zone [*Lister et al.*, 1984], then redefined as a thrust [*Huet et al.*, 2009]. An extrusion model was proposed for the Eocene exhumation of the Cycladic Blueschists unit in the Cyclades with the Vari detachment in Syros and the SCSZ in Ios defining respectively the top and the base of the subduction channel or the extrusion wedge [*Jolivet et al.*, 2003; *Ring et al.*, 2007, 2010; *Brun and Faccenna*, 2008; *Huet et al.*, 2009; *Jolivet and Brun*, 2010]. Cropping out also within the Hellenides in the Olympos, Ossa and Pelion tectonic windows (figure 2.7), the Cycladic Blueschists unit displays here a similar bivergent ductile deformation with both top-to-the NE and top-to-the WSW senses of shear associated with the exhumation of the H*P*-L*T* parageneses (figure 2.4) [*Godfriaux*, 1968; *Blake et al.*, 1981; *Schermer*, 1993; *Lips et al.*, 1998; *Lacassin et al.*, 2007].

Following this, the Cycladic Blueschists unit underwent a brief M*T*-M*P* metamorphic overprint in the early Oligocene (i.e. ~9 kbar, 550-570 °C) followed by a greenschist-facies retrogration, such as in Andros, Tinos and Kea islands (figure 2.7) [*Altherr et al.*, 1982; *Parra et al.*, 2002; *Bröcker et al.*, 2004; *Jolivet and Brun*, 2010; *Grasemann et al.*, 2012; *Huet et al.*, 2014] and in the Olympos, Ossa and Pelion tectonic windows [*Schermer*, 1993; *Lips et al.*, 1999; *Lacassin et al.*, 2007]. In the lower Miocene, a H*T*-M*P* metamorphism (i.e. 5-8.5 kbar, 500-700°C) and associated migmatites also developed in the central Cyclades, such as in Naxos, Paros, Mykonos and Ikaria islands [*Lister et al.*,

1984; *Urai et al.*, 1990; *Keay et al.*, 2001; *Vanderhaeghe*, 2004; *Duchêne et al.*, 2006; *Laurent et al.*, 2015; *Beaudoin et al.*, in revision]. Exhumation of these rocks as MCCs was accommodated during the Oligocene-Miocene by several ductile-brittle detachment systems (figures 2.5 and 2.7), comprising the top-to-the NE North Cycladic Detachment System (NCDS) [*Faure et al.*, 1991; *Lee and Lister*, 1992; *Gautier and Brun*, 1994; *Mehl et al.*, 2005, 2007; *Brichau et al.*, 2007, 2008; *Jolivet et al.*, 2010a], the top-to-the N Naxos/Paros Extensional Fault System (NPEFS) [*Urai et al.*, 1990; *Gautier et al.*, 1993; *Seward et al.*, 2009; *Bargnesi et al.*, 2013] and the top-to-the SW West Cycladic Detachment System (WCDS) [*Grasemann and Petrakakis*, 2007; *Brichau et al.*, 2010; *Iglseder et al.*, 2011; *Grasemann et al.*, 2012]. The minimum offset of these different extensional structures is estimated at around 60-100 km for the NCDS [*Jolivet et al.*, 2004a; *Brichau et al.*, 2008] and 50 km for the NPEFS (figure 2.4) [*Brichau et al.*, 2006]. Composing the hanging wall of these detachment systems, the low-grade Upper Cycladic unit is an equivalent of the Pelagonian nappe, essentially consisting in ophiolitic material related to the Jurassic Vardar ophiolites (e.g. in Crete) [*Koepke et al.*, 2002] or to the late Cretaceous Lycian and Tauride ophiolites (e.g. in Tinos) [*Katzir et al.*, 1996]. In Mykonos, Ikaria and Naxos, syn-tectonic sedimentary basins were also deposited in the hanging wall of these detachments in the Miocene [*Sánchez-Gómez et al.*, 2002; *Lecomte et al.*, 2010; *Laurent et al.*, 2015]. The lack of clasts belonging to the Cycladic Blueschists unit indicates a late exposure of this unit in the late Miocene at the earliest [*Sánchez-Gómez et al.*, 2002].

Following this extensional tectonics, a distributed strike-slip then E-W compressional tectonics developed in the Cyclades in the late Miocene, inducing notably folding and local reactivation of detachment planes with a reverse movement (figure 2.6) [*Ring et al.*, 1999a; *Avigad et al.*, 2001; *Menant et al.*, 2013].

Paleomagnetic studies from middle Miocene syn-extensional intrusions in the Cyclades provide a ~20° clockwise and a ~30° counterclockwise rotation in Mykonos and Naxos respectively (figure 2.4) [*Morris and Anderson*, 1996]. To accommodate these two opposite block rotations, a large-scale dislocation fault has been suggested by *Walcott and White* [1998] (i.e. the so-called Mid-Cycladic Lineament). A similar concept was used by *Philippon et al.* [2012], who proposed the existence of a dextral fault linking the Ikaria Basin and the Mirthes Basin (i.e. the Mirthes-Ikaria strike-slip fault).

Recently, *Jolivet et al.* [2015] proposed instead a wide zone of left-lateral gradient of finite extension covering a large part of the central Aegean region.

Crete and Peloponnese. Located in the southern part of the Aegean domain, the Peloponnese and Crete underwent a H*P*-L*T* metamorphism in the late Oligocene (i.e. 16-18 kbar, 400-550 °C), forming the Phyllite-Quartzite and the Plattenkalk units (figures 2.5 and 2.7) [*Seidel et al.*, 1982; *Theye et al.*, 1992; *Jolivet et al.*, 1996; *Trotet et al.*, 2006]. These units may represent respectively the metamorphosed equivalent of the basement of the Gavrovo-Tripolitza and the Ionian nappes [*Bonneau and Kienast*, 1982; *van Hinsbergen et al.*, 2005c]. Exhumation of these units occurred between 24 and 9 Ma (Ar-Ar crystallization ages on white mica and fission track ages on zircon) in the footwall of the Cretan detachment that has accommodated more than 100 km of displacement (figures 2.4 and 2.6) [*Jolivet et al.*, 1996, 2010c; *Ring et al.*, 2001; *van Hinsbergen and Meulenkamp*, 2006; *Papanikolaou and Royden*, 2007; *Marsellos et al.*, 2010]. Associated deformation is characterized in Crete by a N-S stretching lineation with mainly top-to-the N sense of shear, while in the Peloponnese this stretching lineation evolves from NE-SW in the north to E-W in the south with bivergent kinematic indicators (figure 2.4) [*Jolivet et al.*, 1996, 2010c]. The hanging wall of the Cretan detachment consists in the low-grade Gavrovo-Tripolitza unit and a Miocene to late Pliocene sedimentary basin [*Jolivet et al.*, 1996; *van Hinsbergen and Meulenkamp*, 2006; *Seidel et al.*, 2007]. The lack of metamorphic clasts in the oldest sediments indicates an exposure of the Phyllite-Quartzite nappe ~11-10 Ma ago at the earliest [*van Hinsbergen and Meulenkamp*, 2006; *Seidel et al.*, 2007].

Since the late Miocene, high-angle normal faults developed, crosscutting the Cretan detachment and inducing the uplift of Crete and the opening of the Cretan Sea [*Angelier et al.*, 1982; *van Hinsbergen and Meulenkamp*, 2006]. Finally, additional extensional basins opened in the Peloponnese and along the eastern coast of the Hellenides, within the so-called Central Hellenides Shear Zone [*Papanikolaou and Royden*, 2007; *Royden and Papanikolaou*, 2011]. These basins include the Gulf of Corinth that has accommodated ~15 km of N-S extension since the Pliocene (figure 2.4) [*Armijo et al.*, 1996; *Rohais et al.*, 2007; *Jolivet et al.*, 2010b].

The Black Sea basin. Located north of the Pontides, the Black Sea basin is mainly composed of an oceanic-type crust overlain by ~15 km of sediments (figures 2.2 and 2.5) [*Zonenshain and Le Pichon*, 1986; *Nikishin et al.*, 2015a]. Deep reflection seismic studies show two extensional sub-basins, whose rifting started in the early Cretaceous [*Görür*, 1988; *Hippolyte et al.*, 2010; *Nikishin et al.*, 2015b]. Intense crustal stretching ultimately led to oceanic spreading from Cenomanian to Santonian times (i.e. ~100 to 85 Ma) [*Nikishin et al.*, 2015b]. The Black Sea basin then underwent a compressional deformation (figure 2.6), clearly identified in the late Eocene by reworking of pre-existing structures [*Zonenshain and Le Pichon*, 1986; *Dinu et al.*, 2005; *Nikishin et al.*, 2015b].

The Pontides. The Pontides is an E-W trending orogenic belt extending in the north of Turkey (figures 2.2 and 2.8) and belonging to the Eurasian margin since the closure of the Paleo-Tethys Ocean in Jurassic times [*Yılmaz et al.*, 1997]. Its tectonic evolution, since the late Cretaceous, shows a succession of extensional and compressional or transpressional events (figure 2.6). Late Cretaceous extension thus controlled the opening of sedimentary basins [*Sunal and Tüysüz*, 2002; *Okay et al.*, 2013]. Further south, a forearc basin developed in front of a succession of S-vergent thrust units where several H*P*-L*T* metamorphic events have been recorded during the Cretaceous [*Okay*, 1986; *Okay and Satır*, 2000a; *Okay et al.*, 2013] (figure 2.6). These units have been subsequently exhumed as a syn-orogenic extrusion wedge, such as in the central Pontides and the Biga peninsula [*Okay et al.*, 2006; *Beccaletto et al.*, 2007].

In the Paleocene, the tectonic regime in the Pontides has become compressional with the inversion of the late Cretaceous basins and the development since the late Eocene-Oligocene of a N-vergent fold-and-thrust belt [*Yılmaz et al.*, 1997; *Sunal and Tüysüz*, 2002]. An oroclinal bending also affected the central Pontides that underwent both clockwise and counterclockwise rotations in the latest Cretaceous-Paleocene [*Meijers et al.*, 2010]. In the eastern Pontides, a Paleocene-early Eocene rapid uplift is evidenced [*Boztuğ et al.*, 2004]. The late Cretaceous forearc basin also migrated southward until the Eocene-Oligocene, evolving into a foreland basin, as attested by the deposition of deep-sea, shallow marine and finally continental sediments [*Yılmaz et al.*, 1997; *Okay et al.*, 2001b; *Kaymakci et al.*, 2009]. In the late Oligocene-early Miocene, a H*T*-M*P* metamorphism (i.e. 5 ± 2 kbar, 640 ± 50 °C)

was recorded in the western part of the Pontides (Rb-Sr crystallization ages on muscovite and biotite and fission track ages on apatite, figure 2.6) [*Okay and Satır*, 2000b; *Cavazza et al.*, 2009]. Exhumation of these rocks in a post-orogenic context then allowed the formation of the Kazdağ MCC below the top-to-the N Alakeçi and top-to-the S Şelale detachments (figure 2.8) [*Okay and Satır*, 2000b; *Beccaletto and Steiner*, 2005; *Bonev and Beccaletto*, 2007].

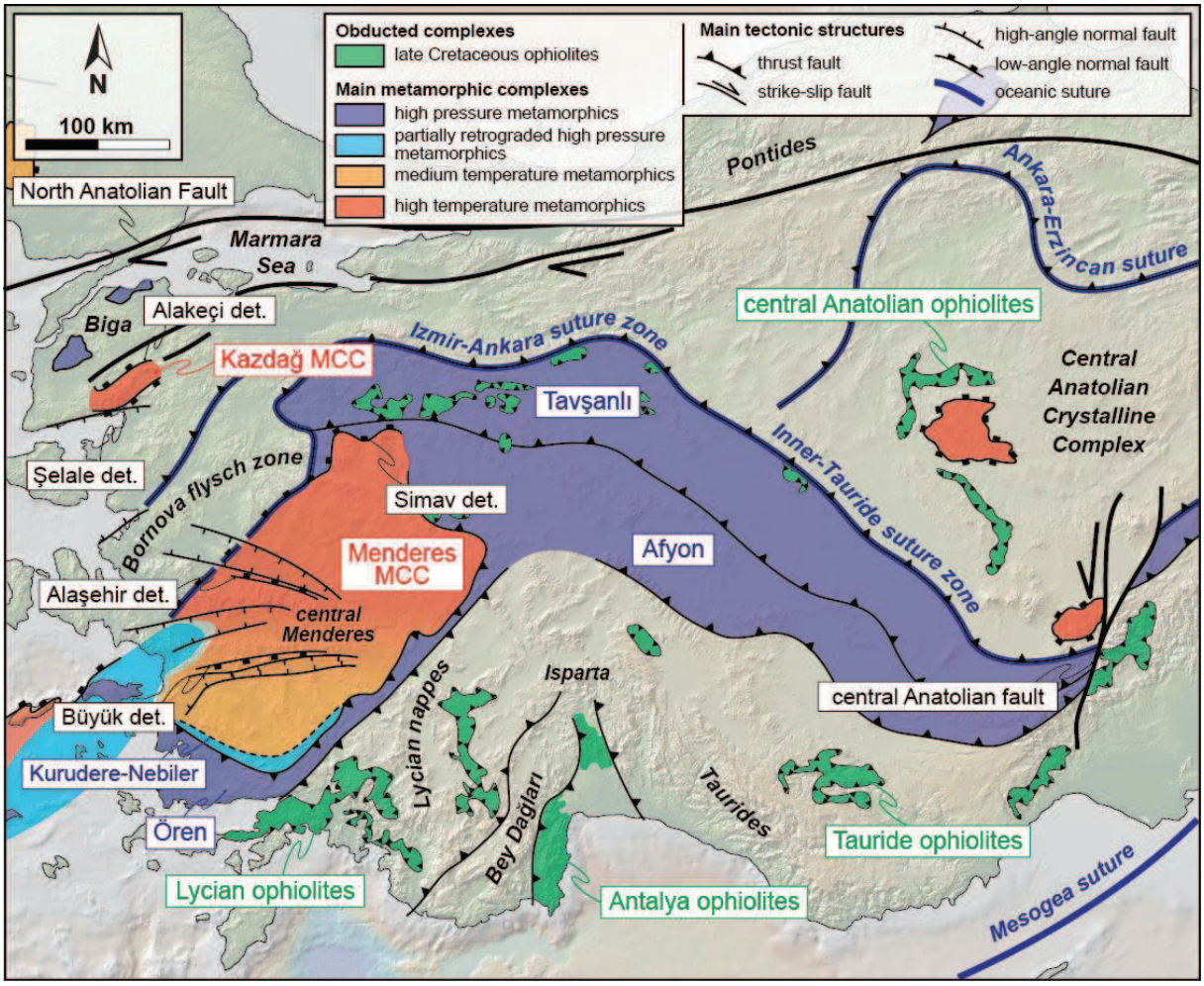

Figure 2.8: detailed tectonic map of the western and central Anatolian region. Base maps made with *GeoMapApp* (*https://www.geomapapp.org*).

Finally, initiated in the eastern Pontides 13-11 Ma ago, the dextral strike-slip North Anatolian Fault (NAF) propagated westward, as a result of the westward extrusion of Anatolia [*Şengör et al.*, 2005]. Although its exact timing is still debated [*Armijo et al.*, 1999; *Yaltirak et al.*, 2000; *Şengör et al.*, 2005; *Le Pichon and Kreemer*, 2010], the NAF seems to localize in the Dardanelle Strait 6-5 Ma ago, opening the Marmara Sea as a pull-apart basin [*Armijo et al.*, 1999; *Melinte-Dobrinescu et al.*, 2009].

The total dextral offset of this structure in its western segment is estimated at around 70-80 km (figure 2.4) [*Armijo et al.*, 1999; *Şengör et al.*, 2005; *Le Pichon and Kreemer*, 2010].

The Central Anatolian Crystalline Complex (CACC). The CACC is a continental domain separated from the Pontides by the Ankara-Erzincan oceanic suture zone (figures 2.2 and 2.8) and mainly constituted by H*T* metamorphic rocks and widespread plutons [*Göncüoğlu et al.*, 1991; *Aydin et al.*, 1998]. It also presents remnants of an ophiolitic unit (the central Anatolian ophiolites), emplaced from an intraoceanic subduction zone and obducted toward the south 90-85 Ma ago [*Yaliniz and Göncüoğlu*, 1998]. Coevally, a regional H*T*-M*P* metamorphism (i.e. ~6 kbar, ~725 °C) affected the CACC whose subsequent exhumation and cooling as a MCC occurred along detachments (figure 2.6) [*Whitney et al.*, 2003; *Lefebvre et al.*, 2011].

The CACC then underwent compressional tectonics since the Paleocene, resulting notably in a complete tectonic reorganization of the complex [*Lefebvre et al.*, 2013] and the oroclinal bending of the late Cretaceous-Oligocene forearc/foreland Çankırı basin, located in the northern part of the CACC [*Kaymakci et al.*, 2003, 2009; *Meijers et al.*, 2010].

Reheating of the southeastern part of the CACC has been dated at ~30 Ma (Ar-Ar crystallization ages on K-felspar) and attributed to a new burial stage associated with the activity of the neighboring transpressional central Anatolian fault (figure 2.8) [*Koçyiğit and Beyhan*, 1998; *Jaffey and Robertson*, 2001; *Idleman et al.*, 2014].

The Bornova flysch zone. In the westernmost part of Turkey, located between the Pontides and the Anatolide-Tauride block (figures 2.2 and 2.8), the Bornova flysch zone mainly consists in a non- or slightly metamorphosed mélange [*Okay et al.*, 2001b, 2012; *Robertson et al.*, 2009]. This mélange is constituted by sedimentary, ophiolitic and rare volcanic blocks, in a latest Cretaceous-Paleocene terrigeneous or ophiolite-derived sedimentary matrix [*Okay et al.*, 2012]. This unit is folded and sheared toward the southwest and unconformably overlaid by undeformed Eocene sediments [*Robertson et al.*, 2009].

The Anatolide-Tauride block. Located south of the Izmir-Ankara and the Inner-Tauride oceanic suture zones (figures 2.2 and 2.8), the Anatolide-Tauride block consists in a series of metamorphic domains in the north (i.e. the Anatolides) and non-metamorphosed sediments in the south (i.e. the Taurides) [*Okay*, 1984]. During the Mesozoic, it consisted in a carbonate platform becoming progressively more pelagic from the Santonian (86-83 Ma), before it underthrusted the Lycian and Tauride ophiolites [*Şengör and Yilmaz*, 1981; *Dilek et al.*, 1999; *Celik et al.*, 2006]. This obduction event resulted from an intraoceanic subduction initiated in the Turonian (94-90 Ma) [*Okay et al.*, 2001b]. Similarly, the Antalya ophiolites overthrusted the southern margin of the Tauride platform, cropping out nowadays south of Isparta region (figure 2.8) [*Robertson*, 2002]. From the Tauride northern margin, this compressional front then migrated southward, carrying the remnants of these late Cretaceous ophiolites [*de Graciansky*, 1967; *Gutnic et al.*, 1979; *Collins and Robertson*, 1998], until the non-metamorphosed Lycian nappes overthrusted the Bey Dağları platform and its foreland basin in the Miocene [*Poisson*, 1977; *van Hinsbergen et al.*, 2010a]. Further east, the late Cretaceous-early Cenozoic subduction of the Mesogean oceanic lithosphere below the southern Tauride margin was followed by the Oligocene subduction then late Oligocene-early Miocene collision of the Arabian plate, allowing the building of the Bitlis belt (figure 2.6) [*Dercourt et al.*, 1986; *Hempton*, 1987; *Jolivet and Faccenna*, 2000; *Agard et al.*, 2005; *Allen and Armstrong*, 2008; *Barrier and Vrielynck*, 2008; *Okay et al.*, 2010b; *McQuarrie and van Hinsbergen*, 2013].

Marking the initiation of the southward migration of the thrust front through the Tauride platform, the buried northern Tauride margin underwent a H*P*-L*T* metamorphism, forming the Tavşanlı unit whose peak conditions (i.e. 24 ± 3 kbar, 430 ± 30 °C) were reached between 88 and 78 Ma (figures 2.6 and 2.8) [*Okay*, 1986, 2002; *Sherlock et al.*, 1999; *Seaton et al.*, 2009; *Plunder et al.*, 2013]. Another H*P*-L*T* metamorphic event was then recorded in the underlying Afyon and Ören units between 70 and 65 Ma [*Rimmelé et al.*, 2003a, 2006; *Candan et al.*, 2005; *Pourteau et al.*, 2010, 2013]. These H*P*-L*T* metamorphic units were subsequently exhumed, reaching the surface as soon as the Eocene [*Özcan et al.*, 1988]. Kinematic criteria related to this cold exhumation show mostly top-to-the NE sense of shear, notably in the Ören unit [*Rimmelé et al.*, 2003a]. Structurally below, the Mesozoic carbonate cover of the southern Menderes massif (also belonging to the Tauride platform) underwent a similar

H*P*-L*T* metamorphism in the Eocene, forming the Kurudere-Nebiler unit (figures 2.6 and 2.8) [*Rimmelé et al.*, 2003b; *Whitney et al.*, 2008; *Pourteau et al.*, 2013]. Coevally, the major part of the Menderes massif underwent a M*T*- to H*T*-M*P* Barrovian-type metamorphism (i.e. 5-8 kbar, 450-660 °C in the central Menderes massif), called the *Main Menderes Metamorphism* (figure 2.6) [*Akkök*, 1983; *Şengör et al.*, 1984; *Bozkurt and Oberhänsli*, 2001; *Lips et al.*, 2001; *Okay*, 2001]. Dated from the Oligocene [*Catlos and Çemen*, 2005; *Bozkurt et al.*, 2010], migmatites largely crop out in the northern Menderes massif and seems to indicate a H*T* event that is more or less continue with the *Main Menderes Metamorphism*. The rest of the massif then experienced a greenschist-facies metamorphism [*Hetzel et al.*, 1995a; *Bozkurt and Oberhänsli*, 2001]. In the northern Menderes massif, this exhumation was accommodated by the top-to-the N Simav detachment, displaying a minimum offset of ~50 km until the late Miocene (i.e. ~8 Ma) [*Işik and Tekeli*, 2001; *Ring et al.*, 2003; *Bozkurt et al.*, 2011]. In the southern Menderes massif, coeval top-to-the S extensional shear criteria have been also recognized and early Miocene volcanoclastic rocks were unconformably deposited (figure 2.5) [*Bozkurt and Satır*, 2000; *Gessner et al.*, 2001a, 2001b; *Ring et al.*, 2003]. From the middle Miocene to the late Miocene-Pliocene, exhumation then localized in the central Menderes massif along the top-to-the NE Alaşehir and the top-to-the S Büyük ductile-brittle detachments (figure 2.8) [*Hetzel et al.*, 1995b; *Gessner et al.*, 2001b; *Lips et al.*, 2001; *Ring et al.*, 2003; *Thomson & Ring*, 2006; *van Hinsbergen et al.*, 2010b]. Additional syn-tectonic sedimentary basins emplaced in the hanging walls of both structures [*Sen and Seyitoglu*, 2009].

The Pliocene-Quaternary final evolution of the Menderes massif is dominated by the N-S opening of several grabens, controlled by high-angle normal faults (figures 2.5 and 2.8) [*Çiftçi and Bozkurt*, 2009; *Sen and Seyitoglu*, 2009]. An additional distributed strike-slip tectonics has been recorded in the western part of the Anatolide-Tauride block since the middle Miocene, notably along the NE-SW Izmir-Balıkesir Transfer Zone [*Ersoy et al.*, 2011].

During its Cenozoic evolution, the Anatolide-Tauride block has recorded several large-scale block rotations. While no significant rotation has been recorded north of the Menderes massif, the central Menderes massif underwent a 25-30°counterclockwise rotation during its exhumation (i.e. 15-5 Ma), coevally with the ~20° counterclockwise rotation recorded in the Lycian nappes and the Bey Dağları

platform (figure 2.4) [*Kissel et al.*, 1993; *van Hinsbergen et al.*, 2010a,b]. Further east, the central Taurides experienced a ~40° clockwise rotation between the middle Eocene-Oligocene (figure 2.4) [*Kissel et al.*, 1993], also affecting the Tavşanlı and Afyon units further north, but with a smaller amount [*Pourteau et al.*, 2010]. Finally, in the eastern Taurides, a ~40° counterclockwise rotation has been evidenced in Eocene volcanic rocks (figure 2.4) [*Kissel et al.*, 2003].

2.4.2. Magmatic features

The geodynamic evolution of the eastern Mediterranean region was accompanied by the emplacement of several magmatic provinces. The spatial and temporal distribution of magmatic centers and the evolution of their geochemical composition can be used to constrain the origin of magmas and associated geodynamic processes. In this section, we compile available information on the nature and origin of the different magmatic provinces since the late Cretaceous.

The Balkans-Pontides magmatic province. During the late Cretaceous and the early Paleocene, a magmatic province developed in the Balkans and the eastern Pontides where both plutonic and volcanic centers have been identified [*Yılmaz et al.*, 1997; *Berza et al.*, 1998; *Ciobanu et al.*, 2002]. In the Pontides, predominant volcanic rocks mostly emplaced between the late Turonian and latest Campanian (~90-70 Ma) (figure 2.6) and seems to display a southward migration through time [*Yılmaz et al.*, 1997; *Bektaş et al.*, 1999; *Okay et al.*, 2001b; *Eyüboğlu et al.*, 2010], similarly as magmatic products in the Balkans [*Ciobanu et al.*, 2002; *von Quadt et al.*, 2005; *Kolb et al.*, 2012].

These rocks mainly display a medium- to high-K calc-alkaline magmatic trend with intermediate composition [*Yılmaz et al.*, 1997; *Berza et al.*, 1998; *von Quadt et al.*, 2005; *Boztuğ et al.*, 2006]. Geochemical and isotopic signatures of these magmas indicate a typical arc-related origin with an increase of their mantle source component through time [*von Quadt et al.*, 2005]. An additional shoshonitic (i.e. high-K alkaline) magmatic trend has been recognized in the eastern Srednogorie region in the latest Cretaceous [*Boccaletti et al.*, 1978]. Finally, mafic alkaline volcanic rocks with a high asthenospheric source component emplaced in the eastern Srednogorie, Banat and Timok regions until Eocene times (figure 2.6) [*Cvetković et al.*, 2004].

The CACC plutonic province. In the CACC (figure 2.2), the late Cretaceous exhumation and cooling of H*T* metamorphic domes were accompanied by the emplacement of numerous intrusions in three successive stages [*Aydin et al.*, 1998; *Ilbeyli et al.*, 2004; *Boztuğ et al.*, 2009]. First, rare peraluminous two-mica leucogranites emplaced, characterized by a high-K calc-alkaline magmatic trend and a major crustal source component. Then, metaluminous high-K calc-alkaline intrusions with composition evolving from quartz monzonite to monzogranite developed with a highly metasomatized mantle source component. Finally, little amount of shoshonitic then silica-undersaturated alkaline intrusions emplaced until the beginning of the Maastrichtian, characterized by a significant asthenospheric source component (figure 2.6).

The Eocene calc-alkaline magmatic province. During the Eocene, an E-W-trending magmatic province developed, extending from the eastern Pontides to the Chalkidiki peninsula, south of the Rhodope massif (figure 2.6). This province is mainly represented by volcano-sedimentary rocks in the east [*Arslan et al.*, 2013] and plutonic bodies in the west [*Harris et al.*, 1994; *Okay and Satır*, 2006].

These rocks mainly follow a medium- to high-K calc-alkaline magmatic trend with both low-silica and high-silica end-members and geochemical and isotopic signatures typical for a subduction-related origin [*Harris et al.*, 1994; *Ersoy and Palmer*, 2013].

The Rhodope magmatic province. From the late Eocene to the Miocene, a widespread magmatic activity developed in the Rhodope massif during the last stages of exhumation of the central and south Rhodope core complexes [*Jones et al.*, 1992; *Marchev et al.*, 2004b, 2005; *Ersoy and Palmer*, 2013].

Emplaced first in the central Rhodope core complex (figure 2.6), these volcanic and plutonic rocks typically crosscut detachment faults [*Marchev et al.*, 2005] with some intrusions displaying a strong marginal foliation associated with an extension-related top-to-the N sense of shear [*Jones et al.*, 1992]. Composition of most of these magmas evolves from high-K calc-alkaline to shoshonitic, including both mafic and silicic rocks [*Marchev et al.*, 2004b; *Ersoy and Palmer*, 2013]. Their geochemical and isotopic signatures reflect both highly metasomatized mantle and a crustal source components, the

latter decreasing from northwest to southeast [*Marchev et al.*, 2004b, 2005; *Ersoy and Palmer*, 2013]. The end of the magmatic activity in the central Rhodope core complex is marked by the emplacement of late Oligocene alkaline dykes displaying a high asthenospheric source component [*Marchev et al.*, 2004b].

In the south Rhodope core complex, syn-tectonic intrusions with a similar composition and origin as the central Rhodope magmatic centers, then emplaced in the early Miocene (figure 2.6), displaying an extensional mylonitic fabric with a top-to-the SW sense of shear [*Dinter and Royden*, 1993; *Dinter et al.*, 1995; *Ersoy and Palmer*, 2013].

The west Anatolian-Aegean magmatic province. In the Biga peninsula (northwest Anatolia, figure 2.8) and on the nearby north Aegean islands, a volcanic activity developed since the Oligocene then migrated southward, reaching the Menderes massif in the Miocene [*Yılmaz et al.*, 2001; *Dilek and Altunkaynak*, 2009]. Several intrusions also emplaced, coevally with the exhumation of MCCs, such as in the Kazdağ massif in the late Oligocene-early Miocene [*Black et al.*, 2013] and in the Menderes massif and the Cyclades in the Miocene (figure 2.6) [*Faure and Bonneau*, 1988; *Altherr and Siebel*, 2002; *Pe-Piper and Piper*, 2006, 2007; *Dilek et al.*, 2009; *Iglseder et al.*, 2009; *Denèle et al.*, 2011; *Laurent et al.*, 2015; *Rabillard et al.*, 2015].

These intrusions are exposed in the footwall of major detachments where they show a strong foliation with extensional kinematic criteria as well as a cataclastic zone at the contact with the detachment [*Faure and Bonneau*, 1988; *Gessner et al.*, 2001a; *Dilek et al.*, 2009; *Iglseder et al.*, 2009; *Denèle et al.*, 2011; *Rabillard et al.*, 2015]. They emplaced first in the northeastern Menderes massif with the Egrigöz and Koyunoba plutons both dated at ~21 Ma (U-Pb crystallization ages on zircon) in the footwall of the Simav detachment [*Ring and Collins*, 2005]. Then, a few intrusions developed below the Alaşehir detachment in the central Menderes massif such as the Salihli pluton dated at ~15 Ma (U-Pb crystallization ages on zircon) although these ages could be affected by dissolution-precipitation reactions [*Glodny and Hetzel*, 2007; *Catlos et al.*, 2010]. In the Cyclades finally, the intrusions emplaced and exhumed in the footwall of the NCDS (in Ikaria, Mykonos and Tinos), the NPEFS (in Naxos) and the WCDS (in Serifos and Lavrion), with ages decreasing from east to west,

from ~15 Ma in Ikaria (U-Pb crystallization ages on zircon) [*Bolhar et al.*, 2010] to ~8 Ma in Lavrion (K-Ar crystallization ages on biotite) [*Altherr et al.*, 1982].

Geochemical data for these volcanic and plutonic rocks indicate a composition evolving from high-K calc-alkaline to shoshonitic [*Ersoy and Palmer*, 2013; *Seghedi et al.*, 2013]. In the Menderes massif and the Cyclades, most of the Miocene intrusions are I-type granites or granodiorites although some S-type granites and pegmatite dikes are also observed in the central Cyclades, associated with migmatites [*Altherr et al.*, 1982; *Altherr and Siebel*, 2002; *Dilek et al.*, 2009; *Stouraiti et al.*, 2010]. As for the Rhodope massif, *Ersoy and Palmer*, [2013] suggest a highly metasomatized mantle source component for these magmas [*Ersoy and Palmer*, 2013], although the sole contribution of several crustal sources (i.e. metasediments and amphibolites) has also been proposed, notably for the Cycladic intrusions [*Altherr and Siebel*, 2002; *Stouraiti et al.*, 2010]. Another interesting observation is the decrease through time, from the northeast (in Ikaria) to the southwest (in Serifos), of the crustal (or felsic) source component of these intrusions relative to their mantle (or mafic) source component [*Jolivet et al.*, 2015].

An additional scattered alkaline volcanism, represented by alkali basalts, emplaced from the late Miocene to the Quaternary in an area extending from the Thrace basin in the north to Patmos island and the Isparta region in the south (figure 2.6) [*Agostini et al.*, 2007; *Ersoy and Palmer*, 2013]. Similarly to the older alkaline magmatic centers, their geochemical and isotopic composition involves a major asthenospheric source component [*Agostini et al.*, 2007].

Finally, an active volcanism has occurred since the Pliocene along a curved narrow arc, notably in the islands of Aegina, Milos, Santorini and Nisyros (figure 2.6). This typical arc-related volcanism mostly presents a medium-potassic calc-alkaline composition [*Fytikas et al.*, 1984; *Pe-Piper and Piper*, 2005; *Ersoy and Palmer*, 2013].

The late Miocene-Quaternary eastern Anatolia volcanic province. In eastern Anatolia, a late Miocene-Quaternary volcanism developed progressively from the eastern Pontides, through the Taurides and the Bitlis belt, to the Arabian foreland basin (figure 2.6) [*Pearce et al.*, 1990; *Keskin*, 2003, 2007]. Composition of these volcanics evolves from high-K calc-alkaline in the north to alkaline

in the south with a compositional ranging from basalt to rhyolite [*Keskin*, 2003]. Evolution of the geochemical and isotopic composition of these magmas suggests a decrease of their metasomatized mantle source component from north to south, correlated with an increase of the asthenospheric source component [*Keskin*, 2003, 2007].

2.5. Kinematic reconstructions of the eastern Mediterranean region

Using all the sedimentary, tectono-metamorphic and magmatic data described above, our kinematic reconstructions of the eastern Mediterranean region were performed from the present to the past. However, for clarity, this tectonic evolution is described in the following section from the late Cretaceous to nowadays, following the geodynamic history of the region. The full set of paleotectonic maps is shown below (figures 2.9a-y), as well as the reconstructed lithospheric-scale cross-sections (figures 2.10 and 2.11). These kinematic reconstructions are also available as a video (cf. *Annexe C, video C.1*). On these reconstructions, the evolution of metamorphic units is displayed from their time of formation to their exhumation at the surface. They are shown with lighter or intense colors when they are respectively still at depth or close to the surface.

Les treize pages suivantes présentent l'ensemble des cartes paléotectoniques extraites du modèle de reconstructions cinématiques et qui intègre l'évolution magmatique de la Méditerranée orientale.

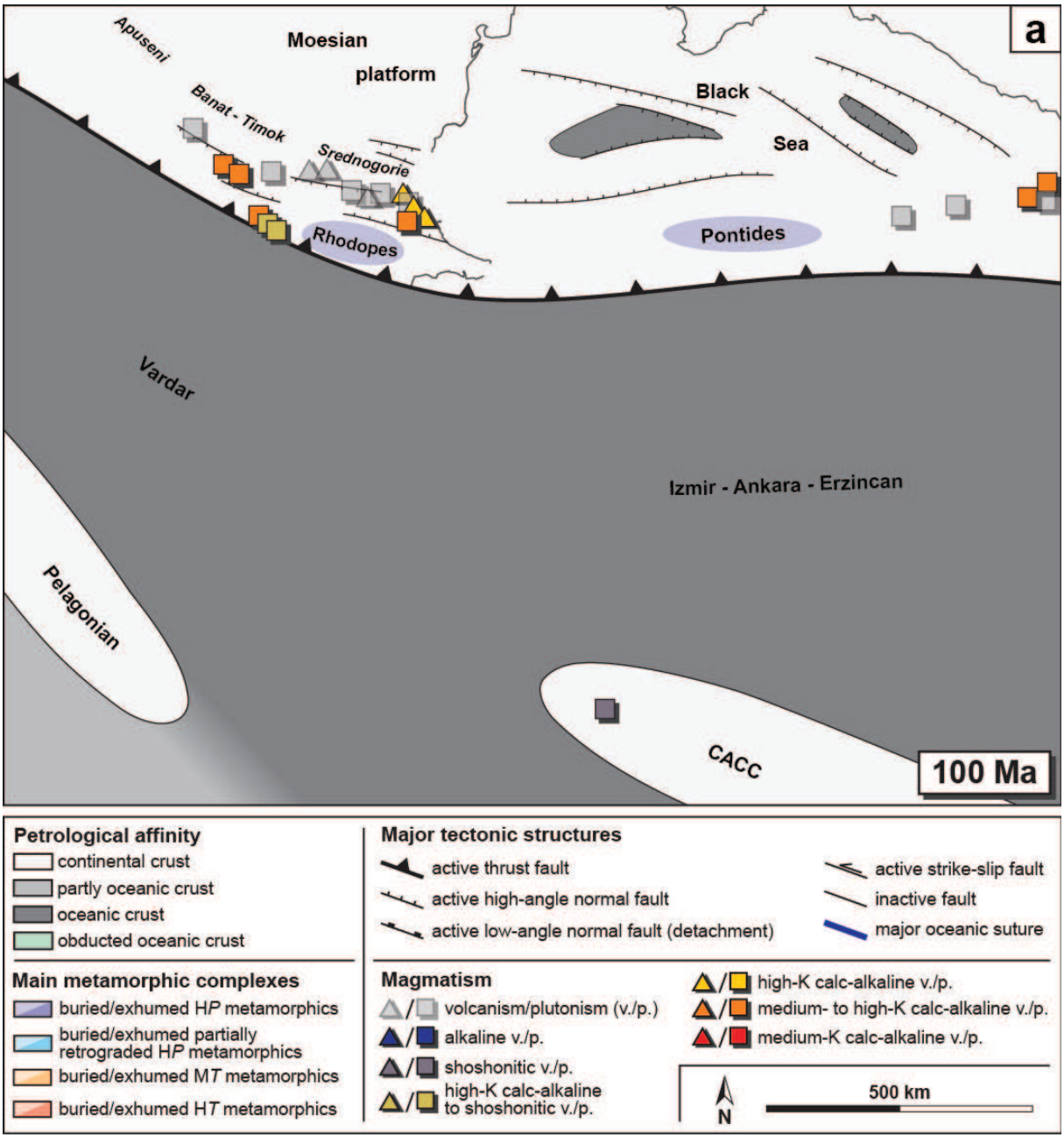

Figure 2.9: (a-y) paleotectonic maps extracted from the kinematic reconstruction model. CACC: Central Anatolian Crystalline Complex. OOP: Olympos-Ossa-Pelion windows.

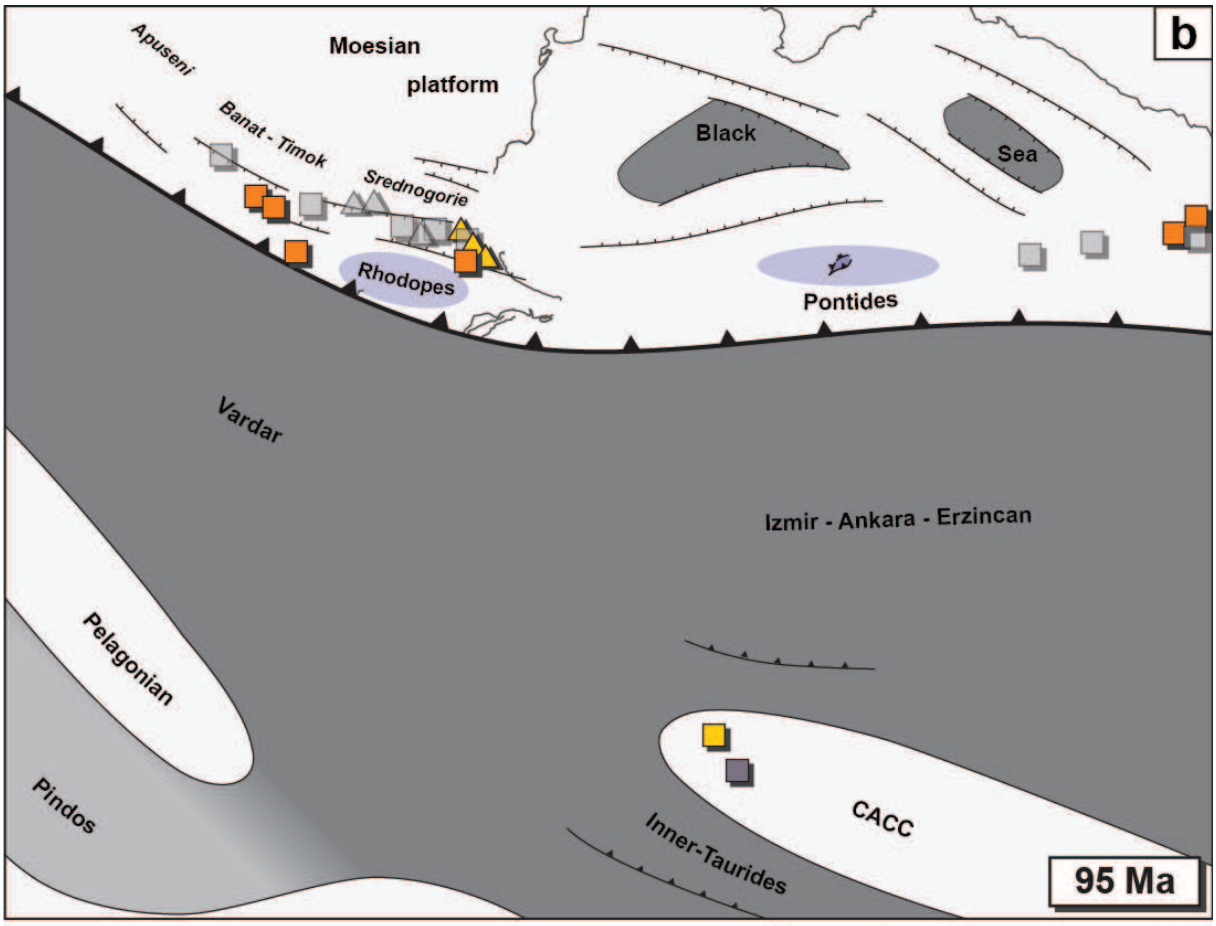
b
Apuseni
Moesian
platform
Banat - Timok
Srednogorie
Black
Sea
Rhodopes
Pontides
Vardar
Izmir - Ankara - Erzincan
Pelagonian
Pindos
CACC
Inner-Taurides
95 Ma

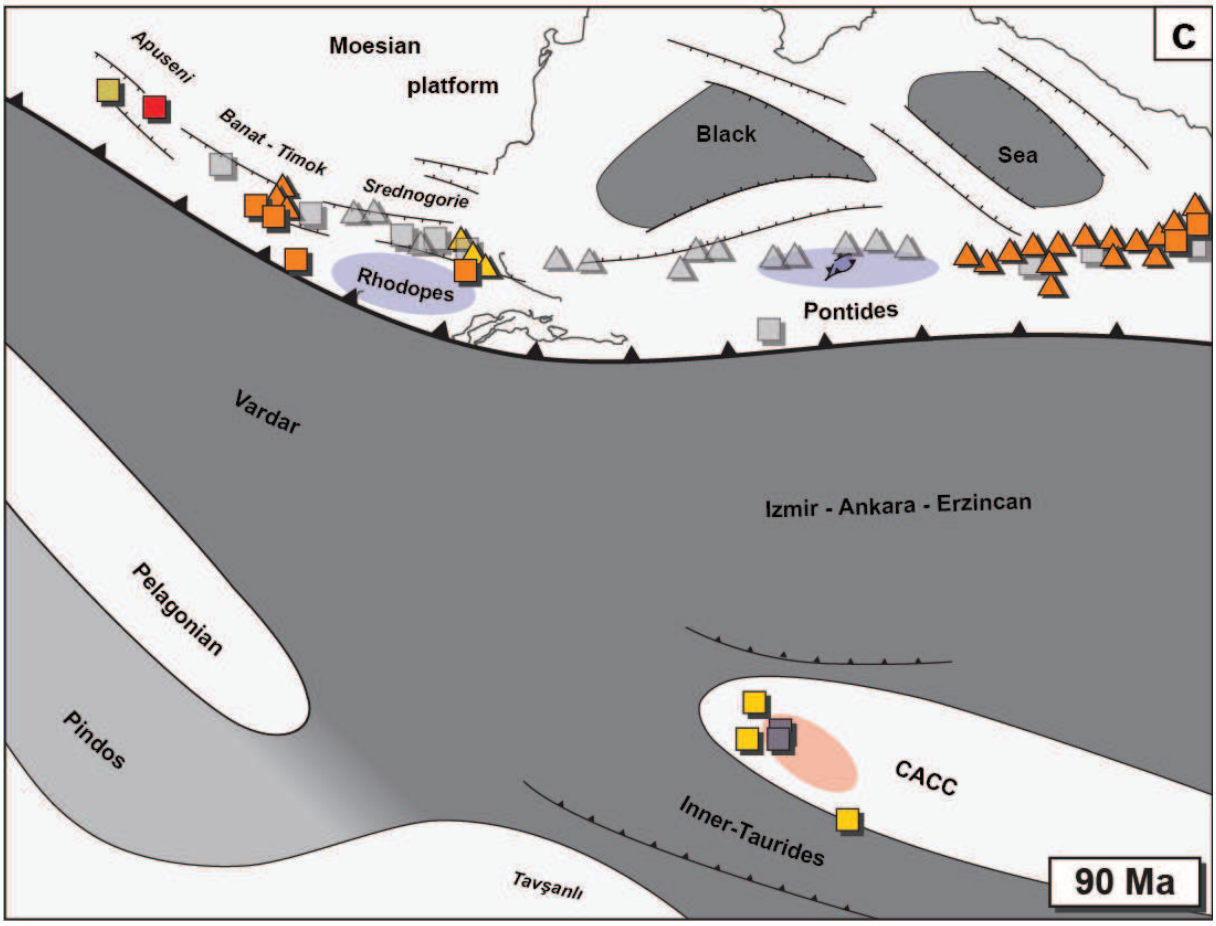
c
Apuseni
Moesian
platform
Banat - Timok
Srednogorie
Black
Sea
Rhodopes
Pontides
Vardar
Izmir - Ankara - Erzincan
Pelagonian
Pindos
CACC
Inner-Taurides
Tavşanlı
90 Ma

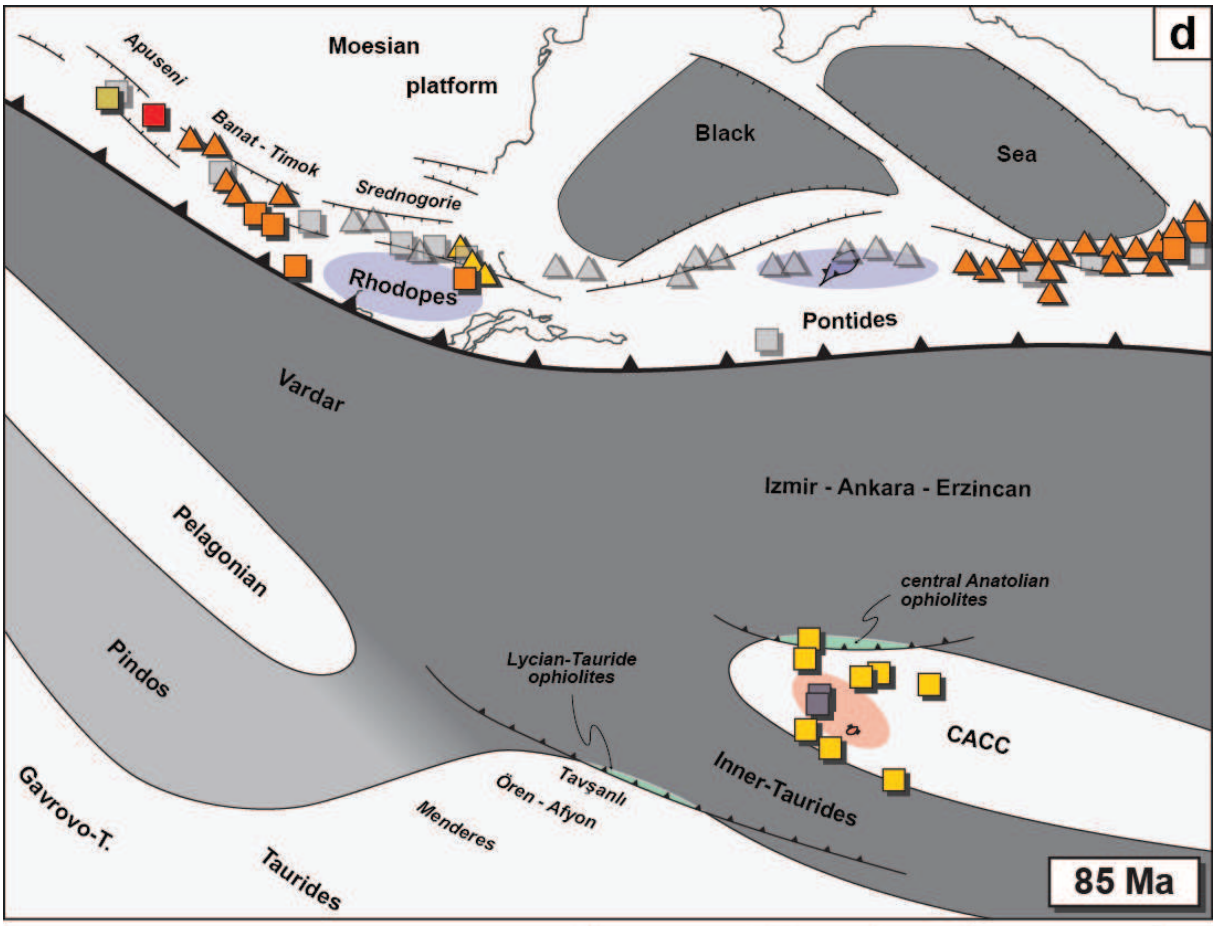
d
Moesian
platform
Apuseni
Banat - Timok
Srednogorie
Rhodopes
Black
Sea
Pontides
Vardar
Izmir - Ankara - Erzincan
Pelagonian
Pindos
central Anatolian
ophiolites
Lycian-Tauride
ophiolites
CACC
Inner-Taurides
Tavşanlı
Ören - Afyon
Menderes
Gavrovo-T.
Taurides
85 Ma

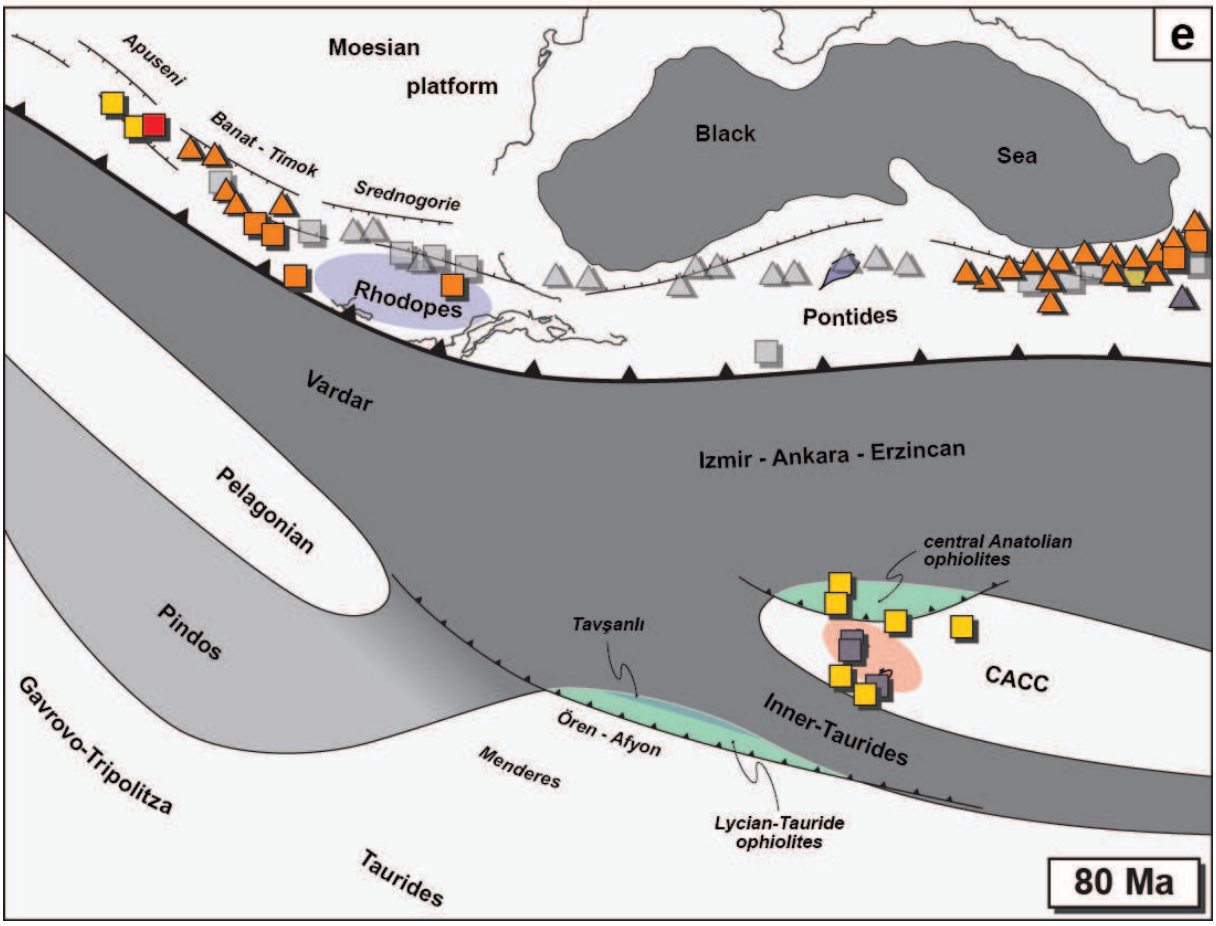
e
Moesian
platform
Apuseni
Banat - Timok
Srednogorie
Rhodopes
Black
Sea
Pontides
Vardar
Izmir - Ankara - Erzincan
Pelagonian
Pindos
central Anatolian
ophiolites
Tavşanlı
CACC
Inner-Taurides
Ören - Afyon
Menderes
Gavrovo-Tripolitza
Lycian-Tauride
ophiolites
Taurides
80 Ma

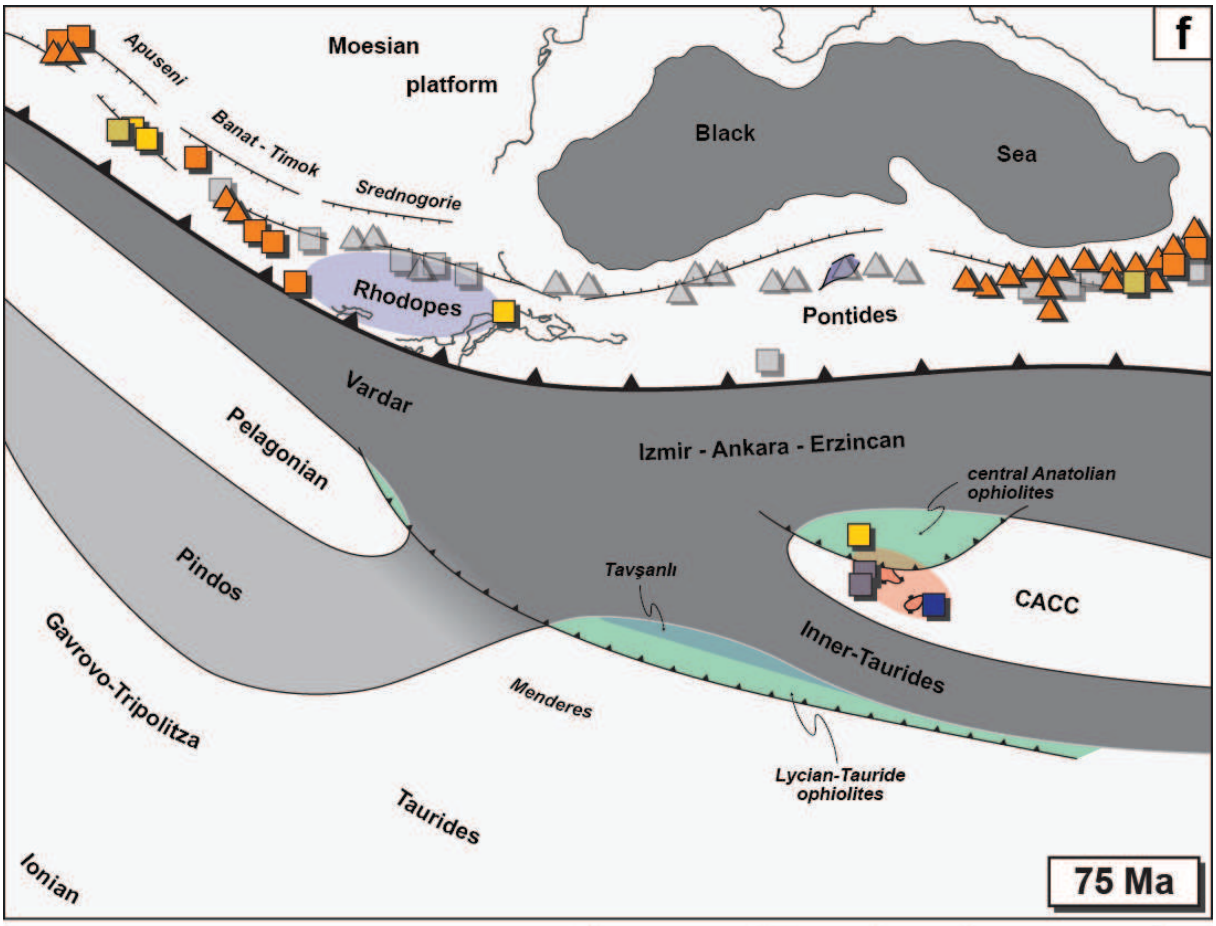
f
Moesian
platform
Apuseni
Banat - Timok
Srednogorie
Black
Sea
Rhodopes
Pontides
Vardar
Pelagonian
Izmir - Ankara - Erzincan
central Anatolian
ophiolites
Pindos
Tavşanlı
CACC
Inner-Taurides
Gavrovo-Tripolitza
Menderes
Lycian-Tauride
ophiolites
Taurides
Ionian
75 Ma

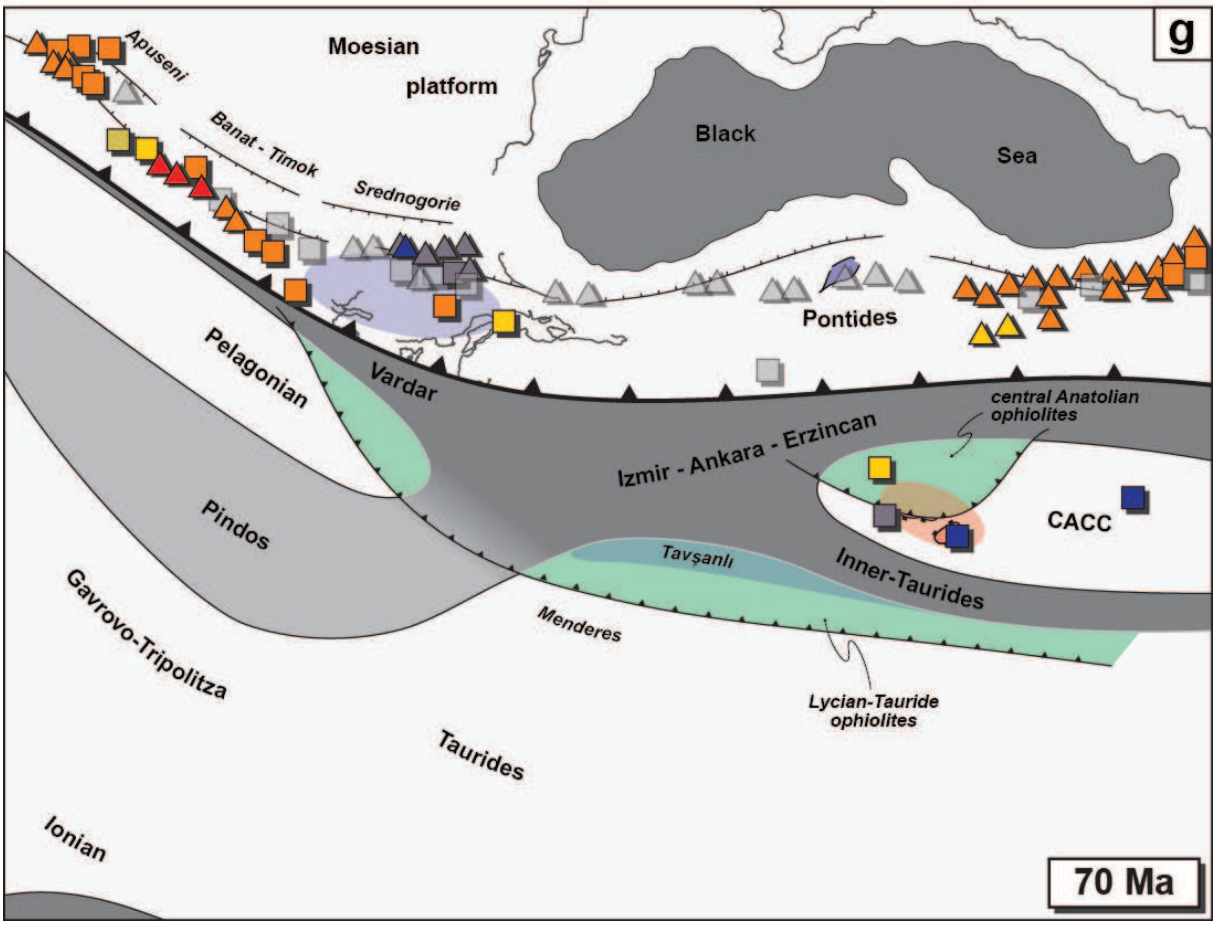
g
Moesian
platform
Apuseni
Banat - Timok
Srednogorie
Black
Sea
Pontides
Pelagonian
Vardar
central Anatolian
ophiolites
Izmir - Ankara - Erzincan
Pindos
CACC
Tavşanlı
Inner-Taurides
Gavrovo-Tripolitza
Menderes
Lycian-Tauride
ophiolites
Taurides
Ionian
70 Ma

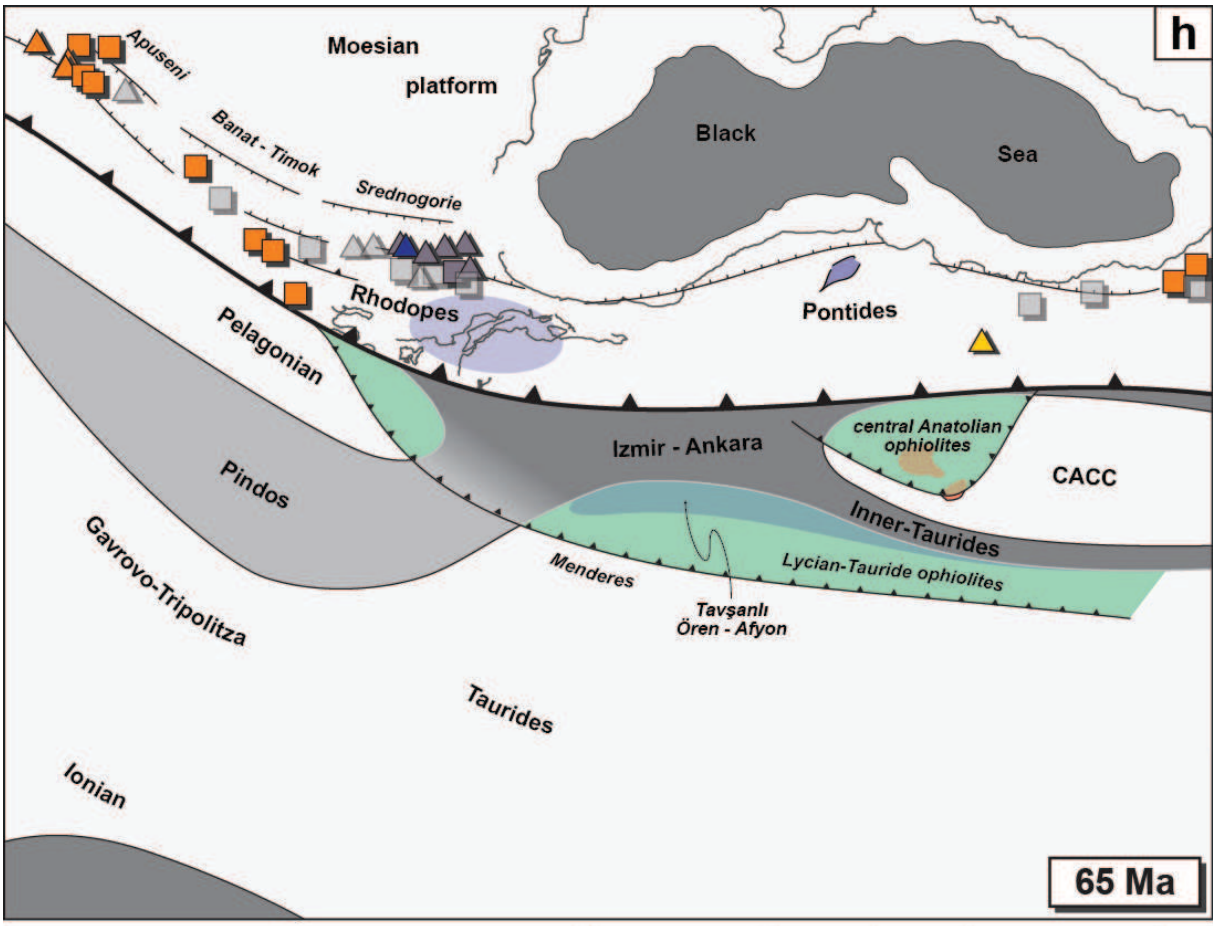
h
Moesian
platform
Apuseni
Banat - Timok
Srednogorie
Black
Sea
Rhodopes
Pontides
Pelagonian
Izmir - Ankara
central Anatolian
ophiolites
CACC
Pindos
Inner-Taurides
Lycian-Tauride ophiolites
Menderes
Tavşanlı
Ören - Afyon
Gavrovo-Tripolitza
Taurides
Ionian
65 Ma

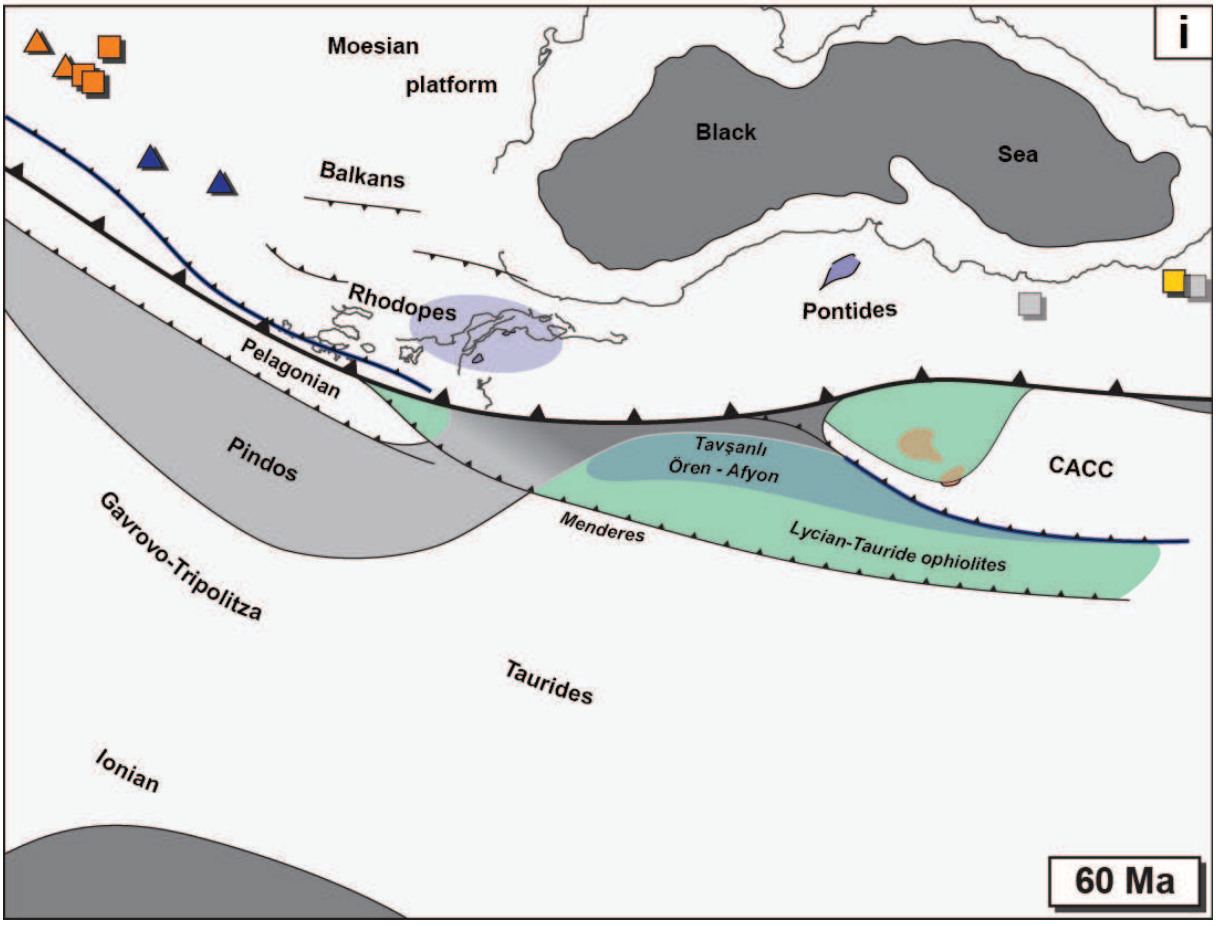
i
Moesian
platform
Black
Sea
Balkans
Rhodopes
Pontides
Pelagonian
Pindos
Tavşanlı
Ören - Afyon
CACC
Menderes
Lycian-Tauride ophiolites
Gavrovo-Tripolitza
Taurides
Ionian
60 Ma

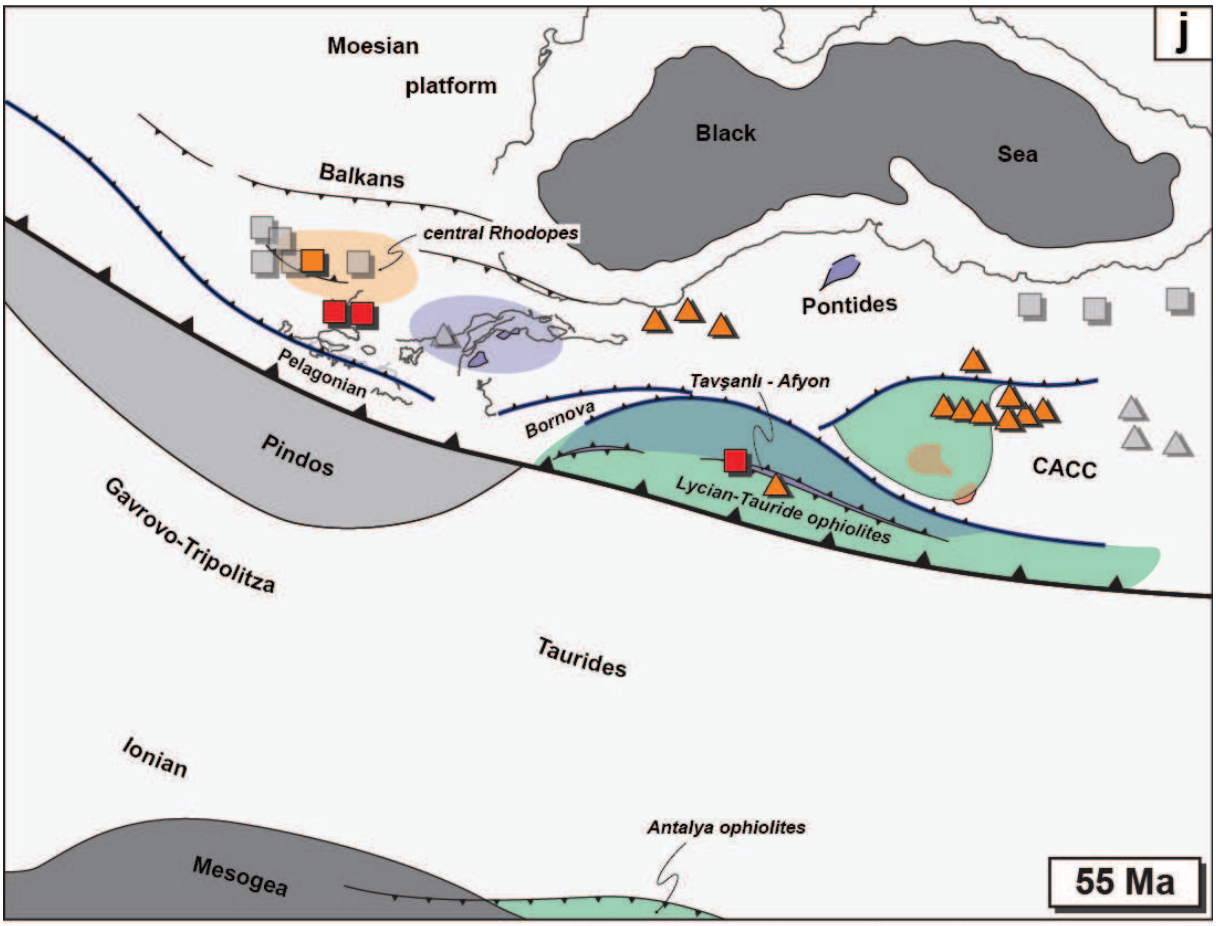
j
Moesian
platform
Black
Sea
Balkans
central Rhodopes
Pontides
Pelagonian
Bornova
Tavşanlı - Afyon
Pindos
CACC
Gavrovo-Tripolitza
Lycian-Tauride ophiolites
Taurides
Ionian
Antalya ophiolites
Mesogea
55 Ma

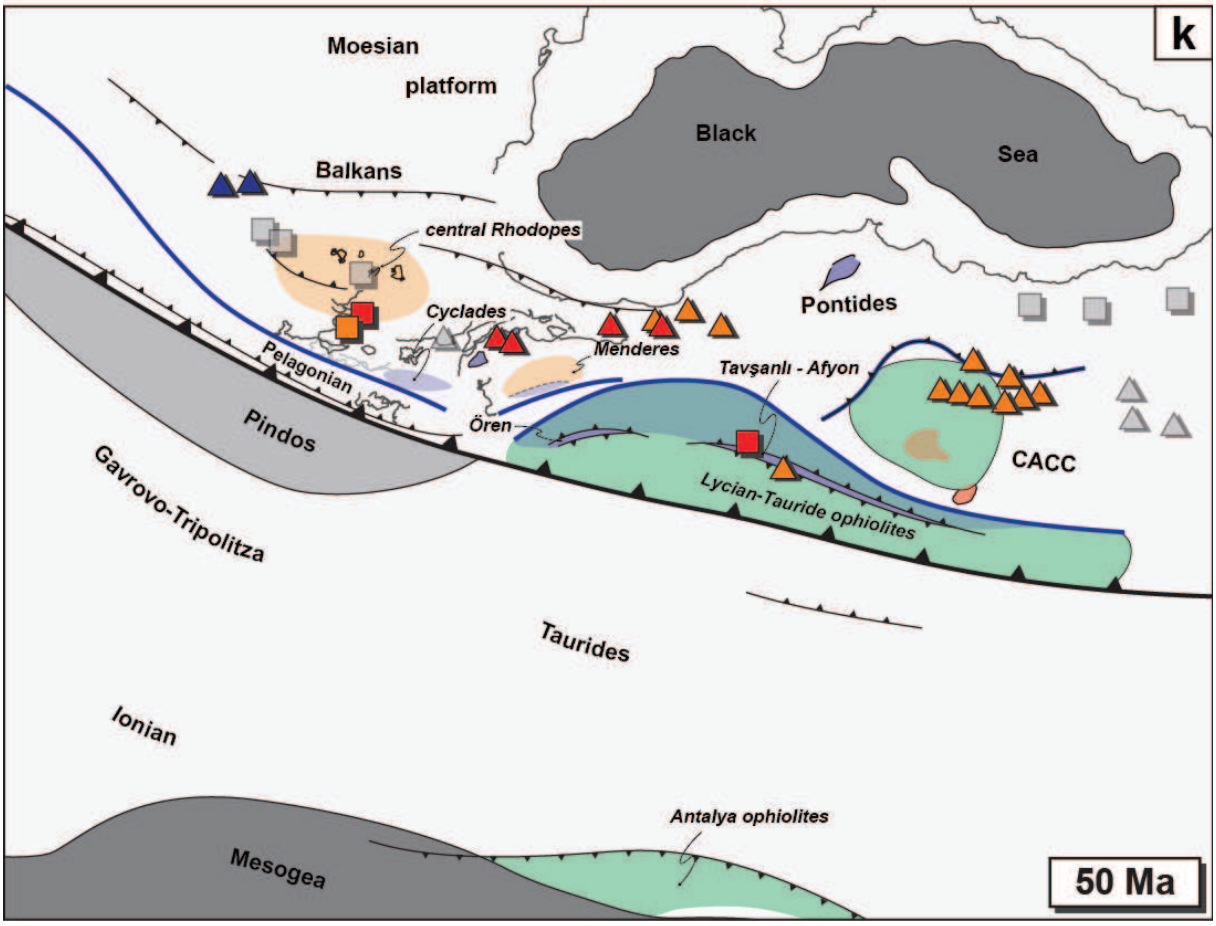
k
Moesian
platform
Black
Sea
Balkans
central Rhodopes
Pontides
Cyclades
Menderes
Pelagonian
Tavşanlı - Afyon
Pindos
Ören
CACC
Gavrovo-Tripolitza
Lycian-Tauride ophiolites
Taurides
Ionian
Antalya ophiolites
Mesogea
50 Ma

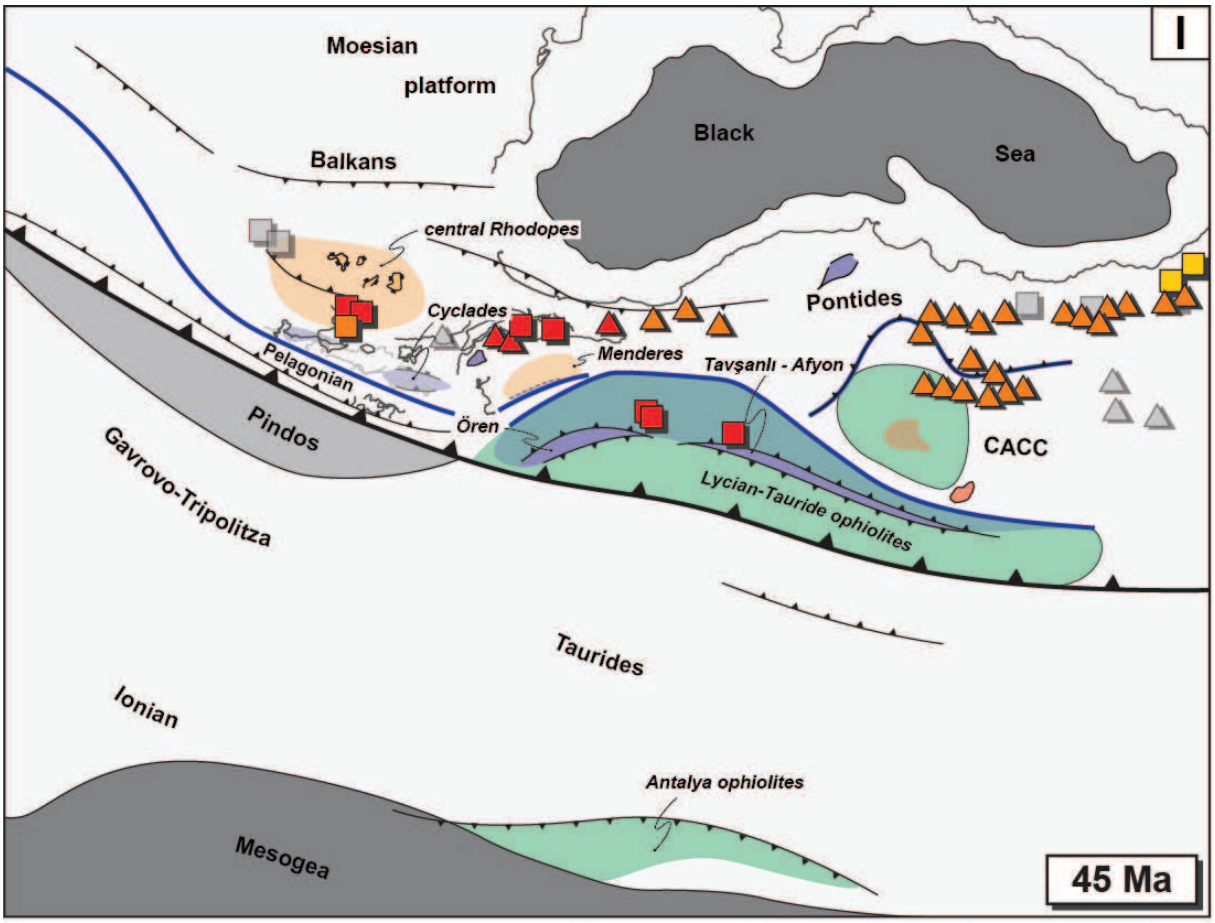
l
Moesian
platform
Balkans
Black
Sea
central Rhodopes
Cyclades
Pontides
Menderes
Tavşanlı - Afyon
Pelagonian
Ören
Pindos
CACC
Gavrovo-Tripolitza
Lycian-Tauride ophiolites
Taurides
Ionian
Antalya ophiolites
Mesogea
45 Ma

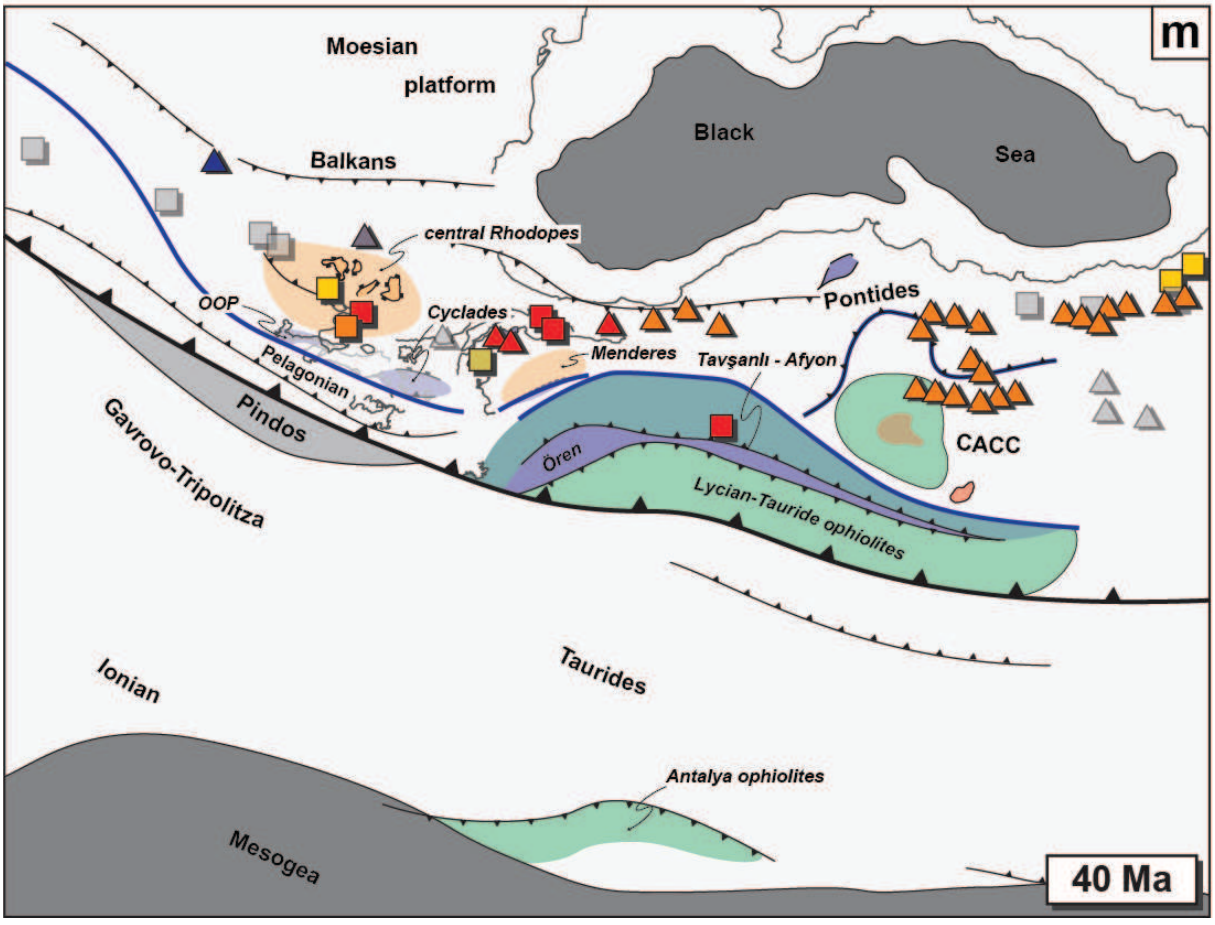
m
Moesian
platform
Balkans
Black
Sea
central Rhodopes
OOP
Cyclades
Pontides
Menderes
Tavşanlı - Afyon
Pelagonian
Pindos
CACC
Gavrovo-Tripolitza
Ören
Lycian-Tauride ophiolites
Taurides
Ionian
Antalya ophiolites
Mesogea
40 Ma

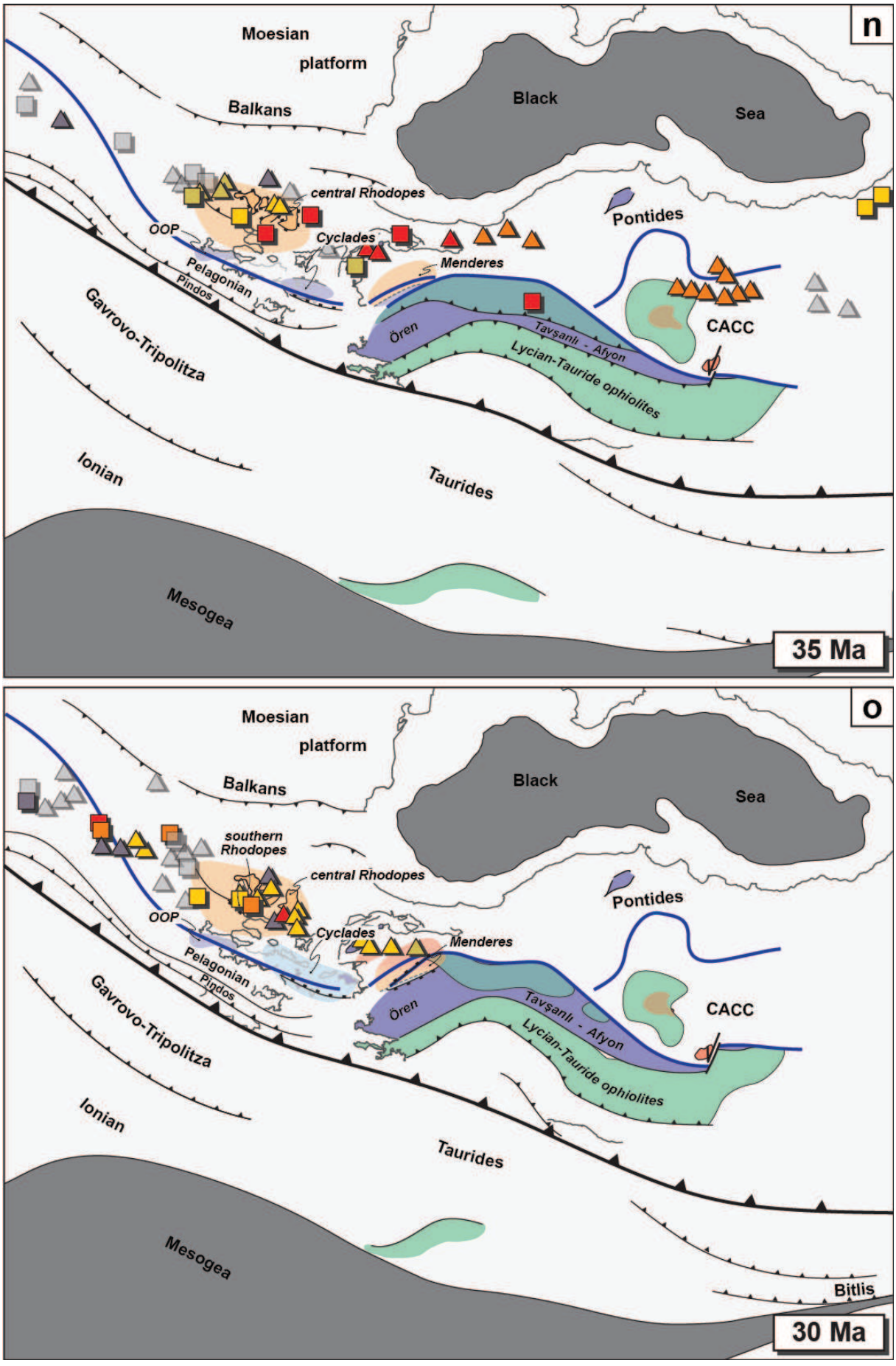
n
Moesian
platform
Balkans
Black
Sea
central Rhodopes
OOP
Cyclades
Menderes
Pontides
Pelagonian
Pindos
Gavrovo-Tripolitza
Ören
Tavşanlı - Afyon
CACC
Lycian-Tauride ophiolites
Ionian
Taurides
Mesogea
35 Ma
o
Moesian
platform
Balkans
Black
Sea
southern
Rhodopes
central Rhodopes
OOP
Cyclades
Menderes
Pontides
Pelagonian
Pindos
Gavrovo-Tripolitza
Ören
Tavşanlı - Afyon
CACC
Lycian-Tauride ophiolites
Ionian
Taurides
Mesogea
Bitlis
30 Ma

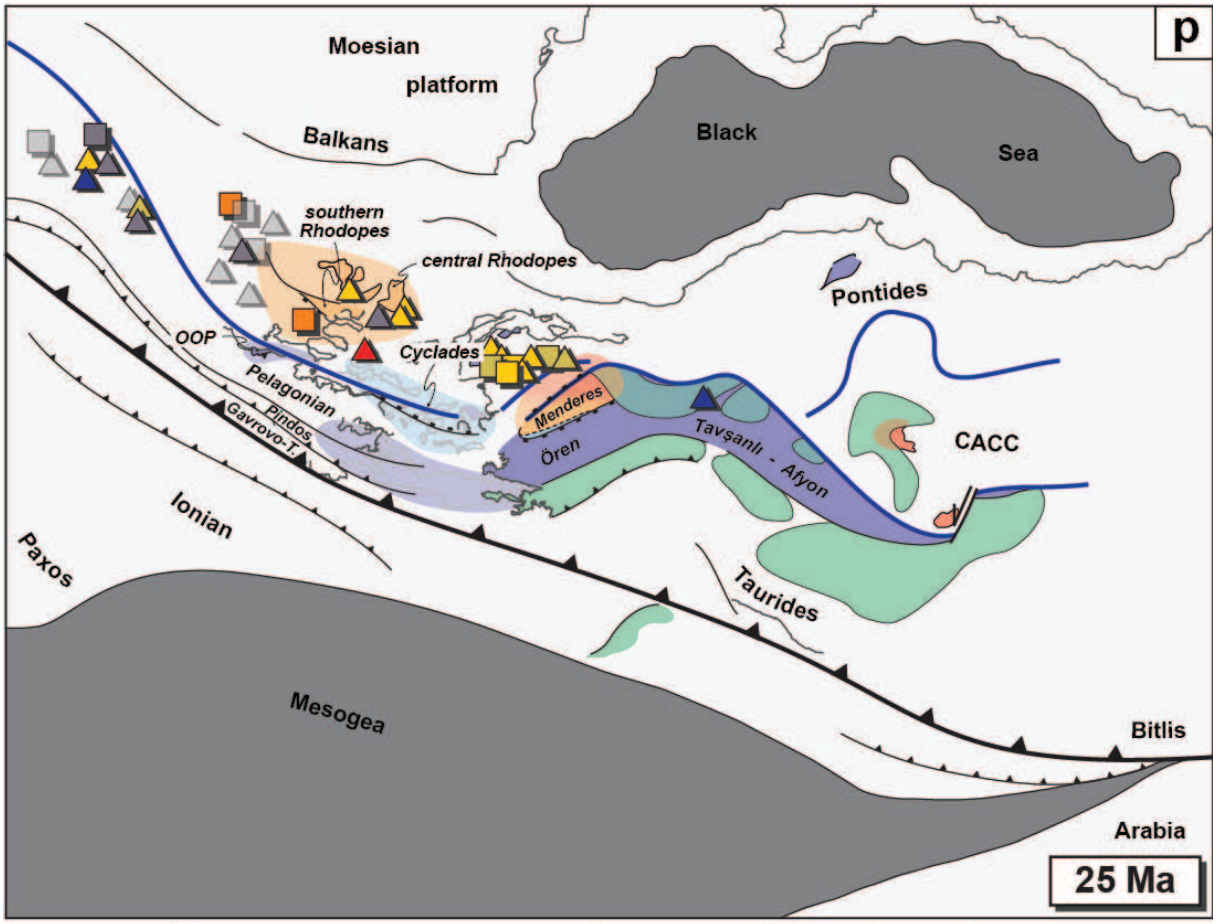
p
Moesian
platform
Balkans
Black
Sea
southern
Rhodopes
central Rhodopes
Pontides
OOP
Cyclades
Pelagonian
Pindos
Gavrovo-T.
Menderes
Ören
Tavşanlı - Afyon
CACC
Ionian
Paxos
Taurides
Mesogea
Bitlis
Arabia
25 Ma

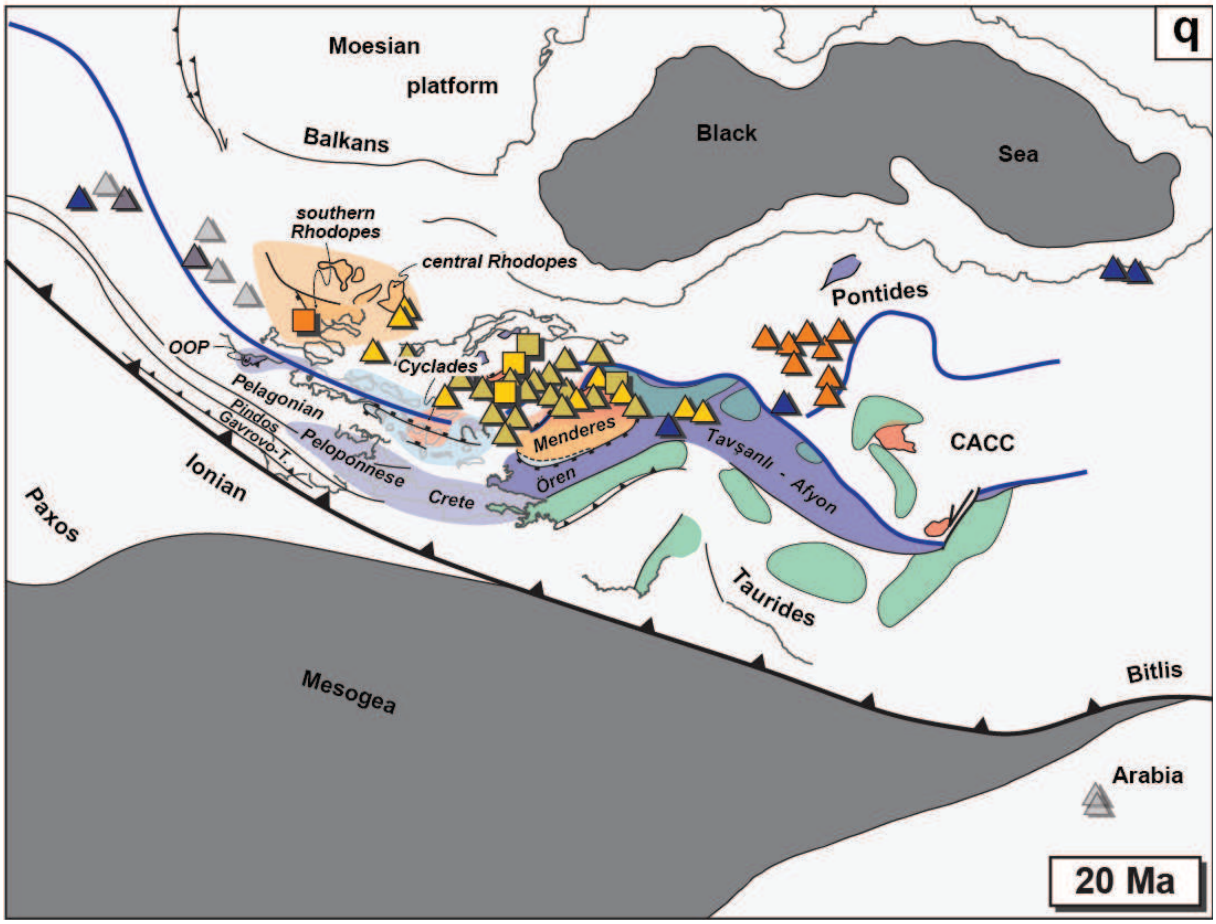
q
Moesian
platform
Balkans
Black
Sea
southern
Rhodopes
central Rhodopes
Pontides
OOP
Cyclades
Pelagonian
Pindos
Gavrovo-T.
Peloponnese
Crete
Menderes
Ören
Tavşanlı - Afyon
CACC
Ionian
Paxos
Taurides
Mesogea
Bitlis
Arabia
20 Ma

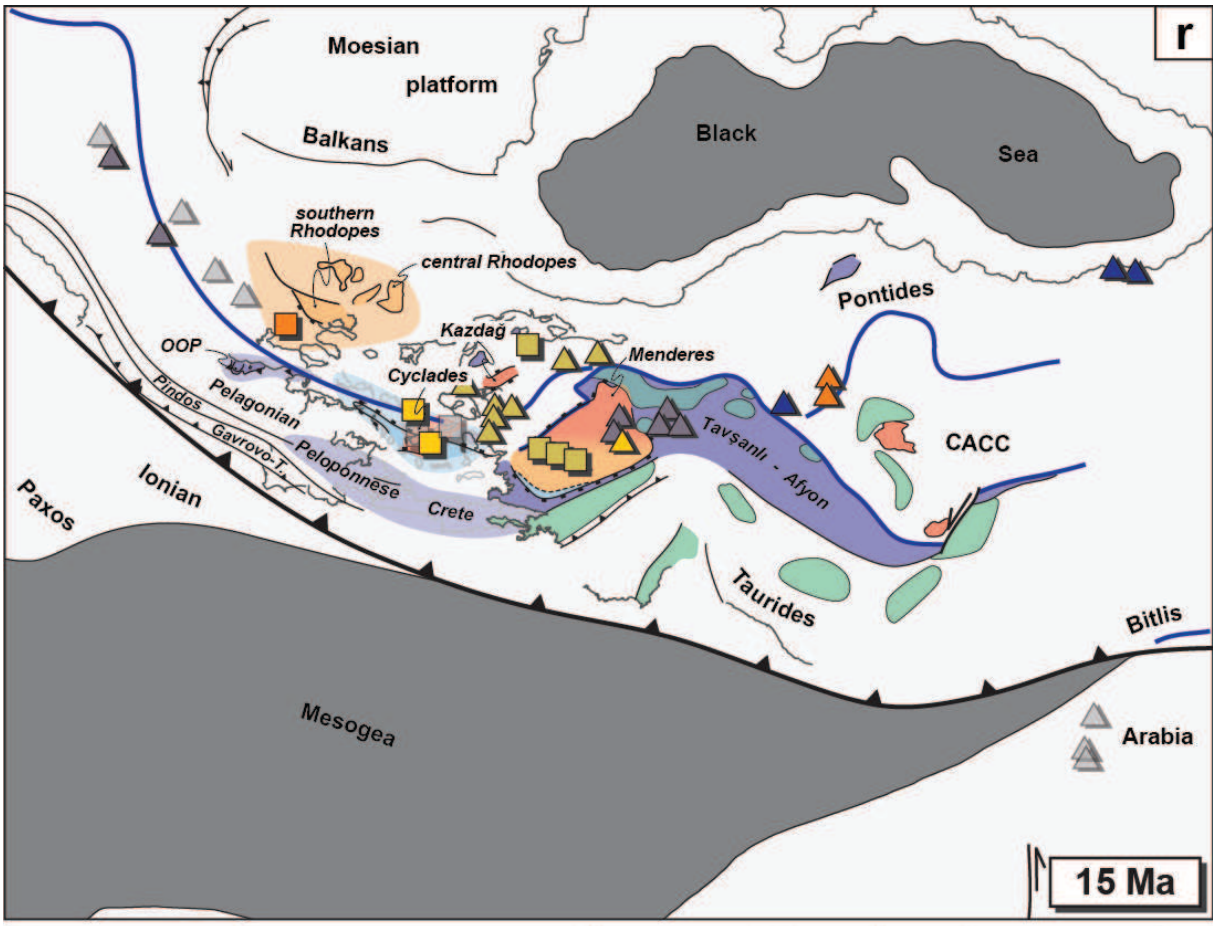
r
Moesian
platform
Balkans
Black
Sea
southern
Rhodopes
central Rhodopes
Pontides
Kazdag
Menderes
OOP
Cyclades
Pindos
Pelagonian
Gavrovo-T.
Peloponnese
Crete
Tavşanlı - Afyon
CACC
Paxos
Ionian
Taurides
Bitlis
Mesogea
Arabia
15 Ma

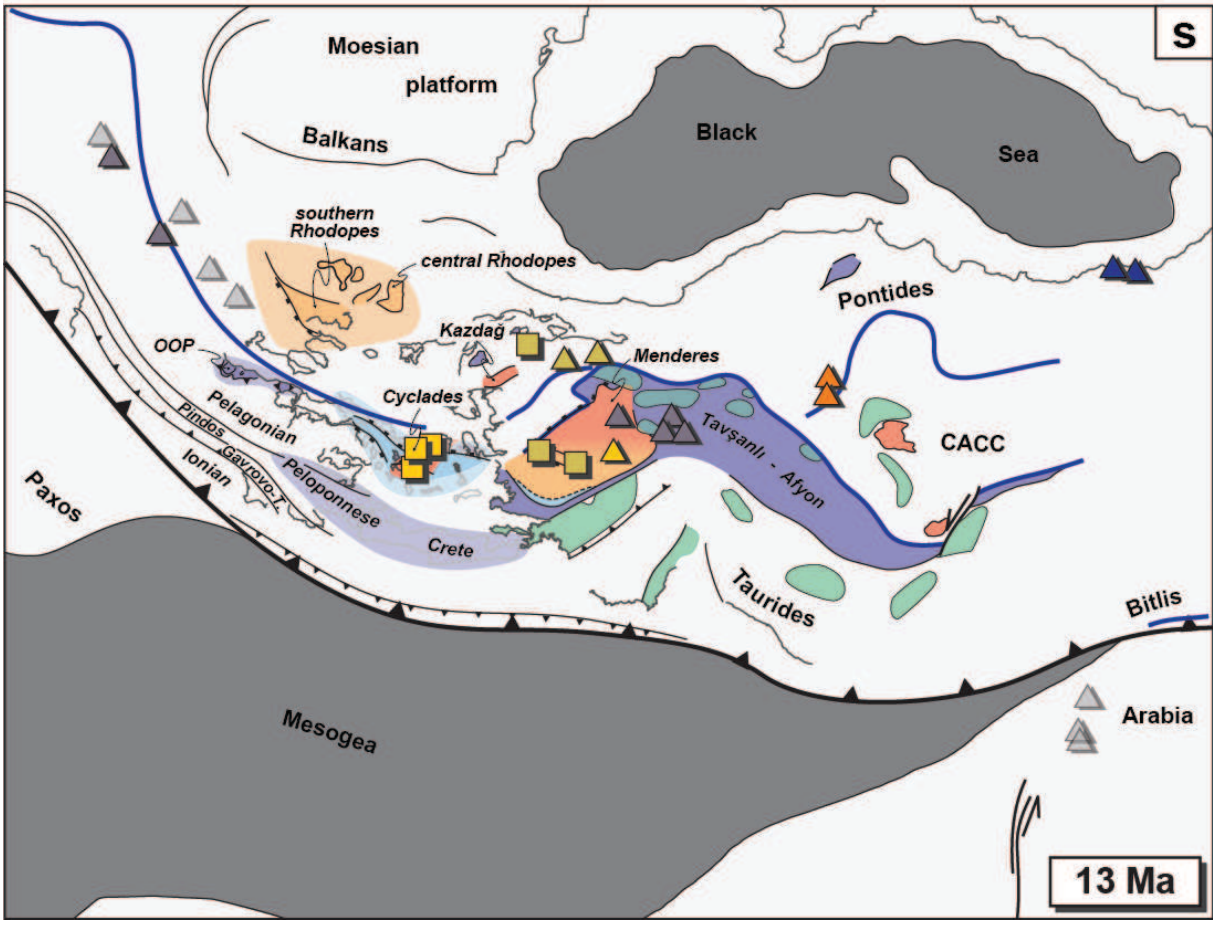
s
Moesian
platform
Balkans
Black
Sea
southern
Rhodopes
central Rhodopes
Pontides
Kazdag
Menderes
OOP
Cyclades
Pindos
Pelagonian
Gavrovo-T.
Ionian
Peloponnese
Crete
Tavşanlı - Afyon
CACC
Paxos
Taurides
Bitlis
Mesogea
Arabia
13 Ma

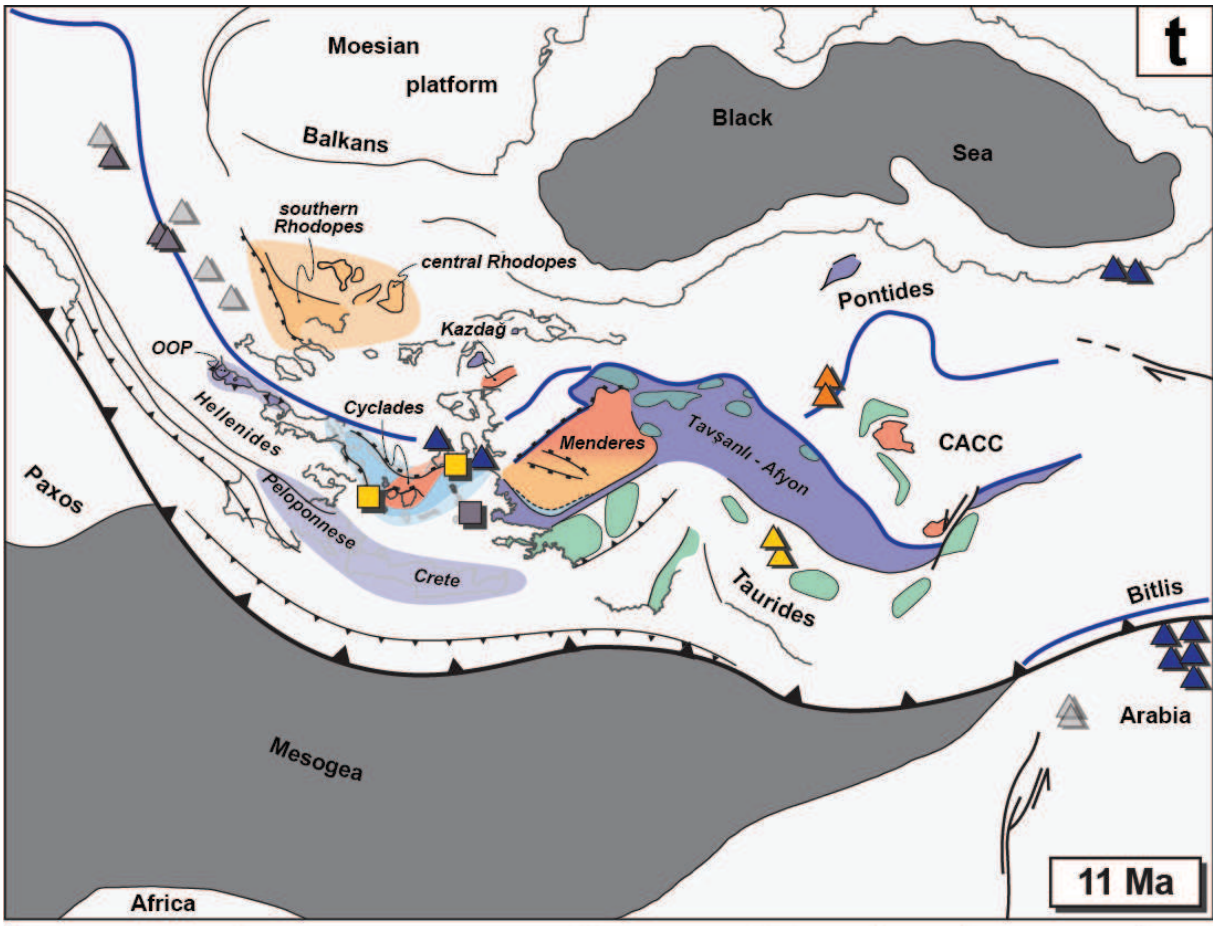
t
Moesian
platform
Balkans
Black
Sea
southern
Rhodopes
central Rhodopes
Pontides
Kazdag
OOP
Hellenides
Cyclades
Menderes
Tavşanlı - Afyon
CACC
Paxos
Peloponnese
Crete
Taurides
Bitlis
Arabia
Mesogea
Africa
11 Ma

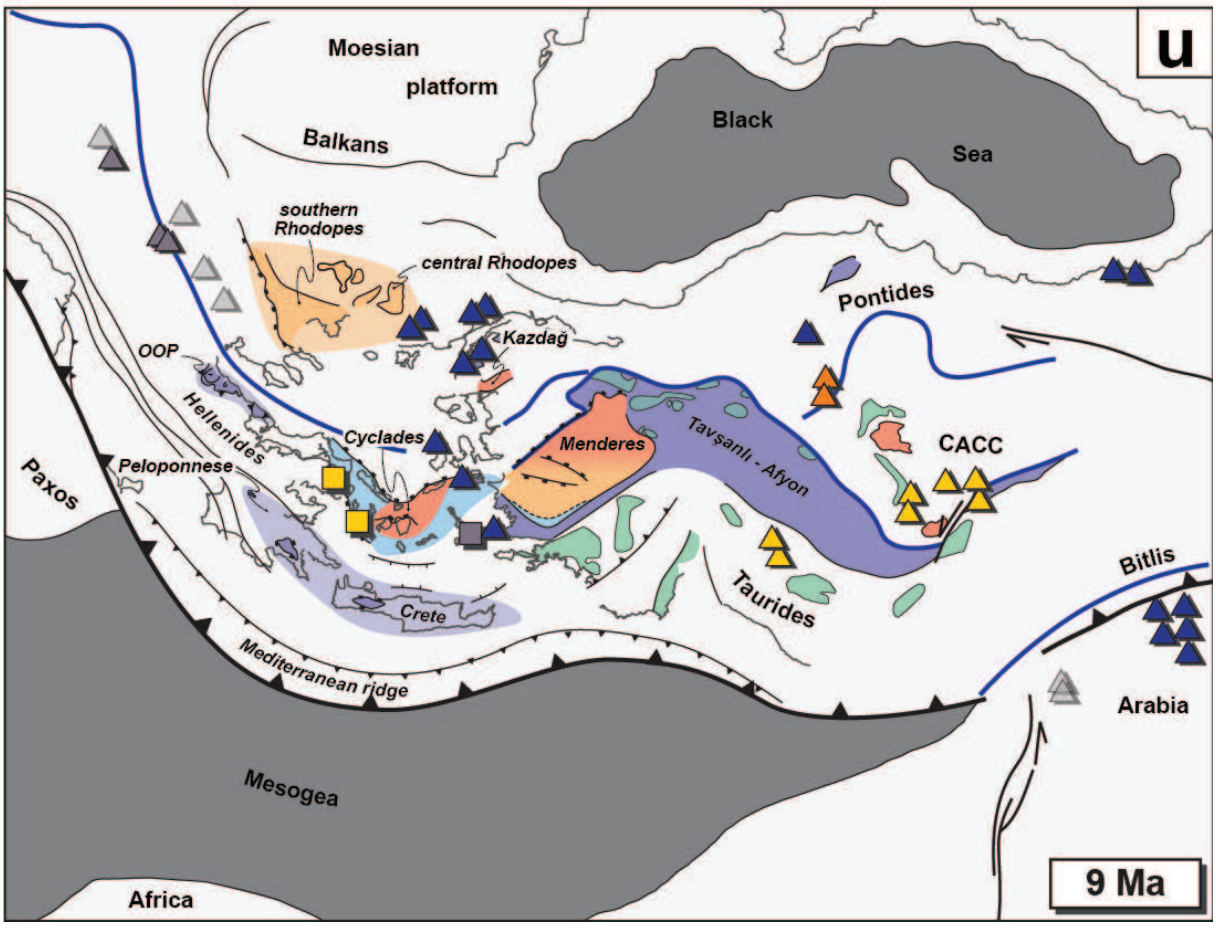
u
Moesian
platform
Balkans
Black
Sea
southern
Rhodopes
central Rhodopes
Pontides
Kazdag
OOP
Hellenides
Cyclades
Menderes
Tavşanlı - Afyon
CACC
Paxos
Peloponnese
Crete
Taurides
Bitlis
Arabia
Mediterranean ridge
Mesogea
Africa
9 Ma

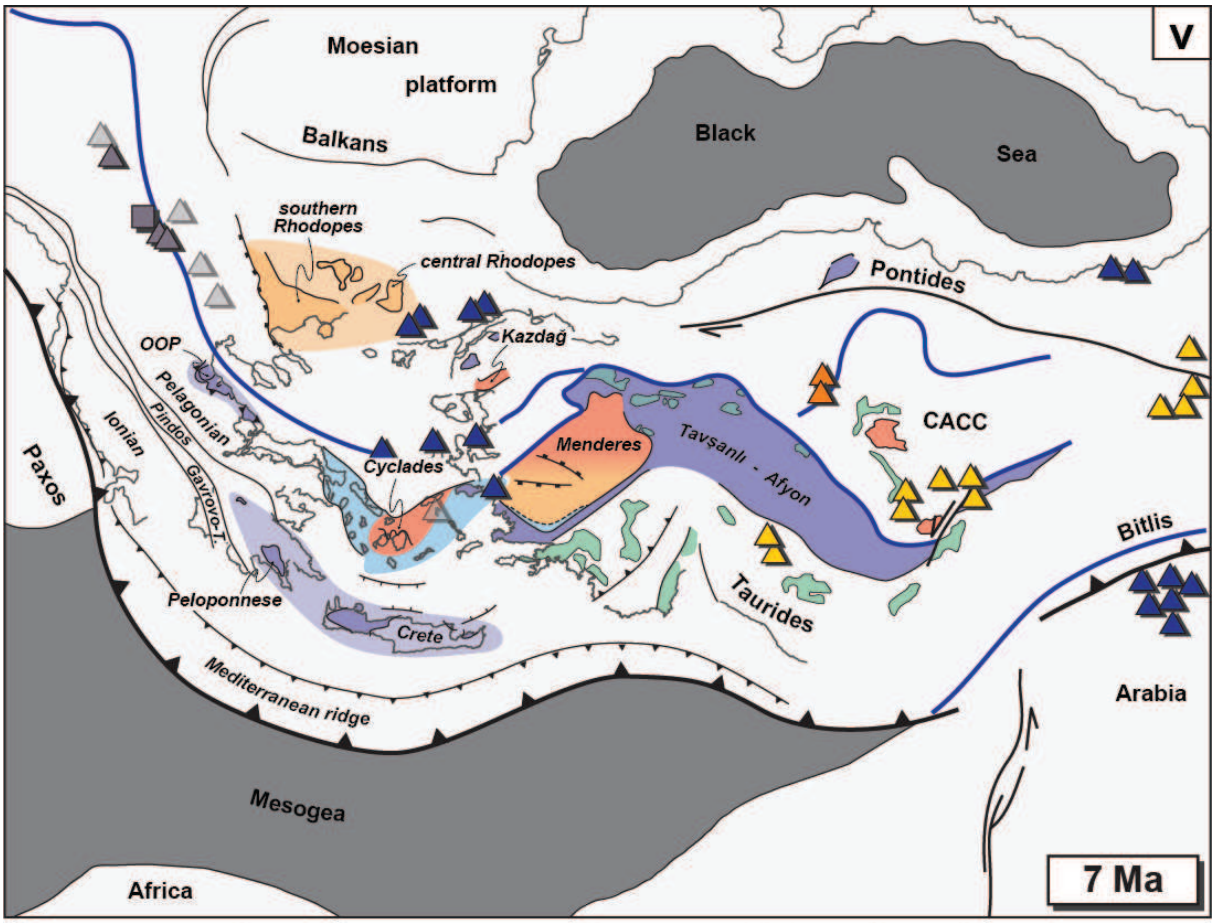
V
Moesian
platform
Balkans
Black
Sea
southern
Rhodopes
central Rhodopes
Pontides
Kazdağ
OOP
Pelagonian
Pindos
Ionian
Gavrovo-T.
Paxos
Cyclades
Menderes
Tavşanlı - Afyon
CACC
Bitlis
Taurides
Peloponnese
Crete
Mediterranean ridge
Arabia
Mesogea
Africa
7 Ma

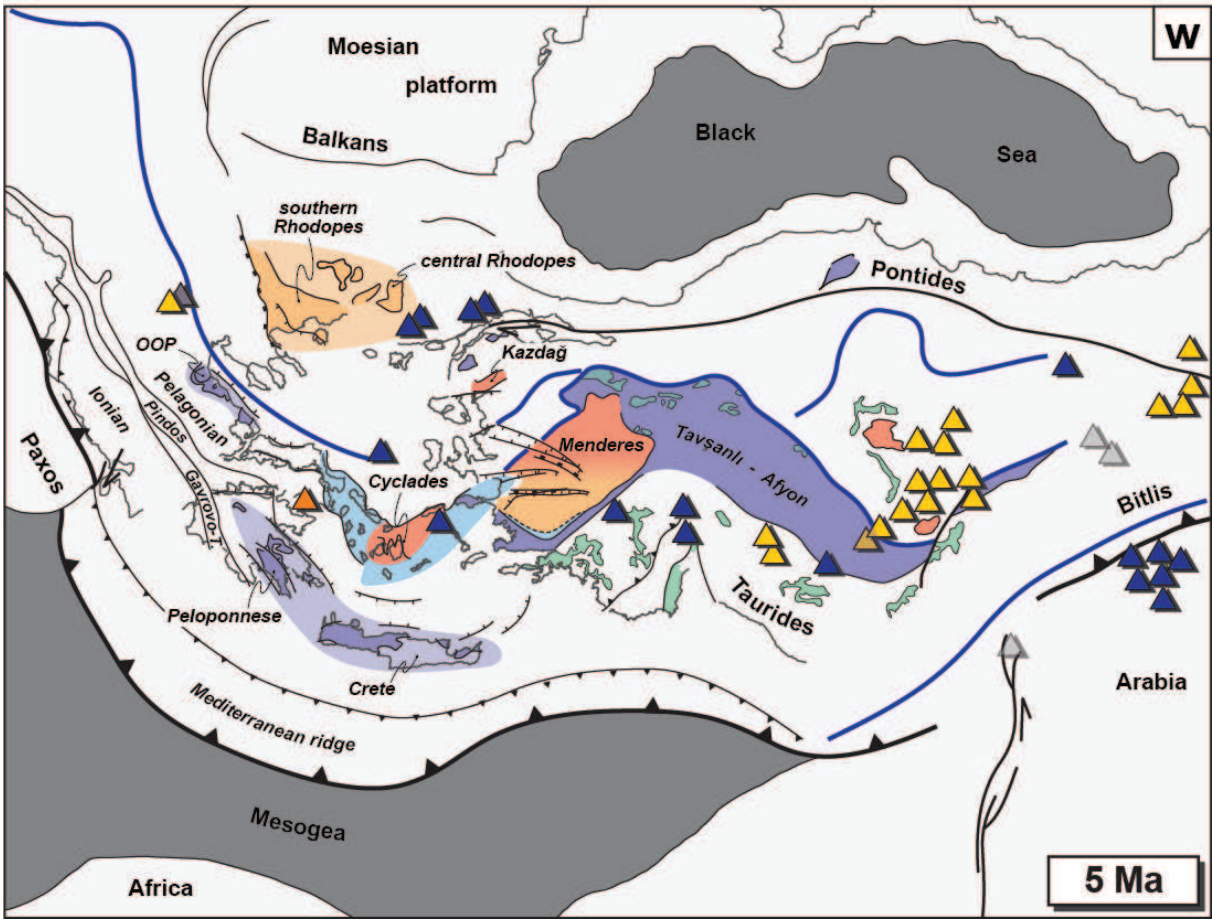
W
Moesian
platform
Balkans
Black
Sea
southern
Rhodopes
central Rhodopes
Pontides
Kazdağ
OOP
Pelagonian
Pindos
Ionian
Gavrovo-T.
Paxos
Cyclades
Menderes
Tavşanlı - Afyon
Bitlis
Taurides
Peloponnese
Crete
Mediterranean ridge
Arabia
Mesogea
Africa
5 Ma

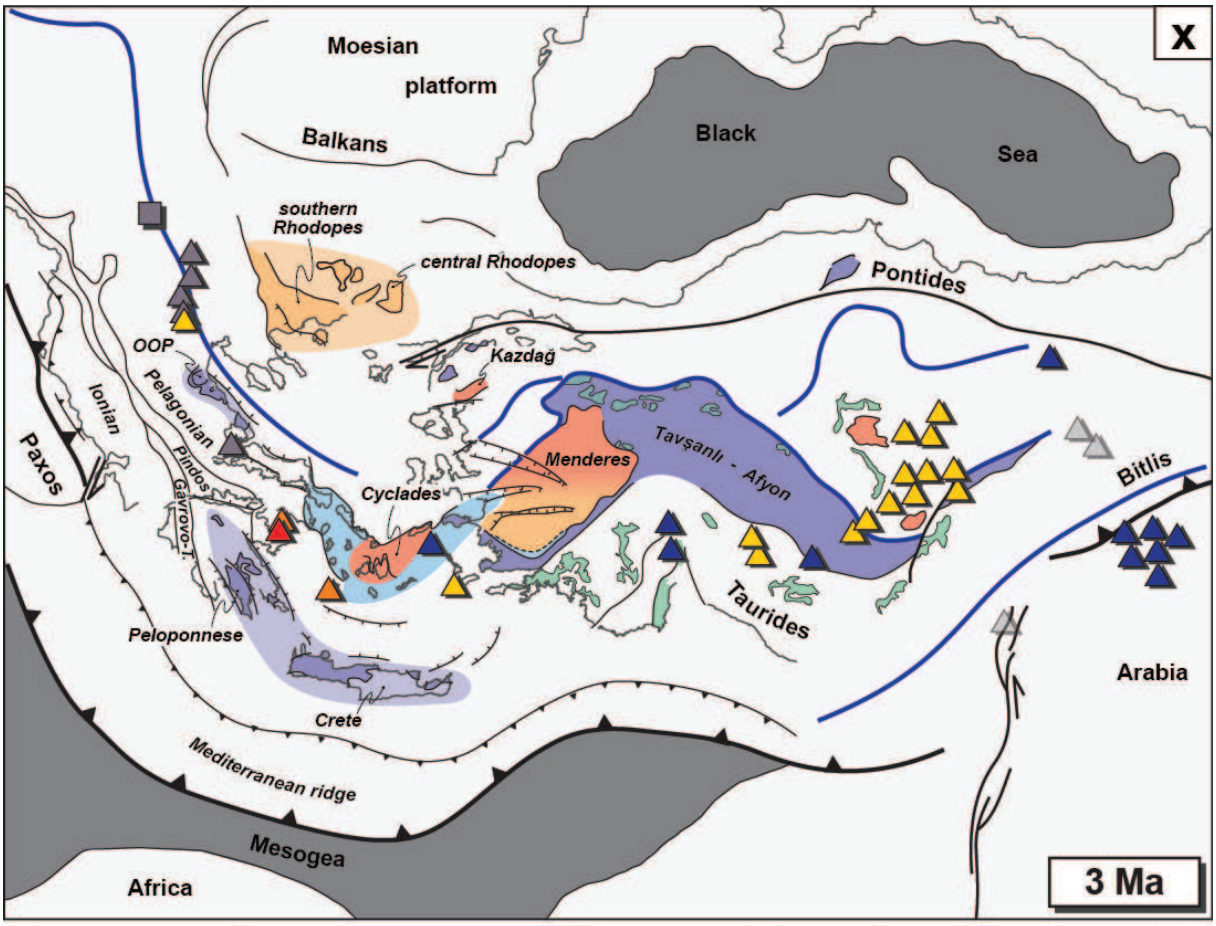
x
Moesian
platform
Balkans
Black
Sea
southern
Rhodopes
central Rhodopes
Pontides
Kazdağ
OOP
Pelagonian
Ionian
Paxos
Pindos
Gavrovo-T.
Menderes
Tavşanlı - Afyon
Cyclades
Bitlis
Taurides
Peloponnese
Arabia
Crete
Mediterranean ridge
Mesogea
Africa
3 Ma

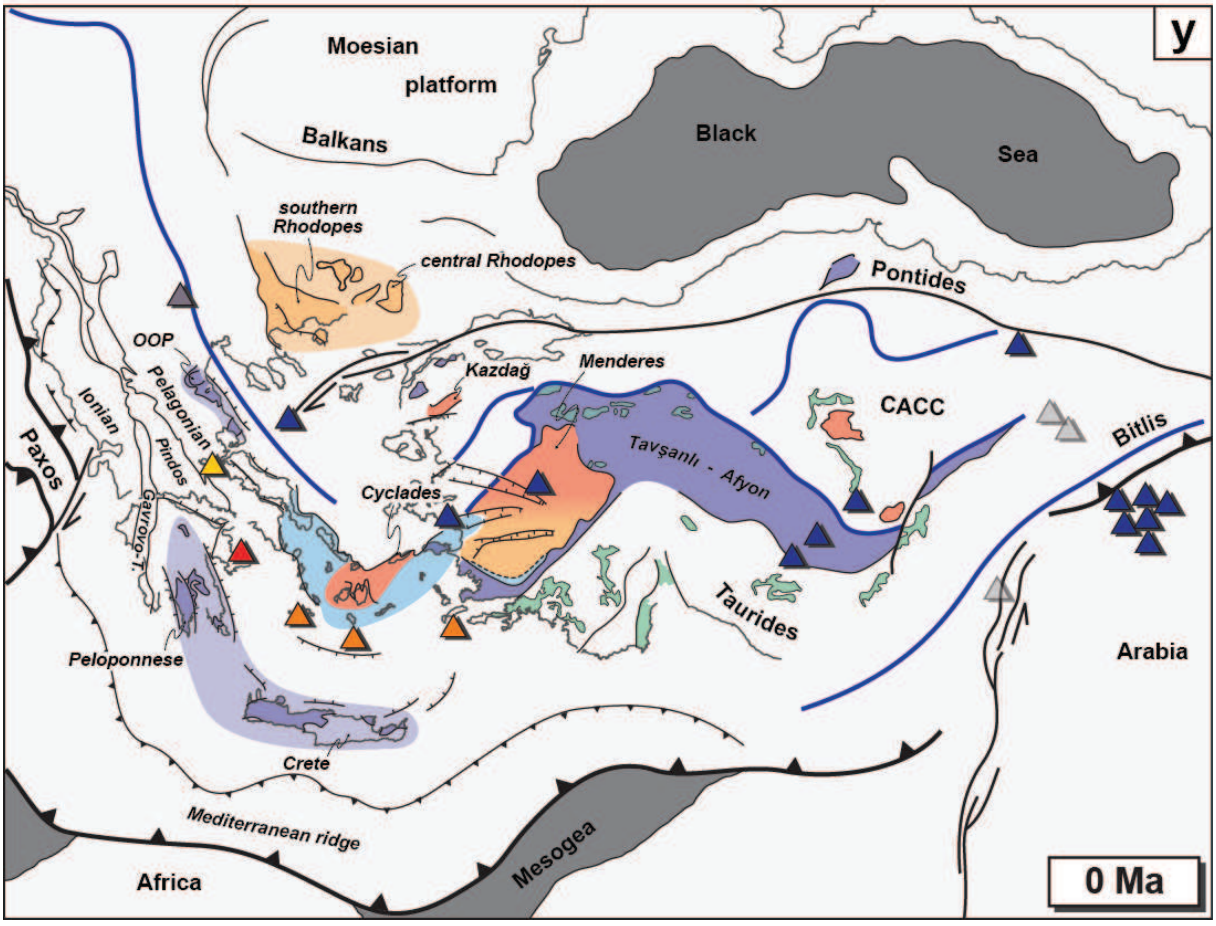
y
Moesian
platform
Balkans
Black
Sea
southern
Rhodopes
central Rhodopes
Pontides
OOP
Kazdağ
Menderes
CACC
Pelagonian
Ionian
Paxos
Pindos
Gavrovo-T.
Tavşanlı - Afyon
Cyclades
Bitlis
Taurides
Peloponnese
Arabia
Crete
Mediterranean ridge
Mesogea
Africa
0 Ma

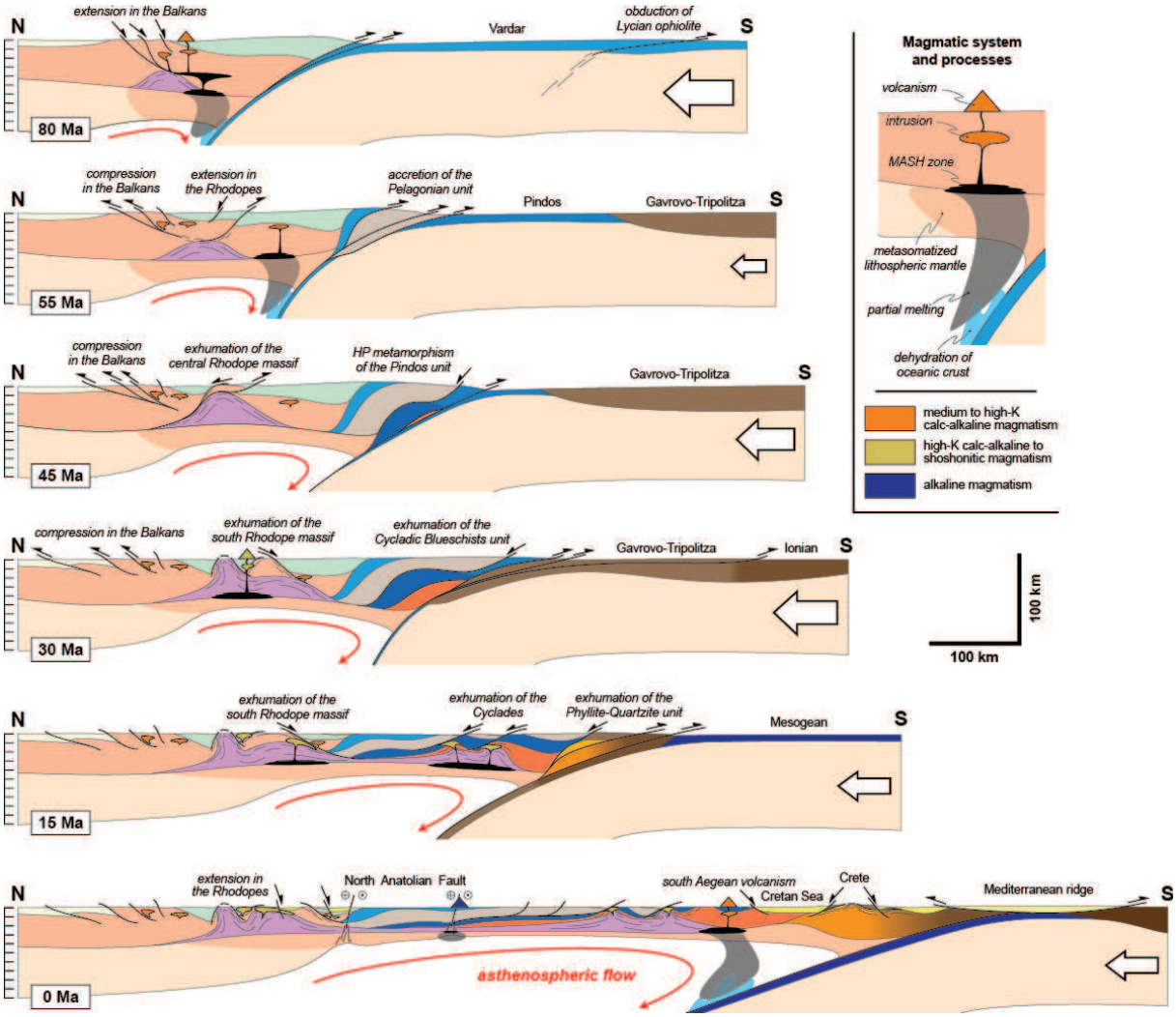

Figure 2.10: reconstructed cross-sections of the Aegean region highlighting the different magma genesis processes. MASH zone: Melting Assimilation Storage and Homogenization zone. See figure 2.5 for detailed legend.

2.5.1. Late Cretaceous (100-65 Ma, figures 2.9a-h)

A linear northward subduction zone along the Eurasian margin. During the late Cretaceous, the Balkans, the Rhodope massif and the Pontides already belonged to the Eurasian margin. Back rotating the early Miocene ~60° clockwise rotation of the Apuseni mountains (figure 2.4) [*Pătraşcu et al.*, 1994], all these domains formed an E-W linear orogenic belt over 2000 km [*Burg et al.*, 1990; *Yılmaz et al.*, 1997; *Georgiev et al.*, 2001; *Okay et al.*, 2001a]. Along this belt, the evidences of H*P*-L*T* metamorphic rocks exhumed as a syn-orogenic extrusion wedge [*Okay*, 1986; *Liati et al.*, 2002; *Okay et al.*, 2006; *Beccaletto et al.*, 2007] and the emplacement of a wide calc-alkaline magmatism [*Yılmaz*

et al., 1997; *Berza et al.*, 1998; *Okay et al.*, 2001b] indicate an active northward subduction zone below Eurasia accommodating Africa-Eurasia convergence. The downgoing lithosphere consisted in a wide oceanic domain, called the Vardar ocean along the Balkan and Rhodope margin and the Izmir-Ankara-Erzincan ocean along the Pontide margin (figures 2.10 and 2.11).

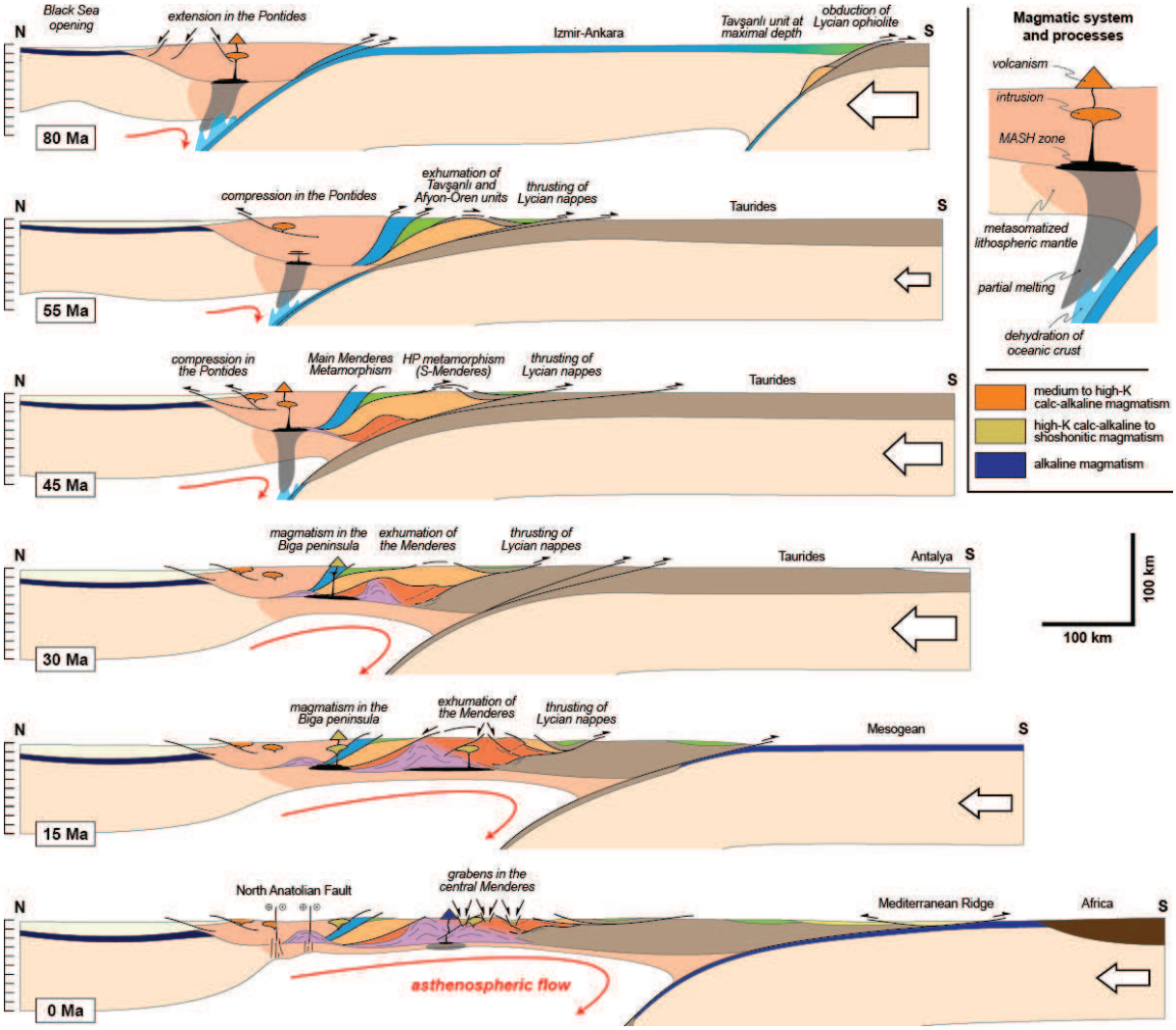

Figure 2.11: reconstructed cross-sections of the western Anatolian region highlighting the different magma genesis processes. MASH zone: Melting Assimilation Storage and Homogenization zone. See figure 2.5 for detailed legend.

Within the upper plate, a thrust belt developed southward in the Rhodope massif and the Pontides [*Burg et al.*, 1990; *Yılmaz et al.*, 1997]. Behind this compressional front, transtensional to extensional tectonics allowed the opening of sedimentary basins [*Willingshofer et al.*, 1999; *Sunal and Tüysüz*, 2002]. Coevally, the magmatic activity seems to migrate southward [*Yılmaz et al.*, 1997; *Ciobanu et*

al., 2002; *von Quadt et al.*, 2005; *Eyüboğlu et al.*, 2010], indicating a southward retreat of the oceanic slab [v*on Quadt et al.*, 2005; *Kolb et al.*, 2012]. Further north, the opening of the two Black Sea basins was associated with an intense stretching of the crust and oceanic spreading in Cenomanian to Santonian times [*Zonenshain and Le Pichon*, 1986; *Görür*, 1988; *Hippolyte et al.*, 2010; *Nikishin et al.*, 2015b]. An additional shoshonitic and alkaline volcanism emplaced coevally in the eastern Srednogorie region, just west of this extensional domain (figures 2.9g-h) [*Boccaletti et al.*, 1978].

Obduction and subduction involving Africa-derived continental blocks. Also governed by the Africa-Eurasia convergence, several continental blocks previously rifted from Africa (i.e. the CACC and Apulia comprising notably the Pelagonian, Gavrovo-Tripolitza, Ionian and Tauride carbonate platforms) moved northward during the late Cretaceous. Probably initiated as intraoceanic subductions, several obduction events then started in the Turonian-Conician (95-85 Ma) (figures 2.9b-d). Thus, a part of the Ankara-Erzincan oceanic domain southward overthrusted the CACC, forming the central Anatolian ophiolites [*Yaliniz and Göncüoğlu*, 1998]. Further south, a part the Inner-Tauride oceanic domain was obducted over the Tauride and the eastern Pelagonian platforms [*Şengör and Yilmaz*, 1981; *Katzir et al.*, 1996; *Dilek et al.*, 1999], forming the Lycian and Tauride ophiolites. A similar process also occurred over the southern Tauride margin with the northward overthrusting of the Antalya ophiolites, belonging to the Mesogean oceanic domain [*Robertson*, 2002].

As a result of this obduction event, the buried northern Tauride margin underwent a H*P*-L*T* metamorphism, forming the Tavşanlı then the Afyon-Ören units (figure 2.11) [*Okay*, 1986, 2002; *Candan et al.*, 2005; *Plunder et al.*, 2013; *Pourteau et al.*, 2013]. Coevally, H*T*-M*P* metamorphism has been recorded in the overriding plate (i.e. the CACC), where several MCCs were subsequently exhumed in a post-orogenic context [*Whitney et al.*, 2003; *Lefebvre et al.*, 2011]. In addition, several high-K calc-alkaline, then shoshonitic and finally alkaline intrusions emplaced in this context [*Aydin et al.*, 1998; *Boztuğ*, 2000; *Boztuğ et al.*, 2009]. These paired H*P*-L*T* and H*T*-M*P* metamorphisms attest for a late Cretaceous subduction-obduction system with an arc and back-arc metamorphic domains [*Lefebvre*, 2011].

2.5.2. Paleocene-Eocene (65-35 Ma, figures 2.9h-n)

Continental accretion along the Eurasian margin. As soon as the latest Cretaceous, an inversion of extensional structures occurred throughout the Balkans and the Pontides [*Yılmaz et al.*, 1997; *Sunal and Tüysüz*, 2002; *Bergerat et al.*, 2010]. In addition, the eastern Pontides recorded a rapid uplift since the Paleocene [*Boztuğ et al.*, 2004]. These features, as well as the end of the magmatic activity along this orogenic belt, indicate a major change in subduction dynamics, probably due to the collision and accretion of the Pelagonian platform and the CACC with Eurasia (figures 8h-i and 10). The indentation of the CACC along the Izmir-Ankara oceanic suture zone induced the oroclinal bending of the central Pontides [*Kaymakci et al.*, 2003, 2009; *Meijers et al.*, 2010] as well as the tectonic reorganization of the CACC [*Lefebvre et al.*, 2013]. In the late Paleocene-early Eocene, a second collisional event between the Eurasian-CACC margin and the Anatolide-Tauride block resulted in the closure of the Inner-Tauride and the Izmir-Ankara oceanic domains as well as of the marine corridor separating the Pelagonian and Tauride platforms (figures 8i-j). In this area, the latest Cretaceous-early Paleocene sedimentary and ophiolitic mélange was then folded and sheared toward the south, forming the Bornova flysch zone [*Robertson et al.*, 2009; *Okay et al.*, 2012]. Another consequence of this second collisional event was the development of a north-vergent fold-and-thrust-belt since the middle-late Eocene along the eastern Balkans and the Pontides (figures 9 and 10) [*Doglioni et al.*, 1996; *Yılmaz et al.*, 1997]. Further south, a new northward subduction zone initiated along the southern Tauride margin, inducing the building of the Bitlis belt and the progressive closure of the Mesogean oceanic domain [*Dercourt et al.*, 1986; *Barrier and Vrielynck*, 2008].

A continuous subduction migrating southward. Immediately after the collision of the Pelagonian platform with Eurasia, the main thrust front shifted along the southern margin of the Pelagonian platform, inducing the subduction of the partly oceanic Pindos basin (figures 2.9i-j and 2.10) [*Aubouin*, 1959]. The latter was partly accreted to the Pelagonian nappe, contributing to the building of the Hellenides while its buried part underwent a H*P*-L*T* metamorphism in the early Eocene, recorded in the Cycladic Blueschists unit and the Cycladic basement [*Bonneau and Kienast*, 1982; *Bonneau*, 1984; *Wijbrans and McDougall*, 1988; *Tomaschek et al.*, 2003; *Lagos et al.*, 2007]. These

units were then progressively exhumed until the end of the Eocene in the Cyclades and in the Olympos, Ossa and Pelion tectonic windows as a syn-orogenic extrusion wedge bounded by the Vari detachment on top (in Syros) and the SCSZ at the base (in Ios) (figure 2.10) [*Jolivet et al.*, 2003; *Ring et al.*, 2007, 2010; *Brun and Faccenna*, 2008; *Huet et al.*, 2009; *Jolivet and Brun*, 2010].

Across the Tauride platform, the main thrust front similarly migrated southward, carrying the remnants of the late Cretaceous Lycian and Tauride ophiolites [*de Graciansky*, 1967; *Gutnic et al.*, 1979; *Collins and Robertson*, 1998]. The late Cretaceous H*P*-L*T* Tavşanlı and Afyon-Ören units were then exhumed along a cold retrograde path, reaching the surface in the early Eocene [*Özcan et al.*, 1988; *Sherlock et al.*, 1999; *Rimmelé et al.*, 2003a; *Ring and Layer*, 2003; *Pourteau et al.*, 2010, 2013]. Structurally below, the major part of the buried Menderes massif underwent a M*T*- to H*T*-M*P* metamorphism (i.e. the *Main Menderes Metamorphism*), excepted in its southern part where a H*P*-L*T* metamorphism was recorded (i.e. the Kurudere-Nebiler unit, figures 2.9l-n and 2.11) [*Şengör et al.*, 1984; *Bozkurt and Oberhänsli*, 2001; *Okay*, 2001; *Rimmelé et al.*, 2003b, 2005; *Whitney et al.*, 2008; *Pourteau et al.*, 2013].

During the Eocene, while the subduction zone migrated southward across the accreted continental blocks, following the retreat of the decoupled part of the downgoing lithosphere, an E-W-trending magmatic province developed, mainly displaying a medium- to high-K calc-alkaline composition figures 2.9j-n) [*Harris et al.*, 1994; *Okay and Satır*, 2006; *Arslan et al.*, 2013].

Back-arc extension in the Rhodope massif. Coevally with the southward retreat of the slab, the lower part of the thickened Rhodope crust was strongly heated, allowing the development of a Paleocene M*T*-M*P* metamorphism associated with migmatites (figure 2.10) [*Burg et al.*, 1996; *Mposkos*, 1998; *Jolivet and Brun*, 2010]. In the central Rhodope massif, these metamorphic rocks then started to exhume as several MCCs below top-to-the NE ductile-brittle detachments, reaching the surface in the late Eocene (figures 2.9j-n) [*Burg et al.*, 1996; *Burchfiel et al.*, 2003; *Bonev et al.*, 2006]. This exhumation was accompanied by a ~11° clockwise rotation of the massif (figure 2.4) [*Brun and Sokoutis*, 2007]. Coevally, the Thrace basin started to open, progressively filled by a thick sedimentary sequence [*Turgut and Eseller*, 2000; *Okay et al.*, 2010a]. At the end of the Eocene, this

extension propagated southward in the southern Rhodope massif [*Brun and Sokoutis*, 2007, 2010; *Wüthrich*, 2009].

2.5.3. Oligocene-early Miocene (35-15 Ma, figures 2.9n-r)

Continuing southward migration of the subduction zone. In the eastern Mediterranean region, contemporaneously with the last compressional increments in the eastern Balkans in the Oligocene [*Doglioni et al.*, 1996] and the early Miocene ~60° clockwise rotation of the western Balkans (figure 2.4) [*Pătraşcu et al.*, 1994], the main thrust front was continuously propagating southward, notably across the Tauride platform with the Lycian nappes reaching the Bey Dağları platform in the early Miocene (figure 2.11) [*Poisson*, 1977; *van Hinsbergen et al.*, 2010a]. Further west, the Gavrovo-Tripolitza and Ionian platforms coevally started to subduct after the closure of the Pindos basin (figure 2.10) [*Sotiropoulos et al.*, 2003; *van Hinsbergen et al.*, 2005a]. The external parts of these carbonate platforms were accreted to the Hellenides, remaining at low pressure while their buried internal parts, comprising their basements, recorded a H*P*-L*T* metamorphism, forming the Phyllite-Quartzite and the Plattenkalk units in Crete and the Peloponnese [*Bonneau and Kienast*, 1982; *Seidel et al.*, 1982; *Theye et al.*, 1992; *Trotet et al.*, 2006; *Jolivet et al.*, 2010b]. These metamorphic units were then exhumed in the footwall of the top-to-the N Cretan detachment since ~25 Ma, following a cold retrograde path [*Jolivet et al.*, 1996, 2010c; *Ring et al.*, 2001]. Similarly to the Cycladic Blueschists unit, the exhumation of the Phyllite-Quartzite and the Plattenkalk units was associated with N-S to NE-SW extension as in Crete (figure 2.4) [*Jolivet et al.*, 1996, 2010c]. The E-W stretching lineation in the Peloponnese results from the subsequent middle-late Miocene clockwise rotation (see details in section 2.5.4).

Back-arc extension in the Cyclades and western Anatolia. Behind this compressional front, back-arc extension propagated southward during the Oligocene-Miocene [*Le Pichon and Angelier*, 1979; *Jolivet and Faccenna*, 2000], leading to a strong crustal thinning observed nowadays in the Aegean-west Anatolian region [*Tirel et al.*, 2004; *Karabulut et al.*, 2013]. Thus, while the exhumation of the central Rhodope core complex ceased in the Oligocene [*Marchev et al.*, 2004a; *Wüthrich*, 2009], the

southern Rhodope massif continued to exhume as a MCC below the top-to-the SW Kerdylion detachment (figures 2.10 and 2.12) [*Brun and Sokoutis*, 2007]. Coeval with this exhumation, a ~30° clockwise rotation affected the hanging wall of the detachment (figure 2.4) [*Kondopoulou and Westphal*, 1986; *Brun and Sokoutis*, 2007].

Further south, Oligocene-early Miocene exhumation of MCCs mainly in greenschist-facies conditions occurred in the Cyclades and the Menderes massif [*Altherr et al.*, 1982; *Lister et al.*, 1984; *Gautier and Brun*, 1994; *Jolivet et al.*, 1994; *Bozkurt and Oberhänsli*, 2001; *Ring et al.*, 2003, 2010; *Catlos and Çemen*, 2005; *Jolivet & Brun*, 2010], associated with an additional H*T*-M*P* metamorphism affecting the northern Menderes massif and the central Cyclades in the Oligocene and early Miocene, respectively (figures 2.9n-r and 2.12) [*Lister et al.*, 1984; *Gautier et al.*, 1993; *Keay et al.*, 2001; *Catlos and Çemen*, 2005; *Bozkurt et al.*, 2010]. In the Cyclades, the NCDS accommodated this exhumation since the Oligocene (figures 2.10 and 2.12) [*Faure et al.*, 1991; *Lee and Lister*, 1992; *Brichau et al.*, 2007, 2008; *Jolivet et al.*, 2010a] while the NPEFS and the WCDS were active later, since the early Miocene [*Urai et al.*, 1990; *Gautier et al.*, 1993; *Brichau et al.*, 2006; *Iglseder et al.*, 2011; *Grasemann et al.*, 2012]. In the hanging wall of these extensional structures, syn-tectonic sediments started to deposit [*Sánchez-Gómez et al.*, 2002; *Kuhlemann et al.*, 2004; *Lecomte et al.*, 2010]. Further east, the exhumation of the Menderes massif was accommodated in the north by the top-to-the N Simav detachment accommodating at least ~50 km of displacement [*Işik and Tekeli*, 2001; *Ring et al.*, 2003; *Bozkurt et al.*, 2011] and in the south by a top-to-the S shearing, just below the overlying Lycian nappes (figures 2.11 and 2.12) [*Bozkurt and Satır*, 2000; *Gessner et al.*, 2001a; *Ring et al.*, 2003]. Volcanoclastic rocks unconformably covering the southern Menderes massif then indicate a surface exposure of these metamorphic rocks in the early Miocene [*Bozkurt and Satır*, 2000]. Finally, the exhumation of the Kazdağ massif started in the late Oligocene in H*T*-M*P* conditions and was accommodated by the top-to-the N Alakeçi and top-to-the S Şelale detachments until the early Miocene (figure 2.12) [*Okay and Satır*, 2000b; *Beccaletto and Steiner*, 2005; *Bonev and Beccaletto*, 2007].

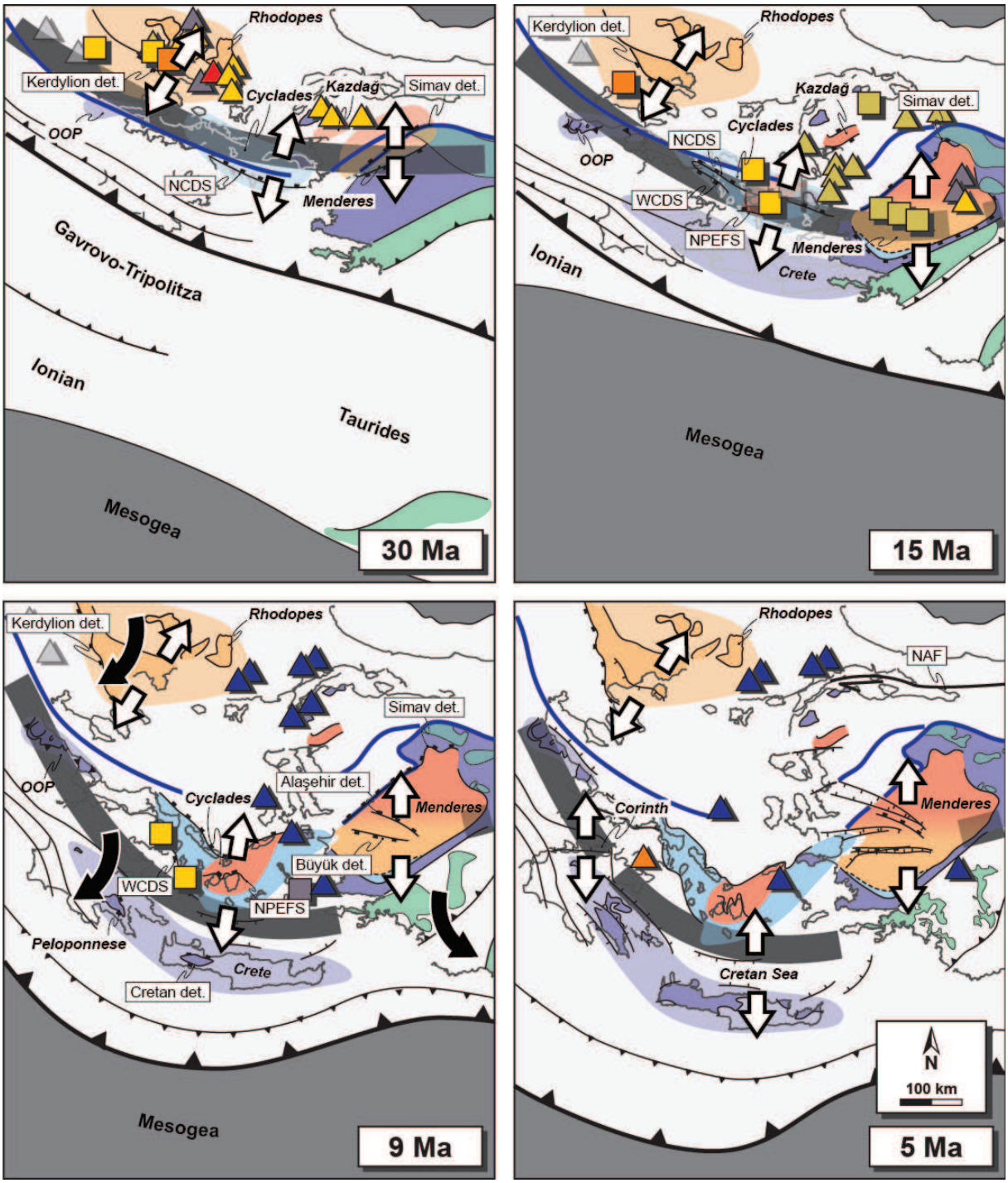

Figure 2.12: detailed paleotectonic maps of the Rhodope-Aegean-west Anatolian region during the Oligocene-Miocene extension. White arrows: direction of stretching. Black arrows: main block rotations. The thick grey line shows the position of the slab at 150 km depth. NAF: North Anatolian Fault. NCDS: North Cycladic Detachment System. NPEFS: Naxos/Paros Extensional Fault System. OOP: Olympos-Ossa-Pelion tectonic windows. WCDS: West Cycladic Detachment System. See figure 2.9 for detailed legend.

During the post-orogenic exhumation of these MCCs, a high-K to shoshonitic magmatism developed and migrated southward. Thus, the first magmatic centers emplaced as soon as the latest

Eocene in the central Rhodope massif (figures 2.10 and 2.12), then in the Biga Peninsula in the Oligocene and finally in the south Rhodope massif and in the northern Menderes massif in the early Miocene [*Jones et al.*, 1992; *Altherr and Siebel*, 2002; *Marchev et al.*, 2004b, 2005; *Pe-Piper and Piper*, 2006, 2007; *Dilek and Altunkaynak*, 2009; *Dilek et al.*, 2009; *Ersoy and Palmer*, 2013].

Eurasia-Arabia collision. Although its timing is debated, the continental subduction of Arabia below the Bitlis-Zagros belt seems to start in the Oligocene, predating the main collisional event probably occurring in late Oligocene-early Miocene times [*Hempton*, 1987; *Jolivet and Faccenna*, 2000; *Agard et al.*, 2005; *Allen and Armstrong*, 2008; *Okay et al.*, 2010b; *McQuarrie and van Hinsbergen*, 2013] and inducing the slowing down of the absolute motion of Africa [*Jolivet and Faccenna*, 2000]. Such lithospheric-scale processes could also induce major tectonic changes within the Anatolide-Tauride block. Thus, *Pourteau et al.* [2010] proposed that the post-Eocene ~40° counterclockwise rotation of the eastern Tauride platform [*Kissel et al.*, 2003] and the middle Eocene-Oligocene ~40° clockwise rotation of the central Tauride platform (figure 2.4) [*Kissel et al.*, 1993] resulted from the indentation of the Arabian plate along the Bitlis-Zagros belt. Displacement of these two rotating rigid blocks could then be accommodated by the central Anatolian fault (figures 2.9n-r) [*Koçyiğit and Beyhan*, 1998; *Jaffey and Robertson*, 2001] as attested by the Oligocene new burial of the Niğde massif in the southern CACC, attributed to the activation (or reactivation) of this transpressional structure [*Idleman et al.*, 2014]. Nevertheless, the timing of these block rotations, especially for the eastern Tauride platform, remains poorly constrained and *Pourteau et al.* [2010] do not exclude that the preceding Eocene collision of the Anatolide-Tauride block with the CACC further north could also induce such block rotations.

2.5.4. Middle-late Miocene (15-5 Ma, figures 2.9r-w)

Continuing syn-orogenic and post-orogenic exhumation. In the middle-late Miocene, the main thrust front continued its southward migration with the accretion of new continental terranes, coeval with ongoing slab retreat. Thus, in the western Hellenides, the Paxos carbonate platform underthrusted the previously accreted Ionian nappe in the western Hellenides [*van Hinsbergen et al.*, 2005a] while

the Mesogean oceanic lithosphere started to subduct in the eastern Hellenides where the Mediterranean ridge also started to grow [*Le Pichon et al.*, 1982, 2002; *Chaumillon et al.*, 1996; *Kopf et al.*, 2003]. Further east, the non-metamorphosed Lycian nappes overthrusted the Bey Dağları platform [*Poisson*, 1977; *van Hinsbergen et al.*, 2010a]. Within the accretionary wedge, the syn-orogenic exhumation of the H*P*-L*T* Phyllite-Quartzite and the Plattenkalk units continued until 9 Ma in the footwall of the Cretan detachment that finally accommodated more than 100 km of northward displacement in Crete (figures 2.4 and 2.12). The metamorphic footwall was exposed at the surface 11-10 Ma ago at the earliest, while sediments were deposited in the hanging wall as soon as the lower Miocene [*Jolivet et al.*, 1996, 2010c; *Ring et al.*, 2001; *van Hinsbergen and Meulenkamp*, 2006; *Seidel et al.*, 2007; *Marsellos et al.*, 2010]. After 9 Ma, the activity of the Cretan detachment ceased and high-angle normal faults formed, inducing the uplift of Crete and the opening of the Cretan Sea (figure 2.12) [*Angelier et al.*, 1982; *van Hinsbergen and Meulenkamp*, 2006].

Behind this compressional belt, post-orogenic extension was still active until the middle-late Miocene. Thus, high-angle normal faults and associated sedimentary basins developed over the south Rhodope core complex that continued to exhume below the Kerdylion detachment (figures 2.10 and 2.12) [*Brun and Sokoutis*, 2007]. In the Cyclades, the exhumation of MCCs ceased ~9-8 Ma ago below the NCDS and the NPEFS and ~6 Ma ago below the WCDS (figures 2.10 and 2.12) [*Brichau et al.*, 2006, 2008, 2010; *Jolivet et al.*, 2010a]. Surface exposure of the metamorphic rocks then occurred in the late Miocene (figure 2.12) [*Sánchez-Gómez et al.*, 2002]. Further east, the Simav detachment activity continued until ~8 Ma [*Bozkurt et al.*, 2011], and is contemporaneous with the exhumation of the central part of the Menderes massif below the top-to-the NE Alaşehir and the top-to-the S Büyük detachments, occurring until the end of the Miocene (figures 2.11 and 2.12) [*Hetzel et al.*, 1995a, 1995b; *Gessner et al.*, 2001b; *Lips et al.*, 2001; *Ring et al.*, 2003; *Thomson & Ring*, 2006; *van Hinsbergen et al.*, 2010b].

Coevally, numerous magmatic centers and notably syn-tectonic intrusive bodies continued to emplace in the footwall of detachment systems such as in the central Menderes massif and the Cyclades [*Faure and Bonneau*, 1988; *Gessner et al.*, 2001a; *Dilek et al.*, 2009; *Iglseder et al.*, 2009; *Lecomte et al.*, 2010; *Denèle et al.*, 2011; *Laurent et al.,* 2015; *Rabillard et al.*, 2015].

Large-scale block rotations during slab retreat. Although the southward trench migration and exhumation processes were similar from the Oligocene to the late Miocene, additional large-scale clockwise and counterclockwise block rotations have been recorded since 15 Ma both in the arc and back-arc domains (figures 2.4 and 2.12). Thus, most of the ~30° clockwise rotation of the south Rhodope core complex occurred after 15 Ma [*Brun and Sokoutis*, 2007; *van Hinsbergen et al.*, 2008]. Similarly, the major part of the Hellenides and the western Cyclades underwent respectively a ~40° and a ~20° clockwise rotation between 15 and 8 Ma [*Kissel and Laj*, 1988; *Morris and Anderson*, 1996; *van Hinsbergen et al.*, 2005b]. In addition, in order to fit the NE-SW to E-W stretching lineation of the Phyllite-Quartzite unit in the Peloponnese (figure 2.4) with the constant N-S to NNE-SSW regional extension related to slab retreat [*Jolivet*, 2001], a similar clockwise rotation has to be applied to this H*P*-L*T* unit during its final exhumation in the Peloponnese. In opposition, large-scale counterclockwise rotations, estimated at around 20-30°, have been coevally recorded further east in the eastern Cyclades, the central Menderes, the Lycian nappes and the Bey Dağları platform (figure 2.4) [*Kissel et al.*, 1993; *van Hinsbergen et al.*, 2010a, 2010b]. These opposite rotations are related to the progressive curvature of the trench during the middle and late Miocene (figure 2.12) with no rotation recorded at the hinge, such as in Crete where the strike of the stretching lineation of the exhumed Phyllite-Quartzite and the Plattenkalk units fits with the regional N-S to NNE-SSW extension (figure 2.4).

Continuing collision and extrusion of Anatolia. In the middle-late Miocene, the northward collision of Arabia along the Bitlis belt was still active (figures 2.9r-w). Eastern Anatolia was then uplifted [*Dewey et al.*, 1986; *Şengör et al.*, 2003; *Okay et al.,* 2010b], coevally with the development of an extensive magmatic province [*Pearce et al.*, 1990; *Keskin*, 2003, 2007]. Some 12 Ma ago, the whole Anatolide-Tauride block started to move westward, mostly accommodated by the dextral strike-slip NAF that propagated throughout the Pontides and reached the Dardanelle Strait 6-5 Ma ago (figures 2.9t-w) [*Armijo et al.*, 1999; *Şengör et al.*, 2005; *Melinte-Dobrinescu et al.*, 2009]. However, as soon as the late Miocene, a distributed strike-slip then E-W compressive tectonics developed, probably as a result of this westward extrusion notably in western Anatolia, along the Izmir-Balıkesir

Transfer Zone [*Ersoy et al.*, 2011] and in the Cyclades with the folding and local reactivation of detachments with a reverse movement [*Avigad et al.*, 2001; *Menant et al.*, 2013].

2.5.5. Pliocene-Quaternary (5-0 Ma, figures 2.9w-y)

Active collision and slab retreat. From the Pliocene to nowadays, while Arabia still collides along the Bitlis-Zagros belt in the east, the southward retreat of the Mesogean slab continues in front of the Aegean domain, coeval with the growing of the Mediterranean ridge that finally reaches the northern African margin (figures 2.9y and 2.10). Further west, the Paxos carbonate platform still accretes to the Hellenides. At the junction between the slowly subducting Paxos continental platform and the fast retreating Mesogean oceanic lithosphere, the dextral strike-slip Kephalonia fault has developed since ~5 Ma, inducing a segmentation of the main thrust front (figures 2.9w-y) [*Finetti*, 1982; *Kreemer and Chamot-Rooke*, 2004; *Royden and Papanikolaou*, 2011]. Behind this subduction front, a medium-potassic calc-alkaline volcanic arc has been active in the south Aegean region (figures 2.9x-y) [*Pe-Piper and Piper*, 2005].

Extrusion and localization of extension. Since 6-5 Ma, the NAF has entered the Aegean domain, accommodating ~80 km of dextral strike-slip displacement in the Dardanelle Strait (figure 2.4) [*Armijo et al.*, 1999; *Şengör et al.*, 2005; *Lacassin et al.*, 2007; *Le Pichon and Kreemer*, 2010]. Coevally, extension ceased in the Cyclades and has localized at the edges of the Aegean domain, comprising Evvia island and Corinth region (forming the Central Hellenic Shear Zone [*Papanikolaou and Royden*, 2007]), Peloponnese, Cretan Sea and Menderes massif [*Armijo et al.*, 1996; *Royden and Papanikolaou*, 2011; *Pérouse et al.*, 2012]. High-angle normal faulting has then developed forming several grabens and half-grabens (figures 2.9w-y). This extensional tectonics has been accompanied in the Hellenides by a clockwise rotation of ~10° and ~23° north and south of the Central Hellenic Shear Zone [*van Hinsbergen et al.*, 2005b; *Bradley et al.*, 2013], increasing the arc curvature. This feature suggests a tectonic decoupling between these two rotating blocks that can be accommodated by the dextral shear distributed across the Central Hellenic Shear Zone [*Royden and Papanikolaou*, 2011].

2.6. Discussion

These new kinematic reconstructions therefore provide many details about the late Cretaceous-Cenozoic geodynamic evolution of the eastern Mediterranean region that have not been necessarily considered in previous larger-scale reconstruction models [*Dercourt et al.*, 1986, 1993; *Ricou*, 1994; *Jolivet et al.*, 2003; *Barrier and Vrielynck*, 2008; *Stampfli and Hochard*, 2009; *van Hinsbergen and Schmid*, 2012]. Using deforming domains allows reconstructing the non-rigid behavior of the lithosphere, especially the stretching of the crust resulting from the dominant trench-perpendicular extension, such as during the Oligocene-Miocene back-arc extension (figure 2.12). Similarly, the small component of trench-parallel extension [*Reilinger et al.*, 2006; *van Hinsbergen and Schmid*, 2012], resulting notably from the progressive curvature of the arc since the middle Miocene, is also considered thanks to these deforming domains (figure 2.12).

Extracting from our reconstructions, the motion paths of different points distributed over the whole region also provide insights about past kinematics and therefore the instantaneous surface deformation of this region (figures 2.13 and 2.14). This kinematic model thus allows discussing the different crustal and mantle processes driving the progressive back-arc opening and the present-day kinematics of the eastern Mediterranean region. Finally, the spatial and temporal distribution of the magmatic activity illustrated in our kinematic reconstructions (figures 2.9a-y) is also discussed in terms of crustal and mantle interactions.

2.6.1. Late Cretaceous and Oligocene to Present slab retreat and back-arc opening

During the late Cretaceous-Cenozoic, two main episodes of southward slab retreat and related back-arc opening have been described: first, during the late Cretaceous along the Balkans and the Pontides (figures 2.9a-h) then since the Oligocene in the Rhodope, Aegean and west Anatolian domains (figures 2.9n-w). These transtensional and/or extensional events are both characterized by opening of sedimentary basins and southward migration of magmatism.

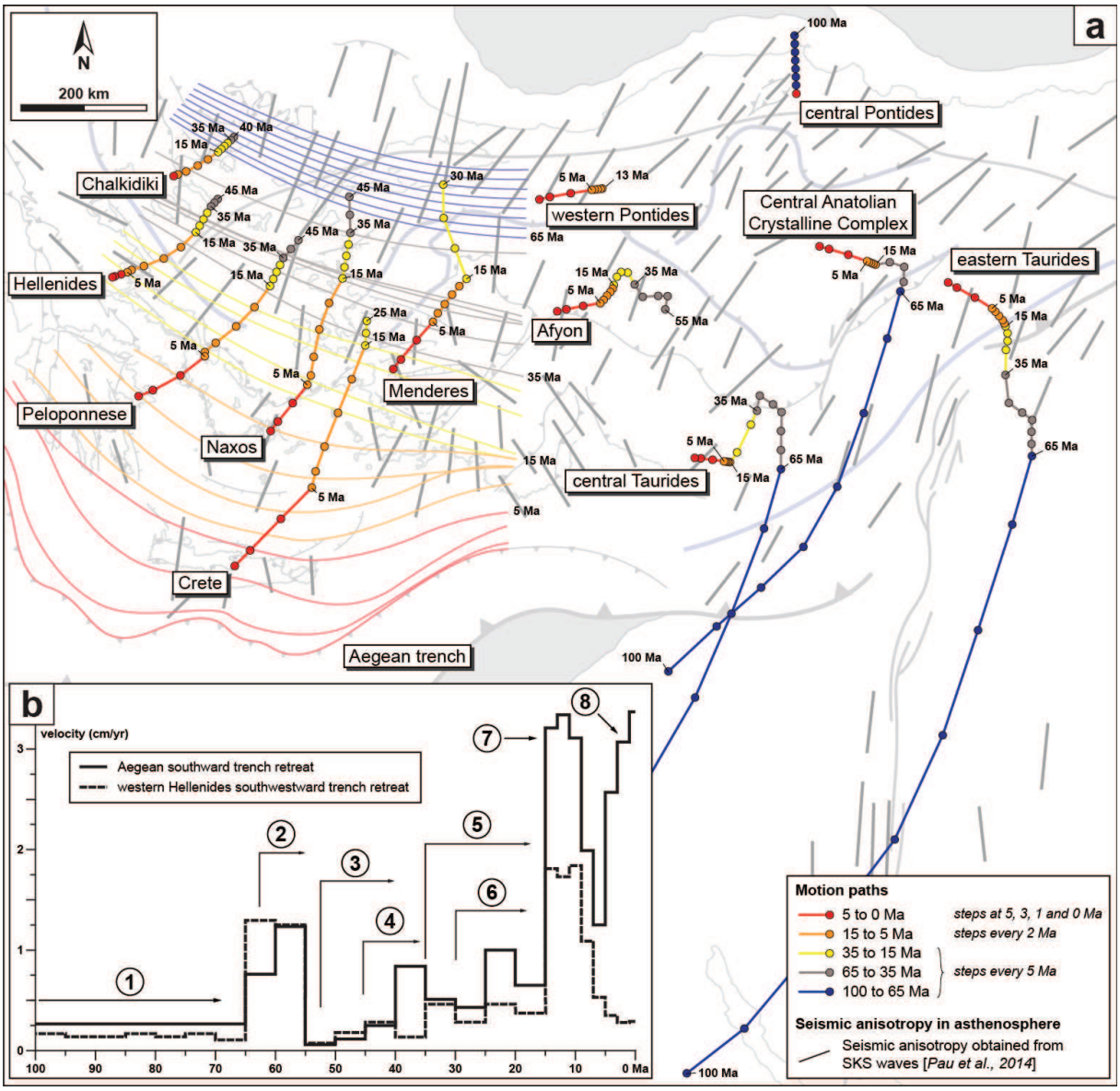

Figure 2.13: (a) different motion paths deduced from the kinematic reconstructions of the eastern Mediterranean region. Migration of the Aegean trench does not include the Mediterranean ridge growth since 15 Ma. SKS fast splitting directions over the eastern Mediterranean region are also represented [*Paul et al., 2014*]. (b) Time-velocity diagram, deduced from the kinematic reconstructions, showing the southward to southwestward trench retreat along the Hellenides and the Aegean region. Main tectono-metamorphic events in the Hellenide-Rhodope-Aegean region are also shown (1: subduction of the Vardar oceanic lithosphere; 2: subduction and accretion of the Pelagonian platform; 3: subduction and accretion of the Pindos basin, formation of the HP Cycladic Blueschists unit, extension in the Rhodope massif; 4: exhumation of the HP Cycladic Blueschists unit; 5: subduction and accretion of the Gavrovo-Tripolitza platform, formation of the HP Phyllite-Quartzite unit, extension in the Aegean domain; 6: exhumation of the HP Phyllite-Quartzite unit; 7: first slab tear and curvature of the trench; 8: second slab tear?).

However, their magnitude is contrasted. Indeed, based on our kinematic reconstructions, the late Cretaceous southward migration of the trench is estimated at around 50-100 km (figure 2.13a), giving a very low rate of N-S extension (i.e. 0.1-0.3 cm/yr), if we make the assumption of a constant velocity in the late Cretaceous. This low trench retreat (figure 2.13b) contrasts with the large crustal stretching and subsequent oceanic spreading occurring coevally in the Black Sea back-arc basin (figures 2.9a-h and 2.11) [*Zonenshain and Le Pichon*, 1986; *Görür*, 1988; *Hippolyte et al.*, 2010; *Nikishin et al.*, 2015b]. Although this retreat can explain the extensional tectonics, its amplitude is obviously not sufficient when considering the ~300 km north-south width of the Black Sea oceanic domain. However, the lack of further geological constraints on the structuration of the Black Sea basement, overlain by the ~15 km of sediments, limits the accuracy of our reconstructions in this region for this period.

In comparison, the total amount of trench retreat since the Oligocene in the Aegean domain is estimated at around 500 km in a NNE-SSW direction (figure 2.13a). The rate of the Hellenic-Aegean trench is thus comprised between 0.5 and 1 cm/yr as soon as the back-arc extension is active in the Rhodope massif (figure 2.13b). During the curvature of the trench, this rate increases drastically up to 3.4 cm/yr between 15 and 8 Ma in the Aegean region while it only reaches ~1.7 cm/yr along the Hellenides that form the flank of this bending trench. Intense crustal stretching behind the hinge of the trench then results in the exhumation of the deepest parts of the crust as migmatitic domes in the central Cyclades.

In our reconstructions the rate of trench retreat however increases as soon as 50 Ma, coevally with inception of extension in the Rhodope massif (figure 2.13b). This Eocene extension is accompanied by a clockwise rotation that is translated at the trench by southward migration. This period is contemporaneous with the subduction, accretion and exhumation of the Cycladic Blueschists unit, which belongs to the Pindos basin. The southward trench migration thus corresponds to the propagation of thrusts within the Pindos basin and the northern part of the Apulian plate. After this period of accretion and exhumation, trench retreat continues, from 35 Ma onward, associated with the subduction of the southern part of the Apulian plate (i.e. the Gavrovo-Tripolitza and the Ionian nappes) and back-arc extension in the Aegean domain. Although the trench has been retreating since

~50 Ma without major acceleration at 35-30 Ma, the magmatic arc has started to move southward only ~30 Ma in our reconstructions (figure 2.13o) (see also *Jolivet et al.* [2004a] and *Jolivet and Brun* [2010]). It thus appears a disconnection between trench retreat and magmatic arc retreat, an observation that may be partly explained by the model of *Brun and Faccenna*, [2008]. In this model the velocity of slab retreat is modified by the nature of the lithosphere entering the trench. When a continental lithosphere enters the trench, slab retreat stops and the slab steepens while thrusts propagate within the subducting continental domain. Once the subducting continental crust has been decoupled from the subducting lithosphere by these thrusts, retreat starts again with progressive shallowing of the slab, and back-arc extension ensues. The period framed between 50 and 35 Ma corresponds to the subduction of the partly oceanic Pindos basin that is progressively incorporated within the nappe stack. One may thus assume that during this period the slab has remained quite steady, progressively steepening, with little migration of the magmatic arc. Afterward the decoupling was sufficient to allow an increase of the rate of retreat with shallowing of the slab, migration of the magmatic arc and back-arc extension. Trench migration and slab migration should thus be considered separately.

Besides the nature of the subducting lithosphere, several other causes should be considered to explain these different extension rates associated with slab retreat in the late Cretaceous and since the Oligocene. Thus, continuous subduction since the Mesozoic implies more subducted lithospheric material and therefore higher slab pull and faster slab retreat since the Oligocene. Another parameter to consider is the slab width. Indeed, the forces resisting slab retreat (reaction of the mantle to slab retreat) are higher with a wide slab [*Faccenna et al.*, 2007; *Schellart et al.*, 2007], such as in the late Cretaceous along the Balkans and the Pontides. The width of this continuous subducting lithosphere was reduced by several episodes of slab tearing, leading to an increase of its retreating rate. Indeed, since the middle Miocene, large-scale block rotations (figure 2.4) and evolution of magmatism in the Cyclades and western Anatolia (see details in section 2.6.5) support the existence of a slab tear below western Anatolia, as suggested by several tomographic models [*de Boorder et al.*, 1998; *Piromallo and Morelli*, 2003; *Dilek and Altunkaynak*, 2009; *Jolivet et al.*, 2009, 2013; *Brun and Sokoutis*, 2010; *Salaün et al.*, 2012]. The reduced width of the slab thus induced its fast retreat and the fast rotation of

the Aegean trench from 15 to 8 Ma (figures 2.12 and 2.13) [*Jolivet et al.*, 2015], probably accentuated by the toroidal mantle flow occurring on its edge. Similarly, the differential Pliocene-Quaternary large-scale counterclockwise rotations in the Hellenides and the Peloponnese (figure 2.4) and the second acceleration of trench retreat since ~5 Ma (figure 2.13b) can be a consequence of a younger slab tear below the Corinth rift, decoupling the surface kinematics and deformation between the Hellenides and the Peloponnese [*Royden and Papanikolaou*, 2011; *Jolivet et al.*, 2013]. It is also not excluded that an older segmentation of the subduction zone may occur, especially during the continental accretion in the late Cretaceous-Paleocene [e.g. *Okay et al.*, 2012]. However, the continuous E-W trending late Cretaceous Balkans-Pontides magmatic arc and Eocene calc-alkaline magmatic province emplaced from the Chalkidiki peninsula to the eastern Pontides suggest a similar first-order E-W trending subduction zone that progressively migrated southward through this time (figures 2.9a-g and k-n).

2.6.2. Strain partitioning in the Aegean region

Recorded in metamorphic rocks of the Aegean region, stretching lineations give information about the strain driving the exhumation of MCCs since the Eocene. Deduced from our reconstructions, exhumation kinematics of the Rhodope, Kazdağ, Cyclades and Menderes MCCs is in line with these kinematic indicators (figure 2.14a). Although stretching lineations relate to strain and not to displacements, the overall parallelism between lineations and displacement trajectories suggests that deformation has been mostly plane with N-S stretching much larger than a possible perpendicular component. This is however associated with the local abnormal trend of lineations such as the WSW-ENE lineation in Syros. The coherent N-S Eocene lineation in the neighboring Sifnos island (figure 2.4) [*Roche et al.*, submitted] suggests that Syros has undergone local rotations responsible for this peculiar strike of the stretching lineation. The same situation can be observed in Mykonos where the main intrusion shows a N70°E lineation trending below the NCDS where the lineation displays a more normal NNE-SSW trend [*Lecomte et al.*, 2010; *Denèle et al.*, 2011]. Similarly, stretching lineations trend almost E-W in the Peloponnese where a late clockwise rotation is documented by paleomagnetic studies [*Kissel and Laj*, 1988; *van Hinsbergen et al.*, 2005b]. The complexity of these

rotations, synthetic to the main clockwise rotation of the Hellenides between 15 and 8 Ma, some of them undated and mostly local, should foster some additional investigations.

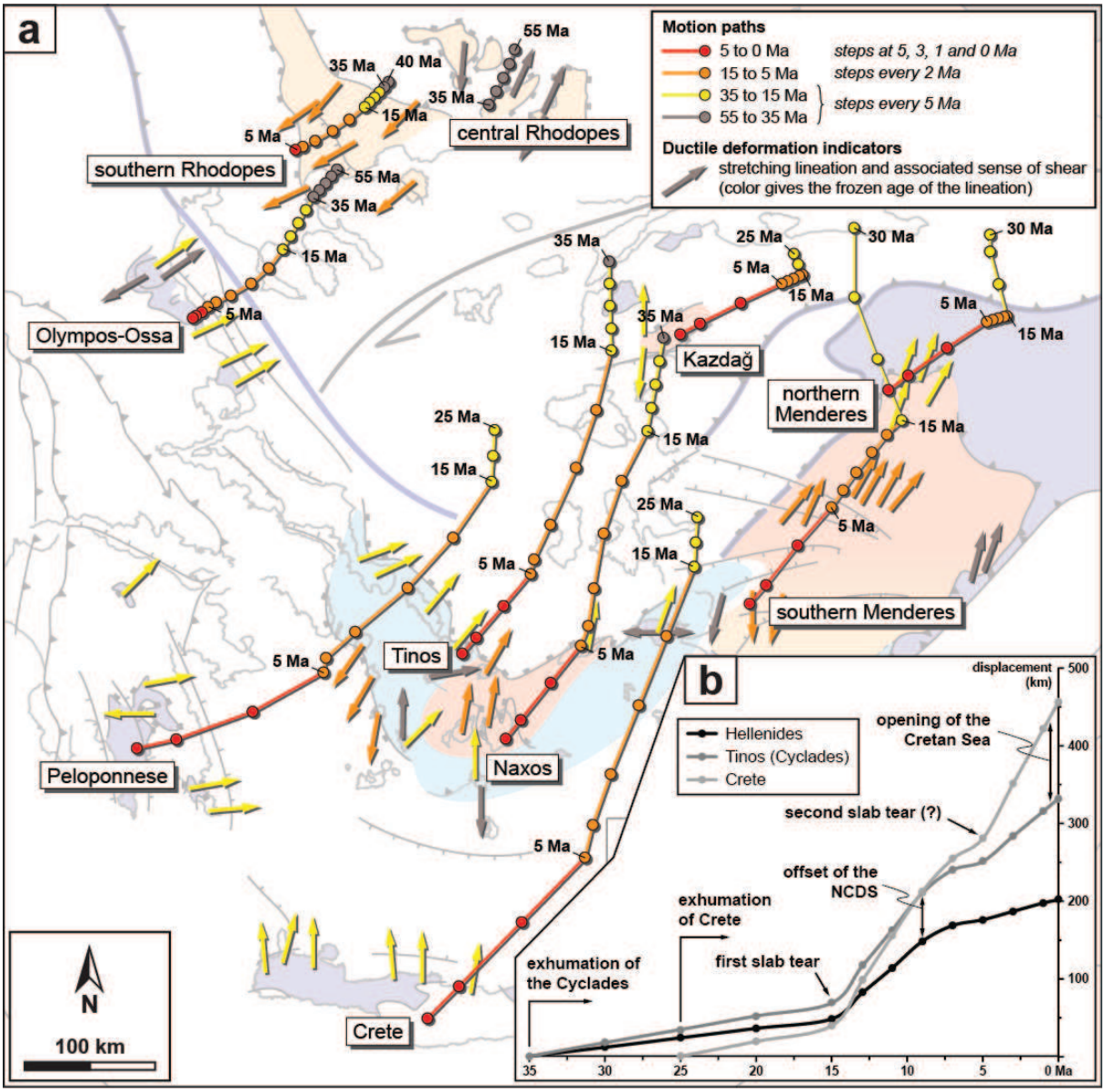

Figure 2.14: (a) **t**ectonic map showing the correlation between deformation (i.e. stretching lineations) and kinematics of exhumation of the MCCs in the Aegean domain since the Eocene (deduced from the reconstructions). (b) Time-displacement diagram, deduced from the kinematic reconstructions, showing the cumulative southward to southwestward displacement of the Hellenides, the Cyclades (Tinos) and Crete since the Oligocene. NCDS: North Cycladic Detachment System.

Since the Oligocene, the post-orogenic exhumation of the MCCs occurred in the footwall of several ductile-brittle detachment systems (figures 2.10 and 2.12). In the Cyclades for instance, three large-scale structures with well-constrained kinematics and timing have been considered: the NCDS,

cropping out in Tinos, Mykonos and Ikaria islands [*Lee and Lister*, 1992; *Gautier and Brun*, 1994; *Mehl et al.*, 2005; *Brichau et al.*, 2007; *Jolivet et al.*, 2010a; *Lecomte et al.*, 2010], the NPEFS, cropping out in Naxos and Paros islands [*Lister et al.*, 1984; *Urai et al.*, 1990; *Gautier et al.*, 1993; *Seward et al.*, 2009; *Bargnesi et al.*, 2013] and the WCDS, cropping out in Serifos island (figures 2.4 and 2.7) [*Grasemann and Petrakakis*, 2007; *Brichau et al.*, 2010; *Iglseder et al.*, 2011; *Grasemann et al.*, 2012]. In our reconstructions, the relative southward motion of Tinos island in the footwall of the NCDS, with respect to the Pelagonian nappe in the Hellenides, considered as the hanging wall of the NCDS, is estimated at around 70 km during the activity of this structure, fitting its estimated offset (i.e. ~60-100 km, figure 2.14b) [*Jolivet et al.*, 2004a; *Brichau et al.*, 2008].

The activity of these detachment systems continued after 15 Ma, while the dynamics of back-arc extension changed with the progressive curvature of the trench, related to slab tearing below western Anatolia (figure 2.12). Accommodation of the two opposite block rotations in the Cyclades has been first attributed to the hypothetic Mid-Cycladic Lineament [*Walcott and White*, 1998]. However, the existence of such fault is mainly based on the deflection of stretching lineations, notably in Paros and no clear strike-slip shear zone has ever been evidenced. In addition, its kinematics remains enigmatic in the literature, presented either as a dislocation zone [*Walcott and White*, 1998] or as a detachment fault [*van Hinsbergen and Schmid*, 2012] or as a dextral strike-slip fault [*Philippon et al.*, 2012]. In our reconstructions, considering fully deforming domains, it appears that such opposite rotations could be accommodated by a wide zone of distributed sinistral transtensional shearing, without the need of a localized fault.

After this fast rotation and the probable slab tear, extension has developed further south with the ~120 km opening of the Cretan Sea since 10-9 Ma (figure 2.14b). In the same time, the stress regime changed during a short time window in the Cyclades with the development of a distributed strike-slip then compressional deformation [*Ring et al.*, 1999a; *Avigad et al.*, 2001; *Menant et al.*, 2013]. Finally, the propagation of the NAF in the northern Aegean region 6-5 Ma ago [*Armijo et al.*, 1999] led to the localization of the deformation at the edges of this region (figures 2.9w-y) [*Papanikolaou and Royden*, 2007; *Pérouse et al.*, 2012].

The exact reason of this late Miocene E-W compression recorded in the Cyclades is unclear. Models of back-arc extension simply driven by slab retreat would not foster compression in this region [*Faccenna et al.*, 2006; *Jolivet et al.*, 2013; *Sternai et al.*, 2014]. Competition between slab retreat, extrusion and mantle flow may render quite complex the distribution of stresses in the back-arc lithosphere during the propagation of the NAF, requiring new investigations on the dynamics of this propagation and its interactions with back-arc extension.

2.6.3. Successive metamorphic events in the Mendres massif

The Menderes massif is often interpreted as an Alpine nappe stack, affecting a Pan-African basement and its sedimentary cover [e.g. *Ring et al.*, 1999b; *Bozkurt & Oberhänsli*, 2001; *Gessner et al.*, 2001a, 2013; *Jolivet et al.*, 2004b]. Following this accretionary event, this massif has then been exhumed in a back-arc extensional context, forming a dome-like structure [e.g. *Gessner et al.*, 2001b; *Lips et al.*, 2001; *van Hinsbergen et al.*, 2010b]. This succession of tectonic events resulted in a complex metamorphic succession that is still largely debated nowadays, notably due to the existence of a pre-Alpine tectono-metamorphic history [*Şengör et al.,* 1984; *Candan et al.,* 2001].

In the Eocene, two metamorphic events have thus been recorded in the Menderes massif with (1) a M*T*- to H*T*-M*P* Barrovian-type metamorphism recorded in the major part of the Menderes massif and called the *Main Menderes Metamorphism* and (2) a H*P*-L*T* metamorphism only preserved in the southern part of the massif. Because of the staggered ages of these metamorphic events, some authors argue that the H*P*-L*T* metamorphism occurred before the *Main Menderes Metamorphism* [e.g. *Rimmelé et al.*, 2003b; *Pourteau et al.*, 2013]. However, the lack of H*P*-L*T* relics in the whole Menderes massif seems to contradict this hypothesis (although rock chemistry restrictions can also be considered [*Rimmelé et al.*, 2003b]) and the overlapping of the metamorphic ages of these two events suggests that they were coeval (figure 2.6). The question is now, how is it possible? According to many authors, the *Main Menderes Metamorphism* resulted from the nappe stacking of the Menderes basement and cover during the Eocene [*Akkök*, 1983; *Şengör et al.*, 1984; *Bozkurt and Oberhänsli*, 2001; *Okay*, 2001]. In our kinematic reconstructions, this unit started to subduct in the late Paleocene-early Eocene and was quickly accreted to the Eurasian margin as the subduction front propagated

southward (figure 2.11). The upper nappes, forming the present-day northern Menderes massif, could thus undergo a M*T*- to H*T*-M*P* metamorphism as a result of crustal thickening. Conversely, the lower nappes could be buried within the subduction zone where they experienced a H*P*-L*T* metamorphism, observed in the southern part of the Menderes massif [*Rimmelé et al.*, 2003b; *Whitney et al.*, 2008; *Pourteau et al.*, 2013]. These synchronous events require however a major tectonic discontinuity which would juxtapose these units displaying a different pressure-temperature history and further investigations are therefore needed to clarify this point [*Whitney et al.*, 2008].

Following this Eocene metamorphic stage, a H*T* metamorphic event has also been recorded in the northern Menderes massif, characterized by migmatites of Oligocene age (figure 2.6). The few geochronological data shows that this event partially overlapped the *Main Menderes Metamorphism*, suggesting a relatively continuous M*T* to H*T* metamorphic event from the Eocene to the Oligocene [*Catlos and Çemen*, 2005; *Bozkurt et al.*, 2010]. These authors however argue that the Oligocene H*T* overprint was coeval with the initiation of the back-arc extension in this region, mainly accommodated at this time by the top-to-the N Simav detachment [*Işik and Tekeli*, 2001; *Ring et al.*, 2003]. Thus, similarly to the Aegean region, the Menderes massif seems to be progressively transferred in late Eocene-early Oligocene times from the compressional arc domain, where it underwent both a subduction-related H*P*-L*T* metamorphism and a nappe stacking-related M*T*- to H*T*-M*P* metamorphism, to the extensional back-arc domain where it was exhumed as a MCC in a H*T* environment (figure 2.11). Converselly, the exhumed parts of the southern Menderes massif only experienced a greenschist-facies metamorphism [*Hetzel et al.*, 1995a; *Bozkurt and Oberhänsli*, 2001], suggesting an exhumation process either at higher rate or in a colder environment.

2.6.4. Driving forces acting on the westward extrusion of Anatolia

Highlighted by GPS measurements, the present-day kinematics of the eastern Mediterranean region is dominated by an overall counterclockwise rotation of velocity vectors from the northward collision of Arabia, westward motion of Anatolia and southward retreat of the Hellenic trench with respect to Eurasia [*Reilinger et al.*, 2006; *Le Pichon and Kreemer*, 2010]. Integrated in our kinematics reconstructions with a rotation pole situated close to the Nile delta, this rotation is mainly

accommodated by the dextral strike-slip NAF after ~12 Ma [*Şengör et al.*, 2005]. The post-12 Ma surface kinematics in our reconstructions fits the present-day kinematics deduced from GPS measurements (figure 2.13), assuming a relatively steady kinematics in the eastern Mediterranean region since the late Miocene.

Several recent studies focused on the contribution of crustal and mantle processes to drive this surface deformation. For *Armijo et al.* [1999], the main force moving Anatolia is the push from the Arabia-Eurasia collision in a typical extrusion model, while in more recent contributions, the main force is slab retreat [*Faccenna et al.*, 2006; *Becker and Faccenna*, 2011; *Sternai et al.*, 2014]. In our reconstructions, the southward migration of the Hellenic trench is sensibly faster than the westward extrusion of Anatolia after the middle Miocene (figure 2.13), reinforcing the idea that slab rollback has played an active role in the westward motion of Anatolia, not only nowadays, but as soon as its inception ~12 Ma ago.

In addition, based on the similarity between mantle-related seismic anisotropy directions and the pattern of deformation in thinned back-arc domains and supported by mantle-related instantaneous 3D velocity fields and high-resolution 3D numerical modeling [*Jolivet et al.*, 2009; *Becker and Faccenna*, 2011; *Sternai et al.*, 2014], it has been proposed that mantle flow codetermines surface deformation. In our reconstructions, the surface kinematics has been dominated since the late Miocene by an overall counterclockwise rotation, in agreement with the pattern of seismic anisotropy observed in the eastern Mediterranean region (figure 2.13) [*Jolivet et al.*, 2013; *Paul et al.*, 2014]. Resulting from the integration of numerous geological data, this observation reinforces the hypothesis of a control, at least partial, of surface deformation by the underlying mantle flow through basal drag [*Jolivet et al.*, 2009; *Sternai et al.*, 2014].

Other external dragging forces, such as the mantle upwelling underneath the Afar region and its northward migration, have been also proposed to explain the present-day kinematics of the eastern Mediterranean region [*Faccenna et al.*, 2013]. Indeed, this hot mantle flow could thermally enhance the major slab break-off suggested on tomographic models in eastern Anatolia, allowing the instauration of the overall toroidal mantle flow highlighted by seismic anisotropy measurements (figure 2.13) [*Jolivet et al.*, 2013; *Paul et al.*, 2014]. In our kinematic reconstructions, the

emplacement of an extensive magmatic province in eastern Anatolia since the middle-late Miocene (figures 2.9t-y) attests for the arrival of hot mantle material at the base of the crust (see detail in section 2.6.6), supporting this slab break-off and related mantle flow hypothesis.

2.6.5. Southward retreat of the subduction zone and magma genesis

Evidenced in our kinematic reconstructions, magmatic activity in the eastern Mediterranean region has migrated southward together with the subduction zone since the late Cretaceous, showing the strong control of subduction dynamics on magma genesis (figures 2.9a-y). In more details, the distribution and petrological and geochemical variations of these magmas suggest that their sources have evolved through time in relation with changes in the subduction geometry and dynamics.

Medium-potassic calc-alkaline magmatism with mostly intermediate composition (commonly called *arc*-related magmatism) suggests primary magmas formed by partial melting of a hydrous mantle source metasomatized during the subduction of an oceanic lithosphere [*Gill*, 1981; *Berza et al.*, 1998]. During their storage in the Melting Assimilation Storage and Homogenization (MASH) zone at the base of the crust then their ascent within the crust, these magmas undergo some degrees of fractionation and crustal assimilation, giving this typical calc-alkaline magmatic trend [*Gill*, 1981; *Hildreth and Moorbath*, 1988; *Harangi et al.*, 2006]. In the eastern Mediterranean region, this medium-potassic calc-alkaline magmatism is represented with the late Cretaceous Balkans-Pontides magmatic province (figures 2.9a-h) [*Yılmaz et al.*, 1997; *Berza et al.*, 1998], the Eocene calc-alkaline magmatic province (figures 2.9j-n) [*Harris et al.*, 1994; *Okay and Satır*, 2006] and the still active south Aegean volcanism (figures 2.9x-y) [*Fytikas et al.*, 1984; *Pe-Piper and Piper*, 2005]. Highlighted by reconstructed cross-sections (figures 2.10 and 2.11), all these magmatic provinces emplace above a dehydrating oceanic slab, allowing the formation of primary magmas in the mantle wedge: the Vardar and Izmir-Ankara-Erzican oceanic lithosphere in the late Cretaceous and Eocene and the Mesogean oceanic lithosphere nowadays. It is noticeable that the emplacement of the late Cretaceous Balkans-Pontides magmatic province and the present-day south Aegean volcanism occurs in a back-arc context associated with transtensional or extensional tectonics. Magmatism with *arc*-related geochemical

characteristics can therefore occur in a *back-arc* context as soon as dehydration of the underlying oceanic slab triggers partial melting in the metasomatized mantle wedge.

When the slab retreats, processes of magma genesis change. In the back-arc region, increased geothermal gradient due to lithospheric thinning and underlying asthenospheric flow thus allow the partial melting of the lower crust and, possibly, of the lithospheric mantle by adiabatic rising, supplying the MASH zone. This lithospheric mantle is often highly metasomatized as a result of the subduction of both continental and oceanic materials [*Hawkesworth et al.*, 1995; *Harangi et al.*, 2006; *Ersoy and Palmer*, 2013]. These magmas then show a higher magmatic alkali content, giving high-K calc-alkaline to shoshonitic compositions. In the eastern Mediterranean region, the late Cretaceous CACC plutonic province (figures 2.9b-g) [*Aydin et al.*, 1998; *Ilbeyli et al.*, 2004; *Boztuğ et al.*, 2009], the latest Cretaceous volcanic activity in the eastern Srednogorie region (figures 2.9g-h) [*Boccaletti et al.*, 1978] and the Oligocene-Miocene Rhodope and west Anatolian-Aegean magmatic provinces (figure 2.12) [*Ersoy and Palmer*, 2013 and references therein] display this typical *back-arc*-related composition. This high-K magmatism often developed during the exhumation of MCCs (figures 2.10 and 2.11). In this context, detachment systems control the exhumation and cooling of syn-tectonic intrusions that show a pervasive co-magmatic to ductile-brittle deformation controlled by the regional extensional stress regime [*Faure and Bonneau*, 1988; *Dinter and Royden*, 1993; *Gessner et al.*, 2001a; *Denèle et al.*, 2011; *Laurent et al.*, 2015; *Rabillard et al.*, 2015]. With this ongoing extensional tectonics, the respective proportions of crustal and mantle (or more generally felsic and mafic) source components in these magmas change with an increase of the mantle (or mafic) source component, often observed notably in the CACC, the Rhodope massif and the Cyclades. This change is probably correlated with the thinning and heating of the lithosphere, allowing the partial melting of the highly metasomatized mantle or a crustal mafic protolith such as amphibolites [*Altherr and Siebel*, 2002; *Ilbeyli et al.*, 2004; *Marchev et al.*, 2005; *Stouraiti et al.*, 2010; *Ersoy and Palmer*, 2013].

If slab rollback continues, the extreme thinning of the upper plate can trigger the partial melting of the underlying asthenosphere, giving alkaline magmas with a major asthenospheric source component, typical for an intraplate-related magmatism. This magmatism developed notably in the Balkans (figures 2.9g-k), the central Rhodope massif and from the Thrace basin to the Isparta angle (figures

2.9t-y), succeeding to the high-K calc-alkaline to shoshonitic magmatism [*Cvetković et al.*, 2004; *Ilbeyli et al.*, 2004; *Marchev et al.*, 2004b; *Agostini et al.*, 2007].

This first-order spatial and compositional evolution of the arc-, back-arc- and then intraplate-related magmatism has already been documented by *Pe-Piper and Piper* [2006]. They involve then several slab break-off or lithospheric delamination events during the earlier Cenozoic, triggering the rise of hot asthenosphere and the change in magma genesis processes with partial melting of hydrated mantle wedge, metasomatized lithospheric mantle and rising asthenosphere. In our opinion, although magma genesis processes remain the same, the subduction dynamics and related asthenospheric flow controlling these processes are different. Indeed, tomographic models show a more than 1,500 km-long single slab in the Rhodope-Aegean-west Anatolian region, suggesting a continuous subduction without any slab break-off since the late Cretaceous at least. The progressive southward retreat of the subduction zone and related lithospheric thinning and underlying asthenospheric flow, notably after 35-30 Ma are the most likely processes controlling the first-order evolution of the magmatism. However, other subduction-related or -unrelated processes, such as lateral slab tearing should also be considered when variations of this *classical* magmatic evolution are observed.

2.6.6. Modulation of magmatic evolution by slab tearing and mantle plumes

The surge of high-K calc-alkaline in the eastern Aegean region from 20 to 15-13 Ma and then alkaline since 12 Ma is not evenly distributed over the entire back-arc domain but instead localized above the slab tear postulated from seismic tomographic models [*de Boorder et al.*, 1998; *Dilek and Altunkaynak*, 2009; *Salaün et al.*, 2012; *Jolivet et al.*, 2013; 2015]. This evolution is contemporaneous with the fast clockwise rotation of the continental Hellenides [v*an Hinsbergen et al.*, 2005b; *Jolivet et al.*, 2013]. So, instead of a regular retreat and magmatic evolution, the distribution of magmatism is compatible with the progressive formation of a tear in the early-middle Miocene.

Similarly, the emplacement of syn-tectonic intrusions in the Menderes massif and the Cyclades with a westward migration in the Miocene (figure 2.12), associated with an increase of the mantle (or mafic) source component of these magmas [*Altherr and Siebel*, 2002; *Stouraiti et al.*, 2010] can be correlated to the slab bending and tearing that occurred coevally below western Anatolia. As shown by

analogue and numerical modeling [*Funiciello et al.*, 2003, 2006; *Piromallo et al.*, 2006; *Faccenda and Capitanio*, 2012; *Li et al.*, 2013; *Sternai et al.*, 2014], slab tearing-related hot asthenospheric flow displays a significant toroidal component that could progressively heat the base of the stretched lithosphere allowing its partial melting.

In eastern Anatolia, the late Miocene-Quaternary volcanism shows a similar evolution to the west Anatolian-Aegean magmatic province with notably a southward migration of volcanism whose composition evolves from high-K calc-alkaline to alkaline (figures 2.9t-y) [*Pearce et al.*, 1990; *Keskin*, 2003]. However, since the Miocene, no significant crustal thinning is observed in this region that is instead supported by a ~45 km thick crust with a 2 km high plateau [*Dewey et al.*, 1986; *Şengör et al.*, 2003]. As discussed above, the slab break-off below the Bitlis belt suggested on tomographic models and the arrival of a hot asthenospheric flow from the Afar hot spot could allow the preservation of a high-elevation plateau and thermal delamination of the lithospheric mantle below eastern Anatolia [*Şengör et al.*, 2003; *Keskin*, 2003, 2007; *Faccenna et al.*, 2013]. Successive partial melting of the lower crust, lithospheric mantle and finally asthenosphere could then control the emplacement of this high-K calc-alkaline to alkaline magmatism.

2.7. Conclusion

Integrating the principle of non-rigid domains, these new kinematic reconstructions describe the late Cretaceous-Cenozoic evolution of the eastern Mediterranean region, notably including the history of rotations, the kinematics of the shear zones, the timing of exhumation of metamorphic units and the distribution and geochemical characteristics of magmatic centers. Extracted from this reconstruction model, the set of tectonic maps and cross-sections allows us to better understand the past geometry of the continuous northward Tethyan subduction zone and its dynamics.

They show that two extensional events and related back-arc opening occurred during the late Cretaceous along the Balkans and the Pontides and since the Eocene-Oligocene in the Rhodope-Aegean-west Anatolian region, separated during the Paleocene by a compressional episode

characterized by the accretion of Africa-derived continental blocks. The extension rate is higher for this second event and associated with an increase of the southward slab retreat rate. This extensional kinematics culminates after 15 Ma while the trench has bent, probably as a result of the formation of a slab tear below western Anatolia.

The kinematic reconstructions show the progressive deformation of the back-arc domain and the formation of the main detachments, such as the NCDS, the WCDS or the Kerdylion detachment. They also show the progressive exhumation of the main metamorphic units from their maximum burial to their arrival at the surface.

The migration of the magmatic activity as well as the evolution of its composition from arc- to back-arc- and finally intraplate-like geochemical signature is in line with this evolution with (1) the first-order southward migration of the magmatic centers related to the southward retreat of the continuous Tethyan subduction zone since the late Cretaceous and (2) the second-order localization of high-K calc-alkaline and alkaline magma emplacement and the westward migration of plutonic bodies from the Menderes massif to the Cyclades during the Miocene, controlled by the tearing of the slab and related hot mantle flow.

Finally, the driving forces of this dynamics may be also discussed in light of these kinematic reconstructions. Thus, the faster migration of the Hellenic trench than the westward extrusion of Anatolia since the late Miocene implies (1) a similar kinematics in the eastern Mediterranean region since the late Miocene and (2) that the retreating slab plays a major role on the crustal kinematics not only nowadays, as shown by GPS measurements, but as soon as the late Miocene. In addition, the coeval emplacement of magmatic centers in eastern Anatolia with a high asthenospheric source component suggest the arrival of a hot mantle flow below this region that may also drive the surface deformation by basal drag where the crust is relatively thin and hot.

Acknowledgments

This work was funded by the French Geological Survey (BRGM), Région Centre, the Institut

Universitaire de France, the European Research Council (ERC) under the 7th Framework Programme of the European Union (ERC Advanced Grant, RHEOLITH) and the Labex VOLTAIRE (ANR-10-LABX-100-01). We thank Laurent Guillou-Frottier and Guillaume Bertrand for their comments. Aral Okay provided helpful comments on an earlier version of the manuscript.

Chapitre 3

Distribution des minéralisations et reconstructions de la dynamique de subduction

Copper or gold? A matter of subduction dynamics

(article soumis au journal *Nature Communications*)

3.1. Extended abstract 160
3.2. Introduction 161
3.3. Ore distribution in eastern Mediterranean since the late Cretaceous 161
3.4. Subduction-related deep processes and ore genesis 163
3.5. Crustal evolution of hydrothermal systems 166
3.6. Conclusion 167

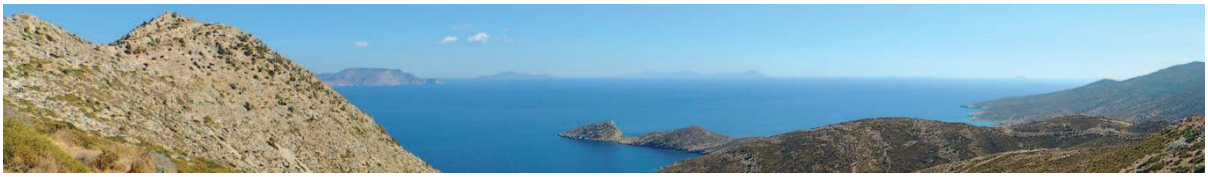

Dans ce chapitre, j'étudie la distribution des gîtes(*) minéralisés en Méditerranée orientale depuis le Crétacé supérieur. Pour ce faire, j'ai compilé une base de données métallogéniques à partir de trois bases de données déjà existantes : (1) la base *ProMine Mineral Deposits* du BRGM [*Cassard et al.*, 2012], (2) la base *Caucase* du BRGM (données non publiées) et (3) la base *Porphyry copper deposits of the World* de l'USGS [*Singer et al.*, 2008] ; ainsi que de nombreuses données publiées dans la littérature [ex. *Ciobanu et al.*, 2002; *Heinrich & Neubauer*, 2002; *Skarpelis*, 2002; *Marchev et al.*, 2005; *Yigit*, 2009, 2012]. J'ai ainsi recensé 317 occurrences minéralisées, caractérisées par leur contenu métallique (i.e. cuivre, or, plomb, zinc), leur typologie (i.e. typique des environnements de subduction, cf. *Section 1.3* : porphyre minéralisé, épithermal acide, neutre ou intermédiaire, skarn ou gîte contrôlé par des failles ou des niveaux sédimentaires) et leur âge de mise en place. J'ai ensuite intégré ces minéralisations au modèle de reconstructions cinématiques présenté dans le chapitre précédent en liant cinématiquement chacune des occurrences au bloc auquel elle appartient, celles-ci se déplaçant alors de manière similaire dans le processus de reconstruction. A partir de ce modèle, j'ai finalement extrait 25 cartes paléotectoniques (figure 3.1a-y, disponibles également sous la forme d'un film, cf. *Annexe D, video D.1*), mettant en évidence l'évolution métallogénique de la Méditerranée orientale depuis le Crétacé supérieur.

Ce travail a fait l'objet d'un article scientifique soumis au journal *Nature Communications* et qui s'intitule *Copper or gold? A matter of subduction dynamics*. Le format de cet article (ex. appel des figures dans le texte, références bibliographiques déplacée dans la section adéquate) a été légèrement modifié par rapport à la version soumise afin de s'adapter à celui de ce manuscrit de thèse.

Dans cet article présenté ci-dessous, après avoir justifié cette démarche, je décris dans un premier temps l'évolution de la distribution spatiale et temporelle des gîtes minéralisés mise en évidence grâce au modèle de reconstructions cinématiques. Ces résultats, ainsi que ceux obtenus sur l'évolution du magmatisme associé (cf. *Chapitre 2*), me permettent ensuite de discuter des processus de genèse de

ces minéralisations qui ont pu intervenir aussi bien dans le domaine d'arc ou d'arrière-arc et ce depuis l'asthénosphère, jusque dans la croûte continentale supérieure.

Principaux résultats

En accord avec les premières observations de *Loiselet et al.* [2010], deux époques fertiles majeures ont été mises en évidence, toutes deux associées à un régime tectonique extensif (ou transtensif) : (1) au Crétacé supérieur-Paléocène inférieur, une ceinture métallogénique s'est mise en place depuis les Balkans jusque dans les Pontides orientales, dominée par des systèmes minéralisés porphyriques et minéralisations associées riches en cuivre (ex. épithermaux acides, skarn) et (2) à l'Oligocène-Miocène, une vaste province riche en plomb-zinc puis en or s'est progressivement développée depuis le massif du Rhodope, jusque dans le domaine Egéen et ouest-Anatolien. Celle-ci est principalement caractérisée par des épithermaux intermédiaires à neutres ainsi que par des gîtes de remplacement sédimentaire de type skarns.

Tout au long de ces deux périodes, ces minéralisations se sont progressivement mises en place vers le sud, de manière synchrone à la migration de premier ordre du magmatisme et du front de subduction, décrite dans le chapitre précédent (figures 2.9a-y). De plus, la migration secondaire de ces systèmes magmatiques et hydrothermaux depuis le massif du Menderes à l'est, vers l'archipel des Cyclades à l'ouest au cours du Miocène vient moduler cette migration globale vers le sud, nécessitant de considérer la complexité 3D de la zone de subduction Hellénique.

Cette évolution résulte du passage d'une zone de subduction linéaire et relativement stable associée à des systèmes magmatiques-hydrothermaux typiques du domaine d'arc (figure 1.5, i.e. similaire à la subduction Andine), à une zone de subduction caractérisée par un retrait rapide du panneau plongeant qui permet l'ouverture d'un vaste domaine d'arrière-arc. Dans ce contexte extensif, les systèmes magmatiques et hydrothermaux permettent la remobilisation de certains métaux depuis la croûte continentale (ex. plomb, zinc, argent), alors que les métaux sidérophiles comme l'or proviendraient de la fusion partielle des résidus sulfurés caractérisés par un rapport Au/Cu élevé et précédemment formés au niveau de la croûte inférieure et du manteau lithosphérique dans le domaine d'arc (figure 1.6).

L'augmentation du taux d'extension dans le domaine d'arrière-arc ainsi que le flux asthénosphérique sous-jacent, tous deux résultant de processus profonds liés à la dynamique de la subduction comme le retrait et la déchirure du panneau plongeant, contrôlent cette transition métallogénique. De plus, l'amincissement crustal accommodé par de grands systèmes de détachements favorise l'ascension rapide des fluides magmatiques et hydrothermaux le long de ces drains, jusque dans la croûte supérieure où les métaux en solution peuvent précipiter et former des concentrations métalliques d'intérêt économique.

Les treize pages suivantes présentent l'ensemble des cartes paléotectoniques extraites du modèle de reconstructions cinématiques et qui intègre l'évolution métalogénique de la Méditerranée orientale.

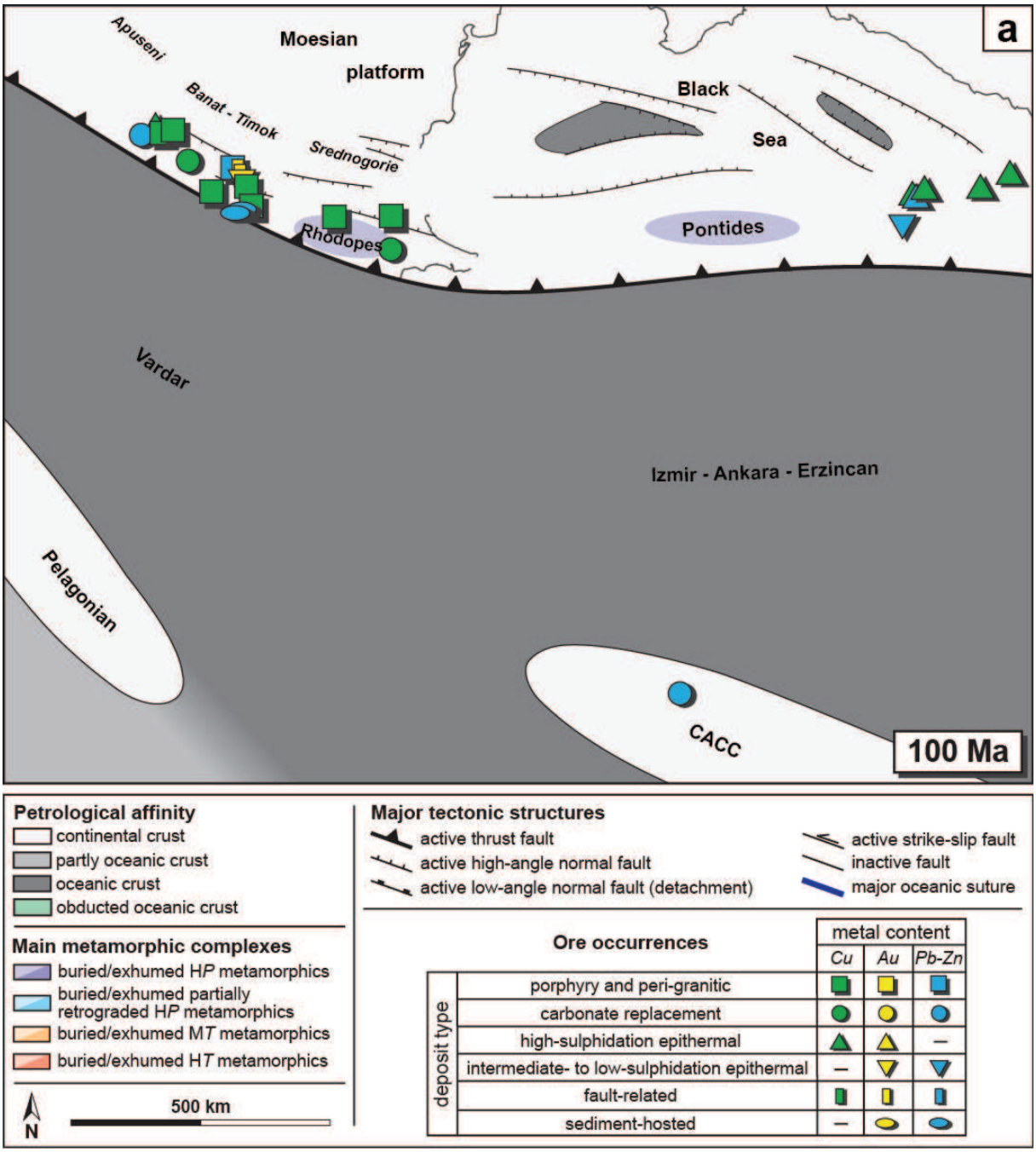

Figure 3.1: (a-y) cartes paléotectoniques extraites du modèle de reconstruction cinématique, mettant en évidence la distribution spatiale et temporelle des occurrences minéralisées en Méditerranée orientale depuis le Crétacé supérieur. CACC: Central Anatolian Crystalline Complex. OOP: Olympos-Ossa-Pelion windows.

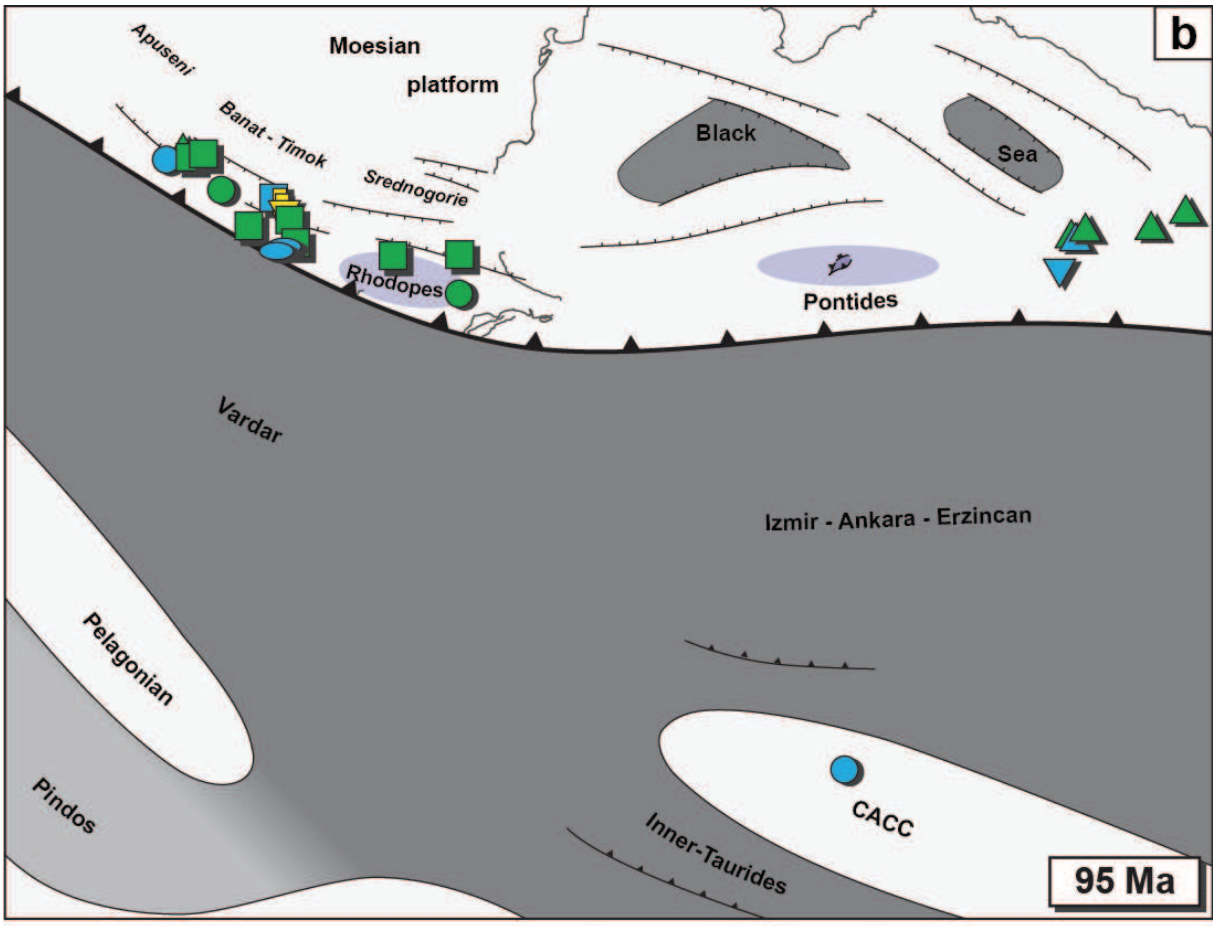
b
Apuseni
Moesian
platform
Banat - Timok
Srednogorie
Black
Sea
Rhodopes
Pontides
Vardar
Izmir - Ankara - Erzincan
Pelagonian
Pindos
CACC
Inner-Taurides
95 Ma

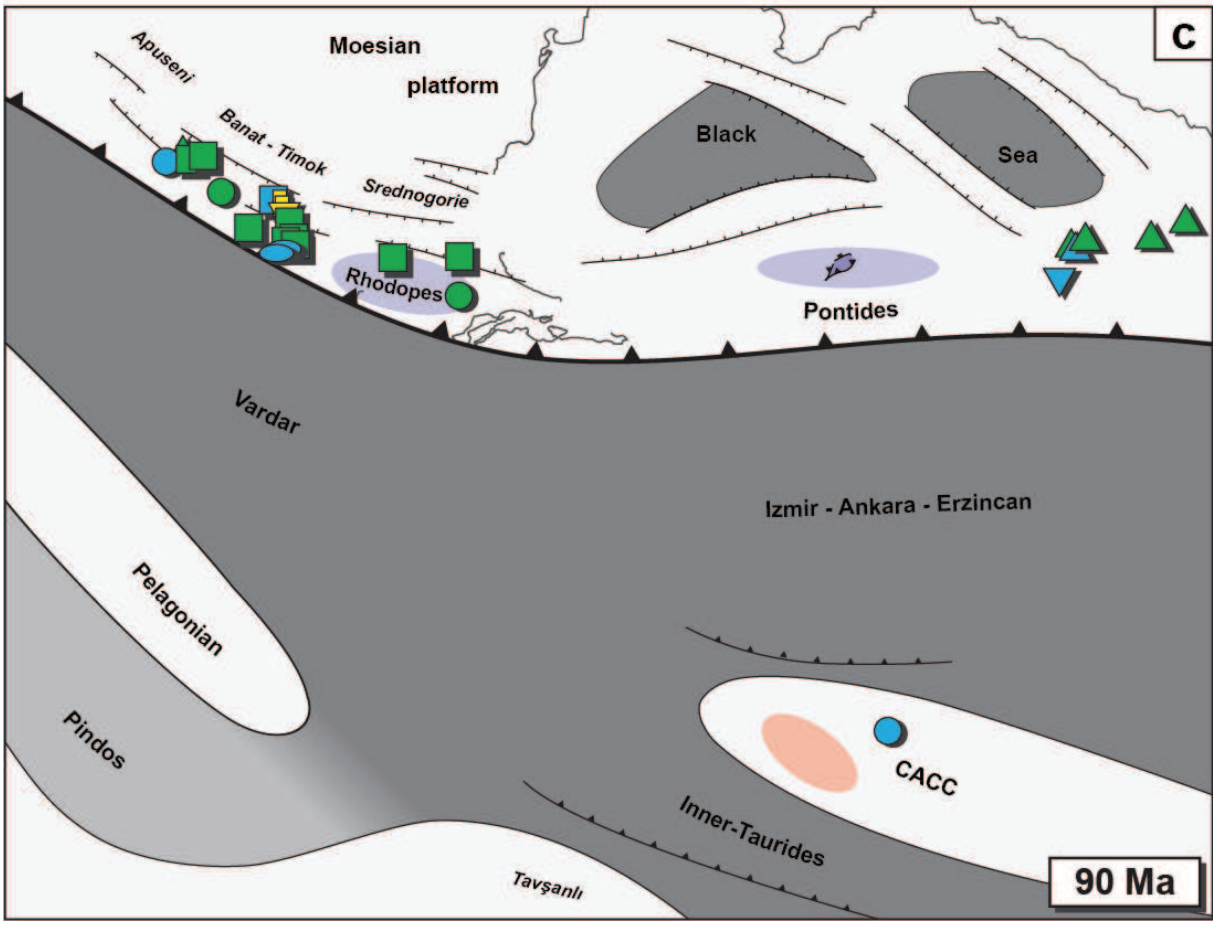
c
Apuseni
Moesian
platform
Banat - Timok
Srednogorie
Black
Sea
Rhodopes
Pontides
Vardar
Izmir - Ankara - Erzincan
Pelagonian
Pindos
CACC
Inner-Taurides
Tavşanlı
90 Ma

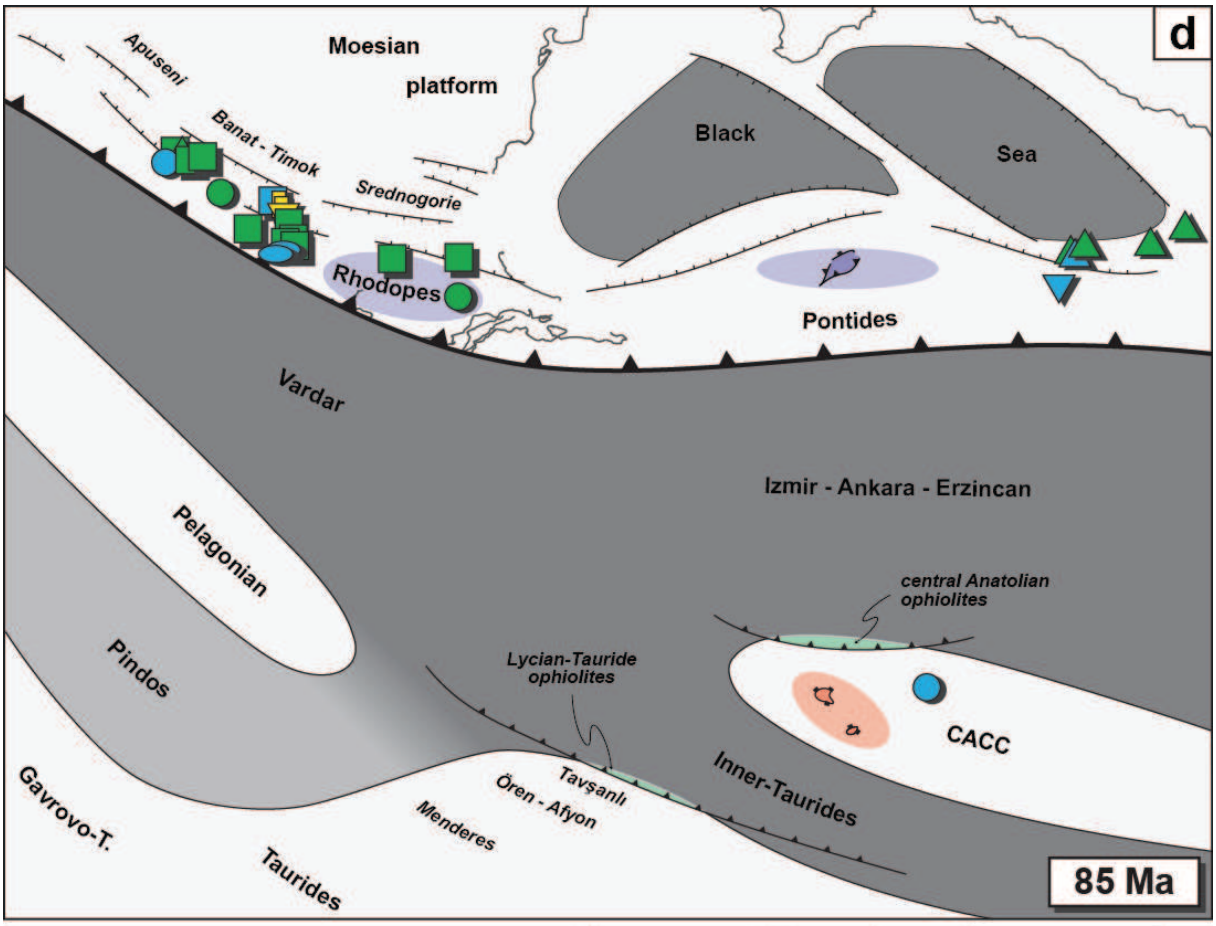
d
Moesian
platform
Apuseni
Banat - Timok
Srednogorie
Rhodopes
Black
Sea
Pontides
Vardar
Izmir - Ankara - Erzincan
Pelagonian
Pindos
central Anatolian
ophiolites
Lycian-Tauride
ophiolites
CACC
Inner-Taurides
Tavşanlı
Ören - Afyon
Menderes
Gavrovo-T.
Taurides
85 Ma

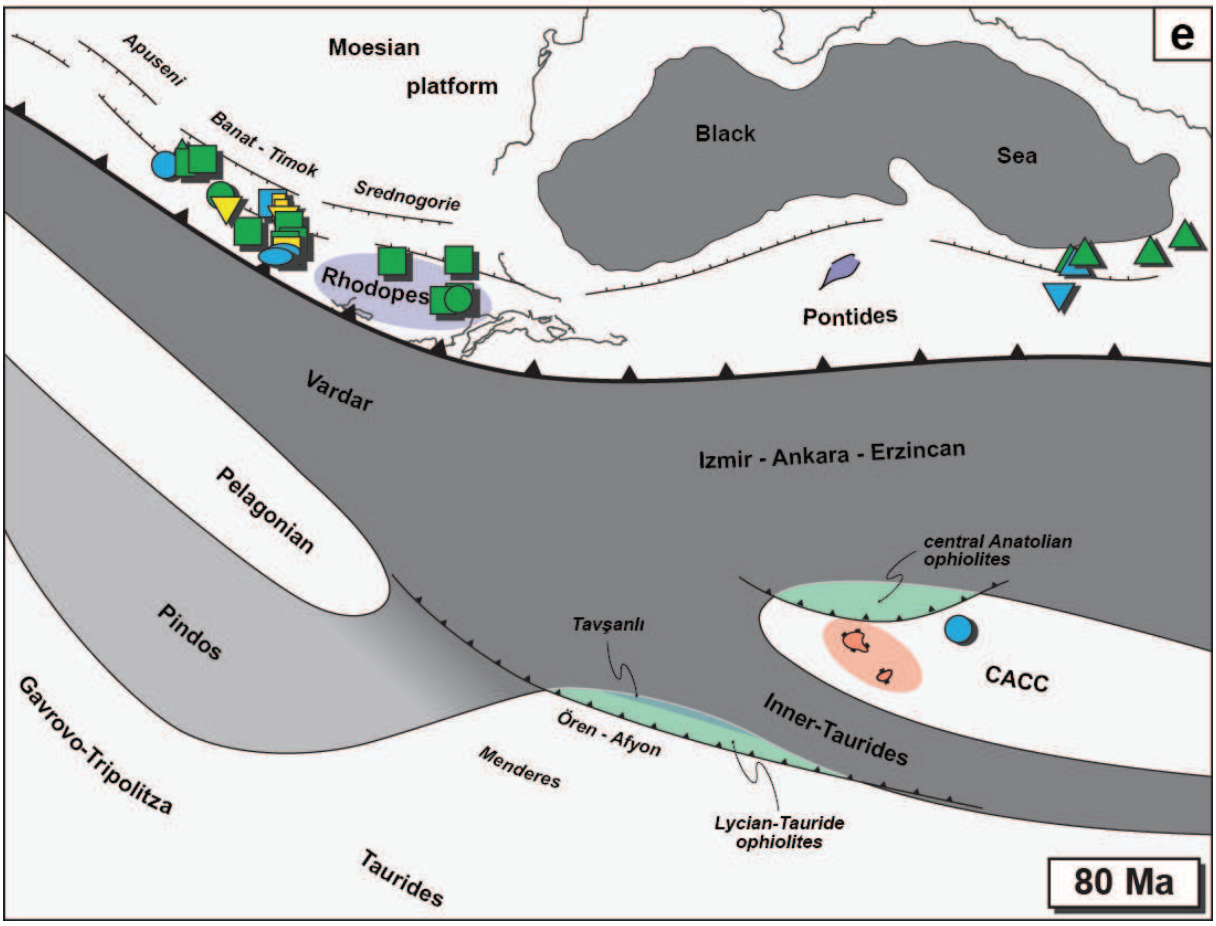
e
Moesian
platform
Apuseni
Banat - Timok
Srednogorie
Rhodopes
Black
Sea
Pontides
Vardar
Izmir - Ankara - Erzincan
Pelagonian
Pindos
central Anatolian
ophiolites
Tavşanlı
CACC
Inner-Taurides
Ören - Afyon
Menderes
Gavrovo-Tripolitza
Lycian-Tauride
ophiolites
Taurides
80 Ma

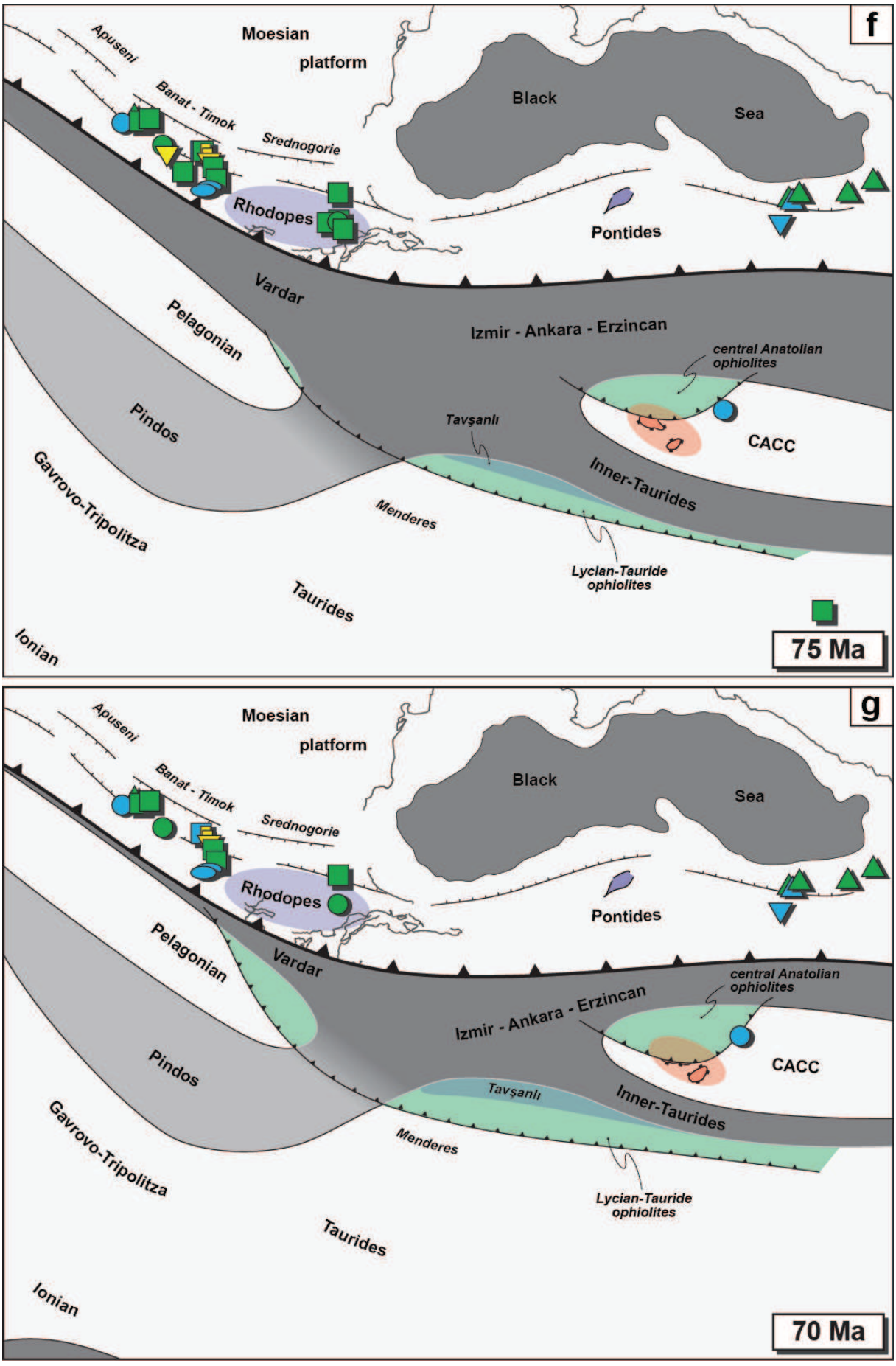
f
Moesian
platform
Apuseni
Banat - Timok
Srednogorie
Rhodopes
Black
Sea
Pontides
Vardar
Izmir - Ankara - Erzincan
central Anatolian
ophiolites
Pelagonian
Pindos
Tavşanlı
CACC
Inner-Taurides
Gavrovo-Tripolitza
Menderes
Lycian-Tauride
ophiolites
Taurides
Ionian
75 Ma
g
Moesian
platform
Apuseni
Banat - Timok
Srednogorie
Rhodopes
Black
Sea
Pontides
Pelagonian
Vardar
central Anatolian
ophiolites
Izmir - Ankara - Erzincan
Pindos
CACC
Tavşanlı
Inner-Taurides
Gavrovo-Tripolitza
Menderes
Lycian-Tauride
ophiolites
Taurides
Ionian
70 Ma

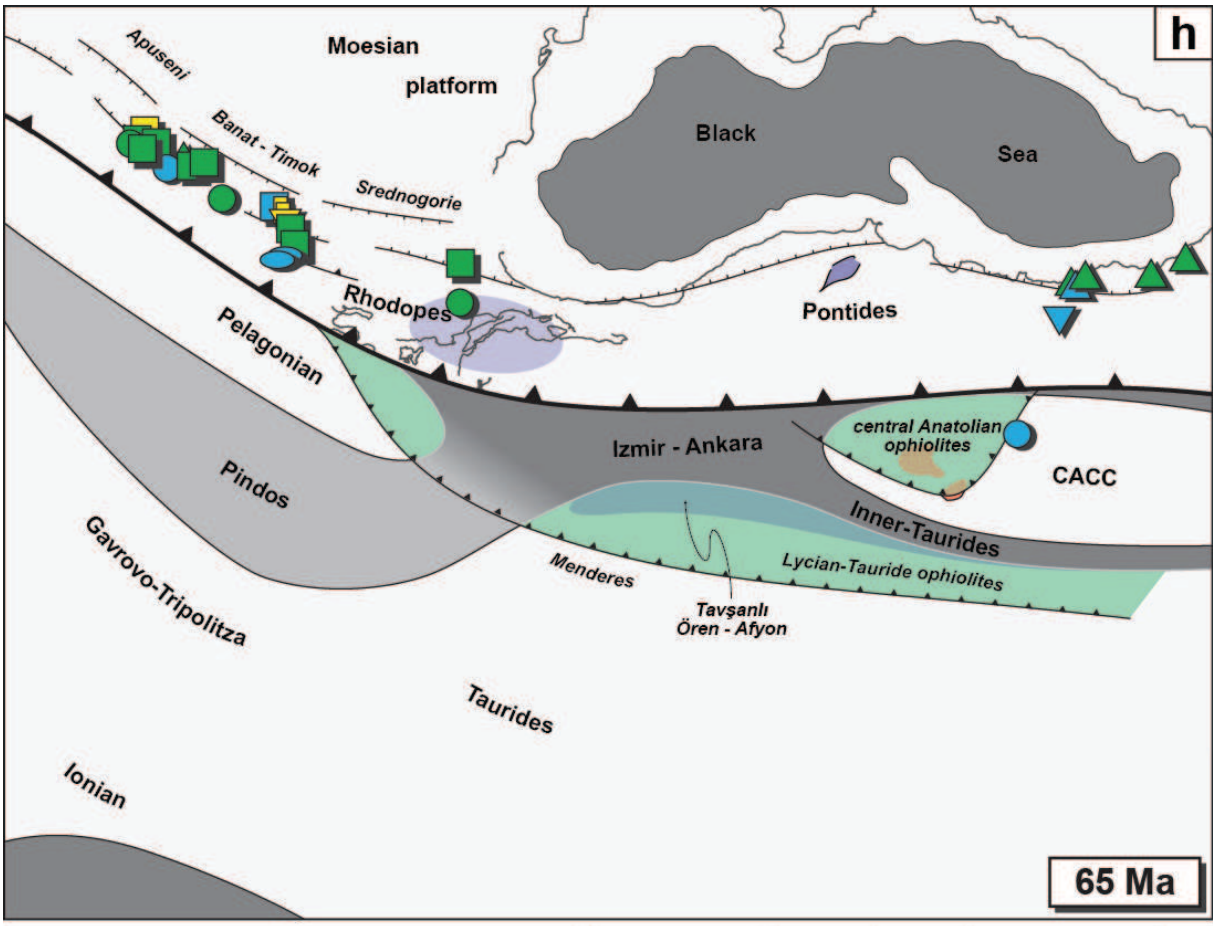
h
Moesian
platform
Apuseni
Banat - Timok
Srednogorie
Black
Sea
Rhodopes
Pontides
Pelagonian
Izmir - Ankara
central Anatolian
ophiolites
CACC
Pindos
Inner-Taurides
Lycian-Tauride ophiolites
Menderes
Tavşanlı
Ören - Afyon
Gavrovo-Tripolitza
Taurides
Ionian
65 Ma

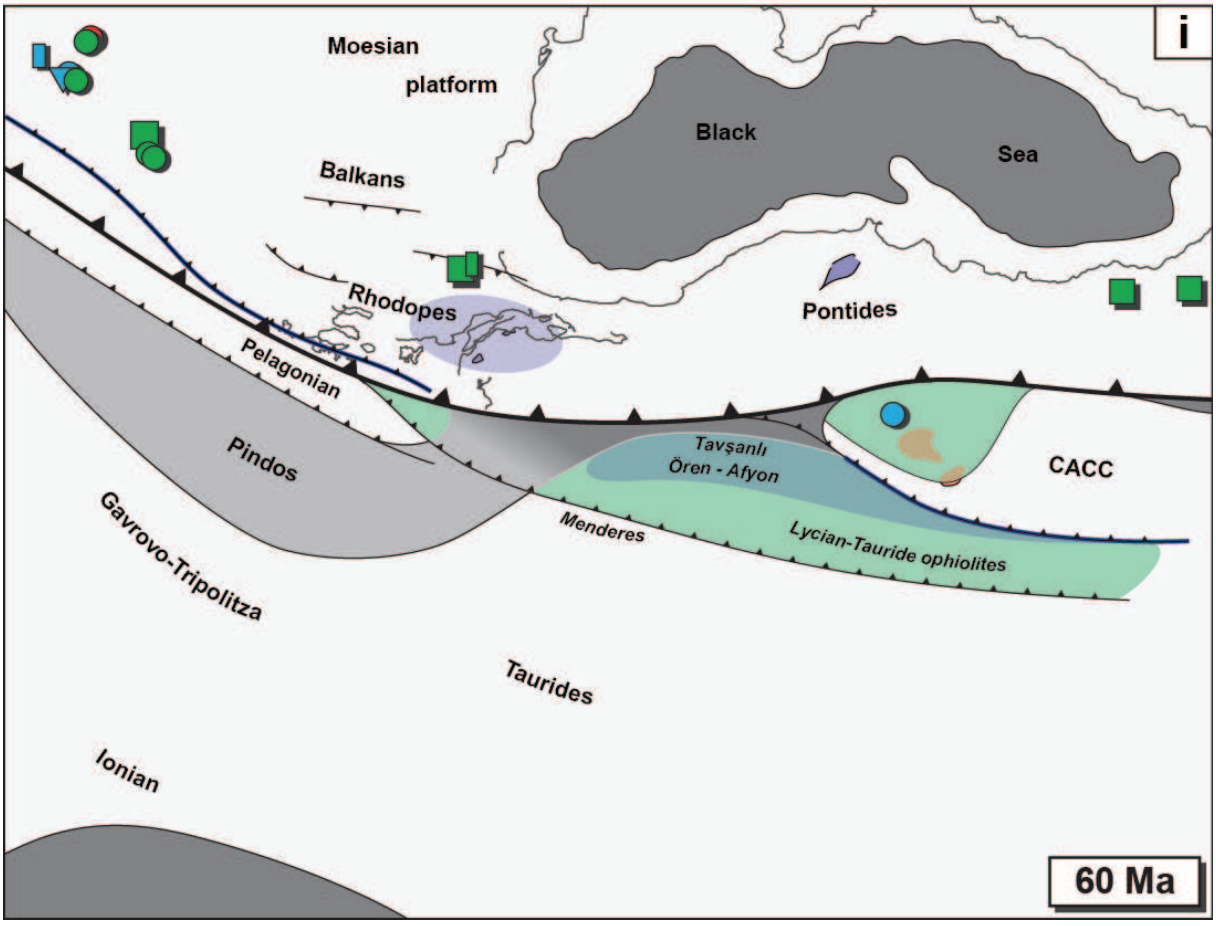
i
Moesian
platform
Black
Sea
Balkans
Rhodopes
Pontides
Pelagonian
Pindos
Tavşanlı
Ören - Afyon
CACC
Menderes
Lycian-Tauride ophiolites
Gavrovo-Tripolitza
Taurides
Ionian
60 Ma

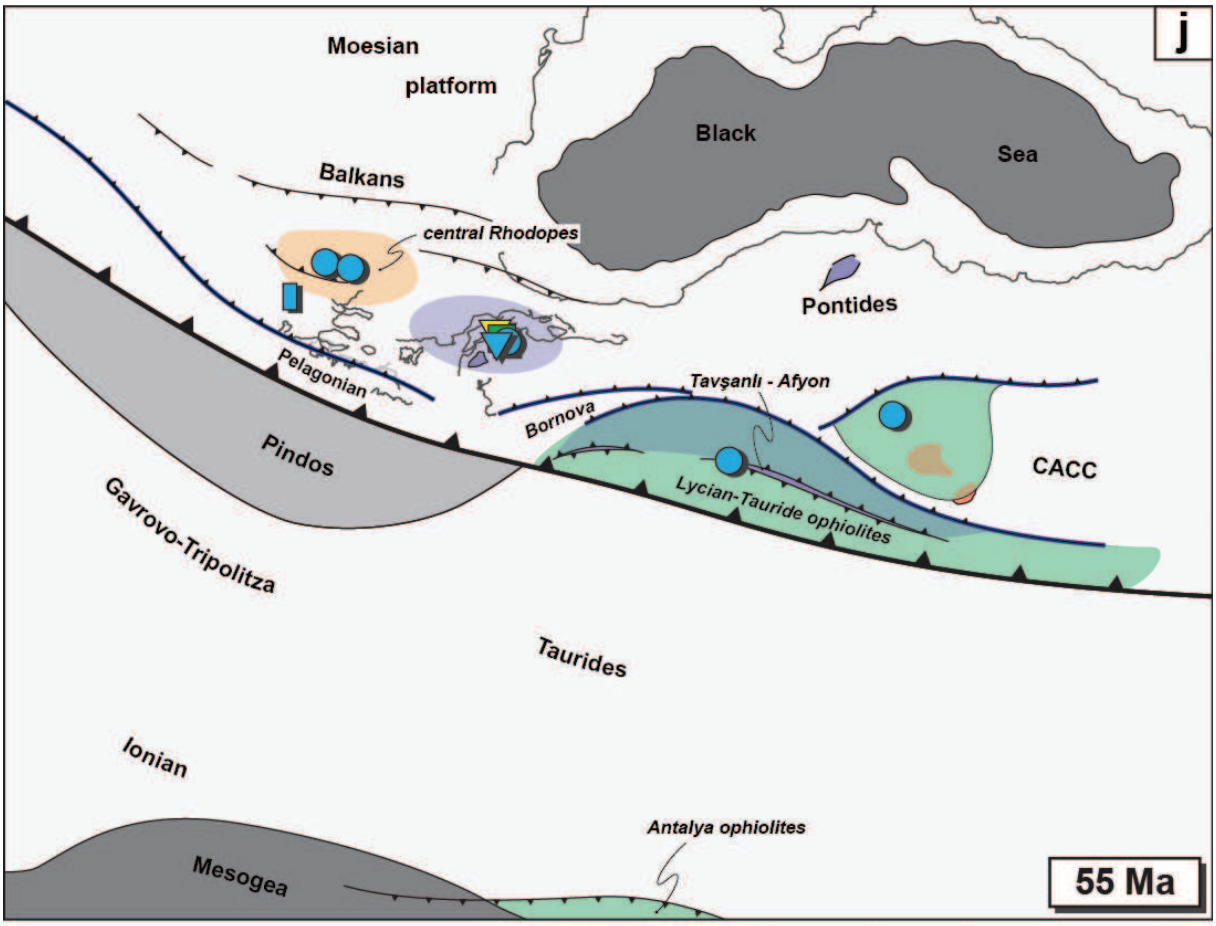
j
Moesian
platform
Black
Sea
Balkans
central Rhodopes
Pontides
Pelagonian
Tavşanlı - Afyon
Bornova
Pindos
CACC
Lycian-Tauride ophiolites
Gavrovo-Tripolitza
Taurides
Ionian
Antalya ophiolites
Mesogea
55 Ma

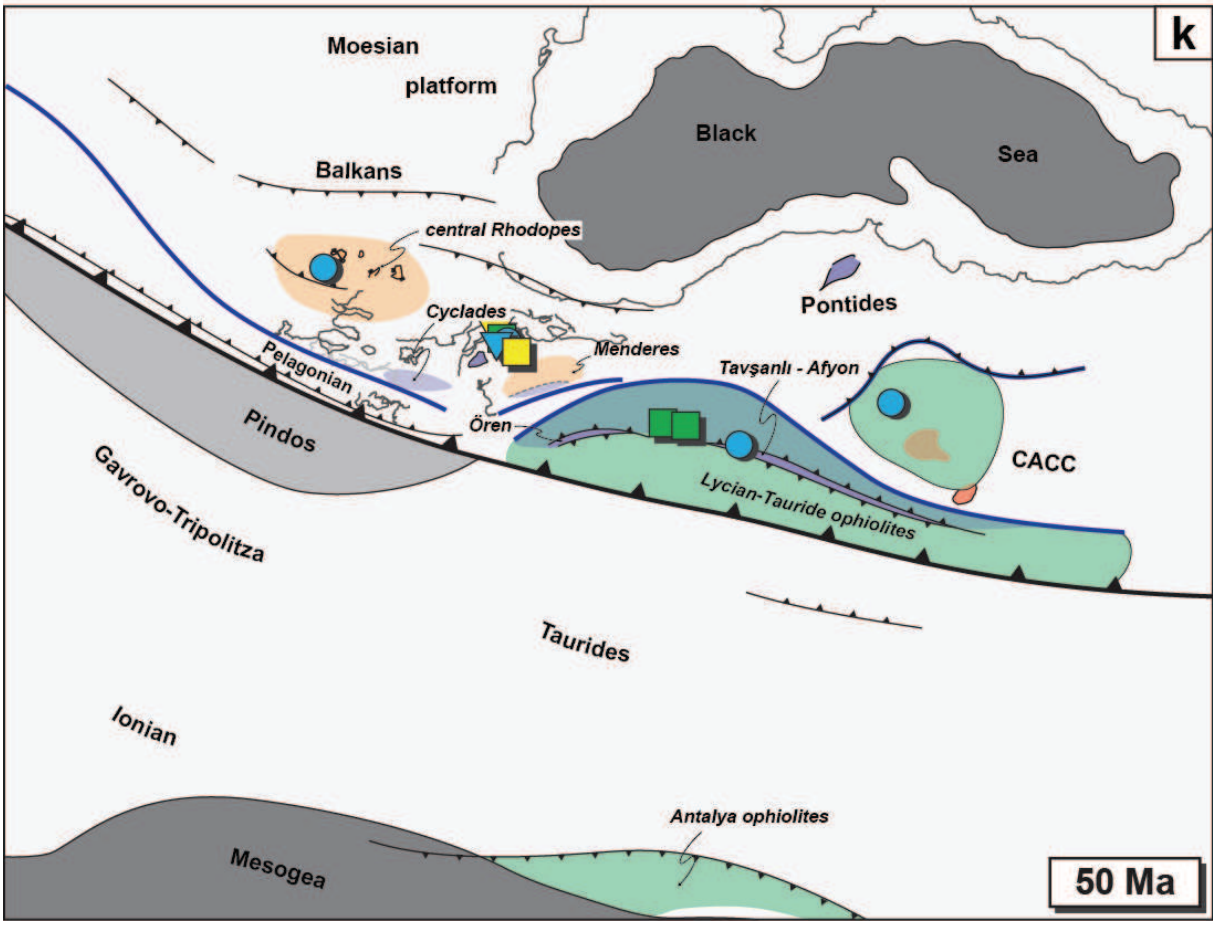
k
Moesian
platform
Black
Sea
Balkans
central Rhodopes
Pontides
Cyclades
Menderes
Pelagonian
Tavşanlı - Afyon
Pindos
Ören
CACC
Lycian-Tauride ophiolites
Gavrovo-Tripolitza
Taurides
Ionian
Antalya ophiolites
Mesogea
50 Ma

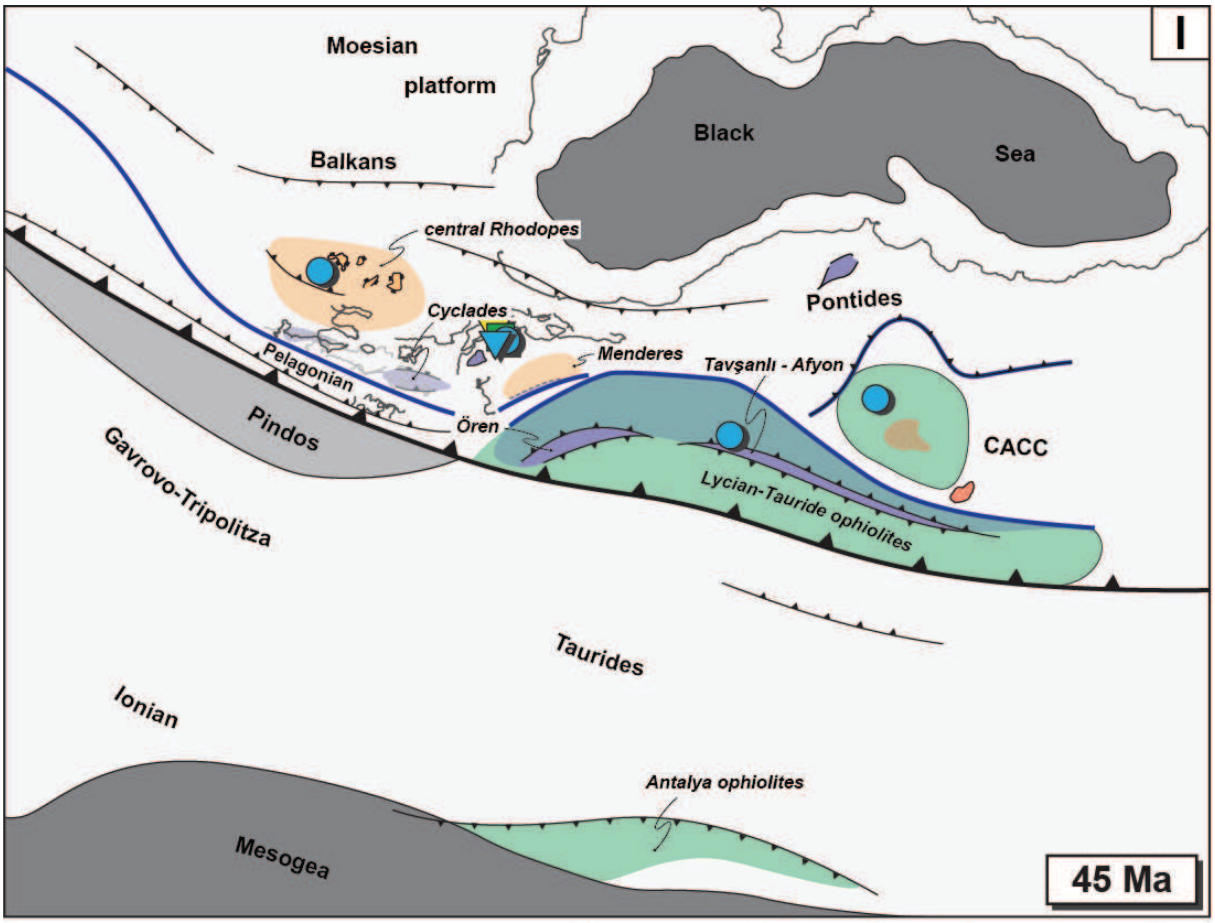
l
Moesian
platform
Balkans
Black
Sea
central Rhodopes
Pontides
Cyclades
Menderes
Tavşanlı - Afyon
Pelagonian
Ören
Pindos
CACC
Gavrovo-Tripolitza
Lycian-Tauride ophiolites
Taurides
Ionian
Antalya ophiolites
Mesogea
45 Ma

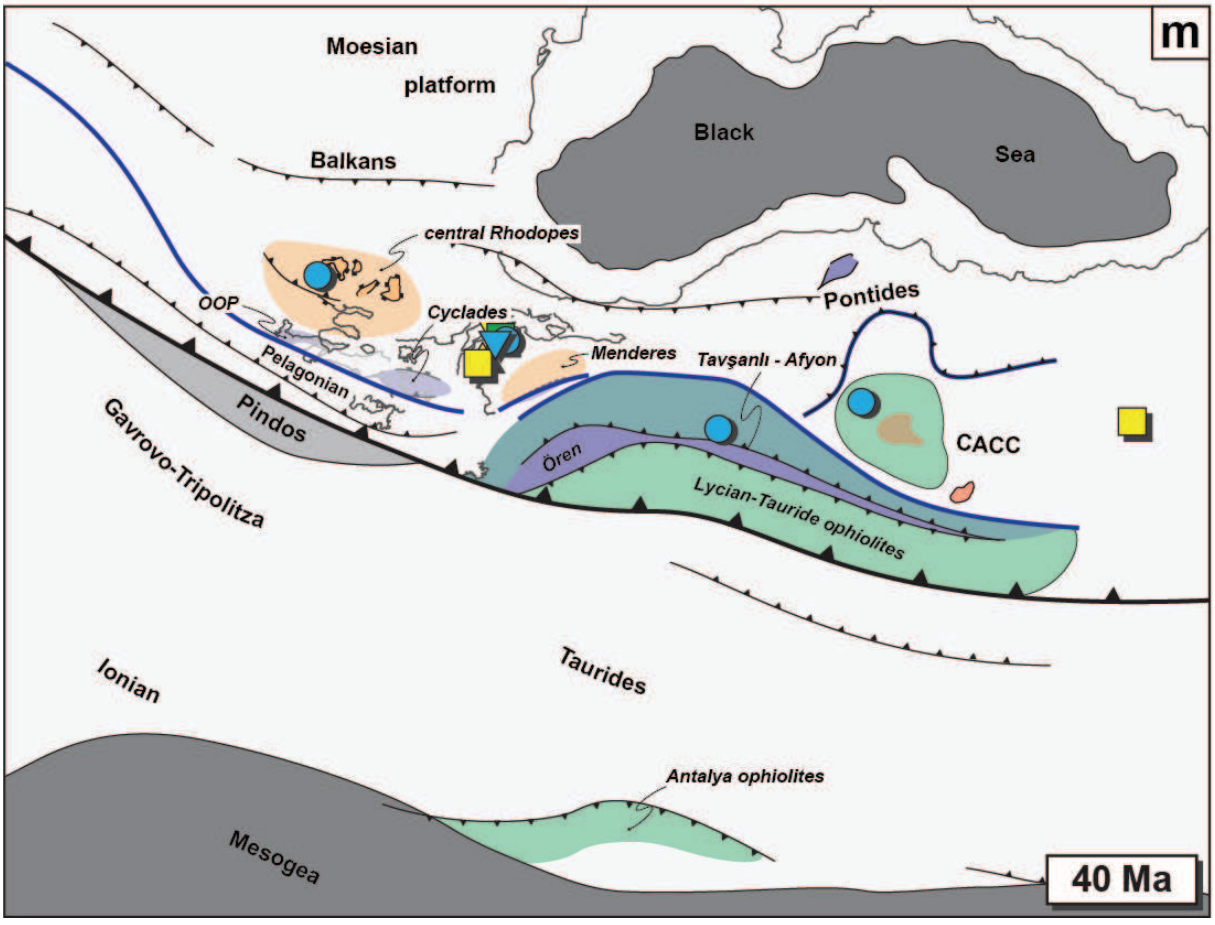
m
Moesian
platform
Balkans
Black
Sea
central Rhodopes
Pontides
OOP
Cyclades
Menderes
Tavşanlı - Afyon
Pelagonian
Pindos
CACC
Gavrovo-Tripolitza
Ören
Lycian-Tauride ophiolites
Taurides
Ionian
Antalya ophiolites
Mesogea
40 Ma

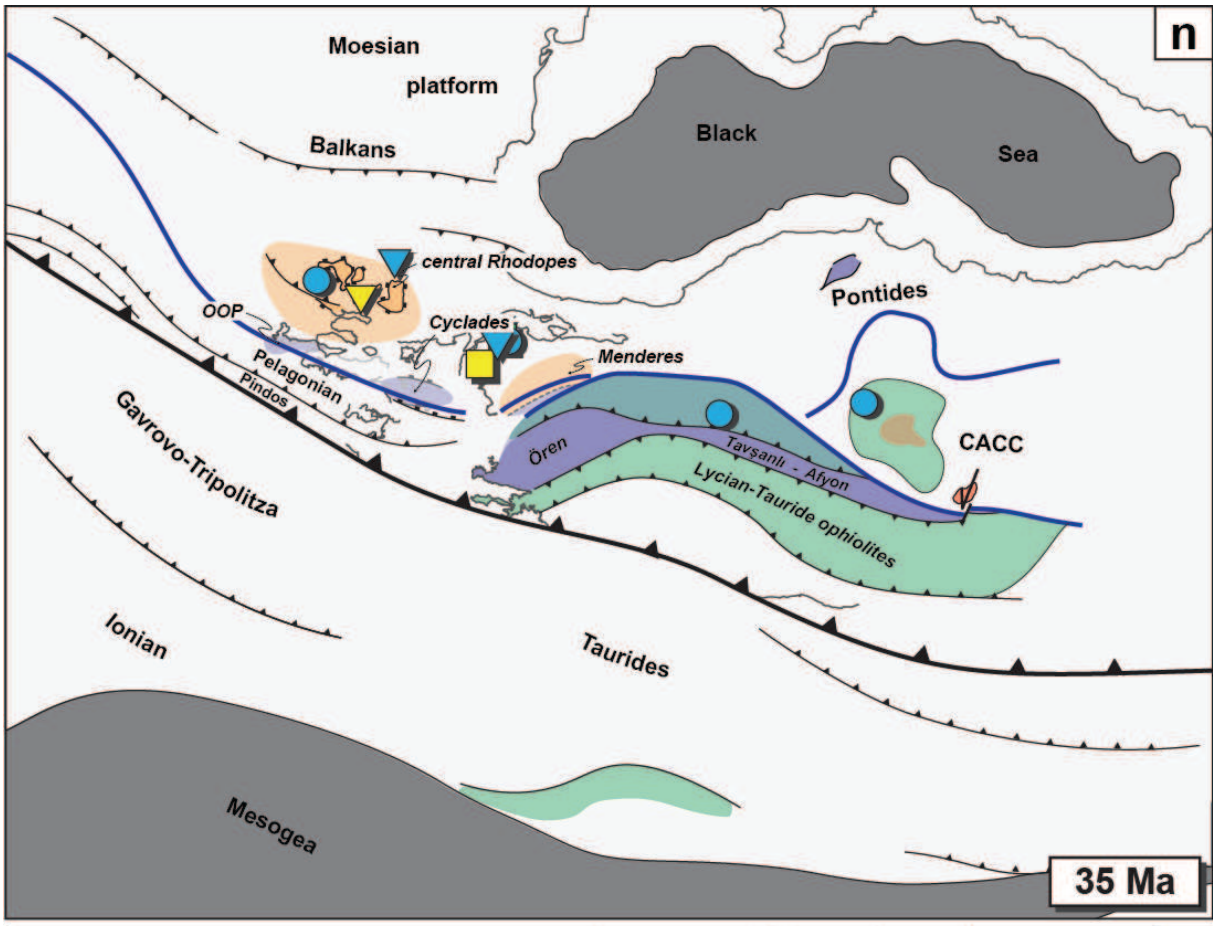
n
Moesian
platform
Balkans
Black
Sea
central Rhodopes
OOP
Cyclades
Menderes
Pelagonian
Pindos
Pontides
Gavrovo-Tripolitza
Ören
Tavşanlı - Afyon
Lycian-Tauride ophiolites
CACC
Ionian
Taurides
Mesogea
35 Ma

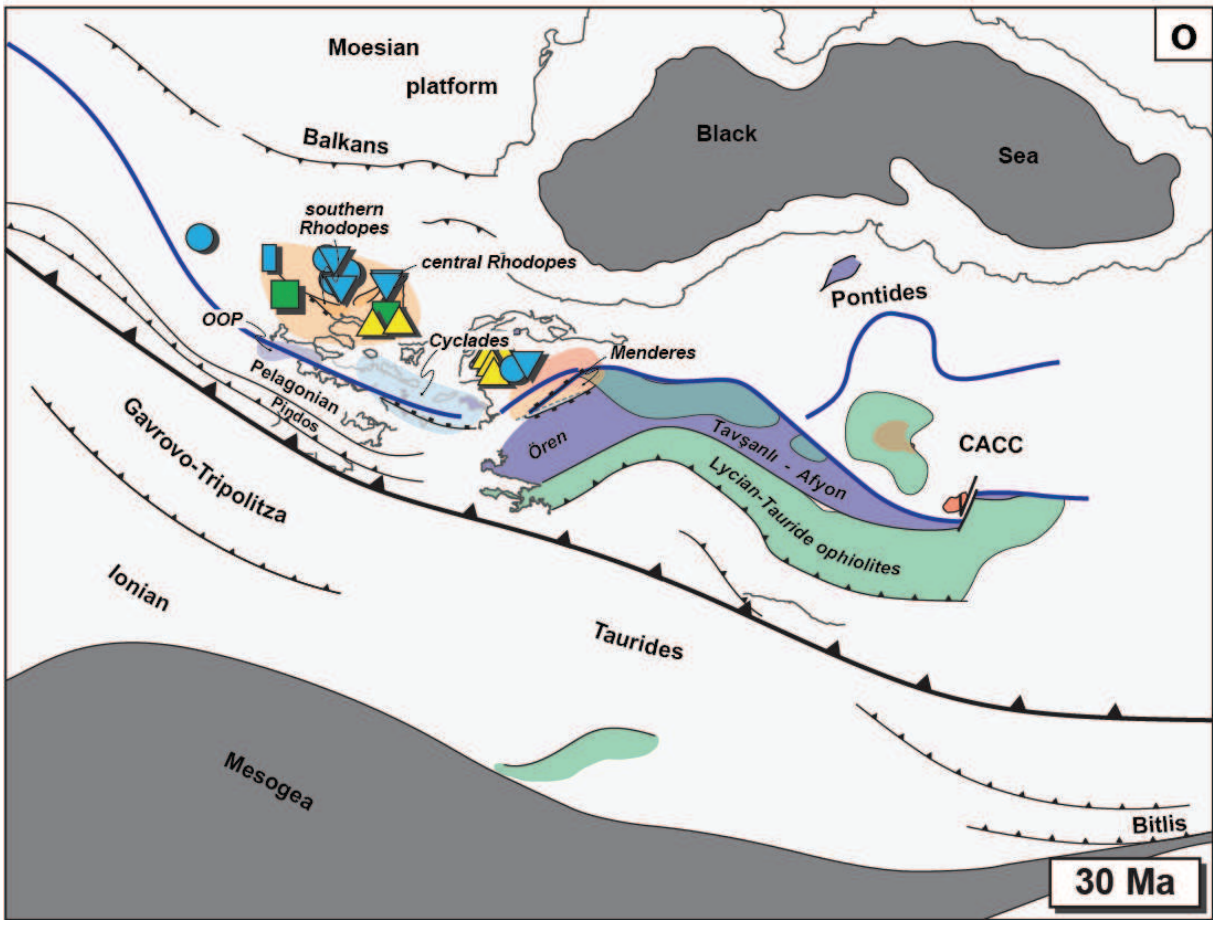
o
Moesian
platform
Balkans
Black
Sea
southern
Rhodopes
central Rhodopes
OOP
Cyclades
Menderes
Pelagonian
Pindos
Pontides
Gavrovo-Tripolitza
Ören
Tavşanlı - Afyon
Lycian-Tauride ophiolites
CACC
Ionian
Taurides
Mesogea
Bitlis
30 Ma

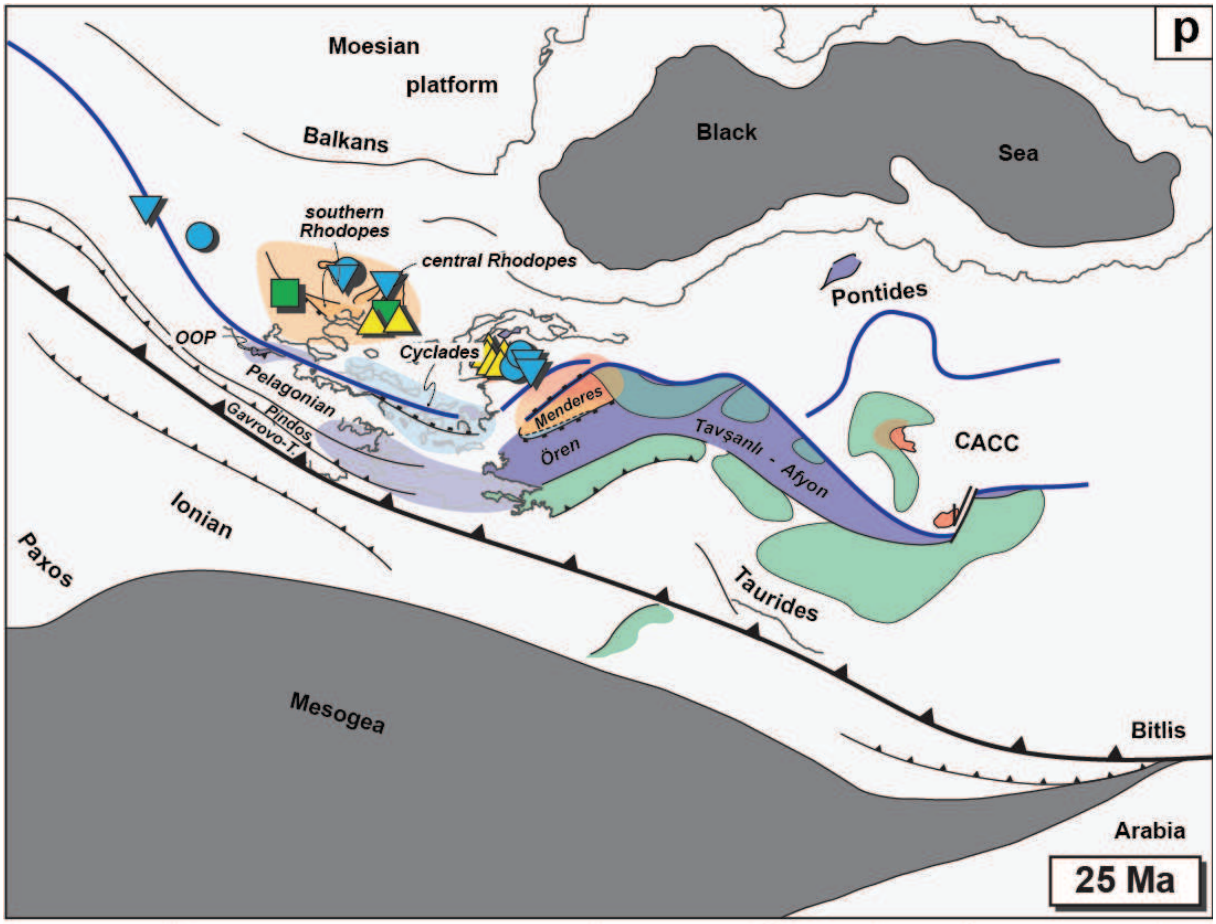
p
Moesian
platform
Balkans
Black
Sea
southern
Rhodopes
central Rhodopes
Pontides
OOP
Cyclades
Pelagonian
Pindos
Gavrovo-T.
Menderes
Ören
Tavşanlı - Afyon
CACC
Ionian
Paxos
Taurides
Mesogea
Bitlis
Arabia
25 Ma

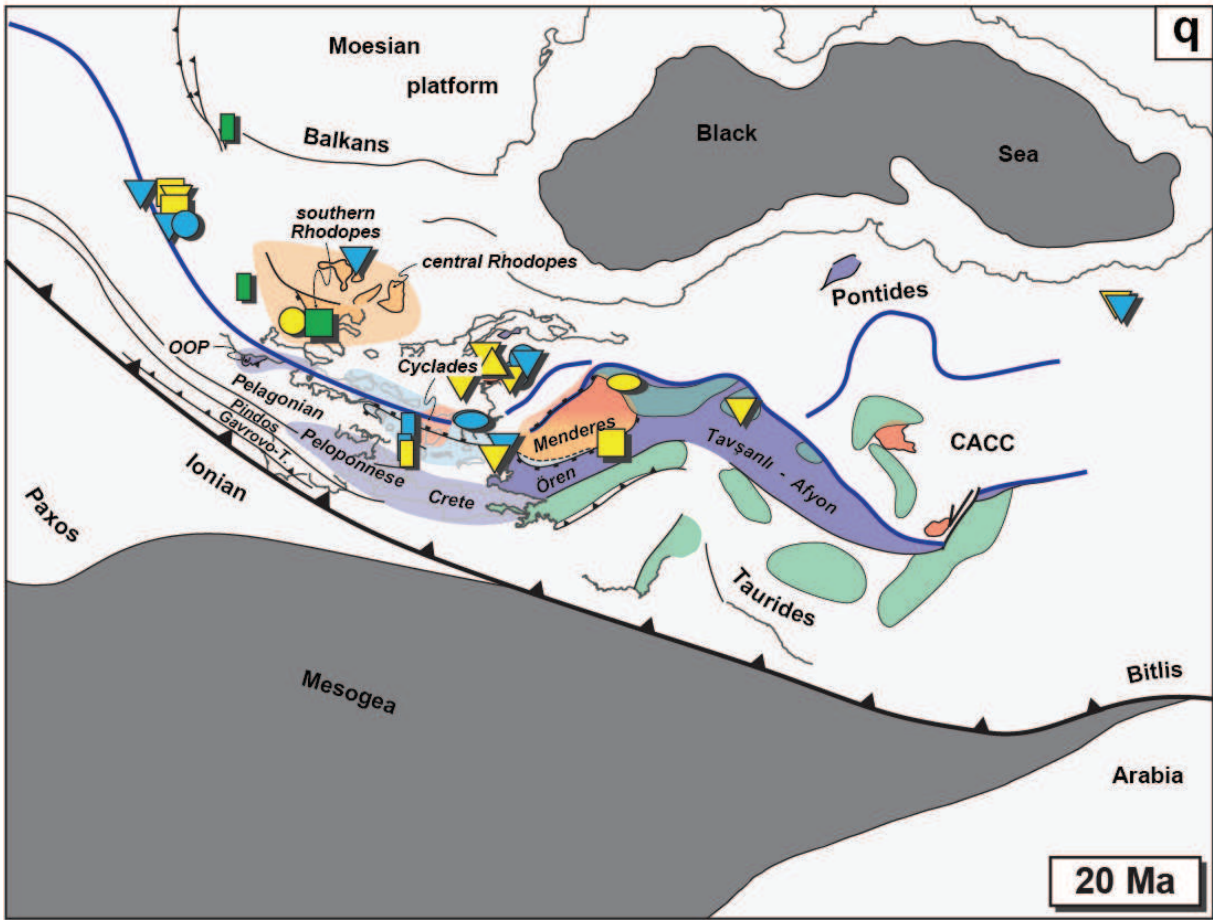
q
Moesian
platform
Balkans
Black
Sea
southern
Rhodopes
central Rhodopes
Pontides
OOP
Cyclades
Pelagonian
Pindos
Gavrovo-T.
Peloponnese
Crete
Menderes
Ören
Tavşanlı - Afyon
CACC
Ionian
Paxos
Taurides
Mesogea
Bitlis
Arabia
20 Ma

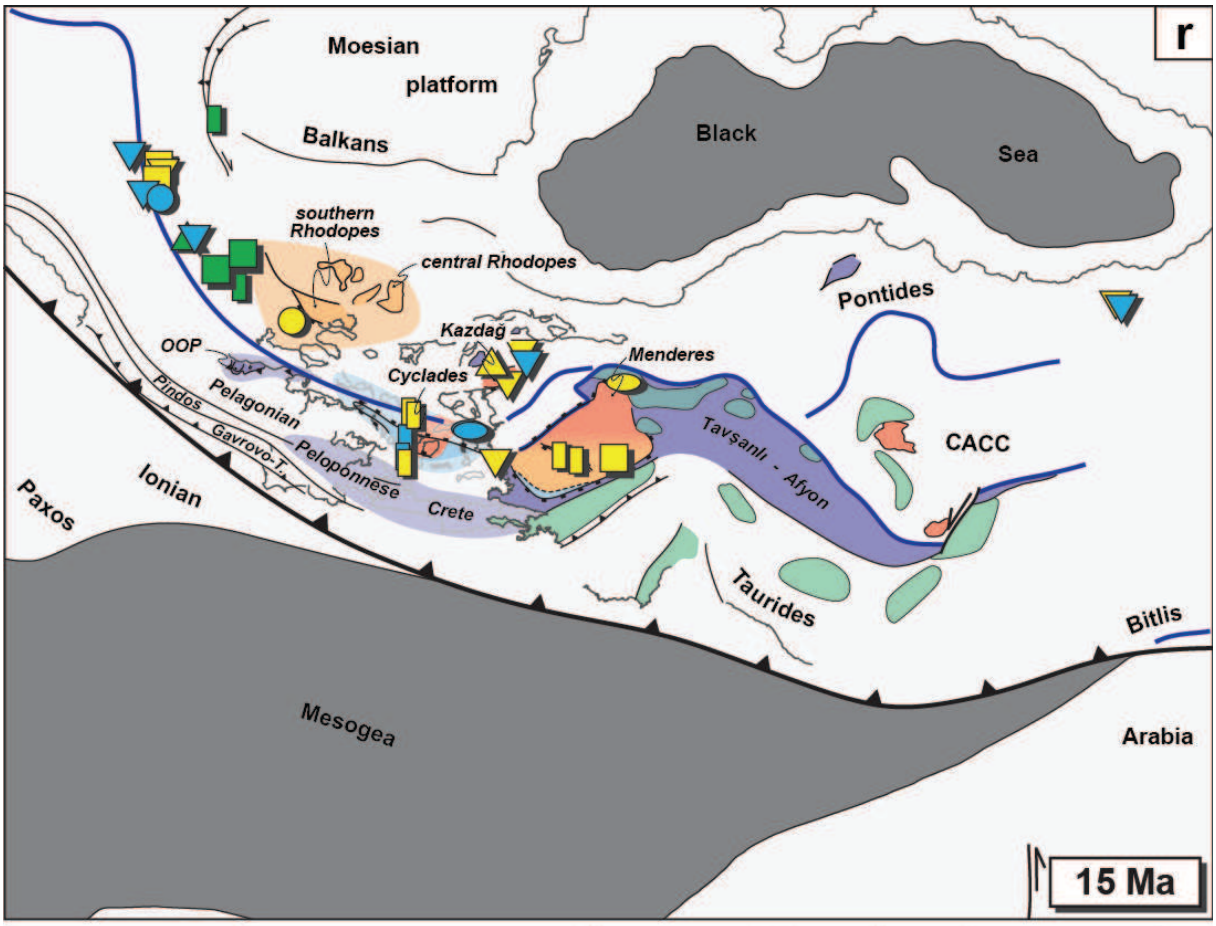
r
Moesian
platform
Balkans
Black
Sea
southern
Rhodopes
central Rhodopes
Pontides
Kazdag
Menderes
OOP
Cyclades
Pindos
Pelagonian
Gavrovo-T.
Peloponnese
Crete
Tavşanlı - Afyon
CACC
Paxos
Ionian
Taurides
Bitlis
Mesogea
Arabia
15 Ma

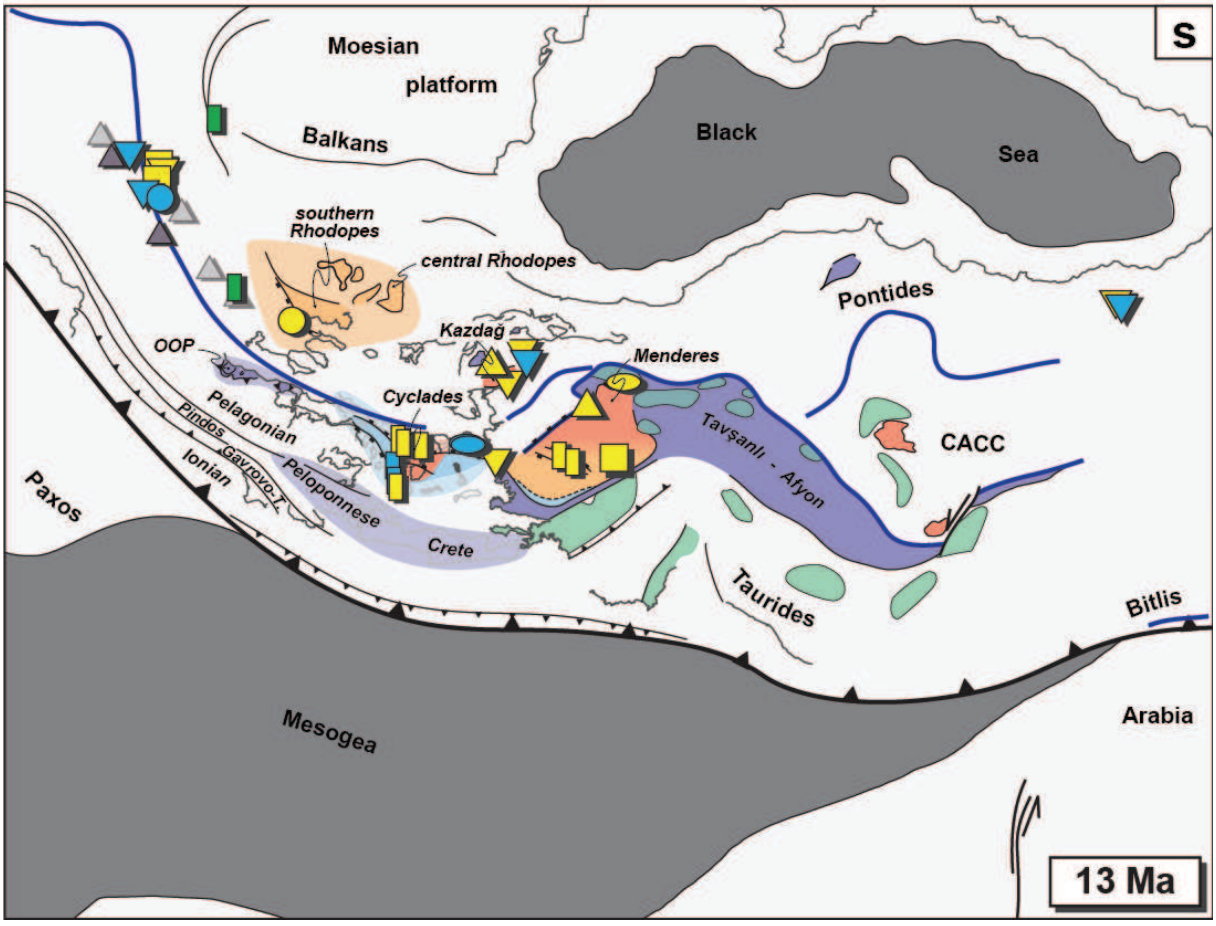
s
Moesian
platform
Balkans
Black
Sea
southern
Rhodopes
central Rhodopes
Pontides
Kazdag
Menderes
OOP
Cyclades
Pindos
Pelagonian
Gavrovo-T.
Ionian
Peloponnese
Crete
Tavşanlı - Afyon
CACC
Paxos
Taurides
Bitlis
Mesogea
Arabia
13 Ma

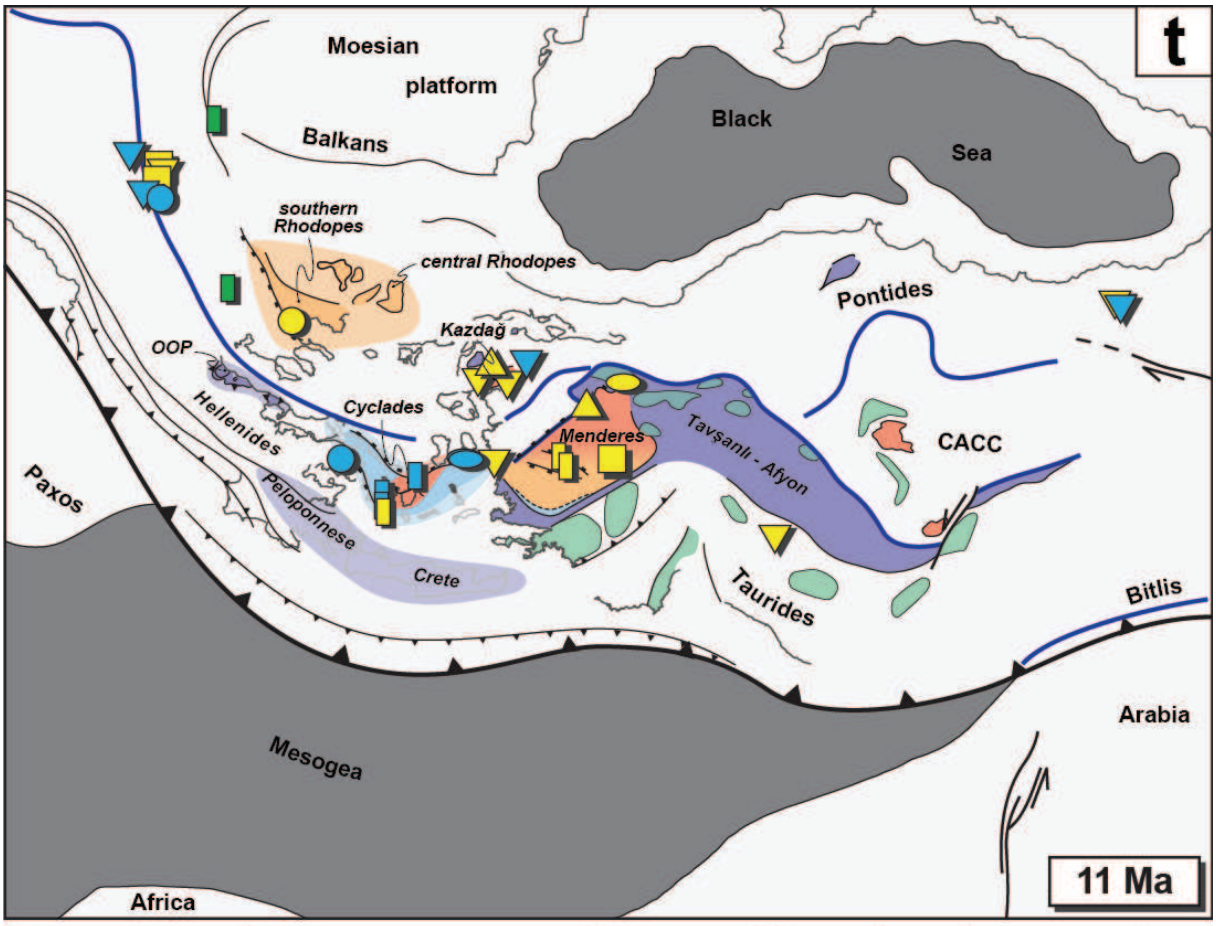
t
Moesian
platform
Balkans
Black
Sea
southern
Rhodopes
central Rhodopes
Pontides
Kazdağ
OOP
Hellenides
Cyclades
Menderes
Tavşanlı - Afyon
CACC
Paxos
Peloponnese
Crete
Taurides
Bitlis
Arabia
Mesogea
Africa
11 Ma

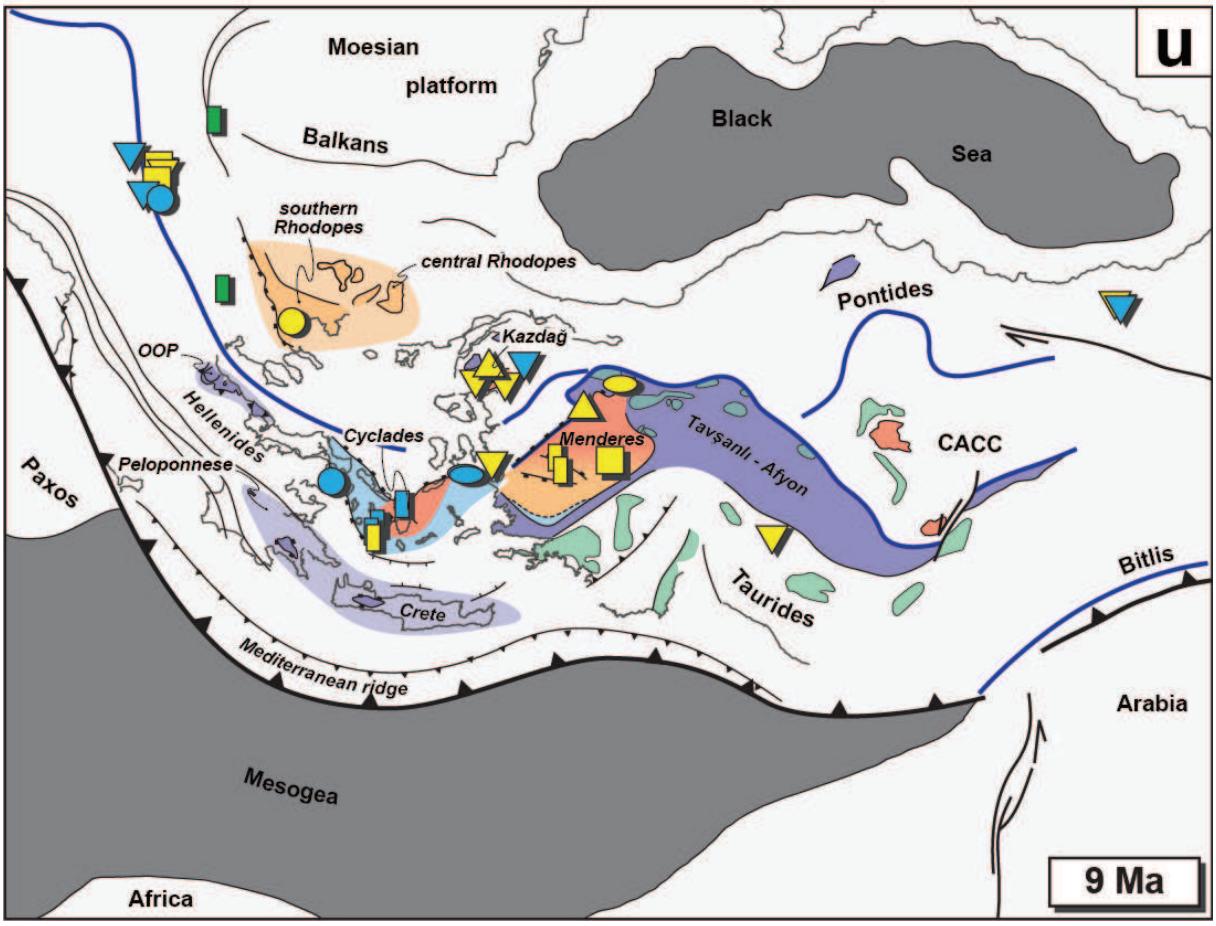
u
Moesian
platform
Balkans
Black
Sea
southern
Rhodopes
central Rhodopes
Pontides
Kazdağ
OOP
Hellenides
Cyclades
Menderes
Tavşanlı - Afyon
CACC
Paxos
Peloponnese
Crete
Taurides
Bitlis
Mediterranean ridge
Arabia
Mesogea
Africa
9 Ma

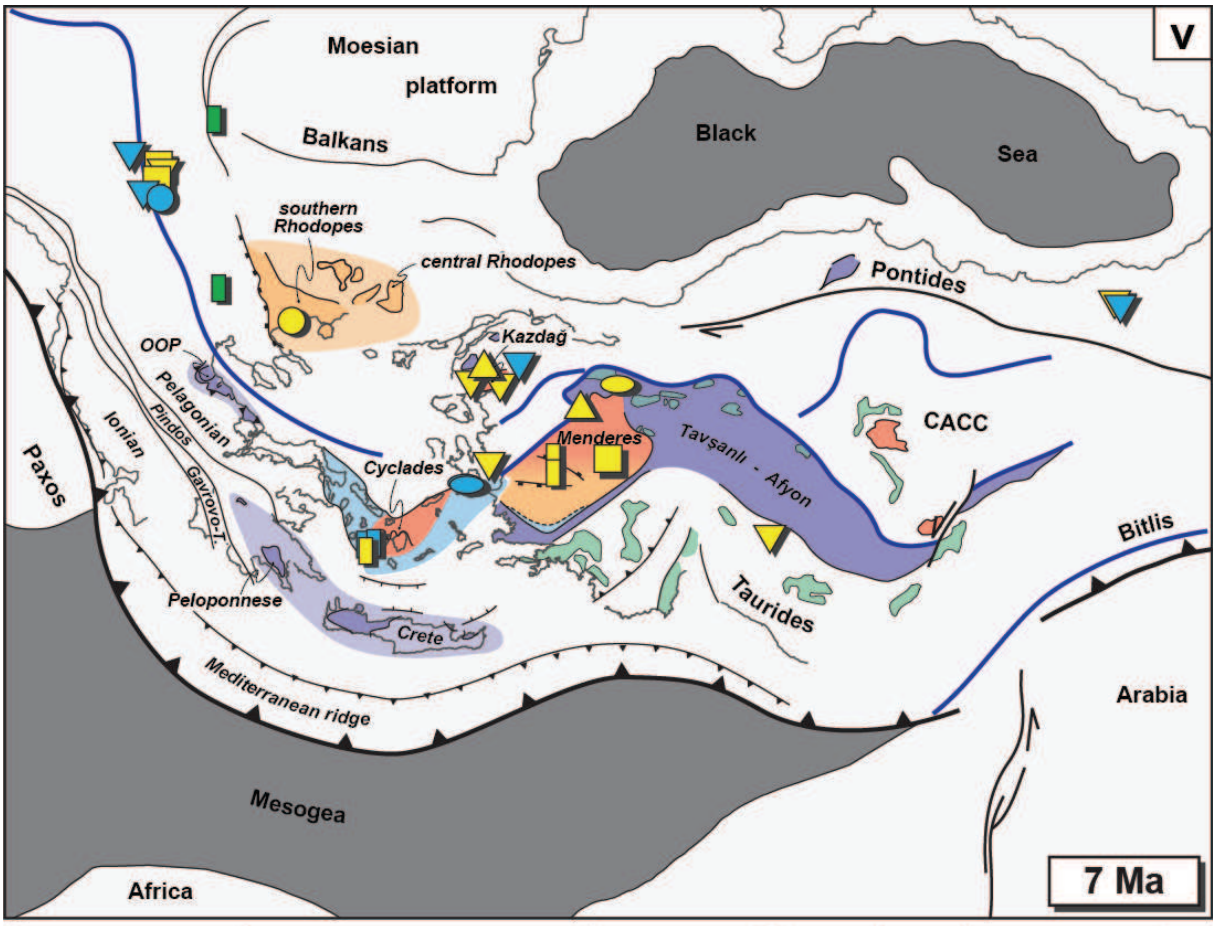
V
Moesian
platform
Balkans
Black
Sea
southern
Rhodopes
central Rhodopes
Pontides
Kazdağ
OOP
Pelagonian
Pindos
Ionian
Gavrovo-T.
Paxos
Cyclades
Menderes
Tavşanlı - Afyon
CACC
Bitlis
Peloponnese
Crete
Taurides
Mediterranean ridge
Arabia
Mesogea
Africa
7 Ma

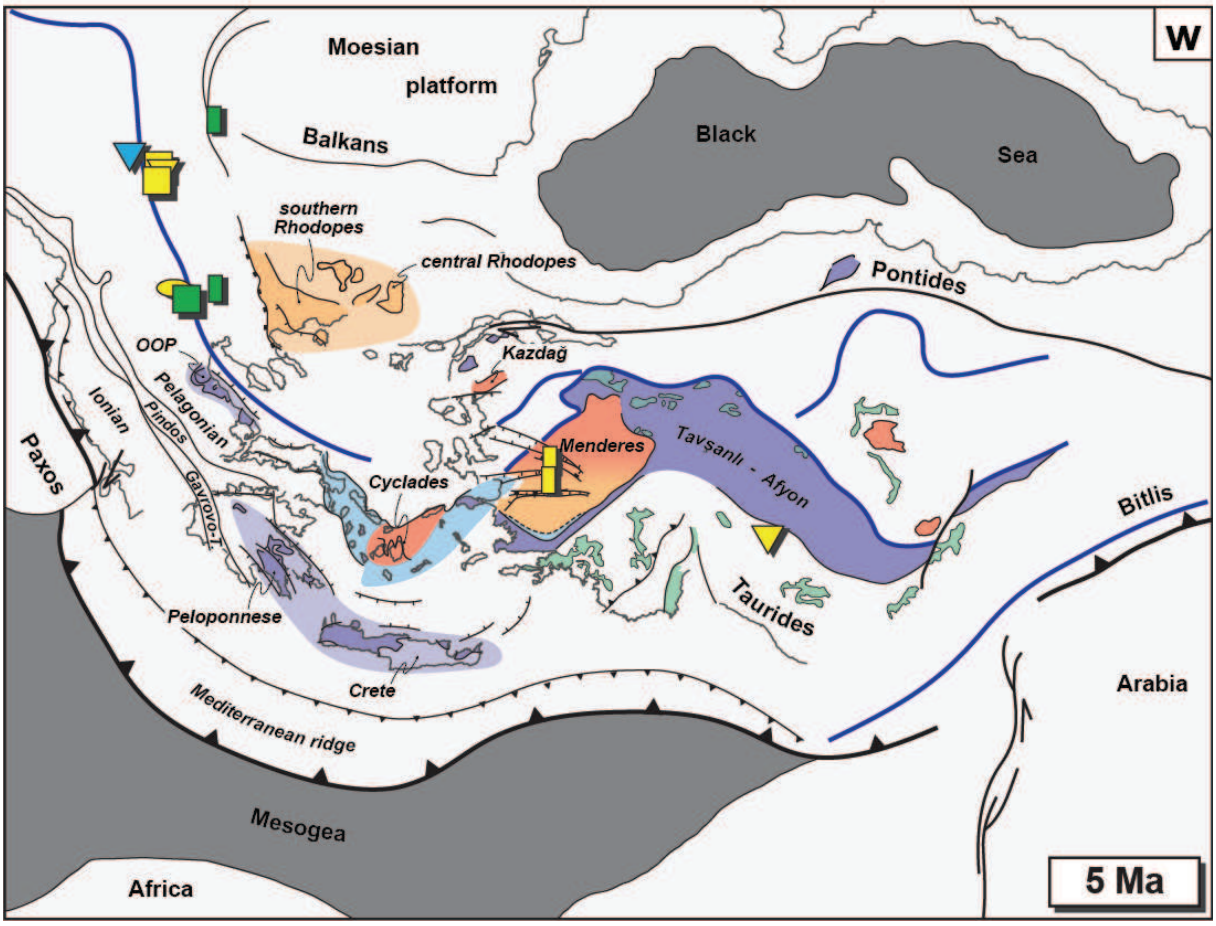
W
Moesian
platform
Balkans
Black
Sea
southern
Rhodopes
central Rhodopes
Pontides
Kazdağ
OOP
Pelagonian
Pindos
Ionian
Gavrovo-T.
Paxos
Cyclades
Menderes
Tavşanlı - Afyon
Bitlis
Peloponnese
Crete
Taurides
Mediterranean ridge
Arabia
Mesogea
Africa
5 Ma

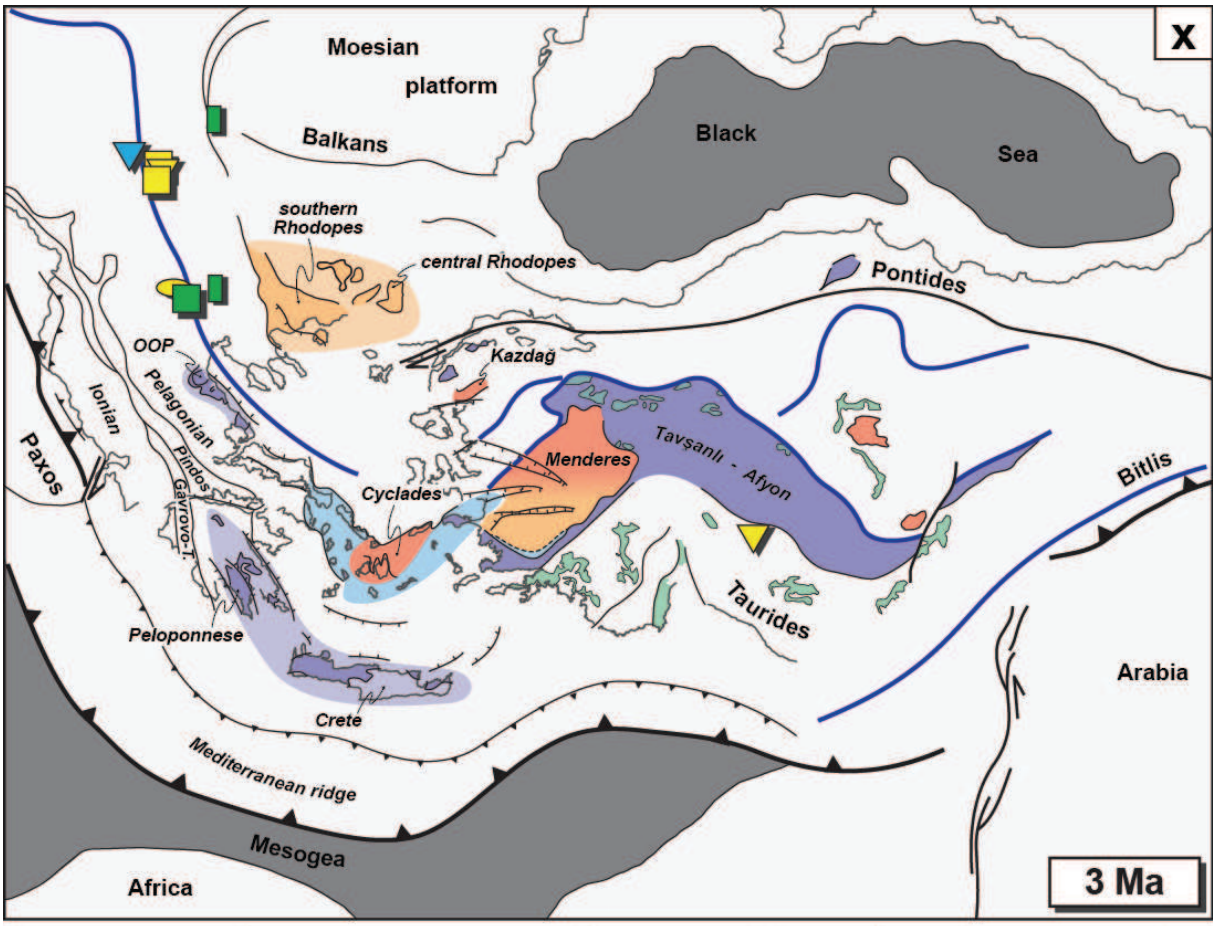
x
Moesian
platform
Balkans
Black
Sea
southern
Rhodopes
central Rhodopes
Pontides
OOP
Kazdağ
Ionian
Pelagonian
Pindos
Gavrovo-T.
Paxos
Menderes
Tavşanlı - Afyon
Bitlis
Cyclades
Taurides
Peloponnese
Arabia
Crete
Mediterranean ridge
Mesogea
Africa
3 Ma

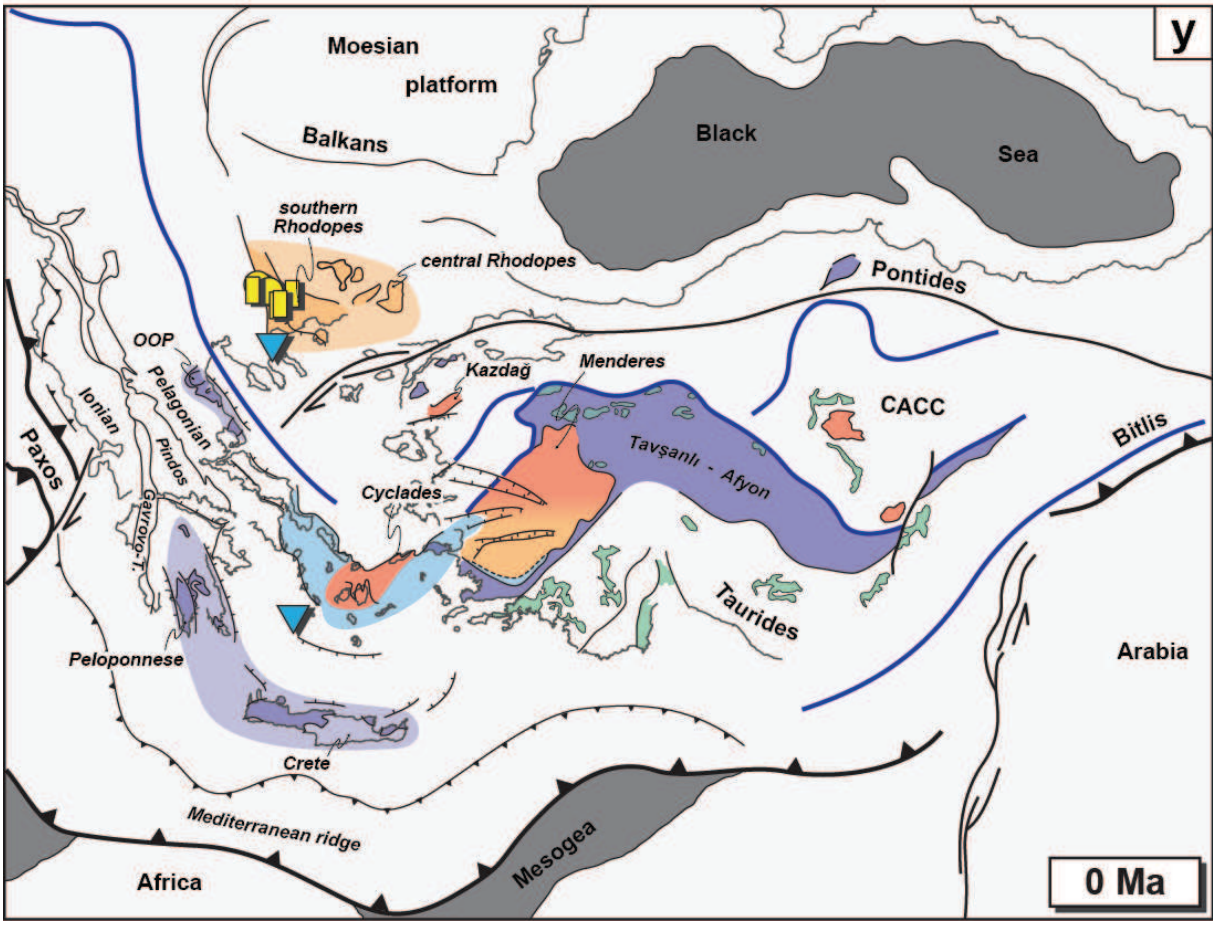
y
Moesian
platform
Balkans
Black
Sea
southern
Rhodopes
central Rhodopes
Pontides
OOP
Kazdağ
Menderes
CACC
Ionian
Pelagonian
Pindos
Gavrovo-T.
Paxos
Tavşanlı - Afyon
Bitlis
Cyclades
Taurides
Peloponnese
Arabia
Crete
Mediterranean ridge
Mesogea
Africa
0 Ma

Copper or gold? A matter of subduction dynamics

Armel Menant [(1,2,3)*], Laurent Jolivet [(1,2,3)], Johann Tuduri [(2,1,3)], Christelle Loiselet [(2,1,3)], Guillaume Bertrand [(2,1,3)], Laurent Guillou-Frottier [(2,1,3)]

(1) Univ d'Orléans, ISTO, UMR 7327, 45071 Orléans, France

(2) BRGM, ISTO, UMR 7327, BP 36009, 45060 Orléans, France

(3) CNRS/INSU, ISTO, UMR 7327, 45071 Orléans, France

* *Corresponding author: Armel Menant – ISTO*
1A, rue de la Férollerie, 45071 Orléans cedex 2
+33(0)2 38 49 46 60
(armel.menant@cnrs-orleans.fr)

3.1. Extended abstract

Active subduction zones display a major economic interest, in terms of mineral resources, with mainly copper and gold deposits, but also molybdenum, lead, zinc and silver concentrations [*Sillitoe*, 1972; *Richards*, 2003; *Camprubí & Albinson*, 2007; *Kouzmanov & Pokrovski*, 2012]. While many studies emphasize on ore-forming mechanisms at different scales [*Hedenquist & Lowenstern*, 1994; *Richards*, 2003, 2011; *Kouzmanov & Pokrovski*, 2012; *Wilkinson*, 2013], the control of tectonic and geodynamic processes on such magmatism-related deposits remains poorly understood with only few published works [*de Boorder et al.*, 1998; *Lips*, 2002; *Grove et al.*, 2006; *Bertrand et al.*, 2014], despite an obvious relation between subduction and magmatism [*Harangi et al.*, 2006; *Pe-Piper & Piper*, 2006]. Studying the effects of changing subduction dynamics on the typology and distribution of ore deposits requires however a detailed space/time evolution of these deposits within a precise 3D tectonic framework, which is rarely available. The eastern Mediterranean region is well suited for this purpose, with a variety of ore deposits [*Heinrich & Neubauer*, 2002; *Richards*, 2014] and a relatively well constrained fast tectonic evolution, mainly governed by the dynamics of laterally constrained subducting slab and related asthenospheric flow [*Faccenna & Becker*, 2010; *Jolivet et al.*, 2013]. Here we show with paleotectonic maps and reconstructed cross-sections that deep-subduction related processes, such as slab retreat and tearing are responsible for the evolution of the distribution and typology of ore resources. Two distinct metallogenic periods are thus revealed: a late Cretaceous-early Paleocene *Cu*-rich period, associated with *arc*-related magmatism, followed by an Oligocene-Miocene *Pb-Zn*- then *Au*-rich period, related to variable degree of partial melting of continental crust and metasomatized lithospheric mantle during slab retreat and hot asthenosphere upwelling, modulated by 3D effects due to slab tearing. These results show, on the one hand, the potential of good comprehension of the 3D large-scale geodynamic evolution for mineral prospection and, on the other hand, how metallogenic data are useful to track geodynamic processes.

3.2. Introduction

Governed by the Eurasia-Africa convergence, the eastern Mediterranean region has been characterized by a southward migrating subduction zone from the late Cretaceous, with subduction and accretion of several oceanic and continental domains (figure 3.2). Within the Eurasian continental upper lithosphere, the tectonic regime has changed due to slab dynamics, resulting in the formation of orogenic belts (e.g. the Balkans, the Hellenides, the Anatolides-Taurides) and back-arc domains (e.g. the Rhodope massif, the Aegean domain). In this context, ore-forming processes evolved through space and time, resulting in an irregular distribution of ore deposits. To make the link with the 3D subduction dynamics, we performed a new detailed kinematic reconstruction model of the region which integrates more than 300 compiled ore occurrences. Resulting paleotectonic maps and reconstructed cross-sections then show the geometry of the subduction zone and the state of the crust at the time of ore deposition (cf. *Annexe D*, *video D.1*). We thus identify two main metallogenic periods, separated by a relatively barren one, in the eastern Mediterranean region since the late Cretaceous (figures 3.2 and 3.3).

3.3. Ore distribution in eastern Mediterranean since the late Cretaceous

During the late Cretaceous-early Paleocene, a ~2,000-km-long *Cu*-rich metallogenic belt developed from the Balkans to the eastern Pontides (figure 3.2a). Among the 51 reported *Cu*-rich occurrences, 29 consist in porphyry *Cu* (-*Au*) deposits, some of them displaying an economic interest (e.g. Bor in Serbia and Elatsite in Bulgaria) [*Heinrich & Neubauer*, 2002]. Remaining ore occurrences mainly consist in high-sulfidation epithermal and skarn *Cu* (-*Au-Pb-Zn*) deposits, often associated with these porphyry systems.

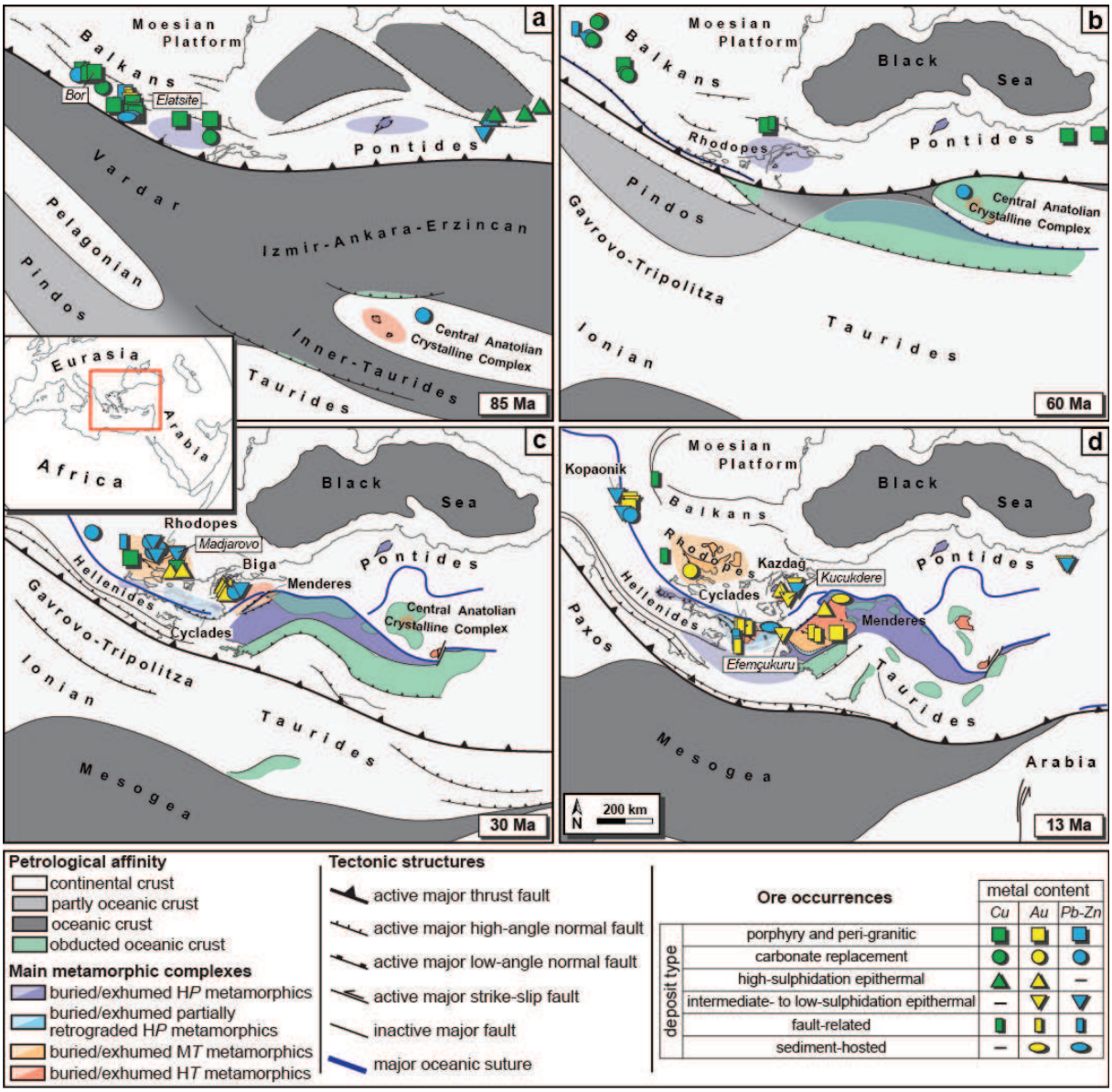

Figure 3.2: kinematic evolution of the eastern Mediterranean subduction zone, showing the spatial distribution of compiled mineral occurrences. (Inset) Location of the studied area (red square). (a, b, c, d) Selected paleotectonic maps extracted from the kinematic reconstruction model (all paleotectonic maps are available as a movie, cf. A*nnexe D, video D.1*).

Following a late Paleocene-Eocene relatively barren period characterized by the subduction and accretion of the Pelagonian and Tauride carbonate platforms (figure 3.2b), a wide *Pb-Zn*- then *Au*-rich metallogenic province has emplaced further south (figures 3.2c and d). In the Oligocene, we report more than 60 *Pb-Zn* (*-Ag*) deposits, comprising carbonate replacement, intermediate- and low-sulfidation epithermal deposits mainly in the Bulgarian Rhodope massif (figure 3.2c), such as the Madjarovo mining district [*Marchev et al.*, 2005]. Coevally, some high- and low-sulfidation

epithermal *Au* (-*Ag*) deposits have also emplaced further south in the Greek Rhodope massif and the Biga peninsula (Turkey). Since the Miocene, *Au* (-*Ag*) deposits have dominated in the Rhodope-Aegean-western Anatolian region and further northwest in the Kopaonik region in Serbia (figure 3.2d). Most of the 36 reported *Au*-rich occurrences consist in low-sulfidation epithermal and fault-related deposits, some of them displaying an economic interest, especially in Turkey (e.g. Kucukdere and Efemçukuru) [*Yigit*, 2009].

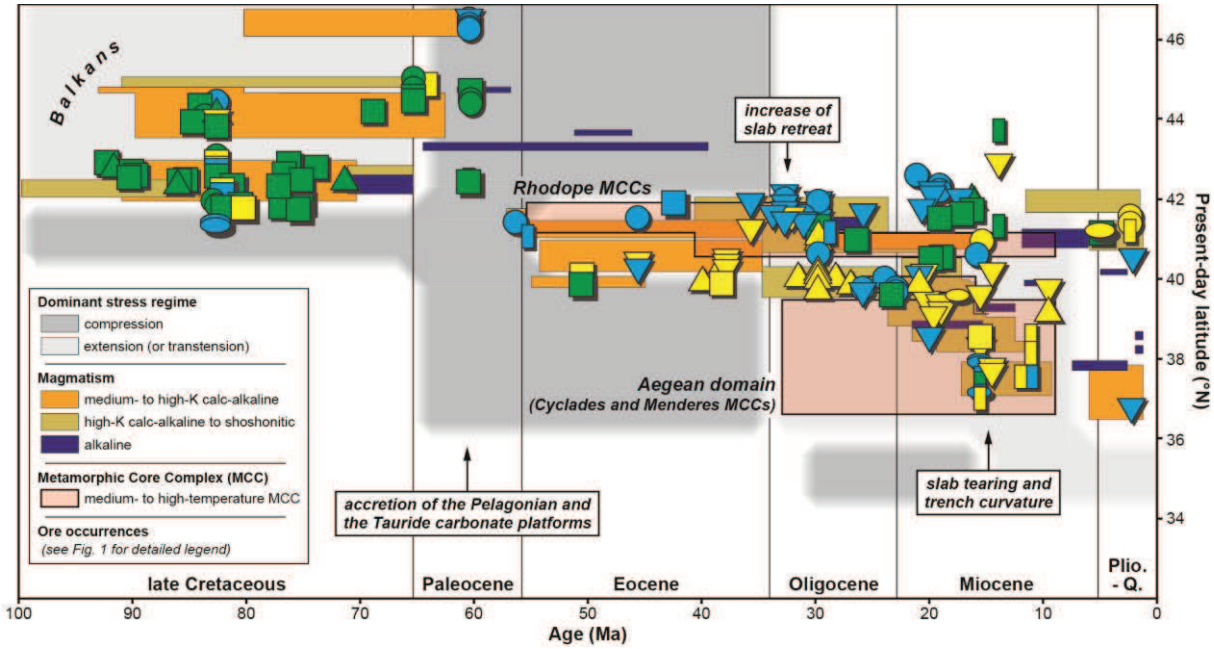

Figure 3.3: spatial and temporal distribution of magmatism and compiled mineral occurrences in the Balkan-Rhodope-Aegean-west Anatolian region since the late Cretaceous. On this latitude/age diagram are represented, for each domain, the dominant active stress regime within the upper plate, the magmatic activity, the exhumation stage of the main metamorphic core complexes (MCCs) and the compiled mineral occurrences.

3.4. Subduction-related deep processes and ore genesis

Spatial and temporal distribution of reported ore occurrences is in line with the southward migration of the subduction zone through time (figure 3.2), similarly to distribution of the magmatic activity displaying geochemical signatures evolving from medium- to high-K calc-alkaline or shoshonitic (i.e. mildly alkaline) and finally alkaline (figure 3.3) [*Harangi et al.*, 2006; *Pe-Piper &*

Piper, 2006]. Our reconstructions therefore strongly supports a control of subduction dynamics on magmatic and ore-forming processes in both arc and back-arc environments.

In the late Cretaceous-early Paleocene, mainly porphyry and high-sulfidation epithermal *Cu* (*-Au*) deposits emplaced along the long and linear extensional Eurasian active margin, associated with typical *arc*-related magmatism, with medium- to high-K calc-alkaline composition (figure 3.3) [*Janković*, 1997; *Berza et al.*, 1998]. First generated by partial melting of the hydrated mantle wedge (figure 3.4a), primary mafic magmas are then stored at the base of the continental crust, forming the Melting, Assimilation, Storage and Homogenization (MASH) zone, where they undergo fractionation and crustal assimilation, giving typical calc-alkaline magmatic trend [*Gill*, 1981; *Hildreth & Moorbath*, 1988].

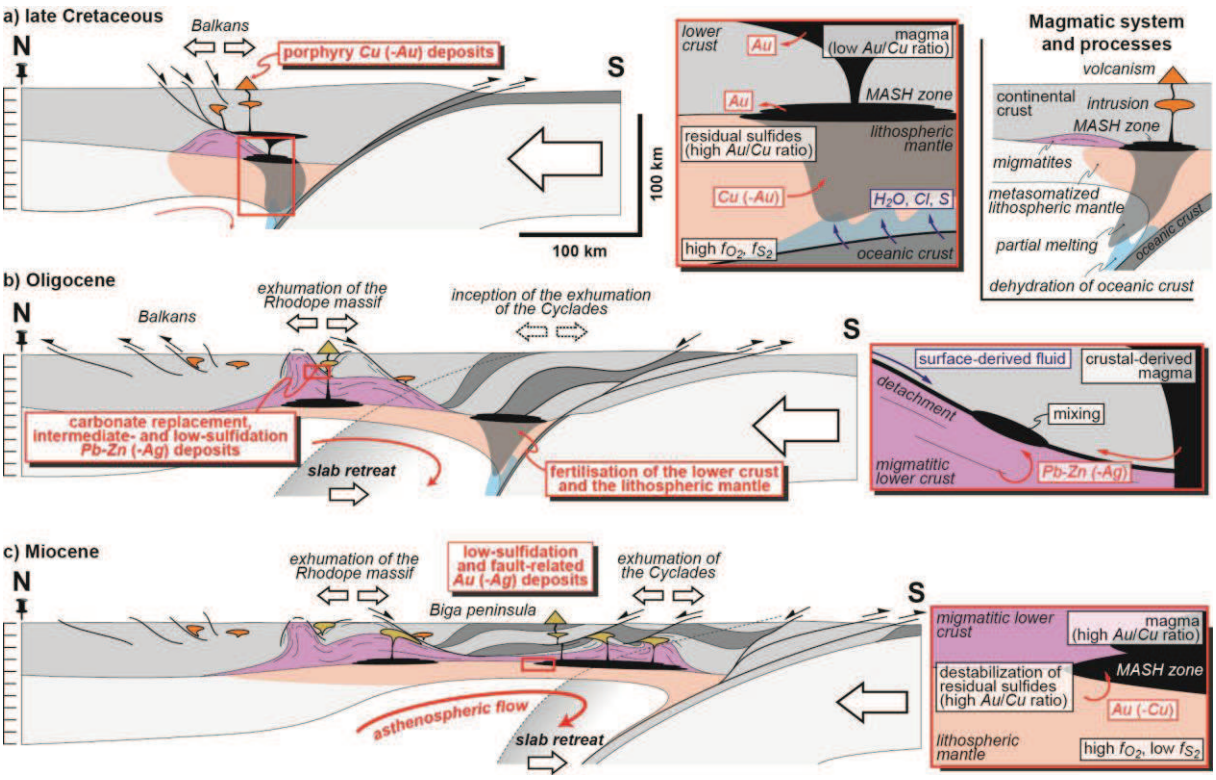

Figure 3.4: reconstructed cross-sections of the subduction zone in the Balkan-Rhodope-Aegean region, showing dominant magmatic and ore-forming processes. (a) Late Cretaceous oceanic subduction, detailing genesis process for *arc*-related *Cu*-rich magmas. (b) Oligocene retreating subduction zone, detailing genesis process for *Pb-Zn* (*-Ag*) deposits. (c) Miocene relatively fast retreating subduction zone, detailing genesis process for *back-arc*-related *Au*-rich magmas. Cross-sections keep the same fixed point to the left-side. See figure 3.3 for detailed legend for magmatism composition.

Release of volatiles (H_2O, *Cl*, *S*) during oceanic crust dehydration, promote high oxidation and sulfur fugacity conditions in the mantle wedge, which control the behavior of chalcophile (e.g. *Cu*) and siderophile (e.g. *Au*) elements initially present as sulfide minerals in the mantle source [*Richards*, 2009]. Because *Au* partitions better than *Cu* into sulfide phases relative to silicate melts [*Peach et al.*, 1990], sulfide melts can exsolve from silicate melts during their ascent, giving a sulfide residue in the lithospheric mantle and lower crust with a high *Au*/*Cu* ratio. Consequently, residual magmas are enriched in *Cu* relative to *Au* (i.e. low *Au*/*Cu* ratio) and therefore fertile to form porphyry *Cu* (-*Au*) deposits (figure 3.4a).

Highlighting in our reconstructions, *Pb-Zn*-rich then *Au*-rich deposits have progressively emplaced southward since the Oligocene, coevally with the opening of a wide back-arc domain where several metamorphic core complexes (MCCs) were exhumed as a result of an increasing rate of slab retreat (figure 3.3) [*Lister et al.*, 1984; *Jolivet et al.*, 2013]. Crustal thinning and underlying asthenospheric flow induce the rising of the upper lithosphere isotherms, partial melting of the lithospheric mantle and lower crust and formation of migmatitic domes and magmatic bodies (figures 3.4b and c). These high-K calc-alkaline to shoshonitic magmas involve both crustal (or felsic) and mantle (or mafic) source components [*Pe-Piper & Piper*, 2006]. *Pb-Zn* (-*Ag*) deposits are spatially associated with magmatic bodies displaying a major crustal source component, suggesting crustal inheritance for these metals, either from the magma or directly from the leaching of surrounding crustal rocks by metamorphic and/or surface-derived fluids (figure 3.4b) [*Marchev et al.*, 2005]. Conversely, the inferred origin for *Au* (-*Ag*) deposits would involve partial melting of the metasomatized lower crust or lithospheric mantle, previously transferred from the arc to the back-arc region with ongoing subduction retreat (figure 3.4c). In such case, sulfide residues with a high *Au*/*Cu* ratio are then destabilized, leading to the genesis of relatively *Au*-rich magmas [*Richards*, 2009]. A closer look at our reconstructions shows a secondary Miocene westward migration of this magmatic-hydrothermal activity from the Menderes massif to the Cyclades, diverging from the overall southward migration (figure 3.5). Coevally, the Hellenides underwent a ~40° clockwise rotation [*van Hinsbergen et al.*, 2005b], interpreted as resulting from a tear in the slab below western Turkey ~15 Ma ago, as suggested by tomographic models [*Jolivet et al.*, 2013]. This slab tear would trigger abnormal hot asthenospheric flow

responsible for the surge of magmatic activity and ore deposition in this region (figure 3.5) [d*e Boorder et al.*, 1998].

Scattered alkaline volcanism also occurring in the eastern Mediterranean region since the late Cretaceous does not show clear relations with any reported ore occurrences (figure 3.3). Major depleted asthenospheric source component inferred for these magmas may explain the relatively barren character of these systems, which require however further investigations, notably considering alkalic-type *Au* deposits [*Richards*, 2014].

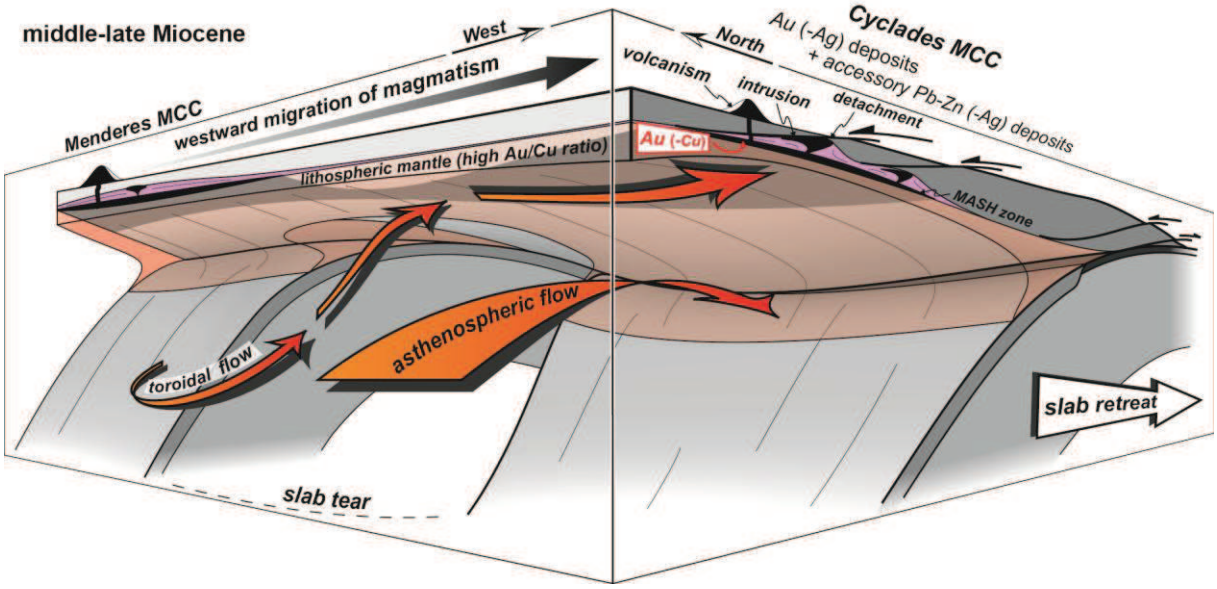

Figure 3.5: 3D lateral view from below of the Eastern Mediterranean subduction zone geometry in the middle-late Miocene. On this cartoon are shown the asthenospheric flows, resulting from both slab retreat and slab tearing. The asthenospheric flow with a dominant toroidal component (i.e. in a horizontal plane) thus results in the westward migration of magmatic activity and associated ore deposition, from the Menderes massif to the Cyclades.

3.5. Crustal evolution of hydrothermal systems

The two metallogenic periods highlighted in our reconstructions are both characterized by an extensional or transtensional tectonics within the upper lithosphere. In the late Cretaceous-early Paleocene, transtensional and extensional faults controlled the emplacement of porphyry and high-sulfidation *Cu* (-*Au*) deposits along the Balkans and the Pontides (figure 3.4a) [*Berza et al.*, 1998; *von*

Quadt et al., 2005], while Oligocene-Miocene *Pb-Zn-* and *Au*-rich occurrences are associated with the last stages of exhumation of MCCs below large-scale detachments (figures 3.2c, d and 3.3). Such an extensional regime therefore promotes crustal thinning, rise of magmas and hydrothermal fluids along crustal-scale extensional structures and subsequent ore deposition within the upper crust (figure 3.4). Decreasing pressure occurring during fast magma ascent up to the upper crust then induces exsolution of a single-phase fluid, scavenging metals from the silicate melt [*Hedenquist & Lowenstern*, 1994; *Richards*, 2011]. Such fluid may later boil in a sub-surface environment, forming a low-density vapor and a hypersaline liquid, which will be key-proxies for metal fractionation and deposition [*Kouzmanov & Pokrovski*, 2012; *Wilkinson*, 2013]. Contribution of surface-derived fluids in these systems can also be significant [*Marchev et al.*, 2005], with massive infiltration of these fluids along large-scale detachments down to 10-15 km (figure 3.4b) [*Famin et al.*, 2004]. Conversely, compressional tectonics within the upper lithosphere, resulting for instance from continental accretion such as in the Paleocene-Eocene (figure 3.2b), prevents the ascent of potentially fertile magmas within the thickening upper lithosphere, giving a relatively barren period in terms of magmatism and ore deposition in the upper crust. However, the storage of these magmas within the MASH zone can fertilize the deepest parts of the lithosphere (figure 3.4b), giving a high *Au*/*Cu* ratio sulfide residue which can be subsequently remobilized in the back-arc domain [*Richards*, 2009].

3.6. Conclusion

The diversity of tectonic contexts associated with fast evolving subduction zones thus leads to the genesis of a variety of ore deposits. Only a better description of this evolution can help to comprehend the distribution such deposits, necessary for large-scale mineral prospection. In the eastern Mediterranean region, transition to a back-arc setting and associated 3D asthenospheric flow are crucial to explain the space/time evolution of ore occurrences, rather than subduction polarity [*Nimis & Omenetto*, 2015]. Indeed, the transition from a late Cretaceous steady subduction zone, similarly to the Andes, to an Oligocene-Miocene fast retreating subduction zone led to the replacement of a *Cu-*

rich province associated with low *Au*/*Cu* ratio magmas by a *Pb*-*Zn*- then *Au*-rich province in a wide extensional back-arc region (figures 3.2 and 3.3). *Pb*-*Zn* (-*Ag*) deposits involve remobilization of metals from the continental crust, while *Au* (-*Ag*) deposits rather involve magmas with high *Au*/*Cu* ratio, originated from metasomatized lower crust and lithospheric mantle. Transition from *Cu*- to *Pb*-*Zn*- and finally *Au*-rich deposits would therefore result from (1) increasing rate of extension and lithospheric thinning and (2) hot asthenospheric flow, both controlled by deep subduction-related processes such as slab retreat and tearing (figures 3.4 and 3.5). During these metallogenic periods, the active extensional tectonics within the upper lithosphere and the formation of crustal-scale structures promote both the fast ascent of fertile magmas and hydrothermal fluids up to the upper crust and the massive infiltration of surface-derived fluids over relatively large depth, forming potentially economically interesting ore deposits.

Acknowledgments

This work was funded by the French Geological Survey (BRGM), the Région Centre, the ERC RHEOLITH project (ERC Advanced Grant n° 290864) and the Labex VOLTAIRE (ANR-10-LABX-100-01). We thank Laurent Bailly for his scientific contribution and his helpful comments.

Author contributions

All authors contributed to write the paper. A.M. performed the kinematic reconstruction model, compiled the GIS database of ore occurrences and interpreted the results. L.J. and L.G.F. elaborated this project and contributed to all stages of this study. J.T. contributed to the discussion on magmatic and metallogenic processes. C.L. made the first observations, resulting in designing this project. G.B. contributed to the discussion on the links between ore deposits distribution and kinematic reconstructions.

Chapitre 4

Dômes extensifs et contrôle structural des systèmes minéralisés : le cas de l'île de Mykonos

The North Cycladic Detachment System and associated mineralization, Mykonos, Greece: Insights on the evolution of the Aegean domain

(article publié au journal *Tectonics*)

4.1. Introduction....175
4.2. Geological and Geodynamic Setting....176
4.3. Detailed Mapping at the Vicinity of the NCDS on Mykonos....178
4.4. Characterization of the Mineralization....179
4.5. Evidence of Successive Tectonic Regimes....183
4.6. Interpretations and Discussion....186
4.7. Conclusion....192

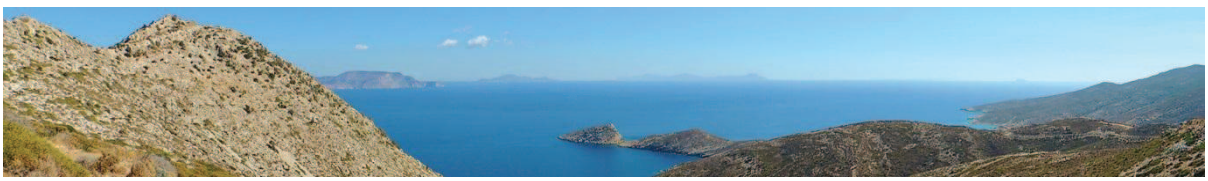

Dans le chapitre précédent, je me suis focalisé sur la distribution des occurrences minéralisées à l'échelle de la zone de subduction est-Méditerranéenne. Il apparaît ainsi qu'à partir de l'Oligocène, un grand nombre de minéralisations à plomb-zinc et à or se sont mises en place dans un environnement extensif d'arrière-arc où ont été exhumés plusieurs dômes métamorphiques (figures 3.1n-y), associés à une forte activité magmatique (figure 3.3). Cette corrélation spatiale entre ces dômes, ce magmatisme et les gîtes métalliques laisse à penser que ces systèmes favorisent la circulation de fluides magmatiques et hydrothermaux potentiellement riches en métaux qui peuvent ensuite précipiter dans la croûte supérieure (figure 3.4b et c).

L'objectif de ce chapitre est d'apporter des preuves à cette hypothèse à partir de l'étude, sur le terrain, de ces objets minéralisés qui affleurent aujourd'hui dans l'archipel des Cyclades, qui constitue l'un de ces dômes métamorphiques exhumés en contexte d'arrière-arc entre l'Oligocène et le Miocène. Je me suis principalement focalisé sur l'étude des systèmes minéralisés de l'île de Mykonos et de leurs liens avec le Système de Détachements Nord-Cycladique (i.e. *NCDS* : *North Cycladic Detachment System*) qui affleure également sur cette île [*Faure et al.*, 1991; *Lee & Lister*, 1992; *Jolivet et al.*, 2010a; *Lecomte et al.*, 2010]. Ce travail a fait l'objet d'un article scientifique publié au journal *Tectonics* et qui s'intitule *The North Cycladic Detachement System and associated mineralization, Mykonos, Greece: Insights on the evolution of the Aegean domain*.

Dans cet article, je décris tout d'abord, la succession des évènements tectoniques, métamorphiques et magmatiques qui ont été mis en évidence dans l'archipel des Cyclades depuis l'Eocène. Puis je me focalise sur l'île de Mykonos, dont l'évolution est principalement caractérisée par la mise en place et le refroidissement d'un pluton sous le *NCDS* au cours du Miocène moyen, alors que cette structure extensive est encore active. Je présente ensuite les principales observations de terrain qui m'ont permis de réaliser une cartographie précise des structures et des minéralisations sur cette île, ainsi qu'une caractérisation de cette minéralisation. Celle-ci s'exprime ainsi sous la forme (1) d'une brèche tectonique aurifère au niveau du système de détachements même et (2) de veines sub-verticales

polymétalliques à barytine et sulfures à cuivre-plomb-zinc-argent, souvent oxydés par l'altération supergène(*). Cette étude structurale me permet également de mettre en évidence une évolution dans le régime tectonique actif sur cette île qui s'est traduit par le passage d'un système extensif orienté NE-SO (i.e. axe de la contrainte minimale : σ_3), vers un système décrochant puis compressif orienté E-O (i.e. axe de la contrainte maximale : σ_1). Toutes ces observations me permettent ensuite de discuter de ces liens entre minéralisations et détachements et d'établir une chronologie précise entre le refroidissement du pluton, activité du *NCDS*, mise en place des différents systèmes minéralisés et ce changement dans le régime de contraintes.

Principaux résultats et discussion complémentaire

Dans cette étude, la découverte de nouveaux sites où affleurent de manière spectaculaire plusieurs détachements dont la morphologie est très similaire à ceux décrits sur l'île voisine de Tinos, permet de confirmer dans un premier temps l'extension du NCDS sur l'île de Mykonos, comme il a déjà été proposé précédemment [*Jolivet et al.*, 2010; *Lecomte et al.*, 2010].

Il apparaît ensuite clairement que les minéralisations aurifères et polymétalliques ont précipité au cours de deux phases minéralisatrices majeures, de manière synchrone à postérieure aux derniers incréments de la déformation extensive enregistrée sur cette île, il y a environ 11-10 millions d'années.

(1) La brèche tectonique, enregistrant des teneurs en or pouvant dépasser les 1 g t^{-1} [*Skarpelis & Gilg*, 2006], se serait mise en place le long du détachement de Mykonos alors que celui-ci était encore actif. D'après l'étude d'inclusions fluides, piégées dans le quartz qui a précipité au sein de cette brèche, celle-ci résulterait de la précipitation d'un fluide hydrothermal modérément salin (~5-6 % d'équivalent en poids de *NaCl*) à une température d'environ 230 °C [*Skarpelis & Gilg*, 2006].

(2) Les veines sub-verticales à barytine et sulfures se seraient, quant à elles, développées de manière synchrone à postérieure à l'activité du *NCDS*. L'étude d'inclusions fluides piégées dans les minéraux de la gangue de ces veines (i.e. barytine et quartz) suggère un fluide de salinité (2-17 % d'équivalent en poids de *NaCl*) et de températures variables (225-370 °C) [*Tombros et al.*, 2015]. Ces données peuvent être néanmoins biaisées, pour ce qui est du fluide piégé dans la barytine, en raison de la fragilité de son réseau cristallin qui facilite la diffusion [*Skarpelis & Gilg*, 2006], mais les résultats

similaires obtenus pour le quartz, semblent attester de leur fiabilité. De plus, les rapports isotopiques $\delta^{34}S$ mesurés dans la barytine et les différents sulfures ainsi que les δD et $\delta^{18}O$ du quartz et de la barytine, laissent à penser à un fluide minéralisateur d'origine magmatique ayant lessivé le pluton encaissant, mobilisant notamment le baryum et la silice [*Tombros et al.*, 2015]. Il se serait ensuite mélangé avec l'eau de mer, entrainant la réduction du soufre (présent initialement sous la forme SO_4^{2-}) en H_2S^- et la précipitation de la minéralisation.

Dans leur étude, *Tombros et al.* [2015] considèrent que la brèche minéralisée et les veines à barytine et sulfures appartiennent au même système minéralisé, argumentant que le fluide hydrothermal circulant dans les veines se serait imprégné le long *NCDS*. Cependant, les critères cinématiques observés dans cette brèche, ainsi que les textures en cocarde(*) du quartz qui y cristallise prouvent que le détachement était encore actif lors de la précipitation de cette minéralisation, alors que les veines, pour la majorité d'entre-elles, recoupent cette structure (cf. article ci-dessous). Il y aurait donc bien (au moins) deux phases minéralisatrices, comme l'évoquaient précédemment *Skarpelis & Gilg* [2006].

Il semble donc évident, que l'activité magmatique a participé à la mise en place des minéralisations sur l'île de Mykonos : (1) en apportant directement des éléments (ex. métaux, soufre) qui ont précipités sous la forme de sulfures ou sulfates et (2) en tant que source probable de chaleur, mobilisant ainsi des fluides qui ont pu contrôler cette précipitation. De plus, le lien très étroit entre ces systèmes magmatiques-hydrothermaux et les détachements à l'échelle de l'île, mais également à l'échelle des Cyclades (figure 4.1), laissent à penser que ces grandes structures extensives ont pu faciliter la remontée rapide de fluides magmatiques et hydrothermaux, à l'origine de ces gîtes minéralisés.

Ce travail réalisé sur l'île de Mykonos nécessiterait d'être étendu à d'autres îles de l'archipel des Cyclades où d'autres minéralisations ont été mises en évidence avec des contenus métalliques et des morphologies variées (figure 4.1) [ex. *Salemink*, 1985; *Liati et al.*, 2002; *Skarpelis*, 2002; *Neubauer*, 2005; *Tombros et al.*, 2007, 2008; *Voudouris et al.*, 2008; *St. Seymour et al.*, 2009; *Bonsall et al.*, 2011; *Kilias et al.*, 2013]. Il serait en effet intéressant : (1) d'apporter des preuves de terrain du

contrôle structural des minéralisations, mis en évidence sur l'île de Mykonos et (2) de comprendre, à partir d'une étude comparative de ces différents systèmes minéralisés, les mécanismes d'échelle locale ou régionale qui contrôleraient cette variabilité métallogénique au sein d'un même dôme métamorphique.

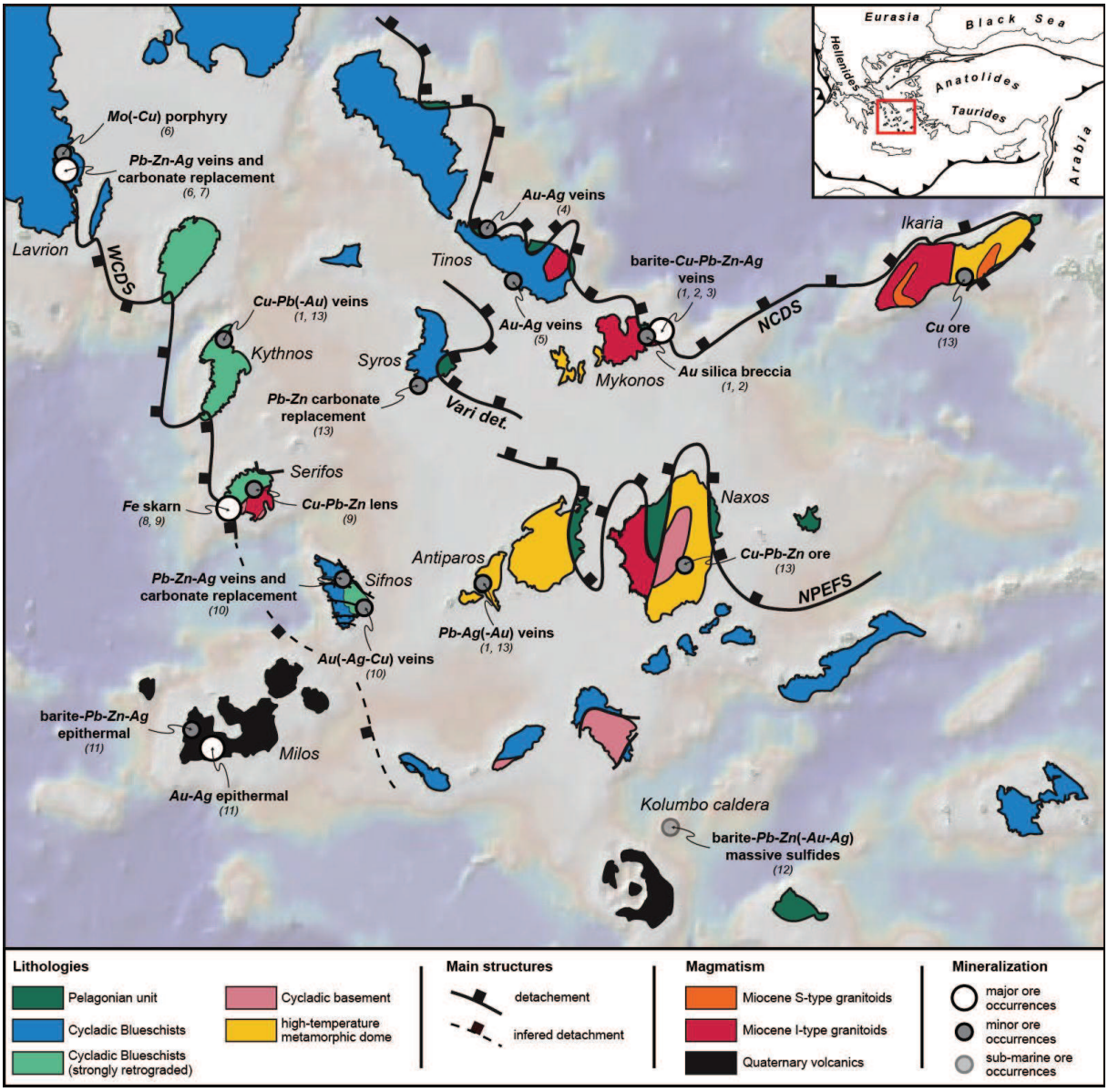

Figure 4.1 : carte tectonique de l'archipel des Cyclades où sont identifiés les principaux gîtes et indices minéralisés. 1 : *Skarpelis* [2002]. 2 : *Menant et al.* [2013], 3 : *Tombros et al.* [2015]. 4 : *Tombros et al.* [2007]. 5 : *Tombros et al.* [2008]. 6 : *Voudouris et al.* [2008]. 7 : *Bonsall et al.* [2011]. 8 : *Salemink* [1985]. 9 : *St. Seymour et al.* [2009]. 10 : *Neubauer* [2005]. 11 : *Kilias et al.* [2001]. 12 : *Sigurdsson et al.* [2006]. 13 : *IGME, Geological map of Greece*. *NCDS* : système de détachements nord-Cycladique. *NPEFS* : système de détachements de Naxos-Paros. *WCDS* : système de détachements ouest-Cycladique. Modifiée d'après *Jolivet et al.* [2015].

TECTONICS, VOL. 32, 1–20, doi:10.1002/tect.20037, 2013

The North Cycladic Detachment System and associated mineralization, Mykonos, Greece: Insights on the evolution of the Aegean domain

Armel Menant,[1,2,3] Laurent Jolivet,[1,2,3] Romain Augier,[1,2,3] and Nikolaos Skarpelis[4]

Received 2 May 2012; revised 2 March 2013; accepted 15 March 2013.

[1] In the Aegean back-arc domain, some 30–35 Ma ago, an increase of the rate of slab retreat led to the initiation of post-orogenic extension, largely accommodated by large-scale structures such as the North Cycladic Detachment System (NCDS). Although this extension is still active nowadays, an E–W compressional regime developed in the Late Miocene with the propagation of the North Anatolian Fault. On Mykonos island (Cyclades), the NE–SW back-arc extension is particularly well expressed with the Livada and Mykonos detachments that belong to the NCDS and that are associated with NW–SE barite veins emplaced during the synkinematic cooling of the Mykonos intrusion. This study shows that the formation of the mineralization occurred when the pluton crossed the ductile-to-brittle transition during its exhumation below the NCDS at ~11–10 Ma. In addition, the kinematics of mineralized structures evolved with time: (1) most of the displacement was accommodated by the top-to-the-NE Livada and Mykonos detachments accompanied by the formation of mineralized normal faults that were (2) reworked in a strike-slip regime with an E–W direction of shortening and a persistent NE–SW stretching and (3) a late post-mineralization E–W compressional stage with a minor reworking of shallow-dipping faults (locally including the detachments themselves). We interpret this increase of the E–W shortening component recorded during the mineral deposition as a consequence of the initiation of the westward motion of Anatolia from 10 Ma, thus 4 Ma before the propagation of the North Anatolian Fault in the Dardanelles Strait and the localization of the strain on the Aegean Sea margins.

Citation: Menant, A., L. Jolivet, R. Augier, and N. Skarpelis (2013), The North Cycladic Detachment System and associated mineralization, Mykonos, Greece: Insights on the evolution of the Aegean domain, *Tectonics*, *32*, doi:10.1002/tect.20037.

1.. Introduction

[2] The Aegean domain in the eastern Mediterranean results from the Tertiary subduction of the African plate below Eurasia. Since the late Cretaceous–Paleocene closure of the Vardar Ocean, continuing convergence has led to the formation of the Hellenic orogenic wedge. Some 35 Ma ago, an increasing rate of slab retreat favored the formation of the Aegean Sea back-arc basin while shortening continued in peripheral areas [*Le Pichon and Angelier*, 1979; *Jolivet and Faccenna*, 2000]. This pervasive NE–SW to N–S Oligocene–Miocene extension was mainly accommodated by a limited number of low-angle normal faults or detachments that controlled the exhumation of a series of metamorphic core complexes (MCCs) [*Lister et al*., 1984; *Gautier and Brun*, 1994a; 1994b; *Jolivet et al*., 1994; *Ring et al*., 2010; *Grasemann et al*., 2012]. In the northern part of Cyclades, this set of detachments is known as the North Cycladic Detachment System (NCDS) that accommodated several tens of kilometers of displacement [*Jolivet et al*., 2010]. Further south, the West Cycladic Detachment System also participated in the exhumation of the metamorphic rocks [*Grasemann et al*., 2012]. More recently, the Anatolian plate started its fast westward movement, revealed especially by Global Positioning System (GPS) and satellite laser ranging data [*Reilinger et al*., 1997; 2010], partly as a consequence of the collision between Eurasia and Arabia [*Armijo et al*., 1996; 1999] and partly as the result of detachments and tears of the African slab in the upper mantle [*de Boorder et al*., 1998; *Govers and Wortel*, 2005; *Faccenna et al*., 2006; *Royden and Papanikolaou*, 2011]. This plate motion is accommodated in particular by a large intracontinental discontinuity: the dextral strike-slip North Anatolian Fault (NAF) that induced the progressive localization of strain in the Aegean region, notably along the Central Hellenic Shear Zone (CHSZ) [*Armijo et al*., 1996; *Royden and Papanikolaou*, 2011]. The

[1]Université d'Orléans, ISTO, Orléans, France.
[2]CNRS/INSU, ISTO, Orléans, France.
[3]BRGM, ISTO, Orléans, France.
[4]Faculty of Geology and Geoenvironment, University of Athens, Department of Economic Geology and Geochemistry, Athens, Greece.

Corresponding author: A. Menant, Université d'Orléans, ISTO, UMR 7327, 45071, Orléans, France. (armel.menant@cnrs-orleans.fr)

©2013. American Geophysical Union. All Rights Reserved.
0278-7407/13/10.1002/tect.20037

NAF entered the Aegean domain through the Dardanelles Strait at ~6–5 Ma [*Armijo et al*., 1999; *Melinte-Dobrinescu et al*., 2009]. However, several studies in Anatolia have suggested that the present-day NAF results from the evolution of a wider dextral shear zone that dates back to the middle Miocene [*Sengör et al*., 2005]. A number of additional observations such as open folds, strike-slip faults, and minor thrusts in the central Aegean domain and in western Turkey suggest, despite the strong back-arc N–S stretching, a significant component of E–W shortening [*Angelier*, 1976; *Buick*, 1991a; 1991b; *Bozkurt and Park*, 1997; *Ring et al*., 1999; *Avigad et al*., 2001; *Bozkurt*, 2003]. This compressional regime could be a consequence of the extrusion of Anatolia [*Avigad et al*., 2001] that would have affected this region before the localization of strain on the edges of the Aegean Sea. The accurate timing for the initiation of this E–W shortening is however not well constrained. A closer look at the tectonic evolution of the central Aegean during the late Miocene allows us to describe more precisely the strain regime change.

[3] On Mykonos island (northern Cyclades), where extensional structures related to the activity of the NCDS have been described in details [*Faure and Bonneau*, 1988; *Lee and Lister*, 1992; *Lucas*, 1999; *Lecomte et al*., 2010; *Denèle et al*., 2011], a syntectonic granitoid intruded the Cycladic basement during the Serravallian and early Tortonian. Radiometric time constraint yielded a 13.5 ± 0.3 Ma U-Pb crystallization age on zircon and 11.5 ± 0.5 Ma to 8.9 ± 0.4 Ma (U-Th)/He final cooling ages on apatite [*Brichau et al*., 2008], at the time of the possible initiation of the westward movement of Anatolia. On the eastern part of the island, two branches of the NCDS have been recognized: the lower ductile-brittle Livada detachment and the upper brittle Mykonos detachment [*Lecomte et al*., 2010]. Located in the vicinity of these structures, numerous mineralized occurrences, mainly barite veins belonging to the Aegean Cenozoic metallogenic province, have been described [*Skarpelis*, 2002]. The orientation of these veins clearly shows a conspicuous relation with the Aegean extensional tectonics [*Lecomte et al*., 2010]. However, detailed geological mapping of the detachments and barite veins as well as detailed observations of the interrelations between strain and veins formation remain still poorly investigated.

[4] Based on field observations, this paper aims at understanding the relationships between mineralization and deformation on Mykonos island. Moreover, recognition of the successive tectonic regimes prior, during, and after mineral deposition has new implications for late Cenozoic geodynamic evolution of the Aegean domain.

2. Geological and Geodynamic Setting

2.1. Late Cenozoic Geodynamic Evolution of the Aegean Domain

[5] In the Mediterranean realm, the collision between the African and Eurasian plates during the Cenozoic led to the formation of several orogenic belts, including the Hellenides formed by accretion of both oceanic and continental units [*Dercourt et al*., 1986; 1993; *Stampfli*, 2000; *van Hinsbergen et al*., 2005]. Within the orogenic wedge, buried units (e.g., the Cycladic Blueschists) were affected by an initial high-pressure and low-temperature metamorphism (H*P*-L*T*) and were partly exhumed in a synorogenic context [*Bonneau and Kienast*, 1982; *Trotet et al*., 2001]. Then, the subduction front started to migrate southward some 35 Ma ago with the collapse of the central part of the Hellenic belt, in direct response to slab retreat. Metamorphic rocks were thus transferred in the back-arc domain where they were exhumed in a post-orogenic extensional context [*Jolivet and Faccenna*, 2000; *Jolivet and Brun*, 2010]. The exact timing of the initiation of the slab retreat and the coeval inception of extension in the upper plate is however still debated and possibly as young as 25 Ma [*Ring et al*., 2010].

[6] In the Cyclades, the H*P*-L*T* Cycladic Blueschists, belonging to the Pindos oceanic domain, reached their peak-pressure during the formation of the Hellenides some 50–45 Ma ago [*Wijbrans and McDougall*, 1986; 1988] and were exhumed during the Eocene as an extrusion wedge within the subduction channel [*Jolivet et al*., 2003; *Ring et al*., 2007; 2010; *Brun and Faccenna*, 2008; *Huet et al*., 2009; *Jolivet and Brun*, 2010]. They are particularly well preserved in Syros and Sifnos islands where synorogenic shear zones are also well exposed [*Trotet et al*., 2001; *Keiter et al*., 2004; *Philippon et al*., 2011]. After 35 Ma, post-orogenic extension started in the Cyclades, due to an increased rate of southward African slab roll-back that induced a delamination of the lower crust and mantle of the upper plate. Therefore, a warmer regime developed in the back-arc region leading to the formation of low-pressure and high-temperature (L*P*-H*T*) mineral assemblages which partly overprinted the former H*P*-L*T* parageneses of the Cycladic Blueschists (e.g., Andros, Tinos, and Naxos islands) and the underlying Cycladic basement (e.g., Ios and Sikinos islands). These L*P*-H*T* units were exhumed as metamorphic core complexes (MCC) between 35 and 8 Ma from the North to the South of the Cyclades [*Lister et al*., 1984; *Gautier and Brun*, 1994a; 1994b; *Vanderhaeghe*, 2004; *Brichau et al*., 2006; 2007; 2008; 2010; *Duchêne et al*., 2006; *Martin et al*., 2006].

[7] The exhumation, whether along H*P*-L*T* or H*T*-L*P* path, is controlled by crustal scale ductile-to-brittle extensional shear zones separating the Cycladic Blueschists in the footwall from the low-grade Upper Cycladic Unit in the hanging wall. In the northern Cyclades, this tectonic contact corresponds to the NCDS that crops out on the islands of Andros, Tinos, Mykonos, and Ikaria (Figure 1a) and shows a consistent top-to-the-NE sense of shear [*Faure et al*., 1991; *Lee and Lister*, 1992; *Gautier and Brun*, 1994a; *Ring and Layer*, 2003; *Kumerics et al*., 2005; *Mehl et al*., 2005; *Brichau et al*., 2007; 2008; *Jolivet et al*., 2010; *Lecomte et al*., 2010]. Syntectonic sediments, related to the activity of the NCDS, were deposited within fault-bounded basins from early (?) to late Miocene on Mykonos island [*Sánchez-Gómez et al*., 2002]. Some 17 Ma ago, back-arc magmatism appeared in the Cyclades leading to the emplacement at mid-crustal levels of several syn-extensional intrusions formed by magmas involving both a mantle-derived mafic component and a voluminous crustal felsic component (e.g., Tinos, Delos, Mykonos, Ikaria, Serifos, and Naxos) [*Altherr et al*., 1982; *Faure et al*., 1991; *Altherr and Siebel*, 2002; *Pe-Piper and Piper*, 2002; 2006; *Denèle et al*., 2011]. Finally, the westward extrusion of Anatolia started, adding an ~E–W shortening to the overall N–S extension of the Aegean domain [*Avigad et al*., 2001]. This motion was then progressively accommodated by the NAF which propagated in the Dardanelles Strait and the North Aegean Trough some 6–5 Ma ago and joined the Evia and Corinth rifts, forming the CHSZ where the deformation is still concentrated nowadays

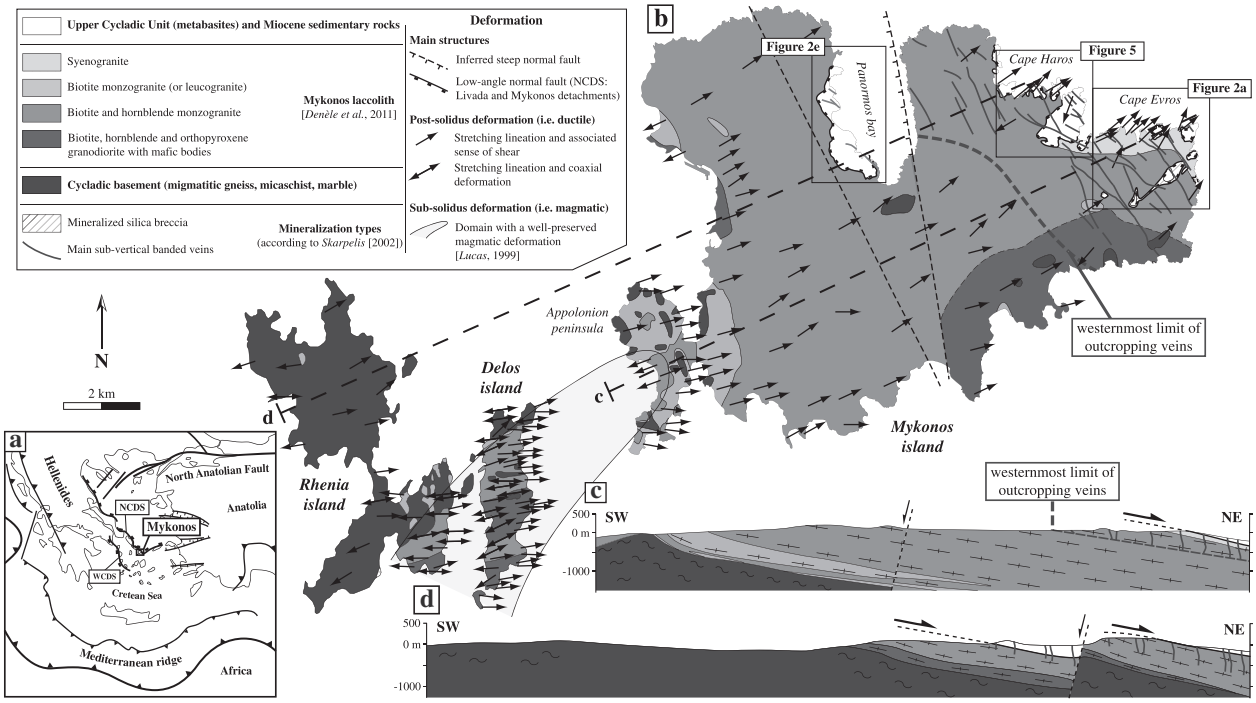

Figure 1. Tectonic and geological maps and location of the study area. (a) Simplified tectonic map of the Aegean domain, given is the location of Mykonos island. (b) Geological map of Mykonos island. (c and d) Cross-sections of Mykonos island oriented parallel to the stretching direction (modified from *Lucas* [1999]; *Lecomte et al.* [2010]; *Denèle et al.* [2011]). The westernmost limit of outcropping veins is reported on the (Figure 1b) geological map and the (Figure 1c) cross-section in order to estimate the current maximal depth of veins.

and generates a significant seismicity [*Armijo et al.*, 1996; *Le Pichon and Kreemer*, 2010; *Royden and Papanikolaou*, 2011].

2.2. Geological and Metallogenic Overview of Mykonos Island

[8] Mykonos island is mainly constituted by an I-type granitoid interpreted as an asymmetrical laccolith-like intrusion with a N70°E long axis [*Denèle et al.*, 2011] whose fast cooling from ~680 to ~60°C occurred between 13 and 9 Ma [*Brichau et al.*, 2008]. This laccolith complex intrudes an extensional migmatitic dome, mainly constituted by paragneisses that belongs to the Cycladic basement cropping out on the Apollonion peninsula and on the neighboring Delos and Rhenia islands (Figure 1) [*Lucas*, 1999; *Pe-Piper et al.*, 2002; *Denèle et al.*, 2011]. The composition of the Mykonos laccolith evolves from a monzogranite to a granodiorite with an inverted zonation (i.e., more mafic toward the pluton center) [*Lucas*, 1999], which indicates a polyphased emplacement by successive pulses of magma injection. The dominant source of this magma corresponds to partial melting of biotite gneiss metasedimentary protolith similar to the metagreywackes of Rhenia island [*Stouraiti et al.*, 2010]. The laccolith displays primarily an intense magmatic fabric over which a protomylonitic to mylonitic deformation is superimposed and intensifies toward the two branches of the NCDS observed on the island (i.e., the Livada and Mykonos detachments; Figure 1c) [*Lucas*, 1999; *Jolivet et al.*, 2010; *Denèle et al.*, 2011]. The stretching lineations draw a curved pattern from ~N90°E in the Apollonion peninsula toward a more northerly direction (N30–20°E) close to the NCDS with conspicuous top-to-the-NE kinematic indicators (Figure 1b). With a stretching lineation trending between N90°E and N60°E in most of the island, Mykonos contrasts with other Cycladic islands where the lineation is dominantly N30–20°E [*Gautier and Brun*, 1994a; 1994b; *Jolivet et al.*, 1994]. *Denèle et al.* [2011] ascribe this curvature of lineation to differential block rotation during exhumation of the laccolith and its progressive cooling while the regional direction of extension remained constant about N20°E [*Walcott and White*, 1998; *Jolivet*, 2001].

[9] The Livada detachment mostly exhibits a top-to-the-NE ductile deformation, locally evolving to brittle that reactivates the intrusive contact between the Mykonos laccolith and the overlying greenschist facies metabasites of the Upper Cycladic Unit. Structurally, above the Mykonos detachment is mainly a top-to-the-NE brittle structure marked by a 5–10-m thick cataclasite body and a conspicuous low-angle normal fault plane that puts late Miocene syn-rift sediments in direct contact with the Upper Cycladic Unit or directly with the Mykonos laccolith [*Avigad et al.*, 2001; *Sánchez-Gómez et al.*, 2002; *Lecomte et al.*, 2010]. A similar kinematics is observed at the scale of the island associated to ductile-to-brittle structures, indicating a continuum of deformation in the laccolith and the host rocks during their emplacement and the subsequent cooling. The NCDS likely accommodated ~30 km of displacement after the intrusion of the Mykonos laccolith [*Brichau et al.*, 2008] with a progressive transfer from the Livada to the Mykonos detachment and a partly contemporaneous activity under brittle conditions [*Lecomte et al.*, 2010].

[10] The hydrothermal mineralization of Mykonos island belongs to the Aegean Cenozoic metallogenic province. It led to the development of a mining activity on the island with barite exploitation and processing by Mykobar Co. S.A. until 1984 and older small-scale sporadic mining for argentiferous galena, cerussite, anglesite, and iron hydroxides [*Skarpelis*, 2002]. The mineral deposits are mainly exposed in the central and the eastern parts of the island where they are preserved in the vicinity of the NCDS, indicating a probable close linkage with this major extensional structure (Figure 1). *Skarpelis* [2002] and *Skarpelis and Gilg* [2006] have distinguished two mineralization types on the basis of the occurrence mode, the ore mineralogy and textures and the origin of hydrothermal fluids. (1) A fragment-dominated sub-economic gold-enriched silica breccia along the Mykonos detachment cataclasite body (Figure 1b) that is filled with hydrothermal minerals including quartz with cockade, crustiform, and comb textures, as well as barite and minor relics of primary sulfides. Gold grades range up to 1 g/t [*Skarpelis*, 2002]. Fluid inclusions study on quartz shows evidence for boiling suggesting a depth of less than 1 km during mineralization [*Skarpelis and Gilg*, 2006]. Quartz was deposited from moderately saline, NaCl-dominated aqueous fluids (5–6 wt% total dissolved solids) at temperatures of ~230°C. (2) A sub-vertical NW–SE-trending barite and Fe-hydroxide veins swarm that cuts the upper part of the Mykonos laccolith, the Upper Cycladic Unit, and the Miocene sediments that are besides heavily impregnated by the hydrothermal mineralization [*Skarpelis*, 2002; *Lecomte et al.*, 2010]. The main banded texture of these veins indicates a successive deposition of the different mineralized contents during the vein opening. Fe-hydroxides and oxides as well as minor secondary Cu minerals result after oxidation of base-metal sulfides and carbonates that are preserved in the deeper parts of veins. Fluid inclusion data on vein barite indicate Ca-rich, highly saline fluids [*Skarpelis and Gilg*, 2006].

3. Detailed Mapping at the Vicinity of the NCDS on Mykonos

[11] In order to understand the interrelations between the mineralization on Mykonos island and the Aegean tectonics, we have carried out a new geological mapping (field mapping as well as satellite images analysis) of key areas (i.e., Cape Evros, Western coast of Panormos Bay, and Cape Haros) where both first-order structures (i.e., the detachments) and mineral deposits are spatially closely associated (Figure 1b).

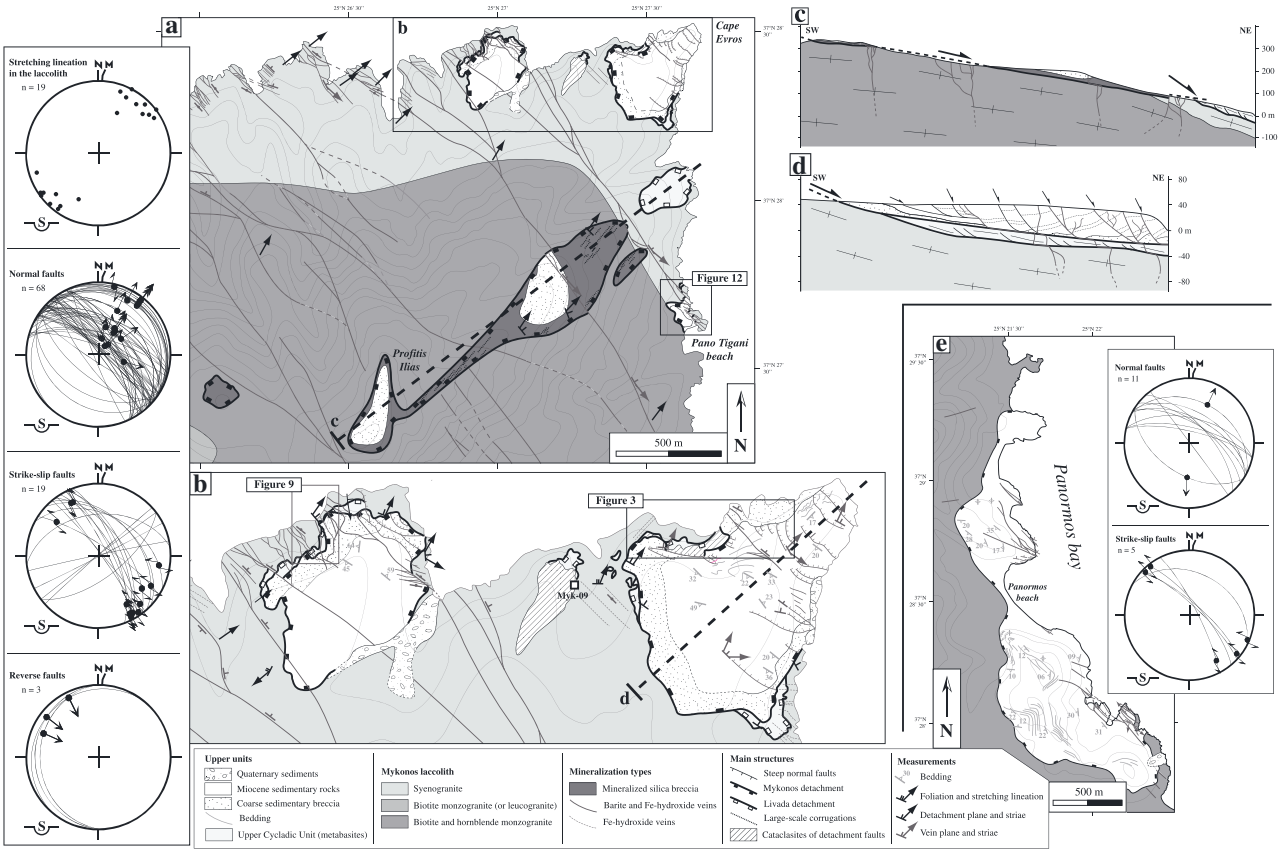

Figure 2. Field geological map of Cape Evros area and western coast of Panormos Bay. (a) Geological map of Cape Evros area. (b) Detailed geological map of Cape Evros area. (c and d) Cross-sections of Cape Evros oriented parallel to the stretching direction. (e) Geological map of western coast of Panormos Bay. See also Figure 1 for location. Fault and vein thicknesses are not to scale. The location of samples used for the chlorite geothermometry study is indicated (see results in Figure 10 and Table 1).

3.1. Cape Evros Area

[12] The first order geological mapping of the Livada and Mykonos detachments in Cape Evros area (Figure 2) was already well documented [*Lecomte et al*., 2010]. The Livada detachment appears as a 10-m scale thick mylonitic shear zone developed at the contact between the Mykonos laccolith and the overlying Upper Cycladic Unit. There, the mylonitic foliation is shallow NE-dipping and carries a N30°E-trending stretching lineation with consistent top-to-the-NE kinematic indicators (Figure 2a) [*Lecomte et al*., 2010]. Late steep and low-angle normal faults either cut or root within the detachment. Structurally, above the Mykonos detachment, roofing the Upper Cycladic Unit, displays a top-to-the-NE intensely hydrothermally altered cataclasite body (Figures 3a and 3b). Its hanging wall is made of syntectonic (i.e., syn-rift) sediments cut by numerous regularly spaced steep normal faults rooting into the detachment and defining a tilted-block geometry (Figure 3c). A 10–20-m thick coarse silicified sedimentary breccia marks the base of the sedimentary sequence. Due to intense normal faulting, the sediments can locally be in direct contact with the mylonitized laccolith with the tectonic omission of the Upper Cycladic Unit (Figure 3a).

[13] The hydrothermal mineralization in Cape Evros area occurs as barite and Fe-hydroxide impregnations in the late Miocene sedimentary unit and as mineralized silica breccia along the main fault zone of the Mykonos brittle detachment (Profitis Ilias; Figures 2 and 4). However, the main expression of this mineralization consists in banded barite and/or Fe-hydroxide veins forming a denser array close to the two branches of the NCDS (see details in part 3). These veins extend over 3 km along strike (Figure 2a). When the veins are emplaced along steep normal faults, they show a ~N110–140°E orientation with mainly a northeastward dip, while some of them may be associated with southwestward dipping antithetic faults (Figure 2). Other veins are also emplaced along strike-slip faults oriented N70–90°E and N120–140°E or within low-angle normal faults that may be reactivated with a reverse kinematics (see details in part 4).

3.2. Western Coast of Panormos Bay

[14] On the western coast of Panormos Bay (Figure 2e), the Mykonos detachment directly juxtaposes the syntectonic sedimentary unit over the top of the Mykonos laccolith through a several meters thick cataclasite zone. The bedding of the sediments dips toward the detachment plane forming a roll-over structure that indicates a flat-and-ramp geometry of the shallow-dipping detachment as described by *Lecomte et al*. [2010]. Numerous steep normal faults root into this first-order structure, affecting the late Miocene sediments.

[15] In this region, the veins present similar orientation (Figure 2e) and composition to those in Cape Evros area but are smaller and less abundant. Within the sediments, approaching the veins considered as feeders, the mineralization is often characterized by a pervasive impregnation or isolated geodic forms because of the replacement of the sedimentary matrix and former limestone pebbles of the conglomeratic layers by barite and/or goethite [*Sánchez-Gómez et al*., 2002]. Moreover, the sediments display a clear color change from yellow- to red-colored, as a possible result of pyrite dispersion followed by supergene weathering to Fe-hydroxides, depicting large-scale halos in the vicinity of the veins.

3.3. Cape Haros Area

[16] Cape Haros area is mostly characterized by the Livada detachment that separates the Mykonos laccolith from the Upper Cycladic Unit (Figure 5). The best outcrop of the contact is exposed on the eastern side of Mersini Beach (Figure 6a). In the footwall, the highly deformed laccolith shows an alternation of shallow-dipping light-colored mylonites and dark ultramylonitic shear bands (Figure 6b). Within this mylonitic foliation, microscopic- to centimeter-scale kinematic indicators, such as shear bands and asymmetric pressure shadows on feldspar porphyroclasts, show a consistent NE–SW stretching lineation associated with an overall top-to-the-NE sense of shear (Figure 6c). In the hanging wall, the Upper Cycladic Unit also displays an intense ductile deformation with a strong foliation and meter-scale top-to-the-NE shear zones within a few meters above the contact. Foliation and shear planes are intruded by aplitic sills and dykes supporting the emplacement of the laccolith within the Upper Cycladic Unit during ductile deformation (Figure 6d). The hanging wall unit is also affected by numerous NW–SE-trending steep and low-angle normal faults that cut ductile structures and aplitic sills and root into or cut through the detachment, showing the superimposition of extensional brittle deformation onto ductile deformation. All these features are similar to the Livada detachment that crops out in the eastern part of Tinos island where the Upper Cycladic Unit and an intrusive granitoid dated at ~14 Ma are affected by a similar top-to-the-NE non-coaxial shearing [*Faure et al*., 1991; *Jolivet and Patriat*, 1999; *Brichau et al*., 2007; *Jolivet et al*., 2010]. The late Miocene sedimentary unit is also observed as a small klippe surrounded by the Mykonos detachment on the west headland of Cape Haros (Figure 7a). The sedimentary unit, overlying the cataclastic Upper Cycladic Unit, is heavily affected by top-to-the-NE steep and low-angle normal faults mimicking at a smaller scale the detachment and associated tilted blocks observed at Cape Evros (Figure 7b).

[17] Similar to Cape Evros and Panormos Bay, the mineralization in Cape Haros area occurs mainly as ~N110–140°E sub-vertical veins (Figure 5) associated with, alternatively, normal and strike-slip kinematics. Some veins trend ~N70–90°E, in particular on Merchias peninsula where numerous small mineralized fault planes with a reverse kinematics are also observed (Figure 5d; see details in part 4).

4. Characterization of the Mineralization

4.1. Description of the Mineralization

[18] Both hydrothermal mineralization types described on Mykonos island [*Skarpelis*, 2002; *Skarpelis and Gilg*, 2006] are strongly structurally controlled. Indeed, the mineralization mostly occurs along sub-vertical NW–SE-trending veins with variable thickness from one centimeter to several meters (Figures 2, 4, 5, and 8a) containing banded barite and/or Fe-hydroxide, mainly goethite. Base-metal sulfides are preserved as patches at the deepest levels of the veins and comprise not only pyrite and marcasite with a colloidal texture (Figures 4 and 8b) but also arsenopyrite, chalcopyrite, galena, sphalerite, tennantite, tetrahedrite, boulangerite, geocronite, and jordanite [*Skarpelis*, 2002]. Quartz and carbonates, mainly siderite, occur as gangue, postdating the barite deposition with rare barite replacement by quartz (Figure 8c). The mineralization may

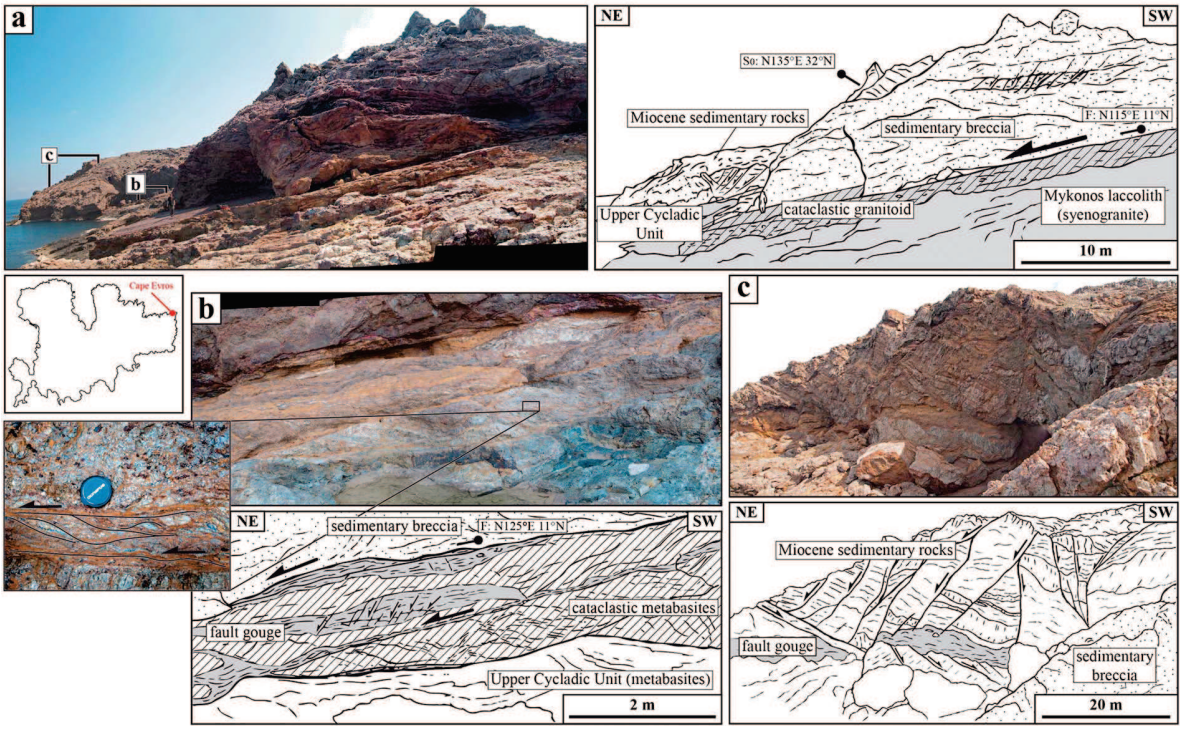

Figure 3. The Mykonos detachment in Cape Evros area. (a) Outcrop picture of the Mykonos detachment highlighted by a cataclasite body that puts the Miocene sediments in direct contact over the Mykonos laccolith. (b) Close-up view of the top-to-the-NE Mykonos detachment zone characterized by hydrothermal cataclasites and a fault gouge. (c) Tilted-block geometry in the Miocene sediments with normal faults rooting in the Mykonos detachment. See also Figure 2 for location.

also occur as a pervasive impregnation of Miocene sediments or as a silica coarse breccia within the Mykonos detachment cataclasite body (Figures 2a and 8d). In the latter, clasts in a Fe-hydroxide matrix are constituted by growth bands of quartz and/or barite that can be replaced by quartz as in banded veins (Figure 8e). This breccia displays top-to-the-NE shear criteria compatible with the kinematics of the Mykonos detachment (Figure 8d).

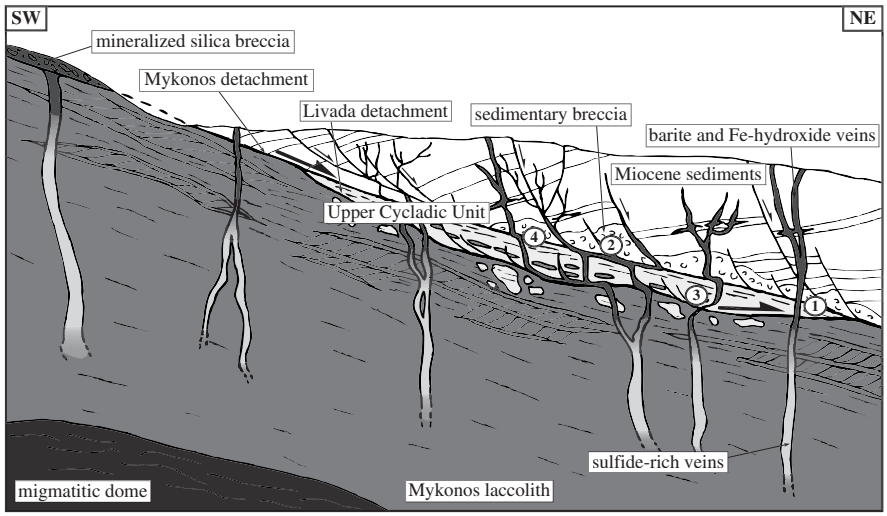

Figure 4. Interpretative diagram of Mykonos hydrothermal system in Cape Evros region showing the different morphologies of mineralization and the four different types of relationships between veins and detachments: (1) veins cut the detachment, (2) mineralization spreads out into the detachment, (3) veins sheared in the detachment, and (4) veins bent in the detachment. Gradual color change of veins corresponds to the evolution of the mineralized filling from sulfides to barite and Fe-hydroxides from the deeper to the upper parts of veins, respectively.

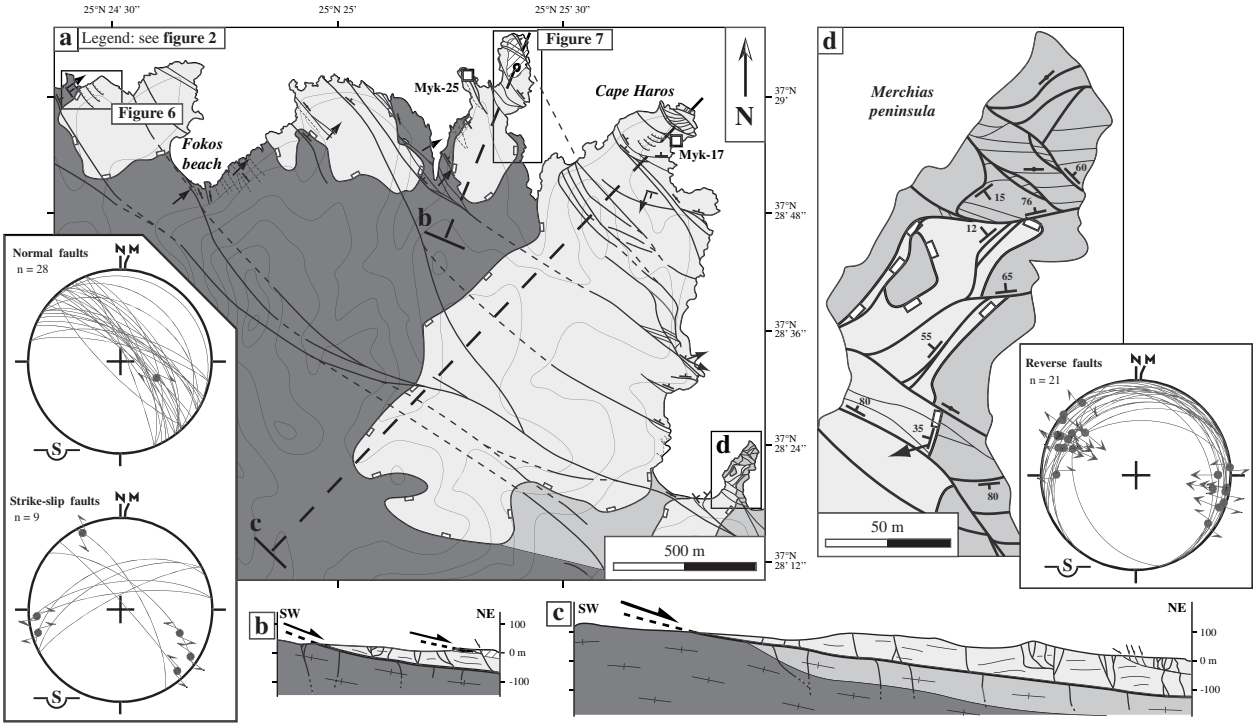

Figure 5. Field mapping of Cape Haros area. (a) Geological map of Cape Haros area. (b and c) Cross-sections of Cape Haros area parallel to the stretching direction. (d) Detailed geological map of Merchias peninsula. See also Figure 1 for location and Figure 2 for detailed legend. Fault and vein thickness is not at scale. The location of samples used for the chlorite geothermometry study is indicated (see results on Figure 10 and Table 1).

[19] The hydrothermal alteration in the Mykonos laccolith wall rocks is characterized by a pervasive silicification and an argillic and phyllic alteration resulting in the replacement of K-feldspar porphyroclasts mainly by kaolinite and sericite and the disappearance of biotite and amphibole (Figure 8f). The mylonitic fabric is however still preserved. In the Upper Cycladic Unit and in the cataclasites of the Mykonos detachment, this hydrothermal alteration is mainly marked by the crystallization of chlorite, quartz, and plagioclase in late fractures (Figure 8g).

[20] The mineralization develops exclusively in the vicinity of the NCDS (Figures 1b, 2, and 5) where veins display four different behaviors when they approach the Livada and Mykonos detachments. (1) Some steep veins cut across the detachments without any deflection or deformation (Figure 9a). (2) Other veins spread out into the detachment zone from steeply-dipping feeders (Figure 9a). Then, the mineralization is often brecciated (Figure 8d) and the mineralized planes are striated. (3) Some veins are sheared and their mineralogical content is deformed in agreement with the kinematics of the detachments (Figure 9b). (4) Finally, many veins show an apparent top-to-the-SW bent shape when they cut across the detachment or within the sedimentary breccia, which appears inconsistent with the top-to-the-NE fault kinematics (Figures 9c and 9d). In this case, barite crystals are devoid of deformation.

4.2. Temperature Conditions of Mineralization Emplacement

[21] Hydrothermal chlorite associated with the mineralization (Figure 8g) provides a useful tool to estimate the temperature that prevailed when the hydrothermal fluid interacted with the host rocks. Accordingly, different chlorite geothermometers have been used. (1) The two thermometers of *Cathelineau and Nieva* [1985] and *Cathelineau* [1988] based on the study of the active geothermal system of *Los Azufres* (Mexico), which use the variation in Al(IV) and octahedral vacations (VI(vac)) in chlorite crystal lattice, are correlated with the crystallization temperature. In these examples, host rocks are constituted by zeolite-, greenschist-, and amphibolite-facies andesites, containing hydrothermal chlorite crystals, associated notably with quartz and epidote. (2) The thermometer of *Kranidiotis and MacLean* [1987] that correlate the temperature of hydrothermal chlorite crystallization in rhyodacite to rhyolite host rocks with the Al(IV) content and the Fe/(Fe + Mg) ratio, particularly within the assemblage quartz-chlorite ± sericite.

[22] These geothermometers are valid for specific mineral phase equilibrium and host rock type because they are based only on substitutions in the chlorite crystal lattice that can depend upon other factors than temperature. The pH of the coexisting fluid [*Walshe*, 1986], the presence of other minerals between chlorite layers [*Jiang et al*., 1994], and the nature and therefore the chemistry of the wall rock also have an influence on chlorite composition. Thus, the use of chlorite geothermometry using data from phase equilibrium experiments [*Vidal et al*., 2001] seems more appropriate.

[23] In this work, chemical analyses of chlorites crystals have been performed on a Cameca SX50 electron microprobe at the University Pierre et Marie Curie (Paris VI). Analytic conditions were 15 kV accelerating voltage and 12 nA beam current using Fe_2O_3 (Fe), $MnTiO_3$

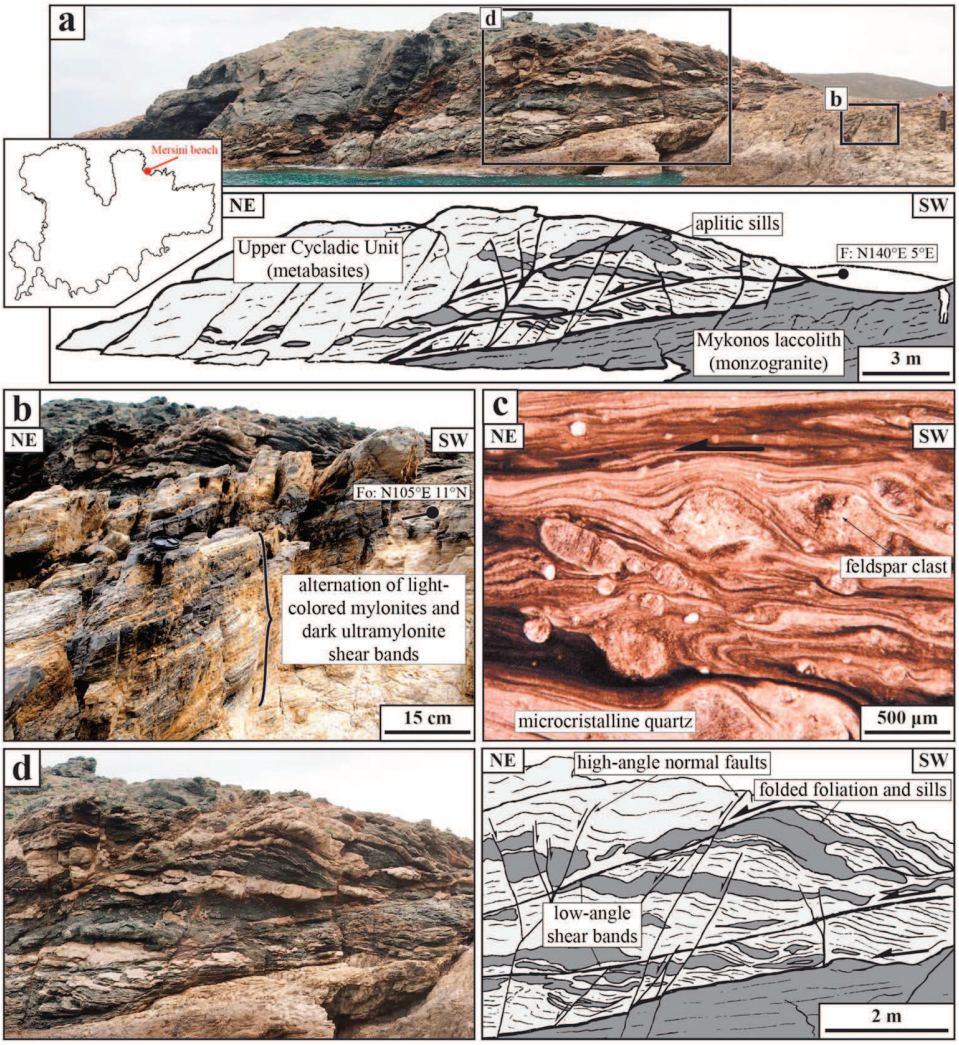

Figure 6. The Livada detachment in Cape Haros area. (a) Landscape picture of the Livada detachment cropping out close to Mersini beach. (b) Close-up view of shallow dipping ductile deformation of Mykonos laccolith close to the Livada detachment. (c) Microscopic view of top-to-the-NE shearing criteria within the mylonitic zone of the laccolith (polarized transmitted light). (d) Detail of intruded aplitic sills in the Upper Cycladic Unit and top-to-the-NE ductile-brittle extensional deformation associated to the Livada detachment. See also Figure 5 for location.

(Mn, Ti), diopside (Mg, Si), CaF_2 (F), orthoclase (Al, K), anorthite (Ca), albite (Na), and vanadinite (Cl) as standards. The counting time was 10 s for all elements. Two types of hydrothermal chlorite crystals have been analyzed: The first type is chlorite crystallizing with quartz and plagioclase in fractures that developed close to barite veins (Figure 8g) within the Upper Cycladic Unit (i.e., metabasites; Myk-25 and Myk-17 samples; Figure 5a). Their composition, enriched in Al_2O_3, evolves between amesite and sudoite end-members (Figure 10) and their Fe/(Fe + Mg) ratio evolves from 0.37 to 0.45. (2) The second type is chlorites formed within the cataclasites of Mykonos detachment associated with quartz (Myk-09 sample; Figure 2b). Richer in SiO_2, these chlorite crystals are comprised between the clinochlore-daphnite and the sudoite end-members (Figure 10) and their Fe/(Fe + Mg) ratio is higher, comprised between 0.43 and 0.5.

[24] Both types of hydrothermal chlorite crystals display Si (IV) content from 5.6 to 6.6 cations per formula unit, that is too high to use Fe-Mg aluminous chlorite geothermometer of *Vidal et al*. [2001]. Crystallization temperatures for the hydrothermal chlorites obtained with the other geothermometers yield a consistent 250–282°C narrow range of temperature in the Upper Cycladic Unit and a lower temperature range of 203–258°C in the cataclasites (Table 1).

[25] This variability is not necessarily the result of different hydrothermal fluid temperatures but can be related to the variable chemistry of the Upper Cycladic Unit and the cataclasites. Nevertheless, the temperature range obtained with chlorite geothermometers is in agreement with the study of fluid inclusions in quartz of the mineralized breccia that yielded a temperature of ~230°C [*Skarpelis and Gilg*, 2006].

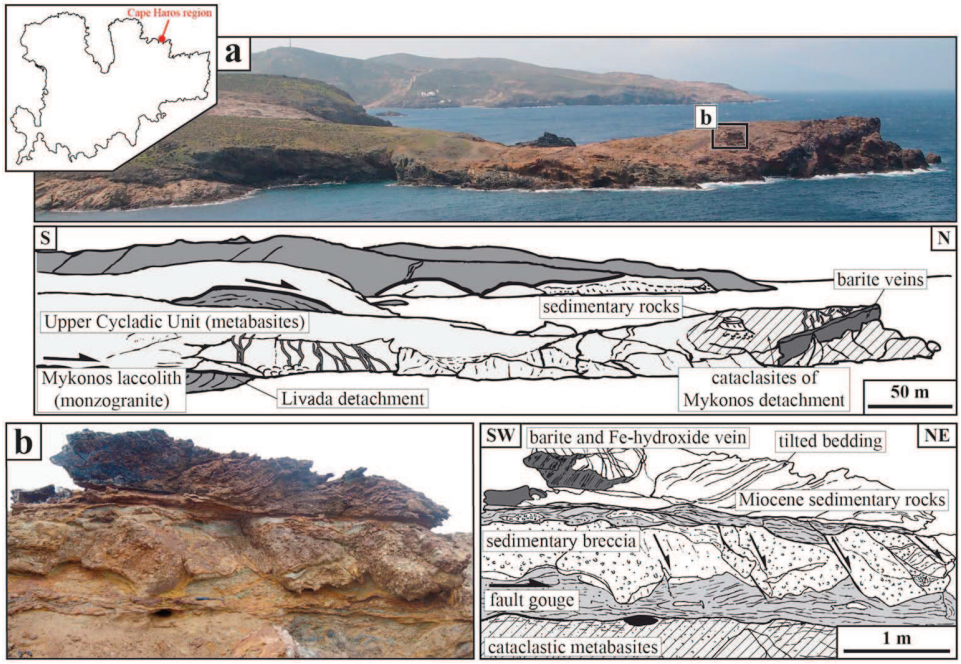

Figure 7. The Mykonos detachment in Cape Haros area. (a) Northern coast of Cape Haros area showing the Livada and Mykonos detachments. (b) Tilted-block geometry within the Miocene sediments in the hanging wall of the Mykonos detachment. See also Figure 5 for location.

5. Evidence of Successive Tectonic Regimes

5.1. Magmatic to Ductile Deformations

[26] The sub-solidus deformation of the Mykonos laccolith is mainly observed in the root zone of the intrusion toward the SW of the study area (Figure 1b). It is characterized notably by a plano-linear magmatic fabric of K-feldspars that is strictly parallel to the ductile fabric of the host migmatitic dome, suggesting a syn-extensional emplacement of the laccolith [*Faure and Bonneau*, 1988; *Faure et al*., 1991; *Denèle et al*., 2011]. The magmatic deformation in the laccolith evolves to a post-solidus deformation forming protomylonitic structures close to the migmatitic dome to ultramylonitic ones in the vicinity of the Livada and Mykonos detachments. Mineral foliation is oriented NW–SE and displays a shallow dip to the NE. The mineral or stretching lineation trends from ~N90°E in the west of the laccolith toward ~N30–20°E close to the NCDS (Figure 1b). Furthermore, numerous kinematic indicators, such as asymmetric folding of the mylonitic foliation, shear bands and asymmetric pressure shadows around porphyroclasts within the mylonitic laccolith and the Upper Cycladic Unit, are consistent with a top-to-the-NE sense of the ductile shear (Figure 6c).

5.2. Brittle Deformation and Relationships With the Mineralization

[27] The brittle deformation is well developed, particularly in contact zones between distinct tectonic units where it partly overprints the ductile structures. The Livada detachment is thus locally reworked by a set of low-angle and steep normal faults rooting into or cutting the contact with the Mykonos laccolith (Figure 6). The Mykonos detachment is exclusively a brittle structure with a thick cataclasite zone and numerous steep normal faults defining a tilted-block geometry (Figures 3 and 7). At the scale of Mykonos island, the strike of these faults that are often mineralized is broadly comprised between N110°E and N150°E with a variable northeastward dip (i.e., 10° to sub-vertical) accompanied by a subordinate set of southwestward dipping faults (Figures 2 and 5). No significant fault orientation variations have been observed between the different regions of the island, and the strike of these extensional faults is consistent with the NE–SW direction of regional stretching (Figures 2 and 5) [*Gautier and Brun*, 1994a; 1994b; *Avigad et al*., 1998]. However, a second set of faults is observed in zones where the veins network is particularly developed. For instance, on Merchias peninsula, N70–90°E-trending veins are conjugated with ~N130°E-trending ones while they both carry sub-horizontal striations (Figure 5d).

[28] Striations on the fault planes are complex with several generations of striae related to a succession of different stress regimes. NW–SE-trending mineralized steep fault planes associated with different mineralization stages display (1) NE–SW dip-slip striae and normal kinematic indicators and (2) sub-horizontal NW–SE striae that show a strike-slip movement (Figure 11a). On low-angle fault planes and notably on the Mykonos detachment plane, two generations of striae are observed: (1) a 10-m scale corrugation accompanied at small scale by a well-marked striation broadly oriented NE–SW and compatible with the top-to-the-NE main extensional movement of the detachment (Figure 2a) and (2) E–W to NW–SE striae associated with reverse kinematic indicators (Figures 5d and 11b).

[29] The overall geometry of veins is also variable and can be used as a strain marker. Indeed, in contrast with most of NW–SE banded veins formed as pure tension gashes

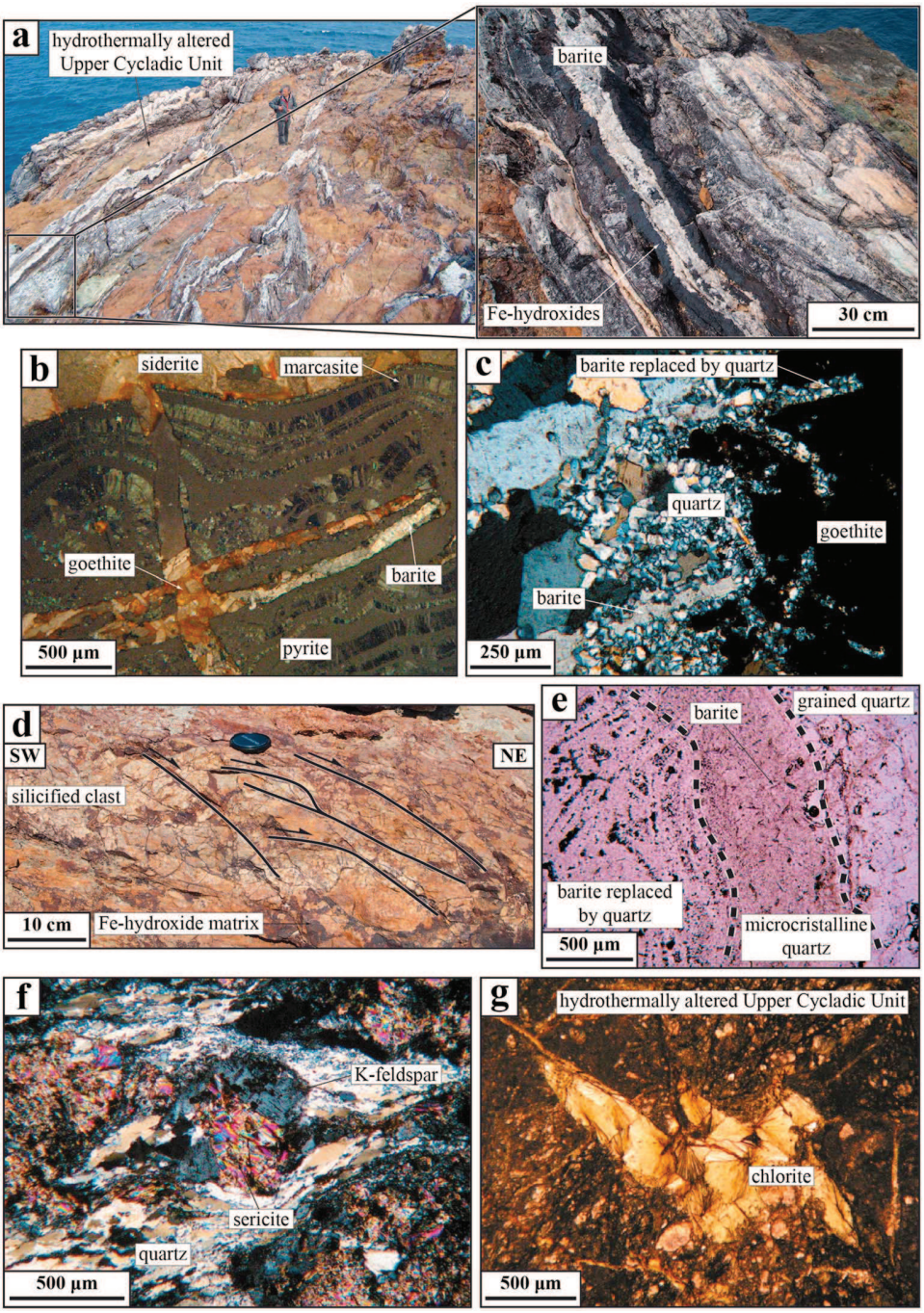

Figure 8. Different morphologies of hydrothermal mineralization and associated hydrothermal alterations. (a) Sub-vertical banded barite and Fe-hydroxide veins network (Cape Haros area). (b) Microscopic view of sulfide mineralization in veins with colloidal pyrite and marcasite crosscut by siderite, barite, and goethite (polarized analyzed reflected light). (c) Microscopic view of banded filling of veins with barite, goethite, and quartz that may replace barite crystals (polarized analyzed transmitted light). (d) Top-to-the-NE shearing criteria in mineralized silica breccia (Cape Evros area). (e) Microscopic view of growth bands of quartz and/or barite of clasts in mineralized breccia (polarized transmitted light). (f) Microscopic view of phyllic alteration of K-feldspars of mylonitic laccolith (polarized analyzed transmitted light). (g) Microscopic view of hydrothermal chlorites in metabasites of Upper Cycladic Unit (polarized transmitted light).

(Figure 8a), other veins, filled with barite or collapse breccia with Fe-hydroxide matrix, display a clear pull-apart morphology compatible with a left-lateral slip for ~N130°E veins (Figure 11c) or a right-lateral one for ~N80°E structures (Figure 11d) forming an obvious conjugate strike-slip faults system (Figure 11e).

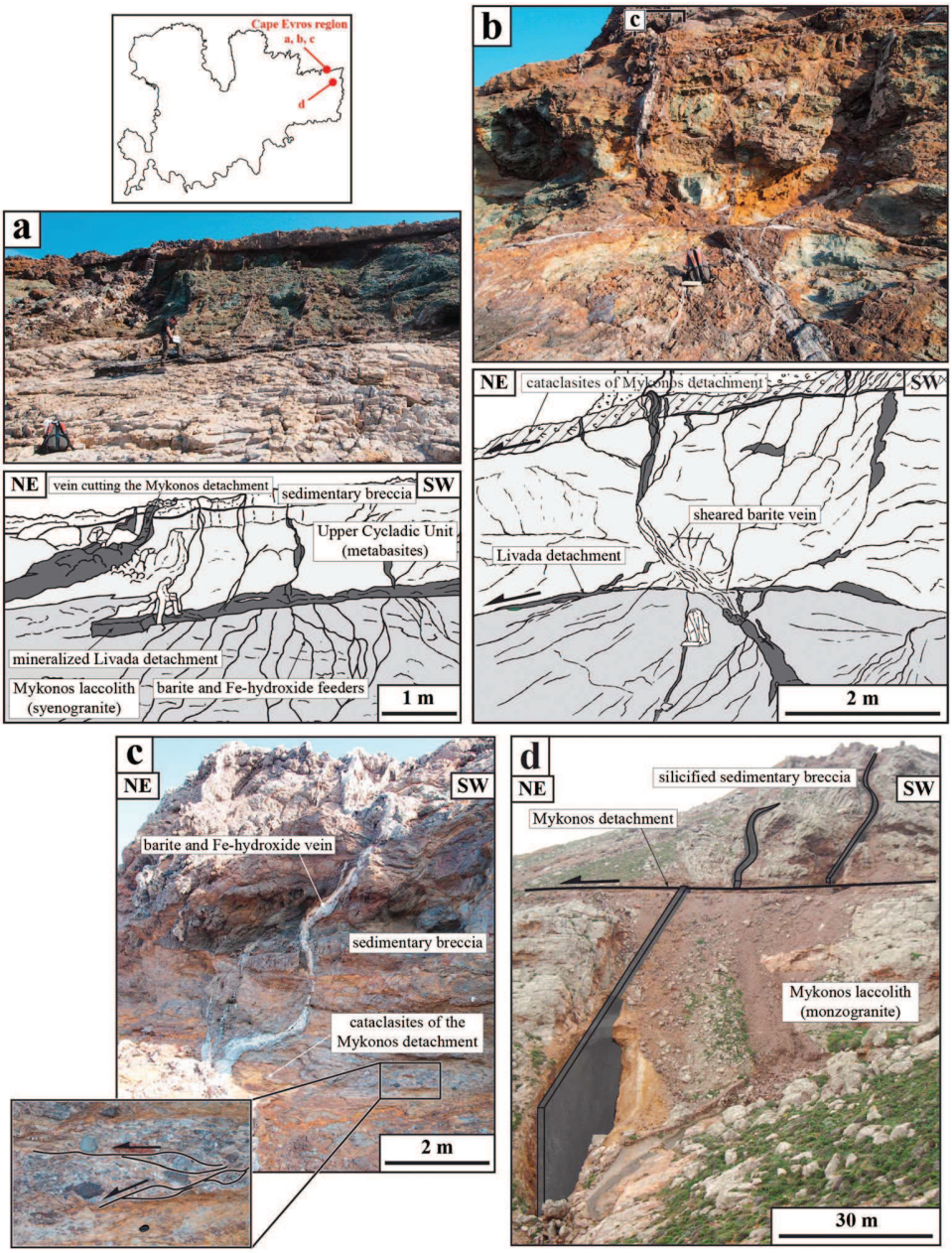

Figure 9. Relationships between veins and detachments. (a) Barite and Fe-hydroxide veins spreading out in the Livada detachment or crosscutting the Mykonos detachment. (b) Top-to-the-NE sheared vein in the Livada detachment. (c) Vein bent in the Mykonos detachment. (d) Exploited vein bent at mining-work scale. See also Figure 4.

5.3. Chronology of the Deformation

[30] As described above, the ductile deformation, observed in the laccolith and surrounding units, is characterized by an NE-shallow dipping foliation and an NE–SW mineral and stretching lineation associated with a top-to-the-NE kinematics (Figure 1b). The Livada detachment between the laccolith and the Upper Cycladic Unit also displayed a ductile activity with the development of top-to-the-NE ductile shear bands (Figure 6). As no significant post-slip tilt of these structures is observed [*Lecomte et al.*, 2010], this deformation is considered as purely extensional.

[31] Then, extensional brittle deformation developed with the reactivation of the Livada detachment and the inception of the Mykonos detachment as top-to-the-NE low-angle normal faults (Figures 3, 6, and 7). Syn-sedimentary NW–SE high-angle normal faults also formed, affecting the Upper Cycladic Unit and the Mykonos laccolith as well as the Miocene sediments. The first-order structure defines a tilted-block geometry compatible with the top-NE motion along the NCDS (Figures 3, 7, and 13a).

[32] Afterward, the low-angle normal faults were cut by strike-slip faults. This feature is particularly well exposed along the eastern coast of Cape Evros area, close to Pano Tigani

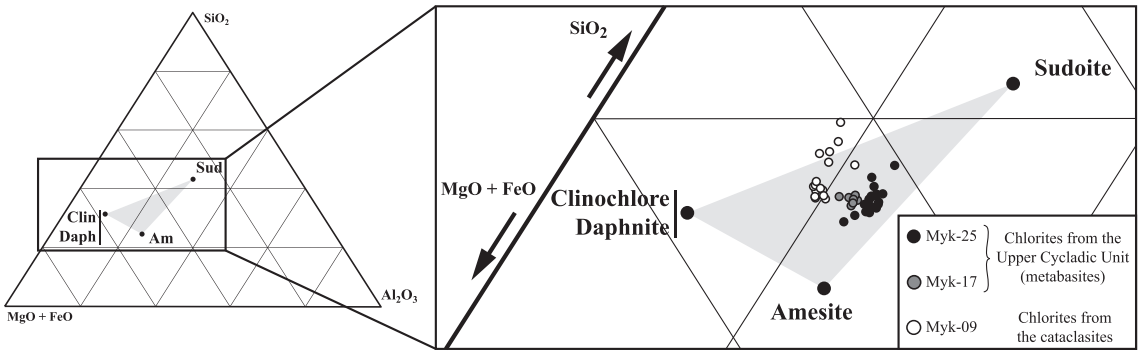

Figure 10. SiO_2-Al_2O_3-FeO + MgO diagram showing the chemical variations of the studied hydrothermal chlorites.

beach (Figure 12a). Indeed, on this outcrop, the Mykonos detachment is dissected by a set of conjugate strike-slip faults (Figures 12b and 12c) and displays a staircase morphology, resulting from a minor vertical component of the dominant left-lateral motion (Figure 12d). Fault planes are often mineralized with several strike-slip striae generations, associated with different pulses of hydrothermal mineral deposition (Figure 12c). These strike-slip faults both reactivated the NW–SE normal faults with a component of left-lateral slip (Figures 11c and 12c) or formed as new fault segments with NE–SW right-lateral slip component (Figure 11d). Moreover, field observations at Cape Evros show that individual faults display evidence for polyphase overprinting by strike-slip and dip-slip extensional kinematic indicators (Figure 11a). This succession indicates that extensional regime alternated with the strike-slip regime during this stage.

[33] The development of small-scale reverse faults (Figure 11b) is in agreement with a late reactivation of the detachments, highlighted on Pano Tigani outcrop. Indeed, the Mykonos detachment plane shows post-mineralization E–W- to NW–SE-trending reverse striae superimposed on the NE–SW extensional kinematic indicators (Figure 12e). In this case, strike-slip faults are also cut by the reworked detachment (Figure 12e).

6. Interpretations and Discussion

6.1. Interrelations and Timing of Mykonos Laccolith Emplacement, Extensional Structures, and Mineralization Deposition

[34] In this study, numerous features show a close linkage of the mineralization and extensional structures: (1) the massive concentration of mineralization in the vicinity of the Livada and Mykonos detachments (Figure 1) demonstrating the ability of these zones to channelize fluid flow as described by *Reynolds and Lister* [1987] in the Basin and Range province, (2) the NW–SE preferential orientation of veins (Figures 2 and 5) and their internal banded texture (Figure 8a) showing that the vein opening is primarily controlled by the NE–SW stretching of the crust, and (3) the different vein geometries (Figures 4 and 9) when these structures interact with the two branches of the NCDS, showing that the mineralization stage lasted during and partly after the extensional brittle activity of the Livada and Mykonos detachments. Indeed, the mineralized veins that are sheared with top-to-the-NE sense along the detachment are tectonically brecciated with angular fragments (Figures 8d and 9b) while other veins cut across these first-order structures (Figure 8a). Moreover, the apparent top-to-the-SW bent shape of many undeformed veins (Figures 9c and 9d) can support the syntectonic deposition of the mineralization. Indeed, one hypothesis to explain this phenomenon is to consider a rotation of principal stresses σ_1 and σ_3 within the detachment zone during its activity as suggested by *Lecomte et al*. [2011]. Thus, σ_1, vertical outside the fault zone, adopts a shallower attitude compatible with both the sense of slip along the fault and the opening of the veins [*Lecomte et al*. 2011, Figure 6]. Another hypothesis is to consider the detachment as a shear zone with a strong coaxial component. However, in this case, the mineralogical content of the vein would be deformed while those bent veins are undeformed (Figure 9c). Thus, according to the first hypothesis, a part of the mineralization occurred contemporaneous with the activity of the NCDS and therefore at the end of the emplacement and cooling of the Mykonos laccolith considering that veins cut the intrusion. The thickness of mineralized zone (i.e., the depth of influence of the veins below the detachments) can be estimated considering the westernmost limit of outcropping veins in Cape Evros and Cape Haros area (Figure 1b) and the shallow dip of the mylonitic foliation. Indeed, this foliation and the veins are all related to the detachments activity. Thus, considering the amount of eroded material, the dip of the foliation and detachments and the hor-

Table 1. Mean Chlorite Crystallization Temperatures Obtained With Different Chlorite Geothermometers[a]

Locality	T_1 (°C)	T_2 (°C)	T_3 (°C)
Myk-25 (Figure 5a)	251	260	282
Hydrothermally altered metabasites 20 analyses	(*17*)	(*10*)	(*17*)
Myk-17 (Figure 5a)	250	271	278
Hydrothermally altered metabasites 8 analyses	(*5*)	(*3*)	(*5*)
Myk-09 Figure 2b)	203	258	236
Hydrothermally altered cataclasites 16 analyses	(*32*)	(*17*)	(*32*)

[a]T_1: Al(IV) thermometer. T_2: VI(vac) thermometer [*Cathelineau and Nieva*, 1985]. T_3: Al(IV) and Fe/(Fe + Mg) thermometer [*Kranidiotis and MacLean*, 1987]. Standard deviation is indicated in italic.

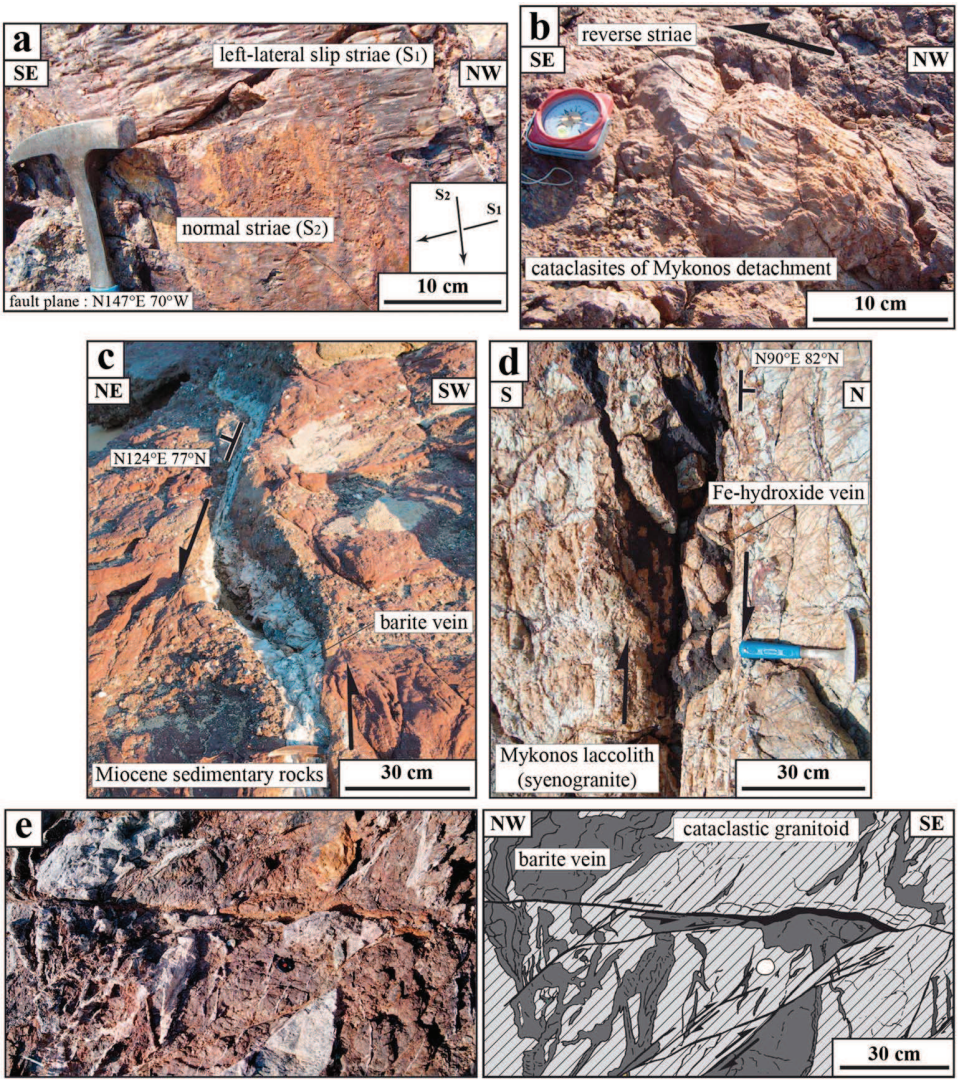

Figure 11. Deformation that affects the veins. (a) Mineralized fault plane showing a first left-lateral slip striae generation associated to quartz and a second normal one associated to Fe-hydroxides (Cape Evros area). (b) Indications for reverse kinematics on minor shallow-dipping fault planes (Cape Evros area). (c and d) Indications for strike-slip kinematics with left-lateral and right-lateral slip pull-aparts (Cape Evros and Panormos area). (e) Conjugate strike-slip faults system (Cape Evros area).

izontal distance to the westernmost vein, maximal depth can be crudely estimated to 700 m, measured perpendicular to the NCDS (Figure 1c).

[35] The emplacement at shallow depth of the hydrothermal mineralization suggested by *Skarpelis and Gilg* [2006] involves meteoric or connate fluids at near-hydrostatic pressure channeled by deviatoric stress-dependant open tensile fractures [*Reynolds and Lister*, 1987]. These conditions occur in the shallower segments of the detachment system above the ductile-brittle transition and are confirmed in our study by the preferential orientation of veins (Figures 2 and 5). Indeed, high fluid pressure that occurs below the ductile-brittle transition, where less-oxidized igneous-derived fluids dominate [*Reynolds and Lister*, 1987], would have preferentially induced a dispersion of vein orientations. Thus, when the laccolith crossed the ductile-brittle transition, an intense fracturing occurred favoring fluid-rock interactions within the pluton and the development of convection cells between the magmatic intrusion and the overlying basin. These modifications of the physico-chemical conditions of the hydrothermal fluids may finally result in a decreasing of metals solubility. Thus, the mineralizing episode probably occurred after this major change until shallow crustal levels. On the basis of variation of fluid inclusions composition, *Skarpelis and Gilg* [2006] have interpreted the veins and the brecciated mineral deposit as two different mineralizing stages. However, these fluid inclusions come from different mineral phases, and this variation is possibly a result of a late hydrothermal fluid modification due to a possible leakage of fluid in barite inclusions [*Skarpelis and Gilg*, 2006]. Thus, a single mineral deposition stage may also be envisaged notably due to the

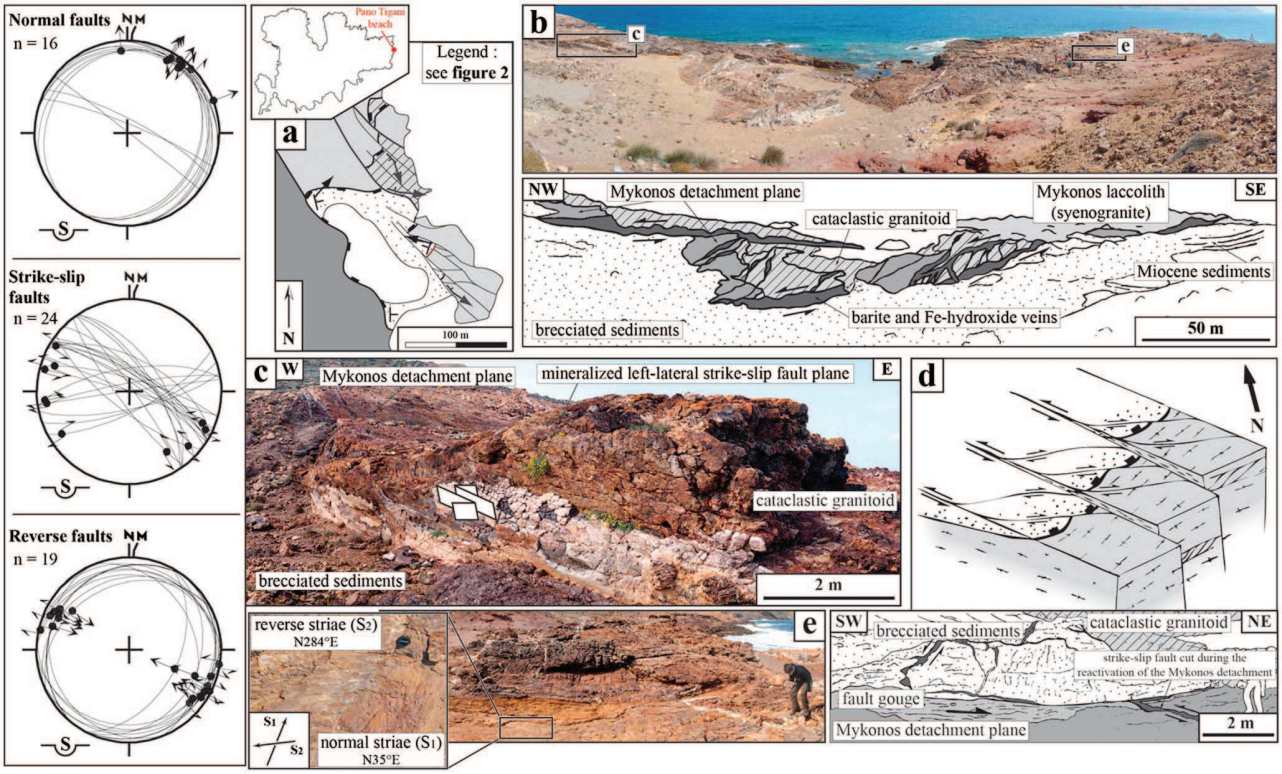

Figure 12. Deformation of the Mykonos detachment in Pano Tigani area. (a) Geological map of Pano Tigani area. (b) Panorama of Pano Tigani outcrop with the Mykonos detachment dissected by strike-slip faults. (c) Mineralized left-lateral slip fault plane dissecting the Mykonos detachment. (d) 3-D diagram synthesizing the brittle deformation observed on Pano Tigani area. (e) Barite vein with reverse striae spreads out in the Mykonos detachment plane. See Figure 2 for location and detailed legend.

similar mineral phases observed in the veins and in the mineralized breccia (i.e., succession of barite and quartz stages with possibly a replacement of barite by quartz; Figures 8c and 8e).

6.2. Age of the Mineralization Emplacement

[36] One of the available models for the formation of hydrothermal ore deposits in detachment zone involves convective fluid flow related to the cooling of a magmatic intrusion. Indeed, the pluton provides heat causing a local steepening of the geothermal gradient and that animates convection cells [*Reynolds and Lister*, 1987]. Using cooling curves of the laccolith in the footwall of the Mykonos detachment defined from a wide range of thermochronometric data [*Brichau et al.*, 2008], the age of barite veins deposition may be estimated assuming that the mineralizing fluids are in thermal equilibrium with the laccolith. Plotting the range of temperatures obtained above for the hydrothermal chlorite crystallization (i.e., 280 and 200°C; Table 1) on the time-temperature diagram (Figure 14), the emplacement age of the mineralization occurred in narrow range between 11 and 10 Ma. This temperature range is consistent with the closure temperature for zircon fission tracks at moderate-to-fast cooling rate (i.e., 280 ± 30°C), which besides fits well with the lower temperature bound of the ductile-brittle transition (Figure 14) [*Stöckhert et al.*, 1999]. Therefore, a similar ~11–10 Ma age may be proposed for the crossing of ductile-brittle transition by the Mykonos laccolith. This age must be considered as the oldest possible age of the mineralization emplacement if the wall rock is not hotter than the mineralizing fluids.

[37] This age is also consistent with (1) a part of the timing of the NCDS activity (14 to 10 Ma for the Livada detachment and 14 to 9 Ma for the Mykonos detachment) [*Brichau et al.*, 2008; *Jolivet et al.*, 2010] and therefore with the syntectonic nature of the mineral deposition and (2) with the timing of the sediments deposition. Indeed, the mineralization is not observed in the upper part of the sedimentary unit while sedimentation continued in the basin until a maximum age of 9–8 Ma, as attested by the 10 Ma old granitoid clasts observed on the top of the conglomeratic sequence [*Sánchez-Gómez et al.*, 2002].

6.3. Temporal Evolution of the Stress Regime

[38] On Mykonos island, previous studies have highlighted an evolution of the deformation, particularly within the Mykonos laccolith, with the development of first magmatic, then ductile and finally brittle extensional fabrics [*Faure and Bonneau*, 1988; *Lee and Lister*, 1992; *Lucas*, 1999; *Lecomte et al.*, 2010; *Denèle et al.*, 2011]. This study shows that final cooling of the Mykonos laccolith was characterized by a progressive change in stress regime contemporaneously with the mineral deposition 11–10 Ma ago (Figures 13a and 14).

[39] Based on these new structural observations, faults and/or veins systems have been systematically measured (Figures 2, 5, and 12). With the strike, dip, and striae data

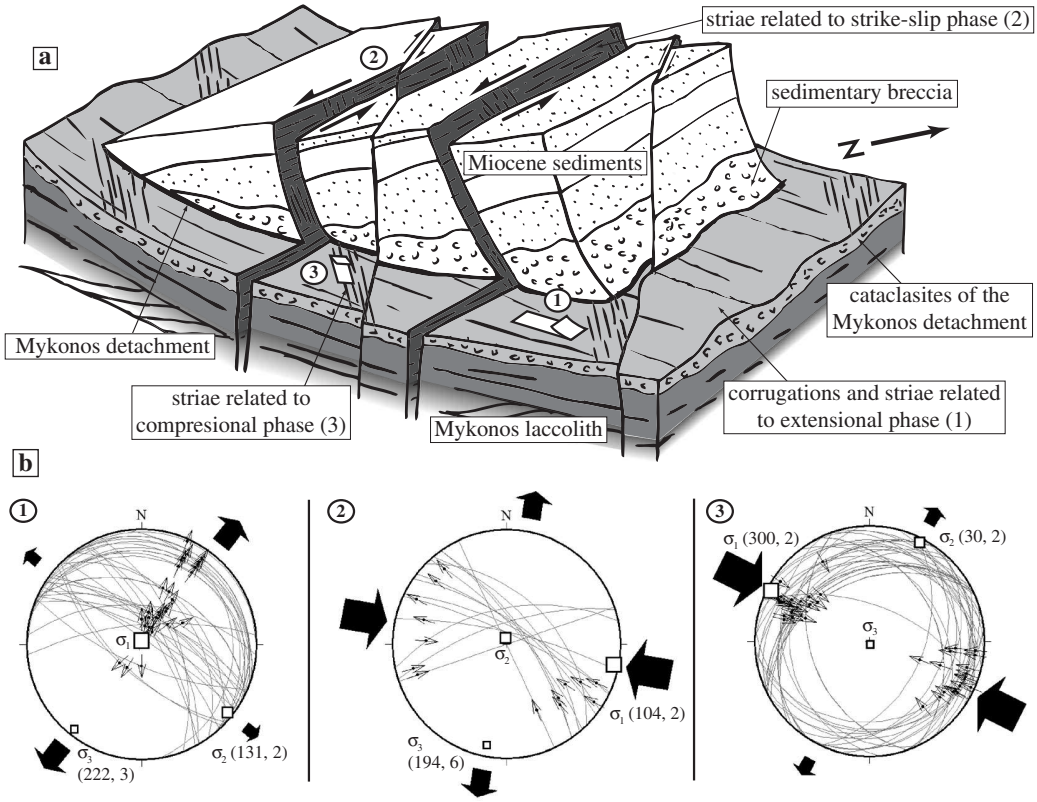

Fault system	n	σ_1		σ_2		σ_3		SDAM	Quality
		direction	dip	direction	dip	direction	dip		
normal	33	5	86	131	2	222	3	11 °	A
strike-slip	14	104	2	355	84	194	6	12 °	A
reverse	39	300	2	30	2	165	87	10 °	A

Figure 13. Evolution of the stress regime on Mykonos island. (a) 3-D diagram showing the ductile and brittle deformation related to the three successive stress regimes. (b1–b3) Palaeostresses results for normal, strike-slip, and reverse faults systems, respectively. Table shows detailed results of palaeostress study. n: number of structural data. SDAM: Standard Deviation of Angular Misfit. Quality A: well-defined palaeostresses.

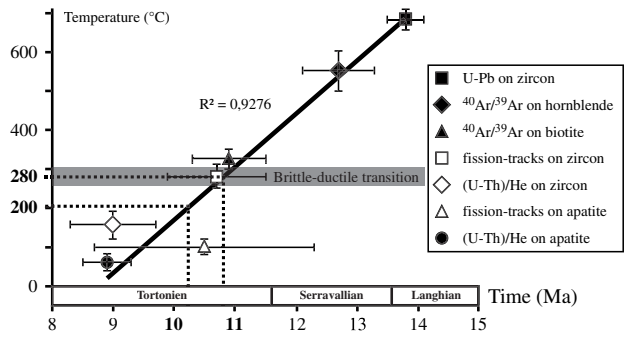

Figure 14. Time-temperature diagram showing the cooling curve of Mykonos laccolith in the footwall of the Mykonos detachment (modified from *Brichau et al*. [2008]). The error bars on both ages and temperatures are at 2σ. The inferred timing for chlorite crystallization is indicated. The temperature of the ductile-brittle transition is according to *Stöckhert et al*. [1999].

collected, we have isolated different sets of faults in order to define the palaeostress orientation patterns by computer-aided inversion method (*T-Tecto 3.0* software [*Žalohar and Vrabec*, 2007]) described in details by *Angelier* [1979, 1994]. Three successive stress tensors have been distinguished. For each of them, the observation that the principal stresses are close to theoretical directions (i.e., two horizontal principal stresses and one vertical one) and the standard deviation of angular misfit parameter (SDAM, equivalent to the ratio υ parameter of the direct inversion method [*Angelier*, 1994]) ensures the reliability of the result (Figure 13b).

[40] First, for the normal faults system with both detachment planes and steep normal faults that are oriented ~N110–140°E, the palaeostress analysis indicates a vertical σ_1 with σ_2 and σ_3 oriented N128°E and N219°E, respectively. Then, for the strike-slip faults system with two different orientations (~N80°E and ~N100–140°E) that correspond to right- and left-lateral strike-slip faults, respectively, the inversion reveals a stress regime characterized by a vertical σ_2 with σ_1 and σ_3

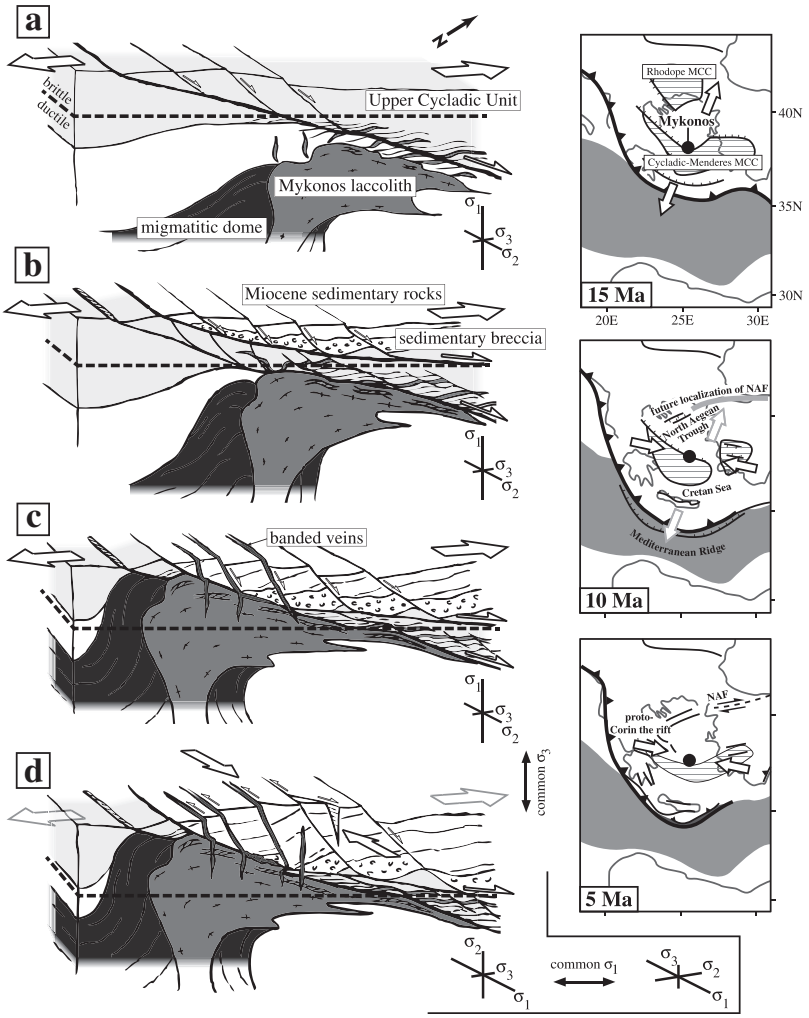

Figure 15. (a–d) 3-D views showing the structural evolution of Mykonos island during and after the activity of the detachments and the mineral deposition. The results of the successive stress regimes experienced by the region are also schematized (modified from *Jolivet and Brun* [2010]).

oriented N93°E and N191°E, respectively. It is noteworthy that the direction of the least principal stress axis is relatively similar to the one of the first normal faults system. Finally, the third faults system associated with E–W to NW–SE-trending reverse kinematic indicators consists in fault planes, sometimes the reworked detachment plane itself, with a wide range of orientation and a low dip. These structures are not compatible with the previous strike-slip and extensional stress regimes and another one is required. This third stress regime therefore shows a vertical σ_3, a σ_2 with a N27°E direction and σ_1 oriented N105°E close to the principal compressional stress axis of the strike-slip faults system.

[41] Integrating these data, we have isolated four to five main stages that characterized the tectonic evolution of Mykonos island.

[42] (1) The first ductile extensional stage is contemporaneous with the emplacement and cooling of the Mykonos laccolith as evidenced by the sub-solidus to post-solidus evolution of its deformation [*Faure and Bonneau*, 1988; *Faure et al*., 1991; *Denèle et al*., 2011] (Figure 15a). Consistent mineral and ductile fabric in the laccolith and in the migmatitic dome indicates that exhumation of these two units occurs under a NE–SW extensional regime and a top-to-the-NE shearing (Figures 1b and 15a), At this stage, the Livada detachment, that affects the Upper Cycladic Unit, had a ductile behavior with the development of top-to-the-NE ductile shear bands (Figure 6).

[43] (2) Then, exhumation of the Mykonos laccolith brought this magmatic body in contact with the Livada detachment (Figure 15b) inducing a reactivation of the initial intrusive contact in ductile conditions. In the footwall, NE-shallow dipping foliation with a top-to-the-NE stretching lineation and mylonitic to ultramylonitic shear bands developed therefore within the laccolith, consistently with the top-to-the-NE extensional stress regime (Figures 6c and 6d). The Upper Cycladic Unit and intruding aplitic sills and dykes in the hanging wall of the Livada detachment were also affected by the top-to-the-NE ductile fabric (Figures 6a and 6b). Structurally, above the Mykonos detachment was initiated under brittle conditions contemporaneously with the deposition of late Miocene syn-rift sediments (Figure 15b). This sedimentary unit was

cut by NW–SE steep normal faults, defining a tilted-block geometry (Figures , 3c, 7b, and 13a).

[44] (3) Then, the continuation of exhumation below the two branches of the NCDS of the Mykonos laccolith and the surrounding migmatitic dome was allowed for these two units to cross the ductile-brittle transition, some 11–10 Ma ago while the Livada detachment was reactivated under brittle conditions (Figure 15c). The Livada detachment is in place tectonically omitted due to intense normal faulting, and the cataclasites of the Mykonos detachment puts the late Miocene sediments in direct contact on top of the Mykonos laccolith (Figure 3). Contemporaneously, a series of sub-vertical banded veins develop during the activity of the detachments (Figures 9 and 15c). Hydrothermal fluids were thus mainly drained by tectonic structures like the NW–SE steep normal faults or the NCDS itself (Figure 4) where the mineralization can be striated with evidence of normal slip or brecciated (Figure 8d). Structural study of these brittle mineralized structures allows us to characterize this brittle extensional stage with a least principal stress (σ_3) oriented ~N40°E (Figure 13b) that supports the formation of banded veins in NW–SE opening fractures (i.e., as tension gashes).

[45] (4) Then, a strike-slip stress regime developed, characterized by a permutation of σ_1 and σ_2, whereas σ_3 kept a consistent N–S to NE–SW orientation (Figure 13b). The NW–SE steep normal faults and veins were thus reactivated as left-lateral strike-slip faults, and some ENE–WSW right-lateral conjugate ones formed (Figures 11 and 15d). Detachment planes were thus dissected by these strike-slip structures as in Pano Tigani area (Figure 12). Some of these strike-slip veins were reactivated as normal faults, suggesting an alternation of stress regime during a transition phase while the mineralization continued to emplace (Figure 11a). Considering that the mineral deposition is a short-lived event, this transition phase may occur quickly after 11–10 Ma.

[46] (5) Finally, a switch of σ_2 and σ_3 could induce a compressional regime with a σ_1 orientation close to N105°E and NE–SW least horizontal stress direction (σ_2) (Figures 13b and 15b). This stage would postdate the mineralization deposition and is characterized by newly formed small-scale reverse faults (Figure 11b) and by a slight local reactivation of the detachment planes with a reverse movement that can cut older strike-slip veins (Figure 12e). All of these structures show striae oriented ~N110°E.

[47] The succession of these different stages first suggests an evolution of a top-to-the-NE extensional deformation from ductile-to-brittle conditions. Then, a fast evolution of the brittle stress regime occurred during the emplacement of veins, 11–10 Ma ago, from a purely NE–SW extensional regime to a strike-slip and, finally, a possible late compressional one with the progressive development of an E–W to NW–SE compression and the persistence of an NE–SW least horizontal principal stress (Figure 13b). This orientation shows however a minor counterclockwise rotation of 10–15° between the extensional and the possible compressional stage that can be related to the rigid clockwise rotation of the Mykonos laccolith during its final cooling [*Morris and Anderson*, 1996; *Avigad et al*., 1998; *Lecomte et al*., 2010; *Denèle et al*., 2011].

[48] The finite strain amount is likely drastically different for each tectonic regime. The first stage is an extensional stage consistent with the Aegean post-orogenic extension, therefore lasted some 25 My at regional scale. It mostly corresponds to several tens of kilometers of slip along the NCDS while the strike-slip stage corresponds to decametric to metric offsets of the detachment and reworking of the normal faults and associated veins. The possible final compressional stage is only associated to striae on the detachment plane and small-scale reverse faults, and no significant offset is observed. The stress regime has thus changed, but the overall structure has not been significantly modified (Figures 13a and 15d). However, this fast and subtle tectonic evolution, occurring at least partially during the mineralization deposition, is essential regarding the late Cenozoic geodynamics of the Aegean region.

6.4. Implication of the Stress Regime Changes for Late Cenozoic Geodynamic Evolution of the Aegean Domain

[49] Evidence for a late E–W shortening has already been described elsewhere within the Cyclades and also farther to the east, in western Turkey [*Angelier*, 1976; *Buick*, 1991a;b; *Bozkurt and Park*, 1997; *Ring et al*., 1999; *Avigad et al*., 2001; *Bozkurt*, 2003]. Based on the existence of fold axes of various scales parallel to the stretching direction in the central and northern Cyclades, *Buick* [1991a; 1991b] and *Avigad et al*. [2001] proposed that the NE–SW extension that has prevailed in the Aegean since the late Oligocene was associated with a component of E–W shortening. *Avigad et al*. [2001] even concluded that during this period, the Aegean crust did not undergo significant thinning due to the combined effects of NE–SW stretching and E–W shortening. Some of these folds can be interpreted differently, as "a-type" folds parallel to the transport direction [*Jolivet et al*., 2004]. However, the late folding of the detachment, seen in Naxos, for instance [*Avigad et al*., 2001], and also the folding of mylonitic foliation in the Menderes massif [*Bozkurt and Park*, 1997], rather suggest a recent component of E–W shortening. Moreover, on the island of Samos in the eastern part of the Aegean Sea and also in the Menderes massif, the deformation of the Miocene–Pliocene sedimentary basins is notably characterized by a short E–W compressional event accompanied by a significant uplift [*Angelier*, 1976; *Ring et al*., 1999; *Bozkurt*, 2003]. The age of this event settled at 9–8.6 Ma [*Weidmann et al*., 1984; *Ring et al*., 1999], that is compatible with our estimation of the timing of the stress regime change on Mykonos island (Figure 14). Thus, although these features indicating a late compressional regime are not well expressed on Mykonos, the presence of contemporaneous compressional structures elsewhere in the region leads us to correlate the reworking of the Mykonos detachment and the development of small-scale reverse faults as a result of this late compressional event.

[50] The question then is the cause of this E–W shortening.

[51] One may argue, as *Sengör and Bozkurt* [2013], that such minor compressional structures could be part of the overall extensional activity of the detachment, but in the case of Mykonos, the compressional features clearly postdate both extensional and strike-slip structures.

[52] One other aspect to consider is the role of the gravitational forces [*Molnar and Lyon-Caen*, 1988; *Vanderhaeghe*, 2012]. Indeed, in their analog experiments, *Gautier et al*. [1999] show that transverse shortening during horizontal spreading of a thick continental lithosphere may develop as a

result of pure gravity spreading, associated with a pattern of faults and rotations. However, the stress regime change on Mykonos island occurred during the deposition of Mykonos mineralization in the early Tortonian (i.e., 11–10 Ma ago) at the earliest (Figure 14). This age is late compared to the timing of the post-orogenic extension in the Aegean domain that started some 35 Ma ago [*Jolivet and Faccenna*, 2000] indicating that the crust was already thinned in the early Tortonian. Therefore, body forces were probably insufficient to explain such stress regime evolution by itself.

[53] Another hypothesis to consider is the influence of exhumation processes on the evolution of stress regime. Indeed, in an extensional context, rock exhumation and crustal thinning are associated with a diminution of the vertical σ_1. If this trend continues, a switch of σ_1 and σ_2 can occur and therefore a strike-slip faults system can develop under brittle conditions. However, this process cannot explain the relatively important offset of the detachment due to the strike-slip stage as well as the late compressional event. Other causes for this evolution of the stress regime have to be considered.

[54] Nowadays, a component of E–W shortening is present in the deformation of the northern Aegean as shown by the GPS data [*Le Pichon and Kreemer*, 2010]. It is due to the westward motion of Anatolia along the North Anatolian Fault. If the NAF has reached the northern Aegean (Dardanelles Strait) some 6 Ma ago as a localized discontinuity [*Armijo et al*., 1999; *Melinte-Dobrinescu et al*., 2009], *Şengör et al*. [2005] proposed that the dextral shear has been active in northern Anatolia since some 13–11 Ma, a timing compatible with our observations on Mykonos (Figures 14 and 15) and also with the late folding of the detachment in Naxos [*Avigad et al*., 2001] and the ~9 Ma E–W compressional event in Samos [*Ring et al*., 1999]. *Faccenna et al*. [2006] further proposed that the westward motion of Anatolia was triggered, at least partly, by a slab detachment event below eastern Turkey, an event that can be related to a surge of volcanism in this region some 10 Ma ago [*Sengör et al*., 2008; *Pearce et al*., 1990]. Here also, the timing of this event is compatible with the late compressional deformation recorded on Mykonos.

7. Conclusion

[55] Our field observations show that mineralization on Mykonos island mainly corresponds to sub-vertical NW–SE extensional veins, developed essentially during the activity of the Livada and Mykonos detachments some 11–10 Ma ago. The veins emplaced shortly after the crossing of the ductile-brittle transition and up to shallow crustal levels during the latest cooling increments of the Mykonos laccolith. This hydrothermal mineralization then shows a clear temporal and kinematics relation with the NE–SW Aegean extensional dynamics.

[56] Finally, this study leads to highlight a change of stress directions during the deposition of the mineralization. Indeed, from purely extensional, the stress regime becomes progressively more compressional with the development of strike-slip faults reactivating some of the veins and even small-scale reverse faults. During this period, the least horizontal stress was consistently oriented NE–SW. The increase of the E–W compressional component from 11–10 Ma ago is probably a consequence of the inception of the westward motion of Anatolia some 4 Ma before the propagation of the NAF in the Aegean domain and the localization of extension on the Aegean Sea margins.

[57] **Acknowledgments.** The authors wish to express their thanks to Olivier Vanderhaeghe, Erdin Bozkurt, and an anonymous reviewer for their constructive comments.

[58] This study was funded by the Institut Universitaire de France and partly by the ERC Advanced Research Grant RHEOLITH.

References

Altherr, R., H. Kreuzer, I. Wendt, H. Lenz, G. A. Wagner, J. Keller, W. Harre, and A. Hohndorf (1982), A Late Oligocene/Early Miocene high temperature belt in the anti-cycladic crystalline complex (SE Pelagonian, Greece), *Geol. Jb.*, *23*, 97–164.

Altherr, R., and W. Siebel (2002), I-type plutonism in a continental back-arc setting: Miocene granitoids and monzonites from the central Aegean Sea, Greece, *Contrib. Mineral. Petrol.*, *143*, 397–415.

Angelier, J. (1976), Sur l'alternance moi-plio-quaternaire de mouvements extensifs et compressifs en Égée orientale: l'île de Samos (Grèce), *C. R. Acad. Sci. Paris*, *283*, 463–466.

Angelier, J. (1979), Determination of the mean principal directions of stress for a given fault population, *Tectonophysics*, *56*, 17–26.

Angelier, J. (1994), Paleostress determinations, in *Continental Deformations*, edited by P. L. Hancock, Pergamon Press, Tarrytown, N.Y., 53–100.

Armijo, R., B. Meyer, G. C. P. King, A. Rigo, and D. Papanastassiou (1996), Quaternary evolution of the Corinth Rift and its implications for the Late Cenozoic evolution of the Aegean, *Int. J. Geophys.*, *126*, 11–53.

Armijo, R., B. Meyer, A. Hubert, and A. Barka (1999), Westward propagation of the north Anatolian into the northern Aegean: Timing and kinematics, *Geology*, *27*(3), 267–270.

Avigad, D., G. Baer, and A. Heimann (1998), Block rotations and continental extension in the central Aegean Sea: palaeomagnetic and structural evidence from Tinos and Mykonos, *Earth Planet. Sci. Lett.*, *157*, 23–40.

Avigad, D., A. Ziv, and Z. Garfunkel (2001), Ductile and brittle shortening, extension-parallel folds and maintenance of crustal thickness in the Central Aegean, *Tectonics*, *20*(2), 277–287.

Bonneau, M., and J. R. Kienast (1982), Subduction, collision et schistes bleus: Exemple de l'Egée, Grèce, *Bull. Soc. géol. France*, *7*, 785–791.

Bozkurt, E., and R. G. Park (1997), Evolution of a mid-Tertiary extensional shear zone in the Southern Menderes Massif, western Turkey, *Bull. Soc. géol. France*, *168*, 3–14.

Bozkurt, E. (2003), Origin of NE-trending basins in Western Turkey, *Geodinamica Acta*, *16*, 61–81.

Brichau, S., U. Ring, R. A. Ketcham, A. Carter, D. Stockli, and M. Brunel (2006), Constraining the long-term evolution of the slip rate for a major extensional fault system in the central Aegean, Greece, using thermochronology, *Earth Planet. Sci. Lett*, *241*, 293–306.

Brichau, S., U. Ring, A. Carter, P. Monie, R. Bolhar, D. Stockli, and M. Brunel (2007), Extensional faulting on Tinos Island, Aegean Sea, Greece: How many detachments?, *Tectonics*, *26*, TC4009, doi:10.1029/2006TC001969.

Brichau, S., U. Ring, A. Carter, R. Bolhar, P. Monié, D. Stockli, and M. Brunel (2008), Timing, slip rate, displacement and cooling history of the Mykonos detachment footwall, Cyclades, Greece, and implications for the opening of the Aegean Sea basin, *J. Geol. Soc. London*, *165*, 263–277.

Brichau, S., S. Thomson, and U. Ring (2010), Thermochronometric constraints on the tectonic evolution of the Serifos detachment, Aegean Sea, Greece, *Int J Earth Sci. (Geol Rundsch)*, *99*, 379–393, doi:10.1007/s00531-00008-00386-00530.

Brun, J. P., and C. Faccenna (2008), Exhumation of high-pressure rocks driven by slab rollback, *Earth Planet. Sci. Lett.*, *272*, 1–7, doi:10.1016/j.epsl.2008.1002.1038.

Buick, I. S. (1991a), Mylonite fabric development on Naxos, Greece, *J. Struct. Geol.*, *13*(6), 643–655.

Buick, I. S. (1991b), The late Alpine evolution of an extensional shear zone, Naxos, Greece, *J. Geol. Soc. London*, *148*, 93–103;

Cathelineau, M., and D. Nieva (1985), A chlorite solid solution geothermometer. The Los Azufres (Mexico) geothermal system, *Contrib. Mineral. Petrol.*, *91*, 235–244.

Cathelineau, M. (1988), Cation site occupancy in chlorites and illites as a function of temperature, *Clay Miner.*, *23*, 471–485.

de Boorder, H., W. Spakman, S. H. White, and M. J. R. Wortel (1998), Late Cenozoic mineralization, orogenic collapse and slab detachment in the European Alpine Belt, *Earth Planet. Sci. Lett.*, *164*, 569–575.

Denèle, Y., E. Lecomte, L. Jolivet, O. Lacombe, L. Labrousse, B. Huet, and L. Le Pourhiet (2011), Granite intrusion in a metamorphic core complex:

The example of the Mykonos laccolith (Cyclades, Greece), *Tectonophysics*, *501*, 52–70, doi:10.1016/j.tecto.2011.1001.1013.
Dercourt, J., et al. (1986), Geological evolution of the Tethys belt from the Atlantic to the Pamir since the Lias, *Tectonophysics*, *123*, 241–315.
Dercourt, J., L. E. Ricou, and B. Vrielinck. (1993), *Atlas Tethys Palaeo environmental maps*, 307 p. pp., Gauthier-Villars, Paris.
Duchêne, S., R. Aïssa, and O. Vanderhaeghe (2006), Pressure-temperature-time evolution of metamorphic rocks from Naxos (Cyclades, Greece): Constraints from thermobarometry and Rb/Sr dating, *Geodinamica Acta*, *19*(5), 299–319.
Faccenna, C., O. Bellier, J. Martinod, C. Piromallo, and V. Regard (2006), Slab detachment beneath eastern Anatolia: A possible cause for the formation of the North Anatolian fault, *Earth Planet. Sci. Lett.*, *242*, 85–97.
Faure, M., and M. Bonneau (1988), Données nouvelles sur l'extension néogène de l'Egée: La déformation ductile du granite miocène de Mykonos (Cyclades, Grèce), *C. R. Acad. Sci. Paris*, *307*, 1553–1559.
Faure, M., M. Bonneau, and J. Pons (1991), Ductile deformation and syntectonic granite emplacement during the late Miocene extension of the Aegean (Greece), *Bull. Soc. géol. France*, *162*, 3–12.
Gautier, P., and J. P. Brun (1994a), Crustal-scale geometry and kinematics of late-orogenic extension in the central Aegean (Cyclades and Evvia island), *Tectonophysics*, *238*, 399–424.
Gautier, P., and J. P. Brun (1994b), Ductile crust exhumation and extensional detachments in the central Aegean (Cyclades and Evvia islands), *Geodinamica Acta*, *7*(2), 57–85.
Gautier, P., J. P. Brun, R. Moriceau, D. Sokoutis, J. Martinod, and L. Jolivet (1999), Timing, kinematics and cause of Aegean extension: A scenario based on a comparison with simple analogue experiments, *Tectonophysics*, *315*, 31–72.
Govers, R., and M. J. R. Wortel (2005), Lithosphere tearing at STEP faults: Response to edges of subduction zones, *Earth Planet. Sci. Lett.*, *236* 505–523.
Grasemann, B., D. A. Schneider, D. F. Stockli, and C. Iglseder (2012), Miocene bivergent crustal extension in the Aegean: Evidence from the western Cyclades (Greece), *Lithosphere*, doi:10.1130/L1164.1131.
Huet, B., L. Labrousse, and L. Jolivet (2009), Thrust or detachment? Exhumation processes in the Aegean: Insight from a field study on Ios (Cyclades, Greece), *Tectonics*, *28*, TC3007, doi:10.1029/2008TC002397.
Jiang, W.-T., D. R. Peacor, and P. R. Buseck (1994), Chlorite geothermomery?–Contamination and apparent octahedral vacancies, *Clays Clay Miner.*, *42*(5), 593–605.
Jolivet, L., J. P. Brun, P. Gautier, S. Lallemant, and M. Patriat (1994), 3-D kinematics of extension in the Aegean from the Early Miocene to the Present, insight from the ductile crust, *Bull. Soc. géol. France*, *165*, 195–209.
Jolivet, L., and M. Patriat (1999), Ductile extension and the formation of the Aegean Sea, in *The Mediterranean Basins: Tertiary Extension within the Alpine Orogen*, edited by B. Durand, L. Jolivet, F. Horváth, and M. Séranne, , *156*, 427–456, Spe. Pub. – Geol. Soc. London.
Jolivet, L., and C. Faccenna (2000), Mediterranean extension and the Africa-Eurasia collision, *Tectonics*, *19*(6), 1095–1106.
Jolivet, L. (2001), A comparison of geodetic and finite strain pattern in the Aegean, geodynamic implications, *Earth Planet. Sci. Lett.*, *5793*, 1–10.
Jolivet, L., C. Faccenna, B. Goffé, E. Burov, and P. Agard (2003), Subduction tectonics and exhumation of high-pressure metamorphic rocks in the Mediterranean orogens, *Am. J. Sci.*, *303*, 353–409.
Jolivet, L., V. Famin, C. Mehl, T. Parra, C. Aubourg, R.Hébert, and P. Philippot (2004), Strain localization during crustal-scale boudinage to form extensional metamorphic domes in the Aegean Sea, *Spe. Pap. – Geol. Soc. Am.*, *380*, 185–210.
Jolivet, L., and J. P. Brun (2010), Cenozoic geodynamic evolution of the Aegean region, *Int. J. Earth Sci.*, *99*, 109–138, doi:10.1007/s00531-00008-00366-00534.
Jolivet, L., E. Lecomte, B. Huet, Y. Denèle, O. Lacombe, L. Labrousse, L. Le Pourhiet, and C. Mehl (2010), The north cycladic detachment system, *Earth Planet. Sci. Lett.*, *289*, 87–104, doi:10.1016/j.epsl.2009.1010.1032.
Keiter, M., K. Piepjohn, C. Ballhaus, M Lagos, and M Bode (2004), Structural development of high-pressure metamorphic rocks on Syros island (Cyclades, Greece), *J. Struct. Geol.*, *26*, 1433–1445.
Kranidiotis, P., and W. H. MacLean (1987), Systematics of chlorite alteration at the Phelps Dodge massive sulfide deposit, Matagami, Quebec, *Econ. Geol.*, *82*(7), 1898–1911, doi:10.2113/gsecongeo.82.7.1898.
Kumerics, C., U. Ring, S. Brichau, J. Glodny, and P. Monié (2005), The extensional Messaria shear zone and associated brittle detachment faults, Aegean Sea, Greece, *J. Geol. Soc.*, *162*(4), 701–721.
Le Pichon, X., and J. Angelier (1979), The Hellenic arc and trench system: A key to the neotectonic evolution of the eastern Mediterranean area, *Tectonophysics*, *60*, 1–42.
Le Pichon, X., and C. Kreemer (2010), The Miocene-to-present kinematic evolution of the Eastern Mediterranean and Middle East and its implications for dynamics, *Annu. Rev. Earth Planet. Sci.*, *38*, 323–351, doi:10.1146/annurev-earth-040809-152419.
Lecomte, E., L. Jolivet, O. Lacombe, Y. Denèle, L. Labrousse, and L. Le Pourhiet (2010), Geometry and kinematics of a low-angle normal fault on Mykonos island (Cyclades, Greece): Evidence for slip at shallow dip, *Tectonics*, *29*, TC5012, doi:10.1029/2009TC002564.
Lecomte, E., L. Le Pourhiet, O. Lacombe, and L. Jolivet (2011), A continuum mechanics approach to quantify brittle strain on weak faults: application to the extensional reactivation of shallow dipping discontinuities, *Int. J. Geophys.*, *184*, 1–11.
Lee, J., and G. S. Lister (1992), Late Miocene ductile extension and detachment faulting, Mykonos, Greece, *Geology*, *20*, 121–124.
Lister, G. S., G. Banga, and A. Feenstra (1984), Metamorphic core complexes of cordilleran type in the Cyclades, Aegean Sea, Greece, *Geology*, *12*, 221–225.
Lucas, I. (1999), *Le pluton de Mykonos-Delos-Rhenee (Cyclades, Grèce): Un exemple de mise en place synchrone de l'extension crustale, 491 pp*, Université d'orléans, Orléans.
Martin, L., S. Duchêne, E. Deloule, and O. Vanderhaeghe (2006), The isotopic composition of zircon and garnet: A record of the metamorphic history of Naxos, Greece, *Lithos*, *87*, 174–192.
Mehl, C., L. Jolivet, and O. Lacombe (2005), From ductile to brittle: evolution and localization of deformation below a crustal detachment (Tinos, Cyclades, Greece), *Tectonics*, *24*, TC4017, doi:10.1029/2004TC001767.
Melinte-Dobrinescu, M. C., et al. (2009), The Messinian salinity crisis in the Dardanelles region: Chronostratigraphic constraints, *Palaeogeogr. Palaeoclimatol. Palaeoecol.*, *278*, 24–39, doi:10.1016/j.palaeo.2009.1004.1009.
Molnar, P., and H. Lyon-Caen (1988), Some simple physical aspects of the support, structure, and evolution of mountain belts, *Spe. Pap. – Geol. Soc. Am.*, *218*, 179–207.
Morris, A., and M. Anderson (1996), First paleomagnetic results from the Cycladic Massif, Greece, and their implications for Miocene extension directions and tectonic models in the Aegean, *Earth Planet. Sci. Lett.*, *142*, 397–408.
Pearce, J. A., J. F. Bender, S. E. Delong, W. S. F. Kidd, P. J. Low, Y. Guner, F. Saroglu, Y. Yilmaz, S. Moorbath, and J. G. Mitchell (1990), Genesis of collision volcanism in eastern Anatolia, Turkey, *J. Volcanol. Geotherm. Res.*, *44*, 189–229.
Pe-Piper, G., and D. J. W. Piper (2002), The igneous rocks of Greece. The anatomy of an orogen, 573 pp., Gebrüder Borntraeger, Berlin-Stuttgart.
Pe-Piper, G., and D. J. W. Piper (2006), Unique features of the Cenozoic igneous rocks of Greece, in *Postcollisional Tectonics and Magmatism in the Mediterranean Region and Asia*, edited by Y. Dilek and S. Pavlides, pp. 259–282,doi: 10.1130/2006.2409(1114), Geol. Soc. of Am., Boulder, Colo.
Philippon, M., J. P. Brun, and F. Gueydan (2011), Tectonics of Syros Island Blueschists (Cyclades, Greece): From subduction to Aegean extension, *Tectonics*, *30*, TC4001, doi:10.1029/2010TC002810.
Reilinger, R. E., S. C. McClusky, M. B. Oral, R. W. King, M. N. Tokzoz, A. A. Barka, I. Kinik, O. Lenk, and I. Sanli (1997), Global positioning system measurements of present-day crustal movements in the Arabia-Africa-Eurasia plate collision zone, *J. Geophys. Res.*, *102*, 9983–9999.
Reilinger, R., S. McClusky, D. Paradissis, S. Ergintav, and P. Vernant (2010), Geodetic constraints on the tectonic evolution of the Aegean region and strain accumulation along the Hellenic subduction zone, *Tectonophysics*, *488*, 22–30.
Reynolds, S. J., and G. S. Lister (1987), Structural aspects of fluid-rock interactions in detachment zones, *Geology*, *15*, 362–366.
Ring, U., S. Laws, and M. Bernet (1999), Structural analysis of a complex nappe sequence and late-orogenic basins from the Aegean Island of Samos, Greece, *J. Struct. Geol.*, *21*, 1575–1601.
Ring, U., and P. W. Layer (2003), High-pressure metamorphism in the Aegean, eastern Mediterranean: Underplating and exhumation from the Late Cretaceous until the Miocene to recent above the retreating Hellenic subduction zone, *Tectonics*, *22*(3), 1022, doi:10.1029/2001TC001350.
Ring, U., T. Will, J. Glodny, C. Kumerics, K. Gessner, S. Thomson, T. Güngör, P. Monie, M. Okrusch, and K. Drüppel (2007), Early exhumation of high-pressure rocks in extrusion wedges: Cycladic blueschist unit in the eastern Aegean, Greece, and Turkey, *Tectonics*, *26*, TC2001, doi:10.1029/2005TC001872.
Ring, U., J. Glodny, T. Will, and S. Thomson (2010), The Hellenic subduction system: High-pressure metamorphism, exhumation, normal faulting, and large-scale extension, *Annu. Rev. Earth Planet. Sci.*, *38*, 45–76, doi:10.1146/annurev.earth.050708.170910.
Royden, L. H., and D. J. Papanikolaou (2011), Slab segmentation and late Cenozoic disruption of the Hellenic arc, *Geochem. Geophys. Geosyst.*, *12*, Q03010, doi:10.1029/2010GC003280.
Sánchez-Gómez, M., D. Avigad, and A. Heiman (2002), Geochronology of clasts in allochthonous Miocene sedimentary sequences on Mykonos and

Paros islands: Implications for back-arc extension in the Aegean Sea, *J. Geol. Soc. London*, *159*, 45–60.

Sengör, A. M. C., O. Tüysüz, C. Imren, M. Sakınç, H. Eyidogan, N. Görür, X. Le Pichon, and C. Rangin (2005), The North Anatolian fault: A new look, *Annu. Rev. Earth Planet. Sci.* , *33*, 37–112, doi:10.1146/annurev.earth.32.101802.120415.

Sengör, A. M. C., M. S. Özeren, M. Keskin, M. Sakinç, A. D. Özbakir, and I. Kayan (2008), Eastern Turkish high plateau as a small Turkic-type orogen: Implications for post-collisional crust-forming processes in Turkic-type orogens, *Earth-Sci. Rev.*, *90*, 1–48.

Sengör, A. M. C., and E. Bozkurt (2013), Layer-parallel shortening and related structures in zones undergoing active regional horizontal extension, *Int. J. Earth Sci.*, *102*, 101–119.

Skarpelis, N. (2002), Geodynamics and evolution of the Miocene mineralization in the Cycladic-Pelagonian belt, Hellenides, *Bull. Geol. Soc. Greece*, *XXXIV*(6), 2191–2206.

Skarpelis, N., and H. A. Gilg (2006), Miocene extensional fault-controlled mineralization in the central Aegean (Mykonos, Cyclades): Deposition from a two-stage hydrothermal system?, *NECAM 2006*, International Conference, Milos.

Stampfli, G. M. (2000), Tethyan oceans, *Spec. Pub. - Geol. Soc. London*, *173*, 1–23.

Stöckhert, B., M. R. Brix, R. Kleinschrodt, A. J. Hurford, and R. Wirth (1999), Thermochronometry and microstructures of quartz–a comparison with experimental flow laws and predictions on the temperature of the brittle-plastic transition, *J. Struct. Geol.*, *21*(3), 351–369.

Stouraiti, C., P. Mitropoulos, J. Tarney, B. Barreiro, A. M. McGrath, and E. Baltatzis (2010), Geochemistry and petrogenesis of late Miocene granitoids, Cyclades, southern Aegean: Nature of source components, *Lithos*, *114*, 337–352, doi:10.1016/j.lithos.2009.09.010.

Trotet, F., L. Jolivet, and O. Vidal (2001), Tectono-metamorphic evolution of Syros and Sifnos islands (Cyclades, Greece), *Tectonophysics*, *338*, 179–206.

Vanderhaeghe, O. (2004), Structural development of the Naxos migmatite dome, *Spe. Pap. – Geol. Soc. Am.*, *380*, 211–227.

Vanderhaeghe, O. (2012), The thermal-mechanical evolution of crustal orogenic belts at convergent plate boundaries: A reappraisal of the orogenic cycle, *J. Geodyn.*, *56–57*, 124–145.

van Hinsbergen, D. J. J., W. J. Zachariasse, M J. R. Wortel, and J. E. Meulenkamp (2005), Underthrusting and exhumation: A comparison between the external Hellenides and the "hot" Cycladic and "cold" South Aegean core complexes (Greece), *Tectonics*, *24*, TC2011, doi:10.1029/2004TC001692.

Vidal, O., T. Parra, and F. Trotet (2001), A thermodynamic model for Fe-Mg aluminous chlorite using data from phase equilibrium experiments and natural pelitic assemblages in the 100° to 600°C, 1 to 25 kb range, *Am. J. Sci.*, *301*, 557–592.

Walcott, C. R., and S. H. White (1998), Constraints on the kinematics of post-orogenic extension imposed by stretching lineations in the Aegean region, *Tectonophysics*, *298*, 155–175.

Walshe, J. L. (1986), A six-component chlorite solid solution model and the conditions of chlorite formation in hydrothermal and geothermal systems, *Econ. Geol.*, *81*(3), 681–703, doi:10.2113/gsecongeo.81.3.681.

Weidmann, M., N. Solounias, R. E. Drake, and G. H. Curtis (1984), Neogene stratigraphy of the eastern basin, Samos island, Greece, *Geobios*, *17*(4), 477–490.

Wijbrans, J. R., and I. McDougall (1986), 40Ar/39Ar dating of white micas from an alpine high-pressure metamorphic belt on Naxos (Greece); the resetting of the argon isotopic system, *Contrib. Mineral. Petrol.*, *93*, 187–194.

Wijbrans, J. R., and I. McDougall (1988), Metamorphic evolution of the Attic Cycladic metamorphic belt on Naxos (Cyclades, Greece) utilizing $^{40}Ar/^{39}Ar$ age spectrum measurements, *J. Metamorph. Geol.*, *6*, 571–594.

Žalohar, J., and M. Vrabec (2007), Paleostress analysis of heterogeneous fault-slip data: The Gauss method, *J. Struct. Geol.*, *29*, 1798–1810.

Chapitre 5

Contrôle mantellique et crustal sur la genèse du magmatisme : approche numérique

3D numerical assessments for mantle flow and magma genesis in laterally constrained subduction zones: the eastern Mediterranean case

(article qui sera soumis au journal *Earth and Planetary Science Letters*)

5.1. Abstract 204
5.2. Introduction 205
5.3. Late Cenozoic evolution of the eastern Mediterranean subduction zone 206
5.4. Numerical modeling 209
5.4.1. Modeling approach and setup 209
5.4.2. Parametric study on rheological implications in natural subduction context 213
5.5. Results 214
5.5.1. Asthenospheric vs. lithospheric flow pattern 215
5.5.2. Genesis and transport of partially molten material 220
5.6. Discussion 225
5.6.1. Magmatism and mantle flow 225
5.6.2. Magmatism and lithospheric deformation 228
5.6.3. Implications for the eastern Mediterranean region 229
5.7. Conclusion 232

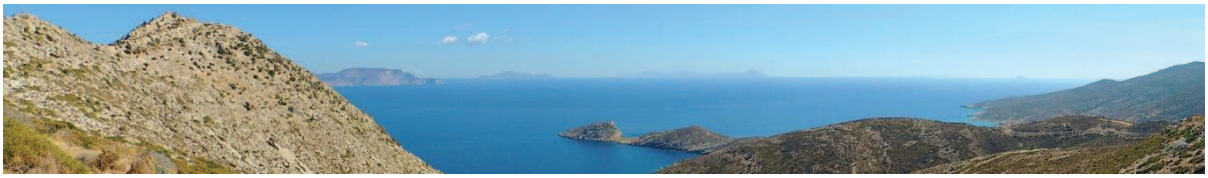

Dans les chapitres précédents, je mets en évidence les liens entre l'évolution de la zone de subduction est-Méditerranéenne depuis le Crétacé supérieur et la distribution du magmatisme et des gîtes minéralisés. Ce travail m'a ainsi permis de proposer un modèle évolutif conceptuel de cette région (en 2D et en 3D) qui montre l'importance des processus profonds (ex. retrait et déchirure du panneau plongeant, flux asthénosphériques associés) sur la mise en place de ces systèmes magmatiques et hydrothermaux enrichis en cuivre ou en or (cf. *Chapitre 3*, figures 3.4 et 3.5).

L'objectif de ce chapitre est de fournir, à l'aide de la modélisation numérique, des contraintes physiques à ces modèles conceptuels afin de les valider (ou non). Il n'existe malheureusement pas de code numérique qui intègre à la fois les processus tectoniques, magmatiques et métallogéniques à l'échelle de la zone de subduction. En revanche, le code *I3ELVIS* développé par Taras Gerya (et collaborateurs) [ex. *Gerya*, 2010] à l'*ETH Zurich* permet de modéliser en 3D et avec une haute résolution, l'évolution géodynamique d'une zone de subduction en intégrant les processus de déshydratation, fusion partielle et transport des fluides (i.e. eau et magmas) [ex. *Zhu et al.*, 2009, 2013]. Les modèles numériques réalisés à partir de ce code permettent donc d'étudier les relations 3D entre flux mantelliques, déformation crustale et magmatisme, pouvant être associés, dans ce contexte de subduction, à des systèmes minéralisés [ex. *Hedenquist & Lowenstern*, 1994]. Je me suis focalisé ici sur l'évolution de la zone de subduction est-Méditerranéenne depuis l'Oligocène qui est caractérisée par (1) le retrait progressif vers le sud de la zone de subduction Hellénique et (2) la collision de la plaque Arabie avec l'Eurasie.

Ce travail a fait l'objet d'un article scientifique qui s'intitule *3D numerical assessments for mantle flow and magma genesis in laterally constrained subduction zones : the eastern Mediterranean case* et qui va être soumis au journal *Earth and Planetary Science Letters*. Le format de cet article (ex. appel des figures dans le texte, références bibliographiques déplacée dans la section adéquate) a été légèrement modifié par rapport à la version qui va être soumise afin de s'adapter à celui de ce manuscrit de thèse.

Dans cet article, après un rappel du contexte géodynamique sur lequel cette étude s'est basée, je présente brièvement les lois physiques implémentées dans le code *I3ELVIS* ainsi que la configuration initiale des différents modèles réalisés. Je décris ensuite l'évolution géodynamique de la zone de subduction en me focalisant sur les flux asthénosphériques, le régime de déformation dans la plaque supérieure et la genèse et le transport du matériel partiellement fondu. Enfin, je discute (1) du contrôle de la dynamique du panneau plongeant et des flux asthénosphériques associés sur l'évolution magmatique (i.e. nature et migration du magmatisme), (2) des interactions dans la lithosphère chevauchante entre magmatisme et déformation crustale et (3) des implications de ces modèles sur l'évolution de la zone de subduction est-Méditerranéenne.

Principe de fonctionnement du code* I3ELVIS *(pour plus de détails, cf.* Annexe E*)

Tout comme une majorité des codes numériques modélisant des processus géologiques (cf. *Section 1.4.4*), le code *I3ELVIS* considère que les roches se comportent, à l'échelle de plusieurs millions d'années, comme un fluide visqueux incompressible. Son mouvement, et donc sa déformation dans les trois directions de l'espace, peut alors être assimilé à un simple écoulement laminaire (i.e. advection), décrit par la loi de *Stokes* (cf. *Annexe E*). Le couplage de cette loi de fluage avec l'équation de transport de la chaleur permet de considérer les effets thermiques dans le modèle qui influencent notamment la densité et la rhéologie des fluides, mais également les processus de déshydratation et fusion partielle (cf. ci-dessous).

Des fluides de compositions différentes sont considérés et ceci afin de représenter différentes lithologies (ex. croûte continentale, océanique, manteau, mais également lithologies hydratées ou partiellement fondues, cf. ci-dessous). Celles-ci sont notamment caractérisées par (1) une densité spécifique dépendante de la température, de la pression (et de la quantité de magma associée, dans le cas de roches partiellement fondues) et (2) une rhéologie visco-plastique non-newtonienne, c'est-à-dire qu'elles peuvent se déformer à la fois de manière ductile (i.e. par fluage-dislocation(*)) et plastique lorsqu'un certain seuil de contraintes (i.e. seuil de plasticité) est atteint (cf. *Annexe E*). Le terme *non-newtonien* indique que la déformation par fluage-dislocation est fonction des contraintes exercées, ce qui se traduit par une relation non linéaire entre la contrainte déviatorique(*) et le taux de déformation.

Pour modéliser le fluage de ces fluides caractérisés par des propriétés non diffusives (ex. fort gradient de viscosité à la limite entre deux lithologies voisines), la technique de *marker-in-cell* est utilisée (figure 5.1a) [*Gerya*, 2010 et références associées]. Elle se traduit par la combinaison (1) de marqueurs mobiles (i.e. marqueurs lagrangiens) et (2) d'une grille de nœuds immobiles (i.e. grille eulérienne) où sont indexées les différentes propriétés du fluide (ex. composition, densité, viscosité). Cette technique permet ainsi de minimiser le phénomène de diffusion *numérique* de ces propriétés au cours du temps (figure 5.1b), permettant leur meilleur conservation (i.e. maintien de forts gradients) au cours de l'advection du fluide [*Gerya*, 2010].

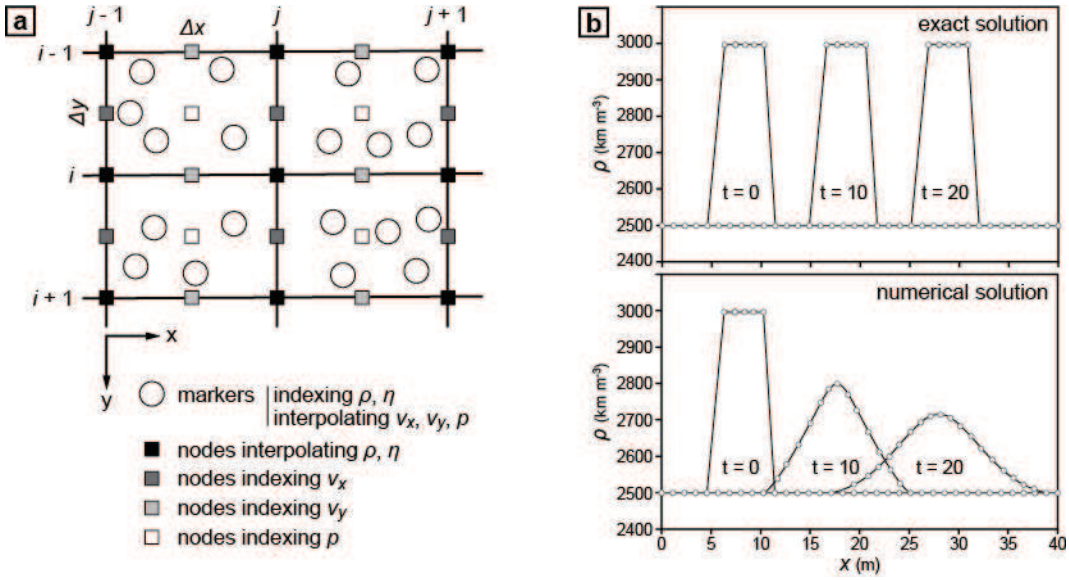

Figure 5.1 : principe de la technique de *marker-in-cell*. (a) Schéma d'une grille 2D combinée à des marqueurs mobiles où sont indexées (ou interpolées) certaines propriétés du fluide. ρ : densité. η : viscosité. p : pression. v_x : vitesse selon l'axe x. v_y : vitesse selon l'axe y. (b) Solution exacte et numérique de l'advection en 1D d'un fort gradient de densité permettant de mettre en évidence le phénomène de diffusion numérique (i.e. *lissage* du gradient). Modifiée d'après *Gerya* [2010].

Enfin, l'un des intérêts majeurs du code *I3ELVIS,* dans le cadre de notre étude, est qu'il intègre dans un espace tridimensionnel les phénomènes de déshydratation et fusion partielle permettant ainsi de modéliser des processus de genèse et transport des magmas (figure 5.2).

Processus de déshydratation. Ce code considère également certaines lithologies comme pouvant contenir de l'eau à l'état stable dans les minéraux. C'est notamment le cas de la croûte océanique (i.e. basaltique) dont la quantité maximale d'eau stable qu'elle peut contenir (X_{H2Omax}) diminue avec

l'augmentation de la température et de la pression (figure 5.2, *étape 1*). Lorsque cette quantité maximale devient inférieure à la quantité réellement contenue dans le basalte ($X_{H2Obasalt}$), le processus de déshydratation s'opère avec la création de marqueurs *eau* caractérisés par une quantité d'eau ($X_{H2Omarker}$) correspondant à celle libérée par le basalte (figure 5.2, *étape 2*).

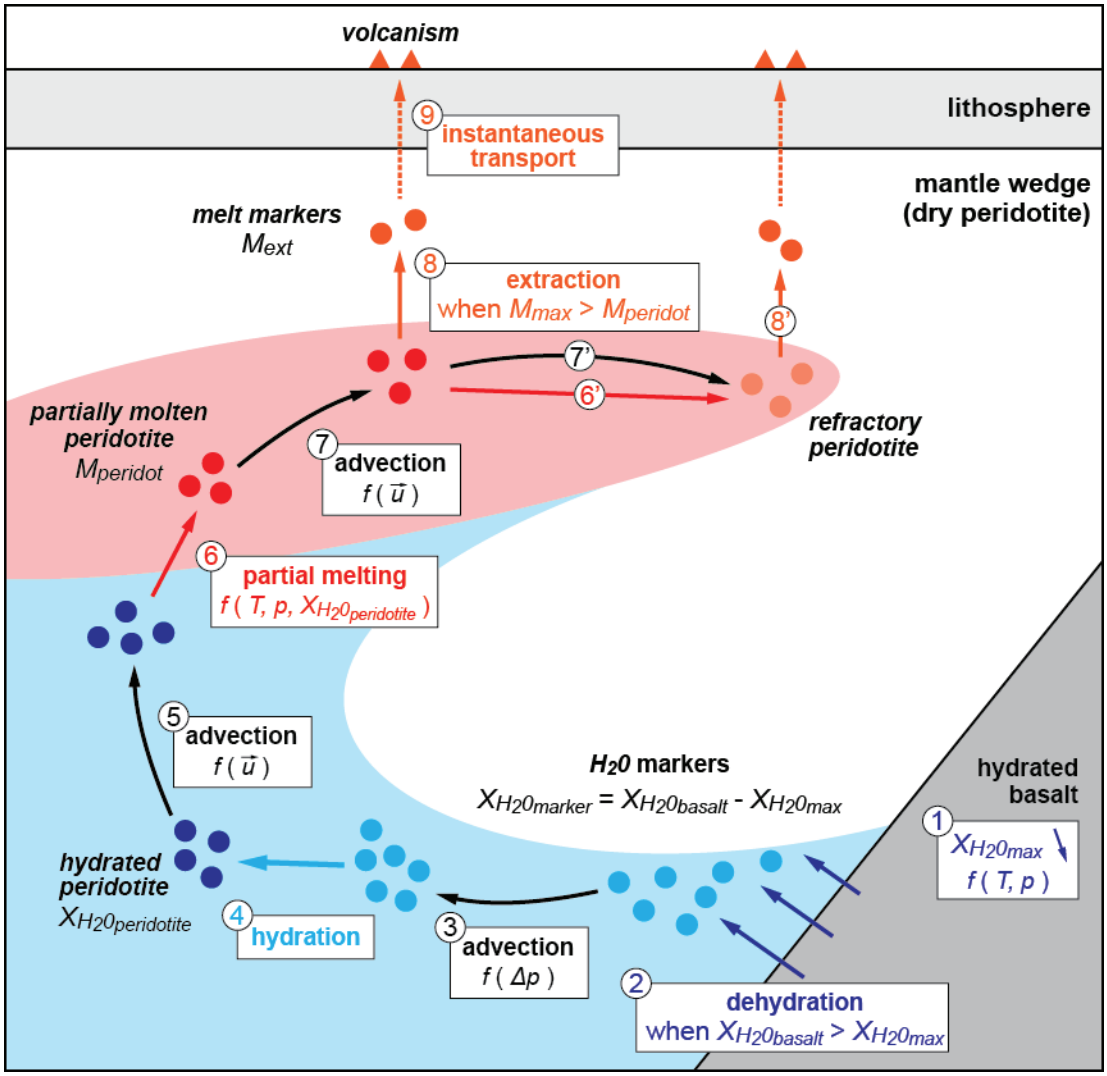

Figure 5.2 : schéma synthétisant les principales étapes implémentées dans le code *I3ELVIS* et qui permettent de modéliser les phénomènes de déshydratation, hydratation, fusion partielle et transport de fluides au niveau du coin mantellique.

Transport de l'eau et processus d'hydratation. Ces marqueurs *eau* peuvent ensuite (1) être advectés suivant le gradient de pression (Δp) caractérisant le milieu (figure 5.2, *étape 3*) ou (2) être absorbés par le manteau environnant, résultant en une péridotite hydratée qui peut contenir une certaine quantité d'eau maximale ($X_{H2Operidot}$) (figure 5.2, *étape 4*).

Processus de fusion partielle. Ce manteau hydraté peut ensuite être advecté, suivant le champ de vitesse calculé ($\vec{u}$) (figure 5.2, *étape 5*), jusqu'à être affecté par un processus de fusion partielle. Celui-ci permet de produire un manteau partiellement fondu caractérisé par une fraction de magma ($M_{peridot}$) dépendante de la température, de la pression et de la quantité d'eau dans le manteau hydraté (figure 5.2, *étape 6*). Ce manteau partiellement fondu peut également être advecté, suivant le champ de vitesse (figure 5.2, *étape 7*).

Processus d'extraction de magmas. Lorsque la fraction de magma dans le manteau partiellement fondu est supérieure à la quantité maximale qu'il peut réellement contenir (M_{max}), des marqueurs *magma* sont formés, caractérisés par une quantité de magma (M_{ext}) correspondant à celle relâchée par le manteau (figure 5.2, *processus 8*). Les processus d'advection, fusion partielle et extraction de magmas peuvent se répéter plusieurs fois pour une même roche partiellement fondue (figure 5.2, *étapes 6', 7' et 8'*), jusqu'à ce que le manteau ait extrait une quantité maximale de magma, auquel cas elle est définie comme réfractaire.

Transport des magmas et formation de volcans en surface. Du fait que le magma libre migre plus rapidement que la roche ne se déforme [*Hawkesworth*, 1997], les marqueurs *magma* générés lors d'un épisode d'extraction sont instantanément transportés à la surface (figure 5.2, *étape 9*). Ils forment alors une roche volcanique dont le volume et la composition sont dépendants respectivement de la quantité de magma extraite et de la nature de la source de ces magmas.

Principaux résultats

Cette étude numérique a permis d'identifier des liens entre processus mantelliques et crustaux et magmatisme dans un environnement de subduction latéralement contraint par une zone de collision (figure 5.3). Il apparait ainsi que la genèse et le transport de roches partiellement fondues depuis le coin mantellique jusqu'à la base de la croûte continentale chevauchante sont largement contrôlés par les flux asthénosphériques 3D (i.e. avec une composante poloidale et toroidale) qui dépendent eux-mêmes de la dynamique de la plaque subduite (ex. processus de courbure, retrait, déchirure). Cette observation cruciale vient confirmer le contrôle de la dynamique profonde de la subduction sur l'activité magmatique au niveau de la marge active. De plus, ces modèles mettent en évidence que

l'ascension de ces roches partiellement fondues dans la plaque supérieure induit un fort contraste rhéologique (i.e. contraste de viscosité) qui permet (1) la localisation de la déformation (qu'elle soit décrochante ou extensive) dans ces zones de plus faible résistance et (2) une meilleure transmission des contraintes depuis le manteau convectif, vers la croûte qui suggère un contrôle (au moins partiel) du flux asthénosphérique sur la déformation de la lithosphère sus-jacente.

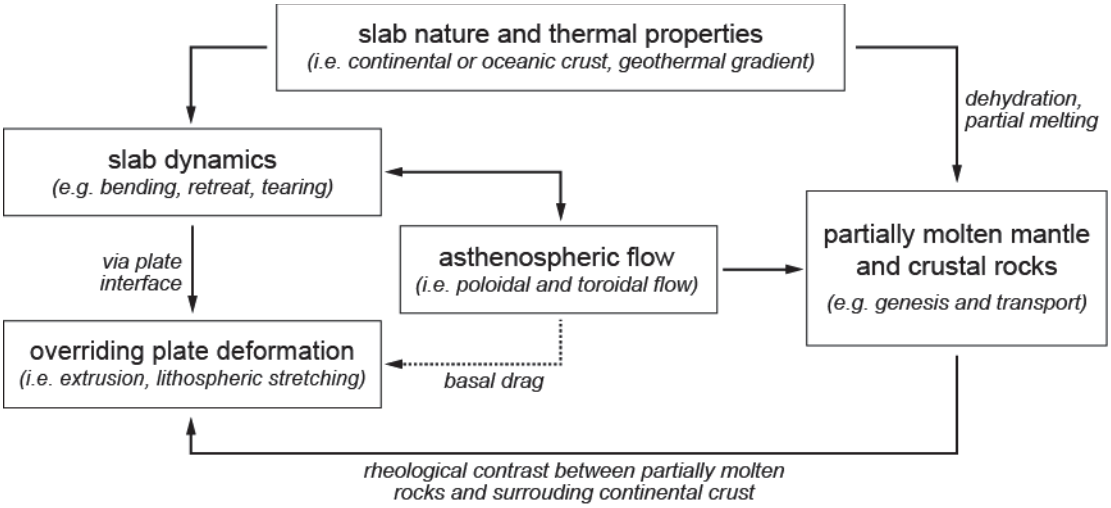

Figure 5.3 : schéma synthétisant l'ensemble les liens (i.e. contrôles et interactions) qui sont mis en évidence à partir de l'observation des modèles numériques 3D entre la dynamique mantellique et crustale d'une zone de subduction et les processus de genèse et transport de roches partiellement fondues (i.e. sources des magmas).

A la lumière de ces résultats, il apparait que l'évolution tectonique et magmatique mise en évidence en Méditerranée orientale depuis l'Oligocène est clairement contrôlée par l'interaction entre la collision Arabie-Eurasie, le retrait vers le sud de la zone de subduction Hellénique, la (ou les) déchirure(s) et/ou détachement(s) du panneau plongeant sous l'Anatolie et les flux asthénosphériques associés. Ces modèles apportent donc une vision globale et robuste du contrôle des processus mantelliques et crustaux liés à la dynamique de la subduction sur l'activité magmatique dans le domaine d'arrière-arc et donc potentiellement sur l'activité hydrothermale associée.

3D numerical assessments for mantle flow and magma genesis in laterally constrained subduction zones: the eastern Mediterranean case

Armel Menant [1,2,3]*, Laurent Jolivet [1,2,3], Laurent Guillou-Frottier [2,1,3]

(4) Univ d'Orléans, ISTO, UMR 7327, 45071 Orléans, France

(5) BRGM, ISTO, UMR 7327, BP 36009, 45060 Orléans, France

(6) CNRS/INSU, ISTO, UMR 7327, 45071 Orléans, France

* *Corresponding author: Armel Menant – ISTO*
1A, rue de la Férollerie, 45071 Orléans cedex 2
+33(0)2 38 49 46 60
(armel.menant@cnrs-orleans.fr)

Pietro Sternai [4]

(7) Division of Geology and Planetary Sciences, California Institute of Technology, Pasadena CA, USA

Taras Gerya [5]

(8) Institute of Geophysics - Swiss Federal Institute of Technology (ETH), Zürich, Switzerland

5.1. Abstract

While the Relationships between subduction dynamics and magmatism have been intensely investigated and several conceptual models derived from geological, geochemical and geophysical data have been proposed, these relations are still poorly understood in complex 3D contexts like laterally constrained subduction zones. Self-consistent numerical models that contain testable mechanical parameters enable verifying and improving these simple conceptual models. Here, we use 3D high-resolution coupled petrological-thermo-mechanical numerical models to quantify the relative contribution of oceanic and continental subduction/collision, slab roll-back and tearing as well as the related asthenospheric flow to the magma genesis and transport processes. Our models suggest that the asthenospheric flow controls the trapping and promotes the ascent of mantle-derived magmatic sources in the mantle wedge, thereby affecting the magmatic activity at the surface. The rheological weakening induced by mantle- and crust-derived magmas localizes strike-slip and extensional zones related to slab roll-back and/or continental collision. We also show that such a lithospheric weakening favors shear stresses transmission from the mantle to the crust. Similarities between our models and the late Cenozoic tectonic and magmatic evolution across the eastern Mediterranean region suggest an efficient control of mantle flow on the magmatic activity in this region which then promotes lithospheric deformation by mantle drag via weakening effects.

5.2. Introduction

Arc magmatism is one of the most typical surface expressions of subduction dynamics, tracking physic-chemical processes from the upper mantle to the crust [*Arculus*, 1994]. It is broadly accepted that the genesis of these magmas is dominated by fluid-fluxed partial melting of a mantle wedge source, as the result of the H_2O release from the subducting oceanic lithosphere [*Arculus*, 1994; *Grove et al.*, 2006]. These primary mafic magmas then ascend through the mantle, reaching the base of the overriding crust where they can be retained in the melting assimilation storage and homogenization (MASH) zone [*Hildreth and Moorbath*, 1988]. During their storage and their subsequent ascent up to the upper crust, these magmas undergo some degrees of fractionation and crustal assimilation, which provide the typical calk-alkaline magmatic trend.

Although geological, geochemical and geophysical data has already been used to link subduction dynamics and associated magmatism, the contribution of the thermal state and rheology of the interacting lithospheres as well as slab kinematics and related asthenospheric flow on arc magmatism remains difficult to ascertain. A large number of numerical experiments, integrating mechanical, thermal and petrological constraints, have been performed to reach a coherent understanding of the interactions between the lithosphere properties, subduction dynamics and magma genesis [*Huw Davies and Von Blanckenburg*, 1995; *Nikolaeva et al.*, 2008; *Zhu et al.*, 2009, 2013; *Gerya and Meilick*, 2011; *Bouilhol et al.*, 2015].

However, the control of complex three-dimensional (3D) subduction dynamics on the magmatic history across laterally constrained subduction zones has been rarely investigated [*Li et al.*, 2013], while more attention has been given to the relationships between the induced asthenospheric flow and lithospheric deformation [*Jadamec and Billen*, 2010; *Li et al.*, 2013; *Capitanio*, 2014; *Duretz et al.*, 2014; *Magni et al.*, 2014; *Sternai et al.*, 2014]. This point is nevertheless crucial to explain the distribution in space and time and the petrological-geochemical variations of the magmatism observed in arc and back-arc environments as a result of fast evolving narrow subduction zones, such those

across the Mediterranean realm [*Pe-Piper and Piper*, 2006; *Dilek and Altunkaynak*, 2009; *Ersoy and Palmer*, 2013; *Jolivet et al.*, 2013].

In this study, we use 3D high-resolution coupled petrological and thermo-mechanical numerical models of subduction zone that involve interacting oceanic and continental lithospheres and account for experimentally calibrated non-Newtonian visco-plastic rheologies and physico-chemical processes such as slab dehydration, fluid transport, partial melting, melt extraction and crustal growth [*Nikolaeva et al.*, 2008; *Gerya and Meilick*, 2011; *Zhu et al.*, 2013]. Our results suggest that slab kinematics and related asthenospheric flow affect the genesis, transport and emplacement of magmatic bodies both in the arc and back-arc domain and that such melts weaken the lithosphere and therefore affect its deformation. Given the tight match between our modeling results and observations from the eastern Mediterranean region, where the late Cenozoic evolution of the subduction zone and associated magmatism is relatively well constrained (figure 5.4), we propose that the asthenospheric flow in response to slab roll-back and tearing was crucial in the magmatic and strain history across this region.

5.3. Late Cenozoic evolution of the eastern Mediterranean subduction zone

The geodynamic evolution of the Mediterranean realm is controlled, since the Mesozoic, by the Africa-Eurasia convergence and involves interactions between several oceanic and continental lithospheres [*Stampfli and Borel*, 2002]. 35-30 Ma ago, an increasing rate of slab retreat controls the opening of back-arc basins, such as in the eastern Mediterranean region where the Hellenic southward slab roll-back led to the opening of the Aegean basin [*Jolivet and Faccenna*, 2000]. In this extensional context, medium- to high-temperature rocks are exhumed as several metamorphic core complexes (MCCs) such as in the Rhodope massif, the Cyclades and the Menderes massif (figure 5.4) [*Lister et al.*, 1984; *Bozkurt and Oberhänsli*, 2001; *Vanderhaeghe*, 2004; *Brun and Sokoutis*, 2007; *Jolivet et al.*, 2013]. Coevally with this extensional tectonics, subduction and collision of the Arabian plate with the southern margin of the Tauride belts occurred further east (figure 5.4c) [e.g. *Jolivet and Faccenna*, 2000]. The present-day kinematics of this region is characterized by an overall counterclockwise

rotation of the surface velocity vectors as recorded by GPS measurements (figure 5.5a) [e.g. *Reilinger et al.*, 2006], associated with the westward extrusion of Anatolia, mainly accommodated by the North Anatolian Fault (NAF) [*Şengör et al.*, 2005].

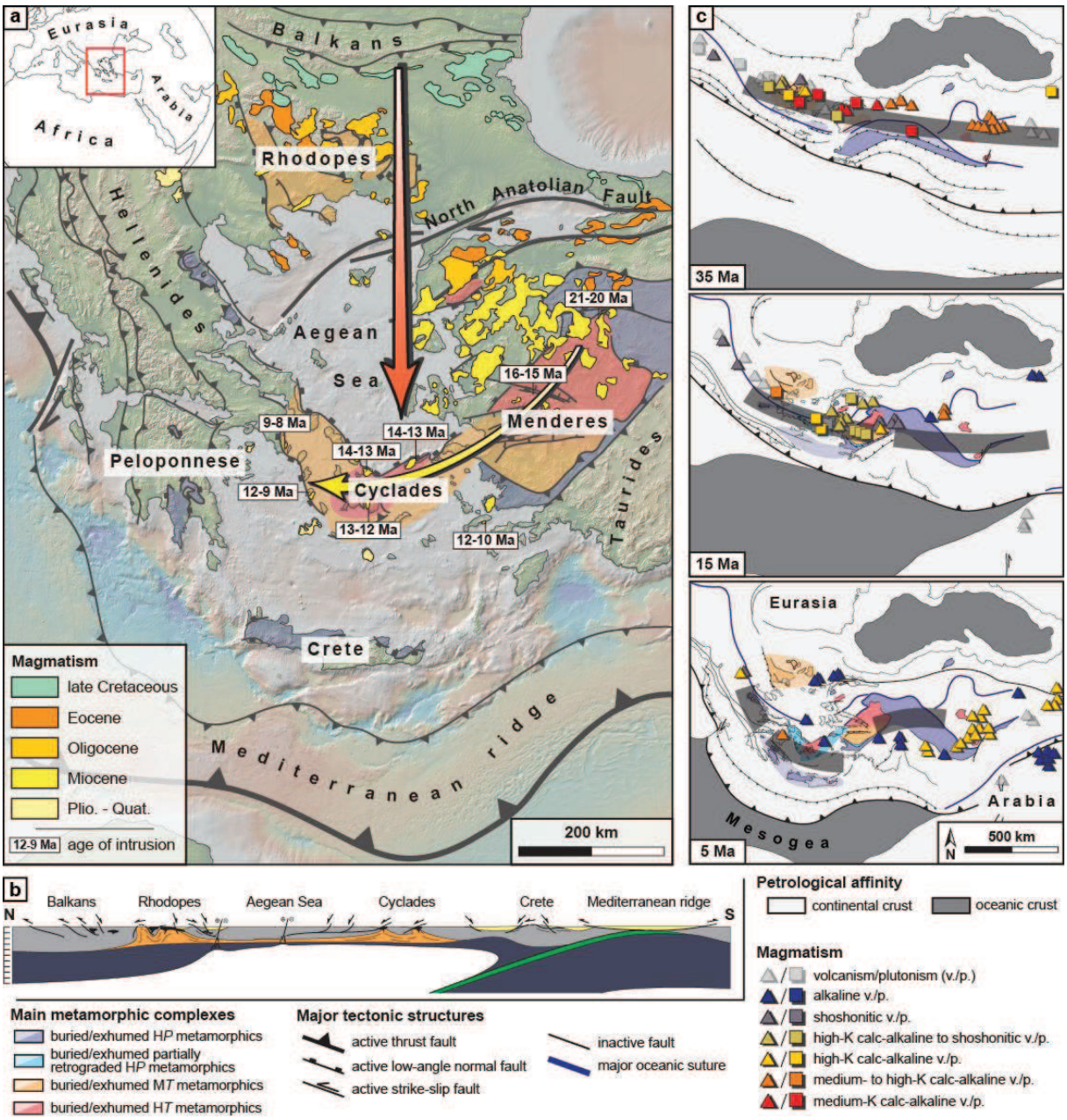

Figure 5.4: late Cenozoic geodynamic evolution of the eastern Mediterranean region. (a) Tectonic map of the eastern Mediterranean region, showing the spatial distribution of the magmatism since the late Cretaceous. Red and yellow arrows show respectively the first-order southward migration of the magmatism since the late Cretaceous and the second-order southwestward migration of the magmatism during the Miocene. (b) Present-day N-S cross-section across the Rhodope-Aegean region. (c) Paleotectonic maps of the eastern Mediterranean region at 35, 15 and 5 Ma, showing the spatial distribution of contemporaneous magmatic occurrences (cf. *Chapitre 2*). The thick grey line shows the position of the slab at 150 km depth.

At depth, tomographic models for the eastern Mediterranean region show trench-parallel variations in seismic velocity, with low-velocity anomalies interpreted as major break-off or tears in the slab that displays a high-velocity anomaly (figure 5.5b) [de *Boorder et al.*, 1998; *Wortel and Spakman*, 2000; *Li et al.*, 2008]. The complex geometry of subducting lithosphere in the region thus resulted in a complex convective mantle pattern including both poloidal and toroidal flows [*Faccenna and Becker*, 2010], the latter imaged by *SKS* splitting anisotropy (figure 5.5c) [*Paul et al.*, 2014].

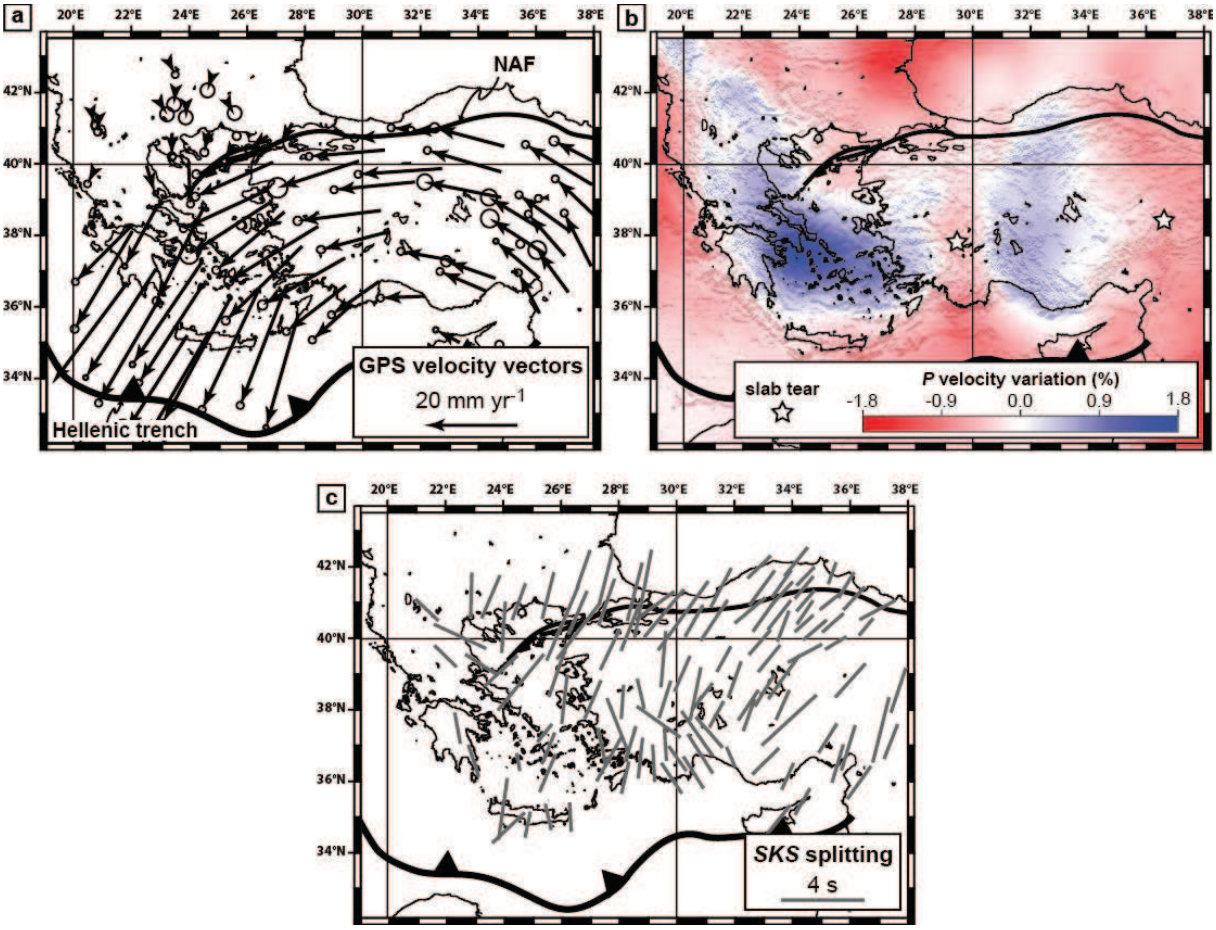

Figure 5.5: geophysical maps of the eastern Mediterranean region. (a) GPS velocities relative to stable Eurasia with 1σ confidence ellipses [*Reilinger et al.*, 2006]. (b) Seismic tomographic model, showing the *Vp* anomalies at ~150 km depth [*Li et al.*, 2008]. Slab tear suspected in the region are highlighted by white stars. (c) Station-averaged SKS splitting data [*Paul et al.*, 2014].

Integrated in this complex tectonic frame, magmatic occurrences show a specific spatial and temporal distribution associated with variable petrological and geochemical composition. Since the Oligocene, mainly high-potassic calc-alkaline to shoshonitic magmatism thus progressively emplaced

southward from the Rhodope massif to the Cyclades and the Menderes massif, associated with the exhumation of MCCs (figures 5.4a and c) [*Pe-Piper and Piper*, 2006; *Dilek and Altunkaynak*, 2009; *Ersoy and Palmer*, 2013]. In addition to this first-order migration, a secondary southwestward migration of the magmatic activity is recorded during the Miocene from the Menderes massif to the Cyclades (figure 5.4a) [*Jolivet et al.*, 2015]. Evolution of geochemical and isotopic composition of this magmatism mainly suggests an increase of mantle source component relative to the crustal source component [*Keskin*, 2003; *Dilek and Altunkaynak*, 2009; *Ersoy and Palmer*, 2013; *Jolivet et al.*, 2015], finally producing alkaline magmas with a major depleted asthenospheric source component [*Ersoy and Palmer*, 2013]. In eastern Anatolia, a wide late Miocene-Quaternary volcanic province also emplaced with composition evolving from high-potassic calc-alkaline to alkaline (figure 5.4c) [*Keskin*, 2003].

5.4. Numerical modeling

We address the relationships between subduction dynamics and magmatism by means of 3D high-resolution numerical geodynamic modeling. In this section we first describe the modeling approach and the initial reference model setup and then outline the main objectives of the parametric study.

5.4.1. Modeling approach and setup

We use the wealth of observations from the eastern Mediterranean region to design and calibrate numerical experiments that could be qualitatively and quantitatively compared to the global evolution of this region during the late Cenozoic. We stress, however, that the main objective of our work is to investigate the links between subduction dynamics and magmatism in the context of constrained subduction zones, and do not claim to provide an exhaustive description of all geodynamics across the area. As such, results may also be applied to other tectonic settings characterized by laterally constrained subduction zones (e.g. central and western Mediterranean region, southeastern Asia).

Numerical modeling was performed, using the code *I3ELVIS*, like in other recent studies [*Zhu et al.*, 2009, 2013; *Li et al.*, 2013; *Duretz et al.*, 2014; *Sternai et al.*, 2014]. The code solves the mass, momentum and heat conservation equations based on a conservative finite-difference scheme combined with a marker-in-cell technique and includes non-Newtonian visco-plastic rheologies (table 5.1) [*Gerya and Yuen*, 2007]. In addition, this code includes physico-chemical processes such as slab dehydration, fluid transport, partial melting, melt extraction and crustal growth at continental margin [*Zhu et al.*, 2013] (for details on the numerical approach used in our numerical experiments, cf. *Annexe E*).

In all our experiments, the model domain measures 1500 × 680 × 656 km in the *x*, *y* and *z* respectively, resolved by 437 × 277 × 149 grid nodes, giving a resolution of 3.4 × 2.5 × 4.4 km (figure 5.6a). Around 130 million additional randomly distributed markers are used for advecting the material properties and temperatures and computing water release, transport and consumption as well as partial melting and melt extraction. The initial setup is designed with an overriding continental lithosphere and a subducting oceanic lithosphere including a small continent (i.e. 500 × 328 km in *x* and *z* directions, respectively), which represent the Eurasian plate and the converging Mesogean and Arabian lithospheres, respectively (figure 5.4c). A 10-km thick trench-parallel weak zone is prescribed at the interface between the overriding and subducting lithospheres in order to initiate subduction. In our reference model, the overriding continental lithosphere is composed by 30 km and 20 km thick of upper and lower crust, respectively, while the subducting continental crust is composed of 20 km and 10 km thick of upper and lower crust, respectively (figures 5.6a and b). Specific initial thermal structure of these continents has been defined for each experiment (see details in section 3.2). This is a laterally uniform and linearly defined thermal gradient with, for the reference model, 0 °C at the surface and 1300 °C at 89 km and 98 km depth for the overriding and subducting continental lithospheres, respectively.

Material	Density ρ_0 (kg m-3)	Isobaric heat capacity C_p (J kg^{-1} K^{-1})	Thermal conductivity k (W m^{-1} K^{-1})	Radiogenic heat production H_r (mW m^{-3})	$T_{solidus}$ (K)	$T_{liquidus}$ (K)	Thermal expansion α (K^{-1})	Compressibility β (MPa^{-1})	Viscous flow law	Creep exponent n	Activation energy E (kJ mol^{-1})	Activation volume V (cm^3 mol^{-1})
Air	1	100	20	0			0	0	Air	1	0	0
Sea water	1000	3330	20	0			0	0	Water	1	0	0
Sediments	2600 (solid)	1000	0.64+807/(*T*-77)	2	889+179/(*P*+54)+20200/(*P*+54)² at $P < 1200$ MPa;	1262+0.09*P*	3×10^{-5}	3×10^{-3}	wet quartzite	2.3	154	0
	2400 (molten)	1500			831+0.06*P* at $P > 1200$ MPa					1		
Upper continental crust	2750 (solid)	1000	0.64+807/(*T*-77)	1	889+179/(*P*+54)+20200/(*P*+54)² at $P < 1200$ MPa; 831+0.06P at P > 1200 MPa	1262+0.09*P*	3×10^{-5}	3×10^{-3}	wet quartzite	2.3	154	0
	2700 (hydrated)											
	2400 (molten)	1500								1	0	
Lower continental crust	2950 (solid)	1000	0.64+807/(*T*-77)	0.5	1327.15+0.0906*P*	1423+0.105*P*	3×10^{-5}	3×10^{-3}	wet quartzite	3.2	238	0
	2900 (hydrated)											
	2400 (molten)	1500								1	0	
Oceanic crust	3000 (solid)	1000	1.18+474/(*T*-77)	0.25	1327.15+0.0906*P*	1423+0.105*P*	3×10^{-5}	3×10^{-3}	Plagiocalse (An_{75})	3.2	238	0
	3000 (hydrated)				973-70400/(*P*+54)+778×10^5/(*P*+354)² at $P < 1600$ MPa;				wet quartzite	2.3	154	
	2900 (molten)	1500			935+0.0035*P*+6.2×10^{-6} at $P > 1600$ MPa				Plagiocalse (An_{75})	1	0	
Mantle	3300 (solid)	1000	0.73+1293/(*T*-77)	0.022	n/a	n/a	3×10^{-5}	3×10^{-3}	dry olivine	3.5	532	0.8
	3300 (hydrated/ serpentinized)				*P-T-H$_2$O* dependent melting model of Katz et al. (2003)				wet olivine	4	470	
	2900 (molten)	1500							dry olivine	1	0	
Weak zone	3300	1000	0.73+1293/(*T*-77)	0.05	n/a	n/a	3×10^{-5}	3×10^{-3}	wet olivine	4	470	0.8

Table 5.1: material properties used in the numerical experiments. See details in the text.

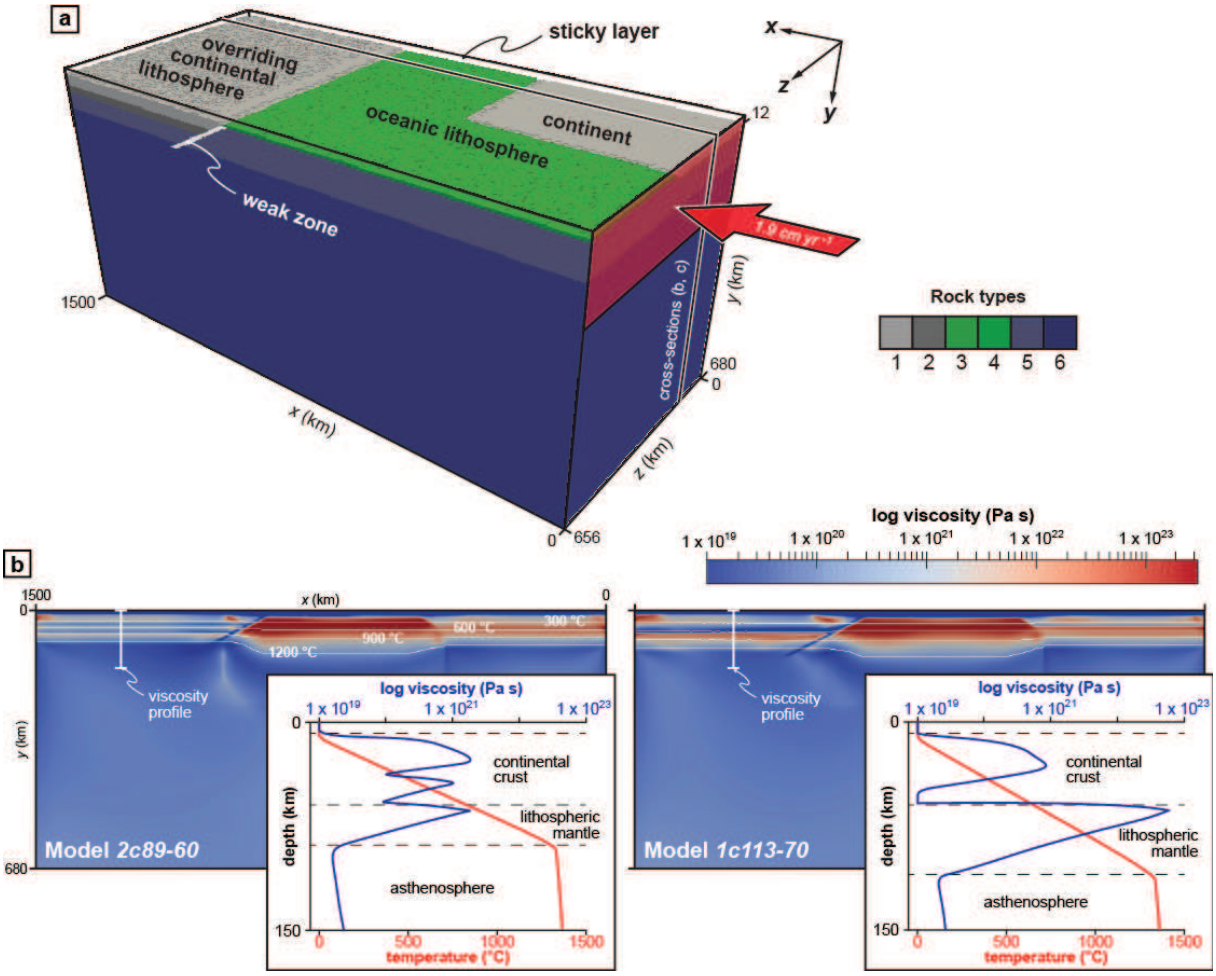

Figure 5.6: initial model setup. (a) 3D model domain with colors representing the different rock types. 1/2 – dry upper/lower continental crust; 3/4 – hydrated/dry oceanic crust; 5 – dry lithospheric mantle; 6 – dry asthenosphere. Air and sea water phases (composing the sticky layer) are cut off for clarity. (b) *x*-*y* viscosity cross-sections of the initial model domain with a bi-phase (left panel) and mono-phase (right panel) continental crust. White lines represent 300, 600, 900 and 1200 °C isotherms. Viscosity (blue) and temperature (red) *y* profiles are shown as inset for each model.

The oceanic lithosphere incorporates a 3 km thick hydrated basaltic crust and a 5 km thick gabbroic crust and its thermal structure, different for each experiment, is defined using for instance a half-space cooling age of 60 Ma for the reference model [*Turcotte and Schubert*, 2002]. These lithospheres overlay an asthenospheric mantle characterized by an initial adiabatic temperature gradient of ~0.5 °C km^{-1}. It is important to remark that physical properties of the lithospheric and asthenospheric mantle are identical and they are shown by different colors to better visualize the lithospheric deformation.

Velocity boundary conditions are free slip at both back and front boundaries (z = 0 and z = 656 km). Material influx is imposed through the right and left boundaries (x = 0 and x = 1500 km). Velocities across these boundaries are null excepted for the first 250 km depth of the right boundary where a ~1.9 cm yr^{-1} influx is applied (Fig 3a), scaled on the African plate absolute motion which estimated as between 1.2 and 2.5 cm yr^{-1} since the Oligocene [*Jolivet and Faccenna*, 2000]. The mass conservation is then ensured by material outflux through the upper and lower permeable boundaries (y = 0 and y = 680 km). The top surface of the lithosphere is calculated dynamically as an internal free surface by using an initial 12-15 km thick low-viscosity layer simulating either air (for y < 12 km) or sea water. The large viscosity contrast caused by this low-viscosity layer minimizes shear stresses at the top of the lithospheres that effectively approximates a free surface [*Schmeling et al.*, 2008].

5.4.2. Parametric study on rheological implications in natural subduction context

Previous studies have shown that the subduction dynamics is largely controlled by the coupling/decoupling at the subduction interface, itself depending on (1) the fluid-related weakening along this plate interface and (2) the rheology of interacting lithospheres, changing their buoyancy and strength [e.g. *Gerya and Meilick*, 2011]. To assess the role of subduction dynamics on the magmatic evolution, a series of numerical experiments with different thermal gradients and rheological properties across continental and oceanic lithospheres were performed (table 5.2). In addition, since there is no consensus on the rheological layering of the lithosphere, especially in the eastern Mediterranean region, either one or two continental crustal layers have been imposed for the continental crust, which allows us to explore a wide range of realistic rheological lithospheric profiles (figures 5.6a and b). In the following, we use acronyms like *2c89-60* for model with two crustal layers, an overriding lithosphere 1300 °C isotherm at 89 km depth and 60-Myr old oceanic lithosphere.

Models with bi-phase continental crust		thermal age of the oceanic lithosphere			
		40 Ma	60 Ma	80 Ma	100 Ma
depth of the 1300 °C isotherm in the overriding lithosphere	84 km	2c84-40	2c84-60	2c84-80	**2c84-100**
	89 km	2c89-40	**2c89-60**	2c89-80	2c89-100
	93 km	2c93-40	2c93-60	2c93-80	2c93-100
	98 km	2c98-40	2c98-60	2c98-80	**2c98-100**

Models with mono-phase continental crust		thermal age of the oceanic lithosphere		
		60 Ma	70 Ma	80 Ma
depth of the 1300 °C isotherm in the overriding lithos.	111 km	1c111-60	1c111-70	1c111-80
	113 km	1c113-60	**1c113-70**	1c113-80
	115 km	1c115-60	1c115-70	1c115-80

Table 5.2: range of performed models with variations in the continental crust structure, and geothermal gradient in the continental and oceanic lithospheres, leading to explore the role of lithosphere rheology on subduction dynamics and magmatic evolution. The overriding lithosphere in dark grey, light grey and white models displays respectively a compressional, minor extensional and major extensional tectonics. Models in bold are described in the text.

5.5. Results

In this section, we outline our numerical results, focusing first on the asthenospheric and lithospheric flow pattern and then on the genesis and evolution of partially molten rocks from the mantle to the crust.

5.5.1. Asthenospheric vs. lithospheric flow pattern

In our reference model *2c89-60* (figures 5.7 and 5.8; cf. *Annexe E, videos E.1 and E.2*), subduction initiates through progressive bending and roll-back of the oceanic slab associated with dominant poloidal asthenospheric flow, initiated at the slab tip and moving upward to the mantle wedge (figure 5.9a), enhancing slab suction (figures 5.8c and d). During this initial phase, the overriding continental lithosphere undergoes a homogeneous minor stretching (figure 5.7a). Subsequent continental subduction then induces along-trench buoyancy variations resulting in progressive bending of the trench due to faster retreat above the oceanic slab (3-6 cm yr^{-1}) than above the continental slab (~2 cm yr^{-1}; figure 5.10a). When the continental slab reaches ~150 km depth, trench-parallel tearing occurs at the transition between the more buoyant continental lithosphere and the oceanic lithosphere (figure 5.7b). The slab tear then propagates vertically along the same compositional boundary, inducing trench-perpendicular tearing (figure 5.7c). Once decoupled from the oceanic lithosphere, the torn continent bends up and collides into the overriding plate while trench retreat in the still active oceanic subduction accelerates (~6 cm yr^{-1}; figure 5.10a) and is associated with slab flattening. Consequently, the overall asthenospheric flow is characterized at this stage by a poloidal flow coming through the newly formed slab windows, which then evolves in a toroidal flow up to the mantle wedge (figures 5.9b and c). Meanwhile, extrusion of the overriding lithosphere towards the oceanic subduction takes place, especially in a restricted zone above the trench-perpendicular slab tear, where the deformation is localized along a strike-slip fault zone (figure 5.9d). Lithospheric and asthenospheric flows in the extensional back-arc domain are sub-parallel and controlled by the slab roll-back (figure 5.9c). , but seem decoupled as demonstrated by the abrupt drop of horizontal velocity through the lithosphere-asthenosphere boundary (see viscosity and velocity profiles in inset of figure 5.9d).

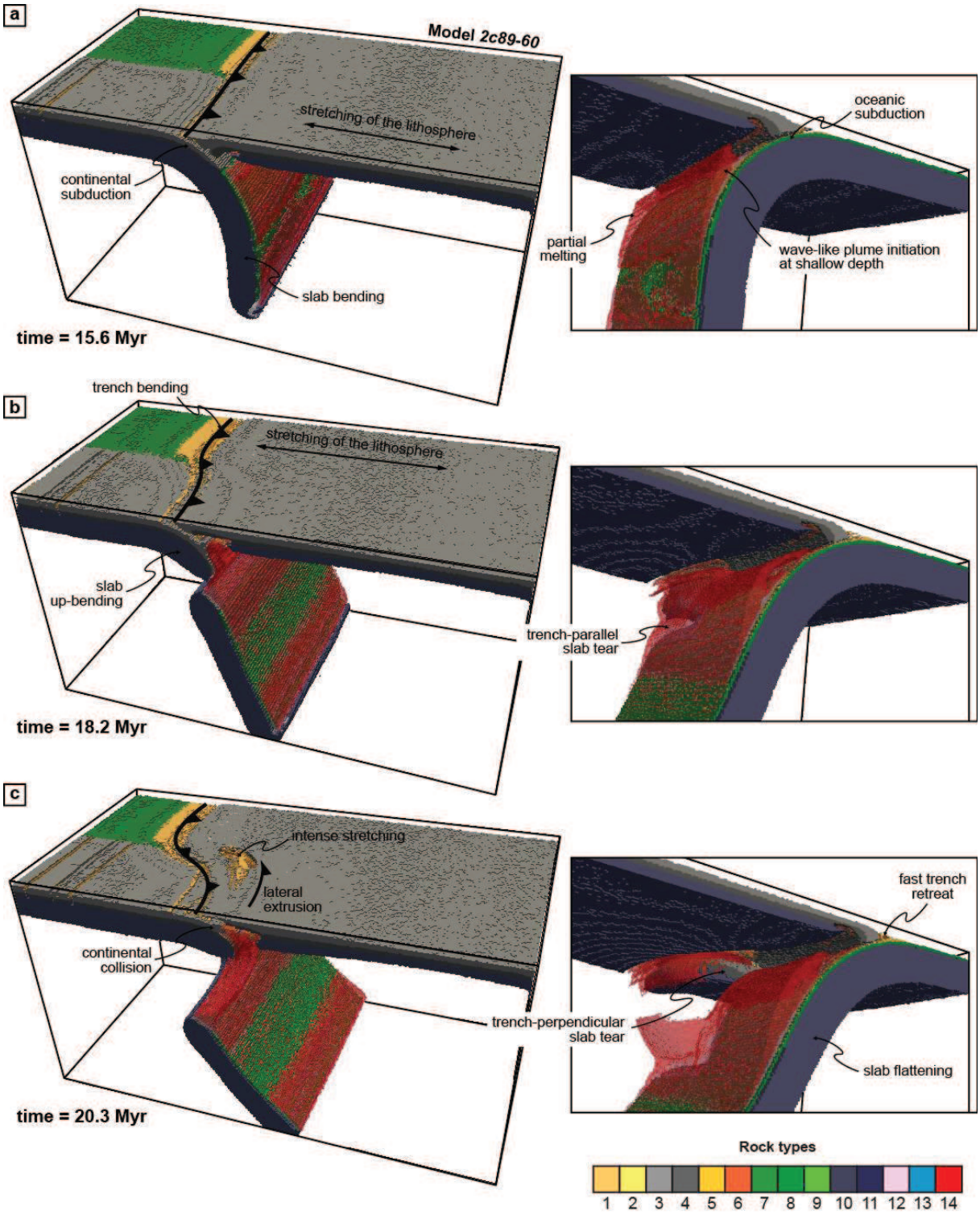

Figure 5.7: evolution of the reference model *2c93-60* (with a bi-phase continental crust). (a, b, c) 3D lateral view of the subduction zone (left panels) and zoom on the mantle wedge (right panels) for selected time steps. Colors represent the different rock types: 1 – sediments; 2 – partially molten sediments; 3/4 – dry upper/lower continental crust; 5/6 – hydrated/partially molten continental crust; 7 – dry oceanic crust; 8/9 – hydrated/partially molten oceanic crust; 10 – dry lithospheric mantle; 11 – dry asthenosphere; 12/13 – hydrated/serpentinized mantle; 14 – partially molten mantle. Asthenosphere and other phases are cut off for clarity.

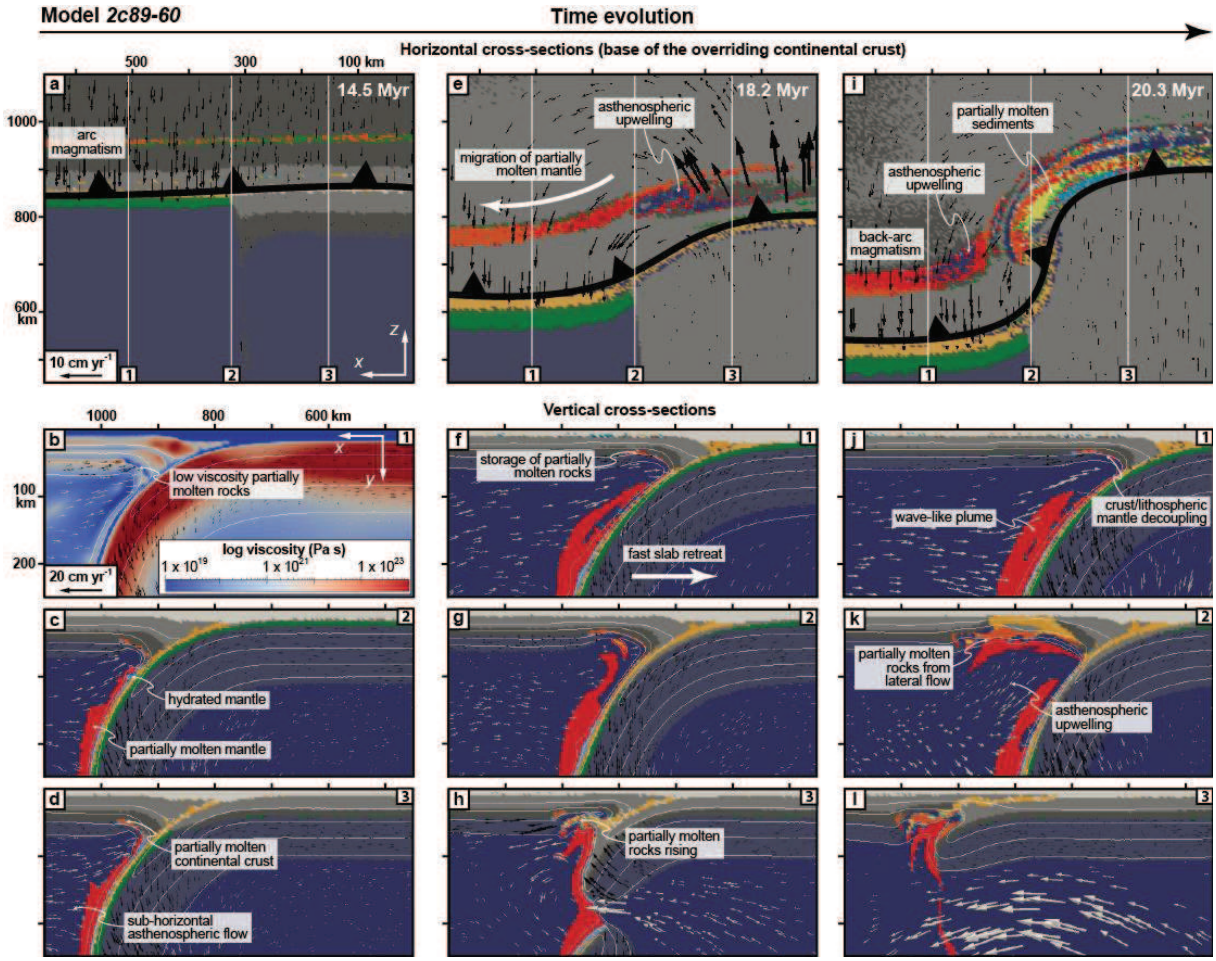

Figure 5.8: evolution of magmatism in reference model *2c93-60*. *x-z* plan views (a, e, i) and *x-y* cross-sections (b, c, d, f, g, h, j, k, l) of the subduction zone for selected time steps. Colors represent the different rock types (see figure 5.7 for detailed legend), excepting for the cross-section (b) where the viscosity is mapped. Black and white arrows represent velocity vectors in the continental crust (top panels) or lithospheric mantle (bottom panels) and the asthenosphere, respectively. Scale of velocity vectors is twice larger in top panels than in bottom panels. White lines (bottom panels) represent 300, 600, 900 and 1200 °C isotherms.

This succession of events is robust through all experiments with two-layer continental crust, except when the lithospheric thermal gradients is low, which leads to overall compression in the overriding lithosphere (model *2c98-100*; figure 5.11a) and slow forward motion of the trench (0.5-2 cm yr^{-1}; figure 5.10b). Conversely, models with higher lithospheric thermal gradients show a sensibly faster trench retreat (reaching up to ~9 cm yr^{-1} above the fast retreating oceanic slab) and more lithospheric stretching (model *2c84-100*; figures 5.10b, 5.12 and 5.13).

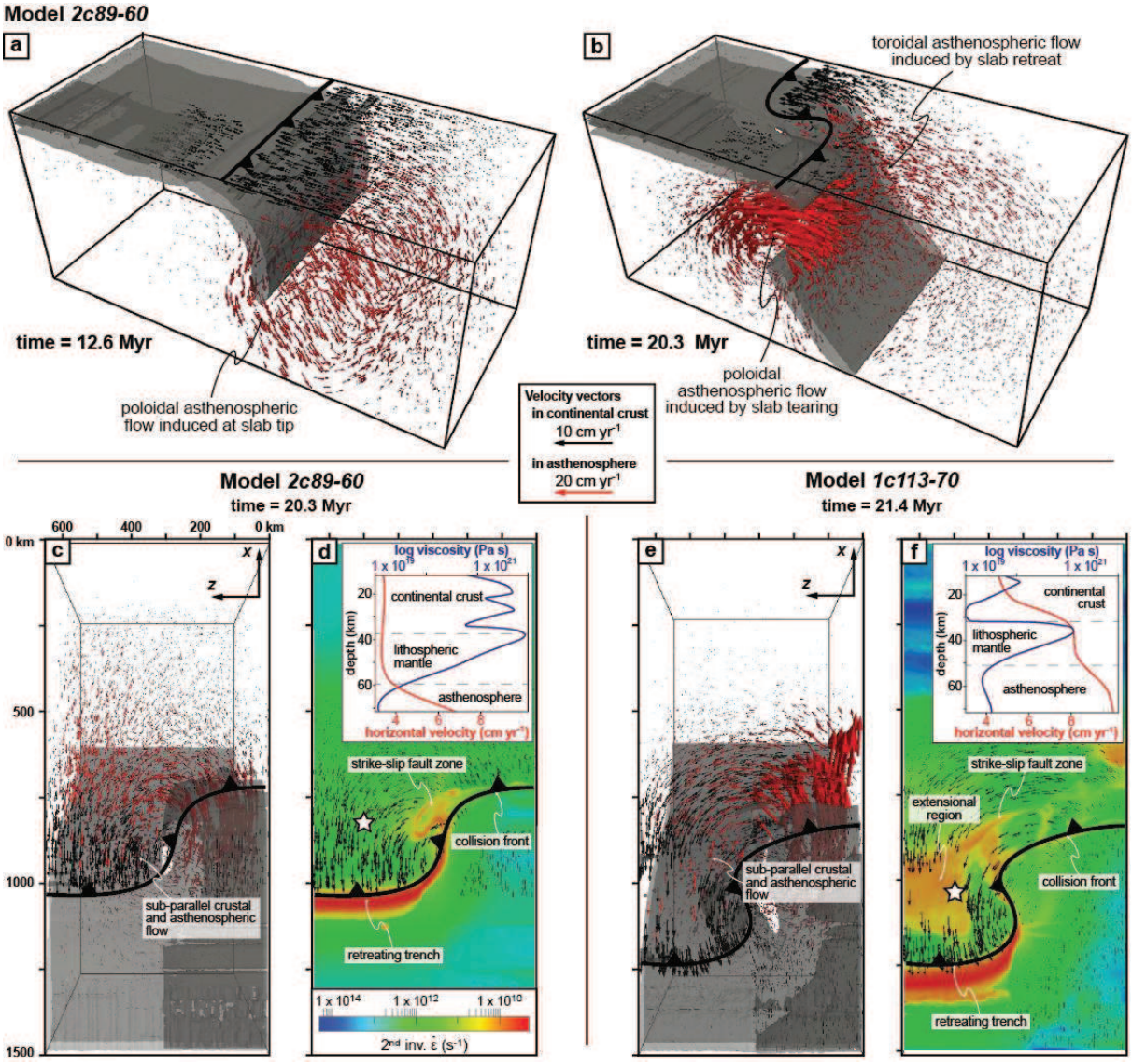

Figure 5.9: asthenospheric and crustal flow evolution and crustal strain rate in performed numerical experiments. (a, b) 3D view of the subduction zone of model *2c93*-60 at two selected time steps (i.e. before and after slab tearing), showing the slab geometry (iso-viscosity contour equal to 10^{23} Pa.s and velocity vectors in the continental crust (black arrows) and asthenosphere (red arrows). (c, e) *x*-*z* plan view of selected time step, showing the velocity vectors in the continental crust and asthenosphere. Scale of velocity vectors is twice larger in continental crust than in asthenosphere. (d, f) *x*-*z* plan view of selected time step, showing the second invariant of the strain rate tensor in interacting lithospheres of models *2c93-60* and *1c113-70*. Viscosity (blue) and velocity (red) *y* profiles are shown as inset for each extensional domain (see the white star for the location of the *y* profile).

Finally, models with one-layer continental crust show faster trench retreat than the reference model (reaching up to ~7 cm yr^{-1} above the fast retreating oceanic slab), but with three noticeable differences (model *1c113-70*; figures 5.10c, 5.14 and 5.15; cf. *Annexe E, videos E.3 and E.4*): (1) a significant

stretching of the subducting continental lithosphere also associated with crustal decoupling, delaying slab tearing (figure 5.14b), (2) a pronounced strike-slip faulting during the upper plate extrusion, reaching a wide extensional region above the fast retreating oceanic slab (figure 5.9f) and (3) a weaker lithosphere in the extensional domain allowing for more efficient transmission of the asthenospheric flow to the overriding lithosphere, as shown by the progressive decrease of the horizontal component of flow velocity from the lithospheric mantle to the upper part of the continental crust (see viscosity and velocity profiles in inset of figure 5.9f).

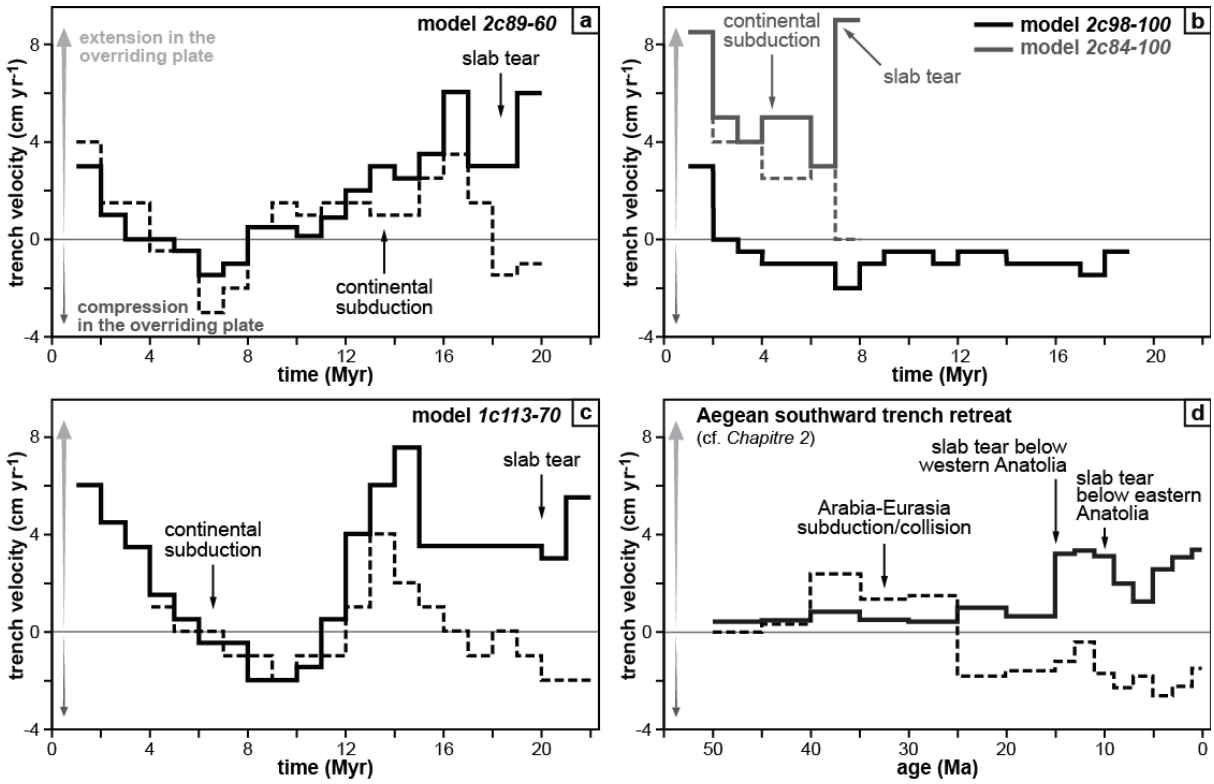

Figure 5.10: time-trench velocity diagram showing the trench migration of both oceanic and oceanic-continental subduction zones obtained from models *2c89-60* (a), *2c98-100*, *2c84-100* (b) and *1c113-70* (c) and from kinematic reconstructions of the eastern Mediterranean region (d) (cf. *Chapitre 2*). Continuous and dashed lines correspond to only oceanic and oceanic-continental subduction zones, respectively. Positive and negative distances correspond to retreating and advancing trench, respectively. The initiation of major lithospheric processes, such as continental subduction and slab tearing are highlighted in each diagram.

It is noteworthy that the apparent lack of lithospheric mantle below the overriding stretched continental crust (especially in model *1c113-70*; figure 5.14) results from the initial geometry of the lithosphere mantle and does not imply that the lithosphere is devoid of rigid mantle and that the crust

lies directly on the asthenosphere. Depending on the evolution of the rheological properties of the peridotite and therefore on the sub-crustal temperature distribution, the thermo-mechanical lithosphere-asthenosphere boundary is indeed better defined considering the 1200-1300 °C isotherms (figure 5.6b).

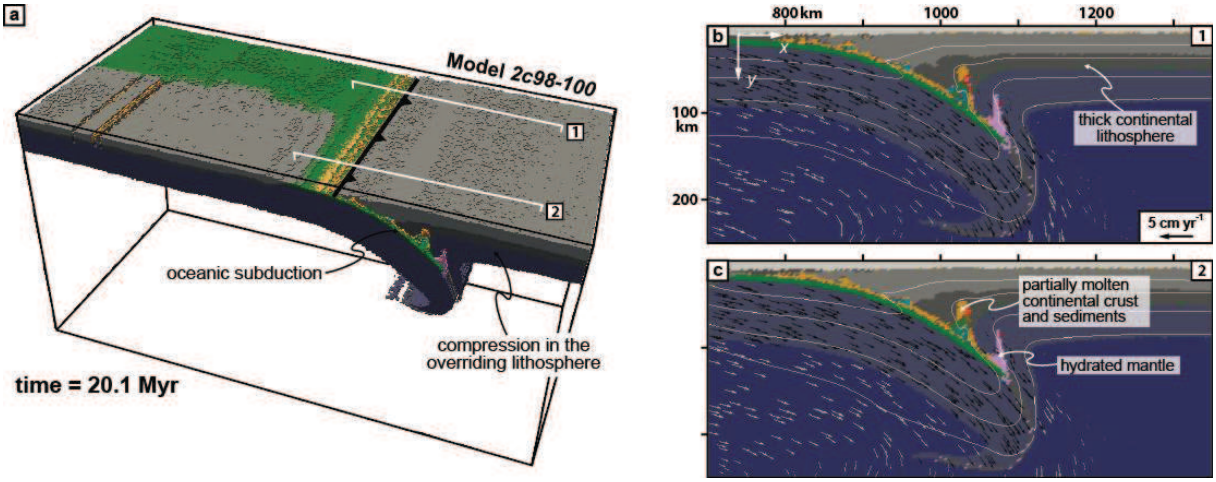

Figure 5.11: subduction geometry of the model *2c98-100*, displaying a relatively strong coupling between both interacting lithospheres. (a) 3D lateral view of the subduction zone, highlighting the compressional tectonics in the overriding continental lithosphere. (b, c) *x*-*y* cross-sections of the subduction zone, highlighting the restrained magmatic activity in the mantle wedge and the low velocity field in both the subducting lithosphere and the underlying asthenosphere (see figure 5.7 for detailed legend).

5.5.2. Genesis and transport of partially molten material

In our reference model *2c89-60*, the first stage of oceanic subduction is associated with water release from the hydrated oceanic crust at ~70 km depth to the mantle wedge (figure 5.8a). Subsequent hydration of the mantle contributes to its partial melting, resulting in a wave-like plume geometry of partially molten mantle (according to the magmatic plume description of *Zhu et al.* [2009]) that starts to ascend at ~150 km depth (figures 5.7a and 5.8a). While the oceanic slab retreats, partially molten mantle and subducted continental crust is stored at the base of the overriding crust, being passively transferred from the arc to the back-arc domain through time (see vertical cross-sections in figure 5.8).

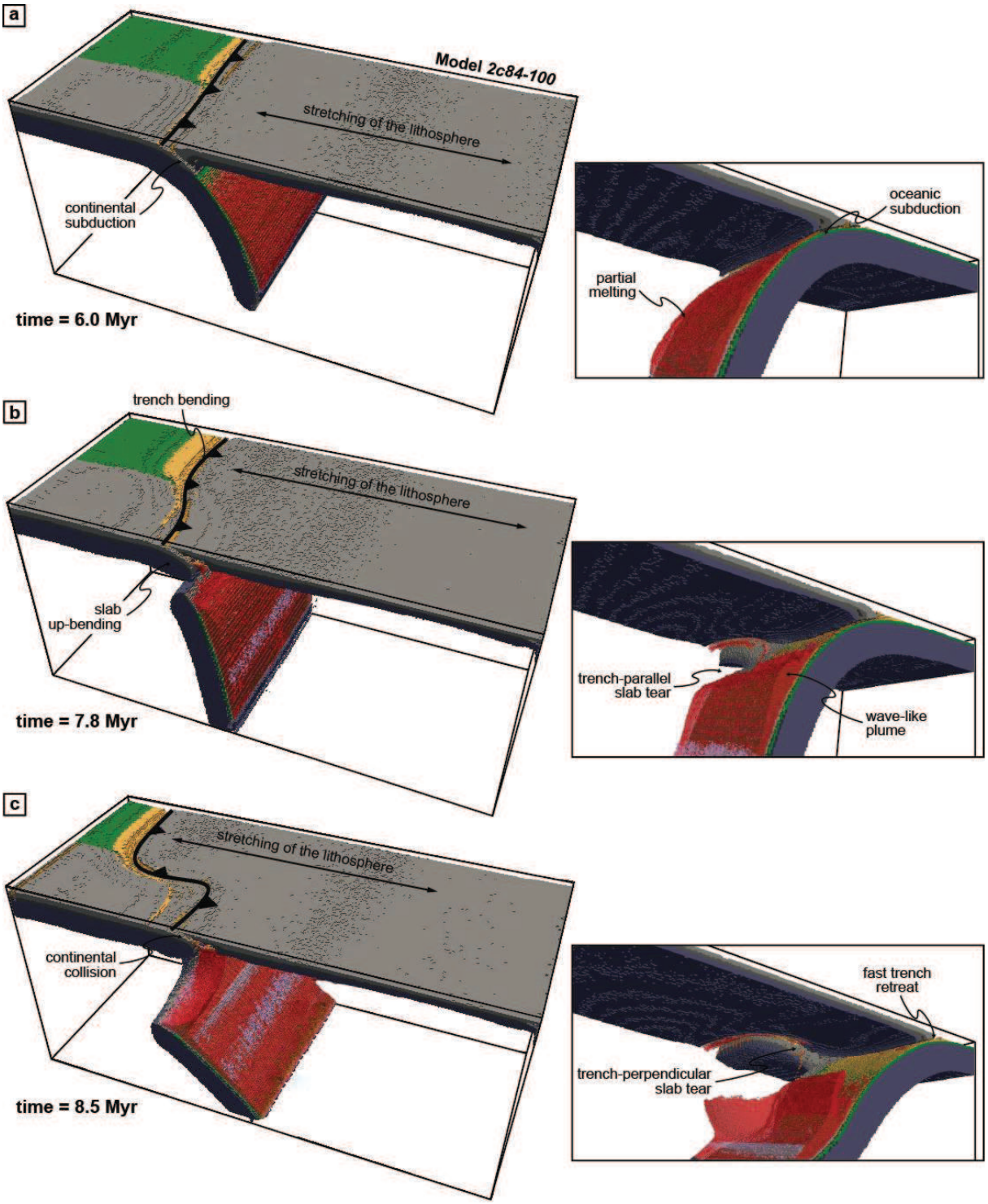

Figure 5.12: evolution of the model *2c84-100*. (a, b, c) 3D lateral view of the subduction zone (left panels) and zoom on the mantle wedge (right panels) for selected time steps. Colors represent the different rock types (see figure 5.7 for detailed legend). Asthenosphere and other phases are cut off for clarity.

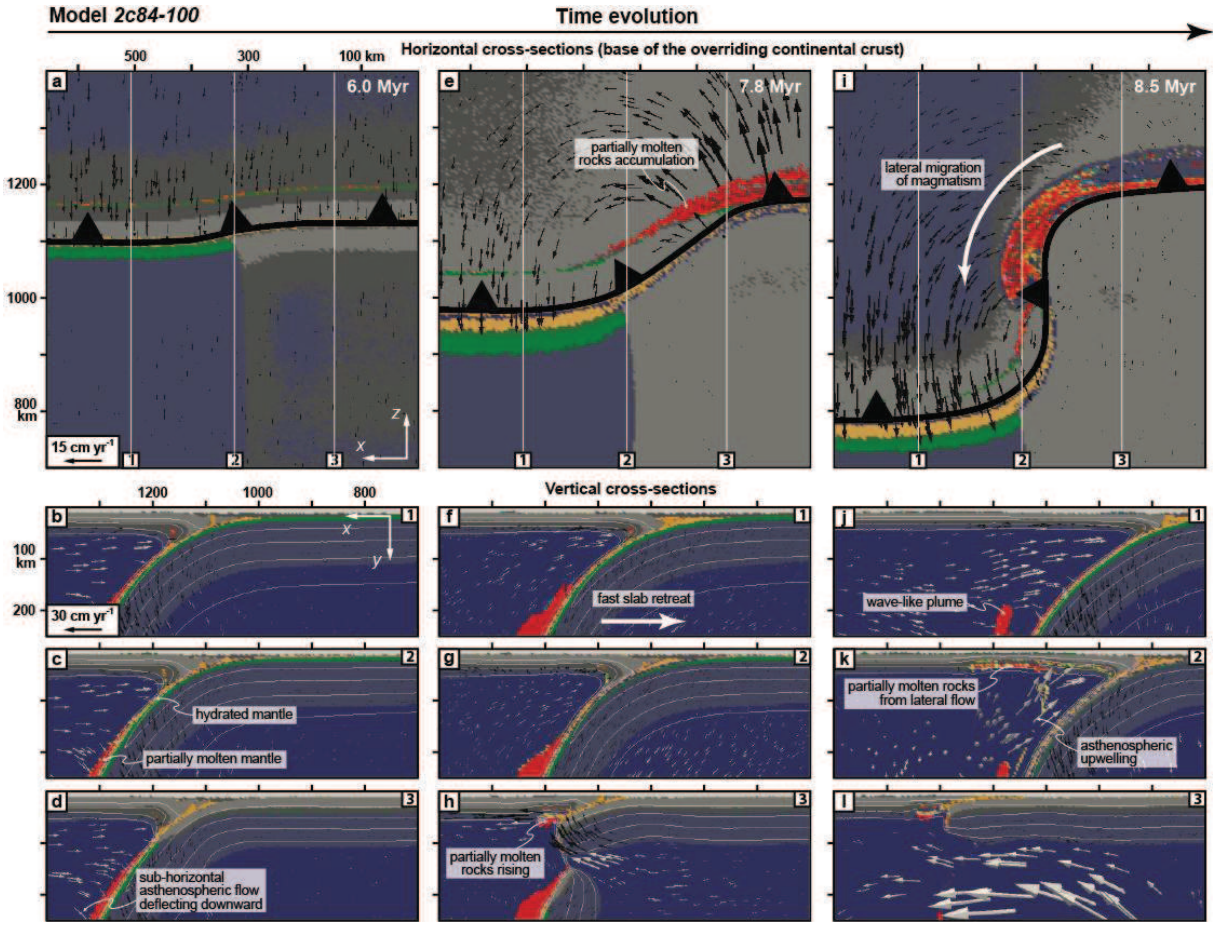

Figure 5.13: evolution of magmatism in model *2c84-100*. *x-z* plan views (a, e, i) and *x-y* cross-sections (b, c, d, f, g, h, j, k, l) of the subduction zone for selected time steps. Colors represent the different rock types (see figure 5.7 for detailed legend). Black and white arrows represent velocity vectors in the continental crust (top panels) or lithospheric mantle (bottom panels) and the asthenosphere, respectively. Scale of velocity vectors is twice larger in top panels than in bottom panels. White lines (bottom panels) represent 300, 600, 900 and 1200 °C isotherms.

The release of the negatively buoyant oceanic lithosphere after the slab tearing event results in the up-bending of the subducted continental lithosphere accompanied by fast rising and accumulation of partially molten mantle and continental crust as well as of dry asthenosphere below the active collision zone (figures 5.8e and h). A significant amount of partially molten sediments is then added to the stacked material, which is laterally transferred through the collision-subduction zone into the back-arc region and exhumed through the stretching crust up to the surface (figures 5.8i and k). Lateral migration of partially molten mantle at the base of the stretched crust above the ongoing subduction zone also takes place (figure 5.8e) and is progressively replaced by dry asthenosphere (figure 5.8i).

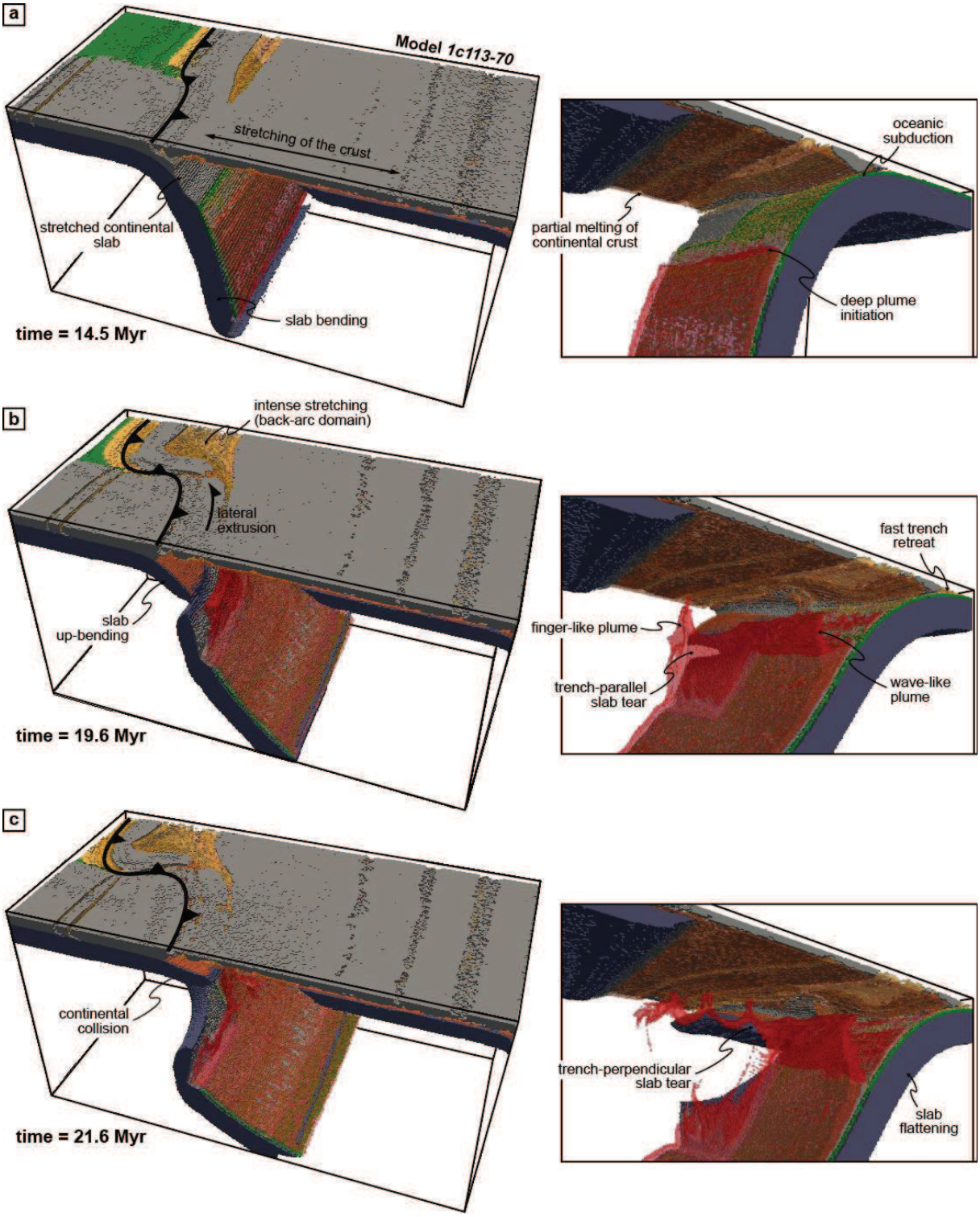

Figure 5.14: evolution of the model 1*c113-70* (with a mono-phase continental crust). (a, b, c) 3D lateral view of the subduction zone (left panels) and zoom on the mantle wedge (right panels) for selected time steps. Colors represent the different rock types (see figure 5.7 for detailed legend). Asthenosphere and other phases are cut off for clarity.

In models displaying slow subduction dynamics associated with a compressional regime (model *2c98*-100; figures 5.11b and c), the magmatic activity is restricted to small amounts of partially molten continental crust and sediments besides the mantle hydration process, slowly ascending within the thickening overriding lithosphere. In models characterized by two-layer continental crust and fast slab roll-back (model *2c84-100*; figure 5.12), the hydrated and partially molten rocks evolution is faster, similar to the reference model *2c89-60*, except that the wave-like plume of partially molten mantle in the mantle wedge develops later (figure 5.13).

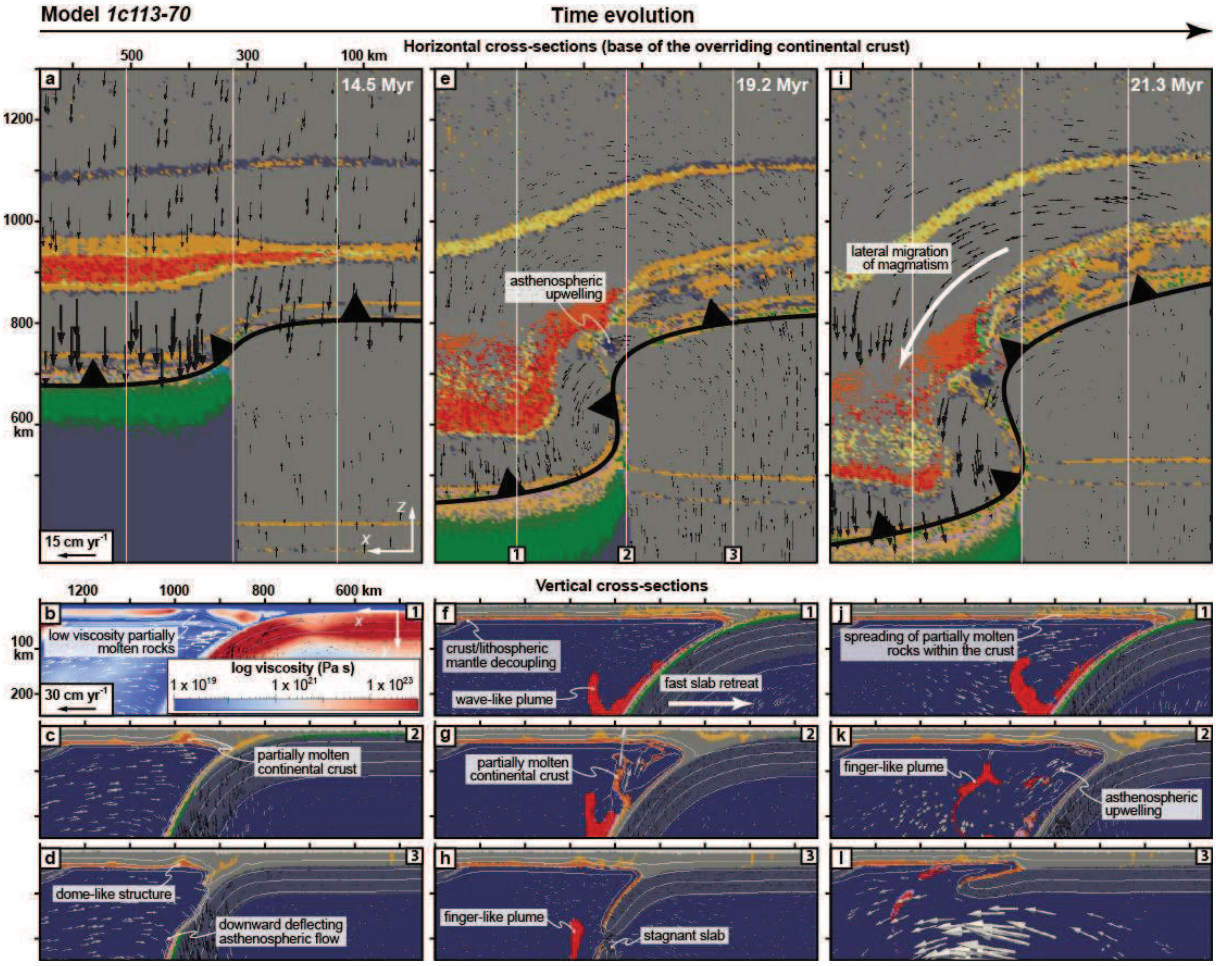

Figure 5.15: evolution of magmatism in model *1c113-70*. *x-z* plan views (a, e, i) and *x-y* cross-sections (b, c, d, f, g, h, j, k, l) of the subduction zone for selected time steps. Colors represent the different rock types (see figure 5.7 for detailed legend), excepting for the cross-section (b) where the viscosity is mapped. Black and white arrows represent velocity vectors in the continental crust (top panels) or lithospheric mantle (bottom panels) and the asthenosphere, respectively. Scale of velocity vectors is twice larger in top panels than in bottom panels. White lines (bottom panels) represent 300, 600, 900 and 1200 °C isotherms.

Finally, the magmatic evolution of models with one-layer continental crust (model *1c113-70*; figures 5.14 and 5.15) shows a number of differences. (1) Dehydration of the oceanic slab and subsequent partial melting of the mantle wedge start deeper, from ~300 km depth (figure 5.14a). The ascent of such partially molten mantle then occurs as a wave-like plume, except around the torn continental slab where it ascends as regularly-spaced finger-like plumes (figures 5.14b and c). (2) The long residence time of continental slab at depth before tearing results in increased partial melting of the crust and subsequently finger-like upwelling of melts (figure 5.15g). (3) An additional partial melting event occurs at the base of the overriding crust (figure 5.14). The partially molten rocks (mainly continental crust) are then progressively exhumed through the stretched crust, forming a high temperature dome-like structure (figures 5.15d and j).

5.6. Discussion

Assuming that partially molten rocks mimic magmatic sources from which magmas with specific composition are potentially extracted, our models provide constraints on the spatial and temporal evolution of magmatic processes in laterally constrained subduction environments. We discuss below the relationships between the magmatism, mantle flow and lithospheric deformation and then compare our findings to observations from the eastern Mediterranean region.

5.6.1. Magmatism and mantle flow

During the initial subduction of the oceanic lithosphere, slab dehydration and then hydrated partial melting result in the progressive accumulation of mantle-derived melts within the mantle wedge, mainly along grain boundaries in the peridotite [*Grove et al.*, 2006]. According to our models, such partially molten mantle rocks with lower viscosity and density rise up as plumes (figure 5.8b). *Zhu et al.* [2009] suggested that this ascent is controlled by competition between the buoyancy force of partially molten mantle (depending on their viscosity and density) and the subduction drag (depending on slab dip notably). The predominance of the buoyancy force would thus result in the development of

Rayleigh-Taylor instabilities at the interface between hydrated/partially molten mantle and dry mantle, initiating plume rising. We add upon this evidence that the asthenospheric flow related to slab dynamics is another crucial parameter affecting the initiation of upwelling and the trajectories of partially molten rocks through the mantle wedge. Initial slab bending and roll-back induces a poloidal asthenospheric flow at the slab tip (figure 5.9a) deflecting downward close to the top of the slab (model *2c89-60*; figures 5.8d and 5.16a). This flow, particularly fast for high slab retreat rates (model *1c113-70*, figures 5.15d and 16c), is responsible for spreading of partially molten rocks along the slab-mantle interface that tends to displace downward the root of the plume [*Zhu et al.*, 2009].

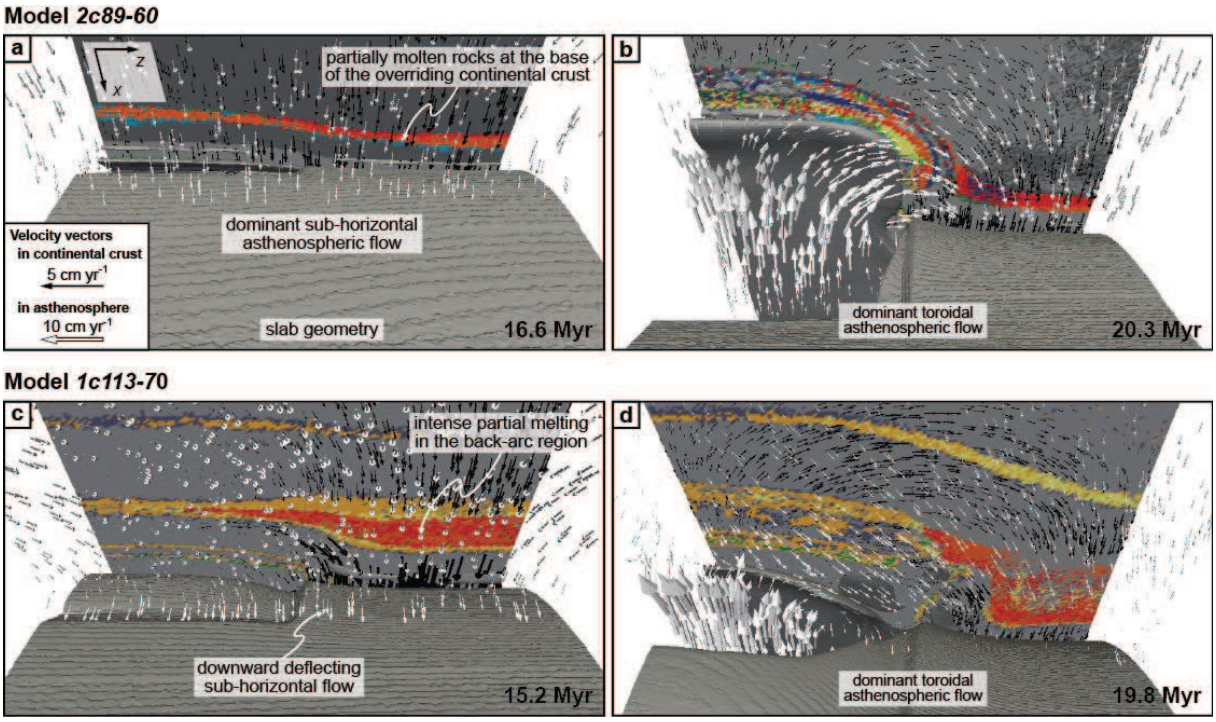

Figure 5.16: view from below of the mantle wedge of selected models, showing the relation between magmatic evolution at the base of the overriding crust and subduction-related asthenospheric flow for two selected time steps. (a, b) *x-z* plan view and slab geometry evolution of reference model *2c93-60*. (c, d) *x-z* plan view and slab geometry evolution of reference model *1c113-70*. On *x-z* plan view, colors represent the different rock types (see figure 5.7 for detailed legend). The slab geometry is visualized through an iso-viscosity contour equal to 10^{23} Pa.s. Black and white arrows represent velocity vectors in the continental crust and the asthenosphere, respectively. Scale of velocity vectors is twice larger in continental crust than in asthenosphere.

In our experiments, hydrated mantle-derived magma sources ascend mainly as wave-like plumes (figures 5.7b and 5.14b), according to the low viscosity of these partially molten rocks with respect to

the solid phases [*Zhu et al.*, 2009]. Finger-like plumes also develop close to the torn continental slab (model *1c113-70*, figures 5.14b and c). *Zhu et al.* [2009] argued that these plume structures are commonly associated with flat slabs but we find that they can also develop above a steep and stagnant slab (figure 5.15h), when the continental slab buoyancy force counterbalances the slab-pull force during a relatively long period of time. In this case, migration of fluids and melts is driven by local pressure gradients resulting from lateral variation of water release by the slab, water percolation at the slab-mantle interface [*Faccenda et al.*, 2009] and progressive growth of hydrated and partially molten mantle as finger-like plumes [*Zhu et al.*, 2013].

Slab tearing results in fast oceanic slab roll-back and promotes a fast and complex 3D asthenospheric flow pattern with both *through-tear* poloidal and toroidal flow (figures 5.9b, 5.16b and d) [*Funiciello et al.*, 2003; *Li et al.*, 2013; *Capitanio*, 2014; *Sternai et al.*, 2014]. Such asthenospheric flow can drag upward both wave- and finger-like partially molten plumes, as a result of a suction phenomenon in the mantle wedge due to slab flattening (figures 5.8k and 5.15k). The major toroidal component of convecting mantle also drives trench-parallel evolution of the magmatism at the base of the overriding continental crust (i.e. in the MASH zone [*Hildreth and Moorbath*, 1988]). Here, both partially molten mantle and crust are stored during the first stage of subduction, with a predominance of crustal-derived magmas, especially in model *1c113-70* where the prescribed upper crust material composing the one-layer continental crust is less refractory than the lower crust material defined for the two-layer continental crust (figures 5.7 and 5.14). The slab tearing promotes upwelling of large amount of both partially molten crust and mantle at the base of the overriding crust (figures 5.8e and 5.15e). Subsequent toroidal asthenospheric flow due to protracted roll-back of the oceanic slab then drags these partially molten rocks from the collision zone to the back-arc region, above the retreating subduction (figures 5.16b and d). In addition, we found a lateral increase of mantle-derived relative to crust-derived melts in the back-arc region (figure 5.8e) and a final upwelling of hot and dry asthenosphere, potentially resulting in the adiabatic melting of depleted mantle and the genesis of alkaline mafic magmas (figures 5.8e, i, 5.15e and i).

The genesis and ascent of mainly mantle-derived magmatic sources is therefore strongly controlled by the asthenospheric flow, itself depending on the slab kinematics. No significant contribution from

partial melting of the oceanic crust was recognized in our experiments, in turn suggesting that most of magmas within the mantle wedge are generated from hydrated mantle, even in warm subduction zones [*Bouilhol et al.*, 2015]. In the MASH zone, such mantle- and crustal-derived magmas may mix and therefore change composition, as if they undergo fractionation and crustal assimilation processes [*Hildreth and Moorbath*, 1988]. Sedimentary materials, likely contributes to the maturation of these magmas in this MASH zone, especially across continental subduction zone where the strong coupling between both continental lithospheres enhances upper plate removal process and therefore the burial of detrital continental crust (figures 5.8i and k) [*Gerya and Meilick*, 2011].

5.6.2. Magmatism and lithospheric deformation

Low-viscosity partially molten rocks exhumed through the overriding continental lithosphere provide a strong rheological contrast with the surrounding high-viscosity rocks (figures 5.8b and 5.15b) and therefore localize the lithospheric deformation. Especially, the storage of partially molten rocks at the base of the crust results in a strong weakening of the lithosphere, promoting the partial decoupling between the continental crust and the underlying lithospheric mantle and intense crustal stretching (figure 5.14c). Reduced upper plate lithospheric strength enhances the decoupling at the subduction interface, which in turn increases the slab roll-back rate, thereby affecting the overriding crustal extrusion and stretching (figure 5.10; comparison between slow evolving models *2c89-60* and *2c98-100* and fast evolving models *1c113-70* and *2c84-100*) [*Gerya and Meilick*, 2011].

Exhuming partially molten rocks can also control the distribution of crustal deformation. Occurring as a dome-like structure (figure 5.15d), the rising of partially molten rocks in our models is initiated from a Rayleigh-Taylor instability, similarly to the plume ascent. Resulting rheological weakening localizes deformation, inducing strike-slip faulting and back-arc-related intense lithospheric stretching, accommodating the lateral extrusion of continental block and fast slab roll-back, respectively (figure 5.9d). Moreover, an intense partial melting induces a longer strike-slip fault zone and a wider back-arc (figure 5.9f) [*Gerya and Meilick*, 2011; *Capitanio*, 2014].

The driving forces of overriding lithosphere deformation across subduction-collision environment have been largely discussed in term of crustal and mantle contributions [e.g. *Royden*, 1996; *Jolivet et*

al., 2009; *Faccenna and Becker*, 2010]. Recently, *Sternai et al.* [2014] have proposed that extrusion tectonics may be jointly driven by continental collision, slab roll-back and associated mantle flow, the latter being particularly effective across hot and thin lithospheres. Indeed, the viscosity contrast between such lithosphere and the underlying asthenosphere is low, which promotes crust/mantle coupling. Our results further suggest that the weakening of the overriding plate by the magmatic input also results in a lower viscosity contrast along the lithosphere-asthenosphere boundary and therefore controls the crust/mantle coupling (inset of figures 5.9d and f). This is a crucial mechanism for transmission of the shear stresses (highlighted in our experiments by the horizontal component of velocity field) from the mantle to the crust. In addition, sub-parallel crustal and asthenospheric velocity fields in the back-arc region where the upper lithosphere is thin, hot and therefore weak (figures 5.9c and e), suggest that the strain is, at least to some extent, controlled by the underlying asthenospheric flow, consistent with field observations [e.g. *Jolivet et al.*, 2009].

5.6.3. Implications for the eastern Mediterranean region

The late Cenozoic geodynamics of the eastern Mediterranean region, in particular coeval retreat of the Hellenic subduction zone and collision across the Arabia-Eurasia margin (figure 5.4c) [*Jolivet and Faccenna*, 2000], are consistently reproduced by our numerical experiments (figures 5.7, 5.12 and 5.14). At depth, slab tearing occurs in these models along the ocean-continent transition, resulting from the along-trench buoyancy variations due to the coeval subduction of oceanic and continental material. Similar lithospheric processes have also been proposed to take place in the eastern Mediterranean region based on different seismic tomographic models, with two possible slab tears beneath western and eastern Anatolia (figure 5.5b) [*De Boorder et al.*, 1998; *Wortel and Spakman*, 2000; *Li et al.*, 2008] and an additional more recent one, further west below the Corinth Rift [*Jolivet et al.*, 2013]. In addition, the toroidal asthenospheric flow in our models is similar to *SKS* fast splitting directions in the eastern Mediterranean region, which can be considered as a proxy for the underlying mantle flow pattern (figures 5.5c and 5.9) [*Paul et al.*, 2014]. The timing of these tearing events is however not well constrained, but considering geological, kinematic and magmatic evidences, several authors suggested that they occurred 15-10 Ma ago [*Faccenna et al.*, 2006; *Dilek and Altunkaynak*,

2009; *Jolivet et al.*, 2015]. *Faccenna et al.* [2006] argued that the slab tearing beneath the Arabia-Eurasia collision zone is responsible for the westward extrusion of the Anatolian crustal block, accommodated by the NAF that initiated ~12 Ma ago in eastern Anatolia [*Şengör et al.*, 2005]. The strike-slip deformation is fairly well reproduced in our experiments, especially in model *1c113-70* (figure 5.9f), and results in a crustal kinematics characterized by an overall counterclockwise rotation from the collisional domain toward the retreating subduction zone, similar to the present-day crustal kinematics across the studied region deduced from GPS measurements (figure 5.5a) [*Reilinger et al.*, 2006]. The magnitude of these crustal velocities is also consistent, with notably the trench motion evolving from -2 cm yr^{-1} (advancing trench) to 3-7 cm yr^{-1} (retreating trench) in models *2c89-60* and *1c113-70* and from 0.5 to 3 cm yr^{-1} for the Hellenic trench, estimated from kinematic reconstructions (figure 5.10). Acceleration of trench retreating, combined with an advancing collisional front in our experiments as well as in the natural case can be related to the inception of slab tears, which would confirm the middle-late Miocene age of slab tearing in the eastern Mediterranean region. Differences in the trench motion rate may be to some extent affected to the imposed free slip conditions at the front and back boundaries (z = 0 and z = 656 km), laterally constraining the crustal and mantle flow. Additional numerical experiments accounting for open boundaries as well as the neighboring plates would then be relevant, leading to more realistic boundaries conditions and therefore more accurate crustal velocities [*Yamato et al.*, 2009].

Another major deformation event consists in the progressive opening of a back-arc basin (i.e. the Aegean-west Anatolian region) where partially molten rocks are exhumed as dome-like structures (model *1c113*-70, figure 5.15d) and mimic high-temperature MCCs with migmatitic core, notably recognized in the Rhodope and Menderes massifs as well as in the Cyclades archipelago [*Lister et al.*, 1984; *Bozkurt and Oberhänsli*, 2001; *Vanderhaeghe*, 2004; *Brun and Sokoutis*, 2007; *Jolivet et al.*, 2013]. Magmatic activity in this back-arc domain is characterized by a first-order southward migration (figure 5.4a) [*Pe-Piper and Piper*, 2006; *Dilek and Altunkaynak*, 2009; *Ersoy and Palmer*, 2013], which is driven by slab roll-back in our model (figures 5.8, 5.15, 5.16a and c). During the Miocene, this magmatic trend is then modulated by a second-order southwestward migration from the Menderes massif to the Cyclades, which is also faithfully reproduced in our model with an along-trench

migration of partially molten rocks at the base of the crust controlled by the toroidal asthenospheric flow related to slab tearing (figures 5.16b and c). This along-trench migration of melts is accompanied by an increase of the mantle-sourced magmas in the natural example, a feature that some experiments fail to reproduce (e.g. model *1c113-70*; figure 5.15e), probably because the mantle signature is buffered by the partially molten crustal layer at the base of the overriding crust. However, this trend is recognized in model *2c89-60* (figures 5.8e and i), where increasing mantle-sourced magmatic component at the base of the overriding crust mimics observations from the Miocene intrusions across the Cyclades [*Jolivet et al.*, 2015]. Eastern Anatolia is further characterized by a wide calk-alkaline to alkaline volcanic province of late Miocene to Quaternary age (figure 5.4c) [*Keskin*, 2003]. In our experiments, partially molten mantle and crust accumulate at the base of the collision zone due to the sub-collisional slab detachment, potentially resulting in such wide magmatic activity (figures 5.8e and h). Later alkaline volcanism in the eastern Mediterranean region [*Keskin*, 2003; *Ersoy and Palmer*, 2013] can be related to the upwelling of asthenospheric flow associated to protracted slab tearing and intense overriding lithospheric stretching (figures 5.8e, i and 5.16b).

Our numerical experiments clearly emphasize the role of subduction dynamics and related asthenospheric flow on the magmatic evolution of the eastern Mediterranean region, especially those characterized by a weak one-layer continental crust (e.g. model *1c113-70*, figure 5.6c). Indeed, this region underwent a complex tectonic story since the early Cenozoic, such as extension in the Rhodope massif since the Eocene [*Brun and Sokoutis*, 2007], which may have significantly weakened the overriding lithosphere. Of course, these 3D models cannot fully assess the natural complexity of the eastern Mediterranean subduction zone, notably characterized by successive oceanic and continental subduction events and possible several slab tearing processes [*Stampfli and Borel*, 2002]. However, consistency between our experiments and the natural case in terms of crustal kinematics and deformation and magmatic evolution suggests that we reproduce the first-order crustal and mantle dynamics of the eastern Mediterranean subduction zone during the late Cenozoic.

Although we focus here on slab roll-back, tearing and the associated asthenospheric flow, other factors such as the plate convergence rate [*Nikolaeva et al.*, 2008] and the interactions between the slab, the 660 km-depth discontinuity [*Guillou-Frottier et al.*, 1995] and the large scale mantle

conveyor belt [*Faccenna et al.*, 2013] have certainly affected the magmatic history in the eastern Mediterranean region, but are left for future works.

5.7. Conclusions

Using 3D high-resolution coupled petrological-thermo-mechanical models integrating experimentally calibrated non-Newtonian crustal and mantle rheologies, we are able to reproduce the first-order geodynamic evolution of a laterally constrained subduction zone characterized by slab roll-back and tearing. We focus on the interactions between the asthenospheric flow and the genesis, transport and emplacement of magmas, and reach the following conclusions.

(1) The slab kinematics and associated mantle flow affect the magma genesis and transport within the hydrated mantle wedge. In particular, bending of the slab and associated downward-deflecting asthenospheric flow promote the trapping of partially molten rocks at the slab/mantle interface. Conversely, a fast slab roll-back promotes the asthenospheric upwelling and therefore the ascent of partially molten rocks as wave-like plumes, while the slower kinematics of a stagnant slab promotes magma ascent as finger-like plumes, mainly driven by pressure gradients in the mantle. Finally, the magmatic sources migrate in response to the asthenospheric flow related to slab tearing which therefore control the emplacement locations of melts at the base of the overriding lithosphere.

(2) During their emplacement, both mantle- and crust-derived magmas contribute to the reduction of the strength of the overriding lithosphere, thereby affecting the deformation pattern. The ascent of large amounts of partially molten rocks within the stretched crust localizes the deformation along dome-like structures. The deformation is characterized by strike-slip faulting and crustal stretching that accommodate the lateral extrusion and slab roll-back, respectively. Such weakening of the crust due to the presence of melts can also facilitate the transmission of the shear stresses from the flow of the weak asthenosphere to the crust, especially if the lithospheric mantle is thin, supporting the hypothesis of the mantle flow dragging the crust and affecting surface deformation.

(3) The initial setup considered in our experiments has been designed to reproduce the late Cenozoic plate configuration of the eastern Mediterranean region. The kinematic, strain and magmatic evolution of this region deduced from geological and geophysical constraints are reasonably well reproduced by our experiments that suggest a strong control of the underlying asthenospheric flow on magma genesis and transport along the eastern Mediterranean subduction zone.

Acknowledgments

This work was funded by the French Geological Survey (BRGM), the Région Centre, the ERC RHEOLITH project (ERC Advanced Grant n° 290864) and the Labex VOLTAIRE (ANR-10-LABX-100-01). We thank Eloise Bessière for her contribution in figures design.

Chapitre 6

Synthèse générale : dynamique de subduction et minéralisations en Méditerranée orientale

6.1. Crétacé supérieur : une chaîne de type Andine, riche en minéralisations cuprifères 238

6.1.1. Dynamique de subduction et processus mantelliques 238

6.1.2. Dynamique de subduction et processus crustaux 241

6.2. Paléocène-Eocène : accrétion continentale et quiescence de l'activité magmatique et hydrothermale 242

6.2.1. Dynamique de subduction et processus mantelliques 243

6.2.2. Dynamique de subduction et processus crustaux 244

6.3. Oligocène : extension d'arrière-arc et minéralisations à plomb-zinc 245

6.3.1. Dynamique de subduction et processus mantelliques 245

6.3.2. Dynamique de subduction et processus crustaux 246

6.4. Miocène : étirement lithosphérique intense et minéralisations aurifères 247

6.4.1. Dynamique de subduction et processus mantelliques 248

6.4.2. Dynamique de subduction et processus crustaux 250

6.5. Conclusion : processus géodynamiques et métallogénie 253

6.6. Perspectives.....255

6.6.1. Quid de l'exploration minérale ? 255

6.6.2. Pistes de recherche 257

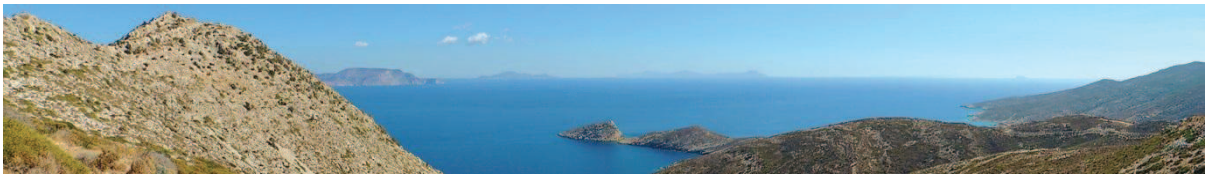

Au cours de ce travail de thèse, j'ai cherché à comprendre les liens entre la dynamique de subduction en Méditerranée orientale et l'activité magmatique et hydrothermale à différentes échelles. Ceci, afin de mettre en évidence les processus d'échelle lithosphérique qui favorisent la genèse de grandes provinces métallogéniques, notamment riches en cuivre et en or. Mon étude a alors porté sur quatre axes majeurs :

(1) une meilleure compréhension de l'évolution tectonique et magmatique de la zone de subduction est-Méditerranéenne, grâce à la réalisation de reconstructions cinématiques précises de la région depuis le Crétacé supérieur (cf. *Chapitre 2*),

(2) une étude de la distribution spatiale et temporelle des minéralisations au cours de l'évolution de cette zone de subduction afin d'associer certains processus mantelliques et crustaux à la mise en place de ces systèmes minéralisés (cf. *Chapitre 3*),

(3) une étude de terrain afin de mettre en évidence, dans un contexte extensif d'arrière-arc, le rôle des structures de type détachement et des systèmes magmatiques associés sur la genèse de concentrations métalliques (cf. *Chapitre 4*),

(4) la réalisation de modèles numériques afin d'apporter des contraintes physiques sur le contrôle de processus profonds liés à la subduction (ex. dynamique du panneau plongeant, flux asthénosphériques associés) sur le régime tectonique et la distribution du magmatisme, potentiellement associés à des systèmes minéralisés, en surface (cf. *Chapitre 5*).

Dans ce chapitre de synthèse, je discute à partir des observations précédentes de l'influence de la dynamique mantellique et crustale associée à chaque régime de subduction identifié en Méditerranée orientale depuis le Crétacé supérieur, sur la genèse et la distribution spatiale des minéralisations. Je reprends ensuite ces résultats afin d'identifier quels processus (mantelliques et crustaux) ont un rôle prépondérant dans la mise en place de grandes provinces métallogéniques dans ces environnements de subduction. Finalement, chaque travail de recherche (celui-ci y compris) soulevant de nouvelles

questions, je propose quelques axes de recherche qui pourraient être intéressants d'explorer afin de préciser ces liens entre géodynamique et métallogénie.

6.1. Crétacé supérieur : une chaîne de type Andine, riche en minéralisations cuprifères

Au Crétacé supérieur, la zone de subduction Téthysienne était située à environ 1000 kilomètres plus au nord de sa position actuelle. La marge active Eurasienne s'étendait alors sur plus de 2000 kilomètres d'ouest en est, depuis les Balkans jusque dans les Pontides (figures 2.9a-h). Cette zone de subduction relativement linéaire a permis le développement d'un arc magmatique typique d'un environnement d'arc (i.e. magmas calco-alcalins, moyennement riches en potassium) [ex. *Yılmaz et al.*, 1997; *Berza et al.*, 1998]. Accompagnant ce magmatisme, de nombreux gîtes minéralisés, pour la plupart riches en cuivre, se sont mis en place dans la croûte supérieure, alors que le régime tectonique actif est transtensif à extensif (figure 2.6). Il s'agit principalement de porphyres cuprifères (ex. le gisement d'Elatsite en Bulgarie) associés à des gisements de type skarn ou épithermal acide (figures 3.1a-h et 3.3) [*Janković*, 1997; *Heinrich & Neubauer*, 2002]. La distribution de ces systèmes minéralisés se caractérise par un alignement de clusters parallèle à la zone de subduction Téthysienne, formant le long de la chaîne des Balkans, la ceinture Apuseni-Banat-Timok-Srednogorie (figure 6.1a) [ex. *Von Quadt et al.*, 2005].

6.1.1. Dynamique de subduction et processus mantelliques

Les similitudes du point de vue du contexte géodynamique et de l'activité magmatique et métallogénique entre cette zone de subduction d'âge Crétacé et la zone de subduction Andine actuelle (et notamment sa partie centrale) (figure 6.1), laissent à penser que les processus de genèse des systèmes minéralisés sont également similaires, s'apparentant donc à ceux décrits dans le *chapitre 1* de ce manuscrit de thèse (cf. *Section 1.3*) (figures 1.5, 1.6 et 1.7) [ex. *Hedenquist & Lowenstern*, 1994; *Sillitoe*, 2010; *Richards*, 2011].

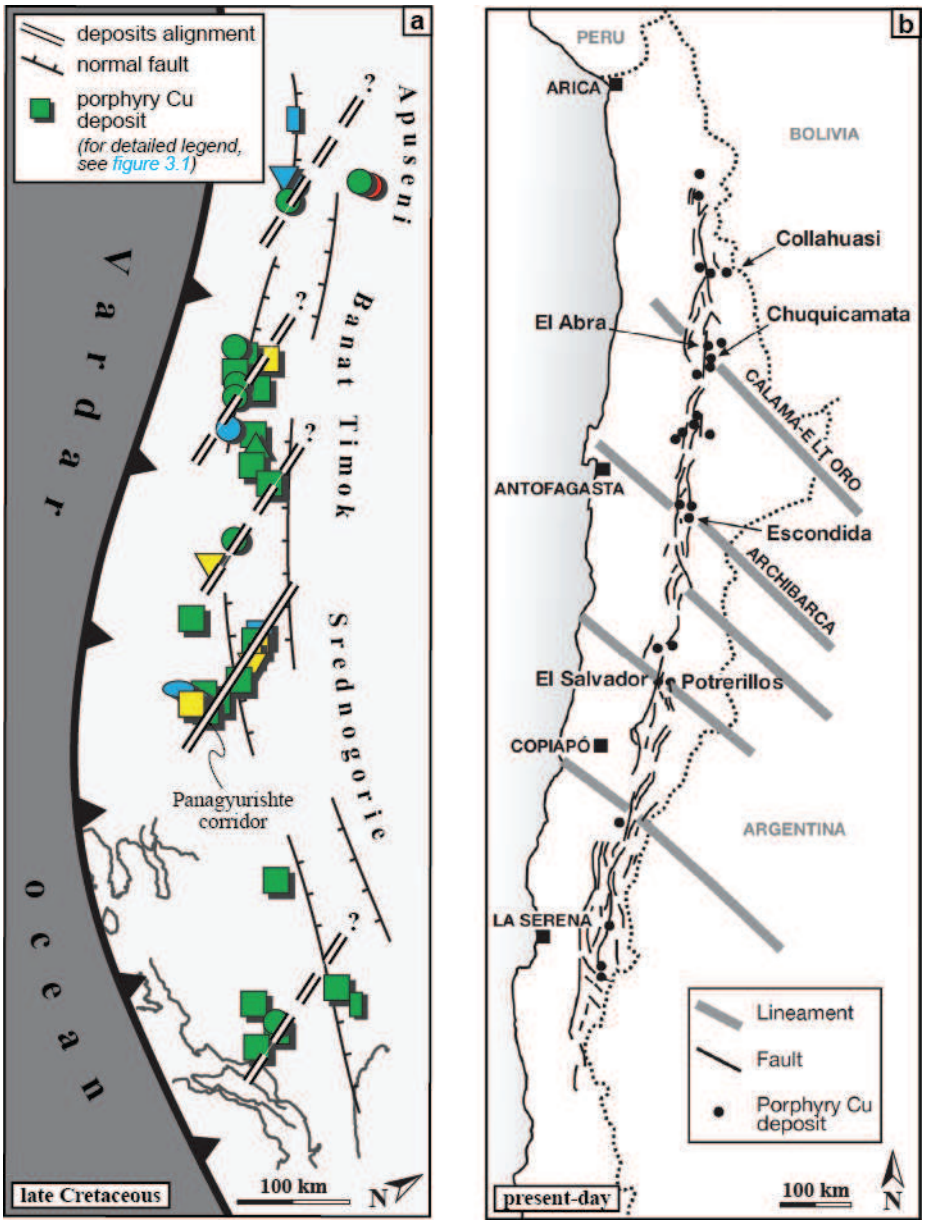

Figure 6.1 : cartes tectoniques comparatives de la répartition des gisements métallifères (principalement des porphyres cuprifère) dans le long de la chaine des Balkans en Méditerranée orientale au Crétacé supérieur (a) (cf. *Chapitre 3*) et le long de la cordillère des Andes à l'actuel (b) [*Sillitoe*, 2010].

Les métaux chalcophiles comme le cuivre auraient alors été préférentiellement mobilisés dans les magmas issus de la fusion partielle hydratée du coin mantellique, tandis que les métaux sidérophiles, tels que l'or, auraient plutôt été piégés sous la forme de cumulats sulfurés, notamment dans le manteau lithosphérique et en base de croûte au niveau de la zone *MASH* (figure 3.4a) [*Peach et al.*, 1990; *Richards*, 2009]. Un tel fractionnement des métaux expliquerait alors la dominance de gîtes minéralisés riches en cuivre dans ces environnements d'arc.

L'influence de processus profonds sur la mise en place de ces systèmes magmatiques et hydrothermaux est difficile à contraindre étant donné le peu d'informations disponibles sur la géométrie du panneau plongeant à cette époque. On sait néanmoins que cette zone de subduction est restée stable sur une longue période de temps (i.e. plusieurs dizaines de millions d'années au cours du Mésozoïque), associée à une convergence rapide entre l'Afrique et l'Eurasie [*Rosenbaum et al.*, 2002] qui a entrainé l'enfouissement d'une grande quantité de matériel lithosphérique. Une telle cinématique aurait alors favorisé une grande production de magmas fertiles dans le coin mantellique, en raison notamment d'un apport continu de matériel océanique hydraté soutenant la fusion partielle du manteau [*Richards*, 2005; *Bertrand et al.*, 2014]. La relative stabilité de la zone de subduction peut également être associée à des flux asthénosphériques lents qui induisent un transport vertical du magma dans le coin mantellique, similairement aux *finger-like magmatic plumes* décrits à partir des modèles numériques réalisés (cf. *Chapitre 5*, figure 5.14b) [*Zhu et al.*, 2009] et qui expliquerait l'alignement des occurrences magmatiques et minéralisées le long d'une bande étroite parallèle à la fosse (figures 6.1 et 6.2) [*Richards*, 2003].

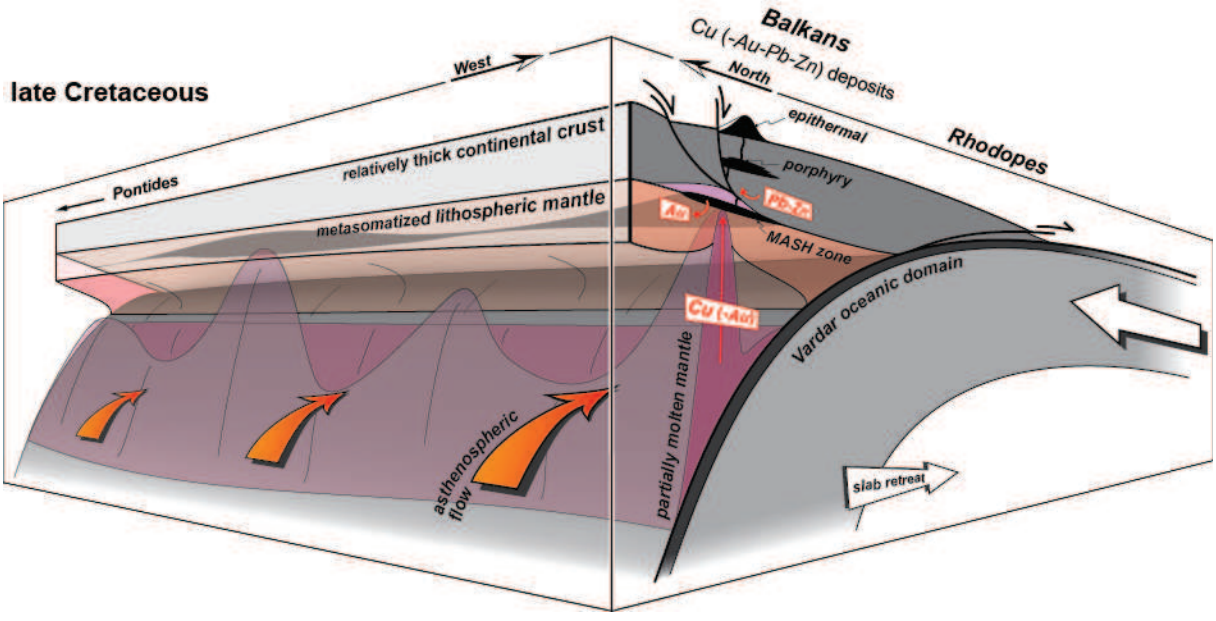

Figure 6.2 : bloc 3D interprétatif de la géométrie de la zone de subduction est-Méditerranéenne au Crétacé supérieur vue de dessous, mettant en évidence une cinématique de cinématique de subduction stable, associée à un faible retrait du panneau plongeant. Cette période est caractérisée par une forte mobilisation du cuivre lors de la genèse de systèmes magmatiques dans le coin mantellique qui induit la formation de gisements cuprifères (i.e. principalement des porphyres minéralisés) dans une croûte continentale en extension (ou transtension).

Cette stabilité dans la cinématique de la subduction peut être liée (1) au fait qu'aucun domaine continental ne vient interagir avec la marge active au cours du Crétacé supérieur (cf. *Chapitre 2*) et (2) à la largeur importante (i.e. plus de 2000 km) de la zone de subduction qui induit une cinématique lente en raison de l'augmentation de la résistance du manteau au déplacement d'une large lithosphère subduite [ex. *Schellart et al.*, 2007; *Loiselet et al.*, 2009]. D'autres processus peuvent également avoir influencé cette activité magmatique et la mobilisation des métaux dans le coin mantellique, comme la subduction d'une ride médio-océanique [*Rosenbaum et al.*, 2005], mais ce dernier reste difficile à discuter étant donné le manque de contraintes sur la dynamique profonde de cette subduction d'âge Crétacé supérieur.

6.1.2. Dynamique de subduction et processus crustaux

Au Crétacé supérieur, la tectonique extensive à transtensive affectant la marge active a favorisé la remontée des magmas fertiles depuis la base de la croûte le long de structures transtensives actives (ex. le corridor de Panagyurishte dans la région de Srednogorie, figure 6.1a [*Von Quadt et al.*, 2005]). La présence de structures similaires le long de cette ceinture métallogénique, cependant non reconnues sur le terrain, pourrait expliquer le regroupement en clusters de ces minéralisations, comme c'est le cas le long de la cordillère des Andes (figure 6.1b) [*Sillitoe*, 2010].

En revanche, il n'y a pas d'indication le long de la chaîne des Balkans d'un changement de régime tectonique qui aurait précédé la précipitation de ces gîtes métalliques, comme le suggère *Tosdal & Richards* [2001] dans leur modèle de genèse des porphyres cuprifères. Le manque de contraintes précises sur l'évolution tectonique des Balkans ne permet cependant pas d'apporter une réponse claire à ce sujet, d'autant plus que dans les Pontides orientales, un épisode compressif daté à 85-80 Ma a été identifié [*Yılmaz et al.*, 1997].

Ce régime tectonique extensif à transtensif peut être dû (1) au faible retrait du panneau plongeant Téthysien vers le sud sur une distance comprise entre 50 et 100 km (cf. *Section 2.6.1,* figure 2.13), associé à une subduction oblique [*Von Quadt et al.*, 2005] et (2) à l'effondrement gravitaire de la chaîne, notamment favorisé par le fluage de la croûte inférieure, si cette dernière est partiellement fondue [*Dewey*, 1988; *Vanderhaeghe*, 2012]. Cependant, la migration vers le sud de l'arc magmatique

dans la chaîne des Balkans [*Ciobanu et al.*, 2002; *von Quadt et al.*, 2005] et des Pontides [*Yılmaz et al.*, 1997] au Crétacé supérieur, tend à privilégier la première hypothèse du retrait du panneau plongeant.

6.2. Paléocène-Eocène : accrétion continentale et quiescence de l'activité magmatique et hydrothermale

A partir du Paléocène, plusieurs domaines continentaux, séparés au cours du Mésozoïque de la plaque Afrique, se sont accrétés à la marge active Eurasienne : la plateforme carbonatée Pélagonienne, le complexe cristallin d'Anatolie centrale (i.e. *Central Anatolian Crystalline Complex* : *CACC*) et la plateforme carbonatée des Taurides (figures 2.9h-n). Ces épisodes de subduction et d'accrétion continentale ont conduit à la formation de chaînes orogéniques comme les Hellénides ou les Anatolides-Taurides [ex. *Aubouin*, 1959; *Collins & Robertson*, 1998; *van Hinsbergen et al.*, 2005a] et à l'instauration d'un régime tectonique compressif le long de la chaîne des Balkans et des Pontides qui a culminé à l'Eocène avec le développement de la *fold-and-thrust-belt* [*Doglioni et al.*, 1996; *Yılmaz et al.*, 1997]. Cette époque est caractérisée par une relative quiescence de l'activité magmatique et hydrothermale (figures 3.1i-m et 3.3). Dans les Balkans, il ne subsiste que de petits centres volcaniques alcalins qui se seraient mis en place au cours de courtes périodes de relâchement des contraintes compressives à partir de faibles taux de fusion partielle d'un matériel asthénosphérique [*Cvetković et al.*, 2004]. L'arc magmatique qui s'étendait le long de cette chaîne a, quant à lui, migré vers le sud où une ceinture magmatique calco-alcaline typique d'un environnement d'arc est mise en évidence à l'Eocène depuis la Péninsule Chalcidique à l'ouest jusqu'au complexe cristallin d'Anatolie centrale à l'est (figures 2.9j-m) [ex. *Harris et al.*, 1994; *Ersoy & Palmer*, 2013]. En revanche, très peu de minéralisations ont été identifiées comme associés à ce magmatisme (figure 3.2b).

6.2.1. Dynamique de subduction et processus mantelliques

L'accrétion continentale le long de la marge Eurasienne et le retrait vers le sud de la zone de subduction qui en résulte, permet d'expliquer la migration de l'arc magmatique (figures 2.10 et 2.11). Cependant, l'absence de systèmes minéralisés associés à cette activité magmatique reste mal comprise.

Il est néanmoins possible que la dynamique lente du retrait du panneau plongeant (figure 2.13) et des flux asthénosphériques associés et la diminution de la vitesse de convergence Afrique-Eurasie [*Rosenbaum et al.*, 2002], n'aient pas permis de renouveler de manière significative le matériel péridotitique dans le coin mantellique qui a alors suivi passivement le retrait de la zone de subduction vers le sud. Ce non renouvellement du coin mantellique, métasomatisé au cours du Crétacé supérieur et donc appauvri en métaux, pourrait alors expliquer le caractère stérile des magmas d'arc d'âge Eocène en Méditerranée orientale (figure 6.3). Une étude géochimique approfondie de ces produits magmatiques serait cependant nécessaire afin de valider (ou non) l'existence d'un tel manteau appauvri en métaux sous cet arc magmatique.

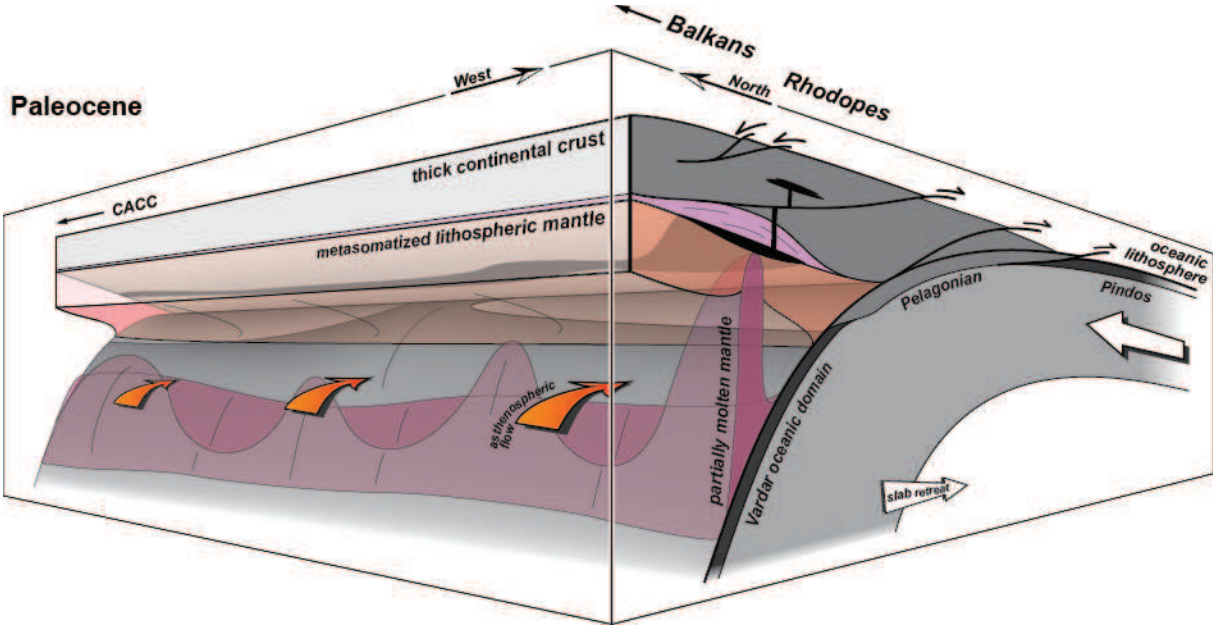

Figure 6.3 : bloc 3D interprétatif de la géométrie de la zone de subduction est-Méditerranéenne au Paléocène vue de dessous, mettant en évidence une cinématique lente de la subduction associée à un épisode d'accrétion continentale. Cette période est caractérisée par une relative quiescence dans l'activité hydrothermale responsable de la genèse de concentrations minéralisées.

Une autre hypothèse est l'apport dans le coin mantellique de matériel continental appartenant aux différents domaines continentaux accrétés qui auraient été entrainés dans le canal de subduction. Il existe des preuves d'un tel mécanisme avec la reconnaissance de roches ayant subi un métamorphisme de haute pression et basse température au niveau du canal de subduction et qui ont ensuite été exhumées (ex. les unités de Tavşanlı et d'Afyon dans la chaîne des Anatolides, figure 2.11) [ex. *Okay*, 1986; *Pourteau et al.*, 2010; *Plunder et al.*, 2013]. Cet apport aurait alors modifié les flux de matière au niveau du coin mantellique (ex. apport d'eau moindre, fusion partielle du matériel crustal), perturbant alors les processus de mobilisation des métaux dans les magmas. Cependant, la signature typique d'arc du magmatisme Eocène invalide cette hypothèse, suggérant le maintien d'un coin mantellique hydraté sus-jacent à une lithosphère plongeante océanique (figure 6.3) [*Harris et al.*, 1994; *Okay & Satır*, 2006].

6.2.2. Dynamique de subduction et processus crustaux

L'instauration d'un régime tectonique compressif à partir du Paléocène a induit un épaississement crustal important au niveau de la marge Eurasienne qui permet d'expliquer le métamorphisme de moyenne température-moyenne pression enregistré dans le massif du Rhodope à cette période (figure 2.6) [*Bonev et al.*, 2006 et références associées]. D'après les modèles métallogéniques de *Sillitoe & Hedenquist* [2003] et de *Cooke et al.* [2005], un tel épaississement crustal favoriserait la genèse de gisements porphyriques et épithermaux de grande taille grâce au développement de larges chambres magmatiques, ce qui n'est pas le cas en Méditerranée orientale à cette époque, probablement en raison de la dynamique profonde décrite ci-dessus. De plus, l'absence de tels gisements à partir de la fin de l'Eocène, lors de l'instauration d'un régime extensif dans le domaine Egéen (cf. *Section 6.3*), semble également invalider l'hypothèse du stockage d'une grande quantité de magmas potentiellement fertiles à la base de la croûte qui aurait ensuite pu remonter dans la croûte, à la faveur d'un relâchement des contraintes tectoniques [*Tosdal and Richards*, 2001; *Richards*, 2005].

6.3. Oligocène : extension d'arrière-arc et minéralisations à plomb-zinc

A l'Oligocène, l'accélération du retrait vers le sud du panneau plongeant Hellénique induit l'effondrement d'une partie de la chaînes des Hellénides et des Anatolides-Taurides et l'ouverture du vaste domaine extensif d'arrière-arc Rhodope-Egée-Anatolie occidentale (figures 2.9n-p et 2.12) [*Le Pichon & Angelier*, 1979; *Bonneau*, 1984; *Jolivet & Faccenna*, 2000]. Associés à cette extension, des dômes métamorphiques sont exhumés le long de grands systèmes de détachements, notamment dans le massif du Rhodope (figure 2.10) [*Burg et al.*, 1996; *Bonev et al.*, 2006; *Brun & Sokoutis*, 2007].

A l'Oligocène, l'essentiel du magmatisme actif dans l'est de la Méditerranée se localise dans ce massif ainsi qu'au niveau de la péninsule de Biga au nord-est de la Turquie [*Yılmaz et al.*, 2001; *Marchev et al.*, 2005]. Ce magmatisme d'affinité calco-alcaline riche en potassium à shoshonitique (i.e. alcalin riche en potassium) est caractérisé par (1) une source crustale dominante et (2) une source mantellique précédemment métasomatisée alors qu'elle se trouvait dans le domaine d'arc [*Marchev et al.*, 2005; *Ersoy & Palmer*, 2013].

Associé à ce magmatisme et à l'exhumation des dômes métamorphiques, un grand nombre de minéralisations à plomb et zinc, principalement des skarns (ou gîtes de remplacement dans des carbonates) et des épithermaux intermédiaires à neutres se mettent en place (ex. le district minier de Madjarovo, figures 3.1n-o) [*Heinrich & Neubauer*, 2002; *Marchev et al.*, 2005].

6.3.1. Dynamique de subduction et processus mantelliques

A l'Oligocène, la quasi-absence de minéralisations de type porphyre minéralisé indique que la genèse de ces minéralisations ne suit plus le modèle métallogénique décrit précédemment et typique du domaine d'arc (figure 1.5). L'accélération du retrait du panneau plongeant Hellénique vers le sud exclut en effet tout contrôle direct du coin mantellique sur la genèse des systèmes magmatiques et hydrothermaux dans le massif du Rhodope (figure 6.4). De plus, l'origine crustale dominante des magmas associés à ces minéralisations [*Marchev et al.*, 2005] semble indiquer que l'influence des flux asthénosphériques sous-jacents au domaine d'arrière-arc et induits par ce retrait se limite

principalement à un simple réchauffement de la base de la lithosphère (i.e. sans épisode de fusion partielle mantellique majeur).

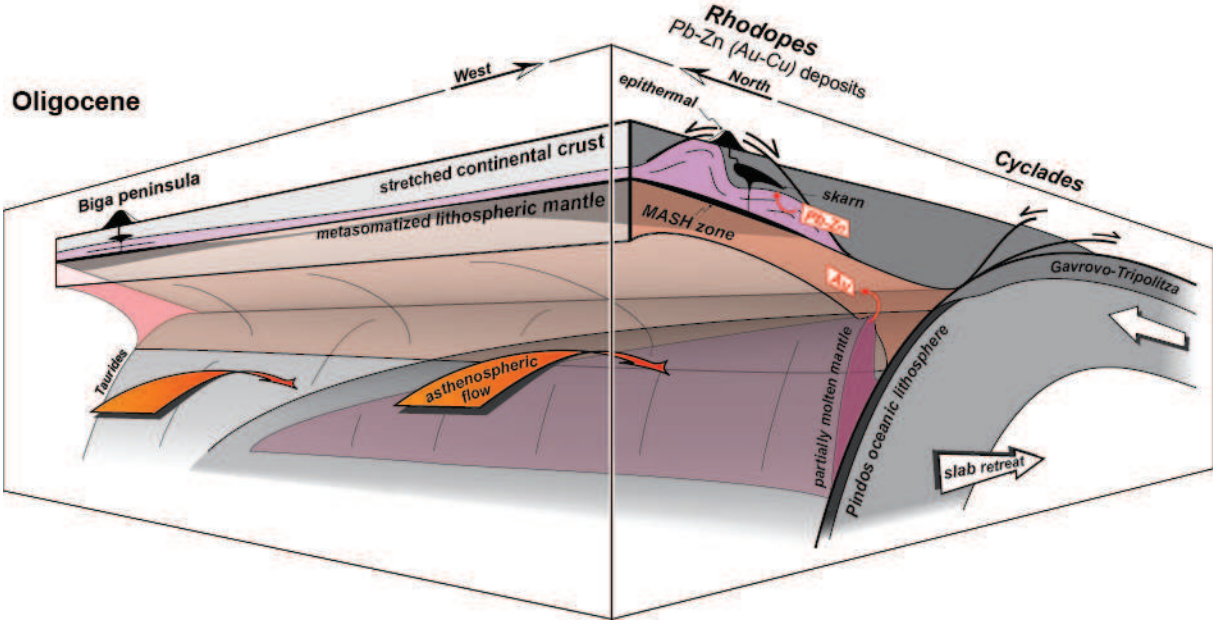

Figure 6.4 : bloc 3D interprétatif de la géométrie de la zone de subduction est-Méditerranéenne à l'Oligocène vue de dessous, mettant en évidence une accélération du retrait du panneau plongeant associée à l'exhumation du dôme métamorphique du Rhodope en contexte d'arrière-arc. Cette période est caractérisée par la genèse de systèmes minéralisés essentiellement enrichis en plomb-zinc.

6.3.2. Dynamique de subduction et processus crustaux

L'origine crustale dominante des magmas ainsi que la signature isotopique des minéralisations suggèrent en revanche que le plomb et le zinc aient été mobilisés depuis la croûte via des fluides métamorphiques liés à l'exhumation du dôme où via les systèmes magmatiques associés [*Marchev et al.*, 2005]. La remontée de ces fluides magmatiques et/ou hydrothermaux fertiles aurait ensuite été guidée par les détachements, similairement aux systèmes minéralisés étudiés sur l'île de Mykonos dans l'archipel des Cyclades (cf. *Chapitre 4*) [*Marchev et al.*, 2004b, 2005]. Leur précipitation aurait ensuite résulté du mélange de ces fluides profonds avec d'autres fluides d'origine météorique (figure 3.4b).

Cette exhumation contrôlée par un régime extensif a été initiée dans le massif du Rhodope dès l'Eocène inférieur, soit environ 20 millions d'années avant la mise en place de ces systèmes minéralisés. Ce timing indique donc que ce n'est pas le relâchement des contraintes mais plutôt la

perduration d'un régime extensif qui aurait permis un amincissement et un réchauffement suffisant de la croûte pour déclencher la genèse de systèmes magmatiques et hydrothermaux fertiles (figure 6.4).

Les causes de cette extension à l'Eocène restent encore mal contraintes. Ailleurs en Méditerranéen orientale, le régime tectonique est plutôt compressif (figure 2.6), ce qui suggère une origine plus locale à ce changement de contraintes. Un épaississement crustal particulièrement développé au niveau du massif du Rhodope, associé à un métamorphisme de moyenne à haute température permettant la fusion partielle de la croûte inférieure [*Bonev et al.*, 2006], pourrait ainsi avoir favorisé son effondrement gravitaire au cours de l'Eocène, en accord avec les modèles de *Dewey* [1988] et *Vanderhaeghe* [2012]. Ce mécanisme n'a cependant pas permis la mise en place de systèmes minéralisés car il a fallu attendre l'accélération du retrait du panneau plongeant à l'Oligocène, pour que l'état de contrainte et l'état thermique de la croûte soit favorable au développement d'occurrences minéralisées.

6.4. Miocène : étirement lithosphérique intense et minéralisations aurifères

Au Miocène, le retrait du panneau plongeant Hellénique se poursuit, entrainant un étirement intense de la croûte et l'exhumation d'autres dômes métamorphiques comme le massif du Kazdağ, du Menderes, ou encore l'archipel des Cyclades le long de grands systèmes de détachements (figure 2.9q-w) [*Bozkurt & Oberhänsli*, 2001; *Bonev & Beccaletto*, 2007; *Jolivet et al.*, 2013]. Cette cinématique de retrait s'accélère à partir du Miocène moyen, s'accompagnant de rotations de blocs d'échelle crustale (figure 2.4) et de la courbure progressive de la fosse, qui constitueraient la réponse crustale d'une déchirure du panneau plongeant sous l'ouest de l'Anatolie, suggérée par de nombreux modèles tomographiques (figures 1.26a et 2.12).

Dans l'est du massif du Rhodope et dans la péninsule de Biga, des minéralisations aurifères, principalement de type épithermal acide ou neutre, se développent dès l'Oligocène (figure 3.1p), ex. gisements de Ağı Dağı et d'Efemçukuru en Turquie) [*Marchev et al.*, 2004; *Yigit*, 2009, 2012; *Voudouris et al.*, 2011]. Cette activité hydrothermale migre ensuite progressivement vers le sud au

cours du Miocène jusqu'à atteindre l'archipel des Cyclades et le massif du Menderes (figures 3.1q-v). Au niveau de ces dômes métamorphiques, ces minéralisation aurifères s'expriment alors sous la forme de brèches tectoniques minéralisées le long des détachements actifs (ex. l'île de Mykonos, cf. *Chapitre 4*) ou de veines de quartz qui peuvent recouper ces détachements (ex. l'île de Tinos) [*Tombros et al.*, 2007].

Tout comme dans le massif du Rhodope dès la fin de l'Eocène, le magmatisme associé à ces systèmes minéralisés est de nature calco-alcaline riche en potassium à shoshonitique avec la participation d'une source mantellique (ou basaltique) métasomatisée et d'une source crustale (ou felsique) [ex. *Altherr & Siebel*, 2002; *Pe-Piper & Piper*, 2006; *Dilek & Altunkaynak*, 2009; *Ersoy & Palmer*, 2013]. Ces magmas diffèrent cependant de ceux précédemment mis en place dans le massif du Rhodope par une augmentation de leur composante mantellique au dépend de leur composante crustale [*Marchev et al.*, 2005].

6.4.1. Dynamique de subduction et processus mantelliques

Le modèle métallogénique associé à ces minéralisations aurifères d'arrière-arc est, là encore, différent de celui classiquement appliqué dans le domaine d'arc (figure 1.6), avec un enrichissement en or contrôlé par la fusion des cumulats sulfurés précédemment formés à la base de la croûte ou dans le manteau lithosphérique sous-jacent alors qu'il se trouvait en domaine d'arc (cf. *Section 3.4*, figure 3.4c et 6.5) [*Richards*, 2009].

Une telle fusion mantellique dont la signature géochimique et isotopique se retrouve dans les magmas d'arrière-arc intervient de manière plus tardive (i.e. principalement à partir du Miocène) dans l'évolution du domaine d'arrière-arc Egéen. Elle s'explique par un régime thermique plus chaud à la base de la lithosphère dû à un amincissement crustal intense et à un flux asthénosphérique sous-jacent important, résultant de l'accélération du retrait de la zone de subduction vers le sud (figure 6.5). La déchirure verticale du panneau plongeant peut également favoriser cette fusion mantellique en induisant (1) un retrait encore plus rapide de la plaque plongeante du fait de la diminution de sa largeur, comme mis en évidence dans le modèle de reconstructions cinématiques et les modèles numériques (cf. *Section 2.12* et *Chapitre 5*, figures 2.13 et 5.10) [*Schellart et al.*, 2007; *Loiselet et al.*,

2009] et (2) en bordure du panneau plongeant, des flux asthénosphériques avec une composante toroidale dominante qui apportent du matériel chaud supplémentaire dans le domaine d'arrière arc (figure 6.5) [ex. *Funiciello et al.*, 2003; *Kincaid & Griffiths*, 2003; *Sternai et al.*, 2014]. Bien mis en évidence dans les modèles numériques réalisés au cours de ce travail de thèse (figures 5.9 et 5.16), ce flux toroidal permet ainsi d'augmenter latéralement la composante mantellique des magmas présents en base de croûte (figure 5.8e).

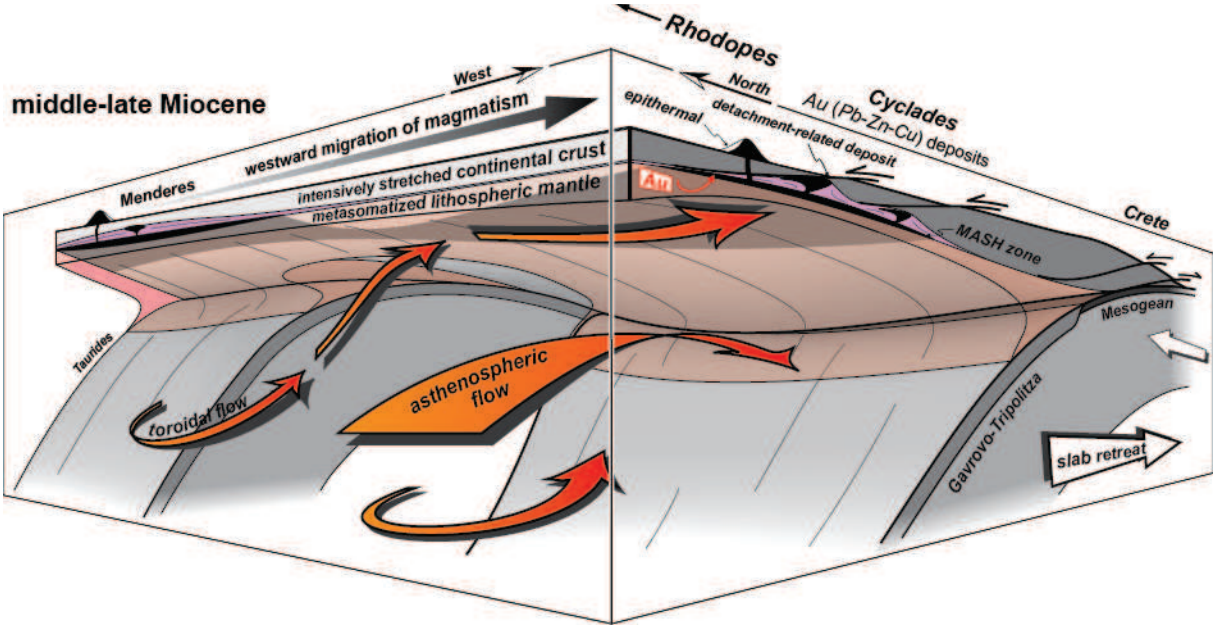

Figure 6.5 : bloc 3D interprétatif de la géométrie de la zone de subduction est-Méditerranéenne au Miocène moyen-supérieur vue de dessous, mettant en évidence une déchirure du panneau plongeant sous le massif du Menderes associée à des flux asthénosphériques toroidaux jusque sous le dôme métamorphique extensif des Cyclades. Cette période est caractérisée par la genèse de systèmes minéralisés essentiellement enrichis en or provenant de la déstabilisation de complexes sulfurés en base de lithosphère.

Ce modèle conciliant retrait et déchirure du panneau plongeant, amincissement lithosphérique et minéralisations aurifères vient préciser celui de *Lips* [2002], ou plus récemment de *Bertrand et al.* [2014], qui invoquait le retrait de la subduction, et la diminution du taux de convergence entre les plaques Afrique et Eurasie, comme un facteur déterminant pour la mise en place de provinces métallifères. Il est également en accord avec les liens mis en évidence par *de Boorder et al.* [1998] entre les domaines d'arrière-arc Méditerranéens, caractérisés par un flux de chaleur important, et les minéralisations à or, mercure et antimoine. Ces auteurs, ainsi que *Neubauer* [2002], invoquent

également un détachement de la lithosphère subduite, notamment sous la chaîne des Carpates (figure 1.15), comme étant responsable du grand nombre de gisements aurifères au niveau du bassin Pannonien. En Méditerranée orientale, un détachement similaire est suspecté au Miocène sous la zone de collision Arabie-Eurasie [ex. *Faccenna et al.*, 2006]. Très peu de minéralisations se mettent en place à l'aplomb de cette déchirure où la lithosphère est épaissie (i.e. ~45 km, figure 3.2d) [*Şengör et al.*, 2003]. Cette observation suggère que c'est bien l'amincissement lithosphérique, lié au retrait du panneau plongeant, qui serait le principal facteur contrôlant la genèse de concentrations aurifères en permettant (1) la formation de cumulats riches en or à la base de la croûte dans le domaine d'arc (figure 3.4a) et (2) la fusion de ces cumulats dans le domaine d'arrière-arc (figure 3.4c). Les processus de déchirure et de détachement du panneau plongeant et les flux asthénosphériques associés ne feraient alors que favoriser cette fusion et décupler l'activité magmatique et hydrothermale aurifère.

Bien que l'origine de l'or reste la même, ce modèle de genèse est une alternative à celui proposé par *Richards* [2009, 2014] qui invoque plutôt des processus d'effondrement orogénique et de délamination lithosphérique pour expliquer la fusion de ces cumulas aurifères à la base de la croûte (figure 1.9c). Un autre modèle invoqué par *Solomon* [1990], considère également le changement de polarité de la zone de subduction (i.e. la plaque chevauchante devient plongeante et vice-versa) comme un facteur crucial au développement de porphyres aurifères, mais également d'épithermaux acides et neutres [*White et al.*, 1995], le long la zone de subduction sud-ouest Pacifique (i.e. depuis la Papouasie-Nouvelle Guinée jusqu'aux îles Fidji). Etant donné les vitesses de retrait rapides des différentes zones de subduction dans cette région (i.e. entre 4 et 16 cm an^{-1}, figure 1.10 [*Schellart et al.*, 2007]), ce modèle métallogénique pourrait également être confronté à celui appliqué à la Méditerranée orientale, sous réserve d'une étude approfondie.

6.4.2. Dynamique de subduction et processus crustaux

Une fois dans la croûte, les systèmes magmatiques puis hydrothermaux formés dans le domaine d'arrière-arc peuvent remonter préférentiellement à la faveur de l'exhumation des dômes métamorphiques (figure 3.4c). Au niveau de ces dômes exhumés (ex. le massif du Rhodope, du Menderes, l'archipel des Cyclades), les minéralisations se présentent principalement sous la forme de

brèches ou de veines, associées aux grands systèmes de détachements qui peuvent drainer les fluides minéralisateurs (cf. *Chapitre 4*). A l'inverse, les épithermaux aurifères sont plutôt associés à des roches volcaniques à volcano-sédimentaires, notamment présentes dans des bassins d'âge Oligocène-Miocène qui reposent sur ces dômes métamorphiques. C'est notamment le cas des systèmes minéralisés de la péninsule de Biga où le dôme sous-jacent affleurerait au niveau du massif du Kazdağ (figure 6.5) [*Bonev & Beccaletto*, 2007]. Ces épithermaux constitueraient alors la partie supérieure de ces systèmes minéralisés aurifères d'arrière-arc alors que les veines et brèches associées aux détachements constitueraient leurs équivalents sous-jacents mis en place à relativement faible profondeur [*Neubauer*, 2005; *Skarpelis & Gilg*, 2006; *Tombros et al.*, 2015].

Des minéralisations riches en plomb et zinc peuvent également accompagner les occurrences aurifères (cf. *Chapitre 4*, figure 4.1), ce qui suggère que des magmas d'origine crustale et/ou des fluides métamorphiques, mobilisant ces métaux d'affinité crustale ont également pu circuler au cours de l'exhumation des dômes métamorphiques [*Marchev et al.*, 2005; *Tombros et al.*, 2015]. Ce modèle métallogénique est identique à celui proposé pour expliquer la genèse des systèmes minéralisés à plomb-zinc à l'Oligocène dans le massif du Rhodope (cf. *Section 6.3*), ce qui suggère que ces deux modèles de genèse ont pu coexister et que la prédominance de l'un ou l'autre serait contrôlé par les contributions relatives entre fluides mantelliques (où de la base de la croûte métasomatisée) et crustaux.

Dans ce contexte d'arrière-arc, les porphyres minéralisés à cuivre et or restent marginaux par rapport aux autres types de gisements présentés ci-dessus (ex. le porphyre de Maronia en Grèce et de Kisladag dans le massif du Menderes, figures 3.2d et 3.3) [*Melfos et al.*, 2002; *Yigit*, 2009]. Bien que ceux-ci puissent être présents en profondeur, le tectonique extensive couplée à une lithosphère largement amincie ne semble pas favoriser la formation de grandes chambres magmatiques mais plutôt la remontée rapide des fluides magmatiques-hydrothermaux, résultant en des systèmes minéralisés de faible profondeur ou de surface tels que les épithermaux.

Enfin, les modèles numériques 3D réalisés au cours de ce travail de thèse, en accord avec de précédentes études [ex. *Gerya & Meilick*, 2011], ont mis en évidence que la présence de roches partiellement fondues dans la lithosphère chevauchante permet de la rendre moins résistante à la

déformation. Dans les cas du domaine d'arrière-arc, ces roches partiellement fondues, qui se retrouvent actuellement à l'affleurement sous la forme de dômes migmatitiques [ex. *Lister et al.*, 1984; *Vanderhaeghe*, 2004], peuvent ainsi avoir favorisé l'amincissement de la lithosphère grâce à (1) une baisse globale de la résistance de la lithosphère, notamment dans les régions où ces roches partiellement fondues s'exhument [*Huet*, 2010] et (2) une diminution du contraste rhéologique à la base de la lithosphère, favorisant la transmission des contraintes cisaillantes depuis le manteau convectif, jusque dans la croûte (cf. *Chapitre 5*, figures 5.9f et 6.6) [*Jolivet et al.*, 2009; *Schellart & Moresi*, 2013; *Sternai et al.*, 2014].

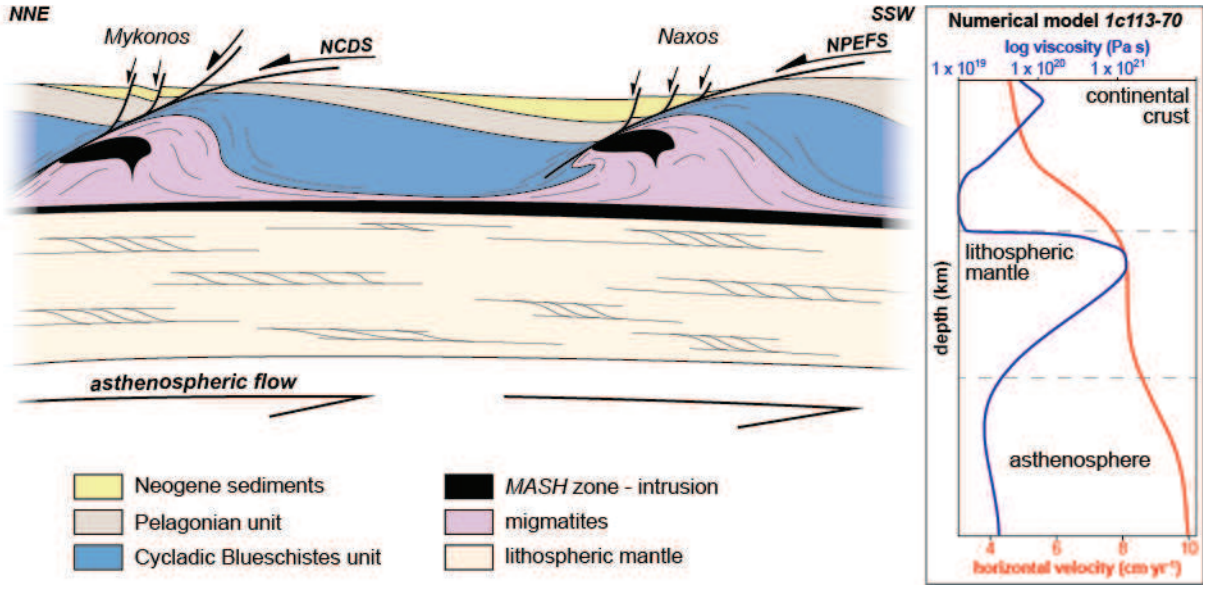

Figure 6.6 : coupe schématique montrant l'exhumation du dôme métamorphique des Cyclades (i.e. dômes de Mykonos et de Naxos), accommodée par de grands systèmes de détachements. *NCDS* : *North Cycladique Detachment System*. *NPEFS* : *Naxos-Paros Extensional Fault System*. La déformation extensive dans cette lithosphère affaiblie par la présence de roches partiellement fondues (i.e. zone *MASH*, migmatites, intrusions) est contrôlée, en partie, par les flux asthénosphériques sous-jacents, comme le suggère le profil de viscosité et de vitesse obtenu à partir des modèles réalisés (cf. *Chapitre 5*), où la vitesse horizontale dans l'asthénosphère est transmise à la lithosphère.

6.5. Conclusion : processus géodynamiques et métallogénie

Ce travail de thèse a permis de faire le lien entre l'histoire géodynamique tridimensionnelle de la zone de subduction est-Méditerranéenne depuis le Crétacé supérieur et la genèse de minéralisations, pour certaines d'intérêt économique. Plusieurs processus asthénosphériques et lithosphériques majeurs dans les environnements d'arc et d'arrière-arc continentaux ont ainsi été identifiés comme favorisant, ou au contraire restreignant, le développement de provinces métallogéniques (figure 6.7).

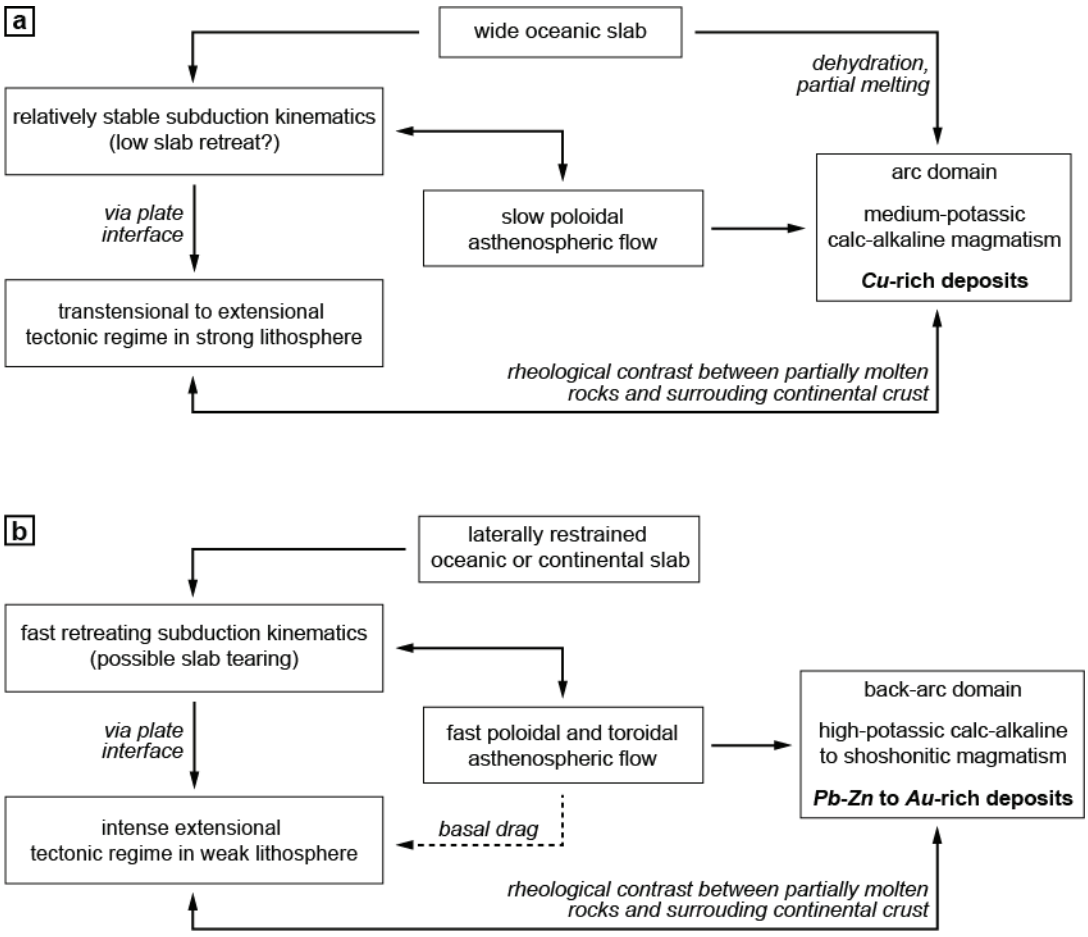

Figure 6.7 : schémas de synthèse, mettant en évidence les principaux liens, mis en évidence dans ce manuscrit de thèse, qui unissent géodynamique et métallogénie en contexte de subduction et qui permettent d'expliquer la genèse de provinces minéralisées riches en cuivre (a) ou en plomb-zinc et or (b).

(1) Une relative stabilité de la cinématique de subduction, caractérisant les larges zones de subduction, semble favoriser la genèse de minéralisations cuprifères, associées à un magmatisme calco-alcalin moyennement potassique, suivant le modèle métallogénique classiquement admis pour les environnements d'arc (figure 6.7a). Elle requiert néanmoins un relâchement de l'état des contraintes dans la lithosphère (i.e. régime transtensif à extensif), liée à un faible retrait du panneau plongeant, afin de faciliter la remontée des fluides magmatiques et hydrothermaux.

(2) Un retrait rapide de la zone de subduction, décuplé par des épisodes de déchirure ou de détachement du panneau plongeant (i.e. zone de subduction étroite, en opposition au point précédent), semble, quant à lui, propice à la mise en place de minéralisations à plomb et zinc puis à or lorsque l'étirement de la lithosphère devient suffisamment intense (figure 6.7b). Ces occurrences minéralisées précipitent essentiellement dans les niveaux crustaux les plus superficiels du domaine extensif d'arrière-arc, associées à de grands systèmes de détachements ayant permis l'ascension de dômes métamorphiques et de systèmes magmatiques calco-alcalins riches en potassium à shoshonitiques.

(3) A l'inverse, une cinématique lente de la subduction, associée à l'accrétion de domaines continentaux et à des flux asthénosphériques sous-jacents lents, ne semble pas favoriser la genèse de minéralisations au sein d'une lithosphère alors soumise à un régime compressif.

Retrait du panneau plongeant, flux asthénosphériques associés et étirement lithosphérique en Méditerranée orientale sont donc des processus cruciaux pour la genèse de systèmes minéralisés qui présentent alors un contenu métallique et une morphologie variable en fonction de l'intensité avec laquelle ces processus influent sur la cinématique de subduction.

L'évolution continue de la subduction, avec le passage des différentes unités tectoniques constituant la marge active dans le domaine d'arc puis d'arrière-arc, montre cependant qu'il ne faut pas uniquement s'intéresser au contexte tectonique synchrone à l'activité hydrothermale mais également considérer l'histoire géodynamique antérieure de ces régions où se sont développées ces grandes provinces métallogéniques.

6.6. Perspectives

Citius, Altius, Fortius (*plus loin, plus haut, plus fort*), comme le dit si bien Pierre de Coubertin, ce travail de recherche peut être poussé plus loin…

Je présente ici quelques réflexions sur l'implication que peut avoir cette étude en termes d'exploration minérale et d'axes innovants de recherche.

6.6.1. Quid de l'exploration minérale ?

Il n'est pas facile d'utiliser directement des résultats de recherche à des fins plus appliquées d'exploration minérale. Cependant, ce travail de thèse permet de soulever quelques points cruciaux qui peuvent apporter de nouvelles réflexions du point de vue de la gîtologie prévisionnelle.

Les domaines extensifs d'arrière-arc constituent des cibles majeures pour l'exploration minérale, en particulier pour la recherche de ressources aurifères. Dans ces environnements où l'amincissement lithosphérique est important, hormis quelques occurrences porphyriques à cuivre-or-molybdène, les systèmes minéralisés sont plutôt de type épithermal (acide ou neutre) ou contrôlés par de grands systèmes de failles extensives.

En Méditerranée orientale, certaines zones sont apparemment dépourvues de minéralisations, sans pour autant signifier qu'elles n'existent pas. La partie ouest de la chaîne des Pontides fait le lien entre la ceinture minéralisée cuprifère des Balkans et celle des Pontides orientales, mais elle semble stérile (figure 6.8). Une variation latérale dans la dynamique de subduction Téthysienne au Crétacé supérieur aurait-elle inhibé la formation de gisements similaires dans cette région-là spécifiquement ? Ou bien, sont-ils préservés à de plus grandes profondeurs dans la croûte, sous les nombreux bassins sédimentaires Cénozoïques de la région qui auraient alors recouvert cet arc magmatique [*Sunal & Tüysüz*, 2002; *Okay et al.*, 2013] ? Un autre exemple concerne le domaine d'arrière-arc d'âge Crétacé supérieur situé dans le complexe cristallin d'Anatolie centrale (*CACC*) (cf. *Chapitre 2*). La présence de plusieurs dômes métamorphiques associés à un magmatisme d'arrière-arc dans cette région [ex. *Whitney et al.*, 2003; *Lefebvre*, 2011] laisse en suspens la question de son potentiel

métallogénique, notamment en termes de concentration métalliques à plomb, zinc ou encore à or (figure 6.8).

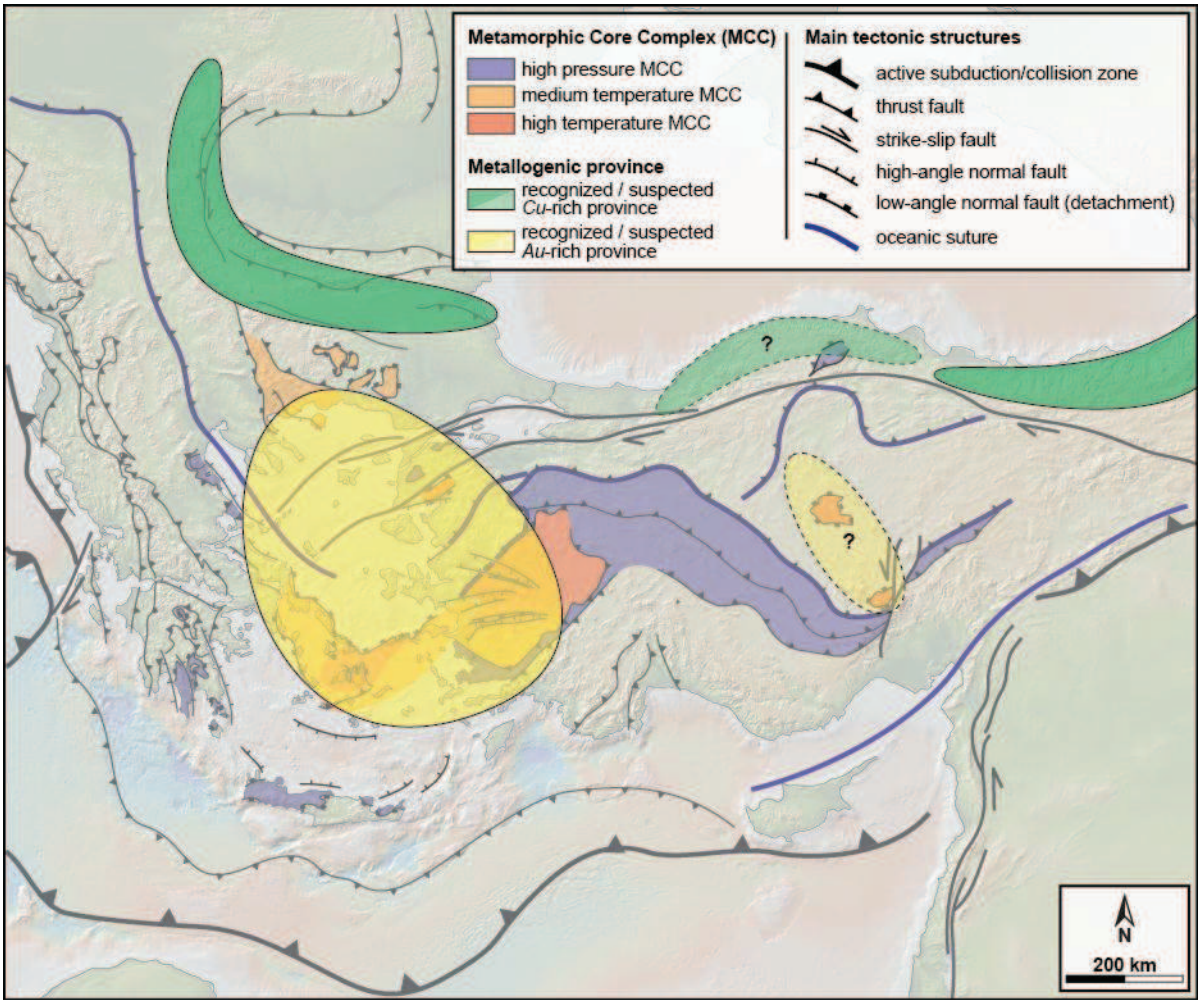

Figure 6.8 : carte tectonique de la Méditerranée orientale montrant les principales provinces métallogéniques reconnues ainsi que celles suspectées, au vue du contexte géodynamique similaire.

Enfin, bien que distribuées de manière sporadique, des occurrences magmatiques alcalines de composition basaltique ont été reconnues en Méditerranée orientale, notamment dans les domaines d'arrière-arc (cf. *Chapitre 2*). Au vue du potentiel aurifère de tels édifices volcaniques [ex. *Jensen & Barton*, 2000], ces derniers nécessiteraient une étude plus approfondie afin de déterminer s'ils peuvent présenter un réel intérêt économique.

6.6.2. Pistes de recherche

D'un point de vue plus fondamental, il serait intéressant de pousser l'étude comparative entre les différents systèmes minéralisés mis en place lors de l'exhumation du dôme métamorphique des Cyclades (cf. *Chapitre 4*), afin de comprendre quels facteurs contrôlent la variabilité minéralogique et morphologique de ces occurrences hydrothermales.

L'étude de la distribution spatiale et temporelle des systèmes minéralisés couplée à des modèles de reconstructions paléogéographiques peut être appliquée à d'autres zones de subduction, ou même à d'autres contextes tectoniques, dans le but de mieux appréhender les relations entre processus géodynamiques et métallogénie.

Similairement, ce travail peut être également étendu à d'autres types de ressources, notamment énergétiques. Un projet a ainsi été monté en partenariat entre le laboratoire ISTO (Institut des Sciences de la Terre et d'Orléans, France) et le BRGM (Bureau de Recherche Géologique et Minière, Orléans, France) et a pour but de comprendre les mécanismes mantelliques et/ou crustaux qui contrôlent l'activité géothermale importante observée actuellement dans l'ouest de la région Anatolienne.

Enfin, les modèles numériques réalisés au cours de cette étude à partir du code *I3ELVIS* ont permis de mettre en évidence des liens entre l'évolution complexe 3D d'une zone de convergence et la genèse et le transport de magmas. Toujours dans le but de faire le lien entre dynamique de subduction et métallogénie, il serait utile d'intégrer à ces modèles des processus de transport des métaux via les phases magmatiques. Ce projet est cependant loin d'être trivial car de nombreux paramètres physico-chimiques peuvent influencer la mobilité des métaux dans les magmas (ex. pression, température, pH, fO_2, fS_2). Il conviendrait donc de considérer les facteurs majeurs contrôlant cette mobilité afin d'implémenter dans le code numérique les réactions de solubilités des métaux les plus simples (mais les plus justes) possible.

Références bibliographiques

Agard P., J. Omrani, L. Jolivet, and F. Mouthereau (2005), Convergence history across Zagros (Iran): constraints from collisional and earlier deformation, *Int. J. Earth Sci.*, *94*, 401-419, doi:10.1007/s00531-005-0481-4.

Agostini, S., C. Doglioni, F. Innocenti, P. Manetti, S. Tonarini, & M. Y. Savaşçin (2007), The transition from subduction-related to intraplate Neogene magmatism in the Western Anatolia and Aegean area, *Spec. Pap. - Geol. Soc. Am.*, *418*, 1–15.

Akkök, R. (1983), Structural and Metamorphic Evolution of the Northern Part of the Menderes Massif: New Data from the Derbent Area and Their Implication for the Tectonics of the Massif, *J. Geol.*, *91*(3), 342-350.

Allen, M. B., & H. A. Armstrong (2008), Arabia–Eurasia collision and the forcing of mid-Cenozoic global cooling, *Palaeogeogr., Palaeoclimatol., Palaeoecol.*, *265*(1-2), 52–58, doi:10.1016/j.palaeo.2008.04.021.

Allmendinger, R. W., J. W. Sharp, D. Von Tish, L. Serpa, L. Brown, S. Kaufman, J. Oliver, & R. B. Smith (1983), Cenozoic and Mesozoic structure of the eastern Basin and Range province, Utah, from COCORP seismic-reflection data, *Geology*, *11*(9), 532, doi:10.1130/0091-7613(1983)11<532:CAMSOT>2.0.CO;2.

Altherr, R., M. Schliestedt, M. Okrusch, E. Seidel, H. Kreuzer, W. Harre, H. Lenz, I. Wendt, & G. A. Wagner (1979), Geochronology of high-pressure rocks on Sifnos (Cyclades, Greece), *Contrib. Mineral. Petrol.*, *70*(3), 245–255, doi:10.1007/BF00375354.

Altherr, R., H. Kreuzer, I. Wendt, H. Lenz, G. A. Wagner, J. Keller, W. Harre, & A. Höhndorf (1982), A late Oligocene/early Miocene high temperature belt in the Attic-Cycladic crystalline complex (SE Pelagonian, Greece), *Geol. Jahrb., Reihe E*, *23*, 97–164.

Altherr, R., & W. Siebel (2002), I-type plutonism in a continental back-arc setting: Miocene granitoids and monzonites from the central Aegean Sea, Greece, *Contrib. Mineral. Petrol.*, *143*(4), 397–415, doi:10.1007/s00410-002-0352-y.

Angelier, J., N. Lybéris, X. Le Pichon, E. Barrier, & P. Huchon (1982), The tectonic development of the hellenic arc and the sea of crete: A synthesis, *Tectonophysics*, *86*(1-3), 159–196, doi:10.1016/0040-1951(82)90066-X.

Annen, C. (2006), The Genesis of Intermediate and Silicic Magmas in Deep Crustal Hot Zones, *J. Petrol.*, *47*(3), 505–539, doi:10.1093/petrology/egi084.

Arculus, R. J. (1994), Aspects of magma genesis in arcs, *Lithos*, *33*(1-3), 189–208, doi:10.1016/0024-4937(94)90060-4.

Armijo, R., B. Meyer, G. C. P. King, A. Rigo, & D. Papanastassiou (1996), Quaternary evolution of the Corinth Rift and its implications for the Late Cenozoic evolution of the Aegean, *Geophys. J. Int.*, *126*(1), 11–53, doi:10.1111/j.1365-246X.1996.tb05264.x.

Armijo, R., B. Meyer, A. Hubert, & A. Barka (1999), Westward propagation of the North Anatolian fault into the northern Aegean: Timing and kinematics, *Geology*, *27*(3), 267, doi:10.1130/0091-7613(1999)027<0267:WPOTNA>2.3.CO;2.

Arslan, M., İ. Temizel, E. Abdioğlu, H. Kolaylı, C. Yücel, D. Boztuğ, & C. Şen (2013), 40Ar–39Ar dating, whole-rock and Sr–Nd–Pb isotope geochemistry of post-collisional Eocene volcanic rocks in the southern part of the Eastern Pontides (NE Turkey): implications for magma evolution in extension-induced origin, *Contrib. Mineral. Petrol.*, *166*(1), 113–142, doi:10.1007/s00410-013-0868-3.

Aubouin, J. (1959), Contribution à l'étude de la Grèce septentrionale; les confins de l'Epire et de la Thessalie, *Ann. Geol. Pays Hellen.*, *10*, 1–483.

Avigad, D., A. Ziv, & Z. Garfunkel (2001), Ductile and brittle shortening, extension-parallel folds and maintenance of crustal thickness in the central Aegean (Cyclades, Greece), *Tectonics*, *20*(2), 277–287, doi:10.1029/2000TC001190.

Aydin, N. S., M. C. Göncüoğlu, & A. Erler (1998), Latest Cretaceous magmatism in the Central Anatolian Crystalline Complex: review of field, petrographic and geochemical features, *Turk. J. Earth Sci.*, *7*, 259–268.

Bargnesi, E. A., D. F. Stockli, N. Mancktelow, & K. Soukis (2013), Miocene core complex development and coeval supradetachment basin evolution of Paros, Greece, insights from (U–Th)/He thermochronometry, *Tectonophysics*, *595-596*, 165–182, doi:10.1016/j.tecto.2012.07.015.

Barrier, E., & B. Vrielynck (2008), MEBE Atlas of Paleotectonic maps of the Middle East, *Commission for the Geological Map of the World*.

Bauer, C., D. Rubatto, K. Krenn, A. Proyer, & G. Hoinkes (2007), A zircon study from the Rhodope metamorphic complex, N-Greece: Time record of a multistage evolution, *Lithos*, *99*(3-4), 207–228, doi:10.1016/j.lithos.2007.05.003.

Beaty, D. W., G. P. Landis, & T. B. Thompson (1990), Carbonate-Hosted Sulfide Deposits of the Central Colorado Mineral Belt: Introduction, General Discussion, and Summary, edited by D. W. Beaty, G. P. Landis, and T. B. Thompson, *Econ. Geol. Monog.*, *7*, 1–18.

Beaudoin, A., V. Laurent, R. Augier, L. Jolivet, A. Lahfid, L. Arbaret, A. Rabillard, & A. Menant (in revision), Geometry and thermal structure of the Ikaria metamorphic core complex (eastern Cyclades, Greece), *J. Geodyn.*

Beccaletto, L., & C. Steiner (2005), Evidence of two-stage extensional tectonics from the northern edge of the Edremit Graben, NW Turkey, *Geodinamica Acta*, *18*(3-4), 283–297, doi:10.3166/ga.18.283-297.

Beccaletto, L., N. Bonev, D. Bosch, & O. Bruguier (2007), Record of a Palaeogene syn-collisional extension in the north Aegean region: evidence from the Kemer micaschists (NW Turkey), *Geol. Mag.*, *144*(02), 393, doi:10.1017/S001675680700310X.

Becker, T. W., & C. Faccenna (2011), Mantle conveyor beneath the Tethyan collisional belt, *Earth Planet. Sci. Lett.*, *310*(3-4), 453–461, doi:10.1016/j.epsl.2011.08.021.

Bektaş, O., C. Şen, Y. Atici, and N. Köprübaşi (1999), Migration of the Upper Cretaceous subduction-related volcanism towards the back-arc basin of the eastern Pontide magmatic arc (NE Turkey), *Geol. J.*, *34*(1-2), 95-106, doi:10.1002/(SICI)1099-1034(199901/06)34:1/2<95::AID-GJ816>3.0.CO;2-J.

Benioff, H. (1955), Seismic Evidence for Crustal Structure and Tectonic Activity, *Spec. Pap. - Geol. Soc. Am.*, *62*, 61–74.

Bercovici, D. (2003), The generation of plate tectonics from mantle convection, *Earth Planet. Sci. Lett.*, *205*(3-4), 107–121, doi:10.1016/S0012-821X(02)01009-9.

Bergerat, F., D. Vangelov, & D. Dimov (2010), Brittle deformation, palaeostress field reconstruction and tectonic evolution of the Eastern Balkanides (Bulgaria) during Mesozoic and Cenozoic times, *Spec. Publ. - Geol. Soc. London*, *340*(1), 77–111, doi:10.1144/SP340.6.

Berk Biryol, C., S. L. Beck, G. Zandt, & A. A. Özacar (2011), Segmented African lithosphere beneath the Anatolian region inferred from teleseismic P-wave tomography, *Geophys. J. Int.*, *184*(3), 1037–1057, doi:10.1111/j.1365-246X.2010.04910.x.

Bertrand, G., L. Guillou-Frottier, & C. Loiselet (2014), Distribution of porphyry copper deposits along the western Tethyan and Andean subduction zones: Insights from a paleotectonic approach, *Ore Geol. Rev.*, *60*, 174–190, doi:10.1016/j.oregeorev.2013.12.015.

Berza, T., E. Constantinescu, & Ş.-N. Vlad (1998), Upper Cretaceous Magmatic Series and Associated Mineralisation in the Carpathian - Balkan Orogen, *Resour. Geol.*, *48*(4), 291–306, doi:10.1111/j.1751-3928.1998.tb00026.x.

Bijwaard, H., W. Spakman, & E. R. Engdahl (1998), Closing the gap between regional and global travel time tomography, *J. Geophys. Res.*, *103*(B12), 30055, doi:10.1029/98JB02467.

Billa, M., D. Cassard, A. L. . Lips, V. Bouchot, B. Tourlière, G. Stein, & L. Guillou-Frottier (2004), Predicting gold-rich epithermal and porphyry systems in the central Andes with a continental-scale metallogenic GIS, *Ore Geol. Rev.*, *25*(1-2), 39–67, doi:10.1016/j.oregeorev.2004.01.002.

Black, K. N., E. J. Catlos, T. Oyman, & M. Demirbilek (2013), Timing Aegean extension: Evidence from in situ U–Pb geochronology and cathodoluminescence imaging of granitoids from NW Turkey, *Lithos*, *180-181*, 92–108, doi:10.1016/j.lithos.2013.09.001.

Blake, M. C., M. Bonneau, J. Geyssant, J. R. Kienast, C. Lepvrier, H. Maluski, & D. Papanikolaou (1981), A geologic reconnaissance of the Cycladic blueschist belt, Greece, *Geol. Soc. Am. Bull.*, *92*(5), 247, doi:10.1130/0016-7606(1981)92<247:AGROTC>2.0.CO;2.

Boccaletti, M., P. Manetti, A. Peccerillo, & G. Stanisheva-Vassileva (1978), Late Cretaceous high-potassium volcanism in eastern Srednogorie, Bulgaria, *Geol. Soc. Am. Bull.*, *89*(3), 439, doi:10.1130/0016-7606(1978)89<439:LCHVIE>2.0.CO;2.

Bolhar, R., U. Ring, & C. M. Allen (2010), An integrated zircon geochronological and geochemical investigation into the Miocene plutonic evolution of the Cyclades, Aegean Sea, Greece: Part 1: Geochronology, *Contrib. Mineral. Petrol.*, *160*(5), 719–742, doi:10.1007/s00410-010-0504-4.

Bonev, N., J.-P. Burg, & Z. Ivanov (2006), Mesozoic–Tertiary structural evolution of an extensional gneiss dome—the Kesebir–Kardamos dome, eastern Rhodope (Bulgaria–Greece), *Int. J. Earth Sci.*, *95*(2), 318–340, doi:10.1007/s00531-005-0025-y.

Bonev, N., & L. Beccaletto (2007), From syn- to post-orogenic Tertiary extension in the north Aegean region: constraints on the kinematics in the eastern Rhodope Thrace, Bulgaria Greece and the Biga Peninsula, NW Turkey, *Spec. Publ. - Geol. Soc. London*, *291*(1), 113–142, doi:10.1144/SP291.6.

Bonneau, M., & J. R. Kienast (1982), Subduction, collision et schistes bleus; l'exemple de l'Egée (Grèce), *Bull. Soc. Geol. Fr.*, *4*, 785–791.

Bonneau, M. (1984), Correlation of the Hellenide nappes in the south-east Aegean and their tectonic reconstruction, *Spec. Publ. - Geol. Soc. London*, *17*(1), 517–527, doi:10.1144/GSL.SP.1984.017.01.38.

Bonsall, T. A., P. G. Spry, P. C. Voudouris, S. Tombros, K. S. Seymour, & V. Melfos (2011), The Geochemistry of Carbonate-Replacement Pb-Zn-Ag Mineralization in the Lavrion District, Attica, Greece: Fluid Inclusion, Stable Isotope, and Rare Earth Element Studies, *Econ. Geol.*, *106*(4), 619–651, doi:10.2113/econgeo.106.4.619.

Bouilhol, P., V. Magni, J. van Hunen, & L. Kaislaniemi (2015), A numerical approach to melting in warm subduction zones, *Earth Planet. Sci. Lett.*, *411*, 37–44, doi:10.1016/j.epsl.2014.11.043.

Boyden, J. A., R. D. Muller, M. Gurnis, T. H. Torsvik, J. A. Clark, M. Turner, H. Ivey-Law, R. J. Watson, & J. S. Cannon (2011), Next-generation plate-tectonic reconstructions using GPlates, in *Geoinformatics*, edited by G. R. Keller, C. Baru, G. R. Keller, and C. Baru, pp. 95–114, Cambridge University Press, Cambridge.

Boztuğ, D. (2000), S-I-A-type Intrusive Associations: Geodynamic Significance of Synchronism Between Metamorphism and Magmatism in Central Anatolia, Turkey, *Spec. Publ. - Geol. Soc. London*, *173*(1), 441–458, doi:10.1144/GSL.SP.2000.173.01.21.

Bozkurt, E., & M. Satır (2000), The southern Menderes Massif (western Turkey): geochronology and exhumation history, *Geol. J.*, *35*(3-4), 285–296, doi:10.1002/gj.849.

Bozkurt, E., & R. Oberhänsli (2001), Menderes Massif (Western Turkey): structural, metamorphic and magmatic evolution - a synthesis, *Int. J. Earth Sci.*, *89*(4), 679–708, doi:10.1007/s005310000173.

Bozkurt, E., M. Satır, and Ç. Buğdaycıoğlu (2010), Timing of post-orogenic extension in the Gördes migmatite dome, Western Turkey: Insights from U-Pb and Rb-Sr chronology, *Tectonic Crossroads: Evolving Orogens of Eurasia-Africa-Arabia*, Ankara, Turkey.

Bozkurt, E., M. Satır, and Ç. Buğdaycıoğlu (2011), Surprisingly young Rb/Sr ages from the Simav extensional detachment fault zone, northern Menderes Massif, Turkey, *J. Geodyn.*, *52*(5), 406-431, doi: 10.1016/j.jog.2011.06.002.

Boztuğ, D., A. İ. Erçin, M. K. Kuruçelik, D. Göç, İ. Kömür, & A. İskenderoğlu (2006), Geochemical characteristics of the composite Kaçkar batholith generated in a Neo-Tethyan convergence system, Eastern Pontides, Turkey, *J. Asian Earth Sci.*, *27*(3), 286–302, doi:10.1016/j.jseaes.2005.03.008.

Boztuğ, D., R. C. Jonckheere, M. Heizler, L. Ratschbacher, Y. Harlavan, & M. Tichomirova (2009), Timing of post-obduction granitoids from intrusion through cooling to exhumation in central Anatolia, Turkey, *Tectonophysics*, *473*(1-2), 223–233, doi:10.1016/j.tecto.2008.05.035.

Bradley, K. E., E. Vassilakis, A. Hosa, & B. P. Weiss (2013), Segmentation of the Hellenides recorded by Pliocene initiation of clockwise block rotation in Central Greece, *Earth Planet. Sci. Lett.*, *362*, 6–19, doi:10.1016/j.epsl.2012.11.043.

Brichau, S., U. Ring, R. A. Ketcham, A. Carter, D. Stockli, & M. Brunel (2006), Constraining the long-term evolution of the slip rate for a major extensional fault system in the central Aegean, Greece, using thermochronology, *Earth Planet. Sci. Lett.*, *241*(1-2), 293–306, doi:10.1016/j.epsl.2005.09.065.

Brichau, S., U. Ring, A. Carter, P. Monié, R. Bolhar, D. Stockli, & M. Brunel (2007), Extensional faulting on Tinos Island, Aegean Sea, Greece: How many detachments?, *Tectonics*, *26*(4), doi:10.1029/2006TC001969.

Brichau, S., U. Ring, A. Carter, R. Bolhar, P. Monie, D. Stockli, & M. Brunel (2008), Timing, slip rate, displacement and cooling history of the Mykonos detachment footwall, Cyclades, Greece, and implications for the opening of the Aegean Sea basin, *J. Geol. Soc. London*, *165*(1), 263–277, doi:10.1144/0016-76492006-145.

Brichau, S., S. Thomson, & U. Ring (2010), Thermochronometric constraints on the tectonic evolution of the Serifos detachment, Aegean Sea, Greece, *Int. J. Earth Sci.*, *99*(2), 379–393, doi:10.1007/s00531-008-0386-0.

Bröcker, M., D. Bieling, B. Hacker, & P. Gans (2004), High-Si phengite records the time of greenschist facies overprinting: implications for models suggesting mega-detachments in the Aegean Sea, *J. Metamorph. Geol.*, *22*(5), 427–442, doi:10.1111/j.1525-1314.2004.00524.x.

Brun, J.-P., & D. Sokoutis (2007), Kinematics of the Southern Rhodope Core Complex (North Greece), *Int. J. Earth Sci.*, *96*(6), 1079–1099, doi:10.1007/s00531-007-0174-2.

Brun, J.-P., & C. Faccenna (2008), Exhumation of high-pressure rocks driven by slab rollback, *Earth Planet. Sci. Lett.*, *272*(1-2), 1–7, doi:10.1016/j.epsl.2008.02.038.

Brun, J.-P., & D. Sokoutis (2010), 45 m.y. of Aegean crust and mantle flow driven by trench retreat, *Geology*, *38*(9), 815–818, doi:10.1130/G30950.1.

Burchfiel, B. C., & L. H. Royden (1985), North-south extension within the convergent Himalayan region, *Geology*, *13*(10), 679, doi:10.1130/0091-7613(1985)13<679:NEWTCH>2.0.CO;2.

Burchfiel, B. C., R. Nakov, & T. Tzankov (2003), Evidence from the Mesta half-graben, SW Bulgaria, for the Late Eocene beginning of Aegean extension in the Central Balkan Peninsula, *Tectonophysics*, *375*(1-4), 61–76, doi:10.1016/j.tecto.2003.09.001.

Burg, J.-P., Z. Ivanov, L.-E. Ricou, D. Dimor, & L. Klain (1990), Implications of shear-sense criteria for the tectonic evolution of the Central Rhodope massif, southern Bulgaria, *Geology*, *18*(5), 451, doi:10.1130/0091-7613(1990)018<0451:IOSSCF>2.3.CO;2.

Burg, J.-P., L.-E. Ricou, Z. Ivano, I. Godfriaux, D. Dimov, & L. Klain (1996), Syn-metamorphic nappe complex in the Rhodope Massif. Structure and kinematics, *Terra Nova*, *8*(1), 6–15, doi:10.1111/j.1365-3121.1996.tb00720.x.

Burov, E., L. Jolivet, L. Le Pourhiet, & A. Poliakov (2001), A thermomechanical model of exhumation of high pressure (HP) and ultra-high pressure (UHP) metamorphic rocks in Alpine-type collision belts, *Tectonophysics*, *342*(1-2), 113–136, doi:10.1016/S0040-1951(01)00158-5.

Burov, E., T. Francois, P. Yamato, & S. Wolf (2014), Mechanisms of continental subduction and exhumation of HP and UHP rocks, *Gondwana Res.*, *25*(2), 464–493, doi:10.1016/j.gr.2012.09.010.

Camprubí, A., & T. Albinson (2007), Epithermal deposits in México—Update of current knowledge, and an empirical reclassification, *Spec. Pap. - Geol. Soc. Am.*, *422*, 377–415.

Candan, O., O. Ö. Dora, R. Oberhänsli, M. Çetinkaplan, J. H. Partzsch, F. C. Warkus, and S. Dürr (2001), Pan-African high-pressure metamorphism in the Precambrian basement of the Menderes Massif, western Anatolia, Turkey, *Int. J. Earth Sci.*, *89*, 793-811, doi:10.1007/s005310000097.

Candan, O., M. Çetinkaplan, R. Oberhänsli, G. Rimmelé, & C. Akal (2005), Alpine high-P/low-T metamorphism of the Afyon Zone and implications for the metamorphic evolution of Western Anatolia, Turkey, *Lithos*, *84*(1-2), 102–124, doi:10.1016/j.lithos.2005.02.005.

Candela, P. A., & P. M. Piccoli (2005), Magmatic processes in the development of porphyry-type ore systems, *Econ. Geol.*, *100th Anniversary Volume*, 25–37.

Capitanio, F. A. (2014), The dynamics of extrusion tectonics: Insights from numerical modeling, *Tectonics*, *33*(12), 2361–2381, doi:10.1002/2014TC003688.

Cassard, D. et al. (2012), ProMine pan-European Mineral Deposit database: a new dataset for assessing primary mineral resources in Europe, Nancy, France.

Catlos, E. J., and I. Çemen (2005), Monazite ages and the evolution of the Menderes Massif, western Turkey, *Int. J. Earth Sci.*, *94*(2), 204-217, doi: 10.1007/s00531-005-0470-7.

Catlos, E. J., C. Baker, S. S. Sorensen, I. Çemen, & M. Hançer (2010), Geochemistry, geochronology, and cathodoluminescence imagery of the Salihli and Turgutlu granites (central Menderes Massif, western Turkey): Implications for Aegean tectonics, *Tectonophysics*, *488*(1-4), 110–130, doi:10.1016/j.tecto.2009.06.001.

Cavazza, W., A. I. Okay, & M. Zattin (2009), Rapid early-middle Miocene exhumation of the Kazdağ Massif (western Anatolia), *Int. J. Earth Sci.*, *98*(8), 1935–1947, doi:10.1007/s00531-008-0353-9.

Celik, O. F., M. Delaloye, & G. Feraud (2006), Precise 40 Ar– 39 Ar ages from the metamorphic sole rocks of the Tauride Belt Ophiolites, southern Turkey: implications for the rapid cooling history, *Geol. Mag.*, *143*(02), 213, doi:10.1017/S0016756805001524.

Chamot-Rooke, N., J.-M. Gaulier, & F. Jestin (1999), Constraints on Moho depth and crustal thickness in the Liguro-Provencal basin from a 3D gravity inversion: geodynamic implications, *Spec. Publ. - Geol. Soc. London*, *156*(1), 37–61, doi:10.1144/GSL.SP.1999.156.01.04.

Chase, C. G. (1978), Extension behind island arcs and motions relative to hot spots, *Journal of Geophysical Research*, *83*(B11), 5385, doi:10.1029/JB083iB11p05385.

Chaumillon, E., J. Mascle, & H. J. Hoffmann (1996), Deformation of the western Mediterranean Ridge: Importance of Messinian evaporitic formations, *Tectonophysics*, *263*(1-4), 163–190, doi:10.1016/S0040-1951(96)00035-2.

Çiftçi, N. B., & E. Bozkurt (2009), Evolution of the Miocene sedimentary fill of the Gediz Graben, SW Turkey, *Sedim. Geol.*, *216*(3-4), 49–79, doi:10.1016/j.sedgeo.2009.01.004.

Ciobanu, C., N. Cook, & H. Stein (2002), Regional setting and geochronology of the Late Cretaceous Banatitic Magmatic and Metallogenetic Belt, *Miner. Deposita*, *37*(6-7), 541–567, doi:10.1007/s00126-002-0272-9.

Coats, R. R. (1962), Magma Type and Crustal Structure in the Aleutian Arc, in *The Crust of the Pacific Basin*, edited by G. A. Macdonald and H. Kuno, pp. 92–109, Amer. Geophys. Union, Washington, US.

Collins, A. S., & A. H. F. Robertson (1998), Processes of Late Cretaceous to Late Miocene episodic thrust-sheet translation in the Lycian Taurides, SW Turkey, *J. Geol. Soc. London*, *155*(5), 759–772, doi:10.1144/gsjgs.155.5.0759.

Coltice, N., B. R. Phillips, H. Bertrand, Y. Ricard, & P. Rey (2007), Global warming of the mantle at the origin of flood basalts over supercontinents, *Geology*, *35*(5), 391, doi:10.1130/G23240A.1.

Coltice, N., M. Seton, T. Rolf, R. D. Müller, & P. J. Tackley (2013), Convergence of tectonic reconstructions and mantle convection models for significant fluctuations in seafloor spreading, *Earth Planet. Sci. Lett.*, *383*, 92–100, doi:10.1016/j.epsl.2013.09.032.

Conrad, C. P., & C. Lithgow-Bertelloni (2002), How Mantle Slabs Drive Plate Tectonics, *Science*, *298*(5591), 207–209, doi:10.1126/science.1074161.

Cooke, D. R., P. Hollings, & J. L. Walshe (2005), Giant Porphyry Deposits: Characteristics, Distribution, and Tectonic Controls, *Econ. Geol.*, *100*(5), 801–818, doi:10.2113/gsecongeo.100.5.801.

Courtillot, V., A. Davaille, J. Besse, & J. Stock (2003), Three distinct types of hotspots in the Earth's mantle, *Earth Planet. Sci. Lett.*, *205*(3-4), 295–308, doi:10.1016/S0012-821X(02)01048-8.

Cvetković, V., D. Prelević, H. Downes, M. Jovanović, O. Vaselli, & Z. Pécskay (2004), Origin and geodynamic significance of Tertiary postcollisional basaltic magmatism in Serbia (central Balkan Peninsula), *Lithos*, *73*(3-4), 161–186, doi:10.1016/j.lithos.2003.12.004.

Davaille, A., & C. Jaupart (1993), Transient high-Rayleigh-number thermal convection with large viscosity variations, *J. Fluid Mech.*, *253*(-1), 141, doi:10.1017/S0022112093001740.

de Boorder, H., W. Spakman, S. H. White, & M. J. R. Wortel (1998), Late Cenozoic mineralization, orogenic collapse and slab detachment in the European Alpine Belt, *Earth Planet. Sci. Lett.*, *164*(3-4), 569–575, doi:10.1016/S0012-821X(98)00247-7.

de Graciansky, P. C. (1967) Existence d'une nappe ophiolitique à l'extrémité occidentale de la chaîne sud-anatolienne : relations avec les autres unités charriées et avec les terrains autochtones (Province de Muğla, Turquie), *C. R. Acad. Sci. Paris*, *264*, 2876-2879.

Denèle, Y., E. Lecomte, L. Jolivet, O. Lacombe, L. Labrousse, B. Huet, & L. Le Pourhiet (2011), Granite intrusion in a metamorphic core complex: The example of the Mykonos laccolith (Cyclades, Greece), *Tectonophysics*, *501*(1-4), 52–70, doi:10.1016/j.tecto.2011.01.013.

Dercourt, J. et al. (1986), Geological evolution of the tethys belt from the atlantic to the pamirs since the Lias, *Tectonophysics*, *123*(1-4), 241–315, doi:10.1016/0040-1951(86)90199-X.

Dercourt, J., L. E. Ricou, & B. Vrielynck (1993), Atlas Tethys Palaeoenvironment Maps, 14 maps.

Dewey, J. F. (1980), Episodicity, sequence and style at convergent plate boundaries, in *The Continental Crust and its Mineral Deposits*, pp. 553–573, Stangway D. W.

Dewey, J. F., M. R. Hempton, W. S. F. Kidd, F. Saroglu, and A. M. C. Şengör (1986), Shortening of continental lithosphere: the neotectonics of Eastern Anatolia - a young collision zone, *Spec. Publ. - Geol. Soc. London*, *19*(1), 1-36, doi:10.1144/GSL.SP.1986.019.01.01.

Dewey, J. F. (1988), Extensional collapse of orogens, *Tectonics*, *7*(6), 1123–1139, doi:10.1029/TC007i006p01123.

Dietz, R. S. (1961), Continent and Ocean Basin Evolution by Spreading of the Sea Floor, *Nature*, *190*(4779), 854–857, doi:10.1038/190854a0.

Dilek, Y., P. Thy, B. Hacker, & S. Grundvig (1999), Structure and petrology of Tauride ophiolites and mafic dike intrusions (Turkey): Implications for the Neotethyan ocean, *Geol. Soc. Am. Bull.*, *111*(8), 1192–1216, doi:10.1130/0016-7606(1999)111<1192:SAPOTO>2.3.CO;2.

Dilek, Y., & S. Altunkaynak (2009), Geochemical and temporal evolution of Cenozoic magmatism in western Turkey: mantle response to collision, slab break-off, and lithospheric tearing in an orogenic belt, *Spec. Publ. - Geol. Soc. London*, *311*(1), 213–233, doi:10.1144/SP311.8.

Dilek, Y., & E. Sandvol (2009), Seismic structure, crustal architecture and tectonic evolution of the Anatolian-African Plate Boundary and the Cenozoic Orogenic Belts in the Eastern Mediterranean Region, *Spec. Publ. - Geol. Soc. London*, *327*(1), 127–160, doi:10.1144/SP327.8.

Dilek, Y., S. Altunkaynak, & Z. Oner (2009), Syn-extensional granitoids in the Menderes core complex and the late Cenozoic extensional tectonics of the Aegean province, *Spec. Publ. - Geol. Soc. London*, *321*(1), 197–223, doi:10.1144/SP321.10.

Dinter, D. A., & L. Royden (1993), Late Cenozoic extension in northeastern Greece: Strymon Valley detachment system and Rhodope metamorphic core complex, *Geology*, *21*(1), 45, doi:10.1130/0091-7613(1993)021<0045:LCEING>2.3.CO;2.

Dinter, D. A., A. Macfarlane, W. Hames, C. Isachsen, S. Bowring, & L. Royden (1995), U-Pb and </sup>40</sup> Ar/ ^{39} Ar geochronology of the Symvolon granodiorite: Implications for the thermal and structural evolution of the Rhodope metamorphic core complex, northeastern Greece, *Tectonics*, *14*(4), 886–908, doi:10.1029/95TC00926.

Dinter, D. A. (1998), Late Cenozoic extension of the Alpine collisional orogen, northeastern Greece: Origin of the north Aegean basin, *Geol. Soc. Am. Bull.*, *110*(9), 1208–1230, doi:10.1130/0016-7606(1998)110<1208:LCEOTA>2.3.CO;2.

Dinu, C., H. K. Wong, D. Tambrea, & L. Matenco (2005), Stratigraphic and structural characteristics of the Romanian Black Sea shelf, *Tectonophysics*, *410*(1-4), 417–435, doi:10.1016/j.tecto.2005.04.012.

Doglioni, C., C. Busatta, G. Bolis, L. Marianini, & M. Zanella (1996), Structural evolution of the eastern Balkans (Bulgaria), *Mar. Pet. Geol.*, *13*(2), 225–251, doi:10.1016/0264-8172(95)00045-3.

Duchêne, S., R. Aïssa, & O. Vanderhaeghe (2006), Pressure-Temperature-time Evolution of Metamorphic Rocks from Naxos (Cyclades, Greece): Constraints from Thermobarometry and Rb/Sr dating, *Geodinamica Acta*, *19*(5), 301–321, doi:10.3166/ga.19.301-321.

Duretz, T., T. V. Gerya, & W. Spakman (2014), Slab detachment in laterally varying subduction zones: 3-D numerical modeling, *Geophys. Res. Lett.*, *41*(6), 1951–1956, doi:10.1002/2014GL059472.

Einaudi, M. T., & D. M. Burt (1982), Introduction; terminology, classification, and composition of skarn deposits, *Econ. Geol.*, *77*(4), 745–754, doi:10.2113/gsecongeo.77.4.745.

Elger, K., O. Oncken, & J. Glodny (2005), Plateau-style accumulation of deformation: Southern Altiplano: ALTIPLANO DEFORMATION, *Tectonics*, *24*(4), doi:10.1029/2004TC001675.

Ersoy, Y. E., C. Helvacı, & M. R. Palmer (2011), Stratigraphic, structural and geochemical features of the NE–SW trending Neogene volcano-sedimentary basins in western Anatolia: Implications for associations of supra-detachment and transtensional strike-slip basin formation in extensional tectonic setting, *J. Asian Earth Sci.*, *41*(2), 159–183, doi:10.1016/j.jseaes.2010.12.012.

Ersoy, E. Y., & M. R. Palmer (2013), Eocene-Quaternary magmatic activity in the Aegean: Implications for mantle metasomatism and magma genesis in an evolving orogeny, *Lithos*, doi:10.1016/j.lithos.2013.06.007.

Eyüboğlu, Y. (2010), Late Cretaceous high-K volcanism in the eastern Pontide orogenic belt: implications for the geodynamic evolution of NE Turkey, *Int. Geol. Rev.*, *52*(2-3), 142-186, doi:10.1080/00206810902757164.

Faccenda, M., L. Burlini, T. V. Gerya, & D. Mainprice (2008), Fault-induced seismic anisotropy by hydration in subducting oceanic plates, *Nature*, *455*(7216), 1097–1100, doi:10.1038/nature07376.

Faccenda, M., T. V. Gerya, & L. Burlini (2009), Deep slab hydration induced by bending-related variations in tectonic pressure, *Nat. Geosci.*, *2*(11), 790–793, doi:10.1038/ngeo656.

Faccenda, M., & F. A. Capitanio (2012), Development of mantle seismic anisotropy during subduction-induced 3-D flow, *Geophys. Res. Lett.*, *39*(11), doi:10.1029/2012GL051988.

Faccenna, C., M. Mattei, R. Funiciello, & L. Jolivet (1997), Styles of back-arc extension in the Central Mediterranean, *Terra Nova*, *9*(3), 126–130, doi:10.1046/j.1365-3121.1997.d01-12.x.

Faccenna, C., L. Jolivet, C. Piromallo, & A. Morelli (2003), Subduction and the depth of convection in the Mediterranean mantle, *J. Geophys. Res.*, *108*(B2), doi:10.1029/2001JB001690.

Faccenna, C., C. Piromallo, A. Crespo-Blanc, L. Jolivet, & F. Rossetti (2004), Lateral slab deformation and the origin of the western Mediterranean arcs, *Tectonics*, *23*(1), doi:10.1029/2002TC001488.

Faccenna, C., O. Bellier, J. Martinod, C. Piromallo, & V. Regard (2006), Slab detachment beneath eastern Anatolia: A possible cause for the formation of the North Anatolian fault, *Earth Planet. Sci. Lett.*, *242*(1-2), 85–97, doi:10.1016/j.epsl.2005.11.046.

Faccenna, C., A. Heuret, F. Funiciello, S. Lallemand, & T. W. Becker (2007a), Predicting trench and plate motion from the dynamics of a strong slab, *Earth Planet. Sci. Lett.*, *257*(1-2), 29–36, doi:10.1016/j.epsl.2007.02.016.

Faccenna, C., F. Funiciello, L. Civetta, M. D'Antonio, M. Moroni, & C. Piromallo (2007b), Slab disruption, mantle circulation, and the opening of the Tyrrhenian basins, *Spec. Pap. - Geol. Soc. Am.*, *418*, 153–169.

Faccenna, C., & T. W. Becker (2010), Shaping mobile belts by small-scale convection, *Nature*, *465*(7298), 602–605, doi:10.1038/nature09064.

Faccenna, C., T. W. Becker, C. P. Conrad, & L. Husson (2013a), Mountain building and mantle dynamics, *Tectonics*, *32*(1), 80–93, doi:10.1029/2012TC003176.

Faccenna, C., T. W. Becker, L. Jolivet, & M. Keskin (2013b), Mantle convection in the Middle East: Reconciling Afar upwelling, Arabia indentation and Aegean trench rollback, *Earth Planet. Sci. Lett.*, *375*, 254–269, doi:10.1016/j.epsl.2013.05.043.

Faccenna, C. et al. (2014), Mantle dynamics in the Mediterranean, *Rev. Geophys.*, *52*(3), 283–332, doi:10.1002/2013RG000444.

Famin, V., P. Philippot, L. Jolivet, & P. Agard (2004), Evolution of hydrothermal regime along a crustal shear zone, Tinos Island, Greece, *Tectonics*, *23*(5), doi:10.1029/2003TC001509.

Faure, M., & M. Bonneau (1988), Données nouvelles sur l'extension néogène de l'Égée: la déformation ductile du granite miocène de Mykonos (Cyclades, Grèce), *C. R. Acad. Sci. Paris*, *307*(II), 1553–1559.

Faure, M., M. Bonneau, & J. Pons (1991), Ductile deformation and syntectonic granite emplacement during the late Miocene extension of the Aegea (Greece), *Bull. Soc. Geol. Fr.*, *162*(1), 3–11.

Finetti, I. (1982), Structure and Evolution of the Central Mediterranean (Pelagian and Ionian Seas), *Boll. Geofis. Teor. Appl.*, *24*, 247–312.

Fukao, Y., M. Obayashi, H. Inoue, & M. Nenbai (1992), Subducting slabs stagnant in the mantle transition zone, *J. Geophys. Res.*, *97*(B4), 4809, doi:10.1029/91JB02749.

Funiciello, F., C. Faccenna, D. Giardini, & K. Regenauer-Lieb (2003), Dynamics of retreating slabs: 2. Insights from three-dimensional laboratory experiments, *J. Geophys. Res.*, *108*(B4), doi:10.1029/2001JB000896.

Funiciello, F., M. Moroni, C. Piromallo, C. Faccenna, A. Cenedese, & H. A. Bui (2006), Mapping mantle flow during retreating subduction: Laboratory models analyzed by feature tracking, *J. Geophys. Res.*, *111*(B3), doi:10.1029/2005JB003792.

Fytikas, M., F. Innocenti, P. Manetti, A. Peccerillo, R. Mazzuoli, & L. Villari (1984), Tertiary to Quaternary evolution of volcanism in the Aegean region, *Spec. Publ. - Geol. Soc. London*, *17*(1), 687–699, doi:10.1144/GSL.SP.1984.017.01.55.

Gautier, P., J.-P. Brun, & L. Jolivet (1993), Structure and kinematics of Upper Cenozoic extensional detachment on Naxos and Paros (Cyclades Islands, Greece), *Tectonics*, *12*(5), 1180–1194, doi:10.1029/93TC01131.

Gautier, P., & J.-P. Brun (1994), Crustal-scale geometry and kinematics of late-orogenic extension in the central Aegean (Cyclades and Ewia Island), *Tectonophysics*, *238*(1-4), 399–424, doi:10.1016/0040-1951(94)90066-3.

Gerst, M. D. (2008), Revisiting the Cumulative Grade-Tonnage Relationship for Major Copper Ore Types, *Econ. Geol.*, *103*(3), 615–628, doi:10.2113/gsecongeo.103.3.615.

Georgiev, G., C. Dabovski, & G. Stanisheva-Vassileva (2001), *East Srednogorie-Balkan Rift Zone*, Mem. Mus. Nati. Hist. Nat.

Gerya, T. V., B. Stöckhert, & A. L. Perchuk (2002), Exhumation of high-pressure metamorphic rocks in a subduction channel: A numerical simulation, *Tectonics*, *21*(6), 6–1–6–19, doi:10.1029/2002TC001406.

Gerya, T. V., & D. A. Yuen (2007), Robust characteristics method for modelling multiphase visco-elasto-plastic thermo-mechanical problems, *Phys. Earth Planet. Inter.*, *163*(1-4), 83–105, doi:10.1016/j.pepi.2007.04.015.

Gerya, T. (2010), *Introduction to Numerical Geodynamic Modelling*, Cambridge University Press., Cambridge, UK.

Gerya, T. V., & F. I. Meilick (2011), Geodynamic regimes of subduction under an active margin: effects of rheological weakening by fluids and melts, *J. Metamorph. Geol.*, *29*(1), 7–31, doi:10.1111/j.1525-1314.2010.00904.x.

Gessner, K., S. Piazolo, T. Güngör, U. Ring, A. Kröner, & C. Passchier (2001a), Tectonic significance of deformation patterns in granitoid rocks of the Menderes nappes, Anatolide belt, southwest Turkey, *Int. J. Earth Sci.*, *89*(4), 766–780, doi:10.1007/s005310000106.

Gessner, K., U. Ring, C. Johnson, R. Hetzel, C. W. Passchier, and T. Güngör (2001b), An active bivergent rolling-hinge detachment system: Central Menderes metamorphic core complex in western Turkey, Geology, 29(7), 611-614, doi:10.1130/0091-7613(2001)029<0611:AABRHD>2.0.CO;2.

Gessner, K., L. A. Gallardo, V. Markwitz, U. Ring, & S. N. Thomson (2013), What caused the denudation of the Menderes Massif: Review of crustal evolution, lithosphere structure, and dynamic topography in southwest Turkey, *Gondwana Res.*, *24*(1), 243–274, doi:10.1016/j.gr.2013.01.005.

Gill, J. B. (1981), *Orogenic andesites and plate tectonics*, Minerals and rocks 16, Springer-Verlag, Berlin ; New York.

Glodny, J., & R. Hetzel (2007), Precise U–Pb ages of syn-extensional Miocene intrusions in the central Menderes Massif, western Turkey, *Geol. Mag.*, *144*(02), 235–246, doi:10.1017/S0016756806003025.

Godfriaux, I. (1968), Etude géologique de la région de l'Olympe (Grèce), Université de Lille, Faculté des Sciences.

Göncüoğlu, M. C., V. Toprak, I. Kuşcu, A. Erler, and E. Olgun (1991), Geology of the Western Part of the Central Anatolian Massif, Part 1: Southern Section, *Turkish Petroleum Corporation (TPAO)*, *Report 2909*, 140 pp.

Görür, N. (1988), Timing of opening of the Black Sea basin, *Tectonophysics*, *147*(3-4), 247–262, doi:10.1016/0040-1951(88)90189-8.

Govers, R., & M. J. R. Wortel (2005), Lithosphere tearing at STEP faults: response to edges of subduction zones, *Earth Planet. Sci. Lett.*, *236*(1-2), 505–523, doi:10.1016/j.epsl.2005.03.022.

Grasemann, B., and K. Petrakakis (2007), Evolution of the Serifos Metamorphic Core Complex, in *Inside the Aegean Metamorphic Core Complexes*, *Journal of the Virtual Explorer*, edited by G. Lister, M. Forster, and U. Ring, *27*(2), 1-17.

Grasemann, B., D. A. Schneider, D. F. Stockli, & C. Iglseder (2012), Miocene bivergent crustal extension in the Aegean: Evidence from the western Cyclades (Greece), *Lithosphere*, *4*(1), 23–39, doi:10.1130/L164.1.

Grove, T., N. Chatterjee, S. Parman, & E. Medard (2006), The influence of H2O on mantle wedge melting, *Earth Planet. Sci. Lett.*, *249*(1-2), 74–89, doi:10.1016/j.epsl.2006.06.043.

Groves, D. I., and F. P. Bierlein (2007), Geodynamic settings of mineral deposit systems, *J. Geol. Soc. London*, *164*(1), 19–30, doi:10.1144/0016-76492006-065.

Guillou-Frottier, L., & E. Burov (2003), The development and fracturing of plutonic apexes: implications for porphyry ore deposits, *Earth Planet. Sci. Lett.*, *214*(1-2), 341–356, doi:10.1016/S0012-821X(03)00366-2.

Guillou-Frottier, L., & C. Jaupart (1995), On the effect of continents on mantle convection, *J. Geophys. Res.*, *100*(B12), 24217, doi:10.1029/95JB02518.

Guillou-Frottier, L., J. Buttles, & P. Olson (1995), Laboratory experiments on the structure of subducted lithosphere, *Earth Planet. Sci. Lett.*, *133*(1-2), 19–34, doi:10.1016/0012-821X(95)00045-E.

Gurnis, M. (1988), Large-scale mantle convection and the aggregation and dispersal of supercontinents, *Nature*, *332*(6166), 695–699, doi:10.1038/332695a0.

Gurnis, M., M. Turner, S. Zahirovic, L. DiCaprio, S. Spasojevic, R. D. Müller, J. Boyden, M. Seton, V. C. Manea, & D. J. Bower (2012), Plate tectonic reconstructions with continuously closing plates, *Computers & Geosciences*, *38*(1), 35–42, doi:10.1016/j.cageo.2011.04.014.

Gutnic, M., O. Monod, A. Poisson, and J.-F. Dumont (1979), Géologie des Taurides Occidentales (Turquie), *Mem. Soc. Geol. Fr.*, *137*, 1-112.

Hager, B. H., & R. J. O'Connell (1981), A simple global model of plate dynamics and mantle convection, *J. Geophys. Res.*, *86*(B6), 4843, doi:10.1029/JB086iB06p04843.

Halter, W. E., C. A. Heinrich, & T. Pettke (2005), Magma evolution and the formation of porphyry Cu-Au ore fluids: evidence from silicate and sulfide melt inclusions, *Miner. Deposita*, *39*(8), 845–863, doi:10.1007/s00126-004-0457-5.

Harangi, S., H. Downes, & I. Seghedi (2006), Tertiary-Quaternary subduction processes and related magmatism in the Alpine-Mediterranean region, *Geol. Soc. London, Memoirs*, *32*(1), 167–190, doi:10.1144/GSL.MEM.2006.032.01.10.

Harris, N. B. W., S. Kelley, & A. I. Okay (1994), Post-collision magmatism and tectonics in northwest Anatolia, *Contrib. Mineral. Petrol.*, *117*(3), 241–252, doi:10.1007/BF00310866.

Hawkesworth, C., S. Turner, K. Gallagher, A. Hunter, T. Bradshaw, & N. Rogers (1995), Calc-alkaline magmatism, lithospheric thinning and extension in the Basin and Range, *J. Geophys. Res.*, *100*(B6), 10,271–10,286, doi:10.1029/94JB02508.

Hawkesworth, C. J. (1997), U-Th Isotopes in Arc Magmas: Implications for Element Transfer from the Subducted Crust, *Science*, *276*(5312), 551–555, doi:10.1126/science.276.5312.551.

Hedenquist, J. W., & J. B. Lowenstern (1994), The role of magmas in the formation of hydrothermal ore deposits, *Nature*, *370*(6490), 519–527, doi:10.1038/370519a0.

Hedenquist, J. W., A. Arribas, & T. J. Reynolds (1998), Evolution of an intrusion-centered hydrothermal system; Far Southeast-Lepanto porphyry and epithermal Cu-Au deposits, Philippines, *Econ. Geol.*, *93*(4), 373–404, doi:10.2113/gsecongeo.93.4.373.

Heinrich, C. A., & F. Neubauer (2002), Cu – Au – Pb – Zn – Ag metallogeny of the Alpine – Balkan – Carpathian – Dinaride geodynamic province, *Miner. Deposita*, *37*(6-7), 533–540, doi:10.1007/s00126-002-0271-x.

Heinrich, C. A., D. Günther, A. Audétat, T. Ulrich, & R. Frischknecht (1999), Metal fractionation between magmatic brine and vapor, determined by microanalysis of fluid inclusions, *Geology*, *27*(8), 755, doi:10.1130/0091-7613(1999)027<0755:MFBMBA>2.3.CO;2.

Heinrich, C. A., T. Driesner, A. Stefánsson, & T. M. Seward (2004), Magmatic vapor contraction and the transport of gold from the porphyry environment to epithermal ore deposits, *Geology*, *32*(9), 761, doi:10.1130/G20629.1.

Hempton, M. R. (1987), Constraints on Arabian Plate motion and extensional history of the Red Sea, *Tectonics*, *6*(6), 687–705, doi:10.1029/TC006i006p00687.

Herzberg, C. T., W. S. Fyfe, & M. J. Carr (1983), Density constraints on the formation of the continental Moho and crust, *Contrib. Mineral. Petrol.*, *84*(1), 1–5, doi:10.1007/BF01132324.

Hess, H. H. (1962), History of ocean basins, in *Petrologic Studies*, pp. 599–620, Engel, A. E. J. et al., New York, US.

Hetzel, R., U. Ring, C. Akal, and M. Troesch (1995a), Miocene NNE-directed extensional unroofing in the Menderes Massif, southwestern Turkey, *J. Geol. Soc., 152*(4), 639-654, doi: 10.1144/gsjgs.152.4.0639.

Hetzel, R., C. W. Passchier, U. Ring, & Ö. O. Dora (1995b), Bivergent extension in orogenic belts: The Menderes massif (southwestern Turkey), *Geology*, *23*(5), 455, doi:10.1130/0091-7613(1995)023<0455:BEIOBT>2.3.CO;2.

Heuret, A., and S. Lallemand (2005), Plate motions, slab dynamics and back-arc deformation, *Phys. Earth Planet. Inter.*, *149*(1-2), 31–51, doi:10.1016/j.pepi.2004.08.022.

Hildreth, W., & S. Moorbath (1988), Crustal contributions to arc magmatism in the Andes of Central Chile, *Contrib. Mineral. Petrol.*, *98*(4), 455–489, doi:10.1007/BF00372365.

Hildreth, W., & S. Moorbath (1988), Crustal contributions to arc magmatism in the Andes of Central Chile, *Contrib. Mineral. Petrol.*, *98*(4), 455–489, doi:10.1007/BF00372365.

Hippolyte, J.-C., C. Muller, N. Kaymakci, & E. Sangu (2010), Dating of the Black Sea Basin: new nannoplankton ages from its inverted margin in the Central Pontides (Turkey), *Spec. Publ. - Geol. Soc. London*, *340*(1), 113–136, doi:10.1144/SP340.7.

Holmes, A. (1931), XVIII. Radioactivity and Earth Movements, *Trans. Geol. Soc. Glasgow*, *18*(3), 559–606, doi:10.1144/transglas.18.3.559.

Huet, B., L. Labrousse, & L. Jolivet (2009), Thrust or detachment? Exhumation processes in the Aegean: Insight from a field study on Ios (Cyclades, Greece), *Tectonics*, *28*(3), doi:10.1029/2008TC002397.

Huet, B., L. Labrousse, P. Monié, B. Malvoisin, & L. Jolivet (2014), Coupled phengite 40Ar–39Ar geochronology and thermobarometry: P-T-t evolution of Andros Island (Cyclades, Greece), *Geol. Mag.*, 1–17, doi:10.1017/S0016756814000661.

Husson, L. (2012), Trench migration and upper plate strain over a convecting mantle, *Phys. Earth Planet. Inter.*, *212-213*, 32–43, doi:10.1016/j.pepi.2012.09.006.

Huw Davies, J., & F. von Blanckenburg (1995), Slab breakoff: A model of lithosphere detachment and its test in the magmatism and deformation of collisional orogens, *Earth Planet. Sci. Lett.*, *129*(1-4), 85–102, doi:10.1016/0012-821X(94)00237-S.

Idleman, L., M. A. Cosca, M. T. Heizler, S. N. Thomson, C. Teyssier, & D. L. Whitney (2014), Tectonic burial and exhumation cycles tracked by muscovite and K-feldspar 40Ar/39Ar thermochronology in a strike-slip fault zone, central Turkey, *Tectonophysics*, *612-613*, 134–146, doi:10.1016/j.tecto.2013.12.003.

Iglseder, C., B. Grasemann, D. A. Schneider, K. Petrakakis, C. Miller, U. S. Klötzli, M. Thöni, A. Zámolyi, & C. Rambousek (2009), I and S-type plutonism on Serifos (W-Cyclades, Greece), *Tectonophysics*, *473*(1-2), 69–83, doi:10.1016/j.tecto.2008.09.021.

Iglseder, C., B. Grasemann, A. H. N. Rice, K. Petrakakis, & D. A. Schneider (2011), Miocene south directed low-angle normal fault evolution on Kea Island (West Cycladic Detachment System, Greece), *Tectonics*, *30*(4), doi:10.1029/2010TC002802.

Ilbeyli, N., J. A. Pearce, M. F. Thirlwall, & J. G. Mitchell (2004), Petrogenesis of collision-related plutonics in Central Anatolia, Turkey, *Lithos*, *72*(3-4), 163–182, doi:10.1016/j.lithos.2003.10.001.

Işik, V., & O. Tekeli (2001), Late orogenic crustal extension in the northern Menderes massif (western Turkey): evidence for metamorphic core complex formation, *Int. J. Earth Sci.*, *89*(4), 757–765, doi:10.1007/s005310000105.

Jadamec, M. A., & M. I. Billen (2010), Reconciling surface plate motions with rapid three-dimensional mantle flow around a slab edge, *Nature*, *465*(7296), 338–341, doi:10.1038/nature09053.

Jaffey, N., & A. H. F. Robertson (2001), New sedimentological and structural data from the Ecemis Fault Zone, southern Turkey: implications for its timing and offset and the Cenozoic tectonic escape of Anatolia, *J. Geol. Soc. London*, *158*(2), 367–378, doi:10.1144/jgs.158.2.367.

James, D. E. (1971), Andean crustal and upper mantle structure, *J. Geophys. Res.*, *76*(14), 3246–3271, doi:10.1029/JB076i014p03246.

Janković, S. (1997), The Carpatho-Balkanides and adjacent area: a sector of the Tethyan Eurasian metallogenic belt, *Miner. Deposita*, *32*(5), 426–433, doi:10.1007/s001260050110.

Jarrard, R. D. (1986), Relations among subduction parameters, *Rev. Geophys.*, *24*(2), 217, doi:10.1029/RG024i002p00217.

Jébrak, M., & E. Marcoux (2008), *Géologie des ressources minérales*, Bibliothèque et Archives nationales du Québec., Géologie Québec, Canada.

Jégo, S., & R. Dasgupta (2013), Fluid-present melting of sulfide-bearing ocean-crust: Experimental constraints on the transport of sulfur from subducting slab to mantle wedge, *Geochim. Cosmochim. Acta*, *110*, 106–134, doi:10.1016/j.gca.2013.02.011.

Jensen, E. P., & M. D. Barton (2000), Gold deposits related to alkaline magmatism, in *Gold in 2000: Rev. in Econ. Geol.*, edited by S. G. Hagemann and P. E. Brown, pp. 279–314.

Johnson, H. P., & M. J. Pruis (2003), Fluxes of fluid and heat from the oceanic crustal reservoir, *Earth Planet. Sci. Lett.*, *216*(4), 565–574, doi:10.1016/S0012-821X(03)00545-4.

Johnson, R. W., D. E. Mackenzie, & I. E. M. Smith (1978), Delayed partial melting of subduction-modified mantle in papua new guinea, *Tectonophysics*, *46*(1-2), 197–216, doi:10.1016/0040-1951(78)90114-2.

Jolivet, L., J. M. Daniel, C. Truffert, & B. Goffé (1994), Exhumation of deep crustal metamorphic rocks and crustal extension in arc and back-arc regions, *Lithos*, *33*(1-3), 3–30, doi:10.1016/0024-4937(94)90051-5.

Jolivet, L., B. Goffé, P. Monié, C. Truffert-Luxey, M. Patriat, & M. Bonneau (1996), Miocene detachment in Crete and exhumation P-T-t paths of high-pressure metamorphic rocks, *Tectonics*, *15*(6), 1129–1153, doi:10.1029/96TC01417.

Jolivet, L., & C. Faccenna (2000), Mediterranean extension and the Africa-Eurasia collision, *Tectonics*, *19*(6), 1095–1106, doi:10.1029/2000TC900018.

Jolivet, L. (2001), A comparison of geodetic and finite strain pattern in the Aegean, geodynamic implications, *Earth Planet. Sci. Lett.*, *187*(1-2), 95–104, doi:10.1016/S0012-821X(01)00277-1.

Jolivet, L., C. Faccenna, B. Goffé, E. Burov, & P. Agard (2003), Subduction tectonics and exhumation of high-pressure metamorphic rocks in the Mediterranean orogens, *Am. J. Sci.*, *303*(5), 353–409, doi:10.2475/ajs.303.5.353.

Jolivet, L., V. Famin, C. Mehl, T. Parra, C. Aubourg, R. Hébert, & P. Philippot (2004a), Strain localization during crustal-scale boudinage to form extensional metamorphic domes in the Aegean Sea, *Spec. Pap. - Geol. Soc. Am.*, *380*, 185–210.

Jolivet, L., G. Rimmelé, R. Oberhänsli, B. Goffé, and O. Candan (2004b), Correlation of syn-orogenic tectonic and metamorphic events in the Cyclades, the Lycian nappes and the Menderes massif. Geodynamic implications, *Bull. Soc. Geol. Fr.*, *175*(3), 217-238.

Jolivet, L., R. Augier, C. Faccenna, F. Negro, G. Rimmele, P. Agard, C. Robin, F. Rossetti, & A. Crespo-Blanc (2008), Subduction, convergence and the mode of backarc extension in the Mediterranean region, *Bull. Soc. Geol. Fr.*, *179*(6), 525–550, doi:10.2113/gssgfbull.179.6.525.

Jolivet, L., C. Faccenna, & C. Piromallo (2009), From mantle to crust: Stretching the Mediterranean, *Earth Planet. Sci. Lett.*, *285*(1-2), 198–209, doi:10.1016/j.epsl.2009.06.017.

Jolivet, L., & J.-P. Brun (2010), Cenozoic geodynamic evolution of the Aegean, *Int. J. Earth Sci.*, *99*(1), 109–138, doi:10.1007/s00531-008-0366-4.

Jolivet, L., E. Lecomte, B. Huet, Y. Denèle, O. Lacombe, L. Labrousse, L. Le Pourhiet, & C. Mehl (2010a), The North Cycladic Detachment System, *Earth Planet. Sci. Lett.*, *289*(1-2), 87–104, doi:10.1016/j.epsl.2009.10.032.

Jolivet, L., L. Labrousse, P. Agard, O. Lacombe, V. Bailly, E. Lecomte, F. Mouthereau, & C. Mehl (2010b), Rifting and shallow-dipping detachments, clues from the Corinth Rift and the Aegean, *Tectonophysics*, *483*(3-4), 287–304, doi:10.1016/j.tecto.2009.11.001.

Jolivet, L., F. Trotet, P. Monié, O. Vidal, B. Goffé, L. Labrousse, P. Agard, & B. Ghorbal (2010c), Along-strike variations of P–T conditions in accretionary wedges and syn-orogenic extension, the HP–LT Phyllite–Quartzite Nappe in Crete and the Peloponnese, *Tectonophysics*, *480*(1-4), 133–148, doi:10.1016/j.tecto.2009.10.002.

Jolivet, L. et al. (2013), Aegean tectonics: Strain localisation, slab tearing and trench retreat, *Tectonophysics*, *597-598*, 1–33, doi:10.1016/j.tecto.2012.06.011.

Jolivet, L., A. Menant, P. Sternai, A. Rabillard, L. Arbaret, R. Augier, V. Laurent, A. Beaudoin, B. Grasemann, B. Huet, L. Labrousse, & L. Le Pourhiet (2015), The geological signature of a slab tear below the Aegean, *Tectonophysics*, doi:10.1016/j.tecto.2015.08.004.

Jones, C. E., J. Tarney, J. H. Baker, & F. Gerouki (1992), Tertiary granitoids of Rhodope, northern Greece: Magmatism related to extensional collapse of the Hellenic Orogen?, *Tectonophysics*, *210*(3-4), 295–314, doi:10.1016/0040-1951(92)90327-3.

Karabulut, H., A. Paul, T. Afacan Ergun, D. Hatzfeld, D. M. Childs, & M. Aktar (2013), Long-wavelength undulations of the seismic Moho beneath the strongly stretched Western Anatolia, *Geophys. J. Int.*, *194*(1), 450–464, doi:10.1093/gji/ggt100.

Kárason, H., & R. D. van der Hilst (2000), Constraints on Mantle Convection From Seismic Tomography, in *Geophys. Monogr. Series*, vol. 121, edited by M. A. Richards, R. G. Gordon, and R. D. van der Hilst, pp. 277–288, American Geophysical Union, Washington, D. C.

Karato, S., H. Jung, I. Katayama, & P. Skemer (2008), Geodynamic Significance of Seismic Anisotropy of the Upper Mantle: New Insights from Laboratory Studies, *Annual Review of Earth and Planetary Sciences*, *36*(1), 59–95, doi:10.1146/annurev.earth.36.031207.124120.

Katz, R. F., M. Spiegelman, & C. H. Langmuir (2003), A new parameterization of hydrous mantle melting, *Geochem. Geophys. Geosyst.*, *4*(9), doi:10.1029/2002GC000433.

Katzir, Y., A. Matthews, Z. Garfunkel, M. Schliestedt, and D. Avigad (1996), The tectono-metamorphic evolution of a dismembered ophiolite (Tinos, Cyclades, Greece), *Geol. Mag.*, *133*(03), 237, doi:10.1017/S0016756800008992.

Kaymakci, N., C. E. Duermeijer, C. Langereis, S. H. White, & P. M. van Dijk (2003), Palaeomagnetic evolution of the Çankırı Basin (central Anatolia, Turkey): implications for oroclinal bending due to indentation, *Geol. Mag.*, *140*(3), 343–355, doi:10.1017/S001675680300757X.

Kaymakci, N., Y. Ozcelik, S. H. White, & P. M. van Dijk (2009), Tectono-stratigraphy of the Cankiri Basin: Late Cretaceous to early Miocene evolution of the Neotethyan Suture Zone in Turkey, *Spec. Publ. - Geol. Soc. London*, *311*(1), 67–106, doi:10.1144/SP311.3.

Keay, S., G. Lister, & I. Buick (2001), The timing of partial melting, Barrovian metamorphism and granite intrusion in the Naxos metamorphic core complex, Cyclades, Aegean Sea, Greece, *Tectonophysics*, *342*(3-4), 275–312, doi:10.1016/S0040-1951(01)00168-8.

Keiter, M., K. Piepjohn, C. Ballhaus, M. Lagos, & M. Bode (2004), Structural development of high-pressure metamorphic rocks on Syros island (Cyclades, Greece), *J. Struct. Geol.*, *26*(8), 1433–1445, doi:10.1016/j.jsg.2003.11.027.

Kerrich, R., R. Goldfarb, D. Groves, S. Garwin, & Y. Jia (2000), The characteristics, origins, and geodynamic settings of supergiant gold metallogenic provinces, *Sci. China, Ser. D: Earth Sci.*, *43*(S1), 1–68, doi:10.1007/BF02911933.

Keskin, M. (2003), Magma generation by slab steepening and breakoff beneath a subduction-accretion complex: An alternative model for collision-related volcanism in Eastern Anatolia, Turkey, *Geophys. Res. Lett.*, *30*(24), doi:10.1029/2003GL018019.

Keskin, M. (2007), Eastern Anatolia: A hotspot in a collision zone without a mantle plume, *Spec. Pap. - Geol. Soc. Am.*, *430*, 693–722.

Kilias, S. P., J. Naden, I. Cheliotis, T. J. Shepherd, H. Constandinidou, J. Crossing, & I. Simos (2001), Epithermal gold mineralisation in the active Aegean Volcanic Arc: the Profitis Ilias deposit, Milos Island, Greece, *Miner. Deposita*, *36*(1), 32–44, doi:10.1007/s001260050284.

Kincaid, C., & R. W. Griffiths (2003), Laboratory models of the thermal evolution of the mantle during rollback subduction, *Nature*, *425*(6953), 58–62, doi:10.1038/nature01923.

Kissel, C., & C. Laj (1988), The Tertiary geodynamical evolution of the Aegean arc: a paleomagnetic reconstruction, *Tectonophysics*, *146*(1-4), 183–201, doi:10.1016/0040-1951(88)90090-X.

Kissel, C., O. Averbuch, D. Frizon de Lamotte, O. Monod, & S. Allerton (1993), First paleomagnetic evidence for a post-Eocene clockwise rotation of the Western Taurides thrust belt east of the Isparta reentrant (Southwestern Turkey), *Earth Planet. Sci. Lett.*, *117*(1-2), 1–14, doi:10.1016/0012-821X(93)90113-N.

Kissel, C., C. Laj, A. Poisson, & N. Görür (2003), Paleomagnetic reconstruction of the Cenozoic evolution of the Eastern Mediterranean, *Tectonophysics*, *362*(1-4), 199–217, doi:10.1016/S0040-1951(02)00638-8.

Koçyiğit, A., & A. Beyhan (1998), A new intracontinental transcurrent structure: the Central Anatolian Fault Zone, Turkey, *Tectonophysics*, *284*(3-4), 317–336, doi:10.1016/S0040-1951(97)00176-5.

Koepke, J., E. Seidel, & H. Kreuzer (2002), Ophiolites on the Southern Aegean islands Crete, Karpathos and Rhodes: composition, geochronology and position within the ophiolite belts of the Eastern Mediterranean, *Lithos*, *65*(1-2), 183–203, doi:10.1016/S0024-4937(02)00165-2.

Kolb, M., A. von Quadt, I. Peytcheva, C. A. Heinrich, S. J. Fowler, & V. Cvetkovic (2012), Adakite-like and Normal Arc Magmas: Distinct Fractionation Paths in the East Serbian Segment of the Balkan-Carpathian Arc, *J. Petrol.*, *54*(3), 421–451, doi:10.1093/petrology/egs072.

Kondopoulou, D., & M. Westphal (1986), Paleomagnetism of the Tertiary intrusives from Chalkidiki (northern Greece), *J. Geophys.*, *59*(1), 62–66.

Kopf, A., J. Mascle, & D. Klaeschen (2003), The Mediterranean Ridge: A mass balance across the fastest growing accretionary complex on Earth, *J. Geophys. Res.*, *108*(B8), doi:10.1029/2001JB000473.

Kouzmanov, K., & G. S. Pokrovski (2012), Hydrothermal Controls on Metal Distribution in Porphyry Cu (-Mo-Au) Systems, *Spec. Publ. - Soc. Econ. Geol.*, *16*(22), 573–618.

Kreemer, C., & N. Chamot-Rooke (2004), Contemporary kinematics of the southern Aegean and the Mediterranean Ridge, *Geophys. J. Int.*, *157*(3), 1377–1392, doi:10.1111/j.1365-246X.2004.02270.x.

Kreemer, C., N. Chamotrooke, & X. Lepichon (2004), Constraints on the evolution and vertical coherency of deformation in the Northern Aegean from a comparison of geodetic, geologic and seismologic data, *Earth Planet. Sci. Lett.*, *225*(3-4), 329–346, doi:10.1016/j.epsl.2004.06.018.

Kuhlemann, J., W. Frisch, I. Dunkl, M. Kázmér, & G. Schmiedl (2004), Miocene siliciclastic deposits of Naxos Island: Geodynamic and environmental implications for the evolution of the southern Aegean Sea (Greece), *Spec. Pap. - Geol. Soc. Am.*, *378*, 51–65.

Kydonakis, K., K. Gallagher, J.-P. Brun, M. Jolivet, F. Gueydan, & D. Kostopoulos (2014), Upper Cretaceous exhumation of the western Rhodope Metamorphic Province (Chalkidiki Peninsula, northern Greece), *Tectonics*, *33*(6), 1113–1132, doi:10.1002/2014TC003572.

Lacassin, R., N. Arnaud, P. H. Leloup, R. Armijo, & B. Meyer (2007), Syn- and post-orogenic exhumation of metamorphic rocks in North Aegean, *eEarth*, *2*(2), 51–63, doi:10.5194/ee-2-51-2007.

Lagos, M., E. Scherer, F. Tomaschek, C. Munker, M. Keiter, J. Berndt, & C. Ballhaus (2007), High precision Lu–Hf geochronology of Eocene eclogite-facies rocks from Syros, Cyclades, Greece, *Chem. Geol.*, *243*(1-2), 16–35, doi:10.1016/j.chemgeo.2007.04.008.

Lallemand, S., A. Heuret, & D. Boutelier (2005), On the relationships between slab dip, back-arc stress, upper plate absolute motion, and crustal nature in subduction zones, *Geochem. Geophys. Geosyst.*, *6*(9), doi:10.1029/2005GC000917.

Lay, T. et al. (2005), The Great Sumatra-Andaman Earthquake of 26 December 2004, *Science*, *308*(5725), 1127–1133, doi:10.1126/science.1112250.

Lee, C.-T. A., P. Luffi, E. J. Chin, R. Bouchet, R. Dasgupta, D. M. Morton, V. Le Roux, Q. -z. Yin, & D. Jin (2012), Copper Systematics in Arc Magmas and Implications for Crust-Mantle Differentiation, *Science*, *336*(6077), 64–68, doi:10.1126/science.1217313.

Laurent, V., A. Beaudoin, L. Jolivet, L. Arbaret, R. Augier, A. Rabillard, and A. Menant (2015), Interrelations between extensional shear zones and synkinematic intrusions: the example of Ikaria island (NE Cyclades, Greece), *Tectonophysics*, *651*, 152-171, doi: 10.1016/j.tecto.2015.03.020.

Le Pichon, X. (1968), Sea-floor spreading and continental drift, *J. Geophys. Res.*, *73*(12), 3661–3697, doi:10.1029/JB073i012p03661.

Le Pichon, X., & J. Angelier (1979), The hellenic arc and trench system: A key to the neotectonic evolution of the eastern mediterranean area, *Tectonophysics*, *60*(1-2), 1–42, doi:10.1016/0040-1951(79)90131-8.

Le Pichon, X., N. Lybéris, J. Angelier, & V. Renard (1982), Strain distribution over the east Mediterranean ridge: A synthesis incorporating new Sea-Beam data, *Tectonophysics*, *86*(1-3), 243–274, doi:10.1016/0040-1951(82)90069-5.

Le Pichon, X., S. . Lallemant, N. Chamot-Rooke, D. Lemeur, & G. Pascal (2002), The Mediterranean Ridge backstop and the Hellenic nappes, *Mar. Geol.*, *186*(1-2), 111–125, doi:10.1016/S0025-3227(02)00175-5.

Le Pichon, X., & C. Kreemer (2010), The Miocene-to-Present Kinematic Evolution of the Eastern Mediterranean and Middle East and Its Implications for Dynamics, *Annu. Rev. Earth Planet. Sci.*, *38*(1), 323–351, doi:10.1146/annurev-earth-040809-152419.

Lecomte, E., L. Jolivet, O. Lacombe, Y. Denèle, L. Labrousse, & L. Le Pourhiet (2010), Geometry and kinematics of Mykonos detachment, Cyclades, Greece: Evidence for slip at shallow dip, *Tectonics*, *29*(5), doi:10.1029/2009TC002564.

Lee, J., & G. S. Lister (1992), Late Miocene ductile extension and detachment faulting, Mykonos, Greece, *Geology*, *20*(2), 121, doi:10.1130/0091-7613(1992)020<0121:LMDEAD>2.3.CO;2.

Lefebvre, C. J. C. (2011*), The tectonics of the Central Anatolian Crystalline Complex: a structural, metamorphic and paleomagnetic study*, Dsc thesis, Faculty of Geosciences, Department Earth Sciences, Utrecht.

Lefebvre, C., A. Barnhoorn, D. J. J. van Hinsbergen, N. Kaymakci, & R. L. M. Vissers (2011), Late Cretaceous extensional denudation along a marble detachment fault zone in the Kırşehir massif near Kaman, central Turkey, *J. Struct. Geol.*, *33*(8), 1220–1236, doi:10.1016/j.jsg.2011.06.002.

Lefebvre, C., M. J. M. Meijers, N. Kaymakci, A. Peynircioğlu, C. G. Langereis, & D. J. J. van Hinsbergen (2013), Reconstructing the geometry of central Anatolia during the late Cretaceous: Large-scale Cenozoic rotations and deformation between the Pontides and Taurides, *Earth Planet. Sci. Lett.*, *366*, 83–98, doi:10.1016/j.epsl.2013.01.003.

Li, C., R. D. van der Hilst, E. R. Engdahl, & S. Burdick (2008), A new global model for P wave speed variations in Earth's mantle, *Geochem. Geophys. Geosyst.*, *9*(5), doi:10.1029/2007GC001806.

Li, Z.-H., Z. Xu, T. Gerya, & J.-P. Burg (2013), Collision of continental corner from 3-D numerical modeling, *Earth Planet. Sci. Lett.*, *380*, 98–111, doi:10.1016/j.epsl.2013.08.034.

Liati, A., D. Gebauer, & R. Wysoczanski (2002), U–Pb SHRIMP-dating of zircon domains from UHP garnet-rich mafic rocks and late pegmatoids in the Rhodope zone (N Greece); evidence for Early Cretaceous crystallization and Late Cretaceous metamorphism, *Chem. Geol.*, *184*(3-4), 281–299, doi:10.1016/S0009-2541(01)00367-9.

Lips, A. L. W., S. H. White, & J. R. Wijbrans (1998), 40Ar/39Ar laserprobe direct dating of discrete deformational events: a continuous record of early Alpine tectonics in the Pelagonian Zone, NW Aegean area, Greece, *Tectonophysics*, *298*(1-3), 133–153, doi:10.1016/S0040-1951(98)00181-4.

Lips, A. L. W., J. R. Wijbrans, & S. H. White (1999), New insights from 40Ar/39Ar laserprobe dating of white mica fabrics from the Pelion Massif, Pelagonian Zone, Internal Hellenides, Greece: implications for the timing of metamorphic episodes and tectonic events in the Aegean region, *Spec. Publ. - Geol. Soc. London*, *156*(1), 457–474, doi:10.1144/GSL.SP.1999.156.01.21.

Lips, A. L. W., D. Cassard, H. Sö, H. Yilmaz, & J. R. Wijbrans (2001), Multistage exhumation of the Menderes Massif, western Anatolia (Turkey), *Int. J. Earth Sci.*, *89*(4), 781–792, doi:10.1007/s005310000101.

Lips, A. L. W. (2002), Correlating magmatic-hydrothermal ore deposit formation over time with geodynamic processes in SE Europe, *Spec. Publ. - Geol. Soc. London*, *204*(1), 69–79, doi:10.1144/GSL.SP.2002.204.01.05.

Lister, G. S., G. Banga, & A. Feenstra (1984), Metamorphic core complexes of Cordilleran type in the Cyclades, Aegean Sea, Greece, *Geology*, *12*(4), 221, doi:10.1130/0091-7613(1984)12<221:MCCOCT>2.0.CO;2.

Loiselet, C. (2009), Devenir d'une lithosphère en subduction dans le manteau terrestre : Etude de sa déformation et des flux mantelliques associées, Applied geology, Université Rennes 1, Rennes, France.

Loiselet, C., L. Husson, & J. Braun (2009), From longitudinal slab curvature to slab rheology, *Geology*, *37*(8), 747–750, doi:10.1130/G30052A.1.

Loiselet, C., L. Guillou-Frottier, G. Bertrand, M. Billa, E. Pelleter, F. Maldan, & D. Cassard (2010), Spatial distribution of mineral deposit along eastern Mediterranean subduction zone: a link with 3D mantle flow associated with slab rollback?, Lisbon, Portugal.

Lonergan, L., & N. White (1997), Origin of the Betic-Rif mountain belt, *Tectonics*, *16*(3), 504–522, doi:10.1029/96TC03937.

Long, M. D., & T. W. Becker (2010), Mantle dynamics and seismic anisotropy, *Earth Planet. Sci. Lett.*, *297*(3-4), 341–354, doi:10.1016/j.epsl.2010.06.036.

Long, M. D., & P. G. Silver (2008), The Subduction Zone Flow Field from Seismic Anisotropy: A Global View, *Science*, *319*(5861), 315–318, doi:10.1126/science.1150809.

Love, D. A., A. H. Clark, & J. K. Glover (2004), The Lithologic, Stratigraphic, and Structural Setting of the Giant Antamina Copper-Zinc Skarn Deposit, Ancash, Peru, *Econ. Geol.*, *99*(5), 887–916, doi:10.2113/econgeo.99.5.887.

Magni, V., C. Faccenna, J. van Hunen, & F. Funiciello (2014), How collision triggers backarc extension: Insight into Mediterranean style of extension from 3-D numerical models, *Geology*, *42*(6), 511–514, doi:10.1130/G35446.1.

Malinverno, A., & W. B. F. Ryan (1986), Extension in the Tyrrhenian Sea and shortening in the Apennines as result of arc migration driven by sinking of the lithosphere, *Tectonics*, *5*(2), 227–245, doi:10.1029/TC005i002p00227.

Marchev, P., R. Raicheva, H. Downes, O. Vaselli, M. Chiaradia, & R. Moritz (2004a), Compositional diversity of Eocene–Oligocene basaltic magmatism in the Eastern Rhodopes, SE Bulgaria: implications for genesis and tectonic setting, *Tectonophysics*, *393*(1-4), 301–328, doi:10.1016/j.tecto.2004.07.045.

Marchev, P., B. Singer, D. Jelev, S. Hasson, R. Moritz, & N. Bonev (2004b), The Ada Tepe deposit: a sediment-hosted, detachment fault-controlled, low-sulfidation gold deposit in the Eastern Rhodopes, SE Bulgaria, *Schweiz. Mineral. Petrogr. Mitt.*, *84*, 59–78.

Marchev, P., M. Kaiser-Rohrmeier, C. Heinrich, M. Ovtcharova, A. von Quadt, & R. Raicheva (2005), 2: Hydrothermal ore deposits related to post-orogenic extensional magmatism and core complex formation: The Rhodope Massif of Bulgaria and Greece, *Ore Geol. Rev.*, *27*(1-4), 53–89, doi:10.1016/j.oregeorev.2005.07.027.

Marsellos, A. E., W. S. F. Kidd, & J. I. Garver (2010), Extension and exhumation of the HP/LT rocks in the Hellenic forearc ridge, *Am. J. Sci.*, *310*(1), 1–36, doi:10.2475/01.2010.01.

McCaffrey, R. (2008), Global frequency of magnitude 9 earthquakes, *Geology*, *36*(3), 263, doi:10.1130/G24402A.1.

McGlashan, N., L. Brown, & S. Kay (2008), Crustal thickness in the central Andes from teleseismically recorded depth phase precursors, *Geophys. J. Int.*, *175*(3), 1013–1022, doi:10.1111/j.1365-246X.2008.03897.x.

McInnes, B. I., J. S. McBride, N. J. Evans, D. D. Lambert, & A. S. Andrew (1999), Osmium Isotope Constraints on Ore Metal Recycling in Subduction Zones, *Science*, *286*(5439), 512–516, doi:10.1126/science.286.5439.512.

McInnes, B. I. ., M. Gregoire, R. A. Binns, P. M. Herzig, & M. D. Hannington (2001), Hydrous metasomatism of oceanic sub-arc mantle, Lihir, Papua New Guinea: petrology and geochemistry of fluid-metasomatised mantle wedge xenoliths, *Earth Planet. Sci. Lett.*, *188*(1-2), 169–183, doi:10.1016/S0012-821X(01)00306-5.

McKenzie, D. P., & R. L. Parker (1967), The North Pacific: an Example of Tectonics on a Sphere, *Nature*, *216*(5122), 1276–1280, doi:10.1038/2161276a0.

McQuarrie, N., & D. J. J. van Hinsbergen (2013), Retrodeforming the Arabia-Eurasia collision zone: Age of collision versus magnitude of continental subduction, *Geology*, *41*(3), 315–318, doi:10.1130/G33591.1.

Mehl, C., L. Jolivet, & O. Lacombe (2005), From ductile to brittle: Evolution and localization of deformation below a crustal detachment (Tinos, Cyclades, Greece), *Tectonics*, *24*(4), doi:10.1029/2004TC001767.

Mehl, C., L. Jolivet, O. Lacombe, L. Labrousse, & G. Rimmele (2007), Structural evolution of Andros (Cyclades, Greece): a key to the behaviour of a (flat) detachment within an extending continental crust, *Spec. Publ. - Geol. Soc. London*, *291*(1), 41–73, doi:10.1144/SP291.3.

Meijers, M. J. M., N. Kaymakci, D. J. J. van Hinsbergen, C. G. Langereis, R. A. Stephenson, & J.-C. Hippolyte (2010), Late Cretaceous to Paleocene oroclinal bending in the central Pontides (Turkey), *Tectonics*, *29*(4), doi:10.1029/2009TC002620.

Meinert, L. D. (1997), Application of skarn deposit zonation models to mineral exploration, *Explor. Min. Geol.*, *6*(2), 185–208.

Melfos, V., M. Vavelidis, G. Christofides, & E. Seidel (2002), Origin and evolution of the Tertiary Maronia porphyry copper-molybdenum deposit, Thrace, Greece, *Miner. Deposita*, *37*(6-7), 648–668, doi:10.1007/s00126-002-0277-4.

Melinte-Dobrinescu, M. C. et al. (2009), The Messinian Salinity Crisis in the Dardanelles region: Chronostratigraphic constraints, *Palaeogeogr., Palaeoclimatol., Palaeoecol.*, *278*(1-4), 24–39, doi:10.1016/j.palaeo.2009.04.009.

Menant, A., L. Jolivet, R. Augier, & N. Skarpelis (2013), The North Cycladic Detachment System and associated mineralization, Mykonos, Greece: Insights on the evolution of the Aegean domain, *Tectonics*, *32*(3), 433–452, doi:10.1002/tect.20037.

Miller, M., A. Gorbatov, & B. Kennett (2005), Heterogeneity within the subducting Pacific slab beneath the Izu–Bonin–Mariana arc: Evidence from tomography using 3D ray tracing inversion techniques, *Earth Planet. Sci. Lett.*, *235*(1-2), 331–342, doi:10.1016/j.epsl.2005.04.007.

Morgan, W. J. (1968), Rises, trenches, great faults, and crustal blocks, *J. Geophys. Res.*, *73*(6), 1959–1982, doi:10.1029/JB073i006p01959.

Morris, A., & M. Anderson (1996), First palaeomagnetic results from the Cycladic Massif, Greece, and their implications for Miocene extension directions and tectonic models in the Aegean, *Earth Planet. Sci. Lett.*, *142*(3-4), 397–408, doi:10.1016/0012-821X(96)00114-8.

Mposkos, E. (1998), Cretaceous and tertiary tectonometamorphic events in Rhodope zone (Greece). Petrological and geochronological evidences, *Bull. Soc. Greece*, *32*(3), 59–67.

Neubauer, F. (2002), Contrasting Late Cretaceous with Neogene ore provinces in the Alpine-Balkan-Carpathian-Dinaride collision belt, *Spec. Publ. - Geol. Soc. London*, *204*(1), 81–102, doi:10.1144/GSL.SP.2002.204.01.06.

Neubauer, F. (2005), Structural control of mineralization in metamorphic core complexes, in *Mineral Deposit Research: Meeting the Global Challenge*, edited by J. Mao and F. P. Bierlein, pp. 561–564, Springer Berlin Heidelberg, Berlin, Heidelberg.

New, B. T. E. (2006), Controls of copper and gold distribution in the Kucing Liar deposit, Ertsberg mining district, West Papua, Indonesia, James Cook University, Townsville, Australia.

Nikolaeva, K., T. V. Gerya, and J. A. D. Connolly (2008), Numerical modelling of crustal growth in intraoceanic volcanic arcs, *Phys. Earth Planet. Inter.*, *171*(1-4), 336–356, doi:10.1016/j.pepi.2008.06.026.

Nimis, P., & P. Omenetto (2015), Does subduction polarity control metallogeny? The Mediterranean case, *Terra Nova*, doi:10.1111/ter.12141. Okay, A. I. (1984), Distribution and characteristics of the north-west Turkish blueschists, *Spec. Publ. - Geol. Soc. London*, *17*(1), 455–466, doi:10.1144/GSL.SP.1984.017.01.33.

Okay, A. I. (1986), High-pressure/low-temperature metamorphic rocks of Turkey, *Geol. Soc. London, Memoirs*, *164*, 333–347.

Okay, A. I., & M. Satır (2000a), Upper Cretaceous Eclogite-Facies Metamorphic Rocks from the Biga Peninsula, Northwest Turkey, *Turk. J. Earth Sci.*, *9*, 47–56.

Okay, A. I., & M. Satır (2000b), Coeval plutonism and metamorphism in a latest Oligocene metamorphic core complex in northwest Turkey, *Geol. Mag.*, *137*(5), 495–516, doi:10.1017/S0016756800004532.

Okay, A. I. (2001), Stratigraphic and metamorphic inversions in the central Menderes Massif: a new structural model, *Int. J. Earth Sci., 89*(4), 709-727, doi: 10.1007/s005310000098.

Okay, A., M. Satır, O. Tüysüz, S. Akyüz, & F. Chen (2001a), The tectonics of the Strandja Massif: late-Variscan and mid-Mesozoic deformation and metamorphism in the northern Aegean, *Int. J. Earth Sci.*, *90*(2), 217–233, doi:10.1007/s005310000104.

Okay, A. I., I. Tansel, & O. Tüysüz (2001b), Obduction, subduction and collision as reflected in the Upper Cretaceous–Lower Eocene sedimentary record of western Turkey, *Geol. Mag.*, *138*(02), doi:10.1017/S0016756801005088.

Okay, A. I. (2002), Jadeite-chloritoid-glaucophane-lawsonite blueschists in north-west Turkey: unusually high P/T ratios in continental crust, *J. Metamorph. Geol.*, *20*(8), 757-768, doi: 10.1046/j.1525-1314.2002.00402.x.

Okay, A., & M. Satır (2006), Geochronology of Eocene plutonism and metamorphism in northwest Turkey: evidence for a possible magmatic arc, *Geodinamica Acta*, *19*(5), 251–266, doi:10.3166/ga.19.251-266.

Okay, A. I., O. Tuysuz, M. Satır, S. Ozkan-Altiner, D. Altiner, S. Sherlock, & R. H. Eren (2006), Cretaceous and Triassic subduction-accretion, high-pressure-low-temperature metamorphism, and continental growth in the Central Pontides, Turkey, *Geol. Soc. Am. Bull.*, *118*(9-10), 1247–1269, doi:10.1130/B25938.1.

Okay, A. I., E. Özcan, W. Cavazza, N. Okay, and L. Gyögy (2010a), Basement Types, Lower Eocene Series, Upper Eocene Olistostromes and the Initiation of the Southern Thrace Basin, NW Turkey, *Turk. J. Earth Sci.*, *19*, 1-25, doi:10.3906/yer-0902-10.

Okay, A. I., M. Zattin, and W. Cavazza (2010b), Apatite fission-track data for the Miocene Arabia-Eurasia collision, *Geology*, *38*(1), 35-38, doi:10.1130/G30234.1.

Okay, A. I., İ. İşintek, D. Altıner, S. Özkan-Altıner, and N. Okay (2012), An olistostrome–mélange belt formed along a suture: Bornova Flysch zone, western Turkey, *Tectonophysics*, *568-569*, 282-295, doi: 10.1016/j.tecto.2012.01.007.

Okay, A. I., G. Sunal, S. Sherlock, D. Altıner, O. Tüysüz, A. R. C. Kylander-Clark, & M. Aygül (2013), Early Cretaceous sedimentation and orogeny on the active margin of Eurasia: Southern Central Pontides, Turkey, *Tectonics*, *32*(5), 1247–1271, doi:10.1002/tect.20077.

Oncken, O., D. Hindle, J. Kley, K. Elger, P. Victor, & K. Schemmann (2006), Deformation of the Central Andean Upper Plate System — Facts, Fiction, and Constraints for Plateau Models, in *The Andes*, edited by O. Oncken, G. Chong, G. Franz, P. Giese, H.-J. Götze, V. A. Ramos, M. R. Strecker, and P. Wigger, pp. 3–27, Springer Berlin Heidelberg.

Özbakır, A. D., A. M. C. Şengör, M. J. R. Wortel, & R. Govers (2013), The Pliny–Strabo trench region: A large shear zone resulting from slab tearing, *Earth and Planetary Science Letters*, *375*, 188–195, doi:10.1016/j.epsl.2013.05.025.

Özcan, A., M. Göncüoğlu, N. Turan, Ş. Uysal, K. Senturk, and V. Işık (1988), Late Paleozoic evolution of the Kütahya-Bolkardağ belt. *Middle East Tech. Univ. J. Pure Appl. Sci.*, *21*, 211-220.

Papanikolaou, D. J., & L. H. Royden (2007), Disruption of the Hellenic arc: Late Miocene extensional detachment faults and steep Pliocene-Quaternary normal faults-Or what happened at Corinth?, *Tectonics*, *26*(5), doi:10.1029/2006TC002007.

Parkinson, I. J., & R. J. Arculus (1999), The redox state of subduction zones: insights from arc-peridotites, *Chem. Geol.*, *160*(4), 409–423, doi:10.1016/S0009-2541(99)00110-2.

Parra, T., O. Vidal, & L. Jolivet (2002), Relation between the intensity of deformation and retrogression in blueschist metapelites of Tinos Island (Greece) evidenced

Parsons, B., & D. McKenzie (1978), Mantle convection and the thermal structure of the plates, *J. Geophys. Res.*, *83*(B9), 4485, doi:10.1029/JB083iB09p04485.

Paul, A., H. Karabulut, A. K. Mutlu, & G. Salaün (2014), A comprehensive and densely sampled map of shear-wave azimuthal anisotropy in the Aegean–Anatolia region, *Earth Planet. Sci. Lett.*, *389*, 14–22, doi:10.1016/j.epsl.2013.12.019.

Peach, C. L., E. A. Mathez, & R. R. Keays (1990), Sulfide melt-silicate melt distribution coefficients for noble metals and other chalcophile elements as deduced from MORB: Implications for partial melting, *Geochim. Cosmochim. Acta*, *54*(12), 3379–3389, doi:10.1016/0016-7037(90)90292-S.

Pearce, J. A., J. F. Bender, S. E. De Long, W. S. F. Kidd, P. J. Low, Y. Güner, F. Saroglu, Y. Yilmaz, S. Moorbath, & J. G. Mitchell (1990), Genesis of collision volcanism in Eastern Anatolia, Turkey, *J. Volcanol. Geotherm. Res.*, *44*(1-2), 189–229, doi:10.1016/0377-0273(90)90018-B.

Pe-Piper, G., & D. J. W. Piper (1989), Spatial and temporal variation in Late Cenozoic back-arc volcanic rocks, Aegean Sea region, *Tectonophysics*, *169*(1-3), 113–134, doi:10.1016/0040-1951(89)90186-8.

Pe-Piper, G., & D. J. W. Piper (2005), The South Aegean active volcanic arc: relationships between magmatism and tectonics, in *Dev. Volcanol.*, vol. 7, pp. 113–133, Elsevier.

Pe-Piper, G., & D. J. W. Piper (2006), Unique features of the Cenozoic igneous rocks of Greece, *Spec. Pap. - Geol. Soc. Am.*, *409*, 259–282.

Pe-Piper, G., & D. J. W. Piper (2007), Neogene backarc volcanism of the Aegean: New insights into the relationship between magmatism and tectonics, *Spec. Pap. - Geol. Soc. Am.*, *418*, 17–31.

Pérouse, E., N. Chamot-Rooke, A. Rabaute, P. Briole, F. Jouanne, I. Georgiev, & D. Dimitrov (2012), Bridging onshore and offshore present-day kinematics of central and eastern Mediterranean: Implications for crustal dynamics and mantle flow, *Geochem. Geophys. Geosyst.*, *13*(9), doi:10.1029/2012GC004289.

Philippon, M., J.-P. Brun, & F. Gueydan (2012), Deciphering subduction from exhumation in the segmented Cycladic Blueschist Unit (Central Aegean, Greece), *Tectonophysics*, *524-525*, 116–134, doi:10.1016/j.tecto.2011.12.025.

Pichavant, M., B. . Mysen, & R. Macdonald (2002), Source and H2O content of high-MgO magmas in island arc settings: an experimental study of a primitive calc-alkaline basalt from St. Vincent, lesser antilles arc, *Geochim. Cosmochim. Acta*, *66*(12), 2193–2209, doi:10.1016/S0016-7037(01)00891-2.

Piromallo, C., & A. Morelli (2003), P wave tomography of the mantle under the Alpine-Mediterranean area, *J. Geophys. Res.*, *108*(B2), doi:10.1029/2002JB001757.

Piromallo, C., T. W. Becker, F. Funiciello, & C. Faccenna (2006), Three-dimensional instantaneous mantle flow induced by subduction, *Geophys. Res. Lett.*, *33*(8), doi:10.1029/2005GL025390.

Plunder, A., P. Agard, C. Chopin, & A. I. Okay (2013), Geodynamics of the Tavşanlı zone, western Turkey: Insights into subduction/obduction processes, *Tectonophysics*, *608*, 884–903, doi:10.1016/j.tecto.2013.07.028.

Poisson, A. (1977), *Recherches géologiques dans les Taurides occidentales (Turquie)*, DSc thesis, Université de Paris-Sud, Orsay.

Pourteau, A., O. Candan, & R. Oberhänsli (2010), High-pressure metasediments in central Turkey: Constraints on the Neotethyan closure history, *Tectonics*, *29*(5), doi:10.1029/2009TC002650.

Pourteau, A., M. Sudo, O. Candan, P. Lanari, O. Vidal, & R. Oberhänsli (2013), Neotethys closure history of Anatolia: insights from 40Ar-39Ar geochronology and P-T estimation in high-pressure metasedimentary rocks, *J. Metamorph. Geol.*, *31*(6), 585–606, doi:10.1111/jmg.12034.

Rabillard, A., L. Arbaret, L. Jolivet, N. Le Breton, C. Gumiaux, R. Augier, and B. Grasemann (2015), Interactions between plutonism and detachments during Metamorphic Core Complex formation, Serifos Island (Cyclades, Greece), *Tectonics*, doi:10.1002/2014TC003650.

Ranalli, G. (1995), *Rheology of the Earth*, Chapman & Hall., London, UK.

Reilinger, R. et al. (2006), GPS constraints on continental deformation in the Africa-Arabia-Eurasia continental collision zone and implications for the dynamics of plate interactions, *J. Geophys. Res.*, *111*(B5), doi:10.1029/2005JB004051.

Richards, J. P. (2003), Tectono-Magmatic Precursors for Porphyry Cu-(Mo-Au) Deposit Formation, *Econ. Geol.*, *98*(8), 1515–1533, doi:10.2113/gsecongeo.98.8.1515.

Richards, J. P. (2005), Cumulative factors in the generation of giant calc-alkaline porphyry Cu deposits, in *Super Porphyry Copper & Gold Deposits: A Global Perspective*, vol. 1, pp. 7–25, Porter T. M., Adelaide, Australia.

Richards, J. P. (2009), Postsubduction porphyry Cu-Au and epithermal Au deposits: Products of remelting of subduction-modified lithosphere, *Geology*, *37*(3), 247–250, doi:10.1130/G25451A.1.

Richards, J. P. (2011), Magmatic to hydrothermal metal fluxes in convergent and collided margins, *Ore Geol. Rev.*, *40*(1), 1–26, doi:10.1016/j.oregeorev.2011.05.006.

Richards, J. P. (2014), Tectonic, magmatic, and metallogenic evolution of the Tethyan orogen: From subduction to collision, *Ore Geol. Rev.*, doi:10.1016/j.oregeorev.2014.11.009.

Ricou, L. E., J. Dercourt, J. Geyssant, C. Grandjacquet, C. Lepvrier, & B. Biju-Duval (1986), Geological constraints on the alpine evolution of the Mediterranean Tethys, *Tectonophysics*, *123*(1-4), 83–122, doi:10.1016/0040-1951(86)90194-0.

Ricou, L. E. (1994), Tethys Reconstructed-Plates, Continental Fragments and Their Boundaries since 260-Ma from Central America to South-Eastern Asia, *Geodinamica Acta*, *7*(4), 169–218.

Ricou, L., J. Burg, I. Godfriaux, & Z. Ivanov (1998), Rhodope and Vardar: the metamorphic and the olistostromic paired belts related to the Cretaceous subduction under Europe, *Geodinamica Acta*, *11*(6), 285–309, doi:10.1016/S0985-3111(99)80018-7.

Rimmelé, G., L. Jolivet, R. Oberhänsli, & B. Goffé (2003a), Deformation history of the high-pressure Lycian Nappes and implications for tectonic evolution of SW Turkey, *Tectonics*, *22*(2), doi:10.1029/2001TC901041.

Rimmelé, G., R. Oberhänsli, B. Goffé, L. Jolivet, O. Candan, & M. Çetinkaplan (2003b), First evidence of high-pressure metamorphism in the “Cover Series” of the southern Menderes Massif. Tectonic and metamorphic implications for the evolution of SW Turkey, *Lithos*, *71*(1), 19–46, doi:10.1016/S0024-4937(03)00089-6.

Rimmelé, G., T. Parra, B. Goffé, R. Oberhänsli, L. Jolivet, & O. Candan (2005), Exhumation Paths of High-Pressure-Low-Temperature Metamorphic Rocks from the Lycian Nappes and the Menderes Massif (SW Turkey): a Multi-Equilibrium Approach, *J. Petrol.*, *46*(3), 641–669, doi:10.1093/petrology/egh092.

Rimmelé, G., R. Oberhansli, O. Candan, B. Goffe, & L. Jolivet (2006), The wide distribution of HP-LT rocks in the Lycian Belt (Western Turkey): implications for accretionary wedge geometry, *Spec. Publ. - Geol. Soc. London*, *260*(1), 447–466, doi:10.1144/GSL.SP.2006.260.01.18.

Ring, U., S. Laws, & M. Bernet (1999a), Structural analysis of a complex nappe sequence and late-orogenic basins from the Aegean Island of Samos, Greece, *J. Struct. Geol.*, *21*(11), 1575–1601, doi:10.1016/S0191-8141(99)00108-X.

Ring, U., K. Gessner, T. Güngör, and C. W. Passchier (1999b), The Mendres Massif of western Turkey and the Cycladic Massif in the Aegean – do they really correlate?, *J. Geol. Soc. London*, *156*, 3-6.

Ring, U., P. W. Layer, & T. Reischmann (2001), Miocene high-pressure metamorphism in the Cyclades and Crete, Aegean Sea, Greece: Evidence for large-magnitude displacement on the Cretan detachment, *Geology*, *29*(5), 395, doi:10.1130/0091-7613(2001)029<0395:MHPMIT>2.0.CO;2.

Ring, U., & P. W. Layer (2003), High-pressure metamorphism in the Aegean, eastern Mediterranean: Underplating and exhumation from the Late Cretaceous until the Miocene to Recent above the retreating Hellenic subduction zone, *Tectonics*, *22*(3), 1022, doi:10.1029/2001TC001350.

Ring, U., C. Johnson, R. Hetzel, & K. Gessner (2003), Tectonic denudation of a Late CretaceousTertiary collisional belt: regionally symmetric cooling patterns and their relation to extensional faults in the Anatolide belt of western Turkey, *Geol. Mag.*, *140*(4), 421–441, doi:10.1017/S0016756803007878.

Ring, U., & A. S. Collins (2005), U-Pb SIMS dating of synkinematic granites: timing of core-complex formation in the northern Anatolide belt of western Turkey, *J. Geol. Soc. London*, *162*(2), 289–298, doi:10.1144/0016-764904-016.

Ring, U., T. Will, J. Glodny, C. Kumerics, K. Gessner, S. Thomson, T. Güngör, P. Monié, M. Okrusch, & K. Drüppel (2007), Early exhumation of high-pressure rocks in extrusion wedges: Cycladic blueschist unit in the eastern Aegean, Greece, and Turkey, *Tectonics*, *26*(2), doi:10.1029/2005TC001872.

Ring, U., J. Glodny, T. Will, & S. Thomson (2010), The Hellenic Subduction System: High-Pressure Metamorphism, Exhumation, Normal Faulting, and Large-Scale Extension, *Annu. Rev. Earth Planet. Sci.*, *38*(1), 45–76, doi:10.1146/annurev.earth.050708.170910.

Ring, U., J. Glodny, T. M. Will, & S. Thomson (2011), Normal faulting on Sifnos and the South Cycladic Detachment System, Aegean Sea, Greece, *J. Geol. Soc. London*, *168*(3), 751–768, doi:10.1144/0016-76492010-064.

Robertson, A. H. F., & S. Karamata (1994), The role of subduction-accretion processes in the tectonic evolution of the Mesozoic Tethys in Serbia, *Tectonophysics*, *234*(1-2), 73–94, doi:10.1016/0040-1951(94)90205-4.

Robertson, A. H. . (2002), Overview of the genesis and emplacement of Mesozoic ophiolites in the Eastern Mediterranean Tethyan region, *Lithos*, *65*(1-2), 1–67, doi:10.1016/S0024-4937(02)00160-3.

Robertson, A. H. F., O. Parlak, & T. Ustaömer (2009), Melange genesis and ophiolite emplacement related to subduction of the northern margin of the Tauride-Anatolide continent, central and western Turkey, *Spec. Publ. - Geol. Soc. London*, *311*(1), 9–66, doi:10.1144/SP311.2.

Roche, V., V. Laurent, L. Jolivet, G. L. Cardello, & S. Scaillet (submitted), The anatomy of the Cycladic Blueschists Unit on Sifnos island (Cyclades, Greece).

Rohais, S., S. Joannin, J.-P. Colin, J.-P. Suc, F. Guillocheau, & R. Eschard (2007), Age and environmental evolution of the syn-rift fill of the southern coast of the gulf of Corinth (Akrata-Derveni region, Greece), *Bull. Soc. Geol. Fr.*, *178*(3), 231–243, doi:10.2113/gssgfbull.178.3.231.

Rolf, T., & P. J. Tackley (2011), Focussing of stress by continents in 3D spherical mantle convection with self-consistent plate tectonics, *Geophys. Res. Lett.*, *38*(18), doi:10.1029/2011GL048677.

Rolf, T., N. Coltice, & P. J. Tackley (2012), Linking continental drift, plate tectonics and the thermal state of the Earth's mantle, *Earth Planet. Sci. Lett.*, *351-352*, 134–146, doi:10.1016/j.epsl.2012.07.011.

Rosenbaum, G., G. S. Lister, & C. Duboz (2002), Relative motions of Africa, Iberia and Europe during Alpine orogeny, *Tectonophysics*, *359*(1-2), 117–129, doi:10.1016/S0040-1951(02)00442-0.

Rosenbaum, G., D. Giles, M. Saxon, P. G. Betts, R. F. Weinberg, & C. Duboz (2005), Subduction of the Nazca Ridge and the Inca Plateau: Insights into the formation of ore deposits in Peru, *Earth Planet. Sci. Lett.*, *239*(1-2), 18–32, doi:10.1016/j.epsl.2005.08.003.

Royden, L. (1996), Coupling and decoupling of crust and mantle in convergent orogens: Implications for strain partitioning in the crust, *J. Geophys. Res.*, *101*(B8), 17679, doi:10.1029/96JB00951.

Royden, L. H., & D. J. Papanikolaou (2011), Slab segmentation and late Cenozoic disruption of the Hellenic arc, *Geochem. Geophys. Geosyst.*, *12*(3), doi:10.1029/2010GC003280.

Russo, R. M., & P. G. Silver (1994), Trench-Parallel Flow Beneath the Nazca Plate from Seismic Anisotropy, *Science*, *263*(5150), 1105–1111, doi:10.1126/science.263.5150.1105.

Salaün, G., H. A. Pedersen, A. Paul, V. Farra, H. Karabulut, D. Hatzfeld, C. Papazachos, D. M. Childs, C. Pequegnat, & SIMBAAD Team (2012), High-resolution surface wave tomography beneath the Aegean-Anatolia region: constraints on upper-mantle structure: Tomography of Aegea-Anatolia upper mantle, *Geophys. J. Int.*, *190*(1), 406–420, doi:10.1111/j.1365-246X.2012.05483.x.

Salemink, J. (1985), Skarn and ore formation at Serifos, Greece as a consequence of granodiorite intrusion, Utrecht University, Utrecht, Netherlands.

Sánchez-Gómez, M., D. Avigad, & A. Heimann (2002), Geochronology of clasts in allochthonous Miocene sedimentary sequences on Mykonos and Paros Islands: implications for back-arc extension in the Aegean Sea, *J. Geol. Soc. London*, *159*(1), 45–60, doi:10.1144/0016-764901031.

Savage, M. K. (1999), Seismic anisotropy and mantle deformation: What have we learned from shear wave splitting?, *Rev. Geophys.*, *37*(1), 65, doi:10.1029/98RG02075.

Scaillet, B. (2010), Economic geology: Volatile destruction, *Nat. Geosci.*, *3*(7), 456–457, doi:10.1038/ngeo908.

Schellart, W. P., J. Freeman, D. R. Stegman, L. Moresi, & D. May (2007), Evolution and diversity of subduction zones controlled by slab width, *Nature*, *446*(7133), 308–311, doi:10.1038/nature05615.

Schellart, W. P., & L. Moresi (2013), A new driving mechanism for backarc extension and backarc shortening through slab sinking induced toroidal and poloidal mantle flow: Results from dynamic subduction models with an overriding plate, *J. Geophys. Res.: Solid Earth*, *118*(6), 3221–3248, doi:10.1002/jgrb.50173.

Schermer, E. R. (1993), Geometry and kinematics of continental basement deformation during the Alpine orogeny, Mt. Olympos region, Greece, *J. Struct. Geol.*, *15*(3-5), 571–591, doi:10.1016/0191-8141(93)90149-5.

Schmeling, H. et al. (2008), A benchmark comparison of spontaneous subduction models—Towards a free surface, *Phys. Earth Planet. Inter.*, *171*(1-4), 198–223, doi:10.1016/j.pepi.2008.06.028.

Schmidt, M. W., & S. Poli (1998), Experimentally based water budgets for dehydrating slabs and consequences for arc magma generation, *Earth and Planetary Science Letters*, *163*(1-4), 361–379, doi:10.1016/S0012-821X(98)00142-3.

Schmid, S. M., D. Bernoulli, B. Fügenschuh, L. Matenco, S. Schefer, R. Schuster, M. Tischler, & K. Ustaszewski (2008), The Alpine-Carpathian-Dinaridic orogenic system: correlation and evolution of tectonic units, *Swiss J. Geosci.*, *101*(1), 139–183, doi:10.1007/s00015-008-1247-3.

Seaton, N. C. A., D. L. Whitney, C. Teyssier, E. Toraman, and M. T. Heizler (2009), Recrystallization of high-pressure marble (Sivrihisar, Turkey), *Tectonophysics*, *479*(3-4), 241-253, doi:10.1016/j.tecto.2009.08.015.

Seedorff, E., J. H. Dilles, J. M. Proffett, M. T. Einaudi, L. Zurcher, W. J. A. Stavast, D. A. Johnson, & M. D. Barton (2005), Porphyry deposits: characteristics and origin of hypogene features, *Econ. Geol.*, *100th Anniversary Volume*, 251–298.

Seghedi, I., Y. E. Ersoy, & C. Helvacı (2013), Miocene–Quaternary volcanism and geodynamic evolution in the Pannonian Basin and the Menderes Massif: A comparative study, *Lithos*, *180-181*, 25–42, doi:10.1016/j.lithos.2013.08.017.

Seidel, E., H. Kreuzer, & W. Harre (1982), A late Oligocene/early Miocene high pressure belt in the external Hellenides, *Geol. Jahrb., Reihe E*, *23*, 165–206.

Seidel, M., E. Seidel, & B. Stöckhert (2007), Tectono-sedimentary evolution of lower to middle Miocene half-graben basins related to an extensional detachment fault (western Crete, Greece), *Terra Nova*, *19*(1), 39–47, doi:10.1111/j.1365-3121.2006.00707.x.

Sen, S., & G. Seyitoglu (2009), Magnetostratigraphy of early-middle Miocene deposits from east-west trending Alasehir and Buyuk Menderes grabens in western Turkey, and its tectonic implications, *Spec. Publ. - Geol. Soc. London*, *311*(1), 321–342, doi:10.1144/SP311.13.

Şengör, A. M. C., & Y. Yilmaz (1981), Tethyan evolution of Turkey: A plate tectonic approach, *Tectonophysics*, *75*(3-4), 181–241, doi:10.1016/0040-1951(81)90275-4.

Şengör, A. M. C., M. Satır, and R. Akkök (1984), Timing of tectonic events in the Menderes Massif, western Turkey: Implications for tectonic evolution and evidence for pan-African basement in Turkey, *Tectonics*, *3*(7), 693-707.

Şengör, A. M. C., S. Özeren, T. Genç, & E. Zor (2003), East Anatolian high plateau as a mantle-supported, north-south shortened domal structure, *Geophys. Res. Lett.*, *30*(24), doi:10.1029/2003GL017858.

Şengör, A. M. C., O. Tüysüz, C. İmren, M. Sakınç, H. Eyidoğan, N. Görür, X. Le Pichon, & C. Rangin (2005), The North Anatolian Fault: A New Look, *Annu. Rev. Earth Planet. Sci.*, *33*(1), 37–112, doi:10.1146/annurev.earth.32.101802.120415.

Sengupta, M. K., & M. N. Toksöz (1976), Three dimensional model of seismic velocity variation in the Earth's mantle, *Geophys. Res. Lett.*, *3*(2), 84–86, doi:10.1029/GL003i002p00084.

Seward, D., O. Vanderhaeghe, L. Siebenaller, S. Thomson, C. Hibsch, A. Zingg, P. Holzner, U. Ring, & S. Duchene (2009), Cenozoic tectonic evolution of Naxos Island through a multi-faceted approach of fission-track analysis, *Spec. Publ. - Geol. Soc. London*, *321*(1), 179–196, doi:10.1144/SP321.9.

Sherlock, S., S. Kelley, S. Inger, N. Harris, and A. Okay (1999), 40Ar-39Ar and Rb-Sr geochronology of high-pressure metamorphism and exhumation history of the Tavsanli Zone, NW Turkey, *Contrib. Mineral. Petrol.*, *137*(1-2), 46–58, doi:10.1007/PL00013777.

Sigurdsson, H. et al. (2006), High-Temperature Hydrothermal Vent Field of Kolumbo Submarine Volcano, Aegean Sea: Site of Active Kuroko-Type Mineralization, San Francisco, US.

Sillitoe, R. H. (1972), A Plate Tectonic Model for the Origin of Porphyry Copper Deposits, *Econ. Geol.*, *67*(2), 184–197, doi:10.2113/gsecongeo.67.2.184.

Sillitoe, R. H. (1977), Metallic mineralization affiliated to subaerial volcanism: a review, *Spec. Publ. - Geol. Soc. London*, *7*(1), 99–116, doi:10.1144/GSL.SP.1977.007.01.13.

Sillitoe, R. H. (1997), Characteristics and controls of the largest porphyry copper-gold and epithermal gold deposits in the circum-Pacific region, *Aust. J. Earth Sci.*, *44*(3), 373–388, doi:10.1080/08120099708728318.

Sillitoe, R. H. (2010), Porphyry Copper Systems, *Econ. Geol.*, *105*(1), 3–41, doi:10.2113/gsecongeo.105.1.3.

Sillitoe, R. H., & J. W. Hedenquist (2003), Linkages between Volcanotectonic Settings, Ore-Fluid Compositions, and Epithermal Precious Metal Deposits, *Spec. Publ. - Soc. Econ. Geol.*, *10*.

Silver, P. G. (1996), Seismic Anisotropy Beneath the Continents: Probing the Depths of Geology, *Annu. Rev. Earth Planet. Sci.*, *24*(1), 385–432, doi:10.1146/annurev.earth.24.1.385.

Singer, D. A., V. J. Berger, & C. Moring (2008), *Porphyry copper deposits of the world: Database and grade and tonnage*, U.S. Geological Survey Open-File Report.

Skarpelis, N. (2002), Geodynamics and evolution of the Miocene mineralization in the Cycladic-Pelagonian belt, Hellenides, *Bull. Geol. Soc. Greece*, *34*(6), 2191–2206.

Skarpelis, N., & H. A. Gilg (2006), Miocene extensional fault-controlled mineralization in the central Aegean (Mykonos, Cyclades): deposition from a two-stage hydrothermal system?, in *Neogene Magmatism of the Central Aegean and Adjacent Areas: Petrology, Tectonics, Geodynamics, Mineral Resources and Environment*, Milos, Cyclades, Greece.

Sobolev, S. V., A. Y. Babeyko, I. Koulakov, & O. Oncken (2006), Mechanism of the Andean Orogeny: Insight from Numerical Modeling, in *The Andes*, edited by O. Oncken, G. Chong, G. Franz, P. Giese, H.-J. Götze, V. A. Ramos, M. R. Strecker, and P. Wigger, pp. 513–535, Springer Berlin Heidelberg.

Sokoutis, D., J. P. Brun, J. Van Den Driessche, & S. Pavlides (1993), A major Oligo-Miocene detachment in southern Rhodope controlling north Aegean extension, *J. Geol. Soc. London*, *150*(2), 243–246, doi:10.1144/gsjgs.150.2.0243.

Solomon, M. (1990), Subduction, arc reversal, and the origin of porphyry copper-gold deposits in island arcs, *Geology*, *18*(7), 630, doi:10.1130/0091-7613(1990)018<0630:SARATO>2.3.CO;2.

Sotiropoulos, S., E. Kamberis, M. V. Triantaphyllou, & T. Doutsos (2003), Thrust sequences in the central part of the External Hellenides, *Geol. Mag.*, *140*(6), 661–668, doi:10.1017/S0016756803008367.

St. Seymour, K., D. Zouzias, S. Tombros, & E. Kolaiti (2009), Geochemistry of the Serifos pluton (Cycladic islands) and associated iron oxide and sulfide ores: Skarn or metamorphosed exhalite deposits?, *N. Jb. Miner. Abh.*, *186*(3), 249–270, doi:10.1127/0077-7757/2009/0143.

Stampfli, G. M., & G. Borel (2002), A plate tectonic model for the Paleozoic and Mesozoic constrained by dynamic plate boundaries and restored synthetic oceanic isochrons, *Earth Planet. Sci. Lett.*, *196*(1-2), 17–33, doi:10.1016/S0012-821X(01)00588-X.

Stampfli, G. M., & C. Hochard (2009), Plate tectonics of the Alpine realm, *Spec. Publ. - Geol. Soc. London*, *327*(1), 89–111, doi:10.1144/SP327.6.

Sternai, P., L. Jolivet, A. Menant, & T. Gerya (2014), Driving the upper plate surface deformation by slab rollback and mantle flow, *Earth Planet. Sci. Lett.*, *405*, 110–118, doi:10.1016/j.epsl.2014.08.023.

Stouraiti, C., P. Mitropoulos, J. Tarney, B. Barreiro, A. M. McGrath, & E. Baltatzis (2010), Geochemistry and petrogenesis of late Miocene granitoids, Cyclades, southern Aegean: Nature of source components, *Lithos*, *114*(3-4), 337–352, doi:10.1016/j.lithos.2009.09.010.

Sunal, G., & O. Tüysüz (2002), Palaeostress analysis of Tertiary post-collisional structures in the Western Pontides, northern Turkey, *Geol. Mag.*, *139*(03), doi:10.1017/S0016756802006489.

Tackley, P. J. (2000), Mantle Convection and Plate Tectonics: Toward an Integrated Physical and Chemical Theory, *Science*, *288*(5473), 2002–2007, doi:10.1126/science.288.5473.2002.

Tackley, P. J., D. J. Stevenson, G. A. Glatzmaier, & G. Schubert (1993), Effects of an endothermic phase transition at 670 km depth in a spherical model of convection in the Earth's mantle, *Nature*, *361*(6414), 699–704, doi:10.1038/361699a0.

Tatsumi, Y., M. Sakuyama, H. Fukuyama, & I. Kushiro (1983), Generation of arc basalt magmas and thermal structure of the mantle wedge in subduction zones, *J. Geophys. Res.*, *88*(B7), 5815, doi:10.1029/JB088iB07p05815.

Tatsumi, Y., D. L. Hamilton, & R. W. Nesbitt (1986), Chemical characteristics of fluid phase released from a subducted lithosphere and origin of arc magmas: Evidence from high-pressure experiments and natural rocks, *J. Volcanol. Geotherm. Res.*, *29*(1-4), 293–309, doi:10.1016/0377-0273(86)90049-1.

Tatsumi, Y., Y.-I. Otofuji, T. Matsuda, & S. Nohda (1989), Opening of the Sea of Japan back-arc basin by asthenospheric injection, *Tectonophysics*, *166*(4), 317–329, doi:10.1016/0040-1951(89)90283-7.

Theye, T., E. Seidel, & O. Vidal (1992), Carpholite, sudoite, and chloritoid in low-grade high-pressure metapelites from Crete and the Peloponnese, Greece, *European Journal of Mineralogy*, *4*(3), 487–508, doi:10.1127/ejm/4/3/0487.

Thomson, S. N., and U. Ring (2006), Thermochronologic evaluation of postcollision extension in the Anatolide orogen, western Turkey, *Tectonics*, *25*(3), doi:10.1029/2005TC001833.

Tirel, C., F. Gueydan, C. Tiberi, & J.-P. Brun (2004), Aegean crustal thickness inferred from gravity inversion. Geodynamical implications, *Earth Planet. Sci. Lett.*, *228*(3-4), 267–280, doi:10.1016/j.epsl.2004.10.023.

Tomaschek, F., A. K. Kennedy, I. M. Villa, M. Lagos, and C. Ballhaus (2003), Zircons from Syros, Cyclades, Greece--Recrystallization and Mobilization of Zircon During High-Pressure Metamorphism, *J. Petrol.*, *44*(11), 1977–2002, doi:10.1093/petrology/egg067.

Tombros, S., K. St. Seymour, A. E. Williams-Jones, & P. G. Spry (2007), The Genesis of Epithermal Au-Ag-Te Mineralization, Panormos Bay, Tinos Island, Cyclades, Greece, *Econ. Geol.*, *102*(7), 1269–1294, doi:10.2113/gsecongeo.102.7.1269.

Tombros, S. F., K. St. Seymour, A. E. Williams-Jones, & P. G. Spry (2008), Later stages of evolution of an epithermal system: Au–Ag mineralizations at Apigania Bay, Tinos Island, Cyclades, Hellas, Greece, *Miner. Petrol.*, *94*(3-4), 175–194, doi:10.1007/s00710-008-0019-0.

Tombros, S. F., K. S. Seymour, A. E. Williams-Jones, D. Zhai, & J. Liu (2015), Origin of a barite-sulfide ore deposit in the Mykonos intrusion, Cyclades: Trace element, isotopic, fluid inclusion and raman spectroscopy evidence, *Ore Geol. Rev.*, *67*, 139–157, doi:10.1016/j.oregeorev.2014.11.016.

Tosdal, R. M., & J. P. Richards (2001), Magmatic and structural controls on the development of porphyry Cu±Mo±Au deposits, *Rev. Econ. Geol.*, *14*, 157–181.

Trotet, F., L. Jolivet, & O. Vidal (2001), Tectono-metamorphic evolution of Syros and Sifnos islands (Cyclades, Greece), *Tectonophysics*, *338*(2), 179–206, doi:10.1016/S0040-1951(01)00138-X.

Trotet, F., B. Goffe, O. Vidal, & L. Jolivet (2006), Evidence of retrograde Mg-carpholite in the Phyllite-Quartzite nappe of Peloponnese from thermobarometric modelisation - geodynamic implications, *Geodinamica Acta*, *19*(5), 323–343, doi:10.3166/ga.19.323-343.

Trumbull, R. B., U. Riller, O. Oncken, E. Scheuber, K. Munier, & F. Hongn (2006), The Time-Space Distribution of Cenozoic Volcanism in the South-Central Andes: a New Data Compilation and Some Tectonic Implications, in *The Andes*, edited by O. Oncken, G. Chong, G. Franz, P. Giese, H.-J. Götze, V. A. Ramos, M. R. Strecker, and P. Wigger, pp. 29–43, Springer Berlin Heidelberg.

Turcotte, D. L., & G. Schubert (2002), *Geodynamics*, Cambridge University Press., Cambridge, UK.

Turgut, S., and G. Eseller (2000), Sequence stratigraphy, tectonics and depositional history in eastern Thrace Basin, NW Turkey, *Mar. Pet. Geol.*, *17*(1), 61-100, doi: 10.1016/S0264-8172(99)00015-X.

Underhill, J. R. (1989), Late Cenozoic deformation of the Hellenide foreland, western Greece, *Geol. Soc. Am. Bull.*, *101*(5), 613–634, doi:10.1130/0016-7606(1989)101<0613:LCDOTH>2.3.CO;2.

Urai, J. L., R. D. Schuiling, & J. B. H. Jansen (1990), Alpine deformation on Naxos (Greece), *Spec. Publ. - Geol. Soc. London*, *54*(1), 509–522, doi:10.1144/GSL.SP.1990.054.01.47.

Uyeda, S., & H. Kanamori (1979), Back-arc opening and the mode of subduction, *J. Geophys. Res.*, *84*(B3), 1049, doi:10.1029/JB084iB03p01049.

van Hinsbergen, D. J. J., E. Hafkenscheid, W. Spakman, J. E. Meulenkamp, & R. Wortel (2005a), Nappe stacking resulting from subduction of oceanic and continental lithosphere below Greece, *Geology*, *33*(4), 325, doi:10.1130/G20878.1.

van Hinsbergen, D. J. J., C. G. Langereis, & J. E. Meulenkamp (2005b), Revision of the timing, magnitude and distribution of Neogene rotations in the western Aegean region, *Tectonophysics*, *396*(1-2), 1–34, doi:10.1016/j.tecto.2004.10.001.

van Hinsbergen, D. J. J., W. J. Zachariasse, M. J. R. Wortel, & J. E. Meulenkamp (2005c), Underthrusting and exhumation: A comparison between the External Hellenides and the “hot” Cycladic and “cold” South Aegean core complexes (Greece), *Tectonics*, *24*(2), doi:10.1029/2004TC001692.

van Hinsbergen, D. J. J., & J. E. Meulenkamp (2006), Neogene supradetachment basin development on Crete (Greece) during exhumation of the South Aegean core complex, *Basin Res.*, *18*(1), 103–124, doi:10.1111/j.1365-2117.2005.00282.x.

van Hinsbergen, D. J. J., G. Dupont-Nivet, R. Nakov, K. Oud, & C. Panaiotu (2008), No significant post-Eocene rotation of the Moesian Platform and Rhodope (Bulgaria): Implications for the kinematic evolution of the Carpathian and Aegean arcs, *Earth Planet. Sci. Lett.*, *273*(3-4), 345–358, doi:10.1016/j.epsl.2008.06.051.

van Hinsbergen, D. J. J., M. J. Dekkers, & A. Koç (2010a), Testing Miocene Remagnetization of Bey Dağları: Timing and Amount of Neogene Rotations in SW Turkey, *Turk. J. Earth Sci.*, *19*, 123–156, doi:10.3906/yer-0904-1.

van Hinsbergen, D. J. J., M. J. Dekkers, E. Bozkurt, & M. Koopman (2010b), Exhumation with a twist: Paleomagnetic constraints on the evolution of the Menderes metamorphic core complex, western Turkey, *Tectonics*, *29*(3), doi:10.1029/2009TC002596.

van Hinsbergen, D. J. J., & S. M. Schmid (2012), Map view restoration of Aegean-West Anatolian accretion and extension since the Eocene, *Tectonics*, *31*(5), doi:10.1029/2012TC003132.

van Keken, P. E., S. D. King, H. Schmeling, U. R. Christensen, D. Neumeister, & M.-P. Doin (1997), A comparison of methods for the modeling of thermochemical convection, *J. Geophys. Res.*, *102*(B10), 22477, doi:10.1029/97JB01353.

Vanderhaeghe, O. (2004), Structural development of the Naxos migmatite dome, *Spec. Pap. - Geol. Soc. Am.*, *380*, 211–227.

Vanderhaeghe, O. (2012), The thermal–mechanical evolution of crustal orogenic belts at convergent plate boundaries: A reappraisal of the orogenic cycle, *J. Geodyn.*, *56-57*, 124–145, doi:10.1016/j.jog.2011.10.004.

Vanderhaeghe, O., & C. Teyssier (2001), Partial melting and flow of orogens, *Tectonophysics*, *342*(3-4), 451–472, doi:10.1016/S0040-1951(01)00175-5.

Voudouris, P., V. Melfos, P. G. Spry, T. Bonsall, M. Tarkian, & M. Economou-Eliopoulos (2008), Mineralogical and fluid inclusion constraints on the evolution of the Plaka intrusion-related ore system, Lavrion, Greece, *Miner. Petrol.*, *93*(1-2), 79–110, doi:10.1007/s00710-007-0218-0.

von Quadt, A., R. Moritz, I. Peytcheva, & C. A. Heinrich (2005), 3: Geochronology and geodynamics of Late Cretaceous magmatism and Cu–Au mineralization in the Panagyurishte region of the Apuseni–Banat–Timok–Srednogorie belt, Bulgaria, *Ore Geol. Rev.*, *27*(1-4), 95–126, doi:10.1016/j.oregeorev.2005.07.024.

Wadati, K. (1935), On the activity of deep-focus earthquakes in the Japan Islands and neighbourhoods, *Geophys. Mag.*, *8*(3-4), 305–325.

Walcott, C., & S. White (1998), Constraints on the kinematics of post-orogenic extension imposed by stretching lineations in the Aegean region, *Tectonophysics*, *298*(1-3), 155–175, doi:10.1016/S0040-1951(98)00182-6.

Wegener, A. (1920), *Die enstehung der kontinente und ozeane*, F. Vieweg.

Wernicke, B. (1981), Low-angle normal faults in the Basin and Range Province: nappe tectonics in an extending orogen, *Nature*, *291*(5817), 645–648, doi:10.1038/291645a0.

White, N. C., & J. W. Hedenquist (1990), Epithermal environments and styles of mineralization: Variations and their causes, and guidelines for exploration, *J. Geochem. Explor.*, *36*(1-3), 445–474, doi:10.1016/0375-6742(90)90063-G.

Whitney, D. L., C. Teyssier, A. K. Fayon, M. A. Hamilton, & M. Heizler (2003), Tectonic controls on metamorphism, partial melting, and intrusion: timing and duration of regional metamorphism and magmatism in the Niğde Massif, Turkey, *Tectonophysics*, *376*(1-2), 37–60, doi:10.1016/j.tecto.2003.08.009.

Whitney, D. L., C. Teyssier, S. C. Kruckenberg, V. L. Morgan, & L. J. Iredale (2008), High-pressure–low-temperature metamorphism of metasedimentary rocks, southern Menderes Massif, western Turkey, *Lithos*, *101*(3-4), 218–232, doi:10.1016/j.lithos.2007.07.001.

Wijbrans, J. R., & I. McDougall (1988), Metamorphic evolution of the Attic Cycladic Metamorphic Belt on Naxos (Cyclades, Greece) utilizing 40Ar/39Ar age spectrum measurements, *J. Metamorph. Geol.*, *6*(5), 571–594, doi:10.1111/j.1525-1314.1988.tb00441.x.

Wilkinson, J. J. (2013), Triggers for the formation of porphyry ore deposits in magmatic arcs, *Nat. Geosci.*, *6*(11), 917–925, doi:10.1038/ngeo1940.

Williams-Jones, A. E., & C. A. Heinrich (2005), Vapor Transport of Metals and the Formation of Magmatic-Hydrothermal Ore Deposits, *Econ. Geol.*, *100th Anniversary Volume*, 1287–1312, doi:10.2113/gsecongeo.100.7.1287.

Willingshofer, E., F. Neubauer, & S. Cloetingh (1999), The significance of Gosau-type basins for the late cretaceous tectonic history of the Alpine-Carpathian belt, *Phys. Chem. Earth (A)*, *24*(8), 687–695, doi:10.1016/S1464-1895(99)00100-3.

Wilson, M., & G. Bianchini (1999), Tertiary-Quaternary magmatism within the Mediterranean and surrounding regions, *Spec. Publ. - Geol. Soc. London*, *156*(1), 141–168, doi:10.1144/GSL.SP.1999.156.01.09.

Wortel, M. J. R., & W. Spakman (2000), Subduction and Slab Detachment in the Mediterranean-Carpathian Region, *Science*, *290*(5498), 1910–1917, doi:10.1126/science.290.5498.1910.

Wüthrich, E. D. (2009), Low temperaturethermochronology of the northern Aegean Rhodope Massif, ETH, Zürich.

Yaliniz, K. M., & M. C. Göncüoğlu (1998), General geological characteristics and distribution of the Central Anatolian Ophiolites, *Yerbilimleri*, *20*, 19–30.

Yaltirak, C., M. Sakinç, & F. Y. Oktay (2000), Westward propagation of North Anatolian fault into the northern Aegean:Timing and kinematics: Comment and Reply: COMMENT, *Geology*, *28*(2), 187, doi:10.1130/0091-7613(2000)28<187:WPONAF>2.0.CO;2.

Yamato, P., E. Burov, P. Agard, L. Le Pourhiet, & L. Jolivet (2008), HP-UHP exhumation during slow continental subduction: Self-consistent thermodynamically and thermomechanically coupled model with application to the Western Alps, *Earth Planet. Sci. Lett.*, *271*(1-4), 63–74, doi:10.1016/j.epsl.2008.03.049.

Yamato, P., L. Husson, J. Braun, C. Loiselet, & C. Thieulot (2009), Influence of surrounding plates on 3D subduction dynamics, *Geophys. Res. Lett.*, *36*(7), doi:10.1029/2008GL036942.

Yem, L. M., L. Camera, J. Mascle, & A. Ribodetti (2011), Seismic stratigraphy and deformational styles of the offshore Cyrenaica (Libya) and bordering Mediterranean Ridge: Mediterranean Ridge and offshore Cyrenaica, *Geophys. J. Int.*, *185*(1), 65–77, doi:10.1111/j.1365-246X.2011.04928.x.

Yigit, O. (2009), Mineral Deposits of Turkey in Relation to Tethyan Metallogeny: Implications for Future Mineral Exploration, *Econ. Geol.*, *104*(1), 19–51, doi:10.2113/gsecongeo.104.1.19.

Yigit, O. (2012), A prospective sector in the Tethyan Metallogenic Belt: Geology and geochronology of mineral deposits in the Biga Peninsula, NW Turkey, *Ore Geol. Rev.*, *46*, 118–148, doi:10.1016/j.oregeorev.2011.09.015.

Yılmaz, Y., O. Tüysüz, E. Yiğibaş, Ş. Can Genç, & A. M. C. Şengör (1997), Geology and Tectonic Evolution of the Pontides, in *Regional and petroleum geology of the Black Sea and surrounding region*, vol. AAPG Memoir 68, pp. 183–226, A.G. Robinson.

Yılmaz, Y., Ş. Genç, Z. Karacık, & Ş. Altunkaynak (2001), Two contrasting magmatic associations of NW Anatolia and their tectonic significance, *J. Geodyn.*, *31*(3), 243–271, doi:10.1016/S0264-3707(01)00002-3.

Zajacz, Z., P. A. Candela, P. M. Piccoli, M. Wälle, & C. Sanchez-Valle (2012), Gold and copper in volatile saturated mafic to intermediate magmas: Solubilities, partitioning, and implications for ore deposit formation, *Geochim. Cosmochim. Acta*, *91*, 140–159, doi:10.1016/j.gca.2012.05.033.

Zhang, S., & S. Karato (1995), Lattice preferred orientation of olivine aggregates deformed in simple shear, *Nature*, *375*(6534), 774–777, doi:10.1038/375774a0.

Zhu, G., T. V. Gerya, D. A. Yuen, S. Honda, T. Yoshida, & J. A. D. Connolly (2009), Three-dimensional dynamics of hydrous thermal-chemical plumes in oceanic subduction zones, *Geochem. Geophys. Geosyst.*, *10*(11), doi:10.1029/2009GC002625.

Zhu, G., T. V. Gerya, P. J. Tackley, & E. Kissling (2013), Four-dimensional numerical modeling of crustal growth at active continental margins, *Journal of Geophysical Research: Solid Earth*, *118*(9), 4682–4698, doi:10.1002/jgrb.50357.

Zonenshain, L. P., & X. Le Pichon (1986), Deep basins of the Black Sea and Caspian Sea as remnants of Mesozoic back-arc basins, *Tectonophysics*, *123*(1-4), 181–211, doi:10.1016/0040-1951(86)90197-6.

Annexe A

Lexique

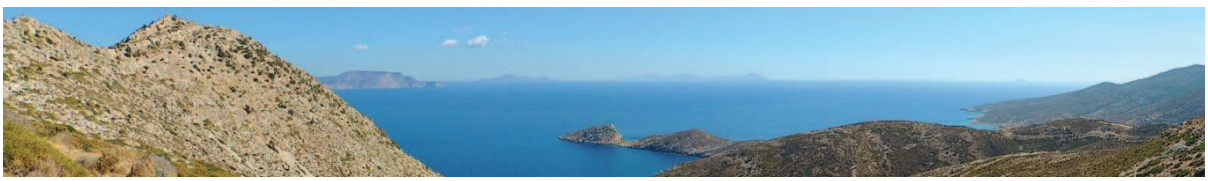

Calco-alcalin (roche –) : roche magmatique relativement riche en éléments alcalins (sodium, potassium) et en calcium et qui se retrouve typiquement dans les environnements de subduction.

Chalcophile : élément chimique qui s'associe préférentiellement au souffre. Ces éléments incluent notamment le cuivre, le zinc, l'argent ou encore l'arsenic.

Convection : transfert de chaleur par le déplacement d'un fluide qui est contrôlé par la variation de densité liée à la structuration thermique du milieu (i.e. un fluide chaud, moins dense, aura tendance à remonter à l'inverse d'un fluide plus froid et donc plus dense).

Déviatorique (contrainte –) : composante du tenseur de contraintes qui est responsable de la distorsion d'une roche (i.e. changement de forme), l'autre composante est définie par la contrainte hydrostatique, correspondant ici à la pression.

Différenciation : mécanisme permettant de faire évoluer un magma de composition basique (i.e. sous-saturé à saturé en silice) vers un magma de composition felsique (i.e. sursaturé en silice).

Epithermal : désigne ici un gîte métallique formé suite à la circulation puis du dépôt de fluides hydrothermaux dans un environnement superficiel (entre 2 km de profondeur et la surface), en lien plus ou moins direct avec un système volcanique aérien.

Fugacité : désigne ici la quantité d'une substance (ex. élément, gaz) présente dans un milieu et qui peut potentiellement interagir chimiquement avec d'autres substances.

Fluage-dislocation : mécanisme de déformation des roches qui s'exprime par la propagation d'imperfections dans la structure du réseau cristallin qui permet la déformation plastique du cristal. Ce mécanisme est fortement dépendant des contraintes appliquées sur la roche, ce qui se traduit par une relation non-linéaire (non-Newtonienne) entre le taux de déformation et la contrainte déviatorique.

Gangue : désigne ici l'ensemble des minéraux associés au minerai dans une concentration minérale, souvent sans grand intérêt économique (ex. quartz, calcite).

Gisement : concentration de substances (ex. métaux, minéraux, pétrole) qui peut être exploitée avec profit.

Gîte : concentration de substances (ex. métaux, minéraux, pétrole) utiles, sans connotation de taille ou d'importance.

***HFSE* (ou *high field strength elements*) :** éléments incompatibles à fort potentiel ionique. Ces éléments incluent le hafnium, le zirconium, le titane, le niobium et le tantale.

Hydraulique (fracturation –) : fracturation de la roche en présence de fluides et qui a lieu lorsque la pression du fluide est supérieure à la pression de la roche environnante sans considérer de contraintes externes (i.e. pression lithostatique).

Hydrothermalisme : circulation d'un fluide aqueux chaud, très souvent chargé en substances (ex. métaux, gaz) dissoutes qui peuvent se déposer sous forme de minéraux en un endroit donné de la croûte, formant ainsi des gîtes dits hydrothermaux.

Incompatible : élément qui tend à se concentrer dans la phase liquide plutôt que la phase solide d'un système donné. Il en existe deux groupes : les éléments lithophiles à large rayon ionique (*large ion lithophile elements* : *LILE*) et les éléments lithophiles à fort potentiel ionique (*high field strength elements* : *HFSE*).

Isostasie : état d'équilibre de la lithosphère *cassante* sur l'asthénosphère *ductile* qui se traduit par une profondeur de compensation à laquelle le poids de la colonne de roche sus-jacente (i.e. pression lithostatique) est le même quelque soit la topographie en surface.

***LILE* (ou *large ion lithophile elements*) :** éléments incompatibles à large rayon ionique. Ces éléments incluent le potassium, le rubidium, le strontium, le césium, le baryum et le plomb.

Manto : gîte métallique à métaux de base ou précieux et qui se met en place de manière disséminée en remplacement de roches sédimentaires ou volcaniques, ou bien sous la forme de veines.

Métallogénie : science qui étudie les mécanismes de formation des gisements métallifères.

Métallotecte : caractéristique géologique, géochimique ou géophysique d'un type de gisement qui peut servir de guide à la recherche d'un gisement similaire.

Métasomatisme : métamorphisme (régional ou de contact) qui s'accompagne d'une modification de la composition chimique globale de la roche.

Minerai : roche contenant une ou plusieurs substances (métaux, minéraux) en proportions suffisamment importantes pour être économiquement exploitable.

***MORB* (ou *mid-oceanic ridge basalt*) :** roche basaltique qui se forme principalement au niveau des dorsales médio-océaniques à la suite de la fusion partielle du manteau primitif sous-jacent qui a la particularité d'être appauvri en éléments incompatibles. Cette caractéristique se retrouve alors dans *MORB*.

Orogène (ou chaîne orogénique) : système montagneux résultant d'une importante compression de la lithosphère qui est alors intensément déformée (ex. plis, chevauchements, nappes de charriage), suite à la convergence entre deux plaques tectoniques.

Paragenèse : association de minéraux à l'équilibre qui se sont déposés de manière synchrone en réponse d'un même processus géologique et/ou géochimique.

***PGE* (ou *platinium group elements*) :** ensemble de métaux précieux, très recherchés pour leur propriétés physiques et chimiques particulières. Ces éléments incluent le platine, le palladium, le rhodium, l'iridium, l'osmium et le ruthenium.

***Pipe* bréchique :** littéralement « cheminée bréchique », roche formant un cylindre sub-vertical composée de fragments de roches dans une matrice pouvant être minéralisée. Cette brèche est souvent formée en réponse à une éruption volcanique de type explosive ou a une surpression de fluides (i.e. fracturation hydraulique) à l'apex d'une chambre magmatique.

Porphyre : désigne ici un gîte métallique associé à un système plutonique (habituellement porphyrique, d'où son nom) qui s'est mis en place au niveau à l'aplomb d'une zone de subduction. Ces gisements sont principalement riches en cuivre (porphyres cuprifères), en molybdène (porphyres à molybdène) ou en or (porphyres à or).

Le terme *porphyre* désigne plus généralement d'une roche magmatique montrant de grands cristaux de feldspath dans une matrice microcristalline.

Réserve : quantité de minerai d'un gisement qui est économiquement et techniquement exploitable au moment au moment de son détermination.

Sidérophile : élément qui s'associe facilement au fer mais également au souffre mais dans une moindre mesure que les éléments chalcophiles. Ces éléments incluent notamment l'or, le nickel, le cobalt ou encore les éléments du groupe du platine (i.e. *PGE*).

Skarn : désigne ici un gîte formé suite au métasomatisme de roches sédimentaires carbonatées au contact ou à proximité d'une intrusion plutonique. On parle alors de skarns proximaux ou distaux.

Solidus : limite séparant le domaine où une phase solide existe seule de celui où elle coexiste avec une phase liquide. Cette limite est définie par des paramètres tels que la pression, la température et la composition de la roche.

Stockwerk : réseau dense de petites veines s'entrecroisant dans toutes les directions.

Supercritique (fluide –) : état d'un fluide lorsqu'il est soumis à une température et une pression élevées, au-delà de sa température et de sa pression critique. La plupart des propriétés du fluide supercritique sont intermédiaires entre son état gazeux et liquide.

Teneur : désigne ici le pourcentage moyen d'un métal ou d'un minéral contenu dans un gisement. La teneur s'exprime en % lorsque cette proportion est élevée et en g t^{-1} lorsqu'elle est faible.

Tonnage : désigne ici la quantité de minerai (extraite et réserves) d'un gisement donné.

Transpression : régime tectonique qui associe une déformation décrochante à une composante de compression. Un tel régime tectonique peut s'exprimer si l'axe de la plus forte contrainte (σ_1) est oblique par rapport à la direction des structures compressives.

Transtension : régime tectonique qui associe une déformation décrochante à une composante d'extension, résultant également en un cisaillement oblique. Ce régime tectonique peut s'exprimer notamment lorsque l'axe de la contrainte la plus faible (σ_3) est oblique par rapport à la direction des structures extensives.

Annexe B

Driving the upper plate deformation by slab rollback and mantle flow

Sternai et al., 2014

(article publié au journal *Earth and Planetary Science Letters*)

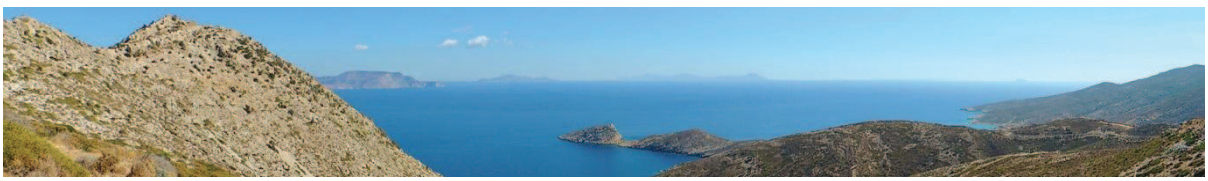

Earth and Planetary Science Letters 405 (2014) 110–118

Contents lists available at ScienceDirect

Earth and Planetary Science Letters

www.elsevier.com/locate/epsl

Driving the upper plate surface deformation by slab rollback and mantle flow

Pietro Sternai [a,*], Laurent Jolivet [a], Armel Menant [a], Taras Gerya [b]

[a] Institut de Sciences de la Terre d'Orléans (ISTO), University of Orléans, France
[b] Institute of Geophysics, Swiss Federal Institute of Technology (ETH), Zürich, Switzerland

ARTICLE INFO

Article history:
Received 19 March 2014
Received in revised form 22 July 2014
Accepted 17 August 2014
Available online xxxx
Editor: Y. Ricard

Keywords:
slab tearing
slab rollback
mantle flow
surface deformation

ABSTRACT

The relative contribution of crustal and mantle processes to surface deformation at convergent plate margins is still controversial. Conflicting models involving either extrusion mechanisms or slab rollback, in particular, were proposed to explain the surface strain and kinematics across the Tethyan convergent domain. Here, we present new high-resolution 3D thermo-mechanical numerical joint models of continental collision, oceanic subduction and slab tearing, which for the first time allow self-consistent reproduction of first-order Tethyan tectonic structures such as back-arc rifting and large-scale strike-slip faults accommodating continental escape. These models suggest that mantle flow due to slab rollback and tearing can modulate the surface strain and kinematics by locally enhancing trench retreat and dragging the upper plate from below. These results highlight the active role of the asthenospheric flow in driving the surface strain, not only by modulating the vertical stresses and producing dynamic topography but also through sub-horizontal motion. We discuss the implications of these findings based on observations across the Aegean–Anatolian and eastern Indian–Eurasian domains, though similar considerations may as well apply to other settings.

© 2014 Elsevier B.V. All rights reserved.

1. Introduction

Plate fragmentation, mountain building, formation of extensional basins, and major strike-slip fault zones characterised the long-term evolution of the Tethyan convergent domains (e.g., Ricou, 1994). Surface deformation is classically attributed to either collision-related processes such as crustal shortening, extrusion and gravitational spreading (e.g., Tapponnier and Molnar, 1976; Le Pichon et al., 1992) or subduction-related mechanisms such as slab pull or rollback and trench retreat (e.g., Dewey, 1988; Royden, 1993). However, subduction of the Tethyan lithosphere and collision along the African, Arabian, Indian and Eurasian margins often coexisted, interacting with each other to set jointly the surface kinematics and strain.

For instance, oceanic subduction below the Hellenic domain coexisted with active convergence across the neighbouring Bitlis–Zagros region since approximately the late Oligocene (e.g., Sengör, 1979; Jolivet and Faccenna, 2000; Allen et al., 2004). GPS measurements show a westward motion of Anatolia and a southward propagation of the Hellenic trench with respect to Eurasia (Reilinger et al., 2010), resulting in an overall counter-clockwise rotation (Fig. 1a). Most of this rotation is accommodated by the north-Anatolian fault (NAF), a strike-slip fault zone joining the Bitlis–Zagros domain to the east and the Aegean/Hellenic extensional back-arc region to the west (e.g., McKenzie, 1972; Sengör, 1979; Armijo et al., 1999). Tomographic models (Li et al., 2008a) show a low-velocity anomaly below western Turkey, which was interpreted as a major tear in the Hellenic slab (De Boorder et al., 1998; Govers and Wortel, 2005) (Fig. 1b). Recent studies foster the hypothesis that the mantle flow induced by slab rollback codetermines the surface deformation (Faccenna et al., 2006, 2013a, 2013b; Jolivet et al., 2009, 2013; Pérouse et al., 2012).

Another example spanning larger scales and a longer temporal evolution is south-eastern Asia in which collision of India with Eurasia and the Andaman–Sumatra subduction contribute jointly to surface deformation across the Himalaya, Indochina and Indonesia since ~45 Ma (e.g., Royden, 1997; Tapponnier et al., 2001; Royden et al., 2008; Replumaz et al., 2013). Geodetic measurements relative to stable Eurasia show a prominent clockwise rotation around the Eastern Himalayan Syntaxes (EHS) characterised by eastward motion of eastern Tibet and western Sichuan, southeastward motion in northern Yunan and south to south-eastward motion in southern Yunan (Zhang et al., 2004; Gan et al., 2007; ArRajehi et al., 2010) (Fig. 1c). Several strike-slip fault zones, which arrange from the convergent domain north of Tibet, such as the

* Corresponding author.
E-mail address: pietro.sternai@univ-orleans.fr (P. Sternai).

http://dx.doi.org/10.1016/j.epsl.2014.08.023
0012-821X/© 2014 Elsevier B.V. All rights reserved.

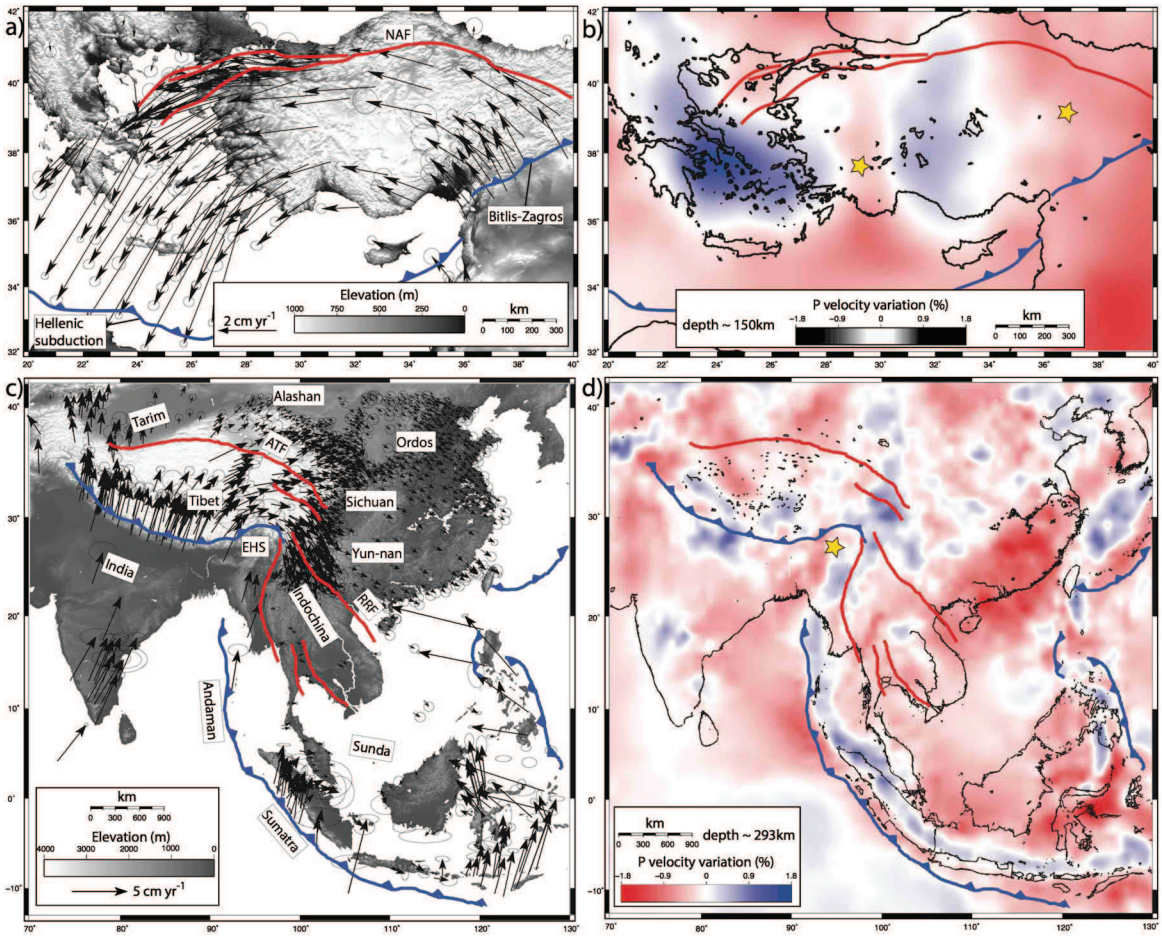

Fig. 1. Maps of the Aegean–Anatolian and Indian–Eurasian systems. a, c) Topography and GPS velocities with 95% confidence ellipses (Zhang et al., 2004; Gan et al., 2007; Reilinger et al., 2010). b, d) Tomographic models (Li et al., 2008a) showing the V_p anomalies at the depths indicated. Stars show the locations of slab tears. Red and blue lines in all panels represent the major strike-slip fault zones and thrusts and subduction fronts, respectively.

Altyn-Tagh Fault, to the extensional domain east and south of it, such as the Red River Fault (RRF), accommodate the majority of this motion (e.g., Molnar and Tapponnier, 1975; Tapponnier and Molnar, 1976). Several basins, such as the South China Sea, have developed east of Tibet and offshore the Indochina peninsula in the Oligocene and Miocene (Tapponnier et al., 1982, 1986; Taylor and Hayes, 1983). The main direction of extension across these regions was N–S and the relationships between the formation of these basins and large-scale shear zones such as the RRF have been widely debated: these topographic lows formed either as a pull-apart basin at the south-easternmost extremity of the RRF (i.e., extrusion: e.g., Tapponnier et al., 1982, 1986) or as more classical back-arc basins behind the retreating subduction (i.e., slab retreat: e.g., Taylor and Hayes, 1983; Jolivet et al., 1994; Fournier et al., 2004). The deep mantle structures associated with subduction of ancient Tethyan lithosphere vary significantly along the collision boundary (Fig. 1d). In particular, while deep and shallow slabs may be still (spatially) connected in the central Himalayas (Li et al., 2008a, 2008b), there is no evidence for such a connection beneath the eastern Himalayas. Tomographic images show a low velocity zone below the EHS at depth larger than ~200 km separating the Indian and Andaman–Sumatra slabs (Li et al., 2008a). This slab tear might have facilitated southward to westward rollback of the Andaman–Sumatra subduction after the onset of collision between India and Eurasia, and the mantle flow through the slab window and around the EHS might have codetermined the surface strain (Fig. 1c, d) (Holt, 2000).

Conflicting models involving extrusion tectonics originated by the Arabia/India–Eurasia collision or rollback of the Tethyan torn slabs were proposed to explain the surface strain and kinematics across both the Aegean–Anatolian and eastern Himalayan regions (e.g., Tapponnier and Molnar, 1976; Tapponnier et al., 1986; Jolivet et al., 1990; Royden, 1997; Armijo et al., 1999; Fournier et al., 2004; Becker and Faccenna, 2011). In addition, slab rollback is often proposed as a passive source of space to accommodate extrusion (e.g., Tapponnier et al., 1982; Armijo et al., 1999). However, the southward migration of the Hellenic trench is sensibly faster than the westward motion of Anatolia (Reilinger et al., 2010) (Fig. 1a), and classical extrusion models fail in predicting widespread extension such as that across the Ordos, Sichuan, Yunan regions in absence of a “free boundary” (e.g., Jolivet et al., 1990, 1994; Royden, 1997; Wang et al., 2001). These flaws suggest that slab rollback is in fact an active player and not just a passive source of space.

These geological, geophysical and geodetic observations, which provide insights on the long-term and recent geologic history, can constrain self-consistent three-dimensional (3D) numerical thermo-mechanical geodynamic models in order to achieve a first-order quantification of the relative contribution of the deep and shallow dynamics in setting the surface deformation across convergent plate boundaries. Previous numerical studies demonstrated along trench variations and complex mantle and crustal processes and surface deformation in subduction–collision systems (e.g., van Hunen and Allen, 2011; Capitanio and Replumaz, 2013;

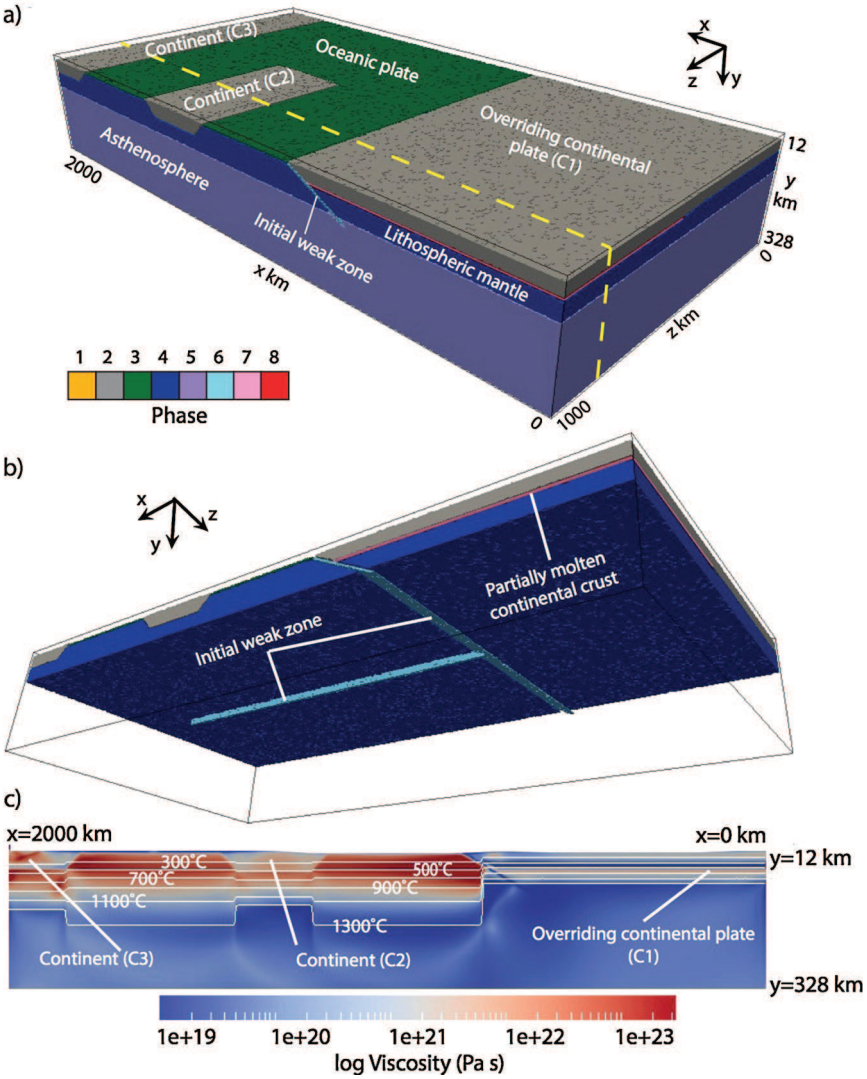

Fig. 2. Model setup. a) The 3D model domain (2000 × 328 × 1000 km in the x, y and z directions, respectively) with colours showing different rock types: 1 – sediments; 2 – continental crust; 3 – oceanic crust; 4 – lithospheric mantle; 5 – asthenospheric mantle; 6 – hydrated/serpentinized mantle (initially imposed "weak fracture zone"); 7 – partially molten continental crust; 8 – partially molten mantle. The top layer ("sticky air", $y < \sim 12$ km) and other phases are cut off for clarity. Convergence is imposed by applying uniform and constant-in-time velocity equal to ~ 1.8 cm yr^{-1} on the $x = 2000$ km model boundary. b) Initial model domain and location of the "weak zones" (i.e., hydrated/serpentinized mantle) into the lithosphere to initialise subduction (z-parallel) and allow slab tearing (x-parallel). The bottom layer (asthenosphere, $y > \sim 105$ km) is cut off for clarity. c) x–y viscosity profile of the initial model domain. The profile location is shown by the yellow dashed line in (a).

Li et al., 2013; Duretz et al., 2014). Although some implications for the large-scale tectonics across the Tethyan domain have been suggested (Li et al., 2013; Duretz et al., 2014), the relative contributions of crustal and mantle flow processes to surface deformation remained widely unaddressed.

2. Methods

The purpose of this paper is to assess the relative contributions of the lithospheric and mantle dynamics in setting the surface deformation at the transition between collisional and subduction domains. To this aim, we use 3D Cartesian thermo-mechanical modelling to resolve self-consistently the joint effects of oceanic subduction, slab tearing and continental collision on mantle flow and surface deformation at high resolution and accounting for realistic crustal and mantle rheologies. In addition to the reference model setup and boundary conditions, we outline below some of the principal features of the numerical model, but more detailed information can be found in Gerya and Yuen (2007), Zhu et al. (2009), Gerya (2010) and Li et al. (2013). Details on the parametric study can be found in the Supplementary Material.

2.1. 3D numerical model, setup and boundary conditions

All numerical experiments were performed with the code "I3ELVIS" (Gerya, 2010), solving the momentum, continuity and energy equations based on a staggered finite difference scheme combined with a marker-in-cell technique. Realistic and non-Newtonian visco-plastic rheologies (Ranalli, 1995) are used in the model. The model domain (Fig. 2) measures 2000 × 328 × 1000 km in the x, y and z dimensions, respectively. This domain is resolved by 501 × 165 × 197 grid points resulting in a resolution of 4, 2 and 5 km in the x, y and z dimensions, respectively. ~130 million randomly distributed markers are used for advecting the material properties and temperatures. The velocity boundary conditions are free slip at the top ($y = 0$ km) and at both the front and back boundaries ($z = 0$ km and $z = 1000$ km). The left and right boundaries ($x = 0$ km and $x = 2000$ km) use constant x-parallel velocities, which define the material influx. Global mass conservation is

Table 1
Material properties used in the numerical experiments. Qz. and Ol. correspond to the abbreviations of Quartzite and Olivine. k denotes the thermal conductivity, ρ_0 is the density, C_p is the specific heat capacity, E_a is the activation energy, V_a is the activation volume, n is the stress exponent, η_0 is the reference viscosity, Hr is the radiogenic heat production, ϕ_{eff} is the effective internal friction angle. Cohesion is 1 MPa for each phase.

Material	k ($W\,m^{-1}\,K^{-1}$)	ρ_0 ($kg\,m^{-3}$)	C_p ($J\,kg^{-1}\,K^{-1}$)	E_a ($kJ\,mol^{-1}$)	V_a ($m^3\,mol^{-1}$)	n	η_0 ($Pa^n\,s$)	Hr ($mW\,m^{-3}$)	Viscous flow law	$\sin(\phi_{eff})$
Sticky-air	20	1	100	0	0	1	1×10^{19}	0	Air	0
Water	20	1000	3330	0	0	1	1×10^{19}	0	Water	0
Sediment	$0.64 + 807/(T + 77)$	2600	1000	154	8	2.3	1.97×10^{17}	2	Wet Qz.	0.15
Cont. crust (C1, C3)	$0.64 + 807/(T + 77)$	2750	1000	154	8	2.3	1.17×10^{17}	2	Wet Qz.	0.15
Cont. crust (C2)	$1.18 + 807/(T + 77)$	2950	1000	238	8	3.2	4.8×10^{22}	2	Wet Qz.	0.15
Oc. crust	$1.18 + 474/(T + 77)$	3000	1000	238	8	3.2	4.8×10^{22}	0.25	Wet Qz.	0.15
Mantle	$0.73 + 1293/(T + 77)$	3300	1000	532	8	3.5	3.98×10^{16}	0.02	Dry Ol.	0.6
Weak zone	$0.73 + 1293/(T + 77)$	3300	1000	47	8	4	5×10^{20}	0.05	Wet Ol.	0

ensured by material outflux through the lower permeable boundary ($y = 328$ km). The top surface of the lithosphere is calculated dynamically as an internal free surface through a 12 km thick layer of "sticky air" (Gerya, 2010). Surface processes are implemented using a highly simplified gross-scale erosion–sedimentation law according to which instantaneous erosion limits mountains height to 4 km above the reference water level ($y = 12$ km), whereas instantaneous sedimentation limits trench depth to 8 km below the water level (Gerya and Yuen, 2007). The initial temperature gradient in the asthenospheric mantle is $\sim 0.5\,^{\circ}C\,km^{-1}$ (adiabatic). The thermal boundary conditions are 0 °C for the upper boundary and nil horizontal heat flux across the vertical boundaries. An infinity-like external temperature condition (Gerya, 2010) is imposed on the lower boundary. All the numerical experiments were performed using 20 cores on the BRUTUS cluster at the ETH-Zürich (the approximate run time of a simulation is two weeks).

2.2. A joint model of continental collision, oceanic subduction and slab tearing

Our numerical experiments were not designed to reproduce any particular case, but can be applied to the transition between a continental indenter flanked by active oceanic subduction. We stress that the ultimate goal of our numerical experiments is to investigate the *effects* of slab tearing on the mantle and surface strain, but the potential *causes* of a tear in the slab are beyond the scope of this work. As such, we impose mechanical weaknesses in the oceanic plate and spatial variations of the upper continental crust (as detailed below), but do not claim that, in natural contexts, slab tears are necessarily generated by these factors.

The reference model is set up as follows. Three continental plates (C1, C2 and C3) are included into the initial model domain (Fig. 2a and Table 1). The crust of C2 and C3 are 50 km and 45 km thick, respectively. By varying the crustal thickness of the upper plate (C1) along the trench-parallel direction (z) one can control the slab descent rates (Nikolaeva et al., 2010) and therefore generate a tear in the slab. In particular, we imposed the crust of C1 as 35 km thick where $z \leq 490$ km and 45 km thick where $z > 510$ km (linear interpolation in between). The initial thermal structure of C1, C2 and C3 is laterally uniform with 0 °C at the surface and 1300 °C at 90, 140 and 150 km depth respectively. An oceanic domain, characterised by a trench-parallel weak fracture zone to initiate subduction and a trench-perpendicular weak fracture zone to allow for slab tearing, separates the three continental plates (Fig. 2a, b). The thermal structure of the oceanic lithosphere is that of a half-space cooling age of 120 Ma (e.g., Turcotte and Schubert, 2002). Uniform and constant in time x-parallel velocities equal to $\sim 1.8\,cm\,yr^{-1}$ (convergence) are imposed to the $x = 2000$ km boundary.

The evolution of the reference model is shown in Fig. 3 and in Video S1, S2 and S3. The details and timing of the model evolution depends upon the assumed thermal and mechanical parameters (see the Supplementary Materials), but the overall sequence of events (Fig. 3) is robust and includes: 1) early subduction of the oceanic domain between C1 and C2 and 2) later subduction of the oceanic domain between C1 and C3. These major events are allowed by tearing of the slab and separated in time by the collision between C1 and C2. Trench retreat, back-arc extension and progressive approach/collision of the continental plates characterise the surface evolution during the entire model run.

3. Results

In this section, we outline the numerical results with particular focus on the relationships between mantle and crustal flow and the effects of slab tearing and continental collision on the surface strain.

3.1. Mantle vs. crustal flow

A toroidal motion (with a minor ascending poloidal component) induced by the down-going slab dominates the deep dynamics during the first subduction event (Fig. 4a). This toroidal flow occurs both below C1 and through the opening slab window. At the surface, extensional and compressional deformation occurs in the back-arc and collisional domain, respectively. Crustal and mantle flows are essentially decoupled and surface deformation seems to be substantially driven by incipient slab rollback and trench retreat within the oceanic domain between C1 and C3 and continental collision between C1 and C2. The rheological stratification of the continental plates is essentially unaffected by this early subduction event, implying that the traction due to mantle flow is imposed at the base of the lithosphere (Fig. 4c).

The model evolution during the second subduction event is highly conditioned by the precedent toroidal flow of hot asthenosphere. This flow warmed the incipiently subducting lithosphere close to the slab tear, enhancing here slab rollback and trench retreat, generating a non-cylindrical (i.e., not parallel to the initial upper plate margin) subduction (Figs. 3, 4b and 4e). This subduction geometry induces a lateral (i.e., with non-nil trench-parallel component of motion), horizontal to sub-horizontal return flow of hot asthenospheric material, which further enhances the asymmetry of subduction (Fig. 4b). The surface deformation across C1 is characterised at this stage by a faster trench retreat in the proximity of the collisional domain and above the slab tear, while localised strike-slip deformation propagating toward the subducting plate as the model progresses accommodates the rotation of a crustal block (Figs. 3b and 4b). The rheological stratification of the upper plate in the back-arc extensional domain is characterised by the absence of a rigid lithospheric mantle and the velocity–depth profile shows particularly fast mantle flow (Fig. 4d), parallel in places to the surface velocity field (Fig. 4b). This translates into shear stresses (σ_{xy}) up to ~100 MPa applied directly to the base of the crust by the asthenospheric flow (Fig. 5).

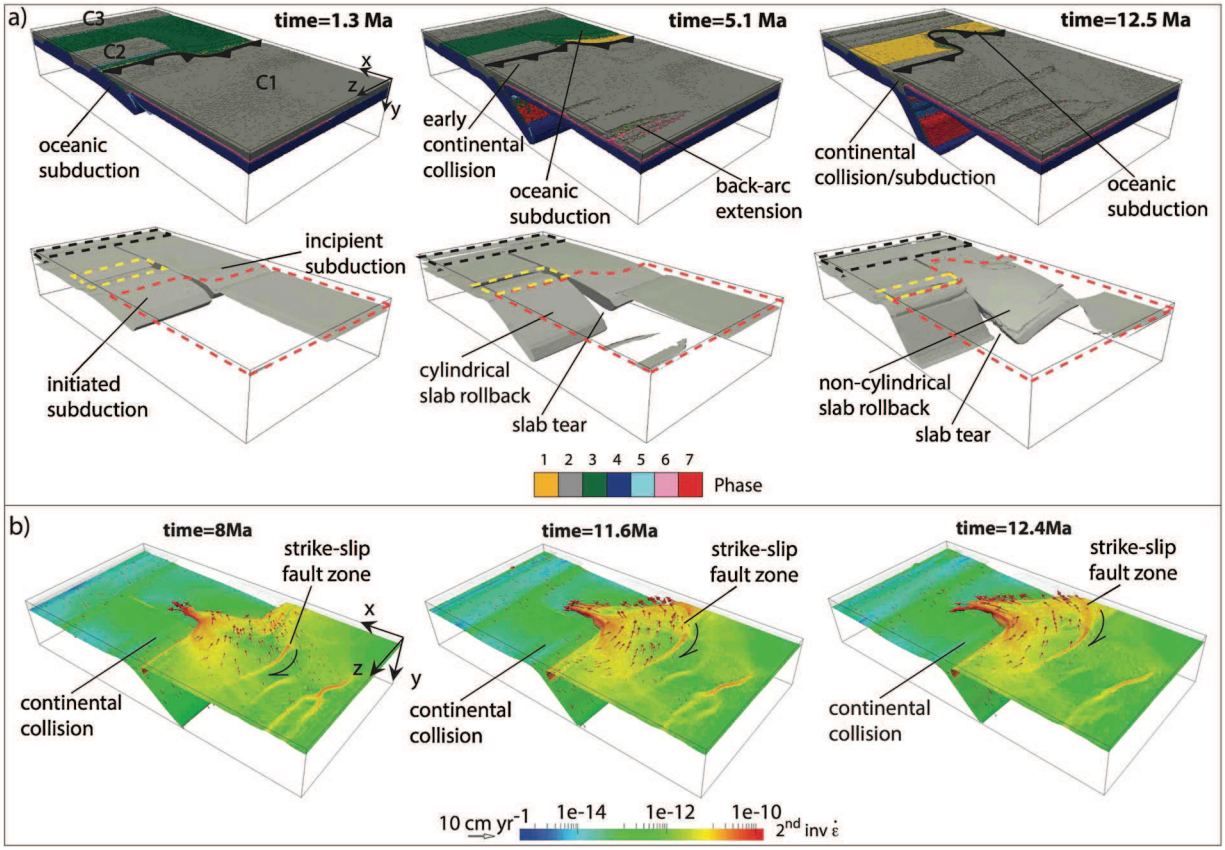

Fig. 3. Evolution of the reference model. a) Colours on the top panels show different rock types: 1 – sediments; 2 – continental crust; 3 – oceanic crust; 4 – lithospheric mantle; 5 – hydrated/serpentinized mantle (initially imposed "weak fracture zone"); 6 – partially molten continental crust; 7 – partially molten mantle. The top layer ("sticky-air", $y <\sim 12$ km), the asthenosphere and other phases are cut off for clarity. The subducting plates shown on the bottom panels are visualised through an iso-viscosity contour equal to 10^{22} Pa s. Red, yellow and black dashed lines on the lower panels show the plan view of C1, C2 and C3, respectively. b) Selected frames showing the 800 °C isotherm (mostly corresponding to the crust–lithospheric mantle transition within the C1 domain), colour-coded by the second invariant of the rate-of-strain tensor on this surface. A strike-slip fault zone (also visible at the surface, Fig. 4b) is generated by the sub-horizontal mantle flow (red arrows) following slab rollback and tearing. Note that the timing of panels in (a) and (b) is different.

3.2. *Effects of slab tearing and continental collision on the surface strain*

By comparing the reference model outputs to similar simulations, but not implying collision between C1 and C2 or slab tearing, one can decouple the first-order crustal and mantle contributions to the surface strain. It appears that strain localisation along a major strike-slip fault zone and thus the onset of a distinctive block-like deformation and surface rotation only occurs when both collision between rigid continental plates and slab tearing take place (Figs. 4b and 6). In particular, the trench parallel component of motion within the upper plate is sensibly reduced in absence of continental collision or slab tearing. Besides, slab tearing allows/enhances rollback of the subducting plate, trench parallel/toroidal migration of the asthenosphere, trench retreat and extension within the upper plate.

It is noteworthy that, when both continental collision and slab tearing allow for a block-like deformation and surface rotation, the velocity fields within the crust and mantle are sensibly faster within the back-arc extensional region and close to the subduction trench than in the collisional domain (Fig. 4b).

4. Discussion

Various combinations of processes such as extrusion tectonics, suction exerted by slab rollback, gravitational collapse of the collisional belt and mantle drag associated with regional plum-like upwelling were proposed to explain the observed surface kinematics across the Tethyan convergent domain (e.g., Tapponnier and Molnar, 1976; Royden, 1997; Armijo et al., 1999; Allen et al., 2004; Alvarez, 2010; Becker and Faccenna, 2011). Most of the proposed models, however, neglected the role played by the dynamical asthenospheric flow originated by slab rollback and tearing. A major outcome of our numerical experiments is that the toroidal motion of the asthenosphere at the edge of a retreating tearing slab is able to modulate the thermal state of the lithosphere, in turn affecting the geometry and dynamics of later subduction events and associated mantle and surface strain. Tectonic inheritance is clearly not a new concept, but it most often refers to the mechanical properties of the lithosphere and mantle (e.g., Thomas, 2006), while we show here that also the thermal and kinematic inheritances can significantly affect the surface evolution. Moreover, the mantle return flow following slab rollback and tearing is able to produce tectonically significant (i.e., up to ∼100 MPa; Bürgmann and Dresen, 2008) shear stresses at the base of the lithosphere and crust. Thus, surface strain across subduction zones is likely to be jointly driven by slab rollback and mantle flow, especially across hot and thinned environments, characterised by the absence of a rigid mantle lithosphere such as the back-arc domains. It was demonstrated that the horizontal traction generated at the base of deep continental roots from regional thermal anomalies within the mantle dragged the continents together along the Tethyan axis and was able to protract convergence even after continental collision and brake-off of the

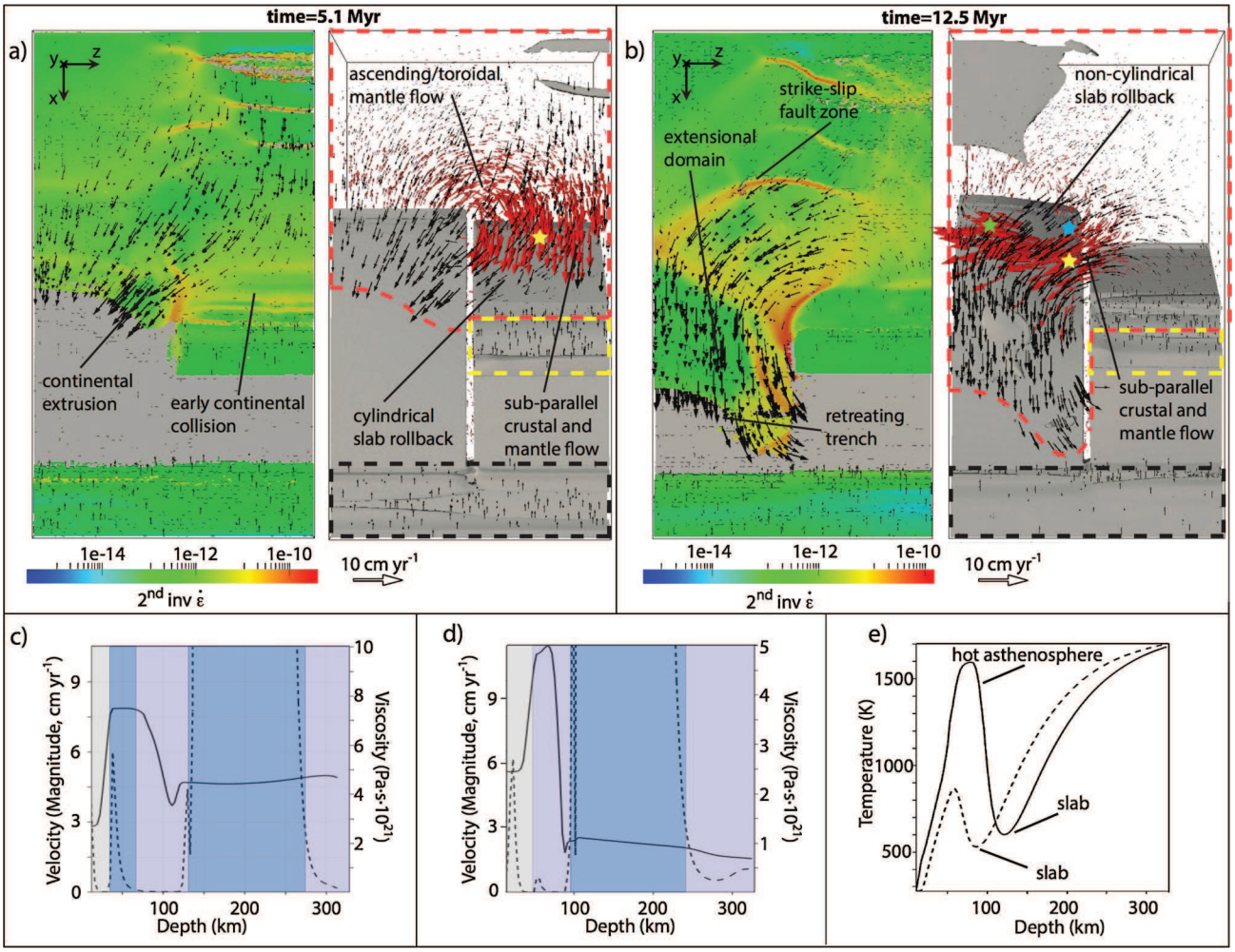

Fig. 4. a–b) Plan view of selected temporal frames. Black and red arrows represent the velocity vectors in the continental crust and asthenosphere, respectively. Colours on the left panel show the second invariant of the rate-of-strain tensor. The subducting plates are shown on the right panel through an iso-viscosity contour equal to 10^{22} Pa s. Red, yellow and black dashed lines on the right panels show the plan view of C1, C2 and C3, respectively. c–d) Depth–velocity–viscosity profiles (y-parallel). The profile location is shown by the yellow stars in (a) and (b). Solid lines, representing the magnitude of the velocity vector, follow the left-axis. Dashed lines, representing the viscosity, follow the right-axis. Shaded background colours show the phase at each depth: grey – continental crust, blue – lithospheric mantle/slab, and purple – asthenospheric mantle. e) Temperature–depth profiles at 12.5 Ma (the green and blue stars in (b) show the locations of the dashed and solid profile, respectively).

Tethyan slabs (Alvarez, 2010). The sub-horizontal mantle flow then seems to be able to actively drive the surface strain and kinematics across both thin and thick continental lithospheres. As such, the sub-horizontal couplings between the Earth's mantle and surface should benefit from the same attention that is paid to the vertical couplings and associated "dynamic topography" (e.g., Braun, 2010).

Our numerical experiments show that the surface strain at the transition between a continental indenter and an oceanic subduction can be dominated by the suction exerted by slab rollback (enhanced by slab tearing) and the associated mantle flow, as demonstrated by faster crustal flow close to the subduction trench than to the collisional domain (Fig. 4b). Although the continental indenter is necessary for setting a block-like deformation and surface rotation, its role is that of a passive bulwark if the overall convergence rates are slower than slab rollback. Thus, the effectiveness of extrusion tectonics, crustal shortening and gravitational collapse at the margins of a collisional belt should be assessed in the light of the dynamics of the neighbouring oceanic subduction (Fig. 7), since the "free boundary" is the most important factor controlling these mechanisms.

We cannot resolve the timing of slab tearing across the Aegean–Anatolian or the eastern Indian–Eurasian margins nor can we address its relationships to slab rollback or continental collision through our modelling. However, trench migration rates are inversely correlated to the width of the subducting plate (Schellart et al., 2007), which implies that the observed tears decoupling the actively subducting slabs from the mantle lithosphere below the collisional domains might have facilitated slab rollback and modulated trench retreat after continental collision, consistently with our numerical experiments. A common feature in the Mediterranean metamorphic core complexes exhumed in back-arc domains from the lower and middle crust is a highly asymmetric deformation with constant sense of shear – i.e., hangingwall motion relative to footwall (Jolivet et al., 2008, 2009). Our modelling results suggest that this asymmetric deformation is substantially controlled by the basal shear stresses imposed to the crust by the asthenospheric return flow.

The modelled surface velocity field shown in Fig. 4b is also similar (regardless of the sense of spin) to the observed surface rotation across the Aegean–Anatolian and the eastern Indian–Eurasian margins (Fig. 1). The majority of the observed surface rotation across the natural examples is accommodated by several fault zones amongst which the NAF, the Kun-Lun, Xianshuihe-Xiaojiang and the Altyn Tagh faults (e.g., Sengör, 1979; Tapponnier et al., 1982), whose kinematics is reasonably well reproduced in our numerical experiments by highly localised strike-slip deformation

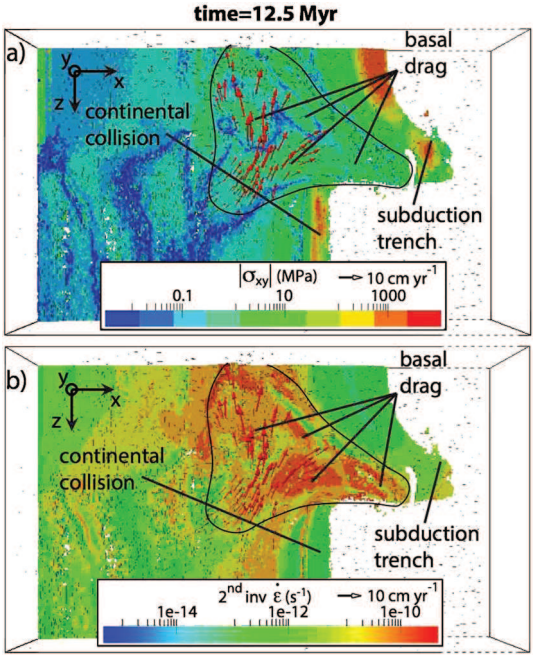

Fig. 5. Shear stress (a) and strain rate (b) distribution at the base of the upper plate continental crust (C1) at 12.5 Myr modelled time on the reference simulation. Red arrows show the velocity field within the asthenosphere. The area inside the black line is where the asthenosphere is at direct contact with the base of the continental crust.

(Figs. 3 and 4b). A faster crustal flow close to the subduction trench than to the collisional domain in our reference model is consistent with GPS measurements across the Aegean–Anatolian region, and suggests that the Aegean extension and extrusion of Anatolia are principally driven by the subduction dynamics and associated mantle flow, instead of collision-related mechanisms (Fig. 7). The arrival of the Australian plate to the Sumatra trench in middle-late Miocene times (Ricou, 1994) might have reduced the suction exerted by oceanic subduction. Nonetheless, the crust along portions of southeastern Tibet has been extending since at least ∼4 Myr (e.g., Royden, 1997; Wang et al., 2001). The many basins and low topographies across the Sichuan, Yunan, Indochina and Sunda provinces as well as the back-arc basins further testify widespread extension, implying that the Andaman–Sumatra and other western Pacific subduction zones substantially affected the surface strain across southeastern Asia during most of the Cenozoic (Jolivet et al., 1990). In addition, tomographic models highlight the presence of hot and shallow asthenospheric material across southeastern Tibet (e.g., Li et al., 2008a, 2008b), which is analogous to the asthenosphere flowing at direct contact with the base of the crust and rotating around the edge of the collisional domain in our numerical experiments. Since a free boundary seems necessary to allow for continental extrusion (e.g., Tapponnier and Molnar, 1976; Tapponnier et al., 1982; Jolivet et al., 1990; Fournier et al., 2004) and this free boundary is provided by oceanic subduction which we proved able to actively drive the surface strain more efficiently than the continental indentation, our experiment confirm that the rollback of the Andaman–Sumatra and the associated mantle return flow actively determined the surface strain east and southeast of the EHS (Fig. 7).

Instantaneous global flow models calculated from mantle density anomalies, suggest that both the pull from the Tethyan slabs and mantle upwelling from underneath the Ethiopia–Afar and Reunion–Carlsberg regions are necessary to reproduce the crustal motion across the Tethyan collisional belts (Becker and Faccenna, 2011; Faccenna et al., 2013a, 2013b; Faccenna and Becker, 2010). Our results suggest that the dynamical mantle flow associated solely with slab rollback and tearing can produce a distinct block-like surface rotation, without the intervention of an external dragging force such as the upwelling from the lower mantle. In our models, however, slab tearing is triggered along the pre-existing weak oceanic fracture zones and modelled slabs are not tied to previously subducted plates as the Tethyan slabs probably were during most of the Cenozoic (Ricou, 1994). Mantle upwellings, thus, have a major role in setting crustal motion at the scale of the whole Tethyan margins by dragging the northern and southern

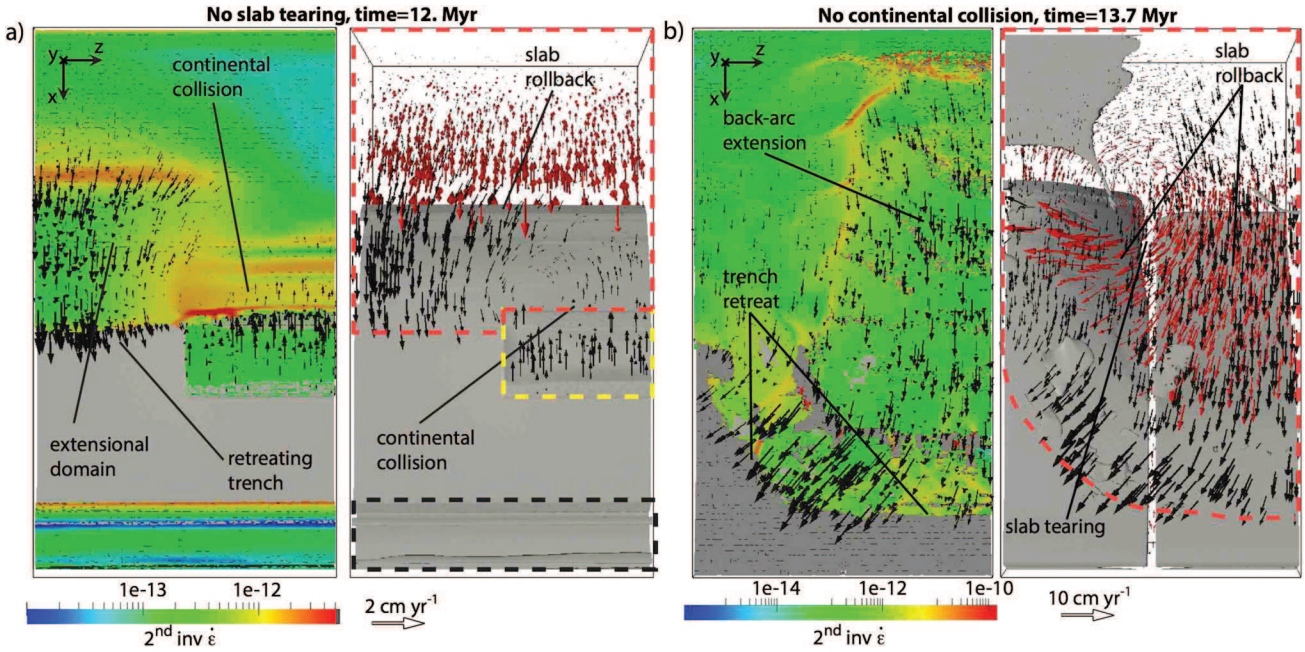

Fig. 6. a) Plan view of a selected temporal frame of a simulation without slab tearing. b) Plan view of a selected temporal frame of a simulation without continental collision. Black and red arrows represent the velocity vectors in the continental crust and asthenosphere, respectively. Colours on the left panels show the second invariant of the rate-of-strain tensor. The subducting plates are shown on the right panel through an iso-viscosity contour equal to 10^{22} Pa s. Red, yellow and black dashed lines on the right panels show the plan view of C1, C2 and C3, respectively.

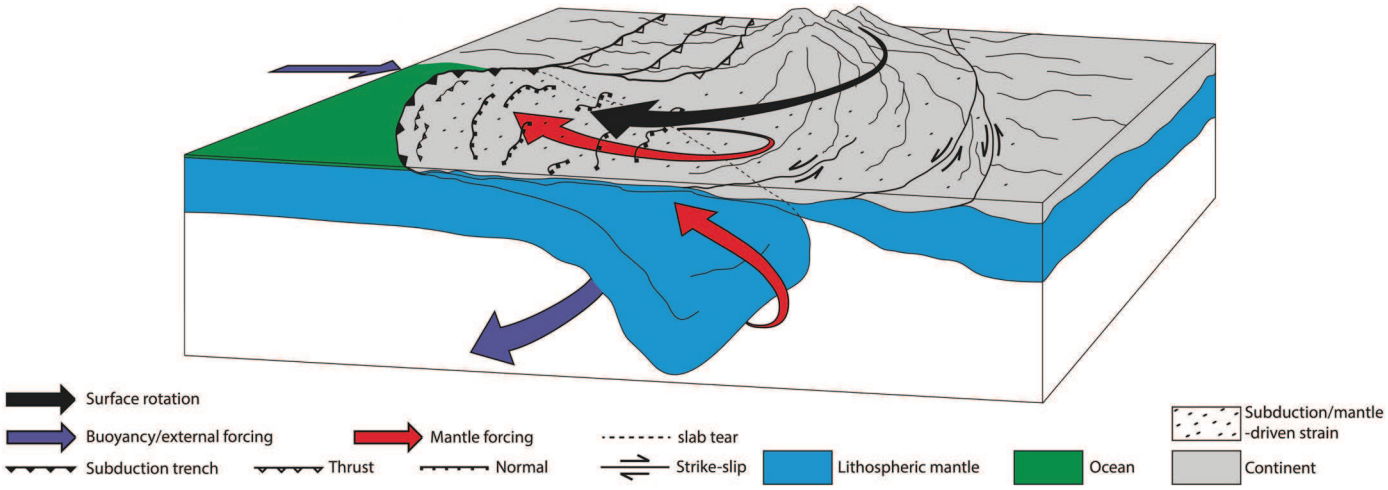

Fig. 7. Illustrative representation of the dynamical interactions between continental collision, oceanic subduction, mantle flow and surface deformation.

continents together along the Tethyan axis (Alvarez, 2010), warming and propelling the upper continental plates (Becker and Faccenna, 2011; Faccenna et al., 2013a, 2013b; Faccenna and Becker, 2010) and, possibly, by thermally enhancing slab tearing, but the rollback of the Tethyan slabs and the associated mantle return flow are likely to be the primary drivers of the surface deformation at the edge of the Tethyan collisional belts.

5. Conclusions

3D Cartesian thermo-mechanical models of self-consistent oceanic subduction, slab tearing and continental collision calibrated on geologic, geophysical and geodetic observations and accounting for realistic crustal and mantle rheologies enabled us to conclude that:

- The dynamical asthenospheric flow originated by slab rollback and tearing is a primary factor controlling the surface evolution at the transition between collisional and subduction domains. In particular, the toroidal motion of the asthenosphere at the edge of a retreating tearing slab is able to modulate the thermal state of the lithosphere, in turn affecting the geometry and dynamics of later subduction events and associated mantle and surface strain. In addition, the sub-horizontal mantle return flow following slab rollback and tearing is able to produce tectonically significant shear stresses at the base of the lithosphere and crust. The surface strain across subduction zones is thus likely to be jointly driven by slab rollback and mantle flow, especially across hot and thinned environments such as the back-arc domains.
- The surface strain at the transition between a continental indenter and an oceanic subduction can be dominated by the suction exerted by slab rollback (enhanced by slab tearing) and the associated mantle flow. The continental indenter acts as a passive bulwark if the overall convergence rates are slower than slab rollback. Thus, the effectiveness of extrusion tectonics, crustal shortening and gravitational collapse at the margins of a collisional belt should be assessed in the light of the dynamics of the neighbouring oceanic subduction.
- A faster crustal flow close to the Hellenic subduction trench than to the collisional domain (consistently reproduced by our numerical models) suggests that the suction exerted by the Hellenic subduction and associated mantle flow is the principal driver of the Aegean extension and extrusion of Anatolia, instead of currently proposed collision-related mechanisms. Our experiment also confirm that the rollback of the Andaman–Sumatra and the associated mantle return flow affected the surface strain east and southeast of the EHS as also suggested by the several basins and low topographies across the Sichuan, Yunan, Indochina and Sunda provinces, which testify widespread extension.
- Mantle upwelling drag and propel the northern and southern continents along the Tethyan axis and possibly thermally enhance slab tearing. The rollback of the Tethyan slabs and the associated mantle return flow, however, are likely to be primary drivers of the surface deformation at the edge of the Tethyan collisional belts.

Acknowledgements

This work has been financially supported by the Laboratoire d'Excellence (LABEX) VOLTAIRE (Convention n° ANR-10-LABX-100-01) of the University of Orléans and the European Research Council (ERC) under the 7th Framework Programme of the European Union (ERC Advanced Grant, grant agreement No. 290864, RHEOLITH). Numerical simulations were performed on the ETH-Zürich cluster BRUTUS. We are thankful to Claudio Faccenna and Thorsten Becker for stimulating discussions and to Kosuke Ueda for constructive comments on an early version of the manuscript and tips for the modelling. The paper benefited from insightful revision by Leigh Royden and two anonymous reviewers.

Appendix A. Supplementary material

Supplementary material related to this article can be found online at http://dx.doi.org/10.1016/j.epsl.2014.08.023.

References

Allen, M., Jackson, J., Walker, R., 2004. Late Cenozoic reorganization of the Arabia–Eurasia collision and the comparison of short-term and long-term deformation rates. Tectonics 23. http://dx.doi.org/10.1029/2003TC001530.

Alvarez, W., 2010. Protracted continental collisions argue for continental plates driven by basal traction. Earth Planet. Sci. Lett. 296, 434–442.

Armijo, R., Meyer, B., Hubert, A., Barka, A., 1999. Westward propagation of the north Anatolian into the northern Aegean: timing and kinematics. Geology 27 (3), 267–270.

ArRajehi, A., McClusky, S., Reilinger, R., Daoud, M., Alchalbi, A., Ergintav, S., Gomez, F., Sholan, J., Bou-Rabee, F., Ogubazghi, G., Haileab, B., Fisseha, S., Asfaw, L., Mahmoud, S., Rayan, A., Bendik, R., Kogan, L., 2010. Geodetic constraints on present

day motion of the Arabian Plate: implications for Red Sea and Gulf of Aden rifting. Tectonics 29, TC3011. http://dx.doi.org/10.1029/2009TC002482.
Becker, T., Faccenna, C., 2011. Mantle conveyor beneath the Tethyan collisional belt. Earth Planet. Sci. Lett. 310, 453–461.
Braun, J., 2010. The many surface expressions of mantle dynamics. Nat. Geosci. 3, 825–833.
Bürgmann, R., Dresen, G., 2008. Rheology of the lower crust and upper mantle: evidence from rock mechanics, geodesy, and field observations. Annu. Rev. Earth Planet. Sci. 36, 531–567.
Capitanio, F., Replumaz, A., 2013. Subduction and slab breakoff controls on Asian indentation tectonics and Himalayan western syntaxis formation. Geochem. Geophys. Geosyst. 14 (9), 3515–3531.
De Boorder, H., Spakman, W., White, S.H., Wortel, M.J., 1998. Late Cenozoic mineralization, orogenic collapse and slab detachment in the European Alpine Belt. Earth Planet. Sci. Lett. 164 (3), 569–575.
Dewey, J.F., 1988. Lithospheric stress, deformation, and tectonic cycles: the disruption of Pangaea and the closure of Tethys. Geol. Soc. (Lond.) Spec. Publ. 37 (1), 23–40.
Duretz, T., Gerya, T., Spakman, W., 2014. Slab detachment in laterally varying subduction zones: 3D numerical modeling. Geophys. Res. Lett. http://dx.doi.org/10.1002/2014GL059472.
Faccenna, C., Becker, T., 2010. Shaping mobile belts by small-scale convection. Nature 465, 602–605.
Faccenna, C., Becker, T.W., Conrad, C.P., Husson, L., 2013a. Mountain building and mantle dynamics. Tectonics 32, 80–93.
Faccenna, C., Becker, T., Jolivet, L., Keskin, M., 2013b. Mantle convection in the Middle East: reconciling Afar upwelling, Arabia indentation and Aegean trench rollback. Earth Planet. Sci. Lett. 375, 254–269.
Faccenna, C., Bellier, O., Martinod, J., Piromallo, C., Regard, V., 2006. Slab detachment beneath eastern Anatolia: a possible cause for the formation of the North Anatolian fault. Earth Planet. Sci. Lett. 242, 85–97.
Fournier, M., Jolivet, L., Davy, P., Thomas, J., 2004. Backarc extension and collision: an experimental approach to the tectonics of Asia. Geophys. J. Int. 157 (2), 871–889.
Gan, W., Zhang, P., Shen, Z., Niu, Z., Wang, M., Wan, Y., Zhou, D., Cheng, J., 2007. Present day crustal motion within the Tibetan Plateau inferred from GPS measurements. J. Geophys. Res. 113.
Gerya, T., 2010. Introduction to Numerical Geodynamic Modelling. Cambridge University Press.
Gerya, T., Yuen, D., 2007. Robust characteristics method for modelling multiphase visco-elasto-plastic thermo-mechanical problems. Phys. Earth Planet. Inter. 163, 83–105.
Govers, R., Wortel, M.J., 2005. Lithosphere tearing at STEP faults: response to edges of subduction zones. Earth Planet. Sci. Lett. 236, 505–523.
Holt, W.E., 2000. Correlated crust and mantle strain fields in Tibet. Geology 28 (1), 67–70.
Jolivet, L., Augier, R., Faccenna, C., Negro, F., Rimmele, G., Agard, P., Robin, C., Rossetti, F., Crespo-Blanc, A., 2008. Subduction, convergence and the mode of backarc extension in the Mediterranean region. Bull. Soc. Géol. Fr. 179 (6), 525–550.
Jolivet, L., Davy, P., Cobbold, P., 1990. Right-lateral shear along the Northwest Pacific Margin and the India–Eurasia Collision. Tectonics 9 (6), 1409–1419.
Jolivet, L., Faccenna, C., 2000. Mediterranean extension and the Africa–Eurasia collision. Tectonics 19.
Jolivet, L., Faccenna, C., Piromallo, C., 2009. From mantle to crust: stretching the Mediterranean. Earth Planet. Sci. Lett. 285, 198–209.
Jolivet, L., Tamaki, K., Fournier, M., 1994. Japan Sea, opening history and mechanism, a synthesis. J. Geophys. Res. 99, 22237–22259.
Jolivet, L., Faccenna, C., Huet, B., Labrousse, L., Le Pourhiet, L., Lacombe, O., Lecompte, E., Burov, E., Denèle, Y., Brun, J.-P., et al., 2013. Aegean tectonics: strain localization, slab tearing and trench retreat. Tectonophysics 597–598, 1–33.
Le Pichon, X., Fournier, M., Jolivet, L., 1992. Kinematics, topography, shortening and extrusion in the India–Eurasia collision. Tectonics 11 (6), 1085–1098.
Li, C., van der Hilst, R., Engdahl, E.R., Burdick, S., 2008a. A new global model for P wave speed variations in Earth's mantle. Geochem. Geophys. Geosyst. 9 (5).
Li, C., van der Hilst, R., Meltzer, A.S., Engdahl, E.R., 2008b. Subduction of the Indian lithosphere beneath the Tibetan Plateau and Burma. Earth Planet. Sci. Lett. 274, 157–168.
Li, Z., Xu, Z., Gerya, T., Burg, J.P., 2013. Collision of continental corner from 3-D numerical modeling. Earth Planet. Sci. Lett. 380, 98–111.
McKenzie, D.P., 1972. Active tectonics of the Mediterranean region. Geophys. J. R. Astron. Soc. 30, 109–185.
Molnar, P., Tapponnier, P., 1975. Cenozoic tectonics of Asia: effects of a continental collision. Science 189 (4201), 419–426.
Nikolaeva, K., Gerya, T., Marques, F.O., 2010. Subduction initiation at passive margins: numerical modeling. J. Geophys. Res. 115. http://dx.doi.org/10.1029/2009JB006549.
Pérouse, E., Chamont-Rooke, N., Rabaute, A., Briole, P., Jouanne, F., Georgiev, I., Dimitrov, D., 2012. Bridging onshore and offshore present-day kinematics of central and eastern Mediterranean: implications for crustal dynamics and mantle flow. Geochem. Geophys. Geosyst. 13 (9). http://dx.doi.org/10.1029/2012GC004289.
Ranalli, G., 1995. Rheology of the Earth, Deformation and Flow Processes in Geophysics and Geodynamics. Chapman & Hall.
Reilinger, R., McClusky, S., Paradissis, D., Ergintav, S., Vernant, P., 2010. Geodetic constraints on the tectonic evolution of the Aegean region and strain accumulation along the Hellenic subduction zone. Tectonophysics 488, 22–30.
Replumaz, A., Guillot, S., Villaseñor, A., Negredo, M., 2013. Amount of Asian lithospheric mantle subducted during the India/Asia collision. Gondwana Res. 24, 936–945.
Ricou, L.E., 1994. Tethys reconstructed: plates, continental fragments and their boundaries since 260 Ma from Central America to South-Eastern Asia. Geodin. Acta 7 (4), 169–218.
Royden, L.H., 1993. The tectonic expression slab pull at continental convergent boundaries. Tectonics 12 (2), 303–325.
Royden, L., 1997. Surface deformation and lower crustal flow in Eastern Tibet. Science 276.
Royden, L.H., Burchfiel, B.C., van der Hilst, R.D., 2008. The geological evolution of the Tibetan Plateau. Science 321, 1054–1058.
Schellart, W.P., Freeman, J., Stegman, D.R., Moresi, L., May, D., 2007. Evolution and diversity of subduction zones controlled by slab width. Nature 446, 308–311.
Sengör, A.M., 1979. The North Anatolian transform fault: its age, offset and tectonic significance. J. Geol. Soc. (Lond.) 136, 269–282.
Tapponnier, P., Molnar, P., 1976. Slip-line field theory and large scale continental tectonics. Nature 264, 319–324.
Tapponnier, P., Peltzer, G., Le Dain, A.Y., Armijo, R., Cobbold, P., 1982. Propagating extrusion tectonics in Asia: new insights from simple experiments with plasticine. Geology 10, 611–616.
Tapponnier, P., Peltzer, G., Armijo, R., 1986. On the mechanics of the collision between India and Asia. In: Coward, M.P., Ries, A.C. (Eds.), Collision Tectonics, pp. 115–157.
Tapponnier, P., Zhiqin, X., Roger, B., Meyer, B., Arnaud, N., Wittlinger, G., Jingsui, Y., 2001. Oblique stepwise rise and growth of the Tibet plateau. Science 294 (5547), 1671–1677.
Taylor, B., Hayes, D.E., 1983. Origin and history of the South China Sea basin. In: Hayes, D.E. (Ed.), The Tectonic and Geologic Evolution of Southeast Asian Seas and Islands, Part 2. AGU, Washington, D.C., pp. 23–56.
Thomas, W.A., 2006. Tectonic inheritance at a continental margin. GSA Today 16 (2).
Turcotte, D.L., Schubert, G., 2002. Geodynamics. Cambridge University Press, Cambridge.
van Hunen, J., Allen, M.B., 2011. Continental collision and slab break-off: a comparison of 3-D numerical models with observations. Earth Planet. Sci. Lett. 203 (1–2), 27–37.
Wang, Q., Zhang, P., Freymueller, J.T., Bilham, R., Larson, K.M., Lai, X., You, X., Niu, Z., Wu, J., Li, Y., Liu, J., Yang, Z., Chen, Q., 2001. Present-day crustal deformation in China constrained by global positioning system measurements. Science 194.
Zhang, Z.K., Wang, M., Gan, W., Bürgmann, R., Wang, Q., Niu, Z., Sun, J., Wu, J., Hanrong, S., Xinzhao, Y., 2004. Continuous deformation of the Tibetan Plateau from global positioning system data. Geology 32, 809–812.
Zhu, G., Gerya, T.V., Yuen, D.A., Honda, S., Yoshida, T., Connolly, J.A., 2009. 3-D dynamics of hydrous thermal–chemical plumes in oceanic subduction zones. Geochem. Geophys. Geosyst. 10, Q11006.

Annexe C

Reconstructions cinématiques : table des rotations et fichier multimédia

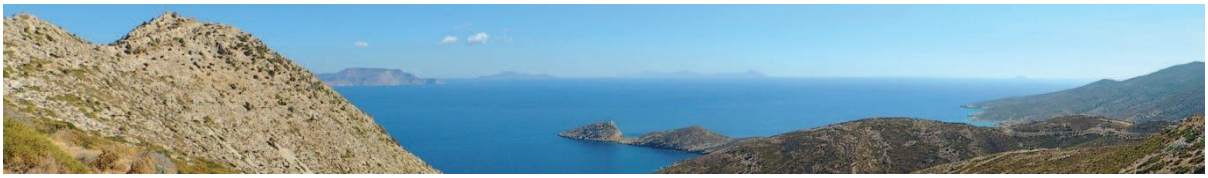

Table C.1: table resuming the succession of total reconstruction poles calculated for each domain. The domain ID, the age of the finite rotation, the latitude and the longitude of the rotation pole, the rotation angle (positive and negative angles depicting respectively clockwise and counterclockwise rotations) and the fixed domain ID are defined for each total reconstruction pole.

Domain ID	Age (Ma)	Latitude (°dec)	Longitude (°dec)	Rotation angle (°)	Reference domaine ID	Description
20029	0	0.0	0.0	0.0	14523	Apuseni mountains relative to Moesian platform
20029	15	0.0	0.0	0.0	14523	
20029	23	43.73	23.34	60.00	14523	
20029	30	43.73	23.34	60.00	14523	
20029	52	43.47	23.89	60.00	14523	
20029	120	43.47	23.89	60.00	14523	
20044	0	0.0	0.0	0.0	14523	Timok region relative to Moesian platform
20044	15	0.0	0.0	0.0	14523	
20044	23	43.94	22.82	60.00	14523	
20044	30	43.94	22.82	60.00	14523	
20044	52	43.67	23.38	60.00	14523	
20044	120	43.67	23.38	60.00	14523	
20041	0	0.0	0.0	0.0	14523	Balkan fold-and-thrust belt relative to Moesian platform
20041	30	0.0	0.0	0.0	14523	
20041	52	02.04	-66.29	-00.50	14523	
20041	68	43.09	19.53	-08.00	14523	
20041	114	43.09	19.53	-08.00	14523	
20030	0	0.0	0.0	0.0	14523	Northern Vardar suture zone relative to Moesian platform
20030	15	0.0	0.0	0.0	14523	
20030	23	43.37	23.23	30.00	14523	
20030	30	43.37	23.23	30.00	14523	
20030	52	43.10	24.43	30.00	14523	
20030	120	43.10	24.43	30.00	14523	
20034	0	0.0	0.0	0.0	14523	Thrace basin relative to Moesian platform
20034	25	0.0	0.0	0.0	14523	
20034	45	41.32	28.6	-2.0	14523	
20034	120	41.32	28.6	-2.0	14523	
20066	0	0.0	0.0	0.0	14523	Central Rhodope massif relative to Moesian platform
20066	35	0.0	0.0	0.0	14523	
20066	55	42.27	22.82	11.00	14523	
20066	120	42.27	22.82	11.00	14523	

Bloc ID	Age (Ma)	Latitude (°dec)	Longitude (°dec)	Rotation angle (°)	Reference bloc ID	Description
20028	0	0.0	0.0	0.0	14523	Chalkidiki peninsula/Kerdilyon detachment relative to Moesian platform
20028	5	00.00	00.00	00.00	14523	
20028	8	42.27	22.82	03.00	14523	
20028	15	42.27	22.82	21.00	14523	
20028	40	42.27	22.82	30.00	14523	
20028	120	42.27	22.82	30.00	14523	
20071	0	0.0	0.0	0.0	14523	Thasos island relative to Moesian platform
20071	5	0.0	0.0	0.0	14523	
20071	15	40.16	25.54	-36.00	14523	
20071	50	40.28	25.84	-50.00	14523	
20077	0	0.0	0.0	0.0	14523	Northern Pelagonian margin relative to Moesian platform
20077	60	0.0	0.0	0.0	14523	
20077	67	38.57	13.73	-00.40	14523	
20077	83	41.66	01.88	-08.90	14523	
20077	95	43.75	02.04	-16.90	14523	
20077	125	47.37	-00.46	-26.80	14523	
20076	0	0.0	0.0	0.0	14523	Southern Pelagonian margin relative to Moesian platform
20076	50	0.0	0.0	0.0	14523	
20076	67	38.57	13.73	-03.50	14523	
20076	83	40.80	05.04	-12.00	14523	
20076	95	42.83	03.81	-20.00	14523	
20076	125	46.29	00.09	-39.80	14523	
20075	0	0.0	0.0	0.0	14523	Northern Gavrovo-Tripolitza margin relative to Moesian platform
20075	35	0.0	0.0	0.0	14523	
20075	42	27.74	76.70	01.50	14523	
20075	47	40.88	33.87	08.40	14523	
20075	67	29.95	-17.97	-05.00	14523	
20075	83	38.11	-08.45	-13.30	14523	
20075	95	41.57	-05.08	-21.20	14523	
20075	125	45.57	-05.60	-31.00	14523	
20021	0	0.0	0.0	0.0	14523	Eastern Hellenides relative to Moesian platform
20021	5	40.35	22.27	10.00	14523	
20021	8	40.82	21.92	10.00	14523	
20021	15	40.62	22.48	50.00	14523	
20021	35	41.00	22.09	50.00	14523	
20021	55	41.19	22.01	53.00	14523	
20021	60	41.19	22.01	53.00	14523	

Bloc ID	Age (Ma)	Latitude (°dec)	Longitude (°dec)	Rotation angle (°)	Reference bloc ID	Description
20017	0	0.0	0.0	0.0	14523	Northwestern Evvia relative to Moesian platform
20017	5	39.72	22.72	23.00	14523	
20017	8	39.81	22.51	23.00	14523	
20017	15	41.82	20.21	23.00	14523	
20017	35	42.46	19.06	23.00	14523	
20017	55	42.56	19.09	26.00	14523	
20017	67	42.56	19.09	26.00	14523	
20031	0	0.0	0.0	0.0	14523	Attica relative to Moesian platform
20031	5	39.75	22.63	23.00	14523	
20031	8	39.73	22.33	23.00	14523	
20031	15	41.86	20.07	23.00	14523	
20031	35	42.43	18.86	23.00	14523	
20031	55	42.48	18.93	26.00	14523	
20031	60	42.48	18.93	26.00	14523	
20018	0	0.0	0.0	0.0	14523	Northern Corinth rift relative to Moesian platform
20018	5	39.73	22.29	23.00	14523	
20026	0	0.0	0.0	0.0	14523	Northwestern Peloponnese relative to Moesian platform
20026	5	40.32	21.79	23.00	14523	
20026	8	40.48	21.38	23.00	14523	
20026	15	40.42	21.48	50.00	14523	
20026	25	40.59	21.03	50.00	14523	
20026	35	40.88	20.71	50.00	14523	
20026	45	41.01	20.69	53.00	14523	
20026	49	41.01	20.69	53.00	14523	
20027	0	0.0	0.0	0.0	14523	Eastern Peloponnese relative to Moesian platform
20027	5	39.94	21.92	23.00	14523	
20027	8	39.96	21.64	23.00	14523	
20027	15	40.13	22.12	50.00	14523	
20027	35	40.50	21.67	50.00	14523	
20027	45	40.69	21.64	53.00	14523	
20027	50	40.69	21.64	53.00	14523	
20027	100	40.69	21.64	53.00	14523	
20035	0	0.0	0.0	0.0	14523	Central Peloponnese/Tripoli relative to Moesian platform
20035	5	39.99	21.63	23.00	14523	
20035	8	40.11	21.21	23.00	14523	
20035	15	40.16	21.43	50.00	14523	
20035	25	40.32	20.93	50.00	14523	
20036	0	0.0	0.0	0.0	14523	Central Peloponnese/Sparta relative to Moesian platform
20036	5	40.14	21.46	23.00	14523	
20036	8	40.25	21.00	23.00	14523	
20036	15	40.25	21.31	50.00	14523	
20036	25	40.42	20.82	50.00	14523	

Bloc ID	Age (Ma)	Latitude (°dec)	Longitude (°dec)	Rotation angle (°)	Reference bloc ID	Description
20037	0	0.0	0.0	0.0	14523	Southwestern Peloponnese relative to Moesian platform
20037	5	40.27	21.33	23.00	14523	
20037	8	40.40	20.81	23.00	14523	
20037	15	40.32	21.20	50.00	14523	
20037	25	40.48	20.72	50.00	14523	
20037	35	40.78	20.42	50.00	14523	
20037	45	40.91	20.42	53.00	14523	
20037	49	40.91	20.42	53.00	14523	
20019	0	0.0	0.0	0.0	14523	Northwestern Cyclades relative to Moesian platform
20019	5	-30.04	88.39	-00.70	14523	
20019	8	48.27	-05.59	02.00	14523	
20019	15	41.09	18.08	20.00	14523	
20019	35	41.16	15.80	20.00	14523	
20019	50	39.67	22.30	60.00	14523	
20024	0	0.0	0.0	0.0	14523	Ikaria island relative to Moesian platform
20024	5	26.21	-87.27	00.80	14523	
20024	8	36.51	-56.47	01.10	14523	
20024	15	34.24	39.37	-10.00	14523	
20024	30	34.14	42.31	-10.00	14523	
20022	0	0.0	0.0	0.0	14523	Samos island relative to Moesian platform
20022	5	26.21	-87.27	00.80	14523	
20022	8	20.93	-81.60	01.00	14523	
20022	15	36.96	32.69	-20.00	14523	
20022	30	37.11	34.50	-20.00	14523	
20032	0	0.0	0.0	0.0	14523	Southwestern Cyclades relative to Moesian platform
20032	5	-35.09	81.91	-00.90	14523	
20032	8	51.72	-14.17	02.00	14523	
20032	15	43.80	09.43	10.00	14523	
20032	35	43.22	04.33	10.00	14523	
20032	50	41.23	13.59	20.00	14523	
20025	0	0.0	0.0	0.0	14523	Central Cyclades relative to Moesian platform
20025	5	29.31	-89.51	00.80	14523	
20025	8	26.50	-86.66	01.00	14523	
20025	15	36.23	30.91	-30.00	14523	
20025	35	36.28	32.43	-30.00	14523	
20025	45	36.49	33.59	-30.00	14523	
20025	100	36.49	33.59	-30.00	14523	
20023	0	0.0	0.0	0.0	14523	Dodecanese/Kos relative to Moesian platform
20023	5	15.69	-75.30	00.80	14523	
20023	8	07.09	90.57	-01.10	14523	
20023	15	36.94	34.17	-20.00	14523	
20023	30	37.14	36.30	-20.00	14523	

Bloc ID	Age (Ma)	Latitude (°dec)	Longitude (°dec)	Rotation angle (°)	Reference bloc ID	Description
20010	0	0.0	0.0	0.0	14523	Crete relative to Moesian platform
20010	5	-33.63	86.38	-01.50	14523	
20010	8	-29.62	90.70	-01.80	14523	
20010	15	-23.22	96.66	-03.50	14523	
20010	25	-21.44	98.22	-03.80	14523	
20010	100	-21.44	98.22	-03.80	14523	
20033	0	0.0	0.0	0.0	14523	Northern Pontides relative to Moesian platform
20033	65	0.0	0.0	0.0	14523	
20033	114	02.11	-57.83	01.10	14523	
20008	0	0.0	0.0	0.0	14523	Southern Pontides relative to Moesian platform
20008	5	32.02	31.96	-05.00	14523	
20008	12	32.02	31.96	-06.00	14523	
20008	120	32.02	31.96	-06.00	14523	
20046	0	0.0	0.0	0.0	14523	Southern Pontide margin relative to Moesian platform
20046	5	32.02	31.96	-05.00	14523	
20046	12	32.02	31.96	-06.00	14523	
20046	65	32.02	31.96	-06.00	14523	
20046	114	31.32	47.78	-06.00	14523	
20045	0	0.0	0.0	0.0	14523	Southern Kazdağ massif relative to Moesian platform
20045	5	32.02	31.96	-5.00	14523	
20045	12	32.02	31.96	-6.00	14523	
20045	15	32.02	31.96	-6.00	14523	
20045	25	32.58	33.55	-6.00	14523	
20045	31	32.58	33.55	-6.00	14523	
20016	0	0.0	0.0	0.0	14523	Lesbos/Balikesir relative to Moesian platform
20016	5	31.86	33.85	-05.00	14523	
20016	12	31.88	33.53	-06.00	14523	
20016	15	31.88	33.53	-06.00	14523	
20016	25	32.32	35.10	-06.00	14523	
20016	120	32.32	35.10	-06.00	14523	
20020	0	0.0	0.0	0.0	14523	Chios/Izmir relative to Moesian platform
20020	5	31.80	35.16	-05.00	14523	
20020	12	31.82	34.63	-06.00	14523	
20020	15	31.82	34.63	-06.00	14523	
20020	25	32.43	36.13	-06.00	14523	
20020	120	32.43	36.13	-06.00	14523	

Bloc ID	Age (Ma)	Latitude (°dec)	Longitude (°dec)	Rotation angle (°)	Reference bloc ID	Description
20042	0	0.0	0.0	0.0	14523	Northern Menderes/Simav detachment relative to Moesian platform
20042	5	31.80	35.16	-05.00	14523	
20042	8	31.82	34.91	-05.40	14523	
20042	12	31.82	35.54	-06.00	14523	
20042	15	31.81	36.25	-06.00	14523	
20042	25	32.22	40.25	-06.00	14523	
20042	30	32.56	40.87	-06.00	14523	
20042	42	32.53	34.26	-06.00	14523	
20042	47	29.81	33.81	-06.00	14523	
20042	50	29.85	32.69	-06.00	14523	
20042	67	-16.75	-26.45	-01.40	14523	
20042	83	33.75	-06.08	-09.20	14523	
20042	95	39.27	-02.71	-17.30	14523	
20042	125	41.62	-01.59	-25.30	14523	
20061	0	0.0	0.0	0.0	14523	Alaşehir detachment relative to Moesian platform
20061	5	31.66	35.81	-05.00	14523	
20061	8	31.68	35.50	-05.40	14523	
20061	12	31.69	36.03	-06.00	14523	
20061	15	31.68	36.75	-06.00	14523	
20062	0	0.0	0.0	0.0	14523	Büyük detachment relative to Moesian platform
20062	5	31.64	36.54	-05.00	14523	
20062	8	35.61	31.94	-14.40	14523	
20062	12	36.59	30.91	-27.00	14523	
20062	15	36.94	30.58	-36.00	14523	
20062	25	37.77	32.03	-36.00	14523	
20062	30	37.96	32.94	-36.00	14523	
20058	0	0.0	0.0	0.0	14523	Southern edge of the Gediz graben (Menderes) relative to Moesian platform
20058	5	31.66	35.81	-05.00	14523	
20059	0	0.0	0.0	0.0	14523	Southern edge of the Ödemiş graben (Menderes) relative to Moesian platform
20059	5	31.64	36.54	-05.00	14523	
20060	0	0.0	0.0	0.0	14523	Southern edge of the Büyük graben (Menderes) relative to Moesian platform
20060	5	31.56	37.12	-05.00	14523	
20043	0	0.0	0.0	0.0	14523	Southern Menderes/Lycian basal thrust relative to Moesian platform
20043	5	31.56	37.12	-05.00	14523	
20043	8	34.69	34.04	-09.60	14523	
20043	12	35.99	33.07	-16.00	14523	
20043	15	36.57	32.71	-20.00	14523	
20043	25	37.68	35.56	-20.00	14523	
20043	30	37.79	37.23	-20.00	14523	

Bloc ID	Age (Ma)	Latitude (°dec)	Longitude (°dec)	Rotation angle (°)	Reference bloc ID	Description
20009	0	0.0	0.0	0.0	14523	Southwestern Taurides relative to Moesian platform
20009	5	31.56	37.12	-05.00	14523	
20009	8	34.69	34.04	-09.60	14523	
20009	12	35.99	33.07	-16.00	14523	
20009	15	36.57	32.71	-20.00	14523	
20009	25	36.87	33.95	-20.00	14523	
20009	30	37.01	34.13	-20.00	14523	
20009	42	37.71	33.04	-20.00	14523	
20009	47	38.25	33.45	-20.00	14523	
20009	50	38.47	33.31	-20.00	14523	
20009	55	38.60	32.30	-20.00	14523	
20038	0	0.0	0.0	0.0	14523	Lycian front relative to Moesian platform
20038	5	31.56	37.12	-05.00	14523	
20038	8	35.48	34.91	-09.60	14523	
20038	12	37.08	34.34	-16.00	14523	
20038	15	37.79	34.22	-20.00	14523	
20038	25	38.18	35.62	-20.00	14523	
20038	30	38.38	35.87	-20.00	14523	
20038	42	39.28	35.09	-20.00	14523	
20038	47	39.87	35.62	-20.00	14523	
20038	50	40.16	35.52	-20.00	14523	
20038	55	40.44	34.58	-20.00	14523	
20038	67	39.34	31.22	-37.00	14523	
20038	83	38.05	27.36	-73.00	14523	
20038	95	38.40	26.34	-81.00	14523	
20038	125	38.70	22.49	-91.00	14523	
20072	0	0.0	0.0	0.0	14523	Bey Dağları platform relative to Moesian platform
20072	5	31.56	37.12	-05.00	14523	
20072	8	34.69	34.04	-09.60	14523	
20072	12	35.99	33.07	-16.00	14523	
20072	15	36.57	32.71	-20.00	14523	
20072	23	36.81	33.70	-20.00	14523	
20072	29	37.67	25.89	-31.00	14523	
20072	42	36.47	21.91	-28.00	14523	
20072	47	34.70	20.72	-21.00	14523	
20072	55	35.27	19.30	-26.00	14523	
20072	67	35.26	17.22	-33.00	14523	
20072	83	35.63	12.89	-41.00	14523	
20072	95	35.32	13.20	-60.00	14523	

Bloc ID	Age (Ma)	Latitude (°dec)	Longitude (°dec)	Rotation angle (°)	Reference bloc ID	Description
20049	0	0.0	0.0	0.0	14523	Northern Central Anatolian Crystalline Complex relative to Moesian platform
20049	5	32.02	31.96	-05.00	14523	
20049	12	32.02	31.96	-06.00	14523	
20049	42	32.02	31.96	-06.00	14523	
20049	47	30.53	32.94	-07.00	14523	
20049	50	31.11	32.54	-08.00	14523	
20049	55	32.03	31.34	-09.00	14523	
20049	67	26.77	26.23	-05.00	14523	
20049	83	36.84	13.29	-13.00	14523	
20049	95	40.37	14.79	-20.00	14523	
20049	125	44.48	08.69	-30.00	14523	
20047	0	0.0	0.0	0.0	14523	Southwestern Central Anatolian Crystalline Complex relative to Moesian platform
20047	5	32.02	31.96	-05.00	14523	
20047	12	32.02	31.96	-06.00	14523	
20047	23	32.02	31.96	-06.00	14523	
20047	30	60.99	33.91	02.00	14523	
20047	40	42.41	34.88	14.00	14523	
20047	42	42.38	35.38	14.00	14523	
20047	47	43.56	35.99	14.00	14523	
20047	50	43.52	36.50	14.00	14523	
20047	55	43.68	37.80	13.00	14523	
20047	67	42.21	37.87	17.00	14523	
20047	83	32.50	60.39	10.00	14523	
20047	95	01.79	-85.63	-05.50	14523	
20047	125	46.92	-41.97	-12.00	14523	
20053	0	0.0	0.0	0.0	14523	Izmir-Ankara suture zone relative to Moesian platform
20053	5	32.02	31.96	-05.00	14523	
20053	12	32.02	31.96	-06.00	14523	
20053	30	32.02	31.96	-06.00	14523	
20053	42	31.70	25.90	-06.00	14523	
20053	47	28.89	25.90	-06.00	14523	
20053	50	28.77	24.83	-06.00	14523	
20053	55	25.07	18.13	-04.00	14523	
20054	0	0.0	0.0	0.0	14523	Western Inner-Tauride suture zone relative to Moesian platform
20054	5	32.02	31.96	-05.00	14523	
20054	12	32.02	31.96	-06.00	14523	
20054	23	32.02	31.96	-06.00	14523	
20054	30	60.99	33.91	02.00	14523	
20054	40	42.41	34.88	14.00	14523	
20054	42	42.38	35.38	14.00	14523	
20054	47	43.56	35.99	14.00	14523	
20054	50	43.52	36.50	14.00	14523	
20054	55	43.02	37.60	14.00	14523	

Bloc ID	Age (Ma)	Latitude (°dec)	Longitude (°dec)	Rotation angle (°)	Reference bloc ID	Description
20055	0	0.0	0.0	0.0	14523	Eastern Inner-Taurides suture zone relative to Moesian platform
20055	5	32.02	31.96	-05.00	14523	
20055	12	35.42	34.14	-13.00	14523	
20055	23	36.79	35.06	-25.00	14523	
20055	30	37.25	35.37	-35.00	14523	
20055	34	37.27	35.16	-40.00	14523	
20055	42	36.94	34.05	-40.00	14523	
20055	47	36.52	34.21	-40.00	14523	
20055	50	36.46	34.03	-40.00	14523	
20055	55	36.45	33.61	-40.00	14523	
20080	0	0.0	0.0	0.0	14523	Northern Tauride margin relative to Moesian platform
20080	50	0.0	0.0	0.0	14523	
20080	67	35.61	44.83	05.80	14523	
20080	83	28.67	-51.47	-05.10	14523	
20080	95	43.67	-21.80	-12.20	14523	
20080	125	49.23	-15.13	-22.00	14523	
20063	0	0.0	0.0	0.0	14523	Western Afyon unit relative to Moesian platform
20063	5	32.02	31.96	-05.00	14523	
20063	12	32.96	33.30	-07.40	14523	
20063	23	33.82	34.56	-09.60	14523	
20063	30	19.50	41.27	-03.00	14523	
20063	40	48.23	29.45	07.00	14523	
20063	42	48.98	29.85	06.60	14523	
20063	47	54.16	28.39	05.60	14523	
20063	50	56.09	28.71	05.00	14523	
20063	55	59.92	32.68	04.00	14523	
20065	0	0.0	0.0	0.0	14523	Eastern Afyon unit relative to Moesian platform
20065	5	32.02	31.96	-05.00	14523	
20065	12	35.59	34.66	-14.40	14523	
20065	23	36.82	35.66	-28.60	14523	
20065	30	37.23	35.95	-40.00	14523	
20065	34	37.28	35.77	-45.80	14523	
20065	40	37.06	35.17	-47.00	14523	
20065	42	37.01	34.98	-47.40	14523	
20065	47	36.68	35.22	-48.40	14523	
20065	50	36.63	35.08	-48.40	14523	
20065	67	36.24	33.75	-42.50	14523	
20065	83	36.02	26.05	-44.50	14523	
20065	95	36.76	22.25	-52.10	14523	
20065	125	38.49	17.60	-61.30	14523	

Bloc ID	Age (Ma)	Latitude (°dec)	Longitude (°dec)	Rotation angle (°)	Reference bloc ID	Description
20040	0	0.0	0.0	0.0	14523	Lycian-Tauride ophiolites relative to Moesian platform
20040	5	32.02	31.96	-05.00	14523	
20040	12	32.69	33.45	-07.40	14523	
20040	23	33.35	34.99	-09.60	14523	
20040	30	17.59	42.92	-03.00	14523	
20040	40	48.98	27.76	07.00	14523	
20040	42	49.80	27.94	06.60	14523	
20040	47	55.22	25.10	05.60	14523	
20040	50	57.41	24.71	05.00	14523	
20040	55	62.17	26.29	04.00	14523	
20040	67	49.76	33.66	07.90	14523	
20040	83	-03.38	-53.45	-03.00	14523	
20040	95	38.81	-05.33	-08.40	14523	
20064	0	0.0	0.0	0.0	14523	Central Taurides relative to Moesian platform
20064	5	32.02	31.96	-05.00	14523	
20064	12	32.02	31.96	-06.00	14523	
20064	23	32.02	31.96	-06.00	14523	
20064	30	40.21	30.83	13.00	14523	
20064	40	38.24	31.87	40.00	14523	
20064	42	38.19	32.05	40.00	14523	
20064	47	38.57	32.30	40.00	14523	
20064	50	38.52	32.47	40.00	14523	
20064	67	37.79	33.89	45.70	14523	
20064	83	33.68	39.12	38.40	14523	
20064	95	27.52	44.04	31.70	14523	
20064	125	12.84	50.37	25.30	14523	
20073	0	0.0	0.0	0.0	14523	Southern Ionian margin relative to Moesian platform
20073	20	13.55	145.15	01.30	14523	
20073	29	39.27	08.60	-20.38	14523	
20073	42	36.54	00.51	-19.01	14523	
20073	47	30.39	-10.83	-12.36	14523	
20073	67	36.20	00.33	-24.36	14523	
20073	83	37.56	-00.48	-32.82	14523	
20073	95	39.32	-00.57	-40.79	14523	
20073	125	41.97	-02.34	-50.49	14523	

Bloc ID	Age (Ma)	Latitude (°dec)	Longitude (°dec)	Rotation angle (°)	Reference bloc ID	Description
20074	0	0.0	0.0	0.0	14523	Southwestern Tauride margin relative to Moesian platform
20074	23	0.0	0.0	0.0	14523	
20074	29	41.09	12.44	-11.00	14523	
20074	42	36.98	-04.07	-09.00	14523	
20074	47	11.10	-46.05	-04.00	14523	
20074	67	36.41	-02.73	-15.00	14523	
20074	83	38.42	-02.60	-23.00	14523	
20074	95	40.57	-01.92	-31.00	14523	
20074	125	43.69	-03.38	-41.00	14523	
20079	0	0.0	0.0	0.0	14523	Southeastern Tauride margin relative to Moesian platform
20079	15	35.52	35.35	-43.00	14523	
20079	23	34.83	33.96	-48.00	14523	
20079	30	34.21	32.58	-52.00	14523	
20079	42	34.03	32.58	-58.00	14523	
20079	47	33.88	31.92	-60.00	14523	
20079	67	33.92	30.28	-49.00	14523	
20079	83	34.00	25.54	-57.00	14523	
20079	95	34.58	22.31	-64.00	14523	
20079	125	35.96	18.11	-73.00	14523	

Video C.1: tectonic evolution of the eastern Mediterranean region since the late Cretaceous deduced from the kinematic reconstructions. Each time step corresponds to 5 Myr between 100 and 15 Ma and 2 Myr after 15 Ma.

Le film est disponible en fichier vidéo (.mp4) attaché à ce manuscrit de thèse.

Annexe D

Reconstructions cinématiques et distribution des minéralisations : fichier multimédia

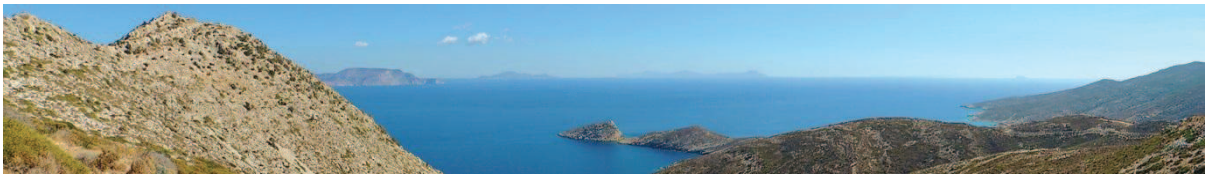

Video D.1: tectonic and metallogenic evolution of the eastern Mediterranean region since the late Cretaceous deduced from the kinematic reconstructions. Each time step corresponds to 5 Myr between 100 and 15 Ma and 2 Myr after 15 Ma.

Le film est disponible en fichier vidéo (.mp4) attaché à ce manuscrit de thèse.

Annexe E

Modélisation numérique : méthode et fichiers multimédias

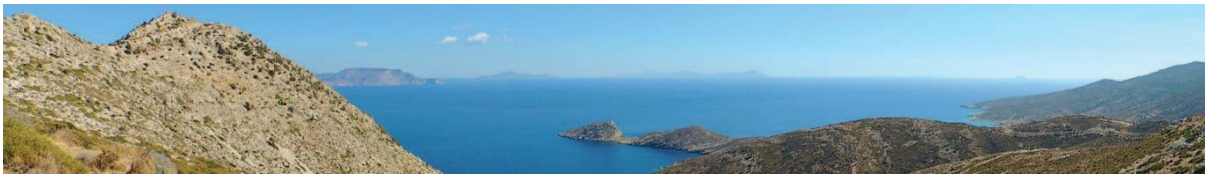

Numerical approach and governing equations

Conservation equations

In our experiments, we model rocks as an incompressible fluid through the 3D mass conservation equation:

$$\nabla \cdot \vec{u} = \frac{\partial v_x}{\partial x} + \frac{\partial v_y}{\partial y} + \frac{\partial v_z}{\partial z} = 0 \quad (1)$$

where v_x, v_y and v_z are the components of the velocity vector $\vec{u}$. The momentum of this incompressible fluid thus occurs as a 3D creeping (or laminar) flow, meaning that the viscous forces are significantly higher than the inertial ones (i.e. Reynolds number << 1). This momentum is then solved using Stokes equation:

$$\begin{aligned} \frac{\partial \sigma_{xx}}{\partial x} + \frac{\partial \sigma_{xy}}{\partial y} + \frac{\partial \sigma_{xz}}{\partial z} &= \frac{\partial p}{\partial x} \\ \frac{\partial \sigma_{yx}}{\partial x} + \frac{\partial \sigma_{yy}}{\partial y} + \frac{\partial \sigma_{yz}}{\partial z} &= \frac{\partial p}{\partial y} - g\,\rho \\ \frac{\partial \sigma_{zx}}{\partial x} + \frac{\partial \sigma_{zy}}{\partial y} + \frac{\partial \sigma_{zz}}{\partial z} &= \frac{\partial p}{\partial z} \end{aligned} \quad (2)$$

where σ_{ij} are the components of the deviatoric stress tensor, p is the pressure, g is the gravitational acceleration and ρ is the density (table 5.1). Finally, heat diffusion in our experiments are solved using the Lagrangian heat conservation equation:

$$\rho\, C_P \frac{\mathrm{D}T}{\mathrm{D}t} = -\frac{\partial q_x}{\partial x} - \frac{\partial q_y}{\partial y} - \frac{\partial q_z}{\partial z} + H_r + H_a + H_s \quad (3)$$

where C_p is the isobaric heat capacity, T is the temperature, t is the time, H_r is the radiogenic heat production, H_a is the adiabatic heat production, H_s is the shear heating and q_x, q_y and q_z are the components of the 3D heat flow solved as:

$$q_x = -k \frac{\partial T}{\partial x}$$
$$q_y = -k \frac{\partial T}{\partial y} \quad (4)$$
$$q_z = -k \frac{\partial T}{\partial z}$$

where k is the thermal conductivity, depending on the temperature and rock composition (table 5.1). Heat advection is then solved based on marker technics [*Gerya and Yuen*, 2007]. Surface processes are implemented using a highly simplified gross-scale erosion-sedimentation law (see details in *Gerya and Yuen* [2007]). Considering these physical laws, the *I3ELVIS* code is able to model multiphase thermo-mechanical flow, approximating ductile-brittle deformation of rocks for long time scales.

Fluid/melt dynamics: dehydration, fluid transport, partial melting and melt extraction computing

In our experiments, each defined lithology can be dry or hydrated, with pressure- and temperature-dependent stable mineralogical water content. Additional porous water content X_{H2O} (wt.%) is prescribed in the sediments and hydrated oceanic crust and decreases linearly from the surface to 75 km depth, also mimicking the effects of low-temperature reactions:

$$X_{H_2O} = X_{H_2O(0)} \left(1 - \frac{\Delta y}{75}\right) \quad (5)$$

where Δy is the depth below the surface and $X_{H2O(0)}$ is the porous water content at the surface [*Johnson and Pruis*, 2003]. During subduction, the local water content of hydrated sediments and oceanic crust can exceed their maximum water content, generating independently moving water markers in the mantle wedge. The 3D velocity of these markers is then solved, according to pressure gradient [*Faccenda et al.*, 2009]:

$$V_{x(water)} = v_x - A \frac{\partial p}{\partial x}$$
$$V_{y(water)} = v_y - A \left(\frac{\partial p}{\partial y} - g\, \rho_{fluid}\right) \quad (6)$$
$$V_{z(water)} = v_z - A \frac{\partial p}{\partial z}$$

where ρ_{fluid} is the fluid density and A is the water percolation constant calculated as:

$$A = \frac{v_{percolation}}{g\,(\rho_{mantle} - \rho_{fluid})} \quad (7)$$

where $v_{percolation}$ is the presumed standard water percolation velocity in the mantle [*Nikolaeva et al.*, 2008] and ρ_{mantle} is the mantle density. Mobile water is then absorbed by the surrounding mantle or crustal rocks by hydration process depending on pressure, temperature and rock composition (see details in [*Zhu et al.*, 2013]).

Partial melting process is also included in our experiments and the volumetric melt fraction is calculated for all rocks, excepted hydrated mantle, as:

$$\begin{aligned} M_0 &= 0 \quad \text{at } T < T_{solidus} \\ M_0 &= \frac{T - T_{solidus}}{T_{liquidus} - T_{solidus}} \quad \text{at } T_{solidus} < T < T_{liquidus} \\ M_0 &= 1 \text{ at } T > T_{solidus} \end{aligned} \quad (8)$$

where M_0 is the volumetric fraction of melt with no previous melt extraction, $T_{solidus}$ and $T_{liquidus}$ are respectively the solidus and liquidus temperatures, depending on the pressure and rock composition (table 5.1). For the hydrated mantle, the degree of partial melting also depends on the water content, according to the parameterization of *Katz et al.* [2003] that is constrained by thermodynamic experimental modeling. Resulting partially molten rocks can then undergo a succession of melt extraction episodes, depending on their melt extraction threshold M_{max} and non-extractable melt fraction M_{min}, both equal to 1 %. Only the exceeding volumetric melt fraction (i.e. > 1 %) is then extracted from partially molten rocks and tracked by partially molten rock markers. For each extraction episode, the melt fraction M_{ext} recorded in the partially molten rock markers is calculated as:

$$M_{ext} = M - M_{min} \quad (9)$$

where M is the volumetric melt fraction in partially molten rock which accounts for previous extraction episodes and is calculated as:

$$M = M_0 - \sum M_{ext} \quad (10)$$

where $\sum M_{ext}$ is the total melt fraction from previous extraction episodes. M varies then dynamically (Eqs. 8 and 10) until remaining solid rock is considered as refractory (i.e. unable to undergo additional partial melting) when $\sum M_{ext} > M_0$. Partially molten rock markers resulting from these extraction episodes are then instantaneously transmitted to the surface as free melt is assumed to propagate upward much faster than rocks deform [*Hawkesworth*, 1997]. At the surface, these markers create volcanic rocks characterized by their volume and composition (i.e. partially molten source).

Rock properties and rheology

The physical properties of rocks used in our experiments are given in table 5.1. Among them, the density of solid rocks ρ_{solid} is calculated as:

$$\rho_{solid} = \rho_{0solid}\left(1 - \alpha\,(T - 298)\right)\left(1 + \beta\,(p - 0.1)\right) \quad (11)$$

where ρ_{0solid} is the standard density of solid rocks and α and β are respectively the thermal expansion and compressibility of rock. For partially molten rocks, their effective density ρ_{eff} is calculated as:

$$\rho_{eff} = \rho_{solid}\left(1 - M + M\,\frac{\rho_{0molten}}{\rho_{0solid}}\right) \quad (12)$$

where $\rho_{0molten}$ is the standard density of molten rock. Non-Newtonian visco-plastic rheologies are used in our experiments, implemented by both ductile and brittle/plastic experimentally constrained laws. Thus, the effective viscosity for dislocation creep, depending on the strain rate, pressure and temperature is calculated as:

$$\eta_{creep} = \dot{\varepsilon}_{II}^{\frac{1-n}{n}}\,A_D^{\frac{-1}{n}}\,exp\left(\frac{E+P\,V}{n\,R\,T}\right) \quad (13)$$

where $\dot{\varepsilon}_{II}$ is the second invariant of the strain rate tensor, n (creep exponent), A_D (pre-exponential factor), E (activation energy) and V (activation volume) are experimentally determined parameters, specific to applied viscous flow law (i.e. wet quartzite, plagioclase (An_{75}), dry olivine and wet olivine flow laws; table 5.1) [*Ranalli*, 1995]. R is the gas constant. This ductile behavior is limited with a

brittle/plastic one, implemented by using the Drucker-Prager criterion σ_{yield} (i.e. plastic strength) [*Ranalli*, 1995] as:

$$\eta_{creep} \leq \frac{\sigma_{yield}}{2\,\dot{\varepsilon}_{II}} \tag{14}$$

where σ_{yield} is calculated as:

$$\sigma_{yield} = c + p\,\sin(\varphi) \tag{15}$$

where c is the cohesion of the rock and φ is the effective internal friction angle, depending on the fluid and melt contents (see details in *Gerya and Meilick* [2011]). The lower and upper cut-off values for the viscosities of all rock compositions in our numerical experiments are 10^{19} and 10^{24} Pa s, respectively.

Video E.1: evolution of the reference model *2c89-60* from a top-down perspective above the collisional domain. Colors represent the different rock types: 1 – sediments; 2 – partially molten sediments; 3/4 – dry upper/lower continental crust; 5/6 – hydrated/partially molten continental crust; 7 – dry oceanic crust; 8/9 – hydrated/partially molten oceanic crust; 10 – dry lithospheric mantle; 11 – dry asthenosphere; 12/13 – hydrated/serpentinized mantle; 14 – partially molten mantle. Asthenosphere and other phases are cut off for clarity.

Le film est disponible en fichier vidéo (.mp4) attaché à ce manuscrit de thèse.

Video E.2: evolution of the reference model *2c89-60* from a bottom-up perspective. For detailed legend see video E.1.

Le film est disponible en fichier vidéo (.mp4) attaché à ce manuscrit de thèse.

Video E.3: evolution of the model *1c113-70* from a top-down perspective above the collisional domain. For detailed legend see video E.1.

Le film est disponible en fichier vidéo (.mp4) attaché à ce manuscrit de thèse.

Video E.4: evolution of the model *1c113-70* from a bottom-up perspective. For detailed legend see video E.1.

Le film est disponible en fichier vidéo (.mp4) attaché à ce manuscrit de thèse.

Armel MENANT

Du manteau à la croûte, dynamique de subduction et systèmes minéralisés en Méditerranée orientale

Les zones de subduction présentent un intérêt majeur en termes de ressources minérales, notamment à cuivre et or. De nombreuses études se sont focalisées sur les mécanismes physico-chimiques de formation de ces minéralisations, mais très peu se sont intéressées aux processus géodynamiques qui contrôlent ces mécanismes. Dans cette étude, j'identifie les processus mantelliques et crustaux, liés à la dynamique tridimensionnelle (3D) de la subduction, qui favorisent la genèse de ces concentrations métalliques. La zone de subduction est-Méditerranéenne présente une évolution tectonique et magmatique complexe, avec de nombreuses données métallogéniques disponibles, ce qui en fait une zone d'étude privilégiée afin d'étudier ces interactions entre subduction et minéralisations. Ce travail a consisté à (1) réaliser un nouveau modèle de reconstructions cinématiques de la région, (2) caractériser la distribution spatiale et temporelle des occurrences magmatiques et minéralisées à partir de ce modèle, (3) mettre en évidence, via une étude de terrain, le contrôle structural de ces minéralisations et (4) apporter des contraintes physiques aux modèles conceptuels alors proposés, à l'aide d'une étude de modélisation numérique thermo-mécanique 3D.
Deux provinces métallogéniques ont ainsi été mises en évidence : (1) au Crétacé supérieur, une province riche en cuivre qui s'est développée dans un environnement d'arc et (2) à l'Oligocène-Miocène, une province riche en plomb-zinc puis en or, qui s'est mise en place dans un contexte d'arrière-arc. Ces épisodes fertiles sont contrôlés par le retrait de la zone de subduction et les flux asthénosphériques associés qui permettent l'instauration d'un régime tectonique extensif (ou transtensif) dans la lithosphère, favorisant la genèse de ces systèmes minéralisés. Leur contenu métallique ainsi que leur typologie est alors fonction (1) de l'intensité avec laquelle ces processus influent sur la cinématique de subduction et (2) de l'histoire géodynamique antérieure de cette zone de subduction.

Mots clés : dynamique de subduction 3D, Méditerranée orientale, cuivre-or, retrait du panneau plongeant, flux asthénosphériques

From mantle to crust, subduction dynamics and mineralization in eastern Mediterranean

Subduction zones display a major economic interest, in terms of mineral resources, with mainly copper and gold deposits. While many studies focus on ore-forming physico-chemical mechanisms, the control of geodynamic processes on such deposits remains poorly investigated. In this study, I track tridimensional (3D) subduction-related mantle and crustal processes that promote ore genesis. The eastern Mediterranean subduction zone is a relevant study area to explore subduction-mineralization interactions, because of its complex tectonic and magmatic evolution and the large number of available metallogenic data. This work consisted in (1) performing a new kinematic reconstruction model of this region, (2) using this model, characterizing the spatial and temporal distribution of magmatic and ore occurrences, (3) evidencing, on the field, the relations between mineralization and large-scale tectonic structures and (4) providing physical constrains to proposed conceptual models, using 3D thermo-mechanical numerical modeling.
Two main metallogenic provinces are evidenced: a late Cretaceous copper-rich and an Oligocene-Miocene lead-zinc- then gold-rich provinces emplaced in an arc and back-arc context, respectively. These metallogenic periods are controlled by the subduction zone retreat and associated asthenospheric flow that results in an extensional (or transtensional) tectonic regime in the overriding lithosphere, promoting ore genesis. Their metal content, as well as their typology then depend on (1) how much these processes affect the subduction kinematics and (2) the past geodynamic evolution of this subduction zone.

Keywords: 3D subduction dynamics, eastern Mediterranean, copper-gold, slab roll-back, asthenospheric flow

Institut des Sciences de la Terre d'Orléans
1A, rue de la Férollerie - 45071 Orléans Cedex 2

Bureau de Recherches Géologiques et Minières
3, avenue Claude Guillemin - 45060 Orléans Cedex 2